International Journal of Fracture Fatigue & Wear

Volume 3, 2015

ISSN 2294-7868

Editor: Professor Magd Abdel Wahab

International Journal of Fracture Fatigue and Wear:

Conference Series proceedings

Volume 3, 2015

Proceedings of 4th International Conference on Fracture Fatigue and Wear, FFW 2015, Ghent University, Belgium, 27-28 August 2015

Published by
Laboratory Soete – Ghent University
Technologiepark Zwijnaarde 903
B-9052 Zwijnaarde, Belgium
http://www.soetelaboratory.ugent.be/
Edited by: Professor Magd Abdel Wahab
ISSN: 2294-7868

4th International Conference on Fracture Fatigue and Wear, FFW 2015, Ghent University, Belgium, 27-28 August 2015

Chairman

Professor Magd Abdel Wahab
Laboratory Soete, Ghent University
Belgium

Co-chairman

Professor Nao-Aki Noda
Kyushu Institute of Technology
Japan

International Scientific Committee

Editorial

The third volume of the International Journal of Fracture Fatigue and Wear contains the proceedings of the fourth International Conference of Fracture Fatigue and Wear (FFW) held in Ghent University, Belgium, 27-28 August 2015.

The organising committee is grateful to Professor Stéphane P.A. Bordas, Faculté des Sciences, de la Technologie et de la Communication, University of Luxembourg, Luxembourg, for agreeing to deliver the keynote lecture, entitled ‘Multiscale isogeometric fracture simulation’, at the opening of the conference.

The sponsorship of Soete laboratory, Ghent University (Belgium), Kyushu Institute of Technology (Japan) and NANOVEA Inc. (Irvine, CA, USA) is highly appreciated.

Most of the papers published in this volume have been sent to reviewers, who are members of Scientific Committee of FFW 2015, to judge their scientific merits. Based on the recommendation of reviewers and the scientific quality of the research work, the papers were accepted for publication in the conference proceedings and for presentation at the conference venue. The organizing committee would like to thank all members of Scientific Committee for their valuable contribution in evaluating the papers.

The efforts of the local organizers of FFW 2015 at Labo Soete Ghent University, Belgium, the team of Professor Abdel Wahab, are highly acknowledged. Special thanks goes to the post-graduate students Hanan Alali, Yue Tongyan, Phuc Phung Van, Tran Vinh Loc, Kyvia Pereira and Junyan Ni.

Finally, the editor would like to thank to all authors, who have contributed to this volume and presented their research work at FFW 2015.

The Editor
Professor Magd Abdel Wahab

Table of Contents

Proceedings of the 4th International Conference on
Fracture Fatigue and Wear, pp. 1-6, 2015

NATURALLY INITIATED SMALL CRACK PROPAGATION BEHAVIORS IN NI-BASE SUPERALLOYS UNDER THERMO-MECHANICAL LOADING

Y. Yamazaki, Y. Hara and T. Maejima

Niigata Institute of Technology, Japan

Abstract: Ni-base superalloys have wide applications in the manufacturing of blades and vane that are used in gas turbine systems for generating electricity. It is of critical need to gain a fundamental understanding of the propagation characteristics of fatigue cracks, especially the early growth of naturally initiated small cracks, under thermo-mechanical fatigue (TMF) conditions. To this end, this study investigates the propagation behaviours of naturally initiated small crack in a polycrystalline Ni-base superalloy under in-phase (IP) and out-of-phase (OP) types of TMF conditions as well as the isothermal low-cycle fatigue (LCF) condition. The crack initiation and propagation mechanisms were discussed base on the crystallographic investigations performed using electron backscatter diffraction (EBSD) analysis. Experimental results revealed that the initiation and propagation morphologies of the naturally initiated crack were significantly affected by the thermo-mechanical loading condition. Under the LCF and IP conditions, the small cracks were initiated and propagated at the grain boundaries perpendicular to the loading axis. On the other hand, under the OP condition, the small cracks were initiated and propagated with the transgranular modes. When the crack growth rates of naturally initiated small crack are correlated with fatigue J-integral, the crack growth rates under the TMF condition were almost similar to those under LCF conditions.

Keywords: Thermo-mechanical fatigue; Small crack; Crack propagation; Polycrystalline Ni-base superalloy

1 INTRODUCTION

Ni-base superalloys are considered as highly reliable alloys in the manufacturing of blades and vanes that are used in gas turbine systems for generating electricity [1-4]. Typically, these alloys are subjected to rather complex stress and temperature cycles due to the temperature gradients that occur during start-up and shut-down or from temperature gradients that occur within the components during steady-state operation. The accumulation of such stress and temperature cycles leads to the possibility of failure caused by thermo-mechanical fatigue (TMF). Therefore, a comprehensive understanding of the crack propagation characteristics under TMF conditions is essential [1, 5]. In particular, the initial growth of naturally initiated small cracks of the order of sub-millimetres can provide some essential information on the life and the remaining life prediction to these failures [6-8]. From the engineering and academic interest perspective, the importance of studying small cracks growth behaviour can be sought to the following reasons: (i) most part of fatigue life under TMF and LCF conditions is generally dominated by the small crack growth process; (ii) given the fact that the small cracks grow with a propagation rate that is significantly higher than that of accompanying physically long cracks (i.e., the difference in propagation rates between small and long cracks), the life prediction based on the traditional long crack results involves strong potential for non-conservative estimation; and (iii) the growth of small cracks is notably affected by microstructures, such as grain boundary and strengthening precipitates, and also by the environment. Nevertheless, most of the earlier studies have dealt with the propagation of physically long cracks, and there is little information on the small crack growth process.

Therefore, this study investigates the propagation behaviours of naturally initiated small cracks in a polycrystalline Ni-base superalloy, IN738LC, under thermo-mechanical fatigue loading. The crack initiation and propagation mechanisms are discussed based on the crystallographic investigations performed using electron backscatter diffraction (EBSD) analysis.

2 EXPERIMENTAL PROCEDURES

The material tested in this study is a conventionally cast polycrystalline Ni-Base superalloy, IN738LC. The chemical composition of IN738LC and the heat-treatment conditions are represented in Table 1. The microstructure of IN738LC and the inverse pole figure (IPF) map obtained using EBSD are shown in Figs. 1(a) and (b), respectively. As is seen, the material comprises the γ matrix strengthened by the randomly distributed γ' precipitates of size ranging from 0.2 μm to 1.5 μm (approximately 40%–45% by volume). Subsequently, solid cylindrical smooth specimen of gauge section diameter 5 mm was machined from the round bar stock of this material. Before the fatigue test, the surface of the specimen was mechanically polished to a mirror surface using 1-μm alumina powders.

Isothermal low-cycle fatigue (LCF) and thermo-mechanical fatigue (TMF) tests were conducted under the test conditions summarized in Table 2. All the tests were performed under a strain-controlled condition, utilizing a fatigue testing machine equipped with an induction heating system. During the TMF tests, mechanical strain was applied such that the thermal free expansion strain is superimposed in a synchronized manner with thermal cycling under the following two phase angle conditions: in-phase (IP) condition and out-of-phase (OP) condition, wherein the phase differences between strain and temperature cycling are 0° and 180°, respectively. In this study, the TMF tests were conducted at temperatures ranging from 400 to 880 °C, while the test temperature of LCF was 880 °C. The strain, temperature, and time correlations of each test conditions are shown in Fig. 2.

To investigate the propagation behaviour of naturally initiated surface small crack, the smooth specimen surface was periodically replicated by the replica method after cooling the specimen to room temperature.

Table 1 Chemical composition and heat treatment conditions of the tested material

(a) Chemical composition (mass %)

C	Si	Cr	Co	Mo	W	Ta	Al	Ni
0.09	0.04	16.0	8.14	1.65	2.58	1.72	3.57	Bal.

(b) Heat treatment conditions

HIP (1200℃ × 111.4 MPA × 4 h in Ar) → Solution heat treatment (1120 ℃ × 2 h in Ar) → aging treatment (1080℃ × 4 h in Ar) → aging treatment (845 ℃ ×24 h)

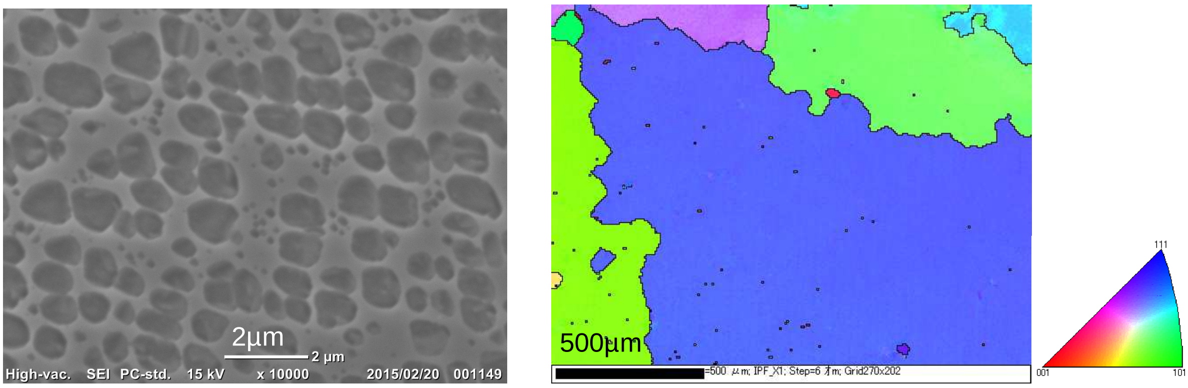

(a) SEM image (b) IPF map by EBSD

Fig. 1 Microstructure of IN738LC used in this study

Table 2 TMF and LCF test conditions

	TMF		LCF
	In-Phase (IP)	Out-of-phase (OP)	
Temp.[°C]	400–800		880
Strain range [%]	0.4		
Strain rate [%/s]	0.002		
Strain ratio	−1		
Phase difference [°]	0	180	-

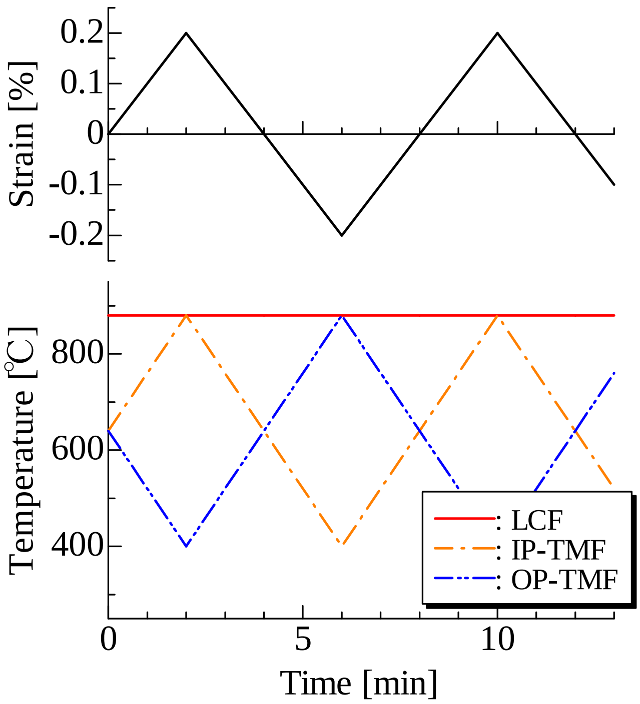

Fig. 2 Strain, temperature, and time correlations of LCF, IP-TMF, and OP-TMF tests

3 RESULTS AND DISCUSSIONS

Figure 3 shows the typical hysteresis loops during LCF and IP- and OP-TMF tests. No inelastic deformation behaviour could be observed in the stress–strain response under the IP- and OP-TMF loading conditions. In addition, the stress–strain curves of the IP- and OP-TMF loadings are asymmetric due to the temperature dependence of the deformation resistance of IN738LC. On the other hand, the stress–strain response under the LCF condition showed a hysteresis loop with in-elastic deformation.

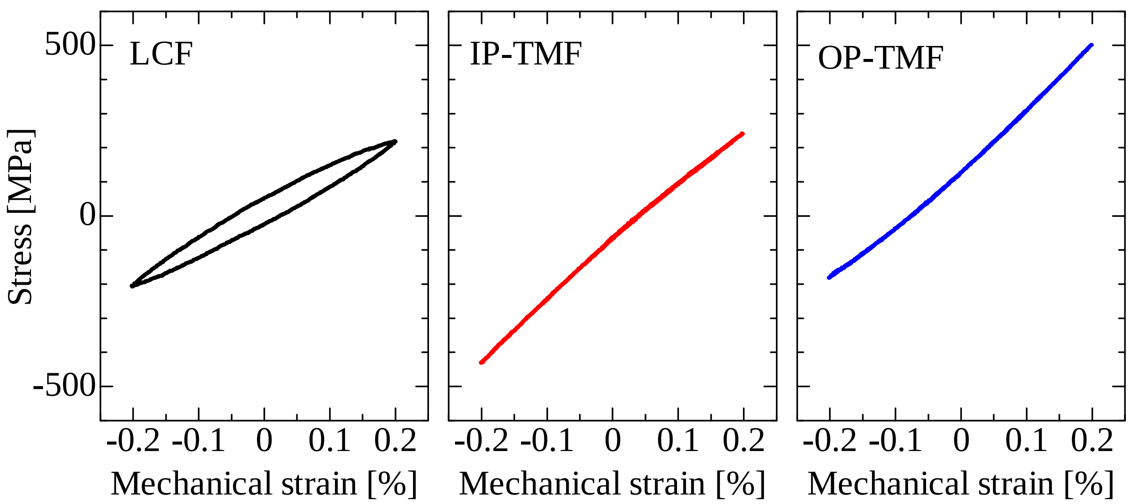

Fig. 3 Typical stress–strain responses during fatigue test: at $N/N_f = 1/2$

Typical examples of small cracks initiated under LCF and TMF loading are shown in Fig. 4. Thus far, they were observed from the specimen surface. Therefore, under the LCF and IP-TMF loadings, the cracks appear to be initiated and propagated at the grain boundary perpendicular to the loading axis, which might be a relatively week region at elevated temperature (Figs. 4(a) and (b)). On the other hand, under OP-TMF loading, of which the tensile loading is applied at lower temperature, the cracks were initiated and propagated via the transgranular mode, as shown in Fig. 4(c). Accordingly, it can be deduced that the initiation and propagation morphologies of naturally initiated small crack are sensitive to the microstructure and test temperature.

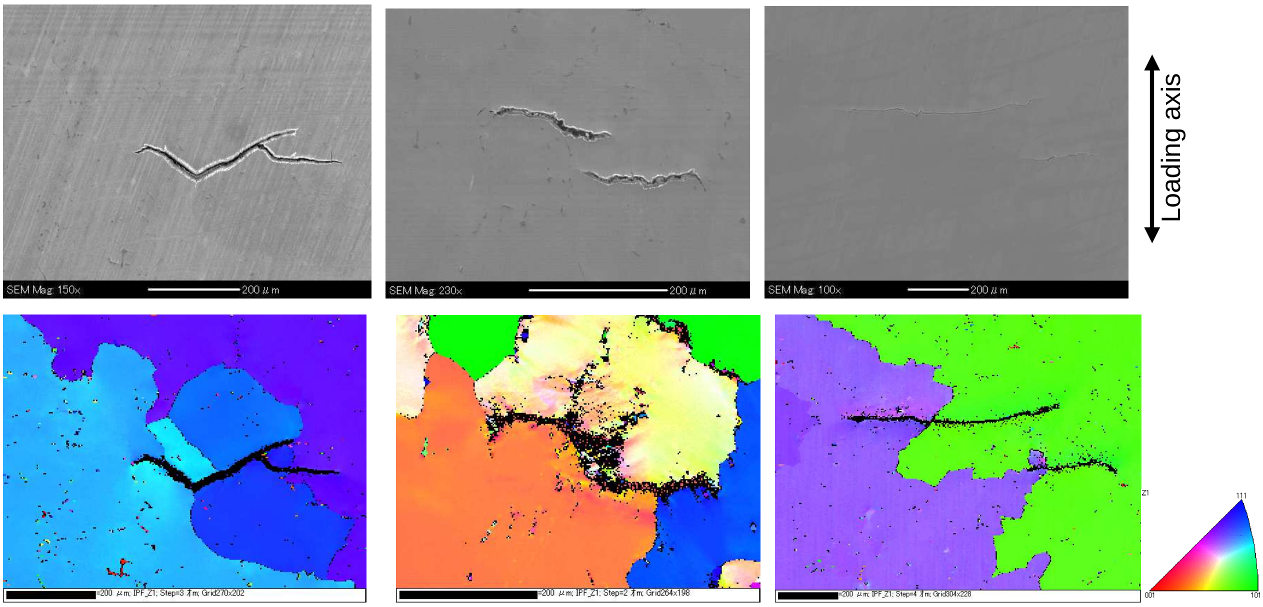

(a) LCF condition (Δε = 0.4%) (b) IP condition (Δε = 0.5%) (c) OP condition (Δε = 0.4%)

Fig. 4 SEM images and Inverse pole figure maps of small cracks initiated on specimen surface

Figure 5 shows the typical small crack growth behaviors. Some small cracks, less than ten cracks, were generated on the surface of a representative smooth specimen under each test condition. The propagation behavior of the small cracks was measured periodically by means of the replica method. The data points in Fig. 5 express the propagation behaviors of multiple small cracks initiated on a representative smooth specimen. Comparing the fatigue lives of IN738LC at the same strain range level (Δε = 0.4%), the fatigue life under the IP-TMF condition was found to be longer than that under the LCF condition. The fatigue lives of IN738LC can be considered to depend on the stress range and mean stress under the TMF condition because they were higher under the OP-TMF. However, under the LCF condition, the stress range was small with a mean stress level of almost zero, even though the fatigue life was shorter under such condition. Besides, the creep damage might also affect the fatigue life under the LCF condition.

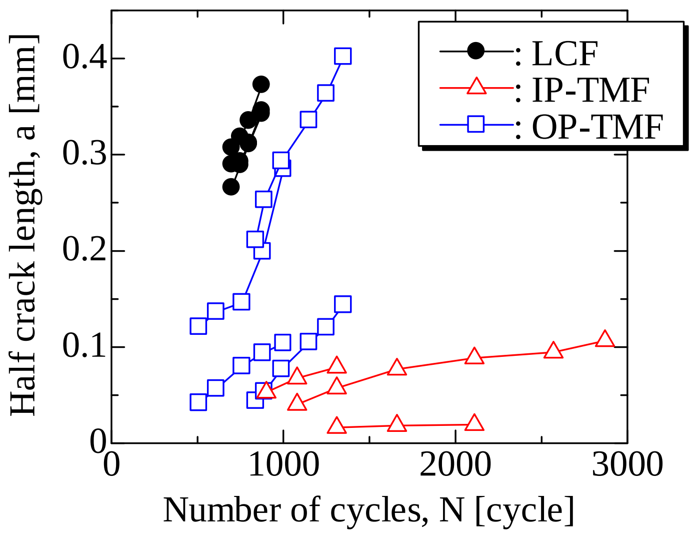

Fig. 5 Propagation behaviors of naturally initiated small cracks; Δε = 0.4%

The data points and the lines in Fig. 6 show the crack growth rates measured for multiple small cracks in a smooth specimen, as a function of the fatigue J integral range, ΔJ_f, wherein ΔJ_f for small cracks was evaluated using the following equation [9, 10].

$$\Delta J_f = F^2\left(\pi\frac{\Delta\sigma^2}{E} + f(n_f)\Delta\sigma\Delta\varepsilon_p\right)a\ , \tag{1}$$

where $\Delta\sigma$ is the stress range, $\Delta\varepsilon_p$ is the plastic strain range, E is the elastic modulus at 880 °C for LCF and at the middle temperature of TMF test (640 °C) for TMF, and n_f is the cyclic hardening exponent. F and $f(n_f)$ are

$$F = 1.12/(1+1.47*\lambda^{1.65})\sqrt{\lambda} \tag{2}$$

and

$$f(n_f) = 3.85(1-n_f)/\sqrt{n_f} + \pi n_f\ , \tag{3}$$

where, λ is the ratio of the crack depth to the surface crack half-length obtained from the fracture surface. For comparison, the physically long crack propagation curves under LCF conditions [11] are also represented in Fig. 6. The small crack propagation rates are considerably higher than those of the long crack. Given the fact that the information obtained from the physically long crack growth rate provides an unrealistic evaluation on the reliability of the actual components, the experimental results obtained in this study illustrate the importance of the investigation of small crack growth behaviour.

As shown in Fig. 6, the rates of small cracks under IP-TMF and OP-TMF loading are almost comparable to those under LCF loading, i.e., the small crack propagation rates can be expressed with a unique curve under LCF, IP-TMF, and OP-TMF conditions, when the propagation rates are correlated with the fatigue J integral range.

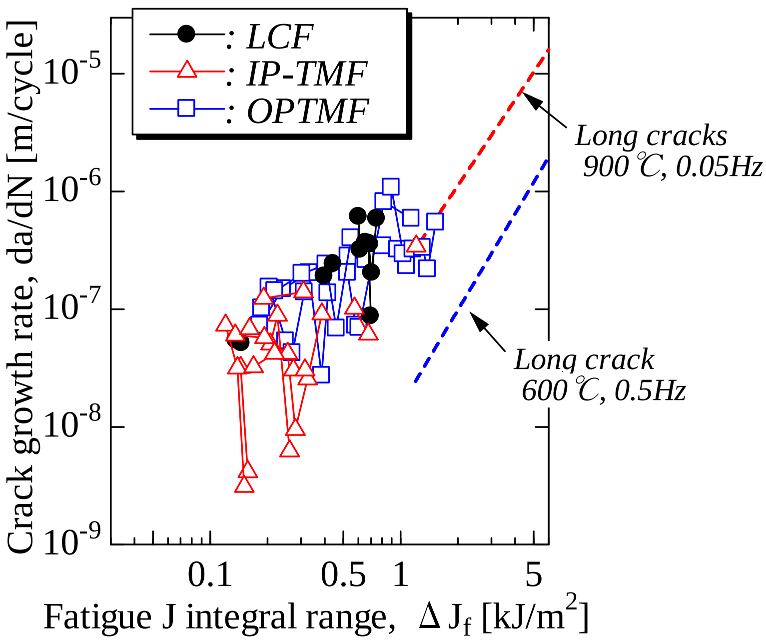

Fig. 6 small crack propagation rates correlated with the fatigue J integral range

4 SUMMARY

In summary, this paper reports the crack propagation behaviour of naturally initiated small cracks in IN738LC under thermo-mechanical fatigue loading. The experimental results indicated beyond ambiguity the importance of the investigation of small crack propagation behaviours. The fatigue lives of IN738LC were varied under different thermo-mechanical fatigue loading conditions. Results suggest that the fatigue life by the creep damage under the LCF condition was relatively shorter. However, when the propagation rates are correlated with the fatigue J integral range, the small crack propagation rates can be expressed with a unique curve, despite the differences in the thermo-mechanical fatigue loading conditions.

5 REFERENCES

[1] M. Okazaki, K. Take, K. Kakehi, M. Sakane, Y. Yamazaki, H. Kaneko, K. Fujiyama, K. Namba, T. Yokomaku, I. Nonaka, M. Arai, Y. Sugita, S. Sakurai, and Y. Harada, Collaborative Research on Thermo-Mechanical and Isothermal Low-Cycle Fatigue Strength of Ni- Base Superalloys and Protective Coatings at Elevated Temperatures in The Society of Materials Science, Japan (JSMS), ASTM STP 1428 (2003) 180–194.

[2] H. L. Bernstein, T. S. Grant, R. C. McClung, and J. M. Allen, Prediction of thermal -mechanical fatigue life for gas turbine blades in electric power generation, ASTM STP 1186 (1993) 212–238,

[3] B.A. Leach and S.D. Antolovich, Fatigue crack propagation behavior of a single crystalline superalloy, Metallurgical and Materials Transactions A, 21 (1990) 2169–2177.

[4] W. Hoffelner, Effects of environment on crack growth behavior of superalloys under various loading conditions, Materials Science and Technology, 3 (1987) 765–771.

[5] M.G. Hocking, V. Vasantathan, and P.S. Sidky, Metallic and ceramic coatings: Longsman Scientific & Technical Publishers, London (1989)

[6] M. Okazaki, H. Yamada, and S. Nohmi, Temperature Dependence of the Intrinsic Small Fatigue Crack Growth Behavior in Ni-Base Superalloys Base on Measurement of Crack Closure, Metall. & Mat. Trans., 26, (1996) 1021–1033.

[7] Kitagawa H and Takahashi S. Applicability of fracture mechanics to very small cracks. In: ASM Proceedings of 2nd International Conference on Mechanical Behavior of Materials (1976) 627–631.

[8] R.Ohtani, T.Kitamura, N.Tada, and S.Iio, Transition from Small Crack to Large Crack on Creep-Fatigue Crack Propagation. Proc. 3rd Int. Conf. Low Cycle Fatigue and ElastoPlastic Behavior of Materials (1992) 533–538.

[9] N. E. Dowling, Cyclic stress-strain and plastic deformation aspects of fatigue crack growth. ASTM STP 637 (1977) 97–121.

[10] C. F. Shih and J. W. Hutchinson, Fully Plastic Solutions and Large Scale Yielding Estimates for Plane Stress Crack Problems, Journal of Engineering Materials and Technology, 98 (1976), 289–295.

[11] H. Kagawa and M. Kurita, Fatigue Crack Propagation Behavior of IN738LC at Elevated Temperature, Proc. Mechanical Engineering Congress, 2012 (2012) 237–238.

Proceedings of the 4th International Conference on
Fracture Fatigue and Wear, pp. 7-12, 2015

BIAXIAL FATIGUE OF CLIP CONNECTORS FOR OFFSHORE DRILLING RISERS UNDER A HIGH MEAN STRESS

V. Gaur[1,2], V. Doquet[1], E. Roguet[2] and E. Persent[2]

[1] LMS, Ecole Polytechnique, UMR CNRS 7649, Palaiseau, France
[2] IFP Energies Nouvelles, 1 et 4 avenue de Bois-Préau, 92852 Rueil-Malmaison, France

Abstract: The riser connectors used in offshore oil drilling undergo cyclic loading with a high mean stress. FE computations revealed in-phase biaxial tension in the critical area, while most fatigue criteria were designed for tension-shear loadings. Both the mean stress effect and the positive biaxiality effect thus need to be addressed. Stress-controlled fatigue tests were run at different R ratios ($\sigma_{min}/\sigma_{max}$). The fatigue lives decreased with increasing R, following Gerber's parabola for the endurance limit and Walker's model for finite lives. Surface crack initiation was observed for R = -1 and -0.5, while positive R ratios triggered internal crack initiation from pores or chemically inhomogeneous areas. The reason for this change in damage mechanism as well as the kinetics of crack nucleation and growth are discussed.

Keywords: Mean stress; internal crack; fish-eye; steel; biaxial fatigue

1. INTRODUCTION: INDUSTRIAL CONTEXT

In order to increase oil production, efforts have to be made for deeper offshore drilling in harsher environments. The riser steel tubes can be conveniently and quickly connected/disconnected using the "clip connector" designed at IFPEN. The assembly experiences external pressure from sea water, internal pressure of the fluid flowing through it, the mass of the riser assembly, buoyancy force and above all, sea waves which induce cyclic bending and potentially, fatigue damage. Two situations are encountered: the "connected mode" with a high mean stress (R = 0.7) and low amplitude constitutes more than 90% of the service life, while the "disconnected mode" with a lower mean stress (R = 0.2) but higher amplitude constitutes less than 10%. A 3D finite element model of 1/4th of a clip connector assembly has been developed in ABAQUS (fig.1a) using quadratic tetrahedral elements and appropriate refinement near the contact areas between the male and female parts. 50 cycles representative of the connected /disconnected modes were simulated, using previously identified elastic-plastic constitutive equations including isotropic softening and non-linear kinematic hardening. A high stress gradient in the region below the lugs and along the thickness is found (fig. 1b) as well as in-phase biaxial tension with different mean stresses in the critical regions, with a biaxiality ratio between 0.2 and 0.3 (fig. 2). Both the mean stress effect and the biaxiality effect thus need to be addressed for a proper design. However, most of the multiaxial fatigue criteria are based on tension-torsion fatigue data and many of those, which include a hydrostatic stress term, do not discriminate the influence of biaxial tension from that of a mean stress [1, 2]. This motivates the present study. The mean stress effect and the positive biaxiality effect are investigated separately, through uniaxial tests at various R ratios for the former and combined tension and internal pressure tests on tubular specimens for the latter.

2. EXPERIMENTAL STUDY

2.1. EXPERIMENTAL PROCEDURES

The clip connectors are made of F22 steel with the composition shown in table 1 and the basic mechanical properties shown in table 2. Its micro-structure is that of a non-textured aged tempered martensite, with a few micron-wide equiaxed grains containing remnants of laths. Aluminum-magnesium-calcium oxide and

Table 1 Measured composition of F22 steel (Wt. %)

C	Cr	Mo	O	Mn	Si	Ni	Cu
3.5	2.5	1.1	1.4	0.6	0.2	0.1	0.1

Table 2 Basic Mechanical properties of F22 steel

Proportional limit	0.2% Yield stress	Ultimate Stress	Vickers Hardness
600 MPa	694 MPa	780 MPa	550

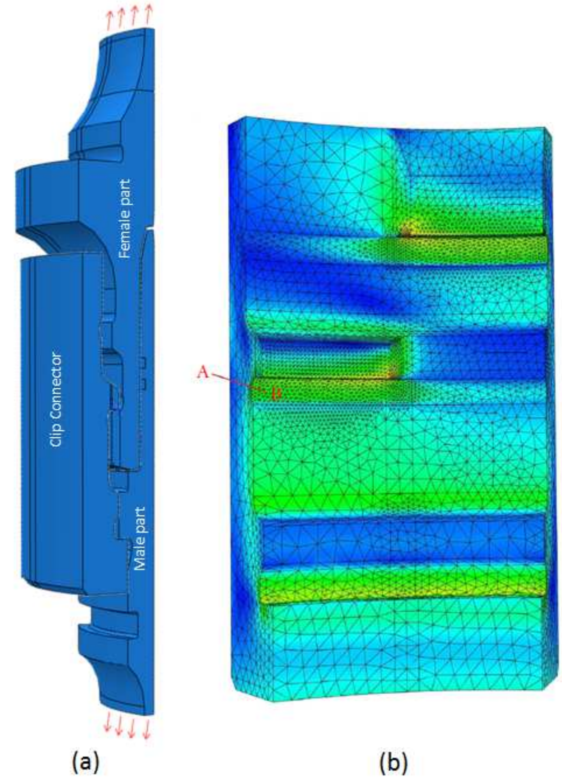

Fig. 1 a) Clip riser F.E. model b) Stress contours at peak load in the connected mode, after 50 cycles.

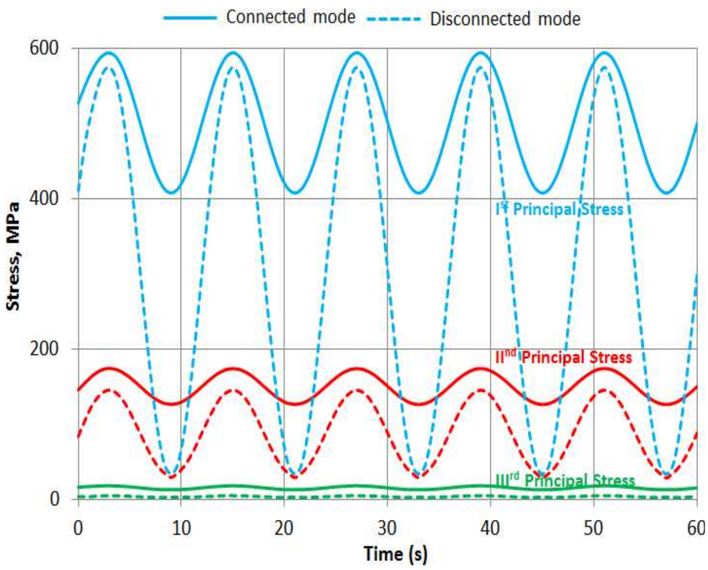

Fig. 2 Computed evolutions of three principal stresses in the critical area under connected/disconnected modes.

manganese sulfide inclusions with an average size of 5 µm are present, but do not seem harmful in fatigue, contrary to some less frequent but larger pores and inhomogeneous zones, as discussed below.

Cylindrical specimens of diameter 8 mm or 7 mm with a surface roughness R_a<0.4 were cut from an actual clip connector and used for stress-controlled push-pull tests at different R ratios (-1, -0.5, 0 and 0.25) in air at 10 Hz. The tests were stopped at 3.10^6, cycles and the corresponding stress amplitude was considered as the endurance limit for that R ratio.

2.2. EXPERIMENTAL RESULTS: FATIGUE LIVES AND DAMAGE MECHANISMS

Both the endurance limit and the slope of the S-N curves drop with increasing R ratio (fig. 3). A Goodman plot (fig. 4) shows that Gerber's parabola provides the most accurate prediction of the endurance limit at different R ratios, while both Goodman's and modified Goodman's lines are too conservative. For finite life, Walker's equation [3] provides reasonable predictions, within a factor of 3 from measured lives (fig. 5).

$$\sigma_a \left(\frac{2}{1-R}\right)^{1-\gamma} = A\, N_f^b \tag{1}$$

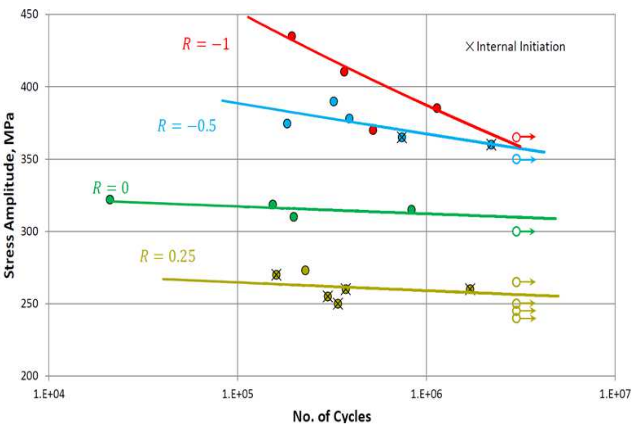

Fig. 3 S-N curves at different R ratios.

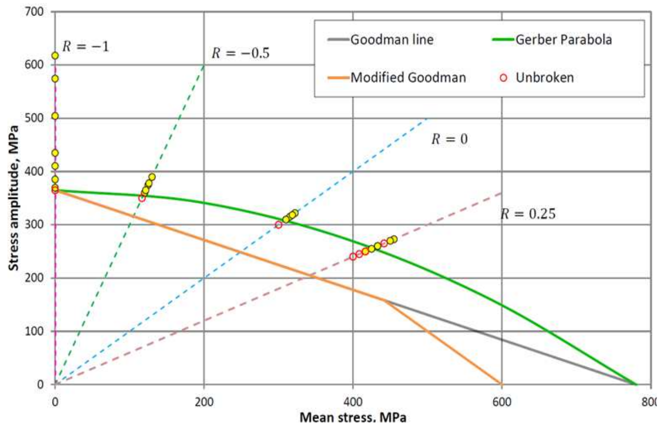

Fig. 4 Goodman Diagram

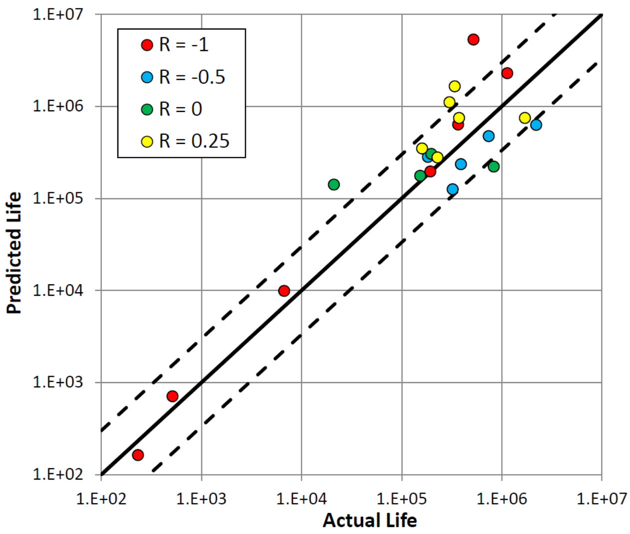

Fig. 5 Measured and predicted lives, using Walker's criterion.

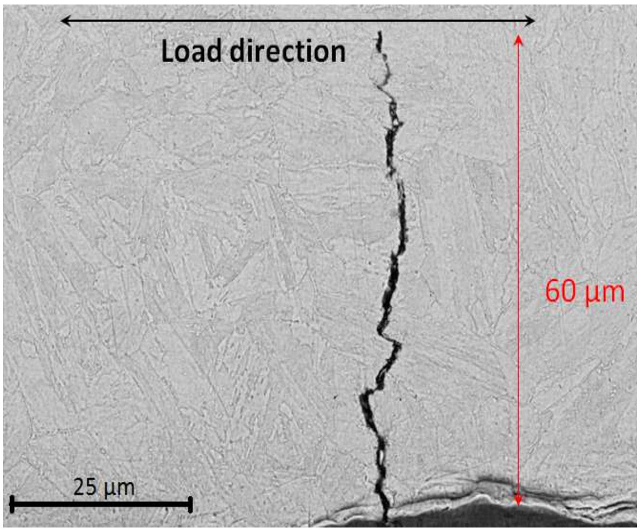

Fig. 6 Surface crack initiation for R = -1

All the fatigue cracks at R=-1 or -0.5 and most of the cracks at R=0 initiated from the surface. SEM observations of longitudinal sections cut from specimens broken after a few thousands cycles under such R ratios, show secondary surface micro-cracks which follow a zig-zag paths with frequent deflections along grain or martensite laths boundaries (fig. 6).

Internal crack initiation from 40-300 µm large pores or inhomogeneities (see table 3) became more and more frequent as the R ratio increased, giving rise to so called "fish eye" patterns (fig. 7a). Topographic analyses of the fracture surfaces around the defects revealed the presence of tilted facets, inclined by 45° relative to the loading axis (fig. 7b), suggesting shear-driven crack initiation of Stage I type. As the crack grows, it becomes normal to the loading axis as if a stage I to stage II transition occured.

The fish eyes look bright under the optical microscope because of the absence of oxide layer on the crack face, as long as the internal crack does not emerge at the free surface and thus propagates without any contact with moist air, as in a vacuum. SEM observations of the border of a fish-eye (fig. 7c) reveal striking differences in the aspects of both sides. The part grown in vacuum is much smoother. It is also featureless, with very few traces of the underlying microstructure and without any striations, in accordance with the literature on fatigue crack growth in vacuum [4]. But as soon as the crack propagates in air, well marked crystallographic patterns evoking laths or grain boundaries, as well as fatigue striations can be observed.

The defects giving rise to internal crack initiation are sometimes pores and sometimes debonded clusters of chemically inhomogeneous material. SEM observations of mating fracture surfaces as shown in fig. 8a-b reveal a crater on one side and a cluster of non-homogeneous material on the other side. Chemical analysis based on Energy Dispersive Spectrometry shows locally much higher oxygen and carbon contents (fig. 8c). This matter has thus different mechanical properties than the matrix and is prone to debonding.

3. DISCUSSION

Internal crack initiation with a fish eye pattern is generally observed in the very high-cycle fatigue (VHCF) regime (10^7-10^{10} cycles). In this regime, a rough Optically Dark Area (ODA) also called Fine Granular Area (FGA), whose formation mechanism is much debated [5-7], surrounds the defect responsible for crack initiation. In the present study internal crack initiation occurred for relatively low fatigue lives (2.10^5 to 3.10^6 cycles) when the R ratio was zero or higher, and no ODA or FGA was observed. While the former result is a bit surprising, the latter is not, since the formation of an ODA/FGA is known to require at least 10^7 fatigue cycles, to be favoured by fully reversed loading and to disappear for positive R ratios, which is consistent with the formation mechanism proposed by Nakamura et al. [5].

All the defects responsible for internal crack initiation were found in the sub-surface area (between 100 µm and 600 µm from the surface) and not randomly distributed on the fracture surface, as the tensile fatigue tests are supposed to produce a uniform stress provided any misalignment, which can induced bending, is avoided, which was checked. This suggests that residual stresses left by the machining process were present in the specimens. Significant plastic flow during the first half cycle at high R ratio might redistribute these residual stresses and thus modify the competition between surface crack initiation and sub-surface

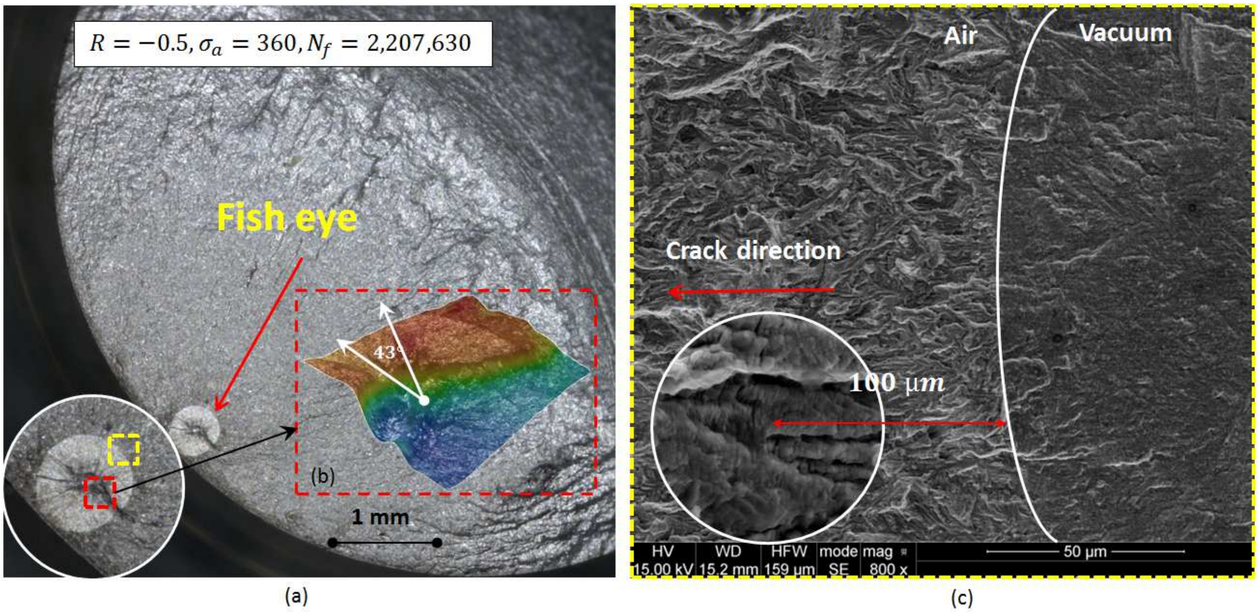

Fig. 7 (a) Fracture surface under optical microscope with "Fish eye" (b) 3D topographic map around the pore (c) SEM observation revealing the difference in aspects of roughness and striations between crack growth in air and vacuum.

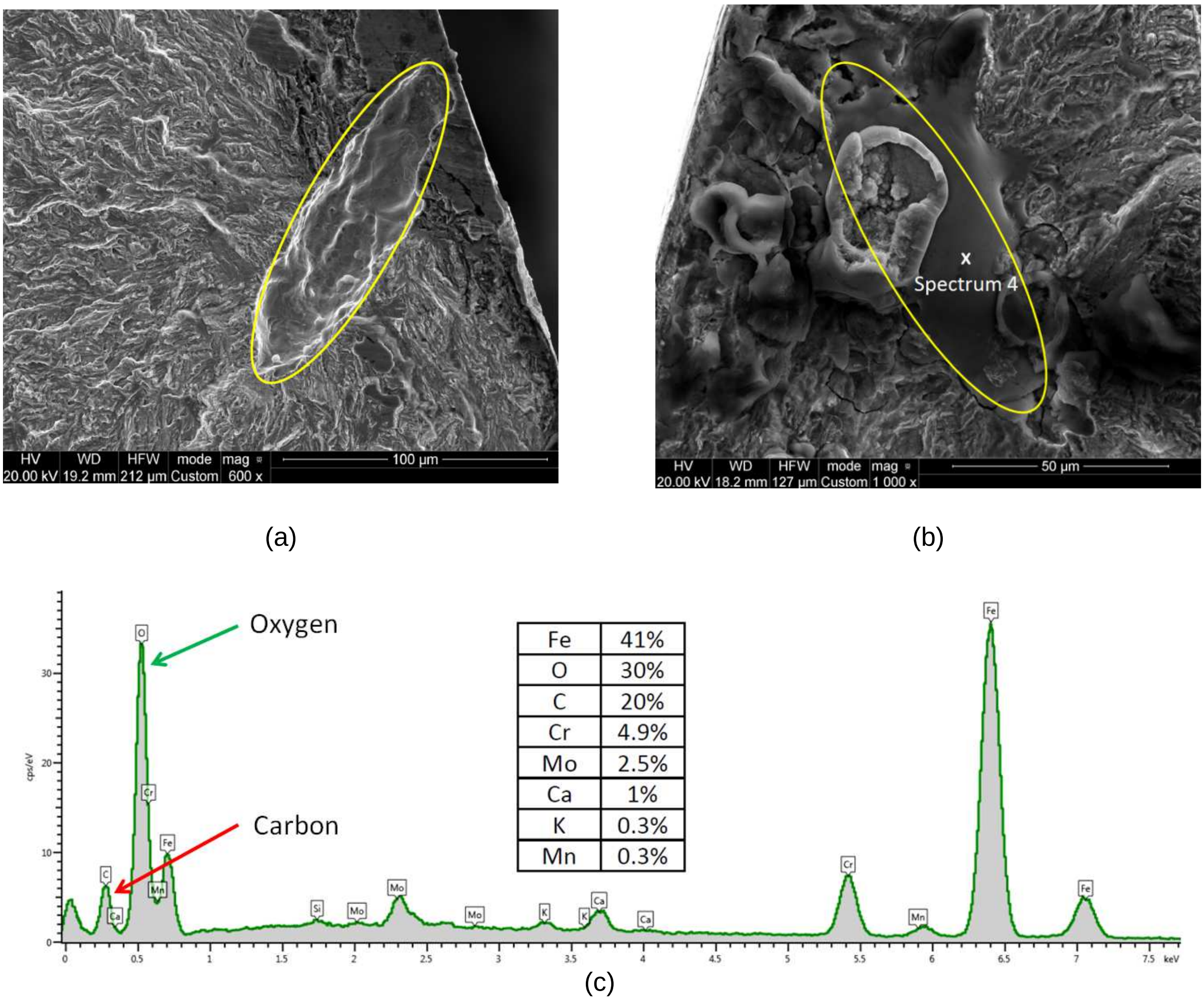

Fig. 8 (a) and (b) SEM image of crack initiation from chemical inhomogeneity of two halves (c) Spectrum obtained on inhomogeneous content using EDS

initiation from defects, in favor of the latter. Measurement of residual stress profiles within the first millimeter from the surface using X-ray diffraction are planned to evaluate the pertinence of this assumption.

For the VHCF regime, there is a consensus about the predominance of the crack initiation stage from an internal defect over the crack growth stage [5-7]. Such a conclusion does not seem to hold in the stress range investigated here. The analytical solution of Goodier [8] for the stress field around a spherical pore in an infinite elastic medium yields a stress concentration factor K_t of 2.04 under uniaxial tension. For the stress cycles corresponding to the endurance limit at R ≥ 0, this is sufficient to induce monotonic and even cyclic plastic flow and ratcheting around a pore. 3D elastic-plastic F.E. simulations of a unit cell model containing 1/8th of a spherical pore were run for cyclic loadings leading to internal crack initiation ($\Delta\sigma = 520$ MPa and $R = 0.25$). An equivalent plastic strain of 1.79% was reached at edge of the pore at the first peak load and after 100 cycles, the steady-state normal strain range was 0.53% with a local R ratio close to 1. Based on available fatigue data, such amplitude should lead to crack initiation after a few thousand cycles only. Note that biaxial tension should make internal crack initiation from internal defects more difficult, as also mentioned by Marquis et al [9], because the stress concentration at a spherical pore is lower in that case, as shown by Goodier's formulae for an elastic matrix [8]: its is 1.36 under equibiaxial tension instead of 2.04 in uniaxial tension.

To analyze the crack growth stage from internal defects, considered as elliptical, their major/minor semi-axes: 'a' and 'b', were measured (see table 3) and the stress intensity factor at any point along the crack front (designated by its angular position) was calculated as:

$$K_{I,max} = \frac{\sigma\sqrt{\pi b}}{E}, \quad E = \int_0^{\pi/2} \left(1 - \left(1 - \frac{b^2}{a^2}\right)\sin^2\phi\right)^{1/2} d\phi \qquad (2)$$

ΔK_I was calculated by taking into account only the tensile part of the cycle. The maximum ΔK value for an elliptical crack occurs at the end point of the minor axis. Both the initial and final maximum ΔK_I (considering the defect as a crack in the former case and at the border of the fish eye in the latter) were computed and reported in table 3. For all the observed defects, the initial ΔK_I is 3.8 to 4.8 MPa√m. This value is much smaller than the threshold ΔK of 7.1 MPa√m measured in similar steel by Suresh et.al. [10], for long cracks in air at R=0. In a reducing atmosphere which nearly suppressed oxide-induced closure, the threshold dropped to 4.5 MPa√m. This is closer to the present values. The internal cracks observed here, which grow in vacuum, are not only free from oxide-induced closure but they are also short and rather smooth cracks and thus, probably undergo very limited plasticity and roughness-induced closure as well.

An evaluation of the number of cycles spent in crack growth from the defect to the border of the fish-eye was attempted, using the kinetics measured by Suresh et.al. [10] in air at R=0.75, which probably corresponds to a closure-free kinetics. The results, denoted by $N_{fish\text{-}eye}$, are reported in table 3. $N_{fish\text{-}eye}$ does not constitute a negligible fraction of the fatigue lives: it reaches to 20% for specimen 18. However, the growth rates of internal cracks growing without any assistance of moist air are probably significantly lower than in air [4]. Beach marks observed within the fish eye in two specimens (23 and 26), submitted

Table 3 Estimated number of cycles for crack growth within the fish eye. Run-out specimens marked (*) were reloaded. In that case, crack growth from the last beach mark was considered. (-) denotes the absence of a fish eye due the proximity of the surface.

Test	R	Δσ (MPa)	Defect size		Fish eye diameter (µm)	$\Delta K_{I,max}$ MPa√m		$N_{failure}$	$N_{fish\text{-}eye}$
			2a (µm)	2b (µm)		Initial	Final		
16	-0.5	480	135	66	471	4.1	8.3	2,207,630	160,000
18	-0.5	487	199	66	660	4.4	10.0	741,938	150,000
23-1*	0	600	120	60	139	4.8	6.2	>3,000,000	50,000
26-1*	0.25	500	304	50	500	4.3	8.9	>3,000,000	110,000
25	0.25	500	95	95	-	3.9	-	339,602	-
24	0.25	510	127	65	-	4.2	-	300,333	-
26-2*	0.25	520	304	50	1028	9.2	13.3	1,704,174	40,000
23-2*	0.25	520	120	60	355	5.3	7.5	373,933	70,000
30	0.25	540	120	40	-	3.8	-	160,277	-

successively to two loading amplitudes, indicated the actual position of the crack front by the end of the first loading block and confirmed that the crack growth kinetics in air overestimated the growth rate of internal cracks. Thus, the growth kinetics collected in vacuum would be more pertinent. However, the fact that $N_{fish\text{-}eye}$ was underestimated reinforces the idea that the internal crack growth stage here constitutes a substantial part of the fatigue lives, which is contrary to what is usually deduced for the VHCF regime |6].

4. CONCLUSIONS AND FURTHER WORK

From the results obtained so far, the following conclusions can be made:

- In-phase biaxial tension with a biaxiality ratio between 0.2 and 0.3 prevails in the critical area of clip connectors, where the R ratio is about 0.7 during 90% of the service life and 0.2 in the remaining 10%.
- The fatigue life of F22 steel depreciates with increasing mean stress following Gerber's parabola for the endurance limit and Walker's model for finite lives.
- While in push-pull (R = -1 or -0.5) fatigue failures initiate from the surface, internal crack initiation from pores or oxygen and carbon rich inhomogeneities becomes predominant at higher R ratios.
- Internal crack growth without any assistance of moist air probably occurs with very limited plasticity and roughness-induced closure and no oxide-induced closure, but does not however, constitute a negligible part of the fatigue life in the range investigated, 10^5 - 3.10^6 cycles.

Combined tension and internal pressure tests on tubular specimens in air and synthetic sea water are in progress, using the tri-axial testing machine described in [11], to analyze the effects of positive load biaxiality and that of a corrosive environment on fatigue lives and formulate an appropriate fatigue criterion.

5. REFERENCES

[1] I. Koutiri, D. Bellett, F. Morel, L. Augustins and J. Adrien, High cycle fatigue damage mechanisms in cast aluminium subject to complex loads, *International Journal of Fatigue,* vol. 47, 44-57, 2013.

[2] V. Bonnand, J. Chaboche, P. Gomez, P. Kanouté and D. Pacou, Investigation of multiaxial fatigue in the context of turboengine disc applications, *International Journal of Fatigue,* vol. 33, 1006-1016, 2011.

[3] K. Walker, The effect of stress ratio during crack propagation and fatigue for 2024-T3 and 7075-T6 aluminum, *ASTM STP 462,* 1-14, 1970.

[4] A. McEvily and J. Gonzalez Velazquez, Fatigue Crack Tip Deformation Processes as Influenced by the Environment, *Metallurgical Transactions A,* vol. 23, 2211-2221, 1992.

[5] T. Nakamura, H. Oguma and Y. Shinohara, The effect of vacuum-like environment inside sub-surface fatigue crack on the formation of ODA fracture surface in high strength steel, *Procedia Engineering,* vol. 2, 2121–2129, 2010.

[6] Y. Murakami, T. Nomoto and T. Ueda, On the mechanism of fatigue failure in the super long life regime ($N>10^7$) cycles. Part II: a fractographic investigation, *Fatigue & Fracture of Engineering Materials & Structures,* vol. 23 , 903-910, 2000.

[7] T. Sakai, H. Harada and N. Oguma, Crack Initiation Mechanism of Bearing Steel in High Cycle Fatigue, *Fracture of Nano and Engineering Materials and Structures,* 1129-1130, 2006.

[8] J. Goodier, Concentration of Stress Around Spherical and Cylindrical Inclusions and Flaws, *Trans. ASME,* vol. 55 (7), 39, 1933.

[9] G. Marquis and P. Karjalainen-Roikonen, Long-life multiaxial fatigue of SG cast iron, *Proc. 6th International Conference on Biaxial/Multiaxial loading and Fracture,* 151-159, 2001.

[10] S. Suresh, G. Zamiski and R. Ritchie, Oxide-induced crack closure: an explanation for near-threshold corrosion fatigue crack growth behavior, *Metallurgical Transactions A,* vol. 12(8), 1435-1443, 1981.

[11] V. Doquet and V. De Greef, Dwell fatigue of a titanium alloy at room temperature under uniaxial or biaxial tension, *International Journal of Fatigue,* vol. 38, 118-129, 2012.

Proceedings of the 4th International Conference on
Fracture Fatigue and Wear, pp. 13-18, 2015

PLASTIC ZONE AROUND INTERACTING CRACKS UNDER ANTI-PLANE DEFORMATION

A. R. Hassani[a] , R. T. Faal[a] and S. J. Fariborz[b*]

[a] Faculty of Engineering, University of Zanjan, P.O. Box 45195-313, Zanjan, Iran
[b]Department of Mechanical Engineering, Amirkabir University of Technology (Tehran Polytechnic) 424, Hafez Avenue, Tehran 158754413, Iran

Abstract: By means of the image method the solution of screw dislocation is obtained in an isotropic elastic layer. The solution is used to derive integral equations for a cracked layer subject to anti-plane deformation. Based on the small scale yielding the solution of these equations, are utilized to determine stress components around a crack tip. Employing von Mises yield criterion the stress components are utilized to define the boundary of plastic region around a crack tip.

Keywords*:* Anti-plane deformation; Crack tip plastic region; Dislocation density; Small-scale yielding

1. INTRODUCTION

Under the hypotheses of linear fracture mechanics, plastic region forms at a crack tip even under small applied loads. In the stress analysis of metallic structures containing cracks the size of plastic region around a crack tip is a factor of utmost importance [1]. Apparently, in ductile materials, as the plastic region extends more energy dissipates reducing the damaged caused by dynamic loads. Furthermore, the direction of crack propagation in mixed mode fracture may be determined by the shape and size of the plastic region [2-4]. Wu and Dzeniz considered an isotropic strip weakened by an edge crack perpendicular to the layer boundary [5]. Adopting Dugdale model they obtained the length of the plastic segment ahead of the crack tip. The plastic region around a crack tip under in-plane loads was the topic of several investigations. For instance, recently, Xin et al., used Hill yield criterion to specify the boundary of the plastic zone in a cracked orthotropic plane under plane-stress conditions [6].

In the present study, under the assumption of small-scale yielding, of the by means image method, stress fields are determined in an isotropic elastic layer containing multiple cracks subjected to anti-plane deformation. The analysis takes into account the interaction between cracks which significantly changes the plastic region. The cracks interaction was not considered in previous investigations. By means of von Mises yield criterion the boundary of plastic region around crack tips is specified.

2. FORMULATION

The solution of a Volterra-type screw dislocation with Burgers vector δ situated at a point with coordinates $(0, h_1)$ in an isotropic infinite-plane is expressed as, [7]

$$w(x,y) = \frac{\delta}{2\pi} tan^{-1}(\frac{y-h_1}{x}) \tag{1}$$

* Corresponding author: Shahriar J. Fariborz,
Email: sjfariborz@yahoo.com
Phone: +98 21 64543460
Fax: +98 21 66419736

We consider a layer with thickness h weakened by the aforementioned dislocation, Fig. 1. The boundary conditions for the layer are

$$\sigma_{yz}(x,0)=0 \qquad (2)$$
$$\sigma_{yz}(x,h)=0$$

To derive the displacement in the layer Eq. (1) in conjunction with the method of images are utilized. To this end, we situate dislocations with Burgers vector δ at the points with coordinates $(0,h_1\pm 2hj), j=0,1,2,\ldots$ and with Burgers vector $-\delta$ at the points with coordinates $(0,-h_1\pm 2hj), j=0,1,2,\ldots$. The result may be written as

$$w(x,y)=\frac{\delta}{2\pi}\{tan^{-1}(\frac{y-h_1}{x})+tan^{-1}(\frac{y+h_1}{x}) \qquad (3)$$
$$+\sum_{j=1}^{\infty}[tan^{-1}(\frac{y-(h_1+2hj)}{x})+tan^{-1}(\frac{y-(h_1-2hj)}{x})$$
$$-tan^{-1}(\frac{y-(-h_1+2hj)}{x})-tan^{-1}(\frac{y-(-h_1-2hj)}{x})]\}$$

Carrying out the summation we arrive at the displacement field as

$$w(x,y)=\frac{\delta}{2\pi}[tan^{-1}(\frac{tan(\kappa\frac{y-h_1}{2})}{tanh(\kappa\frac{x}{2})})-tan^{-1}(\frac{tan(\kappa\frac{y+h_1}{2})}{tanh(\kappa\frac{x}{2})})] \qquad (4)$$

where $\kappa=\pi/h$. We may easily observe that Eq. (4) is multiple-valued on the dislocation cut, $x=0, y=h_1$. The constitutive equations under anti-plane deformation are

$$\sigma_{xz}=G\frac{\partial w}{\partial x} \qquad (5)$$
$$\sigma_{yz}=G\frac{\partial w}{\partial y}$$

where, G is the shear modulus of elasticity of material. From Eqs (4) and (5), stress components become

$$\sigma_{yz}=\frac{\delta G sinh(\kappa x)}{4h}(\frac{1}{cosh(\kappa x)-cos[\kappa(y+h_1)]}-\frac{1}{cosh(\kappa x)-cos[\kappa(y-h_1)]}) \qquad (6)$$
$$\sigma_{xz}=\frac{\delta G}{4h}(\frac{sin[\kappa(y-h_1)]}{cosh(\kappa x)-cos[\kappa(y-h_1)]}-\frac{sin[\kappa(y+h_1)]}{cosh(\kappa x)-cos[\kappa(y+h_1)]})$$

The stress components (6) satisfy boundary conditions (2). Moreover, they behave as

$$\sigma_{yz}(x,h_1)\sim\delta G/2\pi x \qquad as\ x\to 0 \qquad (7)$$
$$\sigma_{xz}(0,y)\sim-\delta G/2\pi(y-h_1) \qquad as\ y\to h_1$$

Therefore, stresses are Cauchy singular at dislocation location.

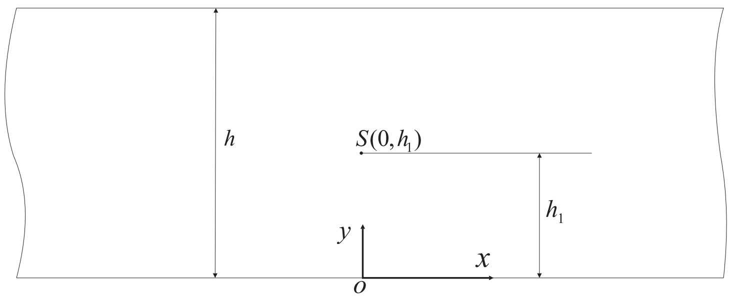

Fig. 1 Schematic view of the strip with a screw dislocation

We consider a strip containing N interacting cracks. The crack configurations may be described in parametric form as

$$x_i = x_i(s) \qquad (8)$$

$$y_i = y_i(s), \qquad -1 \le s \le 1, \quad i \in \{1,2,\dots,N\}$$

The solution of screw dislocation may be utilized to construct integral equations for the anti-plane deformation of a cracked strip. The integral equations are Cauchy singular and are expressed as

$$\sigma_{zni}\big(x_i(s), y_i(s)\big) = \sum_{i=1}^{N} \int_{-1}^{1} b_{zj}(t) K_{ij}(s,t)\,dt \qquad (9)$$

where σ_{zni} is the traction on the i-th crack and $b_{zj}(t)$ is the dislocation density function on the normalized length, $-1 \le t \le 1$ of the j-th crack. From Eq. (6), kernel of integral equation (9) becomes

$$K_{ij}(s,t) = \frac{G}{4h}\sqrt{\frac{x_j'^2(t) + y_j'^2(t)}{x_i'^2(s) + y_i'^2(s)}} \qquad (10)$$

$$[\frac{x_i'(s) sinh\big[\kappa(x_i(s) - x_j(t))\big] + y_i'(s) sin\big[\kappa(y_i(s) - y_j(t))\big]}{cosh\big[\kappa(x_i(s) - x_j(t))\big] - cos\big[\kappa(y_i(s) - y_j(t))\big]}$$

$$-\frac{x_i'(s) sinh\big[\kappa(x_i(s) - x_j(t))\big] + y_i'(s) sin\big[\kappa(y_i(s) + y_j(t) - 2h)\big]}{cosh\big[\kappa(x_i(s) - x_j(t))\big] - cos\big[\kappa(y_i(s) + y_j(t) - 2h)\big]}]$$

For embedded cracks Eq. (9) should be complimented by the following closure condition

$$\int_{-1}^{1}[\sqrt{x_j'^2(t) + y_j'^2(t)}]\, b_{zj}(t)\,dt = 0, \qquad j \in \{1,\dots N\} \qquad (11)$$

The left-hand side of Eq. (9) is

$$\sigma_{zni} = \sigma_{xz}^{E} sin\varphi_i - \sigma_{yz}^{E} cos\varphi_i \qquad (12)$$

where σ_{xz}^{E} and σ_{yz}^{E} are stress components caused by the external traction in the intact strip i.e., strip without cracks, and φ_i is the angle between y-axis and normal to the presumed surface of the i-th crack. The solution to Eqs. (9) and (11) yields the density of dislocation on a crack surface. The dislocation density is substituted into the following equations to determine stress components in the cracked strip

$$\sigma_{yz}(x,y) = \sigma_{yz}^{E}(x,y) \qquad (13)$$

$$+\frac{G}{4h}\sum_{j=1}^{N}\int_{-1}^{1} g_{zj}(t)\{\frac{1}{cosh(\kappa(x - x_j(t))) - cos(\kappa(y - y_j(t)))}$$

$$-\frac{1}{cosh(\kappa(x - x_j(t))) - cos\kappa(y + y_j(t) - 2h)}\}$$

$$sinh(\kappa(x - x_j(t)))\sqrt{[x'_j(t)]^2 + [y'_j(t)]^2}\,dt$$

$$\sigma_{xz}(x,y) = \sigma_{xz}^{E}(x,y)$$

$$+\frac{G}{4h}\sum_{j=1}^{N}\int_{-1}^{1} g_{zj}(t)\{\frac{sin\kappa(\kappa(y + y_j(t) - 2h))}{cosh\big(\kappa(x - x_j(t))\big) - \cos(\kappa(y + y_j(t) - 2h))}$$

$$-\frac{sin\kappa(\kappa(y - y_j(t)))}{cosh(\kappa\big(x - x_j(t)\big)) - \cos(\kappa(y - y_j(t)))}\}$$

$$sinh\left(\kappa\left(x-x_j(t)\right)\right)\sqrt{[x'_j(t)]^2+[y'_j(t)]^2}dt$$

Under the assumption of small scale yielding by invoking von Mises yield criterion, at the boundary of plastic zone in anti-plane deformation, the following relationship holds

$$0.75[\sigma_{xz}^2(x,y)+\sigma_{yz}^2(x,y)]=\tau_y{}^2 \quad (14)$$

where τ_y is the shear yield stress of the material. Therefore, substitution of stress components (13) into Eq. (14) specifies the boundary of plastic zone.

3. NUMERICAL RESULTS

In all the numerical examples, crack length is $2l=h/4$. The stress intensity factor of a crack which is perpendicular to the boundaries of a layer and subjected to uniform anti-plane traction τ_0 is, [8].

$$K_{III}=\tau_0\sqrt{h\,tan(\frac{\pi l}{h})} \quad (15)$$

Utilizing von Mises yield criterion the plastic region caused by the singular terms of stress field around the crack tip is a circle with center at crack tip and radius

$$r=\frac{0.75}{2\pi}\left(\frac{\tau_0}{\tau_y}\right)^2 h\,tan\left(\frac{\pi l}{h}\right) \quad (16)$$

The plastic region around a tip of the crack using Eq. (16) and also stress field (14) for two values of $\tau_0/\tau_y=0.2, 0.4$ are depicted in Fig. 2. The value of $r\left(\tau_y/\tau_0\right)^2$ is constant whereas plastic region obtained from stress field (13) depends upon $\left(\tau_y/\tau_0\right)^2$. Moreover, in the present analysis, by increasing the applied traction plastic zone does not extend in all directions uniformly. In the proceeding examples, uniform traction $\tau_{yz}=\tau_0$ is applied on the layer boundaries. Plastic regions at a crack tip of a horizontal central crack for τ_y are shown in Fig. 3.The common feature of the above two examples is that plastic regions are symmetrical which attributes to the anti-symmetry of the problems with respect to the crack lines. The last example deals with the interaction between a central and an oblique crack, Figs. 4 and 5. The angle between cracks is $5\pi/6$ and the origin of coordinate system is located at the point of intersection of cracks lines. The interaction between cracks widens the plastic region and the area of plastic region on the upper flank of the cracks is larger than that on the lower one.

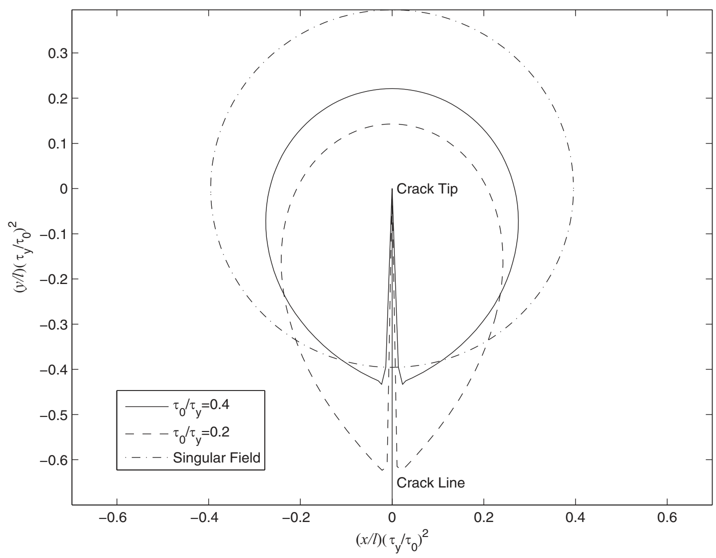

Fig. 2 Plastic region around a tip of a vertical crack

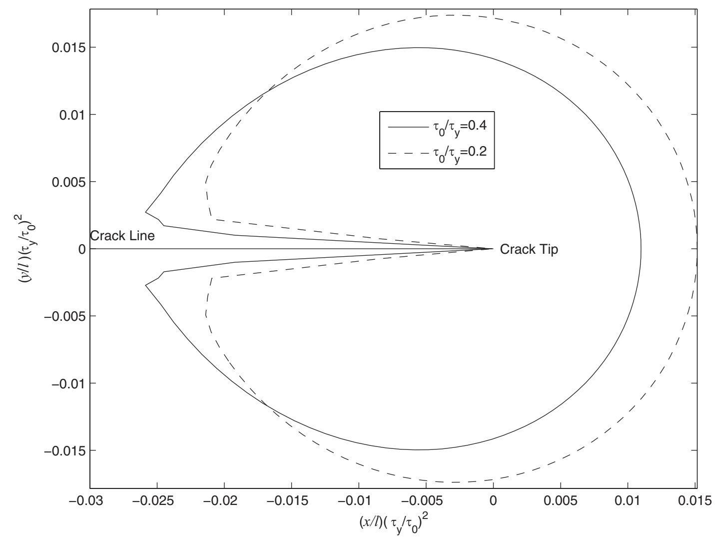

Fig. 3 Plastic region at a tip of a horizontal central crack

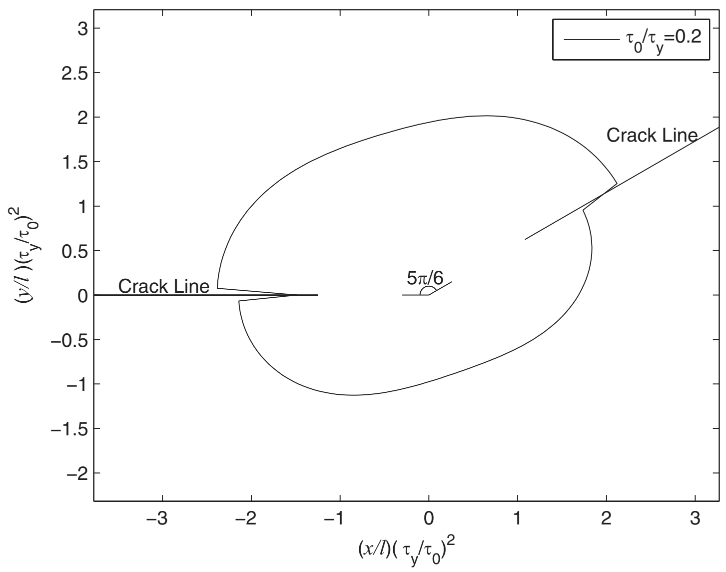

Fig. 4 Plastic region around the tips of two interacting cracks for $\tau_0/\tau_y = 0.2$

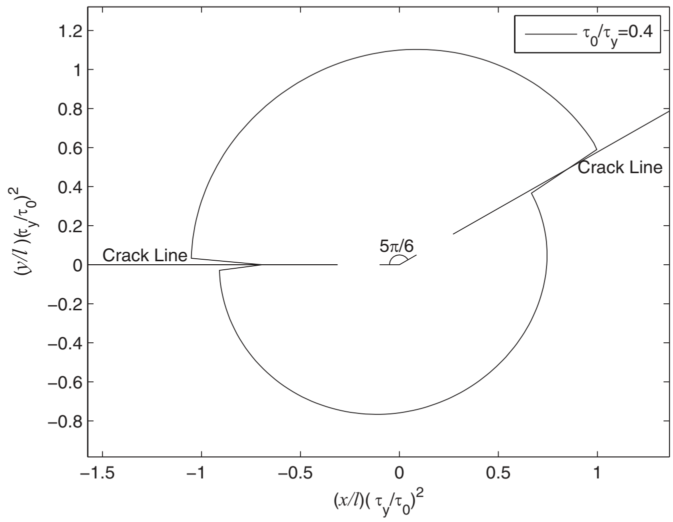

Fig. 5 Plastic region around the tips of two interacting cracks for $\tau_0/\tau_y = 0.4$

4. CONCLUSIONS

Based on the solution of screw dislocation integral equations are derived in a layer containing multiple cracks. These equations are solved numerically to determine dislocation density on the surfaces of cracks. The solution is utilized to determine stress components in the cracked layer under anti-plane deformation. The plastic region around the tips of a crack is specified using von Mises yield criterion. The analysis allows consideration of non-singular terms of stress fields. We observed that interaction between cracks has crucial effect on the shape and size of the plastic region.

5. REFERENCES

[1] T.M. Banks, A. Garlick, The form of crack tip plastic zones, Eng. Fract. Mech., 19 (1984) 571-581.

[2] K. Golos, B. Wasiluk, Role of plastic zone in crack growth direction criterion under mixed mode loading, Int. J. Fract., 102 (2000) 341-353.

[3] S.M.A. Khan, M.K. Khraisheh, Analysis of mixed mode crack initiation angles under various loading conditions, Eng. Fract. Mech., 67 (2000) 397-419.

[4] S.M.A. Khan, M.K. Khraisheh, A new criterion for mixed mode fracture initiation based on the crack tip plastic core region, Int. J. Plast., 20 (2004) 55-84.

[5] X.-F. Wu, Y.A. Dzenis, Closed-form solution for the size of plastic zone in an edge-cracked strip, Int. J. Eng. Sci., 40 (2002) 1751-1759.

[6] G. Xin, W. Hangong, K. Xingwu, J. Liangzhou, Analytic solutions to crack tip plastic zone under various loading conditions, Eur. J. Mech. A. Solids, 29 (2010) 738-745.

[7] J. Weertman, J.R. Weertman, Elementary dislocation theory, Macmillan1964.

[8] B. Michel, Murakami, Y. (ed.), Stress Intensity Factors Handbook. In 2 Volumes. Oxford etc., Pergamon press 1987, ZAMM - Journal of Applied Mathematics and Mechanics, 68 (1988) 259-260.

Proceedings of the 4th International Conference on
Fracture Fatigue and Wear, pp. 19-24, 2015

EVALUATION FORMULAE OF STRESS INTENSITY FACTORS FOR EDGE INTERFACE CRACK IN ELASTIC COATING UNDER THERMAL STRESS

K. Oda[1], Y. Takahata[2], T. Shinmoto[2], Y. Sugita[2] and N. Tsutsumi[1]

[1] Department of Mechanical and Energy Systems Engineering, Oita University, Oita, Japan
[2] Graduate school of Oita University, Oita, Japan

Abstract: This paper deals with the analysis of the thermal stress intensity factor for small edge interfacial crack between thin elastic coating and substrate subjected to uniform temperature change by using the crack tip stress method. In the present method, the stress values at the crack tip calculated by FEM are used under the same mesh pattern and the stress intensity factors are evaluated from the ratio of stress values at the crack-tip-node between a given and a reference problems. This method is based on the fact that the singular stress field near the interface crack tip is controlled by the stress values at the crack tip calculated by FEM. In this study, the small edge interface crack problem under thermal stress is solved by superposing the uniaxial tension problem with edge singularity and the problem subjected to temperature change and uniaxial compression with no edge singularity. The calculation shows that the stress intensity factors of the small edge interface crack under thermal stress can be evaluated from four constant factors related only to the Dundurs' parameter.

Keywords: Stress intensity factor, Interface crack, Thermal stress, Coating layer, Crack tip stress method

1 INTRODUCTION

The between thin elastic coating and substrate, delamination and interface crack at the free edge of interface are often induced by thermal stress due to the elastic and thermal mismatch of the materials. Then, the evaluation of stress intensity factor (SIF) for interface crack under thermal boundary conditions is a subject of practical importance. Although a large number of studies have been made on the interface crack problem under thermal stress [1, 2], little is known about the effect of the free edge singularity on the stress intensity factors of the edge interface crack when the crack is extremely short.

In this paper, single-edge interface crack problem subjected to uniform change of temperature is considered as shown in Fig.1. In Fig.1, G_j, ν_j, η_j (j=1, 2) and ΔT are shear modulus, Poisson's ratio, linear coefficient of thermal expansion and temperature change, respectively. The subscripts j=1, 2 stand for the material 1 and 2. The thermal stress intensity factors for small edge interfacial crack are analysed by using the crack tip stress method [3-6]. This method is based on the fact that the singular stress field near the interface crack tip is controlled by the stress values at the crack-tip-node calculated by FEM. To determine the SIFs under thermal stress, the stresses at the interface crack tip calculated by FEM are used and are compared with the results of reference problem shown in Fig.2 under the same mesh pattern near the crack tip [3-6]. In this study, a small edge interface crack in a bonded rectangular plate will be examined with varying crack length and changing material combination. Then, the effect of material combination and relative crack size on the SIF for interface crack will be discussed.

2 CRACK TIP STRESS METHOD

Recently, the effective method was proposed for calculating the stress intensity factor by using FEM [5-6]. The method utilizes the stress values at the crack tip by FEM. From the stresses σ_y, τ_{xy} near the interface crack tip, stress intensity factors are defined as shown in Eq.1.

$$\sigma_y + i\tau_{xy} = \frac{K_1 + iK_2}{\sqrt{2\pi r}}\left(\frac{r}{2a}\right)^{i\varepsilon}, \quad \varepsilon = \frac{1}{2\pi}\ln\left[\left(\frac{\kappa_1}{G_1}+\frac{1}{G_2}\right)\Big/\left(\frac{\kappa_2}{G_2}+\frac{1}{G_1}\right)\right] \tag{1}$$

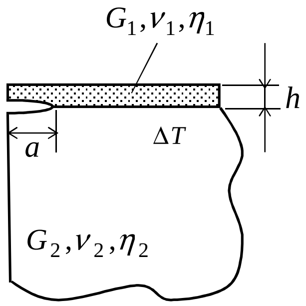

Fig. 1 Small edge interface crack between thin layer and substrate under uniform temperature change

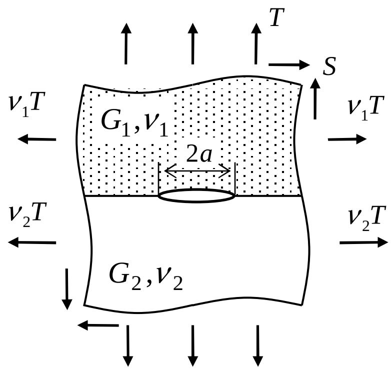

Fig. 2 Reference problem of an interface crack in bonded semi-infinite plates

In Eq.1, G_j is the shear modulus, κ_j=3-4ν_j for plane strain, κ_j=(3-ν_j)/(1+ν_j) for plane stress and ν_j is Poisson's ratio (j=1, 2). From Eq.1, SIFs may be separated as

$$K_1 = \lim_{r\to 0}\sqrt{2\pi r}\,\sigma_y\{\cos Q + (\tau_{xy}/\sigma_y)\sin Q\}\ ,\quad K_2 = \lim_{r\to 0}\sqrt{2\pi r}\,\tau_{xy}\{\cos Q - (\sigma_y/\tau_{xy})\sin Q\}\ , \tag{2}$$

$$Q = \varepsilon \ln\{r/(2a)\}\ . \tag{3}$$

Here, r and Q can be chosen as constant values when the reference and unknown problems have the same crack length and the same material constants. If Eq.4 is satisfied, Eq.5 may be derived from Eqs.2.

$$\tau_{xy}{}^*/\sigma_y{}^* = \tau_{xy}/\sigma_y \tag{4}$$

$$K_1{}^*/\sigma_y{}^* = K_1/\sigma_y\ ,\quad K_2{}^*/\tau_{xy}{}^* = K_2/\tau_{xy} \tag{5}$$

Here, σ_y*, τ_{xy}* are stresses of reference problem near the crack tip, and σ_y, τ_{xy} are stresses of unknown problem in Fig. 1. The asterisk means the value of reference problem. In the FEM analysis, the stresses at the crack tip node, $\sigma_{y0,FEM}$ and, $\tau_{xy0,FEM}$ are obtained as the finite value. By using the stress values at the interface crack tip calculated by FEM under the same mesh pattern, the SIFs of the unknown problem can be determined by

$$K_1 = \frac{\sigma_{y0,FEM}}{\sigma_{y0,FEM}{}^*}K_1{}^*,\quad K_2 = \frac{\tau_{xy0,FEM}}{\tau_{xy,FEM}{}^*}K_2{}^* \tag{6}$$

When the single interface crack in a dissimilar bonded infinite plane subjected to the loads T and S shown in Fig. 2 is selected as the reference problem, the SIFs of the reference problem are evaluated by

$$K_1^* + iK_2^* = (T + iS)\sqrt{\pi a}(1 + 2i\varepsilon) \tag{7}$$

In order to determine the applied loads T and S in Eq.7, the reference problem is expressed by superposing the tension and shear problems [5, 6]. Then, the stresses at the interface crack tip of the reference problem are expressed by

$$\sigma_{y0,FEM}{}^* = T\cdot\sigma_{y0,FEM}^{T=1}{}^* + S\cdot\sigma_{y0,FEM}^{S=1}{}^*,\quad \tau_{xy0,FEM}{}^* = T\cdot\tau_{xy0,FEM}^{T=1}{}^* + S\cdot\tau_{xy0,FEM}^{S=1}{}^* \tag{8}$$

where $\sigma^{T=1}_{y0,FEM}$ stands for the stress σ_y at the crack-tip node calculated by FEM in the condition of T=1 and S=0. From the condition that the crack-tip-stresses between the unknown and the reference problems are the same, we obtain the applied loads T and S as follows,

$$T = \frac{\sigma_{y0,FEM} \cdot \tau^{S=1}_{xy0,FEM}{}^{*} - \sigma^{S=1}_{y0,FEM}{}^{*} \cdot \tau_{xy0,FEM}}{\sigma^{T=1}_{y0,FEM}{}^{*} \cdot \tau^{S=1}_{xy0,FEM}{}^{*} - \sigma^{S=1}_{y0,FEM}{}^{*} \cdot \tau^{T=1}_{xy0,FEM}{}^{*}}, \quad S = \frac{\sigma^{T=1}_{y0,FEM}{}^{*} \cdot \tau_{xy0,FEM} - \sigma_{y0,FEM}{}^{*}\, \tau^{T=1}_{xy0,FEM}{}^{*}}{\sigma^{T=1}_{y0,FEM}{}^{*} \cdot \tau^{S=1}_{xy0,FEM}{}^{*} - \sigma^{S=1}_{y0,FEM}{}^{*} \cdot \tau^{T=1}_{xy0,FEM}{}^{*}} \tag{9}$$

Since the applied loads T and S determined by Eq.9 satisfy the condition that $\sigma_{y0,FEM}{}^{*} = \sigma_{y0,FEM}$ and $\tau_{xy0,FEM}{}^{*} = \tau_{xy0,FEM}$, the SIFs of unknown problem are equivalent to that of reference problem. Therefore, we can obtain the SIFs of unknown problem from Eqs.7 and 9 by using the crack tip stress values calculated by FEM under the same mesh pattern.

3 NUMERICAL RESULTS AND DISCUSSION

In this analysis, eight-node-quadrilateral element is used and the FEM mesh near the crack tip is made fine systematically [3-7]. It should be noted that the same mesh size and pattern near the crack tip have to be used in the calculation of stress values for the unknown and reference problems.

3.1 Effect of singular stress field near the interface edge due to thermal stress

The SIF of the small interface crack is dominated by the singular stress field near the free edge. Figure 3 shows the normalized SIFs for small edge interface crack under uniform temperature change analysed by the crack tip stress method. The dimensionless factors, F_1 and F_2, are defined as follows in this study.

$$K_1 + iK_2 = (F_1 + iF_2)\sigma_0\sqrt{\pi a}(1+2i\varepsilon) \tag{10}$$

$$\sigma_0 = \frac{8G_1G_2(\eta_2^* - \eta_1^*)\Delta T}{G_1(\kappa_2 - 1) - G_2(\kappa_1 - 1) - 2(G_1 - G_2)} \tag{11}$$

Here, σ_0 is the equivalent tensile stress in tension problem which gives the same edge singularity, and $\eta_j^* = (1+\nu_j)\eta_j$ for plane strain, $\eta_j^* = \eta_j$ for plane stress (j=1, 2). As shown in Fig.3, the values of $F_{1,2}$ tend to increase or decrease markedly as the inteface crack becomes short. Furthermore, the values of $F_{1,2}$ are also changed by the layer thickness h/W even when a/W is fixed. There are the reflection of the free edge stress singularity caused by the thermal stress.

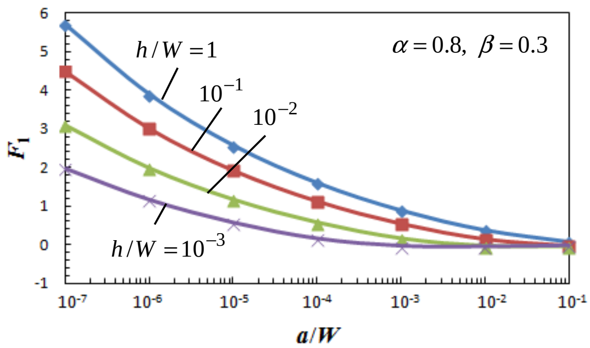

(a) F_1 vs a/W

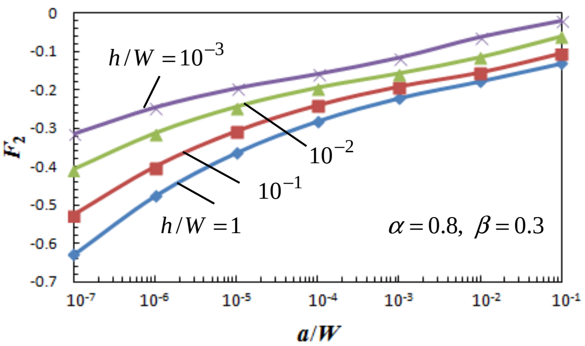

(b) F_2 vs a/W

Fig. 3 Relation between normalized SIFs and the relative crack length a/W when α=0.8 and β=0.3

(α, β are the Dundurs' composite parameters which are determined by elastic constants G_1,G_2, ν_1,ν_2).

3.2 Superposion method to analyze small edge interface crack problem under thermal stress

In this study, the problem of the small interface crack under thermal stress is represented by superposing two different problems as illustrated in Fig.4 [10]. Figure 4(b) is the small edge interface crack problem under tension in y-direction and Fig.4(c) is the problem subjected to compression and uniform temperature change. The problem of Fig.4(b) has the edge singularity and Fig.4(c) has no edge singularity.

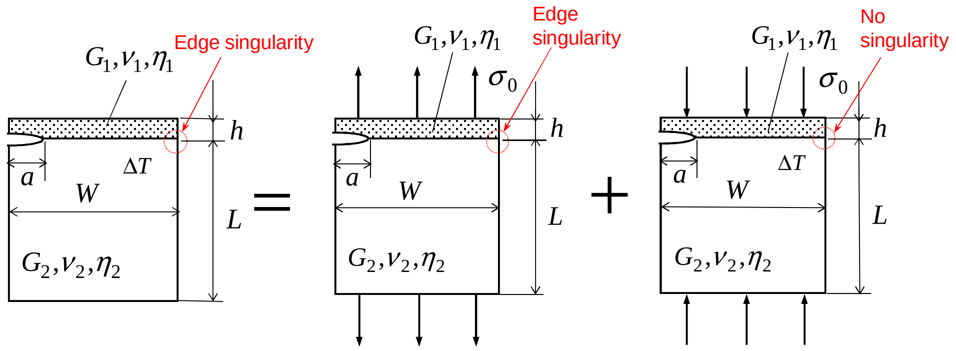

Fig. 4 Superposition method to solve the thermal stress problem

By solving the problems of Fig.4 (b) and (c), the stress intensity factors of Fig.4 (a) can be obtained.

3.2.1 SIF of small edge interface crack under singular stress field (Fig.4b)

The SIF of the short interface crack is dominated by the singular stress field near the free edge as illustrated in Fig.3. The singular stress distribution near the interface free edge is expressed by $\sigma_y=K_\sigma/r^{1-\lambda}$, where r is the distance from free edge and 1-λ is the theoretical index of stress singularity near the interface edge without the crack [8, 9]. We therefore examine the variation of the intensity of the singular stress field K_σ near the interface free edge in Fig.4b without the crack. Figure 5 shows the relation between K_σ the coating layer thickness h/W. In Fig.5, It is found that the intensity K_σ has linear distribution on the double logarithmic plot, that is $K_\sigma \propto (h/W)^m$, when $h/W<10^{-2}$. Table 1 shows the comparison between the slope m and the singular index 1-λ. From Table 1, it is seen that the slope m is close to the index of stress singularity 1-λ. Then, the dimensionless SIFs F_1 and F_2 for tension problem of Fig.4b can be represented by the following expressions.

$$F_1 = C_1(W/a)^{1-\lambda} \cdot (h/W)^{1-\lambda} = C_1 \cdot (h/a)^{1-\lambda}$$
$$F_2 = C_2(W/a)^{1-\lambda} \cdot (h/W)^{1-\lambda} = C_2 \cdot (h/a)^{1-\lambda} \qquad (12)$$

The normalized factors C_1 and C_2 are plotted on a semi-logarithmic chart in Fig. 6when β=0.3. It is seen that the factors $C_{1,2}$ become constant when $a/h<10^{-3}$.

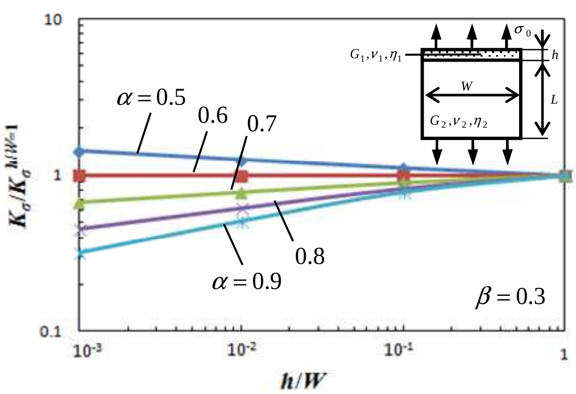

Fig. 5 Relation between the intensity of singular stress at the interface edge K_σ and the relative thin layer thickness h/W when β=0.3.

Table 1 Comparison between *m* and *1-λ* when *β*=0.3.

α	*m* (From Fig.5)	*1-λ* (Theoretical)
0.5	-0.0558	-0.0559
0.6	0.0000	0
0.7	0.0652	0.0652
0.8	0.1344	0.1345
0.9	0.2056	0.2059

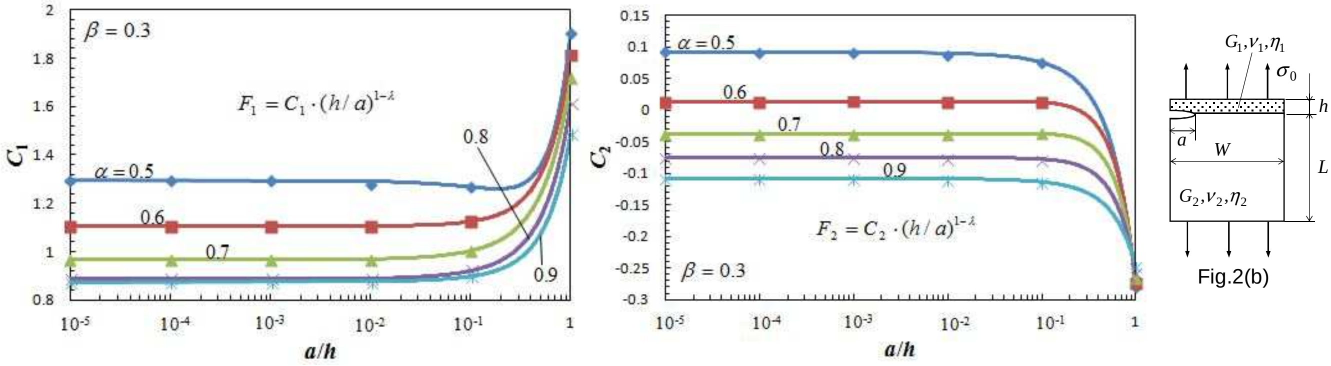

Fig.6 Relation between $C_{1,2}$ (Fig.4b) and the relative crack length a/h when β=0.3.

3.2.2 SIF of small edge interface crack under no stress singularity condition (Fig.4c)

In Fig.4(c), the stress along the interface is the uniform distribution because the singular stress due to the temperature change is counteracted by the singular stress due to the compressive stress σ_0 [10]. The problem of Fig.4(c) has no singularity at the interface edge. Then, the dimensionless SIFs in this problem are shown by using the factors D_1 and D_2.

$$K_1 + iK_2 = (D_1 + iD_2)\sigma_0\sqrt{\pi a}(1+2i\varepsilon) \qquad (13)$$

Figure 7 shows the relation between the normalized factors $D_{1,2}$ and the relative crack length a/h when β=0.3. It is seen that the factors $D_{1,2}$ become constant when $a/h<10^{-2}$.

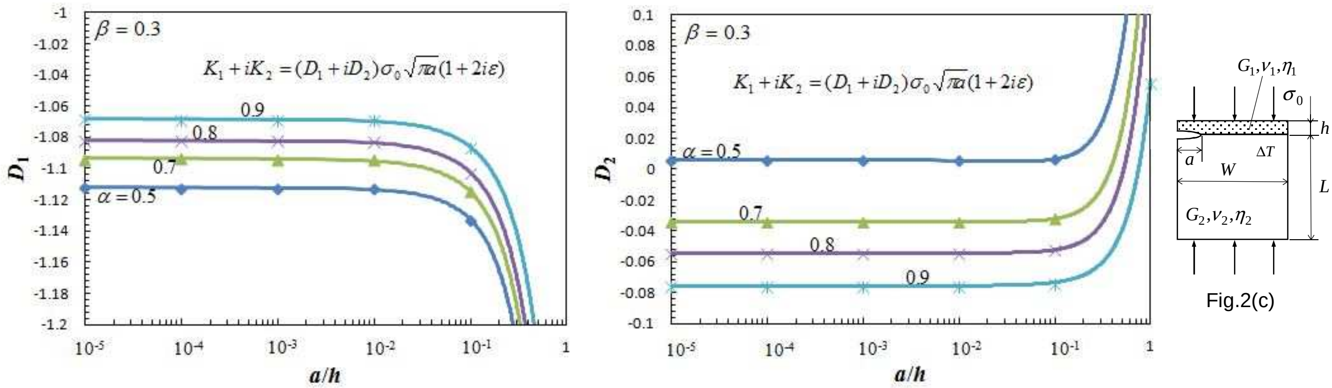

Fig. 7 Relation between $D_{1,2}$ (Fig.4c) and the relative crack length a/h when β=0.3.

3.2.3 Evaluation fomula of SIFs for small edge interface crack under thermal stress

By using the method of superposition, the SIFs of the small interface crack under the uniform temperature change ΔT can be evaluated by using C_1, C_2, D_1 and D_2.

$$K_1 + iK_2 = (F_1 + iF_2)\sigma_0\sqrt{\pi a}(1+2i\varepsilon)\,,\ F_1 = C_1 \cdot (h/a)^{1-\lambda} + D_1\,,\ F_2 = C_2 \cdot (h/a)^{1-\lambda} + D_2\ \ (a/h<10^{-3}) \qquad (14)$$

The factors $C_{1,2}$ and $D_{1,2}$ for the small edge interface crack depend on the material combination α and β. In Table 2, the dimensionless SIFs $F_{1,2}$ evaluated from Eq.14 are compared with the SIFs directly calculated by the crack tip stress method (CTSM). As shown in Table 2, both results are in good agreement with each other. Therefore, the SIFs of the small interface crack under the uniform temperature change can be easily evaluated by using C_1, C_2, D_1 and D_2 when $a/h<10^{-3}$ without FEM analysis for any material combinations.

Table 2 Accuracy of the dimensionless SIFs F_1 and F_2 calculated by Eq.14

β=0.3		$C_{1,2}$		$D_{1,2}$		$F_{1,2}=C_{1,2}(h/a)^{1-\lambda}+D_{1,2}$		$F_{1,2}$ directly obtained by CTSM	
F	a/W	α=0.8	α=0.9	α=0.8	α=0.9	α=0.8	α=0.9	α=0.8	α=0.9
F_1	10^{-5}	0.887	0.875	-1.082	-1.068	3.087	8.293	3.087	8.294
	10^{-4}	0.887	0.875	-1.082	-1.068	1.977	4.763	1.977	4.763
	10^{-3}	0.887	0.875	-1.082	-1.068	1.162	2.558	1.162	2.561
F_2	10^{-5}	-0.0751	-0.1082	-0.0544	-0.0756	-0.4075	-1.233	-0.4075	-1.233
	10^{-4}	-0.0751	-0.1082	-0.0544	-0.0756	-0.3135	-0.7966	-0.3135	-0.7966
	10^{-3}	-0.0751	-0.1082	-0.0544	-0.0756	-0.2447	-0.5242	-0.2447	-0.5245

4 CONCLUSIONS

In this study, the thermal stress intensity factor for small edge interfacial crack between thin elastic coating and substrate subjected to uniform temperature change were analyzed with varying the relative crack length, coating layer thickness and material combinations systematically. The small edge interface crack problem under thermal stress can be solved by superposing the uniaxial tension problem with edge singularity and the problem subjected to temperature change and uniaxial compression with no edge singularity. The calculation showed that the stress intensity factors of the small edge interface crack under thermal stress can be evaluated from the following definition with four factors when the ratio of the crack length and the coating layer thickness $a/h<10^{-3}$:

$$K_1+iK_2=(F_1+iF_2)\sigma_0\sqrt{\pi a}(1+2i\varepsilon)\ ,\ F_1=C_1\cdot(h/a)^{1-\lambda}+D_1\ ,\ F_2=C_2\cdot(h/a)^{1-\lambda}+D_2\ .$$

In above definition, λ is the order of the stress singularity at the interface edge without the crack.

5 REFERENCES

[1] F. Erdogan, Stress Distribution in Bonded Dissimilar Materials with Cracks, *Journal of Applied Mechanics*, Vol.32, pp.403–410, 1965.

[2] T. Ikeda, T. Sun, Stress Intensity Factor Analysis for an Interface Crack between Dissimilar Isotropic Materials under Thermal Stress, *Inter Journal of Fracture*, Vol. 111, pp.229-249, 2001.

[3] H. Nisitani, T. Kawamura, W. Fujisaki, T. Fukuda, Determination of Highly Accurate Values of Stress Intensity Factor or Stress Concentration Factor of Plate Specimen by FEM, *Transactions of the Japan Society of Mechanical Engineering (JSME)*, Vol. 65A, No. 629, pp. 26-31, 1999 (in Japanese).

[4] H. Nisitani, T. Teranishi, K. Fukuyama, Stress Intensity Factor Analysis of a Bimaterial Plate Based on the Crack Tip Stress Method, *Transactions of the JSME*, Vol. 69A, No. 684, pp. 1203-1208, 2003 (in Japanese).

[5] K. Oda, N.-A. Noda, S.N. Atluri, Accurate Determination of Stress Intensity Factor for Interface Crack by Finite Element Method, *Key Engineering Materials*, Vols. 353-358, pp.3124-3127, 2007.

[6] K. Oda, K. Kamisugi, N.-A. Noda, Stress Intensity Factor Analysis of Interface Crack by Proportional Method, *Transactions of the JSME*, Vol. 75A, No. 752, pp. 476-482, 2009 (in Japanese).

[7] N.-A. Noda, X. Lan, K. Michinaka, Y. Zhang. K. Oda, Stress Intensity Factor of an Edge Interface Crack in a Bonded Semi-Infinite Plate, *Transactions of the JSME*, Vol. 76A, No. 770, pp. 1270-1277, 2010 (in Japanese).

[8] K. Oda, X. Lan, N.-A. Noda, K. Michinaka, Effect of Arbitrary Bi-material Combnation and Bending Loading Conditions on Stress Intensity Factors of an edge Interface Crack, *International Journal of Structural Integrity*, Vol. 3, No. 4, pp.457-475, 2012.

[9] D.-H. Chen, H. Nisitani, Intensity of Singular Stress Field near the Interface Edge Point of a Bonded Strip, *Transactions of the JSME*, Vol. 59A, No. 567, pp. 2682-2686, 1993 (in Japanese).

[10] K. Oda, T. Shinmoto, N. Tsutsumi, Stress Intensity Factors for Small Edge Interface Crack in Bonded Dissimilar Plates under Thermal Stress, *International Journal of Fracture Fatigue and Wear*, Vol. 2, pp. 63-69, 2014.

Proceedings of the 4th International Conference on
Fracture Fatigue and Wear, pp. 25-31, 2015

FRACTURE ANALYSIS OF MULTIPLE CRACKS IN A FUNCTIONALLY GRADED PIEZOELECTRIC HALF-PLANE

M. Nourazar and M. Ayatollahi

Faculty of Engineering, University of Zanjan, P. O. Box 45195-313, Zanjan, Iran

Abstract: This paper investigates the analytical method to examine behaviour of several cracks in a functionally graded piezoelectric (FGP) half-plane subjected to anti-plane mechanical and in-plane electrical loading. First, the distributed dislocation technique is used to construct integral equations for FGP materials, in which the unknown variables are dislocation densities. By the use of dislocation densities, the field intensity factors are determined. In this study, we examine the effect of the material parameter and crack geometry upon the field intensity factors. Finally, several examples are solved and the numerical results for the stress intensity factor and electric displacement intensity factor are presented graphically.

Keywords: Functionally graded; piezoelectric; Screw dislocation; Singular integral equations; Half-plane

1. INTRODUCTION

One of the important potential applications of smart material is in the area of high performance structures in the recent years. The electro-mechanical properties of functionally graded piezoelectric (FGP) materials continuously vary in certain directions to compensate sharp change in electro mechanical fields causing catastrophic failures. Therefore, the study of fracture of piezoceramics is receiving considerable attention due to extensive use of piezoelectric materials in adaptive (smart) structures. Commercially available piezoceramics are rather brittle and susceptible to fracture. As is well-known, the extension of the current fundamental fracture concepts in pure elasticity to piezoelectricity is not straightforward since the coupling between the mechanical and electric fields is complicated.

Up to know a number of studies have been performed for the cracked piezoelectric materials. (Deeg, 1980; Park, 1990; Sosa, 1991; Suo et al, 1992; Meguid and Chen, 2001; Kwon and Lee, 2001; mousavi and Paavola, 2013). The distributed dislocation technique is a useful method in the fracture analysis of medium weakened by multiple cracks. It should be mentioned that in order to use the dislocation solution in crack formation, we should have exact solution for the dislocation.

In this paper, we consider the problem for multiple cracks in a piezoelectric half-plane under anti-plane mechanical and in-plane electrical loadings. The Fourier transform is employed to obtain transformed displacement and stress fields. The dislocation solutions are then used to formulate integral equations for a functionally graded piezoelectric half-plane weakened by several cracks. Numerical results for the field intensity factors are shown graphically for functionally graded piezoelectric half-plane.

2. PROBLEM STATEMENT AND METHOD OF SOLUTION

Consider a functionally graded piezoelectric half-plane with the poling axis Z occupies the region, and is thick enough in the Z-direction to allow a state of anti-plane shear. A Volterra-type screw dislocation is located at the origin, Fig.1. Under this anti-plane mechanical loading and in-plane electrical loading, only the out-of plane displacement and in-plane electric fields are non-vanishing. For the anti-plane problem considered here, the out-of plane elastic displacements, in-plane electric potentials satisfy the following governing equations

$$u = 0, v = 0, w = w(x, y) \tag{1}$$

And

$$E_x = -\frac{\partial \phi}{\partial x},\ E_y = -\frac{\partial \phi}{\partial y}. \tag{2}$$

The constitutive relations are as follows:

$$\sigma_{xz} = c_{44}(y)\frac{\partial w}{\partial x} + e_{15}(y)\frac{\partial \phi}{\partial x}, \qquad \sigma_{yz} = c_{44}(y)\frac{\partial w}{\partial y} + e_{15}(y)\frac{\partial \phi}{\partial y}$$

$$D_x = e_{15}(y)\frac{\partial w}{\partial x} - \varepsilon_{11}(y)\frac{\partial \phi}{\partial x}, \qquad D_y = e_{15}(y)\frac{\partial w}{\partial y} - \varepsilon_{11}(y)\frac{\partial \phi}{\partial y} \tag{3}$$

where $c_{44}(y)$, $e_{15}(y)$ and $\varepsilon_{11}(y)$ are the respective elastic shear modulus, piezoelectric coefficient and dielectric constant of the piezoelectric material. In the absence of body forces and body charges, the equilibrium equations for the piezoelectric media are

$$\frac{\partial \sigma_{xz}}{\partial x} + \frac{\partial \sigma_{yz}}{\partial y} = 0, \qquad \frac{\partial D_x}{\partial x} + \frac{\partial D_y}{\partial y} = 0 \tag{4}$$

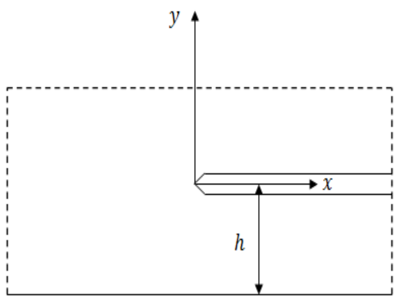

Fig. 1. Schematic view of half-plane with a screw dislocation.

Eqs. 3 in view of Eqs. 4 become:

$$c_{44}(y)\nabla^2 w + e_{15}(y)\nabla^2\phi + \frac{\partial c_{44}(y)}{\partial y}\frac{\partial w}{\partial y} + \frac{\partial e_{15}(y)}{\partial y}\frac{\partial \phi}{\partial y} = 0$$

$$e_{15}(y)\nabla^2 w - \varepsilon_{11}(y)\nabla^2\phi + \frac{\partial e_{15}(y)}{\partial y}\frac{\partial w}{\partial y} - \frac{\partial \varepsilon_{11}(y)}{\partial y}\frac{\partial \phi}{\partial y} = 0 \tag{5}$$

In this paper, we adopt the exponential function as the material constants distribution of piezoelectric half-plane.

$$[c_{44}(y), e_{15}(y), \varepsilon_{11}(y)] = [c_{440}, e_{150}, \varepsilon_{110}]e^{2\lambda y} \tag{6}$$

where λ is the exponent for properties gradation and $[c_{440}, e_{150}, \varepsilon_{110}]$ are the material constant at $y = 0$. Applying Eqs. 6 into Eqs. 5 results in

$$c_{440}\nabla^2 w + e_{150}\nabla^2\phi + 2\lambda c_{440}\frac{\partial w}{\partial y} + 2\lambda e_{150}\frac{\partial \phi}{\partial y} = 0$$

$$e_{150}\nabla^2 w - \varepsilon_{110}\nabla^2\phi + 2\lambda e_{150}\frac{\partial w}{\partial y} - 2\lambda \varepsilon_{110}\frac{\partial \phi}{\partial y} = 0. \tag{7}$$

With the use of Bleustein function [8]

$$\psi(x, y) = \phi - \alpha w(x, y) \tag{8}$$

In which $\alpha = \frac{e_{150}}{\varepsilon_{110}}$, Eqs. 7 can be written as follows:

$$\nabla^2 w + 2\lambda\frac{\partial w}{\partial y} = 0, \ \nabla^2\psi + 2\lambda\frac{\partial \psi}{\partial y} = 0., \tag{9}$$

The constitutive Eqs. 3 can be written as follows

$$\sigma_{xz} = \left[(c_{440} + \alpha e_{150})\frac{\partial w}{\partial x} + e_{150}\frac{\partial \psi}{\partial x}\right]\exp(2\lambda y), \qquad \sigma_{yz} = \left[(c_{440} + \alpha e_{150})\frac{\partial w}{\partial y} + e_{150}\frac{\partial \psi}{\partial y}\right]\exp(2\lambda y)$$

$$D_x = -\varepsilon_{110}\exp(2\lambda y)\frac{\partial\psi}{\partial x}, \qquad D_y = -\varepsilon_{110}\exp(2\lambda y)\frac{\partial\psi}{\partial y} \tag{13}$$

For impermeable case, the boundary, continuity and limiting conditions may be expressed as

$$\sigma_{yz}(x,-h)=0, \quad \sigma_{yz}(x,0^-)=\sigma_{yz}(x,0^+),$$
$$D_y(x,-h)=0, \quad D_y(x,0^-)=D_y(x,0^+),$$
$$w(x,0^-)-w(x,0^+)=b_{mz}H(x), \quad \phi(x,0^-)-\phi(x,0^+)=b_pH(x),$$
$$\lim_{y\to\infty}w=0, \ \lim_{y\to\infty}\phi=0, \tag{14}$$

where in Eqs.14 b_{mz} and b_p designate dislocation Burgers vectors. Although the jump in the electric potential is not a type of dislocation, it is referred here as electric dislocation for convenience. By applying Eq. 8 to the conditions (14), we arrive at

$$\sigma_{yz}(x,-h)=0, \quad \sigma_{yz}(x,0^-)=\sigma_{yz}(x,0^+),$$
$$D_y(x,-h)=0, \quad D_y(x,0^-)=D_y(x,0^+),$$
$$w(x,0^-)-w(x,0^+)=b_{mz}H(x), \ \psi(x,0^-)-\psi(x,0^+)=(b_p-\alpha b_{mz})H(x),$$
$$\lim_{y\to\infty}w=0, \ \lim_{y\to\infty}\psi=0, \tag{15}$$

With the use of complex Fourier transforms, the functions w and ϕ are obtained

$$w(x,y)=\frac{b_{mz}}{4\pi}\int_{-\infty}^{+\infty}[(\beta+\lambda)e^{(\beta-\lambda)y}+\frac{(\beta-\lambda)}{e^{2\beta h}}e^{-(\beta+\lambda)y}]\frac{e^{i\omega x}}{\beta}(\pi\delta(\omega)-i/\omega)d\omega$$
$$-h<y<0$$

$$w(x,y)=\frac{b_{mz}}{4\pi}\int_{-\infty}^{+\infty}[(\beta-\lambda)e^{-(\beta+\lambda)y}]\frac{e^{i\omega x}}{\beta}(e^{-2\beta h}-1)(\pi\delta(\omega)-i/\omega)d\omega \qquad y>0$$

$$\psi(x,y)=\frac{(b_p-\alpha b_{mz})}{4\pi}\int_{-\infty}^{+\infty}[(\beta+\lambda)e^{(\beta-\lambda)y}+\frac{(\beta-\lambda)}{e^{2\beta h}}e^{-(\beta+\lambda)y}]\frac{e^{i\omega x}}{\beta}(\pi\delta(\omega)-i/\omega)d\omega \qquad -h<y<0$$

$$\psi(x,y)=\frac{(b_p-\alpha b_{mz})}{4\pi}\int_{-\infty}^{+\infty}[(\beta-\lambda)e^{-(\beta+\lambda)y}]\frac{e^{i\omega x}}{\beta}(e^{-2\beta h}-1)(\pi\delta(\omega)-i/\omega)d\omega \qquad y>0$$

(16)

where $\beta=\sqrt{\lambda^2+\omega^2}$. With the aid of constitutive equations and use the table of integral transforms [9], it is not difficult to obtain the expressions for the components of the stress and electric displacement. For the sake of brevity, the details of manipulation are not given here. The final results are

$$\sigma_{xz}(x,y)=\frac{[c_{44}(y)b_{mz}+e_{15}(y)b_p]e^{-\lambda y}}{2\pi}[\frac{\lambda(y+2h)}{R}K_1(\lambda R)-\frac{\lambda y}{r}K_1(\lambda r)+\lambda K_0(\lambda r)-\lambda K_0(\lambda R)]$$

$$\sigma_{yz}(x,y)=\frac{[c_{44}(y)b_{mz}+e_{15}(y)b_p]\lambda x e^{-\lambda y}}{2\pi}[\frac{K_1(\lambda r)}{r}-\frac{K_1(\lambda R)}{R}]$$

$$D_x=-\frac{\varepsilon_{11}(y)(b_p-\alpha b_{mz})e^{-\lambda y}}{2\pi}[\frac{\lambda(y+2h)}{R}K_1(\lambda R)-\frac{\lambda y}{r}K_1(\lambda r)-\lambda K_0(\lambda r)+\lambda K_0(\lambda R)]$$

$$D_y = -\frac{\varepsilon_{11}(y)(b_p - \alpha b_{mz})e^{-\lambda y}\lambda x}{2\pi}[\frac{K_1(\lambda r)}{r} - \frac{K_1(\lambda R)}{R}] \tag{17}$$

where $r = \sqrt{x^2 + y^2}$, $R = \sqrt{x^2 + (y + 2h)^2}$ and $K(x)$ is the modified Bessel function of the second kind. The stress components are ready to be used in the distributed dislocation technique to form and analyse the cracked piezoelectric half-plane. It should be mentioned that, as expected, the behaviour of the integrals in stress component depicts that they have singularity in the vicinity of dislocation.

3. MULTIPLE CRACKS PROBLEM

The distributed dislocation technique was used by several investigators for the analysis of cracked bodies under mechanical loading, see e.g., Weertman [10]. We use the solution of dislocation in functionally graded piezoelectric half-plane for the analysis of half-plane with multiple cracks. Let *N* be the number of cracks in the medium. A crack configuration with respect to coordinate system *x*, *y* may be described in parametric form as

$$\begin{aligned} x_i &= x_i(s) \\ y_i &= y_i(s) \qquad i = 1,2,\dots,N \qquad -1 \le s \le 1 \end{aligned} \tag{18}$$

The moveable orthogonal coordinate system (n,t) is chosen such that the origin may move on the crack while t-axis remains tangent to the crack surface. The anti-plane field traction on the surface of *i*-th crack in terms of field components in the Cartesian coordinates (x, y) becomes

$$(\sigma_{nz}, D_n)(x_i, y_i) = [\sigma_{yz}, D_y]\cos\theta_i - [\sigma_{xz}, D_x]\sin\theta_i \tag{19}$$

in which

$$\theta_i(s) = tg^{-1}(\beta_i'(s)/\alpha_i'(s)) \tag{20}$$

Next, covering the crack surfaces by dislocations, the principle of superposition is invoked to obtain the tractions on a given crack surface. The crack is constructed by continuous distribution of dislocations. Therefore, the anti-plane field traction on the surface of *i*-th crack due to the presence of above-mentioned distribution of dislocations on all N cracks yields

$$(\sigma_{nz}, D_n) = \sum_{j=1}^{N}\int_{-1}^{1}\{[\sigma_{yz}, D_y]\cos\theta_i - [\sigma_{xz}, D_x]\sin\theta_i\}\sqrt{[\alpha_j']^2 + [\beta_j']^2}\,dt \tag{21}$$

By virtue of Bueckner's principle (see, e.g., Hills et al., [11]), the left hand side of Eqs. 21 are stress components and the electric displacement at the presumed location of the cracks with negative sign, which implies impermeable crack boundary conditions. Since stress component and electric displacement (17) are Cauchy singular at the dislocation location, the system of integral Eqs. 21 for the density functions are Cauchy singular for $i = j$ as $s \to t$. Employing the definition of density function, the equation for the crack opening displacement and electric potential across j^{th} crack become

$$w_j^-(s) - w_j^+(s) = \int_{-1}^{s} B_{mj}(t)\sqrt{[\alpha_j']^2 + [\beta_j']^2}\,dt$$

$$\phi_j^-(s) - \phi_j^+(s) = \int_{-1}^{s} B_{pj}(t)\sqrt{[\alpha_j']^2 + [\beta_j']^2}\,dt \qquad j = 1,2,\dots,N \tag{22}$$

The closure requirement should be satisfied to ensure single-valued field out of each crack surfaces. Thus, closure requirements for *k*th crack read

$$\int_{-1}^{1} B_{kj}(t)\sqrt{[\alpha_j']^2 + [\beta_j']^2}\,dt = 0 \qquad k \in \{m, p\} \tag{23}$$

The stress fields near a crack tip have the singularity of $1/\sqrt{r}$ where *r* is the distance from a crack tip. Therefore, the dislocation densities are taken in the following forms:

$$B_{kj}(t)=\frac{g_{kj}(t)}{\sqrt{1-t^2}},\quad -1\le t\le 1,\ k\in\{m,p\} \tag{24}$$

The parameters $g_{kj}(t)$ are obtained by solving the system of Eqs. 21, 23. The field intensity factors for impermeable cracks is reduced to [7]

$$(K_{III}^{m})_{Li}=\frac{c_{44}(y_{Li})}{2}\left[[(x_i'(-1)]^2+[y_i'(-1)]^2\right]^{\frac{1}{4}}g_{mi}(-1)+\frac{e_{15}(y_{Li})}{2}\left[[(x_i'(-1)]^2+[y_i'(-1)]^2\right]^{\frac{1}{4}}g_{pi}(-1)$$

$$(K_{III}^{m})_{Ri}=-\frac{c_{44}(y_{Ri})}{2}\left[[(x_i'(1)]^2+[y_i'(1)]^2\right]^{\frac{1}{4}}g_{mi}(1)-\frac{e_{15}(y_{Ri})}{2}\left[[(x_i'(1)]^2+[y_i'(1)]^2\right]^{\frac{1}{4}}g_{pi}(1)$$

$$(K_{III}^{D})_{Li}=\frac{e_{15}(y_{Li})}{2}\left[[(x_i'(-1)]^2+[y_i'(-1)]^2\right]^{\frac{1}{4}}g_{mi}(-1)-\frac{\varepsilon_{11}(y_{Li})}{2}\left[[(x_i'(-1)]^2+[y_i'(-1)]^2\right]^{\frac{1}{4}}g_{pi}(-1)$$

$$(K_{III}^{D})_{Ri}=-\frac{e_{15}(y_{Ri})}{2}\left[[(x_i'(1)]^2+[y_i'(1)]^2\right]^{\frac{1}{4}}g_{mi}(1)+\frac{\varepsilon_{11}(y_{Ri})}{2}\left[[(x_i'(1)]^2+[y_i'(1)]^2\right]^{\frac{1}{4}}g_{pi}(1) \tag{25}$$

For brevity, the details of the derivation of fields intensity factors are not given here.

4. NUMERICAL RESULTS AND DISCUSSION

In the following examples, the half-plane is made up of the PZT-4 piezoelectric ceramic of which material properties are given as follows:

$$c_{44}=2.56\times 10^{10}\frac{N}{m^2},e_{15}=12.7\frac{C}{m^2},\varepsilon_{11}=64.6\times 10^{-10}\frac{C}{Vm}$$

The numerical results given in this section are obtained for a uniform loading $\sigma_{yz}=\sigma_0, D_y=D_0$. The stress intensity is normalized by $K_0=\sigma_0\sqrt{L}$ and the electric intensity factor is normalized by $K_0^D=\sigma_0 e_{15}\sqrt{L}/c_{44}$.

As a first example, the problem of a functionally graded piezoelectric half-plane under constant far field applied traction $(\sigma_{yz}=\sigma_0, D_y=D_0)$ weakened by a straight crack rotating around its center is examined. The effect of crack orientation and FG constant is under consideration and Fig.2 shows the variation of dimensionless stress intensity factors versus the angle of rotation. It was found that for $\theta = 0,\pi$, the stress intensity factors increase with increasing material inhomogeneous parameter. For FGP half-plane, using several values of FG constant, we observed that, the crack opening displacement at the crack tip with smaller shear modulus is higher than the other tip located in higher shear modulus region. The overall effects results in a higher stress intensity factor for the crack tip which is located in the stiffer zone. The minimal value of stress intensity factor occurs at $\theta = \pi/2$.

In the second example, we consider a crack parallel to the boundary of half-plane, inset in Fig.3 and 4. The crack location remain fixed while the crack lengths is changing. The variation of dimensionless fields intensity factors K_M/K_0 and K_D/K_0 are shown in Figs.3 and 4. As it was expected, larger cracks experience more sever field intensity factors. The trend of variation remains the same by changing the FG constant.

In the last example, we consider a half-plane weakened by two embedded cracks with non-dimensionalized length. The crack on the left side is stationary while the crack on the right side rotates around its centre. We observe that the field intensity factor for tip L_2 and R_2 vanishes at $\theta = \frac{\pi}{2}$. Moreover, as it was seen, the variation of stress intensity for the stationary crack is much less significant than that of the rotating crack.

5. CONCLUSION

In the present paper, the closed form dislocation solution of functionally graded piezoelectric half-plane is achieved by the use of Fourier transform. The results for stress and electric displacement exhibit the well-known Cauchy-type singularity at the dislocation location. The dislocation solution is utilized to derive singular integral equations for the analysis of a functionally graded piezoelectric half-plane weakened by several cracks. To study the interaction between cracks, and also the effect of crack orientation field's intensity factors are obtained for four examples.

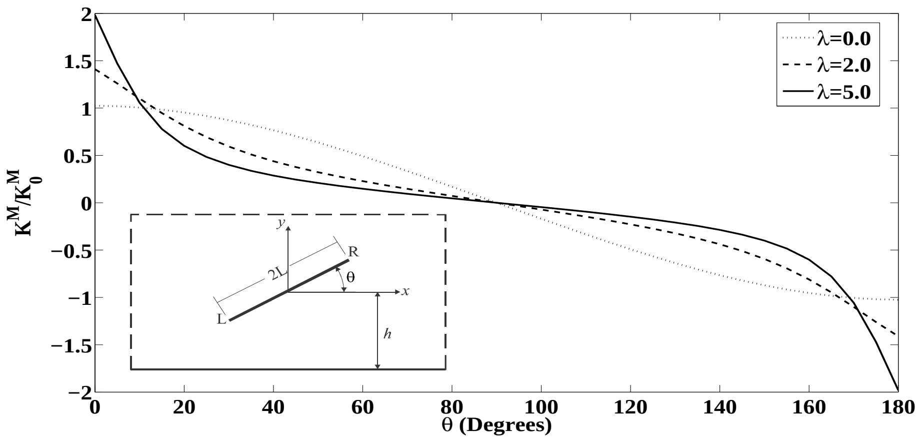

Fig. 2 Variation of stress intensity factors for a rotating crack in a functionally graded half-plane.

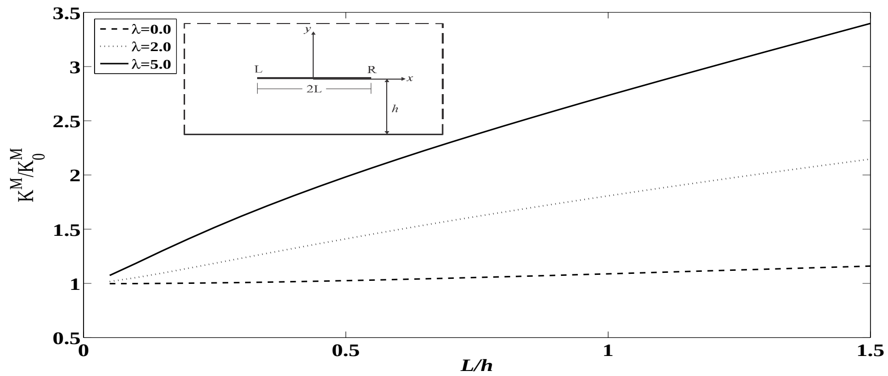

Fig. 3 Variation of stress intensity factors with h/L

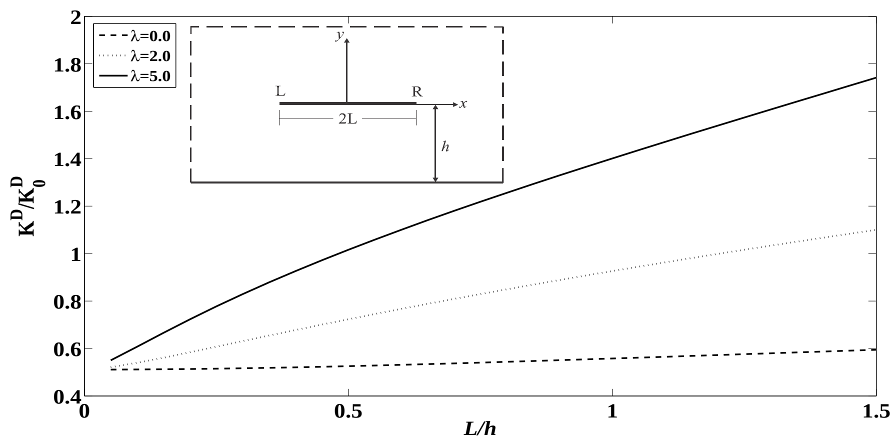

Fig. 4 Variation of electric intensity factors with changing crack length.

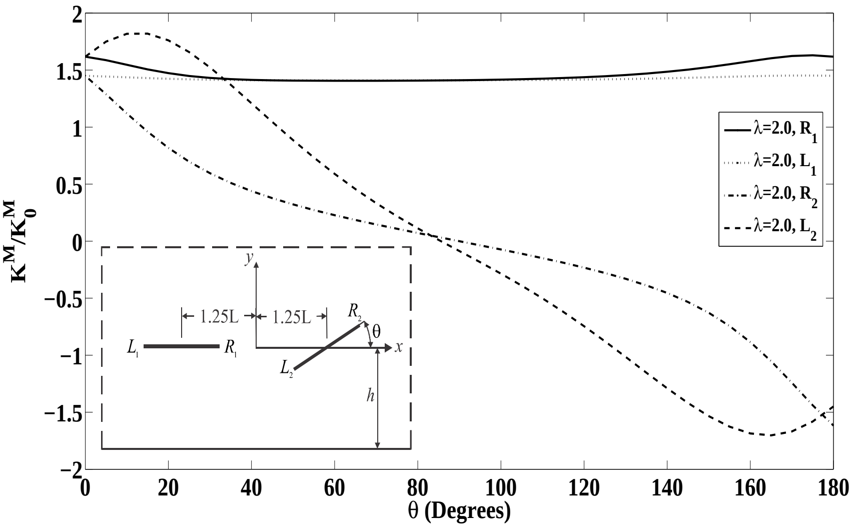

Fig. 5 Variations of stress intensity factor for a stationary and a rotating crack.

6. REFERENCES

[1] W.F. Deeg, Analysis of dislocation crack and inclusion problems in piezoelectric solids, PhD Dissertation, Standford University, 1980.

[2] Y.E. Pak, Crack extension force in a piezoelectric material, Journal of Applied Mechanics 57, 647–653, 1990.

[3] H. Sosa, Plane problems in piezoelectric media with defects, International Journal of Solids and Structures 28, 491–505, 1991.

[4] Z. Suo, C.M. Kuo, D.M. Barnett, J.R. Willis, Fracture mechanics for piezoelectric ceramics, Journal of the Mechanics and Physics of Solids 40, 739–765. 1992.

[5] S.A. Meguid, Z.T. Chen, Transient response of finite piezoelectric strip containing coplanar insulating cracks under electromechanical impact, Mechanics of Materials 33, 85–96. 2001.

[6] S.M. Kwon, K.Y. Lee, Edge cracked piezoelectric ceramic block under electromechanical impact loading, International Journal of Fracture 112, 139–150.

[7] S.M. Mousavi, J. Paavola, Analysis of cracked functionally graded piezoelectric strip, International Journal of Solids and Structures 50, 2449–2456, 2013.

[8] J.L. Bleustein, A new suface wave in piezoelectric materials, Applied physics letters 13, 412-413.

[9] [9] A. Jeffrey and D. Zwillinger, Table of integrals, series and products, sixth ed., Academic press, 2000

[10] J. Weertman, Dislocation Based Fracture Mechanics, Singapore: World Scientifc, 1996.

[11] D. A. Hills, P. A. Kelly, D. N. Dai and A. M. Korsunsky, Solution of Crack Problems: The Distributed Dislocation Technique, Kluwer Academic Publishers, 1996.

Proceedings of the 4th International Conference on
Fracture Fatigue and Wear, pp. 32-37, 2015

SEVERAL SOLUTIONS OF INTENSITY OF SINGULAR STRESS USEFUL FOR EVALUATING BONDED STRENGTH

N.A. Noda[1], Z. Wang[1], F. Ren[1], R. Li[1], T. Miyazaki[2], K. Oda[3],
Y. Takase[1], Y. Sano[1], K. Iida[1] and Y. Zhang[4]

[1] Kyushu Institute of Technology, Kitakyushu, Japan
[2] University of the Ryukyus, Okinawa, Japan
[3] Oita University, Oita, Japan
[4] China University of Petroleum, Beijing, China

Abstract: Adhesive joints are widely used in many industrial sectors since the numerous advantages over other traditional joints. However the mismatch of different materials may cause debonding of the joints. Since few studies are available for evaluating the bonded strength, this study will focuses on the solutions for the intensity of the singular stress for several typical adhesive joints, such as bonded plate and butt joint in plane stress state, bonded cylinder/pipe under axial-symmetric state. In this research, an effective numerical method combined with FEM results is used to obtain the SIFs at corner of adhesive joints in arbitrary material combinations. Here the simple bonded plate, which has already been solved accurately in our previous study, is used as the reference problem. We will discuss the effect of the adhesive thickness in a butt joint, and defined a new parameter for semi-infinite structure; and for the bonded joints in axial-symmetric, the non-singular terms are derived so that the SIFs can be obtained, and it is found that the axial-symmetric problem are quite different since the SIFs cannot be dominated by the Dunders' parameters. And at last, the SIFs for several problems are discussed and compared with each other.

Keywords: Adhesion, Stress Intensity Factor, Fracture Mechanics, Interface, Finite Element Method

1 INTRODUCTION

The adhesive joints have been widely used in automobile, space and aviation engineering recent years since it has number of advantages over the traditional joints, such as no welding residual stress, lightweight, lower costs and easy to process. There are all kinds of adhesive joints in different application area, such as pipe joint (Fig. 1(f)) in couplings, and butt joint (Fig. 1(b)) in microelectronic packaging. Among these adhesive joints, the most fundamental one is a bonded strip composed by two different materials (Fig. 1(a)).

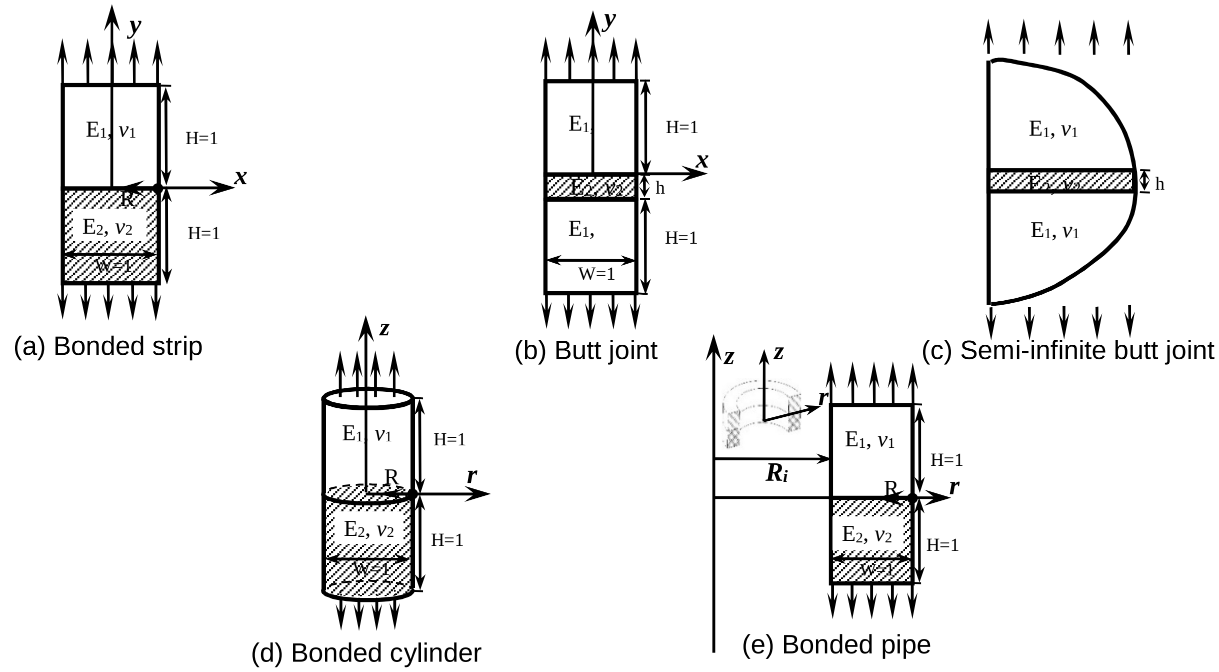

Fig. 1 Several bonded structures having singularity at interface corner in the form $\sigma_{ij} \propto K_\sigma / r^{1-\lambda}$

It is known that different material properties cause singular stress at the end of interface which leads to the failure of these structures. All these problems need to consider the intensity of singular stress.

So far, many studies have been done for these kinds of bonded structures. The fundamental problem of bonded plate in Fig. 1(a) with the expression of intensity of singular stress as Eq.(1) has the has been analysed by Chen-Nisitani[1] and Noda et.al[2]. Fig.2 shows the stress intensity factor of this problem.

$$K_\sigma = \lim_{r\to 0}\left[r^{1-\lambda} \times \sigma_{\theta|\theta=\frac{\pi}{2}}(r) \right], \quad F_\sigma = \frac{K_\sigma}{\sigma^\infty W^{1-\lambda}}, \tag{1}$$

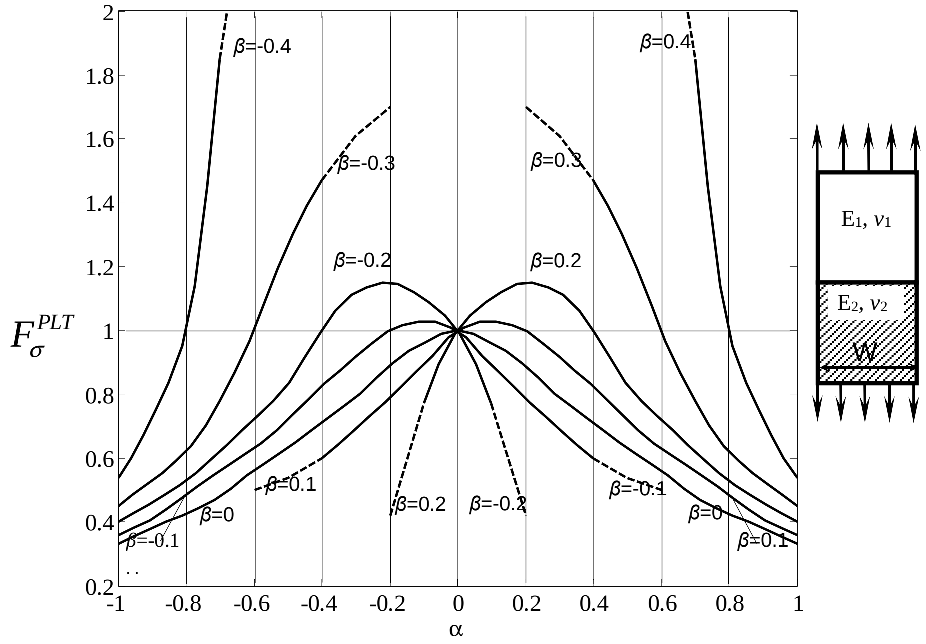

Fig. 2 F_σ for a boned strip in Fig. 2(a)

Also many researchers studied the adhesive thickness effect on the adhesive join shown in Fig. 1(b) [3,4,5]; and this kind of adhesive specimen was also studied under bending tests [6]. In Ref. [7], the effect of adhesive thickness was considered with varying material properties for a bonded cylinder specimen. Zhang and Noda et.al [8] have analysed the effect of adhesive thickness for the butt joint under tension by investigating all material combinations systematically. And in reference [9], it's found that the critical values of the stress intensity factors are almost constant (see Fig.3)

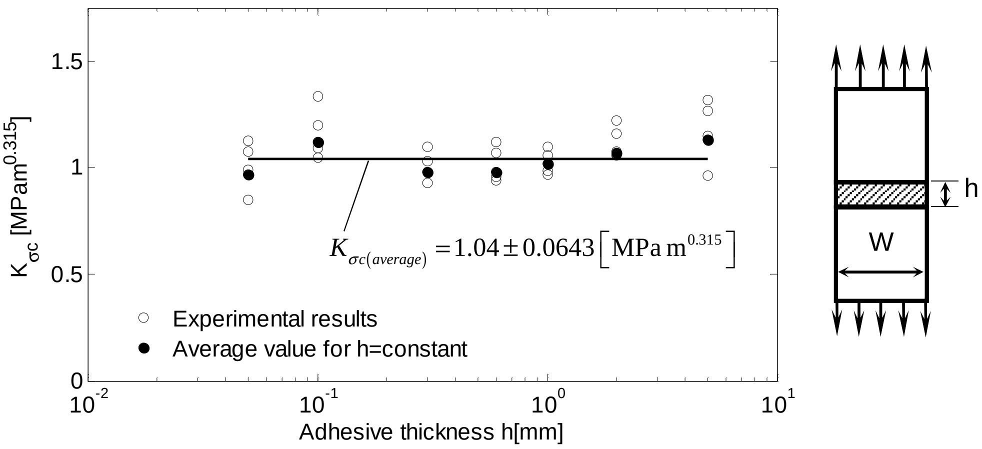

Fig. 3 Relationship between $K_{\sigma c}$ and h

This study will mainly focus on the corner stress intensity factors (SIFs) for several typical adhesive joints as shown in Fig. 1, and aims to give the solutions of SIFs for the future study and application in engineering. In this research, an effective numerical method combined with FEM results is used to obtain the SIFs at corner of adhesive joints in arbitrary material combinations.

2. ANALYSIS ON BUTT JOINT

This section deals with a butt joint as shown in Fig. 1(b), (c). Then, the effect of adhesive thickness on the corner stress intensity factor is discussed. This analytical study focuses on the FEM stress at the first node of interface considering together with the exact solution in Fig. 2 by applying the same mesh division [8, 10]. For the adhesive joint in a bonded finite plate as shown in Fig.1 (b), the dimensionless stress intensity factor F_σ defined in Equation (2) is suitable because F_σ has the same value if the adhesive thickness $h \geq W$ [2].

$$F_\sigma = K_\sigma / \sigma W^{1-\lambda} \tag{2}$$

Here, σ denotes the remote tensile stress. On the other hand, if the adhesive thickness h is much smaller than the adhesive width W ($h/W \to 0$), the results correspond to the solution for bonded semi-infinite plate in Fig. 1 (c). In this case, the dimensionless stress intensity factor F_σ^* defined in Equation (3) is suitable because F_σ^* has the same value if h is small enough.

$$F_\sigma^* = K_\sigma / \sigma h^{1-\lambda} \tag{3}$$

Fig.4 (a) shows an example of the relation between the adhesive thickness h and the corner stress intensity factor. It is seen that F_σ^* becomes constant when adhesive layer is thin enough. In other words, it is found that the adhesive butt joint in Fig.1 (b) can be regarded as the bonded semi-infinite plate in Fig.1 (c) when the ratio $h/W \leq 0.005$. The solution of bonded semi-infinite plate is obtained as shown in Fig.4 (a). Fig. 4 (b) shows the dimensionless stress intensity factor F_σ^* in Fig.1 (c) under arbitrary material combination.

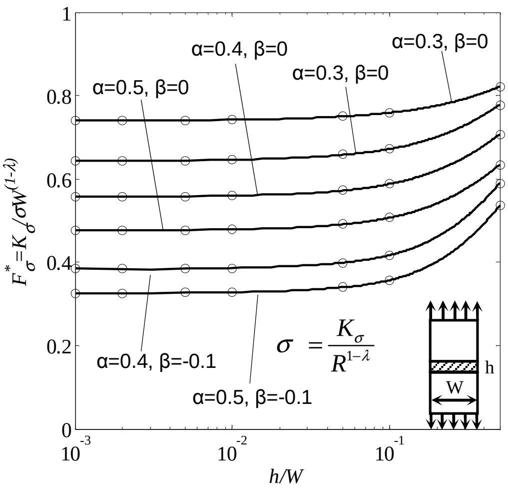

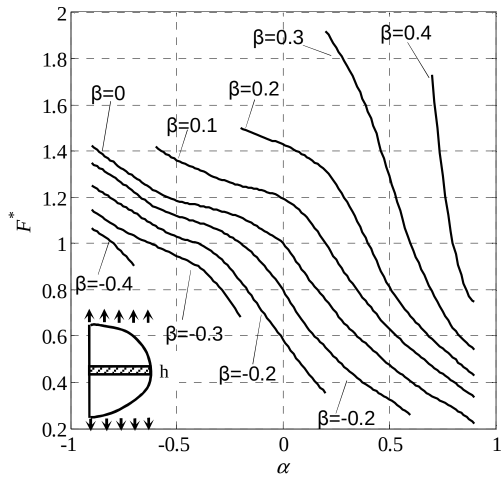

Fig. 4(a) F_σ^* vs. adhesive thickness in Fig. 1 (b)

Fig. 4(b) F_σ^* with varying material combination

3. ANALYSIS ON BONDED CYLINDER AND BONDED PIPE

Here, two extreme solutions are discussed; one is a bonded pipe with $W/R_i \to 0$ in Fig. 1(e), the other is a bonded cylinder equivalent to Fig. 1(d) when $W/R_i \to \infty$. If these two extreme solutions are available under arbitrary material combinations, the authors think general solutions may be conjectured without difficulty.

The singular stresses of the unknown problem in Fig. 1(d) and (e) include the non-singular term σ_{0j}^{AXIL}, τ_{0rz}^{AXIL} and can be expressed as:

$$\sigma_j^{AXIL} = \frac{K_{\sigma_j}^{AXIL}}{R^{1-\lambda}} + \sigma_{0j}^{AXIL} \; (j = r, z, \theta); \quad \tau_{rz}^{AXIL} = \frac{K_{\tau_{xy}}^{AXIL}}{R^{1-\lambda}} + \tau_{0rz}^{AXIL} \tag{4}$$

In our previous paper, the corner stress intensity factor for the bonded strip was analysed accurately, and based on this result, the stress intensity shown in Eq. (4) can be obtained by using the zero element method.

For plane strain problems, the Dunder's parameter α and β can fully control the intensity of singular stress near the end of interface, however, since the bonded pipe and cylinder are axi-symmetric, the corner stress intensity factors cannot be totally dominated by these parameters. Fig.5 indicates an example of the results when (α, β) = (0.8, 0.3). As shown in Fig.5, the range of SIFs is considered when α and β are fixed.

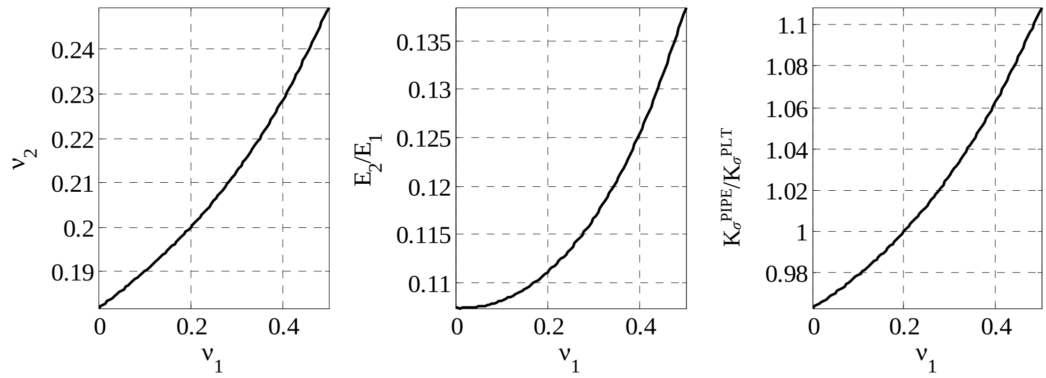

Fig. 5 Stress ratio and material combination varies when (α, β) = (0.8, 0.3)

Although under fixed (α, β) the corner stress intensity factor varies slightly, the maximum value can be used in the design of bonded structures. Therefore in this study the maximum value of the SIF ratio is considered. Fig. 6, and 7 show the results of bonded pipe and bonded cylinder respectively, each curve represents the result of fixed β in the α space.

As shown in the figures, the two problems have similar distributions although the variation of bonded cylinder is larger than that of bonded pipe. And notably, when compared with the result of bonded plate in Fig.2, they all have the similar tendency and distributions, such as the larger value always accompany with large absolute value of β, and all values tend to convergence at approximately 1.

4. CONCLUSIONS

1. For the butt joint, the dimensionless intensity of singular stress F_σ^*, which is controlled by adhesive thickness *h*, tends to be a constant with decreasing adhesive thickness when the ratio $h/W \le 0.005$. The adhesive butt joint can be regarded in a bonded semi-infinite plate if the adhesive layer is thin enough. For a certain value β, it is found that F_σ^* decreases with increasing of α. The material combinations with large α should be used to enhance the interface strength.
2. From the results in Fig.6 and 7, it is found that the maximum value happens when β is 0.4 or -0.4 and α is close to 0.6 or -0.6. And both figure are symmetric, since in the α-β space switching material 1 and 2 (mat. 1↔mat. 2) will only reverse the sings of α and β ((α, β)↔(-α, -β)).
3. Although the results of axis symmetric problems is different from the one of boned plate and cannot be controlled by the Dunder's parameter α and β, they all have similar tendency and distribution.

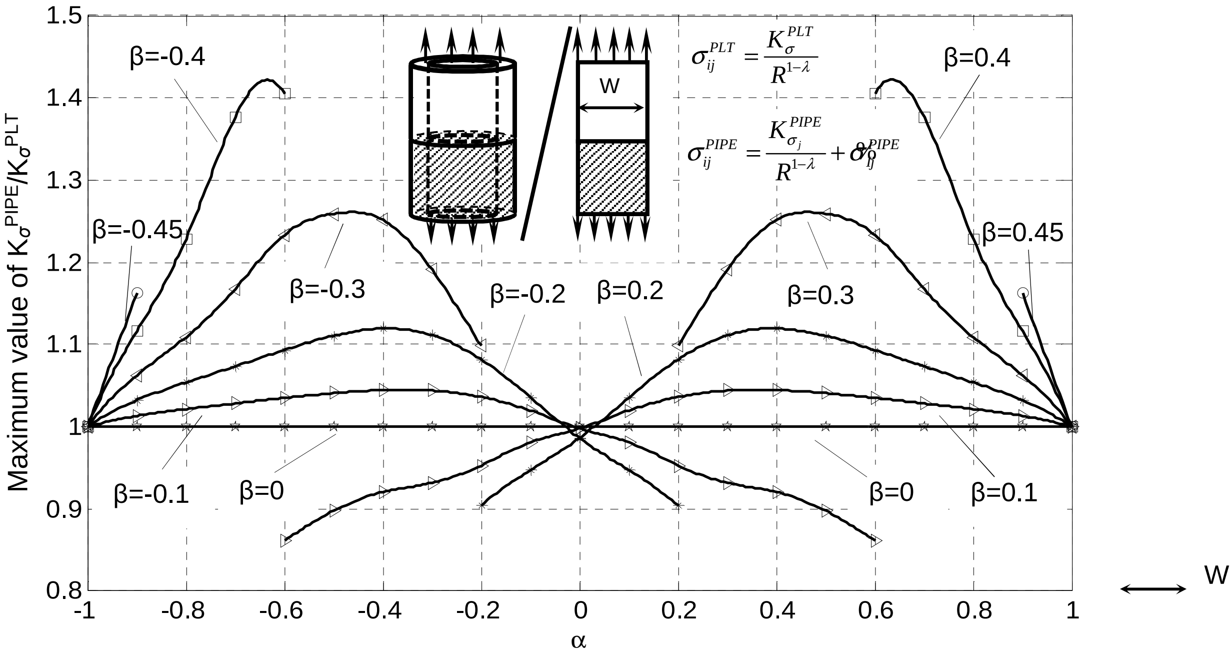

Fig. 6 Maximum value of K_σ^{PIPE}/ K_σ^{PLT} under fixed β when $R_i \to \infty$

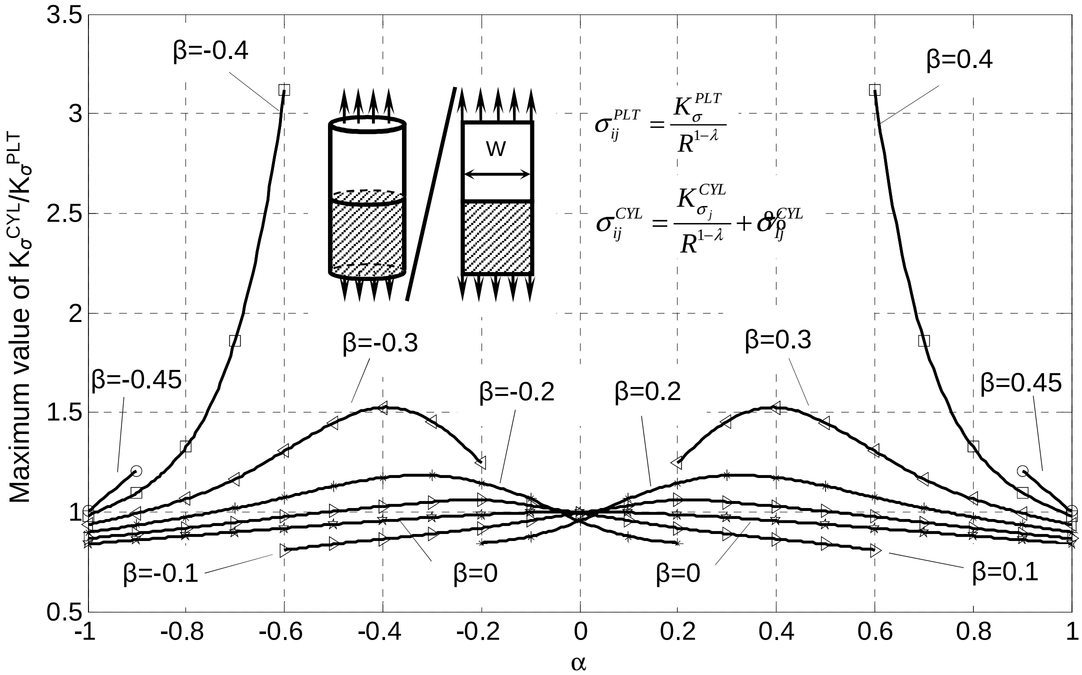

Fig. 7 Maximum value of $K_\sigma^{CYL}/K_\sigma^{PLT}$ under fixed β

5. REFERENCES

[1] Chen, D.H., Nishitani, H., 1993. Intensity of singular stress field near the interface edge point of a bonded strip. Trans. JSME 59, 2682-2686

[2] Noda, N.A, Shirao, R., Li, J. and Sugimoto, J.S., Intensity of Singular Stress at the End of a Fiber under Pull-out Force, International Journal of Solids and Structures, Vol. 44, No.13(2007), pp.4472-4491

[3] Arenas, J., Narbon, J.J., Alia, C. Optimum adhesive thickness in structural adhesives joints using statistical techniques based on Weibull distribution, International Journal of Adhesion&Adhesives, Vol. 30, pp. 160-165, 2010.

[4] Afendi, M., Teramoto, T., Bakri, H. B. Strength prediction of epoxy adhesively bonded scarf joints of dissimilar adherends, International Journal of Adhesion&Adhesives, Vol. 31, pp. 402-411, 2011.

[5] Suzuki, Y. Adhesive Tensile Strengths of Scarf and Butt Joints of Steel Plates, Trans. JSME, Series A, Vol.53, pp. 514-522, 1987.

[6] Hunston, D., Miyagi, Z., Schultheisz, C., Zaghi, S. The sandwich bending specimen for characterizing adhesive properties, Mechanics of Time-Dependent Materials, Vol. 7, pp. 71-88, 2003.

[7] Neves, A.A., Courinho, E., Poitevin, A. Influence of joint component mechanical properties and adhesive layer thickness on stress distribution in micro-tensile bond strength specimens, Dental Materials, Vol. 25, pp. 4-12, 2009.

[8] Zhang, Y., Noda, N.A, Takaishi, K.T, Lan X. Effect of Adhesive Thickness on the Interface of Singular Stress at the Adhesive Dissimilar Joint. Transactions of the Japan Society of Mechanical Engineers Series A ,77(774), 360-372, 2011

[9] Noda, N.A, Miyazaki, T., Uchikoba, T., Li, R., Sano, Y., Takase, Y. Convenient Debonding Strength Evaluation Based on the Intensity of Singular Stress for Adhesive Joints. Journal: Transactions of The Japan Institute of Electronics Packaging, vol. 17, no. 2, pp. 132-142, 2014

[10] Teranishi T, Nisitani H. Determination of highly accurate values of stress intensity factor in a plate of arbitrary form by FEM. Trans JSME 1999;A65:16 – 21.

International Journal of Fracture Fatigue and Wear, Volume 3

Proceedings of the 4th International Conference on
Fracture Fatigue and Wear, pp. 38-42, 2015

RESIDUAL STRESS GENERATION MECHANISM FOR HOT STRIP COMPOSITE ROLLS DURING QUENCHING PROCESS

Kejun Hu[1], Yoshikazu Sano[1*], Nao-Aki Noda[1], Katsma Ono[1] and Chengwei Wu[2]

[1] Department of Mechanical Engineering, Kyushu Institute of Technology, Kitakyushu, Japan
[2]State Key Laboratory of Structural Analysis for Industrial Equipment, Dalian University of Technology, Dalian, China

Abstract: Composite rolls are widely used in hot rolling mill because of the excellent hardness, wear resistance and high temperature properties. During hot rolling process, composite rolls are subjected to heating-cooling thermal cycles from the hot strip contact and water cooling. The thermal stress is added to already existing residual stress. The thermal fatigue cracking appears at roll surface, and the fracture is possible happen in roll centre when the tensile stress exceeds the centre strength. Therefore, residual stress plays an important role in composite roll. In this paper, FEM (finite element method) simulation is performed to investigate the generation mechanism of the residual stress during quenching process. It should be noted that a large number of experimental data of the core and shell materials are utilized for the wide range of temperature considering the quenching process. The results verify that initially the tensile stress appears on the roll surface but finally the compressive stress occurs.

Keywords: Composite roll; Residual stress; Quenching; FEM.

1 INTRODUCTION

Composite roll is composed of high speed steel as shell material, and ductile iron as core material, as shown in Fig.1. This composite roll is characterized of excellent hardness, wear resistance and high-temperature property on the surface, as well as high strength, high toughness in the centre [1]. In addition, composite roll meets the requirements of better product quality, higher productivity and lower production cost for hot steel rolling industry. However, it’s difficult for conventional single material roll to meet these several requirements at the same time. In this way, the composite roll is widely used for hot strip rolling mill. The residual stresses are always introduced into the composite roll affected by temperature gradient and phase transformation during the heat treatment process. During hot rolling process, thermal stresses are caused by cyclic temperature variation due to hot strip contact and water cooling [2]. As a result, the produced thermal stresses add already existing residual stresses at the roll, resulting in thermal fatigue cracking on roll surface and fracture in roll centre. Hence, residual stress plays an important role in composite rolls services life.

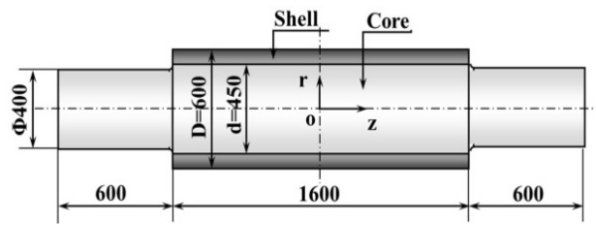

Fig. 1 A schematic diagram of the composite roll (unit: mm)

In previous studies, the residual stress has been evaluated experimentally with a large amount of cost because non-destructive measurement is not possible for large-scale rolls [3]. Meanwhile, a large number of material property data are necessary to calculate the residual stress for composite rolls, which are often difficult to be obtained since the wide ranges of temperature during quenching process. In the past decades, few studies were available for residual stress of composite roll during quenching process. Therefore, the investigation and understanding of stress during heat treatment process is important to improve the quality and reliability for the composite roll. In this study, the numerical simulation using finite element method (FEM) software MSC.Marc2012 is applied to reveal the residual stress during quenching process.

2 GENERATION MECHANISM OF RESIDUAL STRESS FOR SINGLE MATERIAL ROLL

In the first place, by taking an example of single material roll, the residual stress generation mechanism will be considered. Fig.2 shows the simplified single material roll considered in this study. An axisymmetric FEM model is performed, ignoring the phase transformation.

It is known that the axial residual stress σ_z is the most important stress causing roll fracture and spalling during the manufacturing and using process. Therefore, the σ_z residual stress distributions are mainly discussed in this paper. Fig.3 shows the residual stresses σ_z distribution after quenching process. As shown in Fig.3, the compressive stresses appear on the surface, while the tensile stresses appear in the centre. It is seen that σ_z ranges between -115MPa and 101MPa. Both the maximum compressive stress and maximum tensile stress at the central cross section where z=0.

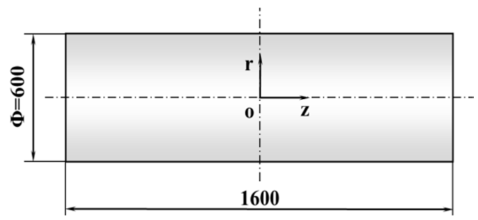

Fig. 2 Model of the single material roll (unit: mm)

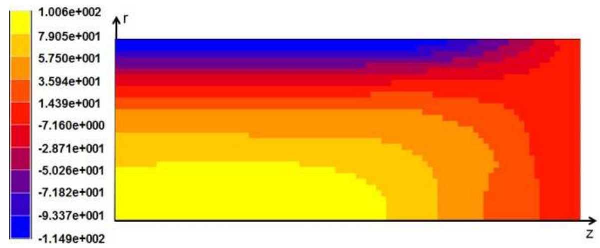

Fig. 3 σ_z of the single material roll after quenching

Fig.4 shows the variation of temperature, residual stress and Young's modulus for the single material roll during quenching process. As is shown in Fig.4, the solid lines represent roll surface and the dotted lines represent roll centre, respectively. Fig.4 (a) shows the temperature history during quenching process. It should be noted that these smooth temperature variation curves are different from the real temperature variation of quenching process, which are simply used to simulate the cooling trend of roll during quenching process. Fig.4 (b) shows the σ_z obtained by the simulation and Fig.4 (c) demonstrates the variations of Young's modulus with the time.

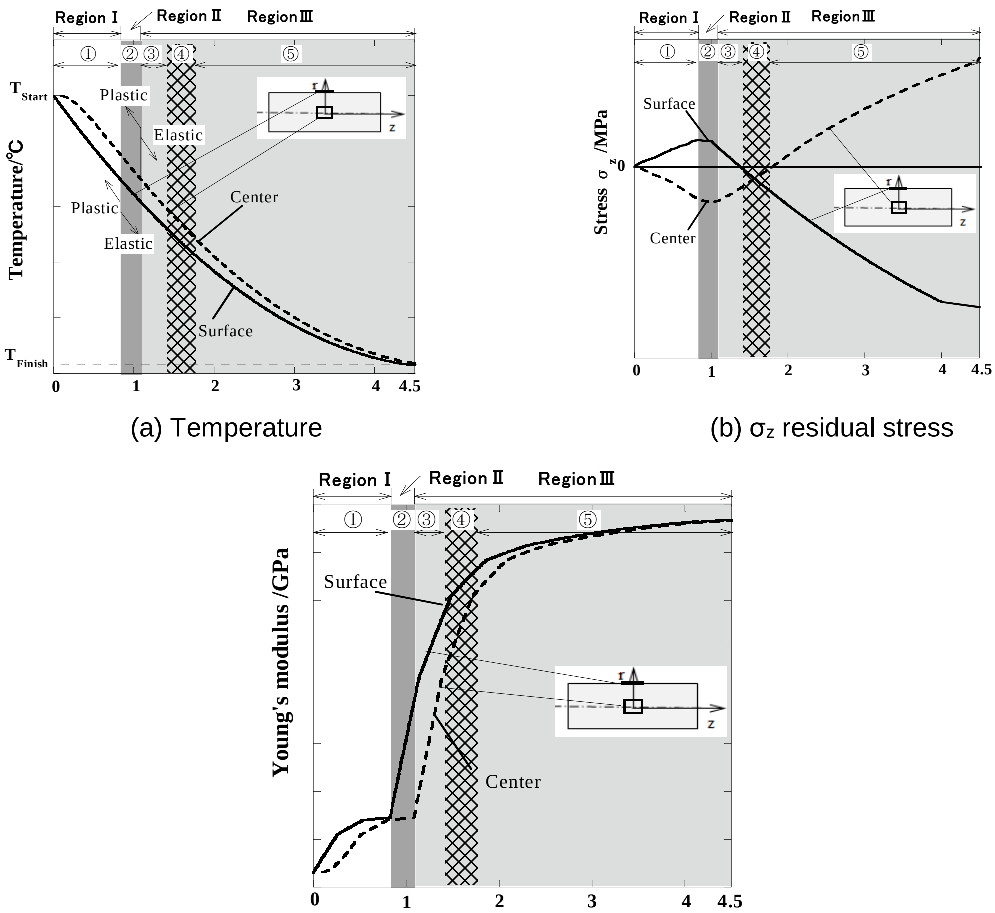

(a) Temperature

(b) σ_z residual stress

(c) Young's modulus

Fig. 4 Residual stress generation mechanism of single material roll

The quenching process can be divided into Region I, Region II and Region□ based on the material state (plastic, elastic-plastic and elastic). Furthermore, these three regions can be separated five regions named as □-□ , which are based on the deformation state and stress state (tensile or compressive). The generation mechanism of residual stress of single material roll during quenching process can be summarized as following.

In Region□, at the beginning of the cooling, the surface temperature drops faster than the centre temperature, leading to the temperature gradient. Afterwards, the roll surface is stretched in the axial direction and result in tensile stress due to the rapid cooling. In order to balance the stresses in the roll interior, the compressive stress is produced in roll centre. With the increase the temperature gradient, the tensile stress on roll surface and the compressive stress in roll centre increase as well continuously.

In Region□, due to the continuous cooling, the roll surface turns to be elastic with the increase of Young's modulus, at the same time, the roll centre is still plastic under the high temperature environments. In this period, the thermal contraction in the centre is restricted because of elastic state on roll surface, resulting in the thermal contraction rate in the centre slowing down. However, the thermal contraction rate in the centre is faster than the rate on the surface, causing the thermal strain differences to decrease. Finally, both surface and centre stresses reach peak values.

In Region □, the thermal contraction rate in roll centre is higher than the rate on roll surface, which cause both surface and centre stresses to decrease, owning to the decrease of thermal contraction difference is shown in the □. As the cooling continues, the surface thermal contraction is approximately equal to the centre thermal contraction, then the stresses state are interchanged from tension to compression and from compression to tension is shown in □. According to region □ and ⑤ in Fig. 4(a), the temperature changes in roll centre is larger than the one on roll surface because the temperature in the centre is higher. Therefore, the centre contraction is larger than the surface thermal contraction, resulting in the tensile stress in roll centre increases and compressive stress increases on roll surface. As is shown in Fig.4(c), since Young's modulus increases in in region Ⅲ and ⑤, the compressive stresses on roll surface increases and tensile stress in roll centre increases at the same time. Eventually, compressive stresses are obtained on the surface and tensile stresses are left in the centre.

3 QUENCHING ANALYSIS OF COMPOSITE ROLL

The composite rolls are manufactured by centrifugal casting method, using high speed steel as outer layer and the ductile iron as inner layer and roll neck, as is shown in Fig.1. The chemical compositions of high speed steel and ductile iron are presented in Table 1, and the material properties at room temperature are given in Table 2.

Table 1 Chemical compositions of high speed steel and ductile iron for composite roll, wt- %

	C	Si	Mn	Ni	Cr	Mo	Co	V	W	Mg	P	S
HSS	1-3	<2	<1.5	<5	2 - 7	<10	<10	3 - 10	<20	<10		
DCI	2.5-4	1.5-3.1		0.4 - 5	0.01-1.5	0.1-1				0.02-0.08	<0.1	<0.1

Table 2 Mechanical property for shell and core at room temperature

Property	Shell	Core
Yield stress /MPa	1282	415
Young's modulus /GPa	233	173
Poisson's ratio	0.3	0.3
Density /kg·m^{-3}	7.6	7.3
Thermal expansion coefficient /K^{-1}	12.6×10^{-6}	13.0×10^{-6}
Thermal conductivity /W(m·K)$^{-1}$	20.2	23.4
Specific heat /J(kg·K)$^{-1}$	0.46	0.46

The heat treatment process of composite roll is given in Fig.5, which includes heating, quenching and tempering. In Fig.5, the whole roll is heated to a uniform temperature of T_{Start} and kept at T_{Start} for some hours, then dropped rapidly to T_{Keep1}. Afterwards, the roll is maintained at T_{Keep1} for several hours, which helps to decrease excessive thermal stresses caused by rapid cooling of surface temperature. After maintained treatment at T_{Keep1}, the roll is transferred into furnace and cooled until temperature drops to T_{Finish}. In this study, only the quenching process is investigated and the tempering process will be studied in the future. To analyse composite roll, the half model is applied to as is shown in Fig.6.

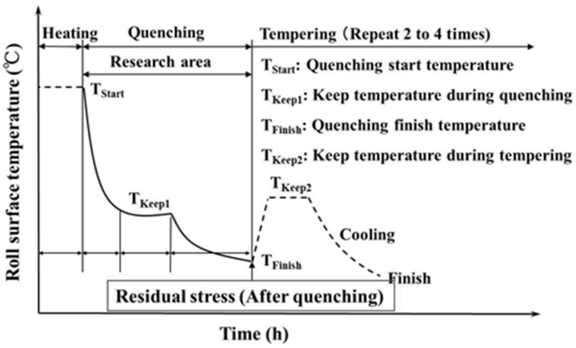

Fig.5 Heat treatment processes for composite roll

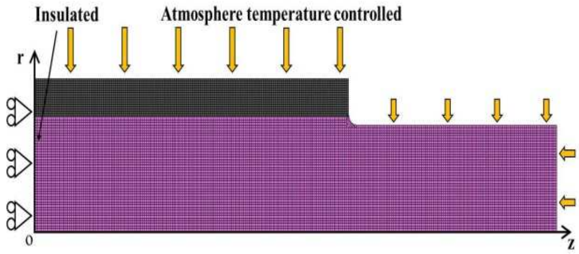

Fig.6 FEM model of composite roll

4 RESULTS AND DISCUSSION OF COMPOSITE ROLL

Fig.7 shows the stress history of composite roll during quenching process. In Region Ⅰ, the roll is cooled from the uniform temperature T_{Start} , in the meantime the surface tensile stress increases continuously because of rapid cooling on the roll surface. In Region Ⅱ, in respect of temperature of T_{EP}, roll surface changes into elastic-plastic from plastic while roll centre is still in elastic. Meanwhile, stress on roll surface moves from tension to compression. After that, thermal contraction in roll centre becomes larger than the one on the surface, resulting in the decrease of compressive stress in the centre. Accordingly, tensile stress on surface has a peak value then reverses to compression. As cooling continues to the temperature $T_{Pearlite}$, pearlite transformation starts from the place that near the interface and expands to the centre. Due to the pearlite transformation, the compressive stress in the centre is reversed to tensile stress rapidly, and jumped back to compressive stress after reaching the peak.

In Region Ⅲ, owing to the high temperature in the roll centre, the roll centre is further contracted, which leads to stresses state interchanged from tension to compression on roll surface and from compression to tension in roll centre. Until cooling to the T_{Keep1}, both surface and centre stresses increase continuously. When keeping at T_{Keep1}, the thermal contraction difference decreases due to the temperature gradient decreasing, contributing to the decrease of stress both surface and centre. At the temperature of $T_{Bainite}$, bainite transformation occurs on surface, causing volumetric expansion, and surface compressive stress increases as followed. To balance the surface compressive stresses in the roll interior, the centre tensile stress also increases. After the bainite phase transformation, the centre thermal contraction becomes larger than surface thermal contraction and the Young's modulus increases with decreasing of temperature. Eventually, both surface and centre residual stresses increase continuously.

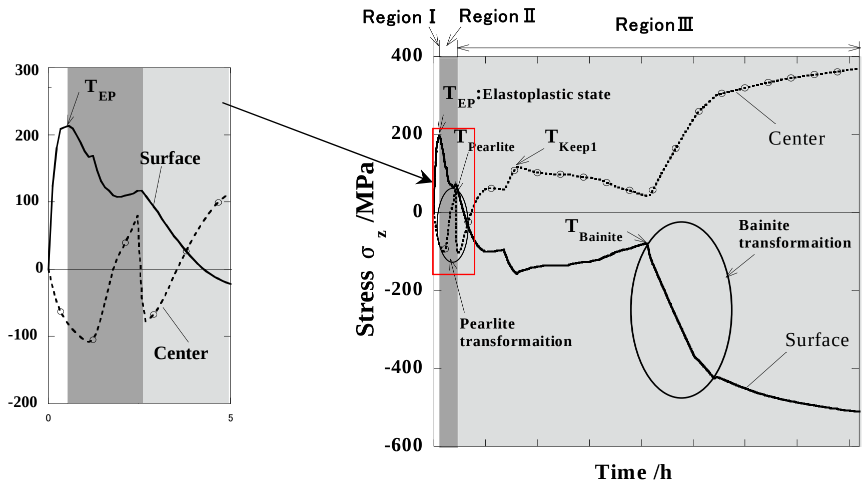

Fig. 7 Residual stress σ_z of composite roll during quenching process

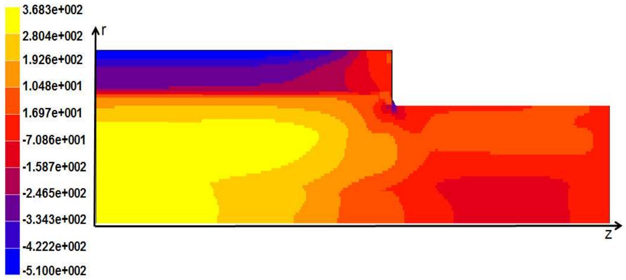

Fig. 8 Distribution of σ_z of composite roll after quenching process

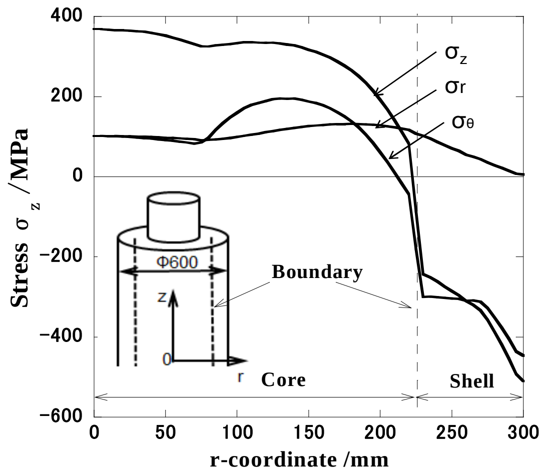

Fig. 9 Distribution of σ_z, σ_θ and σ_r at the central cross section

Fig.8 shows the distribution of σ_z after quenching process. According to the result, the compressive stresses appear on roll surface and the tensile stresses appear in roll centre, which is similar to the single material rolls. It can be found that the residual stresses are much large than the ones of single material roll. Fig.9 shows the distribution of σ_z, σ_θ and σ_r at central cross section where z=0. It can be seen that σ_z range from -510MPa to 368MPa, σ_θ range from -446MPa to 102MPa, σ_r range from 5MPa to 102MPa. This residual stress distribution is similar to the results of alloy roll published by Y. Sano, T. Hattori and M. Haga [4]. However, the maximum tensile stress 368MPa in roll centre is still larger than the previous result and the maximum compressive stress 510MPa on roll surface tends to be larger as well. Differences in previous discussions are mainly resulted from the effect of tempering and the difference of core material.

5 CONCLUSIONS

In this paper, for composite rolls using for hot steel rolling mill, the residual stress distribution during quenching process has been investigated by FEM. The generation mechanisms of residual stress for single material roll and composite roll have been discussed. The results of current study can be summarized as follows.

(1) Prediction of residual stress of composite roll during quenching is realized by FEM with low cost, high accuracy and efficiency compared to experimental measurement. The compressive stress appears at the shell while the tensile stress appears at the core.

(2)The generation mechanism of residual stress during quenching process has been discussed and summarized, which is beneficial for understanding and controlling the residual stress.

Considering the effects of subsequent tempering and the difference of inner material, the simulation result of residual stress are large than the result of alloy roll published in previous. Therefore, the effect of terming process should be discussed and investigated in the future studies.

6 REFERENCES

[1] M. Shimizu, O. Shitamura, S. Matsuo, T. Kamata and Y. Kondo: 'Development of high performance new composite roll', *ISIJ International*, 1992, **32**, (11), 1244-1249.

[2] D. Benasciutti, E. Brusa and G. Bazzaro: 'Finite elements prediction of thermal stresses in work roll of hot rolling mills', *Procedia Engineering,* 2010, **2** (1), 707-716.

[3] P. J. Withers and H. K. D. H. Bhadeshia: 'Residual stress. Part 1–measurement techniques', *Material Science Technology,* 2001, **17**, (4), 355-365.

[4] Y. Sano, T. Hattori and M. Haga: 'Characteristics of High-carbon High Speed Steel Rolls for Hot Strip Mill', *ISIJ International*, 1992, **32**, (11), 1194-1201.

International Journal of Fracture Fatigue and Wear, Volume 3
Proceedings of the 4th International Conference on
Fracture Fatigue and Wear, pp. 43-49, 2015

FATIGUE STRENGTH EVALUATION FOR BOLT-NUT CONNECTIONS HAVING SLIGHT PITCH DIFFERENCE CONSIDERING INCOMPLETE THREADS OF NUT

Yasushi Takase[a], Nao-Aki Noda[a], Xin Chen[a,b], Yoshikazu Sano[a],
Ryota Fujisawa[a], Hikaru Maruyama[a] and Magd Abdel Wahab[b]

[a]Department of Mechanical Engineering, Kyushu Institute of Technology,Kitakyushu 804-8550, Japan
[b]Department of Mechanical Construction and Production, Faculty of Engineering and Architecture,
Ghent University, 9000 Ghent, Belgium

Abstract: The high strength bolts and nuts are widely used in various fields. In this study the effect of slight pitch difference is considered when the nut pitch is α μm larger than the bolt pitch. In the first place, the fatigue experiment is conducted with varying pitch difference. The results show that the fatigue life is extended to about 1.5 times by introducing the suitable pitch difference under the high stress amplitude. Next, the detail observation is performed on the fractured specimens including the fractured positions and the crack configurations. It is found that the fractured positions and the crack distributions vary depending on the pitch difference. Finally, to clarify the improvement mechanism of the fatigue strength, the finite element method is applied to calculate the stress amplitude and mean stress at each bolt threads, and the incomplete threads at the nut ends are also considered to obtain the accurate analytical results.

Keywords: Bolt-Nut connections, Pitch Difference, Fatigue Life, Finite Element Analysis

1 INTRODUCTION

Bolt-nut connections are commonly used in engineering structures due to the advantages they offer, such as the ability of clamping, and the ease of disassembly for maintenance or repair. However, fatigue failure problems of bolt are always of concern. High stress concentration factors always occur at the root of bolt thread and it is not easy to improve the fatigue strength of screws. Most previous studies are focusing on the anti-loosening performance for newly developed bolt and nut [1-3].

The effect of the thread shape on the fatigue life of bolt has been investigated [4-6]. A previous study indicated that the fatigue strength may be improved depending on the pitch error [7]. Our previous experiment clarified that the fatigue life is improved by introducing suitable pitch difference under a certain level of stress amplitude [8].

As further work, in the present study, two types of specimens will be investigated systematically, including the standard bolt-nut connections and the connections having a slight pitch difference α. Figure 1 shows the schematic diagram of bolt and nut connection. First, the fatigue experiment will be carried out for the two types of specimens with varying stress amplitude systematically. Afterwards, the fractured specimens will be investigated. Finally, to clarify the improvement mechanism of the fatigue strength, the finite element analysis will be applied to calculate the stress amplitude and mean stress at each bolt threads. In order to obtain the accurate analytical results, the longitudinal section of nut specimen was investigated as shown in Fig. 2. It's noticeable the incomplete end threads may have an effect on the contact status between bolt and nut, therefore, we will pay attention to the incomplete threads of nut in the FE analysis.

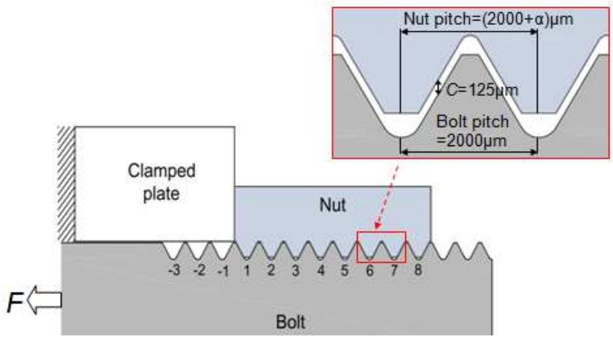

Fig. 1 Schematic diagram of bolt-nut connection

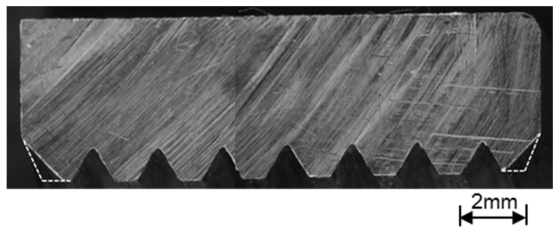

Fig. 2 Incomplete threads at nut ends

2 EXPERIMENTAL SET-UP

2.1 Materials

In this study, the Japanese Industrial Standard (JIS) M16 bolts and nuts are employed. The strength grade of bolt and nut is 8.8 and 8, respectively. Table 1 presents the material property of bolt and nut. The standard M16 bolt and nut have the same pitch dimension as 2000 μm. Herein, the nut pitch is assumed to be (2000+α) μm, and α is named as pitch difference. Motivated by the results of previous study, two types of pitch differences, i.e. α=0 (standard bolt nut connection) and $\alpha=\alpha_m$ are considered in this study. The clearance between bolt and nut has a standard dimension as 125 μm as shown in Fig. 1.

Table 1 Material Property of Bolt and Nut

	Young's modulus (GPa)	Poison's ratio	Yield strength (MPa)	Tensile strength (MPa)
SCM435 (Bolt)	206	0.3	800	1200
S45C (Nut)	206	0.3	530	980

2.2 Fatigue tests

The fatigue experiment is conducted by using 392 kN Servo Fatigue Testing Machine. A series cyclic loading were applied to the specimens. Table 2 summarizes the experimental loading conditions and the corresponding stress with considering the bottom cross sectional area of bolt as A_R=141 mm^2. The cycling frequency of the loadings is 8 Hz.

2.3 Experimental Results

Figure 3 shows the fractured specimens which underwent a stress amplitude of σ_a=100 MPa. For the standard bolt-nut connection, it is confirmed that the fracture always occurs at the bottom of thread No.1. For the specimens of $\alpha=\alpha_m$, the fracture takes place nearby No.1 thread, and the fracture surface shows noticeably different characteristics.

Table 2 Experimental loading conditions

Load (kN)		Stress (MPa)	
Mean load	Load amplitude	Mean stress	Stress amplitude
30	22.6	213	160
30	18.3	213	130
30	14.1	213	100
30	11.3	213	80
30	8.5	213	60
30	7.1	213	50

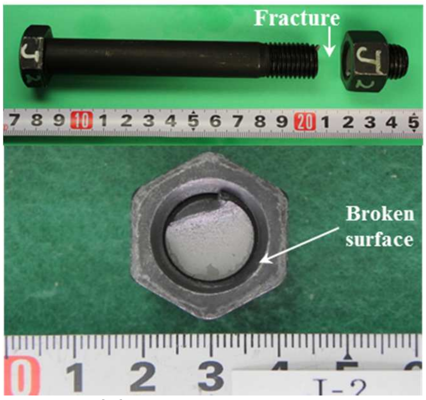

(a) $\alpha=0$, σ_a=100MPa

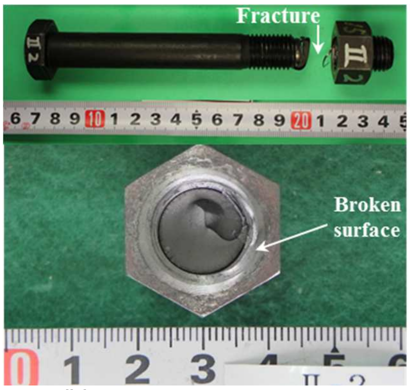

(b) $\alpha=\alpha_m$, σ_a=100MPa

Fig. 3 Fractured specimens

The S-N curves with fatigue limit at N=2×10^6 stress cycles are obtained as depicted in Fig.4. It is found that the pitch differences effects the fatigue life significantly. When the stress amplitude is above 80 MPa, the fatigue life for $\alpha=\alpha_m$ is about 1.5 times of the standard bolt-nut connections (α=0). However, near the fatigue limit, the fatigue lives of the two types of specimens are similar, and the fatigue limits remain at the same value of 60 MPa.

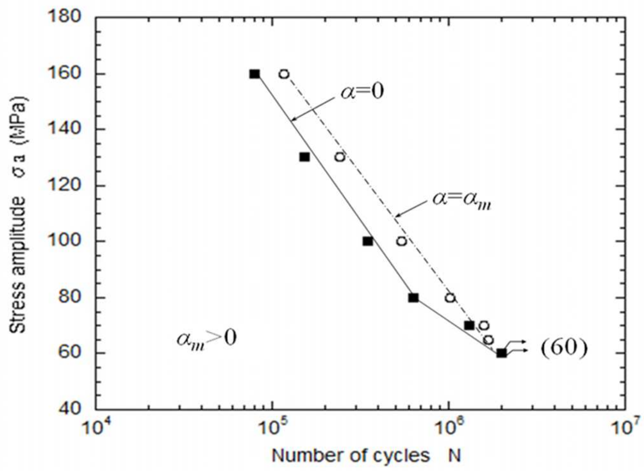

Fig. 4 S-N curves

3 CRACK OBSERVATION

Figure 5 and Figure 6 show the observed trajectory of cracks along the longitudinal cross section of the specimens at the fatigue stress amplitudes σ_a=60 MPa and 100 MPa. For the standard bolt-nut connections, it can be seen that the initial crack may occur at thread No.2, and final fracture happens at No.1 thread. For $\alpha=\alpha_m$, the initial crack may start at No.5 thread or No.6 thread, extending toward thread No.1 and finally fracture happen nearby thread No.1. From the S-N curves and the observations of crack trajectories, we can conclude that the fatigue life of the bolt-nut connections may be extended by introducing a pitch difference because the changes in crack propagation trajectory may take place.

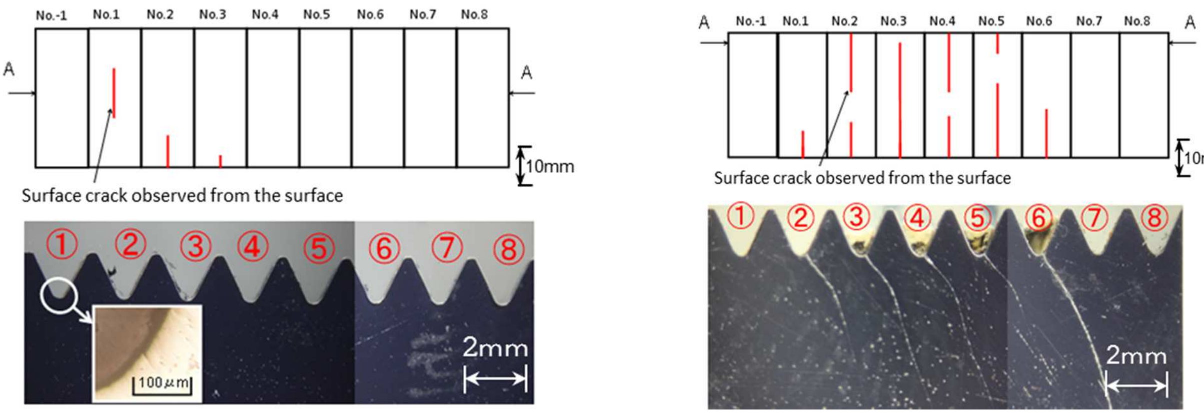

(a) α=0 (b) $\alpha=\alpha_m$

Fig. 5 Crack configuration observed from the surface and at the longitudinal section of the bolt when σ_a=60MPa

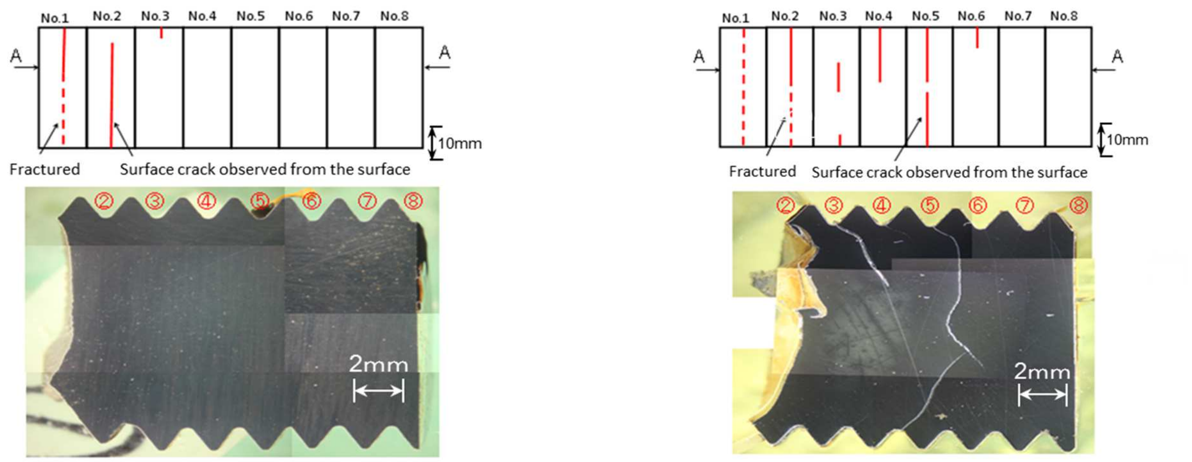

(a) α=0 (b) $\alpha=\alpha_m$

Fig. 6 Crack configuration observed from the surface and at the longitudinal section of the bolt when σ_a=100MPa

4 FINITE ELEMENT ANALYSIS

To analyse the stress at the bolt threads, the axisymmetric model of the bolt-nut connection is created by using FEM code MSC.Marc/Mentat 2012. The elastic-plastic FE analysis is performed. The multifrontal sparse solver is used. Friction coefficient of 0.3 is entered in contact table and Coulomb friction is used.

Considering the incomplete threads of nut shown in Fig. 2, here, the complete thread model and the incomplete thread model are created as shown in Fig. 7. In accordance with the experimental specimens, two types of pitch differences, i.e. α=0 and $\alpha=\alpha_m$ are analysed by using both the complete thread model and incomplete thread model. At the roots of bolt threads a very fine mesh with a minimum size of 0.01mm is used. The clamped plate is fixed in the horizontal direction and the bolt head is subjected to cyclic load F. For each bolt thread from No.-2 thread to No.8 thread, the maximum stress amplitude and the mean stress are investigated at the point where the maximum stress amplitude appears. According to these stress components, the endurance limit diagrams are obtained to evaluate the relative danger level of the bolt threads. Figure 8 shows the endurance limit diagrams analysed by using the complete thread model when the load F=30±14.1kN. In the endurance limit diagram, the Soderberg line is plotted. It should be noted that because of the stress gradient, the maximum stress amplitude for fracture of notched specimens is always larger than that of the plain specimens. Therefore, the stress data plotted beyond the Soderberg line does not represent the real fracture at the bolt thread.

For α=0, Fig. 8 (a) indicates that thread No.1 has the highest stress amplitude. On the other hand, for $\alpha=\alpha_m$, Fig. 8 (b) shows that No.7 and No.8 thread become more dangerous. However, these analytical results do not correspond to the crack observation results very well, because the crack may initiate at No.2 thread for α=0, and large crack occurs at No.5 thread for $\alpha=\alpha_m$ when σ_a=100 MPa as illustrated in section 3.

Figure 9 shows the endurance limit diagrams analysed by using the incomplete thread model. For α=0, thread No.2 becomes the most dangerous thread in accordance with the observed crack. For $\alpha=\alpha_m$, the stress amplitude at No.6 thread increases while that at No.7 thread decreases, and these results become more closer to the crack configuration in Fig.6 (b) where the large crack occurs at No.5 thread.

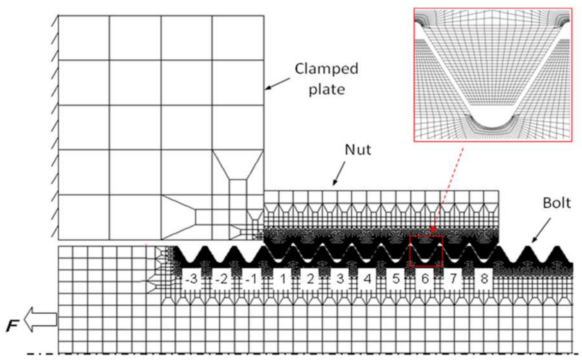

(a) Complete thread model

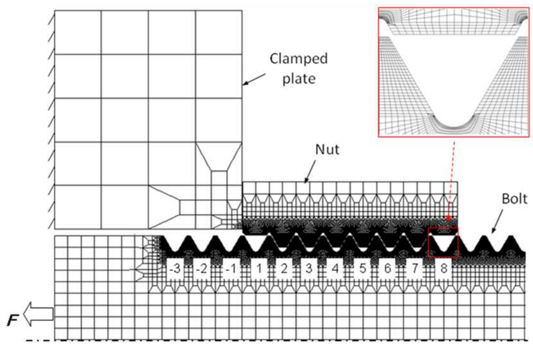

(b) Incomplete thread model

Fig. 7 Axi-symmetric finite element model of bolt-nut connection

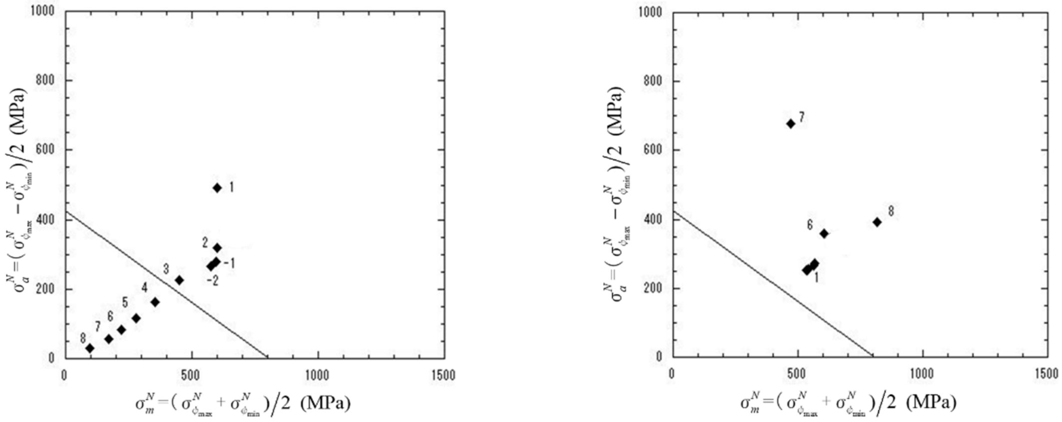

(a) α=0 (b) $\alpha=\alpha_m$

Fig. 8 Endurance limit diagram, σ_a=100MPa (Complete thread model)

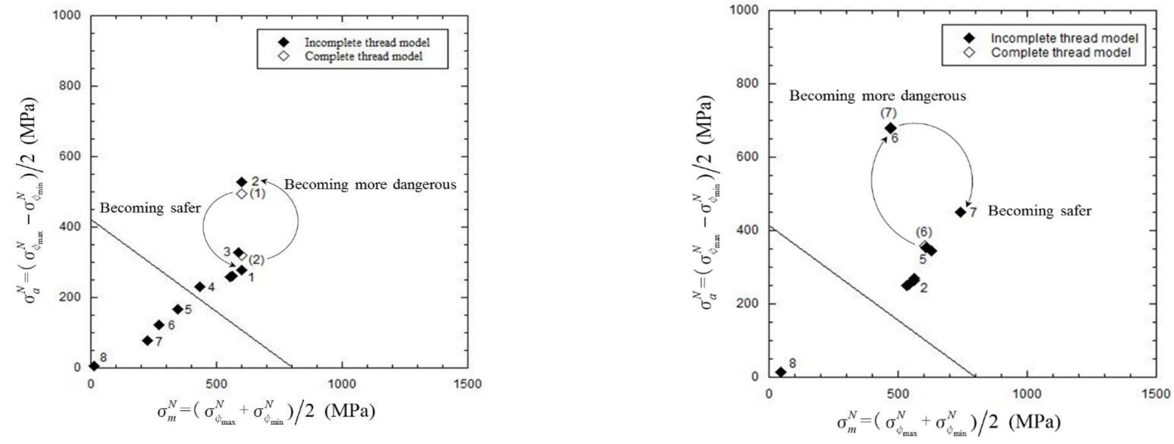

(a) α=0 (b) $\alpha=\alpha_m$

Fig. 9 Endurance limit diagram, σ_a=100MPa (Complete thread model vs Incomplete thread model)

5 CONCLUSIONS

A slight pitch difference α is considered between the M16 bolt-nut connections. The fatigue experiment has been conducted for two types of pitch difference, i.e. α=0 and $\alpha=\alpha_m$. The stress amplitude and mean stress at each bolt threads have been numerically analysed using the finite element method with considering the incomplete threads of nut. The conclusions can be summarized as follows:

(1) For α=0, the incomplete thread model explains that the crack initiates at No.2 thread as shown in Fig. 9 (a).

(2) For $\alpha=\alpha_m$, the incomplete thread model explains the crack initiates at No.5 or No.6 threads as shown in Fig. 9 (b).

6 REFERENCES

[1] Hard Lock Industry KK, Looseness Preventing Nut, Patent Abstracts of Japan, Publication No.: 2002–195236, 2002-7-10.

[2] Izumi, S., Yokoyama, T., Teraoka, T., Iwasaki, A., Sakai, S., Saito, K., Nagawa, M., Noda, H.,Verification of anti-loosening performance of super slit nut by finite element method, Transaction of the Japan Society of Mechanical Engineers, Series A, Vol.71, No.703(2005), pp.380-386 (in Japanese).

[3] Xiao, Y., Kuhara, M., Noda, N.-A., Saito, K., Nagawa, M. and Yumoto, A., Optimum dimensions of thin walled tube on the mechanical performance of super stud bolt, Transaction of the Japan Society of Mechanical Engineers, Series A, Vol.74, No.743(2008), pp.954-960 (in Japanese).

[4] Kawahara, S., et al., A study on the thread shape of the high strength bolt, Summaries of technical papers of annual meeting Architectural Institute of Japan, (1990), pp.1545-1546 (in Japanese).

[5] Nishida, S-I., Urashima, C., and Tamasaki, H., A new method for fatigue life improvement of screws, European Structural Integrity Society, No.22(1997), pp.215-225.

[6] Xiao, Y., Wan, Q., Noda, N.-A., Akaishi, Y.-I., Takase, Y. and Nishida, S.-I., Stress reduction effect of tapering thread bolts and nuts which have slightly different pitches, Transactions of Society of Automotive Engineers of Japan, Vol.42, No.4(2011), pp.927-933 (in Japanese).

[7] Maruyama, K., Stress analysis of a bolt-nut Joint by the finite element method and the copper-electroplating method (3rd report), Transaction of the Japan Society of Mechanical Engineers, Vol.19, No.130(1976), pp.360-368.

[8] Akaishi, Y.-I., Chen, X., Yu, Y., Tamasaki, H., Noda, N.-A., Sano, Y. and Takase, Y., Fatigue strength analysis for bolts and nuts which have slightly different pitches considering clearance, Transactions of Society of Automotive Engineers of Japan, Vol.4, No.44(2013), pp.1111-1117 (in Japanese).

Proceedings of the 4th International Conference on
Fracture Fatigue and Wear, pp. 50-56, 2015

EFFECT OF SPECIMEN-THICKNESS ON FATIGUE CRACK CLOSURE BEHAVIOR IN A7075-T6 ALLOY

K. Masuda[1], S. Ishihara[2], M. Okane[2] and S. Nishino[3]

[1] University of Toyama, Toyama, Japan
[2] National Institute of Technology, Toyama College, Toyama, Japan
[3] National Institute of Technology, Anan College, Anan, Japan

Abstract: In this study, fatigue tests were conducted on aluminium alloy 7075-T6 to study fatigue crack growth and crack closure behaviour of the material. The experiments included the determination of the crack-opening levels K_{op} as a function of ΔK, the rate of fatigue crack growth da/dN as a function of ΔK_{eff}, where ΔK_{eff} ($=K_{max}$-K_{op}) is the effective stress intensity factor range. In addition, a change in the value of K_{op} due to the specimen-surface removal and a crack front shape were also investigated. It was concluded that the aluminium alloy 7075-T6 exhibits plasticity-induced fatigue crack closure. Moreover, the specimen thickness effect on the crack closure behaviour was also investigated. It was concluded that the crack-opening levels decreased with increasing the specimen thickness. The crack growth rates and crack opening behaviour were in good agreement with similar results in the literature.

Keywords: Fatigue crack; Crack propagation; Crack closure; Specimen thickness, Aluminium alloy

1 INTRODUCTION

Crack closure has been accepted as a phenomenon in fatigue crack propagation. Especially the changes of crack opening levels have a significant effect on crack growth rates. Therefore it is necessary to evaluate the crack opening values exactly to predict the fatigue life. In many materials, crack closure can occur while the force is above the minimum force in the cycle even when the minimum force is tensile. After reloading from the minimum force, some increment of tensile loading must be applied before the crack is fully open.

In the 1970s, Elber [1, 2] introduced the important topic of fatigue crack closure into the literature and showed by means of experiments with the aluminum alloy 2024-T3 (yield strength [YS] = 350 MPa) that at a given R value, the crack-opening level increased with ΔK. Similar results have been obtained with other low- and medium-strength aluminum alloys. This type of crack closure is referred to as plasticity-induced fatigue crack closure (PIFCC), and Elber proposed that PIFCC was caused by the residual stretch of material present in the wake of the crack tip. Soon after Elber's initial studies, other forms of crack closure were found, including a type of material-related crack closure now known as roughness-induced fatigue crack closure (RIFCC). In this type of crack closure, the crack-opening level in the macro crack range is constant and independent of the ΔK level, in contrast to PIFCC. Schivje in his review article on crack closure [3] pointed out that the crack-opening level at the surface of a plane specimen, the plane-stress region, is higher than in the interior plane-strain region.

Newman et al. [4] found that the aluminum alloy 7075-T6 showed PIFCC behavior. Figure 1(a) shows the relations of ΔK, ΔK_{eff} and da/dN for Newman's results [4]. Based on Fig. 1(a), the K_{op} level can be derived as shown in Fig. 1(b). As can be seen from the figure, the crack-opening level increases with ΔK. This experimental result indicates that PIFCC controls the crack closure behavior in this material.

Matos et al. [5] investigated the influence of specimen thickness on closure behavior by using the aluminum alloy 6082-T6. They showed that the crack-opening levels K_{op} for the thick specimens are lower than those for the thin specimens.

Purpose of this study is to investigate the thickness effect on crack closure behavior of the aluminum alloy 7075-T6. Surface removal test and crack front observation are conducted for further consideration.

2 MATERIAL, SPECIMEN AND EXPERIMENTAL PROCEDURES

The material tested was the aluminum alloy 7075-T6. Its chemical compositions and mechanical properties are listed in Tables 1 and 2, respectively.

ASTM-type compact specimens [6] were used for the crack growth studies. Figure 2 shows the geometric shape of the specimen. The specimens with W equal to 57.2 mm was used in the tests. The fatigue crack growth (FCG) tests were carried out in a servo controlled hydraulic test system under load control condition in laboratory air at room temperature under stress ratio of R = 0.1. The test frequency was 15 Hz. Crack lengths were measured using the replication technique. The elastic compliance method was used for a determination of the crack-opening level. In the current study, the elastic compliance method using the subtracted strain was used to improve the sensitivity and precision of the determination of the crack-opening load.

In the surface-removal experiments, a fatigue crack was propagated under a constant stress-intensity factor range ΔK. After reaching the steady-state level of fatigue crack closure, the specimen was taken from the fatigue testing machine, and then specimen surfaces were removed by 0.5 mm each using an electric discharge machine. After surface removal, the fatigue crack propagation test was resumed and the K_{op} level was determined anew.

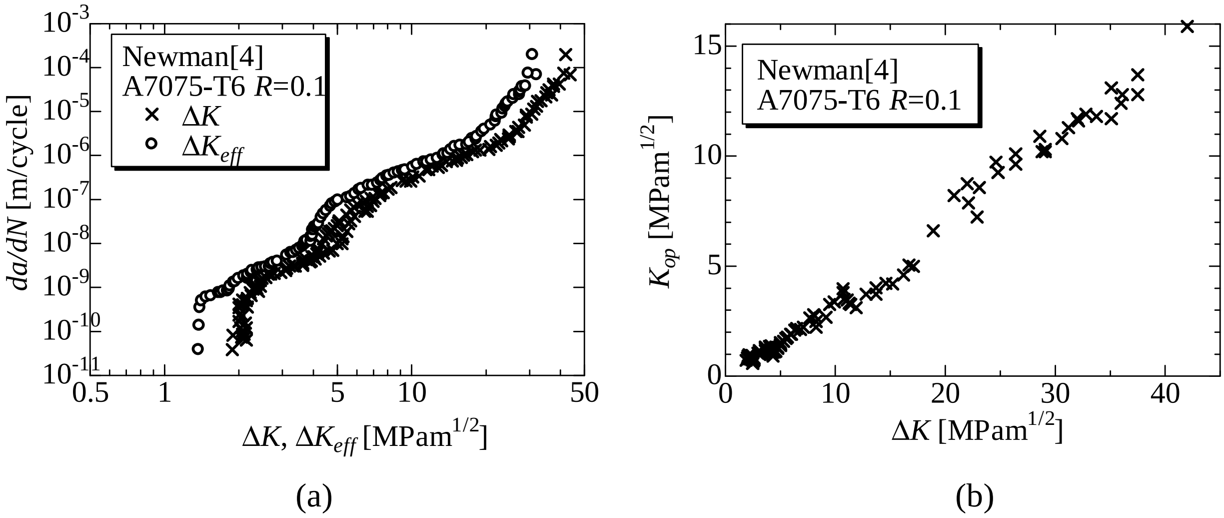

Fig. 1 Newman's results [4] for: *da/dN* vs. ΔK, ΔK_{eff} relations; (b) K_{op} vs. ΔK relation.

Table 1 Chemical compositions of the material used (wt %)

Si	Fe	Cu	Mn	Mg	Cr	Zn	Ti	Al
0.4	0.5	1.6	0.3	2.5	0.24	5.5	0.2	Bal.

Table 2 Mechanical properties of the material used

Yield strength	Tensile strength	Young's modulus	Elongation
510 MPa	577 MPa	70 GPa	12%

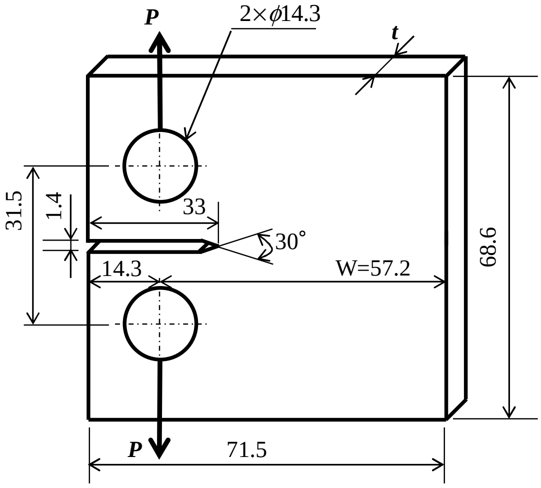

Fig. 2 Geometric shape of the specimen.

3 EXPERIMENTAL RESULTS AND DISCUSSION

3.1 Fatigue Crack Propagation and Crack Closure

Figure 3 shows the comparison between present results and Newman's results for Δ*K* and *da/dN* relation. Right side figure is an extended figure of the left one. Newman's specimen thickness is 5.7 mm, and our specimen thicknesses are 6.0 mm and 11.0 mm. As you can see, the present results are in good agreement with Newman's results. Moreover, the thickness effect in Δ*K* and *da/dN* relation is little.

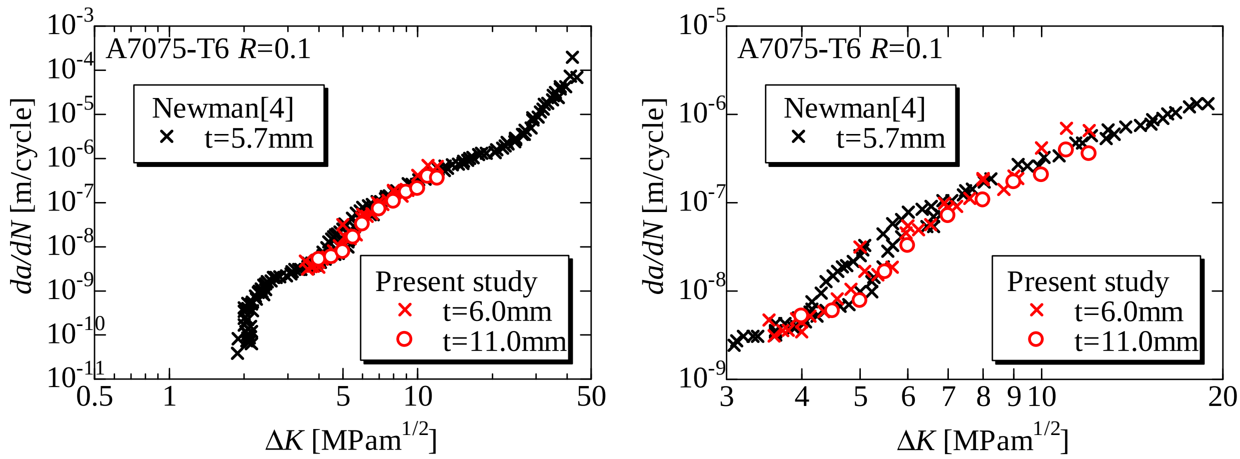

Fig. 3 Comparison between present results and Newman's results for Δ*K* and *da/dN* relation.

Figure 4 shows the comparison between present results and Newman's results for Δ*K* and K_{op} relation. Right side figure is an extended figure of the left one. As can be seen from the figure, the crack-opening level increases with Δ*K* in accord with Newman's findings, which confirms that PIFCC is dominant in these tests (t = 6 mm and 11 mm). From the right-side figure of Fig.4, the value of Kop decreases with an increase in the specimen thickness at the constant Δ*K* condition.

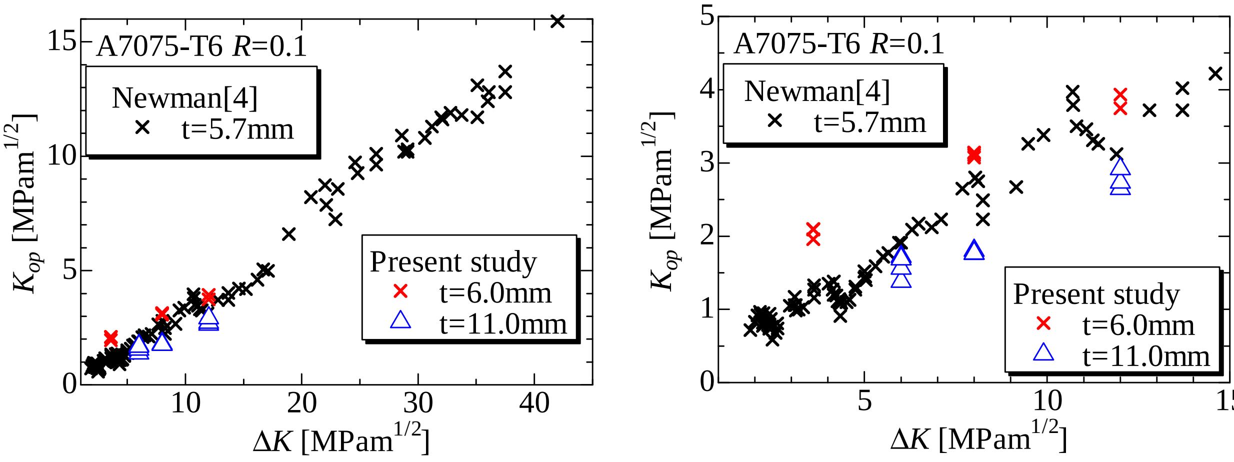

Fig. 4 Comparison between present results and Newman's results for ΔK and K_{op} relation.

Figure 5 shows the relation between specimen thickness t and P_{op}/ P_{max} at the constant ΔK level of 12 MPam$^{1/2}$, where P_{op} is the load at the crack-opening level and P_{max} is the maximum load, respectively. In this figure, Matos's results for the aluminium alloy 6082-T6 are also included for a comparison purpose.

As can be seen from the figure, the crack-opening level P_{op}/ P_{max} (=K_{op}/ K_{max}) decreases with increasing the specimen thickness (t = 6 mm to 11 mm). This present result is common with Matos's one.

Figure 6 show the comparison between the present results and Newman's results for ΔK_{eff} and da/dN relation. As you can see, the present results (t = 6.0 mm) are in good agreement with Newman's results (t = 5.7 mm). It seems that the fatigue crack growth da/dN decreases with increasing the specimen thickness. However, our previous studies with A6061 and JIS S25C [7] and Matos with A6082-T6 [5] showed that the relation of da/dN and ΔK_{eff} does not depend on specimen thickness. So, further study is needed to clarify and to confirm on this point for the present material A7075-T6. FCG tests using specimens with 1 mm and 21 mm thicknesses are preparing for the above purpose, and the results will be reported soon.

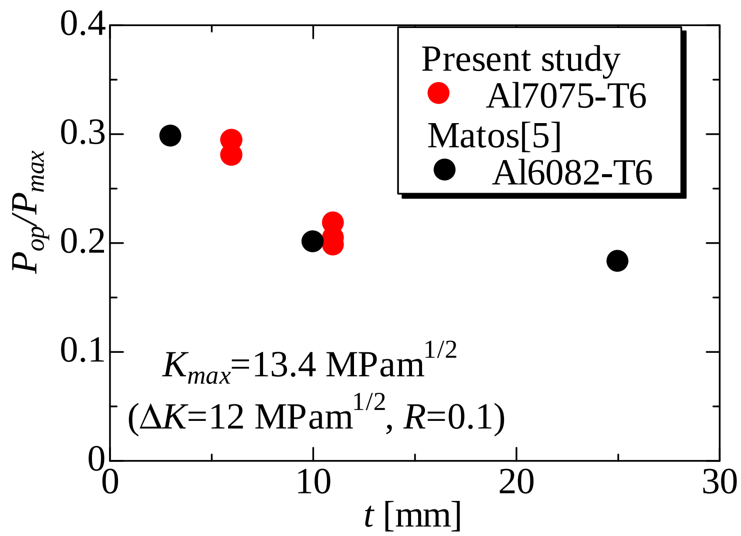

Fig. 5 Comparison between present results and Matos's results for t and P_{op}/ P_{max} relation.

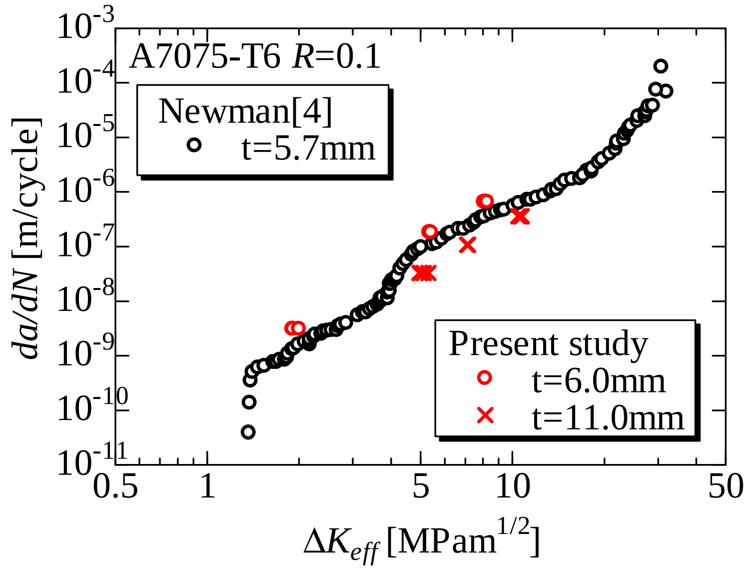

Fig. 6 Comparison between present results and Newman's results for ΔK_{eff} and *da*/*dN* relation.

3.2 Effect of Surface Removal

In this experiment a fatigue crack was grown in a specimen thickness of 6 mm at a ΔK level of 8.0 MPam$^{1/2}$. The specimen was then removed from the testing machine, and 0.5 mm was removed from each specimen surface by electro discharge machining. Then both surfaces were electro polishing. After the surface removal, the crack was advanced further by cyclic loading and crack closure levels were determined. Figure 7 shows how the crack-opening level, K_{op}, varied with crack length, both before and after surface removal.

This result showed a marked effect of surface removal on the crack-opening level of A7075-T6, with the crack closure level at the surface being 1.0 MPam$^{1/2}$ higher than that in the interior. Because A7075-T6 with the specimen thicknesses, 6 mm and 11 mm exhibits PIFCC as shown in Fig. 4, the plane-stress plastic zone at the specimen surface is an important factor in PIFCC [7]. Surface removal test helps understanding of that the crack-opening level K_{op} decreases with increasing of the specimen thickness.

Specimen thickness has an effect on the ratio of surface region and interior. In other word, degree of the surface region effect decreases with increasing the specimen thickness. It is interesting to investigate which patterns (PIFCC or RIFCC) occurs for the case of the thick specimen 21 mm of the present A7075-T6.

3.3 Shape of the Crack Front

For identifying the crack front in the specimen interior, the following procedure was used. At first, the cracks were grown in a specimen thickness of 6 mm at constant ΔK level of 9.0 MPam$^{1/2}$. Then, the specimen was dipped in penetrating dye. After that, the cracks were again grown at constant ΔK level until the failure of the specimen. Figure 8 is a macroscopic view of the fracture surface of the specimen, where the shape of the crack front is indicated in red. It can be observed that because of a higher degree of PIFCC in the aluminum alloy A7075-T6 with a thickness of 6mm, the crack length at the surface is less than in the interior.

4 CONCLUSIONS

In this study, fatigue tests were conducted on aluminium alloy 7075-T6 to study the effect of the specimen thickness on the fatigue crack growth and crack closure behaviour of the material. The following conclusions are reached;

(1) The crack-opening level K_{op} for the specimens with 6 and 11 mm thicknesses increases linearly with the stress intensity factor range, ΔK. This result indicates that A7075-T6 with the specimen thicknesses, 6 mm and 11 mm exhibits the plasticity induced fatigue crack closure (PIFCC) behaviour.

(2) The crack-opening level K_{op} decreases with increasing the specimen thickness from 6mm to 11 mm.

(3) An effect of surface removal on the crack-opening level K_{op} was observed for the 6 mm thick specimen. After removal of the specimen surface, the crack-opening level dropped about 1.0 MPam$^{1/2}$ and then recovered to its original value while propagating.

(4) The crack length at the specimen surface is less than in the interior for the case of the 6 mm thick specimen. This is due to higher crack-opening level K_{op} at the specimen surface than that at the specimen interior.

(5) In the present study, fatigue tests were conducted on specimens with 6 and 11 mm thicknesses. Further FCG study is guaranteed using thicker specimen. It is interesting to investigate which patterns (PIFCC or RIFCC) occurs for the case of the thick specimen of the present A7075-T6.

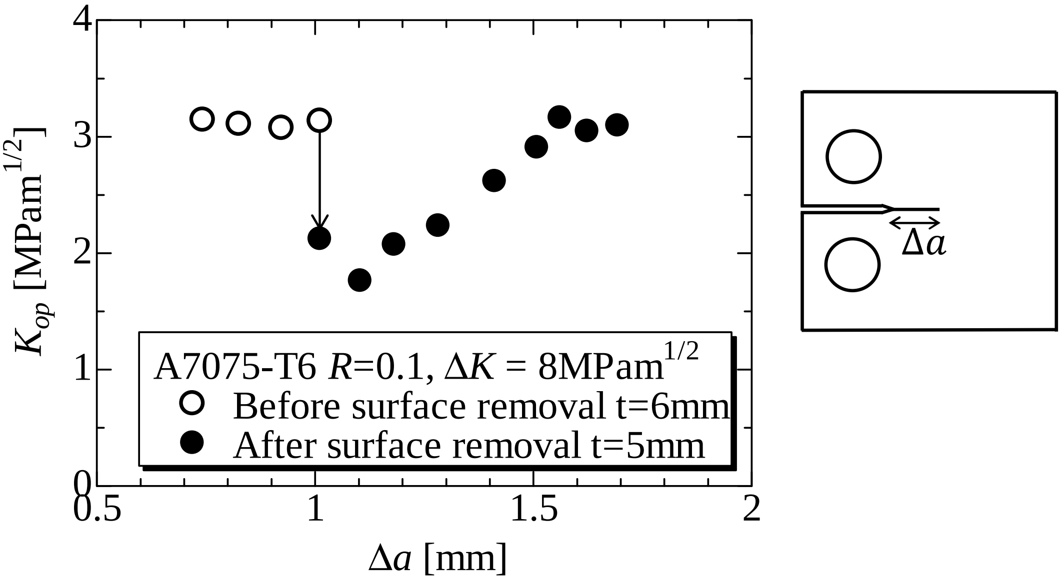

Fig. 7 Effect of surface removal (A7075-T6, ΔK = 8 MPam$^{1/2}$, removal from t= 6mm to 5 mm).

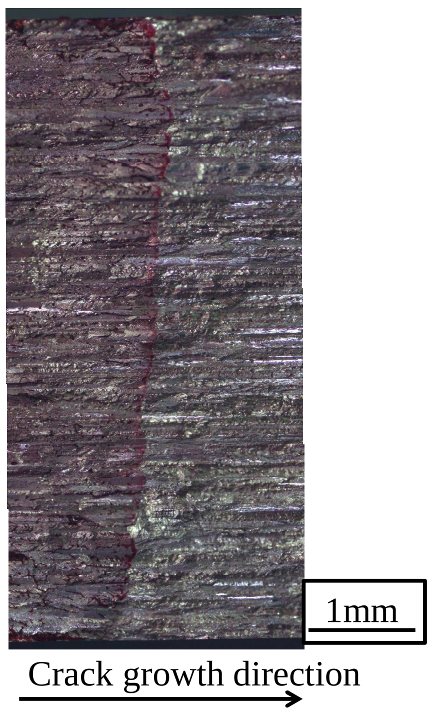

Fig. 8 Macroscopic view of the shape of the crack front propagating under the constant ΔK level of 9.0 MPam$^{1/2}$ (A7075-T6, t= 6 mm).

5 REFERENCES

[1] W. Elber, Eng. Fract. Mech., (1970), Vol. 2, Pp. 37-45.

[2] W. Elber, Astm Stp 486, American Society For Testing And Materials, West Conshohocken, Pa, (1971), pp. 230-42.

[3] J. Schivje, Astm Stp 982, J. Newman And W. Elber, Eds., American Society For Testing And Materials, West Conshohocken, Pa, (1988), pp. 5-34.

[4] J.C. Newman Jr., E.L. Anagnostou And D. Rusk, Fatigue And Crack-Growth Analyses On 7075-T651 Aluminum Alloy Coupons Under Constant- And Variable-Amplitude Loading, Int. J. Fatigue, (2014), Vol. 62, pp.133-143.

[5] P.F.P. De Matos And D. Nowell, Experimental And Numerical Investigation Of Thickness Effects In Plasticity-Induced Fatigue Crack Closure, Int. J. Fatigue, (2009), Vol. 31, pp.1795-1804.

[6] Astm E399-90, Standard Test Method For Plane-Strain Fracture Toughness Of Metallic Materials, (1991), Annual Book Of Astm Standards, pp. 500-02.

[7] S. Ishihara, Y. Sugai, And A. J. Mcevily, On The Distinction Between Plasticity- And Roughness-Induced Fatigue Crack Closure, Metallurgical And Materials Transactions A, (2012), Vol. 43, pp.3086-3096.

Proceedings of the 4th International Conference on
Fracture Fatigue and Wear, pp. 57-64, 2015

EXTENDED ISOGEOMETRIC ANALYSIS IN MODELLING CRACKED STRUCTURES

L. Tran[1], H. Nguyen-Xuan[2] and M. Abdel Wahab[1]

[1] Department of Mechanical Construction and Production, Faculty of Engineering and Architecture, Ghent University, Belgium
[2] Department of Computational Engineering, Vietnamese – German University, Vietnam

Abstract: In this paper, we successfully extended eXtended IsoGeometric Analysis (XIGA) in simulation of stationary and propagating cracks. In this method, IsoGeometric Analysis (IGA) utilizing the Non-Uniform Rational B-Spline (NURBS) functions is incorporated with enrichment functions through the partition of unity. The Heaviside function is enriched to capture the discontinuous phenomenon at the crack faces while the asymptotic functions from analytical solution are incorporated with NURBS to perform the singular field at the crack tips. Based on the NURBS's characteristics, this approach allows us to achieve easily the higher approximation order and continuity of the basic functions. As a result, XIGA can improve accuracy and higher convergence rate as compared with traditional finite element.

Keywords: eXtended IsoGeometric Analysis; Linear Fracture Elastic Mechanics; crack propagation

1 INTRODUCTION

In service, the cracks generated and grown from the defects under a cyclic loading cause a reduction of the load carrying capacity of the structures. Therefore, study of fracture mechanics is virtually important in guarantee of the performance and safety of the structures. The prediction and analysis of the crack problems are the attractive topics for many scientists in general and for computational experts in particular. As a result, a numerous numerical methods have been developed including finite element method (FEM) [1], boundary method [2], meshfree method [3], extended finite element method (XFEM) [4], etc. In these methods, approximated geometries introduce some error in the solutions because different shape functions are utilized in describing geometry and analysis. To overcome this issue, Hughes et al. proposed isogeometric analysis (IGA) [5] which fulfils a seamless bridge link between computer aided design and finite element analysis based on using the same B-Spline or non-uniform rational B-Spline (NURBS) functions in describing the exact geometry of problem as well as constructing finite approximation for analysis. IGA provides a flexible way to make refinement and degree evaluation. It allows us to achieve easily the higher approximation order and continuity of the basic functions as compared with the traditional finite element method. Up-to-now, IGA has been extensively and successfully studied for various fields of engineering and science, including fracture mechanics. For the crack problems, the enrichment functions through the partition of unity method are incorporated into IGA to capture the discontinuous phenomenon at the crack faces and singular filed at the crack tips. Recently, De Luycker et al. [6] has been used XFEM incorporated with IGA for linear fracture of mode I crack. He found that this method gains the greater accuracy and convergence rate. Then, Gorashi et al. [7] kept developing this approach (in short name XIGA) to perform the behaviour of the crack structures in 2D. XIGA also successfully applied in bi-material body with curved interface [8], assessment of collapse load of cracked plate [9], vibration of crack plate [10], cracked thin shell structures [11].

In this paper, we extended XIGA for simulation of stationary and propagating cracks. In this method, the Heaviside function is utilized for model the discontinuous phenomenon at the crack face while the asymptotic functions from analytical solution is used to capture the singular fields at the crack tips. Based on the NURBS, this approach allows us to achieve easily the higher approximation order and continuity of basic functions. As a result, XIGA can improve accuracy and higher convergence rate as compared with XFEM.

2 GOVERNING EQUATIONS OF CRACKED STRUCTURE

Consider a linear elastic solid defined in a domain Ω with a boundary Γ such that $\Gamma = \Gamma_{\mathbf{u}} \cup \Gamma_t \cup \Gamma_c$, $\Gamma_{\mathbf{u}} \cap \Gamma_t \cap \Gamma_c = \varnothing$ where $\Gamma_{\mathbf{u}}$, Γ_t, Γ_c are the Dirichlet and Neumann boundary and crack surfaces, respectively. The body subjected to body forces $\mathbf{b}$ and to surface tractions $\bar{\mathbf{t}}$ on the free portion Γ_t. The governing equations for this problem are

$$\nabla.\boldsymbol{\sigma}+\mathbf{b}=0 \text{ in } \Omega \quad \text{subjected to } \begin{cases} \boldsymbol{\sigma}.\mathbf{n} = \begin{cases} \bar{\mathbf{t}} & \text{on } \Gamma_t \\ 0 & \text{on } \Gamma_c \end{cases} \\ \mathbf{u}=\bar{\mathbf{u}} \quad \text{on } \Gamma_u \end{cases} \tag{1}$$

in which $\mathbf{u}$ is the displacement field which satisfies the compatibility relation

$$\boldsymbol{\varepsilon} = \nabla_s \mathbf{u} \text{ in } \Omega \quad \text{where } \nabla_s = \begin{bmatrix} \partial/\partial x & 0 & \partial/\partial y \\ 0 & \partial/\partial y & \partial/\partial x \end{bmatrix}^T \tag{2}$$

and the Cauchy stress tensor $\boldsymbol{\sigma}$ is obtained from the constitutive relation based on Hooke's law

$$\boldsymbol{\sigma} = \mathbf{D}\boldsymbol{\varepsilon} \text{ in } \Omega \tag{3}$$

where $\mathbf{D}$ is the elastic constant matrix.

The weak form of the equilibrium equations can be expressed as

$$\int_\Omega \boldsymbol{\varepsilon}^T \mathbf{D}\boldsymbol{\varepsilon} \mathrm{d}\Omega = \int_\Omega \mathbf{b}\mathbf{u} \mathrm{d}\Omega + \int_{\Gamma_t} \bar{\mathbf{t}}\mathbf{u} \mathrm{d}\Gamma \tag{4}$$

3 DISCRETIZATION

3.1 A brief of B-spline/NURBS functions

A knot vector $\boldsymbol{\Xi} = \{\xi_1, \xi_2, ..., \xi_{n+p+1}\}$ is a non-decreasing sequence of parameter values ξ_i, $i = 1,...n+p$, where $\xi_i \in R$ called i^{th} knot lies in the parametric space, p is the order of the B-spline and n is number of the basis functions. Using Cox-de Boor algorithm, the univariate B-spline basis functions are defined recursively start with order $p = 0$

$$N_{i,0}(\xi) = \begin{cases} 1 & if \quad \xi_i < \xi < \xi_{i+1} \\ 0 & \text{otherwise} \end{cases} \tag{5}$$

as $p \geq 1$ the basis functions are obtained from

$$N_{i,p}(\xi) = \frac{\xi - \xi_i}{\xi_{i+p} - \xi_i} N_{i,p-1}(\xi) + \frac{\xi_{i+p+1} - \xi}{\xi_{i+p+1} - \xi_{i+1}} N_{i+1,p-1}(\xi) \tag{6}$$

The multivariate B-spline basis functions are generated by a simple way - tensor product of the univariate B-splines

$$N_A(\boldsymbol{\xi}) = \prod_{\alpha=1}^{d} N_{i_\alpha, p_\alpha}(\boldsymbol{\xi}^\alpha) \tag{7}$$

where $d = 1, 2, 3$ is dimensional space. Fig. 1 illustrates an example of bivariate B-spline basis function from tensor product of two univariate B-splines $\boldsymbol{\psi} = \{0,0,0,0,\frac{1}{4},\frac{1}{2},\frac{3}{4},1,1,1,1\}$ and $\boldsymbol{\Xi} = \{0,0,0,\frac{1}{5},\frac{2}{5},\frac{3}{5},\frac{3}{5},\frac{4}{5},1,1,1\}$ in ξ and η direction, respectively.

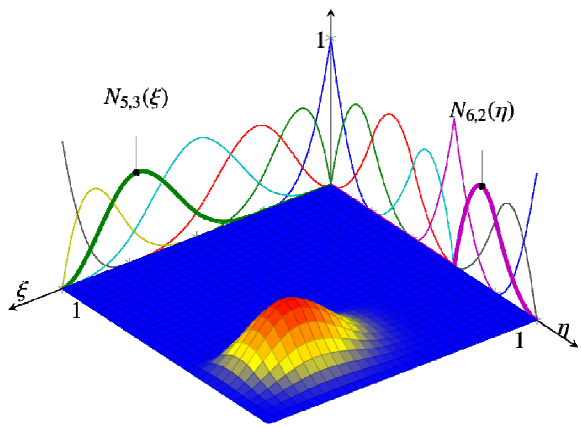

Fig. 1 B-splines basic functions.

To present exactly some conic sections, e.g., circles, cylinders, spheres, etc., non-uniform rational B-splines (NURBS) with an additional weight value $\zeta_A > 0$ for each control point is used.

$$R_A(\xi,\eta) = N_A \zeta_A / \sum_{A}^{m\times n} N_A(\xi,\eta)\zeta_A \tag{8}$$

3.2 Extended isogeometric finite element method

In order to capture the local discontinuous and singular fields, the enriched displacement approximation is introduced according to idea of XFEM as follow:

$$\mathbf{u}^h(\mathbf{x}) = \sum_{I\in S} R_I(\xi)\mathbf{q}_I^{std} + \sum_{J\in S^{enr}} R_J^{enr}(\xi)\mathbf{q}_J^{enr} \tag{9}$$

Here, the NURBS basis functions are utilized instead of the Lagrange polynomials to create a new numerical procedure – so-called eXtended IsoGeometric Analysis (XIGA) [7]. R_J^{enr} are the enrichment functions associated with node *J* located in enriched domain S^{enr} which is splitted up two parts including: a set S^c for crack faces enriched control points and a set S^f for crack tips enriched control points as shown in Fig. 2.

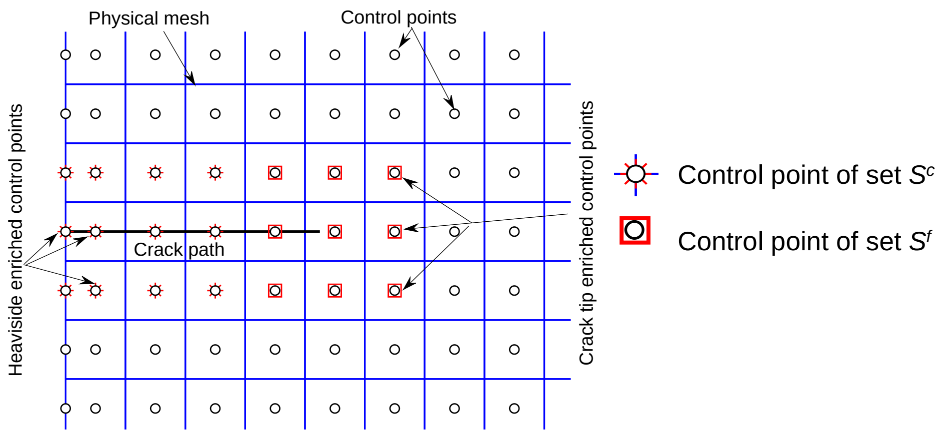

Fig. 2 Illustration of the nodal sets S^c, S^f for a quadratic NURBS mesh.

To model the discontinuous displacement at crack faces, the Heaviside function, which otherwise becomes +1 if physical coordinate is above the crack and -1, is incorporated in the enriched functions:

$$R_J^{enr}(\xi) = R_J(\xi)\left(H(\mathbf{x}) - H(\mathbf{x}_J)\right) \tag{10}$$

The analytical displacement field of linear elastic fracture problem at crack tips in polar coordinate (r,θ) is expressed as below [12]:

$$\begin{Bmatrix} u \\ v \end{Bmatrix} = \frac{K_I}{2\mu}\sqrt{\frac{r}{2\pi}}\begin{Bmatrix} \cos\frac{\theta}{2}\left(\kappa-1+2\sin^2\theta\right) \\ \sin\frac{\theta}{2}\left(\kappa+1-2\cos^2\theta\right) \end{Bmatrix} + \frac{K_{II}}{2\mu}\sqrt{\frac{r}{2\pi}}\begin{Bmatrix} \sin\frac{\theta}{2}\left(\kappa+1+2\cos^2\frac{\theta}{2}\right) \\ \cos\frac{\theta}{2}\left(\kappa-1-2\sin^2\frac{\theta}{2}\right) \end{Bmatrix} \tag{11}$$

where K_I and K_{II} are the stress intensity factors of mode I and mode II, respectively.

From the analytical displacement, the enriched functions for crack tips are chosen as [13]:

$$R_J^{enr}(\xi) = R_J(\xi)\left(\sum_{L=1}^{4}\left(\psi(r,\theta)-\psi(r_J,\theta_J)\right)\right) \tag{12}$$

where

$$\psi(r,\theta) = \sqrt{r}\left\{\sin\frac{\theta}{2} \quad \cos\frac{\theta}{2} \quad \sin\frac{\theta}{2}\sin\theta \quad \cos\frac{\theta}{2}\sin\theta\right\} \tag{13}$$

3.3 Discretization

Now, substituting Eq. (9) into Eq. (2), the strain can be expressed follow the nodal displacement as

$$\boldsymbol{\varepsilon} = \sum_{I=1}^{m\times n}\mathbf{B}_I{}^T\mathbf{q}_I \tag{14}$$

where the strain matrix $\mathbf{B}$ is given by

$$\mathbf{B}_I = \left[\mathbf{B}_I^{std} \middle| \mathbf{B}_I^{enr}\right] \tag{15}$$

in which $\mathbf{B}^{std}$ and $\mathbf{B}^{enr}$ are the standard and enriched part of matrix $\mathbf{B}$ defined in the following form

$$\mathbf{B} = \begin{bmatrix} \bar{R}_{,x} & 0 & \bar{R}_{,y} \\ 0 & \bar{R}_{,y} & \bar{R}_{,x} \end{bmatrix}^T \tag{16}$$

where $\bar{R}$ can be either the NURBS basic functions $R(\xi)$ or enriched functions R^{enr}.

Substituting Eq.(14) into Eq.(4), the linear static equation for crack problem is obtained

$$\mathbf{Kq} = \mathbf{F} \tag{17}$$

with the global stiffness and force vector

$$\mathbf{K} = \int_\Omega \mathbf{B}^T\mathbf{D}\mathbf{B}\,\mathrm{d}\Omega \qquad \text{and} \qquad \mathbf{F} = \int_\Omega \bar{R}\mathbf{b}\,\mathrm{d}\Omega + \int_{\Gamma_t}\bar{R}\bar{\mathbf{t}}\,\mathrm{d}\Gamma \tag{18}$$

4 NUMERICAL RESULTS

In this section, we study linear elastic fracture mechanics in some numerical examples with rectangular geometry such as: an infinite plate under in-plane tension, the static crack and crack propagation of an edge cracked plate subjected to shear stress. In all numerical examples, plane strain state is assumed. Herein, we illustrated the present method using meshing of cubic elements.

4.1 An infinite plate subjected to tension

Firstly, let us consider an isotropic infinite plate with material parameters of $E = 10^7$ N/mm², $\nu = 0.3$ containing a centre crack of length $2a$ subjected to a remote uniform stress $\sigma = 10^2$ N/mm². A unit shaded domain, as shown in Fig. 3, with crack length of 0.5 mm is modelled. To evaluate the present method, Fig. 4 reveals the comparison between XFEM and XIGA in investigation of the relative error and convergence rate of displacement and energy which are given by

$$\|\mathbf{u}\| = \left[\int_\Omega \left(\mathbf{u}-\mathbf{u}^h\right)^T \left(\mathbf{u}-\mathbf{u}^h\right) d\Omega \Big/ \int_\Omega \mathbf{u}^T \mathbf{u}\, d\Omega\right]^{1/2} \tag{19}$$

$$\|\mathbf{e}\| = \left[\int_\Omega \left(\boldsymbol{\varepsilon}-\boldsymbol{\varepsilon}^h\right)^T \left(\boldsymbol{\sigma}-\boldsymbol{\sigma}^h\right) d\Omega \Big/ \int_\Omega \boldsymbol{\varepsilon}^T \boldsymbol{\sigma}\, d\Omega\right]^{1/2} \tag{20}$$

It is noted that as $p = 1$, XIGA formulation is identical to XFEM. As compared to XFEM, it is observed that present method archives supper accuracy and higher convergence rate in displacement error norm as well as energy error norm. Fig. 5 displays the contour plots of displacements and stress distributions in x and y directions, respectively.

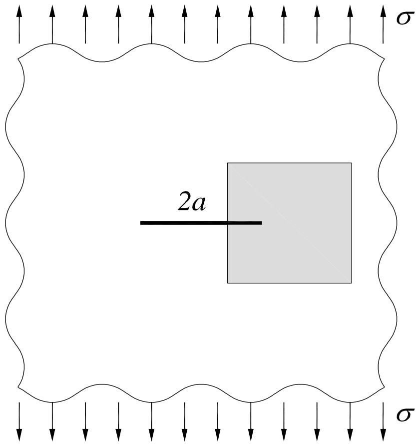

Fig. 3 Infinite crack plate in tension.

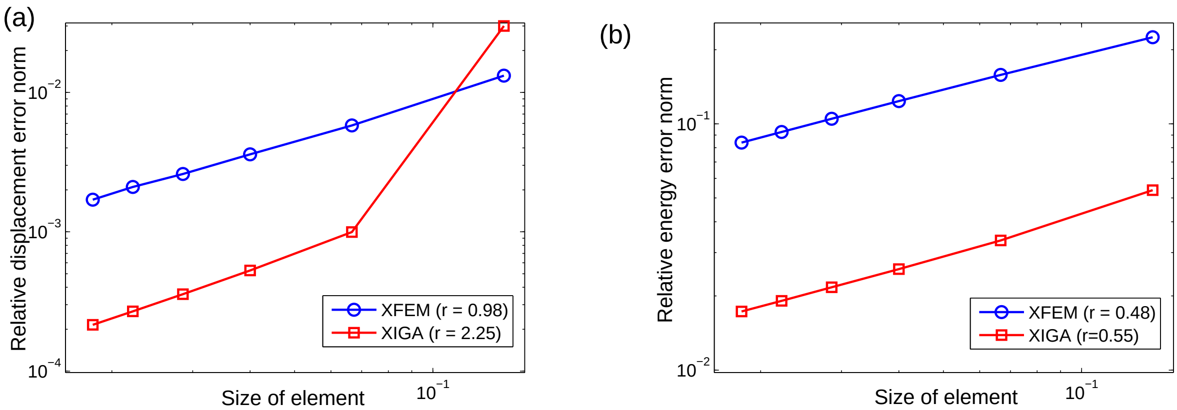

Fig. 4 Comparison of relative error norm of: (a) displacement, (b) energy.

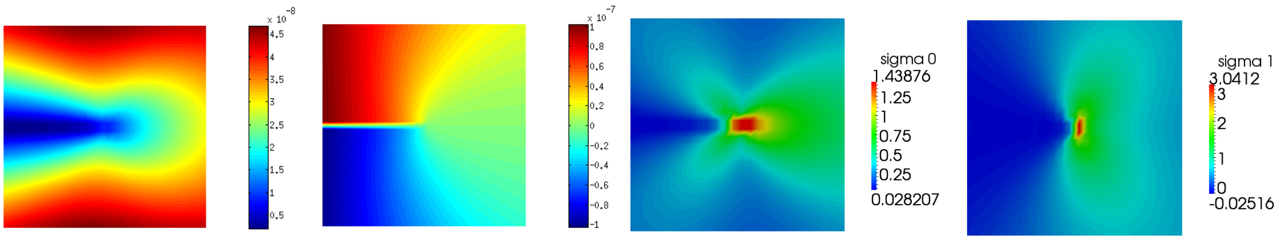

(a) Displacement U_x (b) Displacement U_y (c) Axial stress σ_{xx} (d) Axial stress σ_{yy}

Fig. 5 Contour plot of the displacements and stresses distribution.

4.2 An edge cracked plate under shear stress

In next example, we consider a rectangular plate subjected to a shear stress $\tau = 1$ N/mm² as shown in Fig. 6 with material parameters of $E = 3\text{x}10^7$ N/mm², $\nu = 0.25$. Fig. 7a and b show the relations between relative error of stress intensity factor (SIF) via number of degrees of freedom (DOFs) and CPU time, respectively. It is again seen that present method archives more accurate than XFEM. Indeed, to get the accuracy of SIF K_I with error lower than 0.1%, XIGA needs approximate 4300 DOFs while XFEM uses more than 25000 variables with nearly two time computational cost. Fig. 8 plots the distribution of axial stress, shear stress and displacement along y direction. For comparison purpose of displacement U_y, 3D elastic solid is also modelled by XIGA with meshing of 13x27x3 elements. The same contour plot of displacement is observed in Fig. 8c and d.

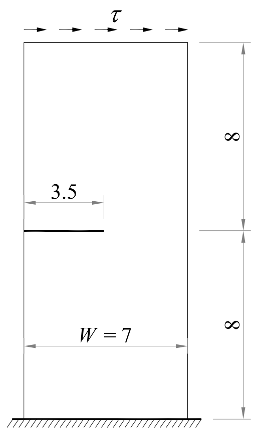

Fig. 6 Edge crack plate under shear

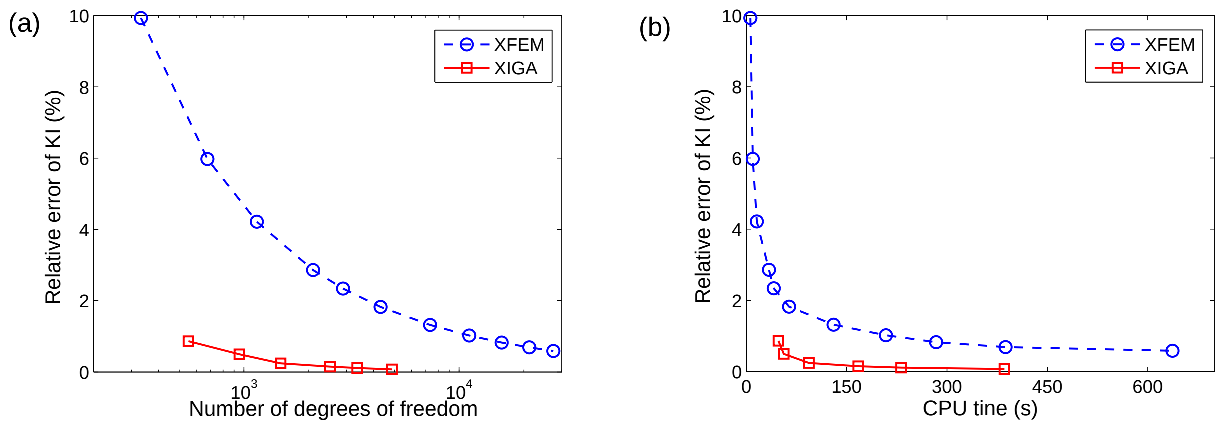

Fig. 7 Comparison between XIGA and XFEM.

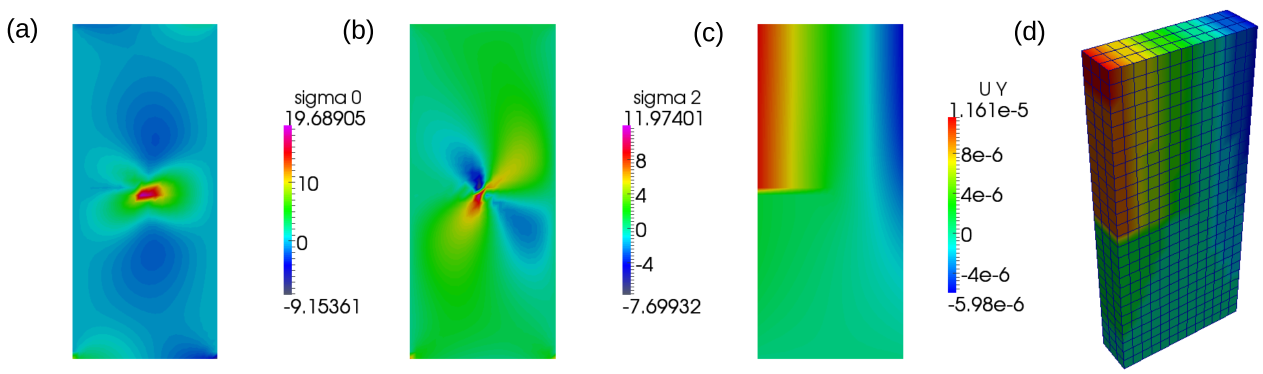

Fig. 8 Contour plot of the stresses and displacements: (a) σ_{xx}, (b) σ_{xy}, U_y in 2D (c) and 3D (d).

4.3 Crack propagation of an edge cracked plate under mixed mode loading

In this section, we want to show the capacity of present method in crack growth simulation without re-meshing. For this problem, two important parameters need to be specified during the crack growth procedure: crack growth direction θ_c and incremental crack length Δa. The crack growth angle can be identified follow to several available criteria such as: the critical plane approach, the maximum circumferential stress, the maximum energy release rate, the minimum strain energy density (see review in [14]). In this present work, we adopt the maximum circumferential stress to evaluate the crack growth direction [15]

$$\theta_c = 2\text{atan}\left(-2(K_{II}/K_I)/(1+\sqrt{1+8\left(K_{II}/K_I\right)^2})\right) \tag{21}$$

The incremental crack length is commonly determined from Paris's law. However, in this example, for simple, a constant crack increment length of $\Delta a = 0.3$ mm is set for each step. Fig. 9 shows the meshes at the step number #1 and #8 with the axial stress distributions σ_{xx}, respectively. It is observed that, during the crack growth, the mesh is unchanged while the position of crack tip downwards as oblique path. It leads to change the enrichment status of the control points, for instance, from being tip-enriched to Heaviside enriched or some standard control points becomes the enriched ones.

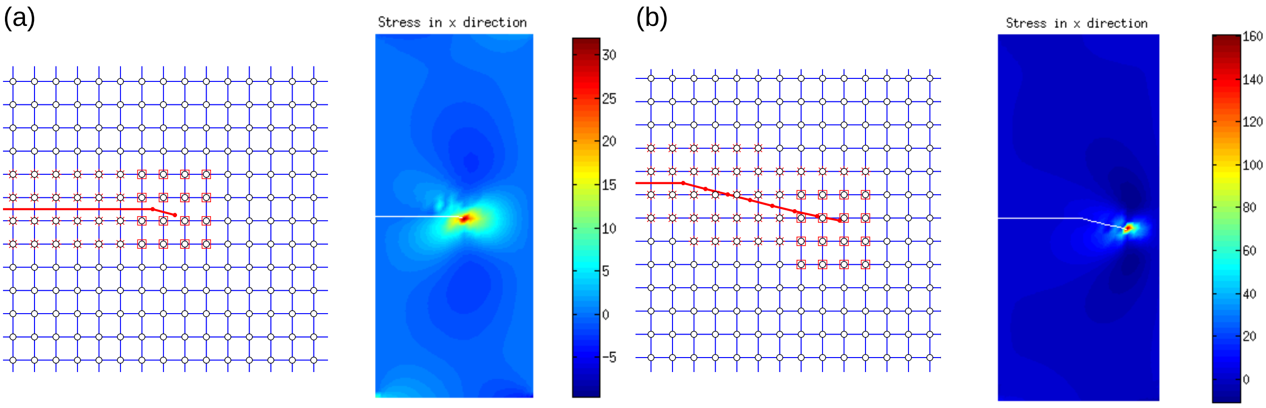

Fig. 9 Propagation of an edge crack under shear stress after step 1 (a) and step 8 (b).

5 CONCLUSIONS

In this paper, an eXtended IsoGeometric Analysis (XIGA) is extended to simulate the stationary and propagation of the crack problems. Based on idea of XFEM, the enrichment functions through the partition of unity method are integrated to capture the local discontinuous and singular fields. The advantage of present method is based on the NURBS which allows us to achieve easily the higher approximation and continuity in order of basic functions as compared with the traditional FEM. As a results, XIGA gains better accuracy and higher convergence rate than XFEM. Furthermore, the stresses and displacement are also plotted smoothly and continuous through the element boundaries.

6 REFERENCES

[1] Barsoum RS. On the use of isoparametric finite elements in linear fracture mechanics. International Journal for Numerical Methods in Engineering. 1976;10:25-37.

[2] Chang C, Mear ME. A boundary element method for two dimensional linear elastic fracture analysis. International Journal of Fracture. 1985;74:219-51.

[3] Belytschko T, Lu Y, Gu L. Crack propagation by element-free Galerkin methods. Engineering Fracture Mechanics. 1995;51:295-315.

[4] Dolbow J, Belytschko T. A finite element method for crack growth without remeshing. Int J Numer Meth Engng. 1999;46:131-50.

[5] Hughes TJR, Cottrell JA, Bazilevs Y. Isogeometric analysis: CAD, finite elements, NURBS, exact geometry and mesh refinement. Computer Methods in Applied Mechanics and Engineering. 2005;194:4135-95.

[6] De Luycker E, Benson D, Belytschko T, Bazilevs Y, Hsu M. X-FEM in isogeometric analysis for linear fracture mechanics. International Journal for Numerical Methods in Engineering. 2011;87:541-65.

[7] Ghorashi SS, Valizadeh N, Mohammadi S. Extended isogeometric analysis for simulation of stationary and propagating cracks. International Journal for Numerical Methods in Engineering. 2012;89:1069-101.

[8] Haasemann G, Kästner M, Prüger S, Ulbricht V. Development of a quadratic finite element formulation based on the XFEM and NURBS. International Journal for Numerical Methods in Engineering. 2011;86:598-617.

[9] Nguyen-Xuan H, Tran LV, Thai CH, Le CV. Plastic collapse analysis of cracked structures using extended isogeometric elements and second-order cone programming. Theoretical and Applied Fracture Mechanics. 2014;72:13-27.

[10] Tran L, Phung Van P, Phu Nguyen P, A AW, Nguyen-Xuan H. Vibration analysis of cracked plate using higher-order shear deformation theory. 3rd International Journal of Fracture Fatigue and Wear. 2014;2:127-33.

[11] Nguyen-Thanh N, Valizadeh N, Nguyen M, Nguyen-Xuan H, Zhuang X, Areias P, et al. An extended isogeometric thin shell analysis based on Kirchhoff–Love theory. Computer Methods in Applied Mechanics and Engineering. 2015;284:265-91.

[12] Anderson TL. Fracture mechanics: fundamentals and applications: CRC press, 2005.

[13] Bordas S, Nguyen PV, Dunant C, Guidoum A, Nguyen-Dang H. An extended finite element library. International Journal for Numerical Methods in Engineering. 2007;71:703-32.

[14] Pais MJ. Variable amplitude fatigue analysis using surrogate models and exact XFEM reanalysis: University of Florida, 2011.

[15] Sukumar N, Prévost J-H. Modeling quasi-static crack growth with the extended finite element method Part I: Computer implementation. International Journal of Solids and Structures. 2003;40:7513-37.

Proceedings of the 4th International Conference on
Fracture Fatigue and Wear, pp. 65-70, 2015

FRACTURE OF T91 MARTENSITIC STEEL IN LIQUID METALS

J.-B. Vogt and I. Proriol Serre

Université Lille1 Sciences et Technologies, Unité Matériaux Et Transformations, France

Abstract: The paper presents some key results on embrittlement of T91 steel by liquid lead-bismuth eutectic and by liquid sodium gained during research programs conducted this last decade. It is shown that both sodium and lead-bismuth eutectic can embrittle T91 but this depends as well on the microstructural state of T91 as on experimental parameters such as temperature, loading rate and chemistry of the liquid metal. The assessment of liquid metal embrittlement conditions allows materials to be used in safe conditions.

Keywords: small punch test – brittle fracture – liquid metal embrittlement– sodium - lead bismuth eutectic

1 INTRODUCTION

T91 martensitic steel is a modified grade of the 9Cr1Mo steel family. It exhibits excellent combination of strength and ductility which can be achieved by control of the heat treatment. In addition, with the level of chromium and molybdenum, the resistance to corrosion is somewhat acceptable. It is therefore employed for structural components in all industrial fields working at high temperatures and in severe environments as for instance in refineries or power plants. The apparently ductile alloys however can undergo a ductile to brittle behaviour under the action of an agent which affects either the bulk of the material or the surface or only a small part of the materials. Typically, temperature or irradiation act at the scale of the bulk while the effect of environment tends to occur at the surface or at crack tip.

The Gen IV forum aims at providing the basis for identifying and selecting six nuclear energy systems. Two of them taken into consideration should be cooled by liquid metals. Lead or lead bismuth eutectic (LBE) are employed in the lead fast reactor (LFR) and sodium is employed for the sodium fast reactor (SFR). For these reactors, T91 is a candidate material. Nevertheless, the question of liquid metal embrittlement (LME) needs to be examined. When strained in liquid metals, an otherwise ductile material can exhibit a loss of ductility and, sometime a brittle fracture. Many metals, pure or alloyed, are known to be sensitive to LME e.g. Al-Ga [1] or Ni-Li [2]. Generally speaking, it can be stated that no material can be considered as immune against liquid metal embrittlement. So to ensure the reliability of the material employed in these reactors, it is necessary to find the conditions leading to LME.

The objective of this paper is to present some key results obtained in the laboratory UMET during the last decade in the frame of European collaborations such as TECLA, Megapie-TEST, DEMETRA, GETMAT or in the frame of French research program such as Gedepeon or NEEDS. Indeed, the behaviour of T91 martensitic steel in presence of LBE or sodium has been extensively studied at UMET. For the study of LME, several loading conditions and mechanical tests were considered: monotonic and cyclic loading [3]; tensile, small punch test, low cycle fatigue, fatigue crack propagation tests were performed. The paper will be restricted SPT since it has pointed out amazing and differentiating results.

2 MATERIAL

The material studied during these research programs was a conventional T91 martensitic steel containing 8.5 - 8.8 %Cr, 0.1%C, 1% Mo, 0.06 % Nb, 0.20-0.25 % V. Several heats coming from different suppliers were tested. They all fulfilled the required chemical composition.

The standard heat treatment of this steel comprises an austenitisation at 1050 °C for 1h followed by air cooling and a subsequent tempering for 1h at 750 °C (noted ‘TR750’). It is very important to respect the recommended heat treatment especially the tempering temperature because it strongly impacts the microstructure. Changing the tempering temperature modifies the precipitation state and the structure of dislocations, and this modifies the hardness and the strain hardening response. Since the literature suggests that hard materials are more sensitive to LME, it was decided to submit the T91 steel to another heat treatment. It consisted in normalizing the material at 1050 °C for 1 h followed by air cooling but in tempering for 1 h at 500 °C or 550 °C (noted TR500 and TR550). Also, the absence of tempering has also been taken into account (T material). The macro hardness HV_{10} of TR750 material was 278 HV while TR500 material has a hardness of 446 HV and T material a hardness of 380 HV. By the way, the austenitic grain size was not changed with these heat treatments and has an average value of 20 µm.

3 MECHANICAL TESTING

The Small Punch Test (SPT) technique, especially designed to perform tests in air and in liquid LBE or liquid sodium at temperatures up to 550 °C, has been employed. It consists of a specimen holder, a pushing rod and a ball. The specimen holder includes a lower die, an upper die which is also used as the tank for the liquid metal and four clamping screws. The load is transferred onto the specimen by means of a pushing rod and a 2.5 mm diameter tungsten carbide ball in contact with the lower surface of the specimen. In this way, the puncher being under the specimen, the upper surface of the specimen is in contact with the liquid metal and is submitted to tensile loading. Specimens were in the form of disk 8.9 mm in diameter or had a squared shape 10 mm x 10 mm. Before testing, the sample surfaces were mechanically polished with SiC paper up to 1200 grade and then electro polished, in order to avoid effects due to the roughness of the surface and residual stresses developed during the mechanical polishing. The final thickness was 500 (±20) µm. More details about this technique can be found in [4].

The composition of LBE was 45 wt% Pb and 55 wt% Bi. The delivered LBE was oxygen saturated and could be further purified thanks a purification unit designed and built in the lab. It consisted in flowing the LBE bath by a mixture of argon/hydrogen gas which allowed decreasing the oxygen content up to 10^{-8} wt % at 450 °C. Tests were performed in oxygen saturated LBE or in low oxygen LBE. They were carried out inside a cell which atmosphere was controlled thanks to a purification unit. The latter allows removing water vapour and oxygen by flux sweeping and on use of reactive filters. The oxygen content and the water content in the cell interior could be decreased as low as 0.1~0.5 ppm and 5~20 ppm respectively.

The sodium was rather pure but contained some impurities: 2-10 ppm C, 2-4 ppm Cl^-, 2-4 ppm Br^-, 2-5 ppm Sr, <0.5 ppm Ag, 0.5 – 1 ppm Al, < 1 ppm B, < 4 ppm Fe. The experiments in liquid sodium were performed in an environment-controlled cell which test zone was continuously spread out by an argon flow. Solid sodium was sliced into small pieces, deposited and gently pressed at the SPT specimen surface. The oxygen content in the sodium bath was determined from Noden's calculations. When sodium is in contact with saturated oxygen air, the maximum oxygen content in sodium at 300 °C is 96 ppm.

SPT were performed using an INSTRON electro- mechanical machine which can control the experimental cross-head displacement velocities from 0.5 mm/min to 0.005 mm/min.

4 MECHANICAL BEHAVIOUR OF T91 STEEL IN LIQUID SODIUM

4.1 Effect of microstructure

The standard T91-TR750 steel showed a similar mechanical behaviour in air and sodium environment at 400 °C, and at a cross head displacement of 0.05 mm/min (Fig. 1a). However, TR550 steel exhibited a load–displacement curve which was different whether the material was tested in air or in liquid sodium (Fig. 1b). Indeed even if the curves superimposed at the beginning of test in the elastic part, they diverge in the plastic domain. In air, TR550 exhibited high mechanical resistance involving a maximum load F_m value of 2385 ± 40 N, and a displacement to fracture d_f of 1.35 mm. These values were strongly reduced to 1355 N and 0.75 mm respectively in sodium.

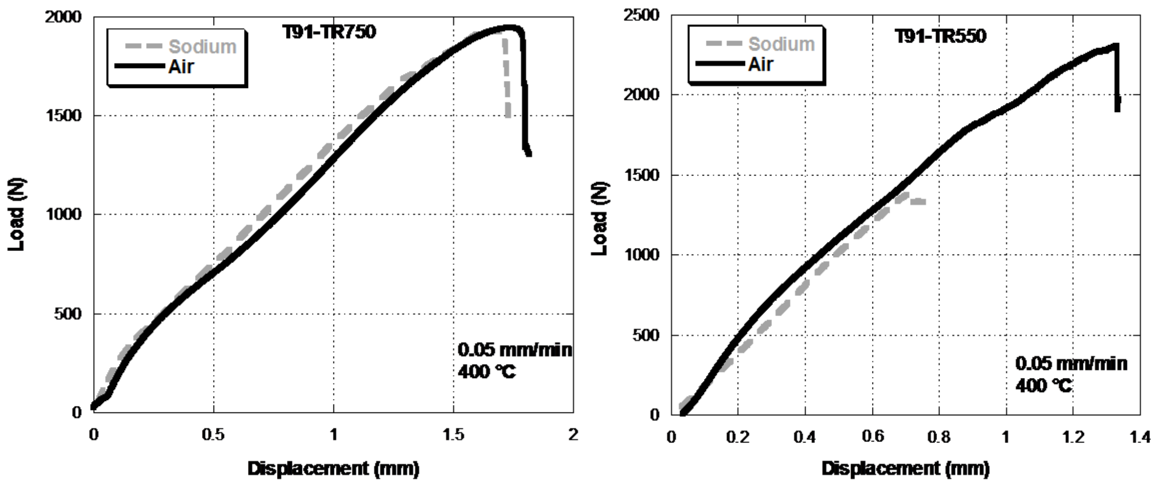

Fig. 1 SPT curves in air and in liquid sodium at 400°C, at 0.05 mm/min of: a) TR750 steel, b) TR550 steel

Scanning Electron Microscopy (SEM) observations at low and high magnifications of the fractured specimens revealed also a difference depending on whether the test was performed in air or in liquid sodium. For each material fractured at 400°C in air but also for the TR750 steel fractured at 400°C in liquid sodium, the specimen dome contained a circular crack (Fig. 2a) and the fracture surface contained dimples typical of ductile rupture (Fig. 2b).

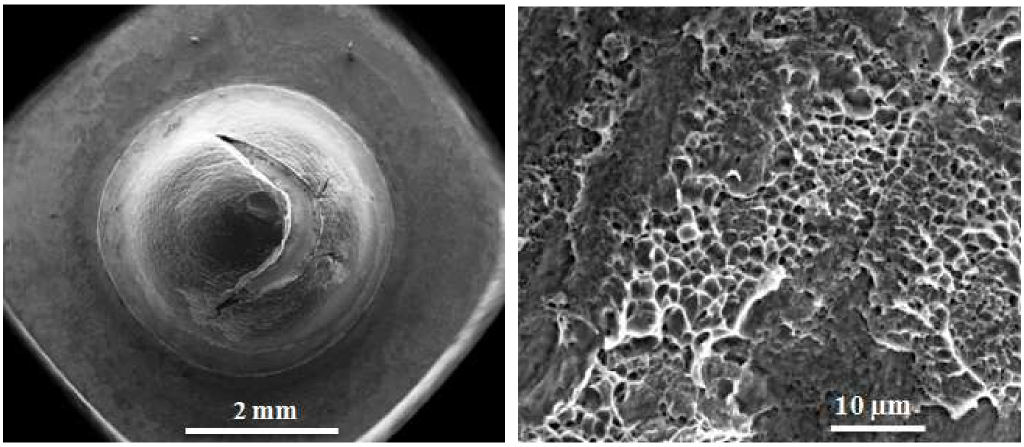

Fig. 2 Fracture in TR750 specimen a) Principal crack in air, b) Ductile fracture surface in air

The general tendency for TR550 material fractured at 400°C in liquid sodium is that cracking contained very limited circular parts with large radial cracks (Fig.3a). The weak mechanical properties of this material were associated with a fully brittle fracture mode. The brittle fracture surface comprised an intergranular zone (Fig. 3b) close to the external surface in contact with the liquid sodium which changes for transgranular one in the rest of the specimen. Sodium penetration at grain and lath boundaries is the cause of the embrittlement [5].

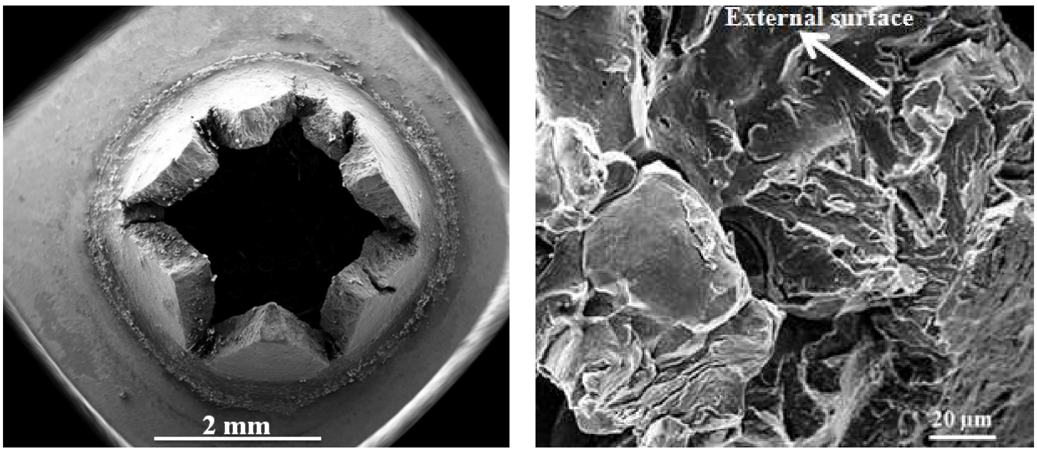

Fig. 3 Fracture in TR550 specimen a) Principal crack in sodium, b) Brittle fracture surface, showing intergranular decohesion near the exposed surface

4.2 Effect of temperature

LME being a temperature dependent phenomenon, TR750 and TR550 steels have been tested at 150 °C, 200 °C, 300 °C, 450 °C and 550 °C. The ductility has been used to point out the temperature effect by using a ductility factor (D.F.) defined by D.F. = J_{nfNa} /J_{nfAIR} where J_{nfNa} is the normalized fracture energy (fracture energy divided by thickness of specimen) measured from test in liquid sodium and J_{nfAIR} the normalized fracture energy measured from test in air.

Fig. 4 shows the existence of a ductility trough located at about 250 °C. The location appears to be the same for both alloys. However, the width and the depth of the ductility-trough increase with increasing the strength of the material.

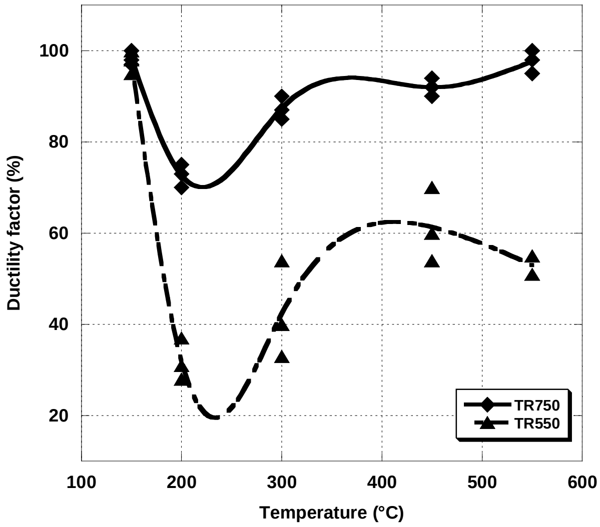

Fig. 4 Evolution of ductility factor with test temperature of TR750 and TR550 materials tested in sodium at a cross head speed of 0.05 mm/min

5 MECHANICAL BEHAVIOUR OF T91 STEEL IN LBE

5.1 Effect of microstructure

As for sodium, the behaviour of T91 steel in LBE was investigated according to the heat treatment. SPT were first performed in oxygen saturated LBE bath at 300 °C by using a displacement speed of 0.5 mm/min. As for tests in liquid sodium, the effect of heat treatment on mechanical response was obvious. A strong difference could be seen between both T and TR500 curves and TR750 one. The TR750 curve recorded during test at 300 °C in LBE was similar in terms of shape and numerical values to that obtained after test in air. No obvious difference was noticed from the fractographic observation. A circular crack occurred at the specimen domes and the fracture surfaces were covered by dimples. For the other treated materials, most of the curves were quasi linear right to failure suggesting a quasi-absence of plastic deformation. All the fracture surfaces of the T and TR500 materials tested in LBE were always brittle, essentially transgranular with some occasional intergranular decohesion (Fig. 5b) and the dome exhibited very developed radial cracks providing a star-shaped figure (Fig. 5a)..

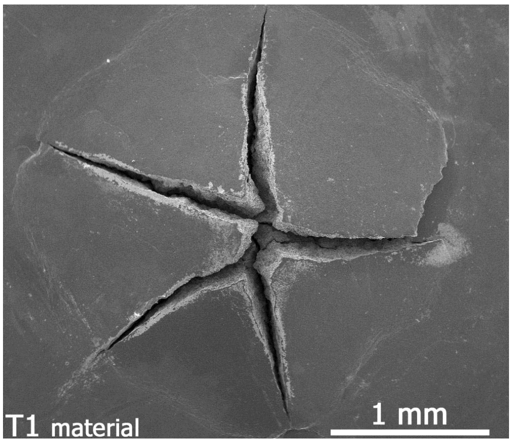

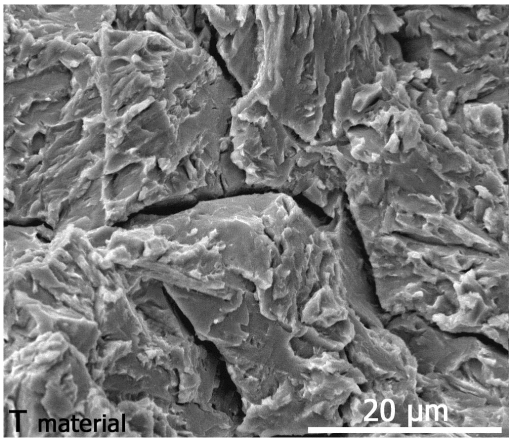

Fig. 5 Fracture in T steel specimen in oxygen saturated LBE at 300 °C at 0.5 mm/min

a) star-shaped principal crack and b) brittle intergranular decohesion

From this study, it can be concluded that T91 in its standard heat treatment is ductile at 300°C as well in air as in oxygen saturated LBE under rather rapid loading rate. LBE embrittlement is possible if unsuitable tempering treatment has been performed.

5.2 Effect of temperature and of LBE chemistry

Tests were done on the TR750 material at different temperatures, at a displacement speed of 0.5 mm/min in liquid LBE purified by argon and hydrogen. Then the results were compared with those obtained after SPT in oxygen saturated LBE.

Fig. 6a gives the load-displacement curves of TR750 SPT specimens tested at 200℃, 300℃ and 400℃ in purified liquid LBE and in oxygen saturated LBE. It seems that the curves obtained from tests performed in purified LBE and those obtained in oxygen saturated LBE do not exhibit very obvious differences.

SEM observations of TR750 SPT specimens fractured in oxygen saturated LBE (Fig. 6b) and in purified LBE (Fig. 6c) revealed that the shape of the cracks was circular with some small radial cracks.

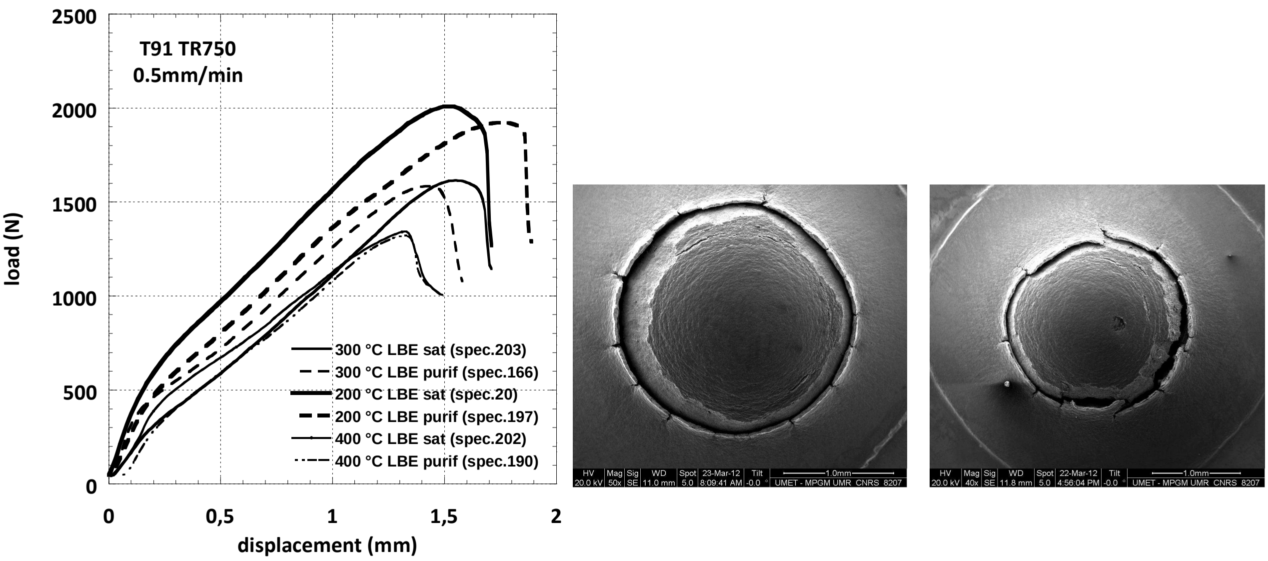

Fig. 6 a) SPT curves of TR750 material tested at 300 °C at a displacement speed of 0.5 mm/min in oxygen saturated LBE (LBE sat) and in purified LBE (LBE purif) and SEM image of the dome of the TR750 material after test at 300 °C b) in oxygen saturated LBE and c) in purified LBE

5. 3 Effect of loading rate

In order to analyze the role of loading rate or strain rate, tests were performed on the TR750 material in purified LBE at 300 °C at two displacement speeds: 0.5 mm/min and 0.005 mm/min. SPT curves are reported in Fig. 7a and the SPT curve related to the test performed in the oxygen saturated bath at a speed of 0.5 mm/min is also included for comparison.

SPT curves show a strong dependence on displacement speed. First, for the lowest displacement speed, the maximum load was strongly reduced as compared to the other tests performed at high speed by a factor of two third. Second, the displacement at maximum load was decreased in the same way.

Analysis of the fractured specimen also pointed out an effect of the displacement velocity as well at the macroscopic scale as at the microscopic one. All the SPT specimens exhibited circular and radial cracks but the decrease in the displacement velocity promoted radial cracking. For the lowest displacement velocity, the number of radial cracks was much reduced as compared to the other tests but the radial cracks were also much longer (Fig. 7b). In addition, transgranular brittle fracture was observed (Fig. 7c).

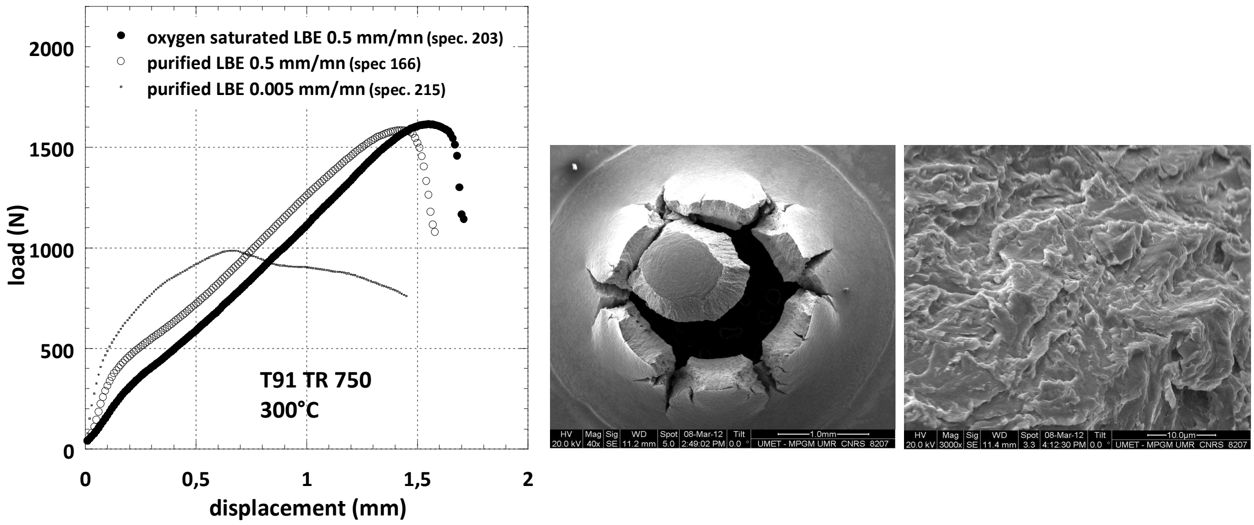

Fig. 7 a) SPT curves of TR750 material tested at 300 °C at displacement speeds of 0.5 mm/min and 0.005 mm/min in oxygen saturated LBE and in purified LBE and SEM image b) of the dome and c) of the fracture surface of the TR750 material after test in purified LBE at 300°C at a displacement speed of 0.005 mm/min

It has been also shown that decreasing both the loading rate and the dissolved oxygen in LBE accelerated the phenomenon [6].

6. CONCLUDING REMARKS

The program research conducted this last decade showed that liquid metal embrittlement is a damage mode difficult to be assessed due to the very large number of parameters that can act. The considered T91 alloy exhibits a certain degree of LME sensitivity in LBE or in liquid sodium. While in the hard condition the occurrence of LME was not so surprising, the brittle fracture in the recommended heat treatment after a slow loading rate test is a real evidence of the scientific and technological interest for understanding liquid metal embrittlement.

7 ACKNOWLEDGEMENTS

The authors would like to acknowledge the financial support of European Union and of the French government. All colleagues having taken part in these projects are warmly thanked (J. Golek, D. Creton, C. Ye, O. Hamdame, A. Verleene, G. Nicaise, A. Legris)

8 REFERENCES

[1] W.Y. Chu, X.M. Liu, J.L. Luo, L.J. Qiao, Mechanism of embrittlement of Al alloy by liquid metal (Ga),Canadian Metallurgical Quaterly, 38 (2), pp. 127-132, (1999)

[2] M. G. Nicholas, P. J. Fernback, Tensile properties of high-purity nickel stressed in alkali metal environments, Journal of materials science, (1991)

[3] J.-B. Vogt and I. Proriol Serre, Fatigue behaviour of a martensitic and an austenitic steels in heavy liquid metals, Procedia Engineering, 55, 812 – 818, (2013)

[4] I. Serre, J. B. Vogt, Liquid metal embrittlement of T91 martensitic steel evidenced by small punch test, Nuclear Engineering Design, 237, 667-685 (2007)

[5] O. Hamdane, I. Proriol Serre, J.-B. Vogt, N. Nuns, ToF-SIMS analyses of brittle crack initiation of T91 steel by liquid sodium, Materials Chemistry and Physics, 145, 243-249, (2014)

[6] C. Ye, J.-B. Vogt and I. Proriol Serre, Liquid metal embrittlement of the T91 steel in lead bismuth eutectic: The role of loading rate and of the oxygen content in the liquid metal, Materials Science & Engineering A608, 242–248, (2014)

Proceedings of the 4th International Conference on
Fracture Fatigue and Wear, pp. 71-77, 2015

MODELS OF FRACTURE OF POLYCRYSTALLINE GRAPHENE AND LAYERED METAL-GRAPHENE COMPOSITES

I.A. Ovid'ko[1,2,3] and A.G. Sheinerman[1,2,3]

[1] Institute for Problems in Mechanical Engineering, Russian Academy of Sciences, St. Petersburg, Russia
[2] Department of Mathematics and Mechanics, St. Petersburg State University, St. Petersburg, Russia
[3] Laboratory for Mechanics of New Nanomaterials, St. Petersburg State Polytechnical University, St. Petersburg, Russia

Abstract: We suggest theoretical models which describe fracture of polycrystalline graphene and metal-graphene layered composites. In considering polycrystalline graphene, we consider formation of cracks at grain boundaries (GBs) containing defects (partial disclinations and their dipoles). Such defects at GBs are associated with experimentally observed structural irregularities of real GBs in graphene. Within the suggested model, we calculate the dependences of the critical stress for crack formation on the parameters of individual disclinations and their dipole configurations at GBs. The results of the model explain the experimental data (Huang *et al.* 2011 *Nature* **469** 389; Ruiz-Vargas *et al.* 2011 *Nano Lett.* **11** 2259) on crack formation in polycrystalline graphene at comparatively low levels of the applied stress and their discrepancy with the results of computer simulations of strength exhibited by graphene bi-crystals with structurally perfect, periodic GBs. In consideration of metal-graphene layered composites, we examine the transfer of plastic deformation across a graphene interface and nanocrack formation initiated by stress fields of lattice dislocations stopped near a graphene interface. We reveal strength characteristics of metal-graphene layered composites as functions of their key structural parameters, including the metallic and graphene layer thicknesses, which are well consistent with the corresponding experimental data (Kim et al., Nature Commun. 4 (2013) 2114). The results demonstrate that strong metal-graphene layered composites (against both fracture and macroscopic plastic flow) should contain monolayer graphene inclusions, and for such inclusions the processes of plastic deformation and interface fracture compete and can occur concurrently.

Keywords: graphene; grain boundaries; composites; defects; cracks

1 INTRODUCTION

Graphene – a single carbon atomic sheet with the hexagonal sp^2 covalently bonded crystal structure – with its outstanding mechanical, transport and thermal properties represents the subject of rapidly growing research efforts in applied physics and materials science [1–6]. Of crucial importance from both fundamental and applied viewpoints is the unique behaviour of graphene under mechanical load. In particular, Lee with co-workers have experimentally demonstrated that pristine graphene exhibits the highest ever measured strength of ≈ 130 GPa (Ref. [7]). At the same time, following experimental examinations [8,9], the strength characteristics of graphene sheets containing GBs dramatically degrade compared to the superior strength (≈ 130 GPa) of their pristine counterparts. These experimental data motivate large interest in understanding the physical mechanisms of fracture in graphene and their sensitivity to the presence of defects. Therefore, in the second section of this paper we suggest a theoretical model describing crack generation at elementary irregularities of the GB structure, namely, those associated with partial disclinations and their dipoles.

Also, since graphene monolayer sheets and multilayer nanoplatelets are specified by superior values of strength and elastic moduli, they are very good candidates for the use as reinforcing structural elements in polymer-, ceramic- and metal-matrix composites. For instance, recently, Kim with co-workers [10] have synthesized Cu- and Ni-graphene nanolayered composites exhibiting extremely high strength characteristics (with the flow stress at 5% strain of 1.5 GPa for Cu-graphene composites and 4.0 GPa for Ni-graphene composites). Also, Kim with co-workers [10] experimentally revealed that the above flow stress increases with diminishing the metal layer thickness.

The dominant physical mechanism responsible for superior strength of metal-graphene nanolayered composites is attributed to the role of graphene interfaces as obstacles for lattice dislocation glide [10]. In the case under consideration, it is logical to think that the plastic deformation and fracture processes controlling the flow stress/strength of a metal-graphene layered composite are the transfer of plastic deformation across a graphene interface and the nanocrack formation initiated by stress fields of lattice dislocation stopped near a graphene interface. In the third section we describe the strength-controlling processes (transfer of plastic deformation and nanocrack generation) in metal-graphene layered composites and reveal the dependence of their strength characteristics on the metallic and graphene layer thicknesses.

2 CRACK NUCLEATION AT PARTIAL DISCLINATIONS AT GRAIN BOUNDARIES IN GRAPHENE

In general, GBs in 2D graphene are line defects separating graphene grains (crystallites/domains) whose crystal lattices are tilted by a non-zero angle θ relative to each other [11]. The angle θ serves as the main geometric parameter of a GB and is called the GB misorientation. According to experimental data, computer simulations and theoretical models, low- and high-angle GBs in graphene hexagonal lattices are represented as walls of edge dislocations or, in other terms, pentagon–heptagon pairs [8]. The geometry of the individual geometries of pentagon-heptagon pairs and their spatial arrangement in the corresponding wall configuration determines GB misorientation.

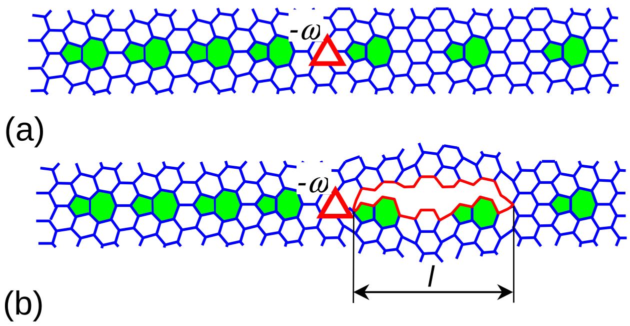

Fig. 1 A partial disclination at grain boundary in graphene bi-crystal. (a) Graphene bi-crystal without cracks. (b) Graphene bi-crystal containing a nanocrack.

Within our model, we consider GB defects associated with elementary changes in the GB misorientation and their effects on crack generation at GBs. Such defects are called partial disclinations in a 2D graphene sheet and represent the points where the GB misorientation changes in a step-like manner (and so does the GB dislocation arrangement; see Fig. 1(a)), so that the jump of misorientation represents the disclination strength ω; see Ref. [11]. With the hexagonal geometry of the graphene crystal lattice, the strengths ω of such partial disclinations can be arbitrary in the range: $-60^{\circ} < \omega < 60^{\circ}$. Partial GB disclinations create stresses that can initiate nanocracks in graphene (Fig. 1(b)).

First, consider crack generation in a flat graphene sheet with a line GB containing a single partial disclination of the strength $-\omega$ (Fig. 1(b)). Within our model, the flat graphene sheet has a circular shape specified by the radius *R*, and the partial disclination is located at its center (Fig. 2). (The radius *R* plays the role of the screening length for the stresses created by the disclination.) Consider the situation where the flat graphene sheet is under a tensile mechanical load σ_0 whose direction is normal to the GB line (Fig. 2). The disclination creates local stresses which, in superposition with the external load, can initiate nanocrack formation. Within our model, the nanocrack nucleates and grows along a GB in the region where the tensile stresses exerted on the crack surfaces by the disclination and the applied load are highest (see Fig. 1(b)).

In order to calculate the conditions for nanocrack growth in graphene, we use the energy criterion [12] suggesting that a crack is favored to grow if the release of the strain energy in the course of crack advance is larger than the effective surface energy of the crack surfaces. With this criterion, using the expressions for the stress field of a wedge disclination in an infinite medium (and modifying these for the case of the plane stress state), one obtains the following condition for catastrophic crack growth: $\sigma > \sigma_c$, where

$$\sigma_c = (8D(2\gamma - \gamma_b)/l_0)^{1/2} - D\omega\left(\ln(4R/l_0) - 2\right). \quad (1)$$

In formula (1), l_0 represents the maximum crack length to which the crack can grow through thermal fluctuations, R is the screening length of the disclination stress field (in our case, R is the graphene circle radius; see Fig. 4), $D = E/(4\pi)$, E is the Young modulus of graphene, γ is the specific surface energy of graphene edges (say, crack edges in graphene), and γ_b is the specific GB energy in graphene. In derivation of formula (1), it is assumed that $l << R$. The quantities γ and γ_b have the meaning of the energy per unit area, that is, the energy of the surface of a graphene edge (or graphene GB energy, respectively) per length of the graphene edge (GB, respectively) divided by the distance (0.34 nm) between the graphene sheets in graphite.

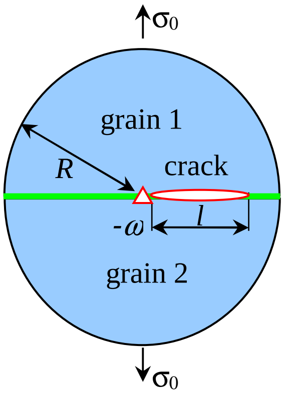

Fig. 2 Nanocrack generation at a grain boundary disclination (triangle) located at center of mechanically loaded circular graphene sheet.

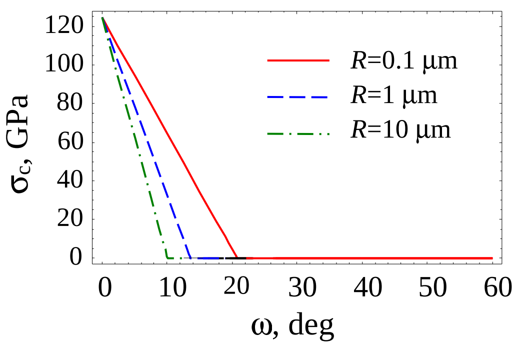

Fig. 3 Dependences of the ultimate stress σ_c on disclination strength ω for various values of the screening length R .

In order to calculate the critical stress σ_c for a GB crack, we use the following typical values of graphene characteristics: $l_0 = 0.72$ nm, $E = 1000$ GPa (Ref. [12]), $\gamma = 10.3$ J/m² [14], and $\gamma_b = 3$ J/m² [15]. The dependences of the critical stress σ_c on the disclination strength ω are calculated and presented in Fig. 3 for various values of the screening length (the radius of the circlular graphene sheet) R . As it follows from Fig. 3, when ω increases, σ_c decreases from 125 GPa at $\omega = 0$ down to zero at certain values of ω (10 to 20 degrees, depending on the value of the screening length R). The calculated low values of the critical stress σ_c for intergranular fracture are consistent with the experimentally documented [9] values (35 GPa or lower) of fracture stresses specifying polycrystalline graphene specimens. As a corollary, individual partial disclinations at GBs can serve as critical defects responsible for experimentally documented [8,9] dramatic decrease in strength of polycrystalline graphene, as compared to its pristine counterpart.

Besides individual disclinations, we have analyzed the effect of disclination dipoles (representing two opposite-sign disclinations) on the critical stress for catastrophic crack growth. The analysis has demonstrated that the critical stress σ_c^{dip} for crack generation at a disclination dipole and its catastrophic growth decreases with increasing the disclination strength and the distance between the dipole disclinations. For large enough values of these parameters, the critical stress σ_c^{dip} is smaller than 35 GPa.

Thus, similar to individual partial disclinations at GBs, their dipoles can be responsible for the experimentally documented [8,9] dramatic decrease in the strength of polycrystalline graphene.

Similar to grain boundaries in graphene, graphene interfaces in metal-graphene layered composites can serve as weak elements that can decrease the strength of such composites. Therefore, nanocrack generation and transfer of plastic flow across graphene interfaces in metal-graphene layered composites will be examined in the next section.

3 COMPETITION BETWEEN NANOCRACK GENERATION AND TRANSFER OF PLASTIC FLOW ACROSS GRAPHENE INTERFACES IN METAL-GRAPHENE LAYERED COMPOSITES - GENERAL ASPECTS

Consider a layered composite solid consisting of repeat metallic layers and graphene interfaces. Let the solid be under the action of a shear stress τ. Consider an ensemble of N rectangular glide dislocation loops with identical Burgers vectors $\boldsymbol{b}=b\boldsymbol{e}_y$ (where $\boldsymbol{e}_y$ is the unit vector directed along the *y*-axis) formed due to the action of a Frank-Read source and stopped near a platelike impenetrable graphene layer (Fig. 4). The action of the applied stress τ and the stress field created by the ensemble of dislocation loops (stopped in the plastically deformed layer located to the left side of the graphene inclusion/interface) can induce homogeneous generation of a new rectangular glide dislocation loop with the Burgers vector $\boldsymbol{b}$ in the neighboring metallic layer located to the right side of the graphene layer (Fig. 4).

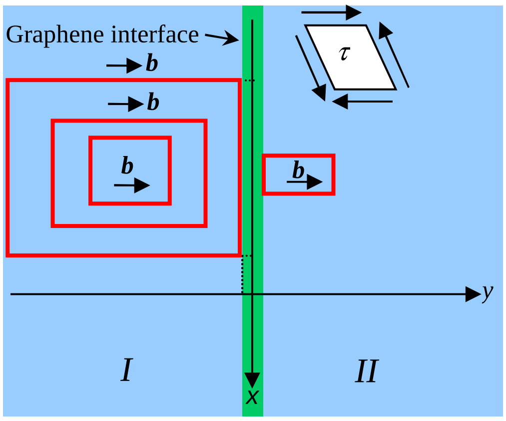

Fig. 4 Transfer of plastic deformation across a graphene interface. Transfer of plastic flow occurs through formation a rectangular glide dislocation loop in a metal layer I under the superposition of the applied shear stress τ and the stress field of an ensemble of rectangular glide dislocation loops located in the neighboring metal layer II.

Within this model, we have calculated the critical shear stress $\tau=\tau_{pl}$ for barrier-free generation of a new rectangular glide dislocation loop in Ni–graphene layered composite. The dependences of the critical shear stress τ_{pl} on the parameter λ characterizing the thickness of Ni layers in the Ni-graphene layered composite are plotted in Fig. 5, for various values of the graphene interface thickness h. It is seen in Fig. 5 that the critical stress τ_{pl} decreases with an increase in the metal layer thickness λ and/or a decrease in the graphene layer thickness h. For a given value of λ, the stress τ_{pl} is minimum in the case of a monolayer graphene interface having the thickness of $h\approx 0.3$ nm. Figure 5 and its extension to the region of small λ also demonstrates that at $\lambda=100$ nm and $h\approx 0.3$ nm, $\tau_{pl}\approx 1.75$ GPa. This value of τ_{pl} is in good agreement with the experimental strength characteristic [10] of the layered Ni-graphene composite with the Ni layer thickness of 100 nm and monolayer graphene interfaces.

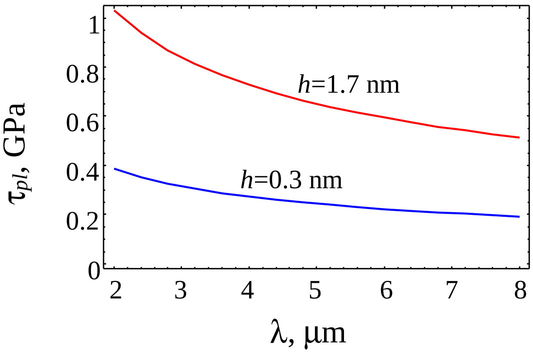

Fig. 5 The critical shear stress τ_{pl} for the barrier-free formation of a dislocation loop at a graphene interface vs the thickness λ of Ni layers in a layered Ni-graphene composite, for different values of the graphene layer thickness h.

Thus, plastic deformation can be transferred through graphene interfaces at high local stresses created by dislocation pileups. At the same time, the high stresses concentrated near the head of a dislocation pileup can induce the formation of a nanocrack: either in the metallic layer, at the angle α to the normal to the layer boundary (Fig. 6(a)), or at the metal-graphene interface (Fig. 6(b)), or within the graphene interface (if this interface represents a multilayer graphene sheet; Fig. 6(c)). We have calculated the condition for the generation of a nanocrack at the head of the dislocation pileup formed under the applied shear stress τ (Fig. 6). This condition has the form $\tau > \tau_{fr}$, where τ_{fr} is the critical stress for nanocrack generation.

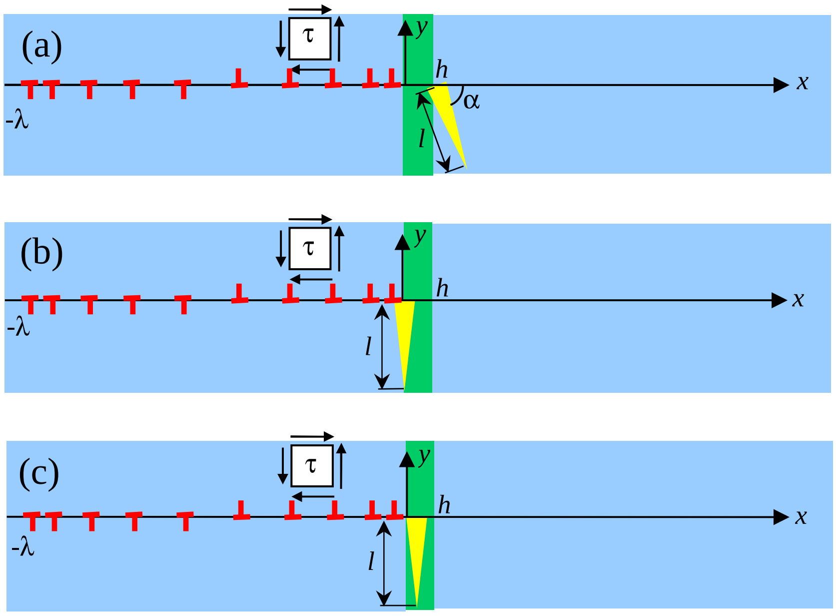

Fig. 6 Generation of nanocracks at a graphene interface in a metal matrix in the stress field of a double dislocation pileup and the applied shear stress τ. (a) Nanocrack forms in the matrix. (b) Nanocrack forms at the matrix–graphene interface. (c) Nanocrack forms inside the graphene inclusion.

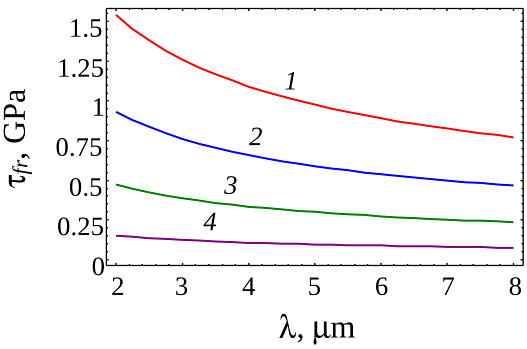

Fig. 7 Dependences of the critical stress τ_{fr} for nanocrack generation on the thickness λ of Ni layers in a layered Ni-graphene composite, for nanocrack in Ni (curves *1* and *2*), Ni–graphene interface (curve *3*) and graphene platelet (curve *4*), with $h = 1.7$ nm (curve *1*) and 0.3 nm (curve *2*). For curves *3* and *4*, graphene inclusion thickness h is arbitrary.

The dependences of the critical stress τ_{fr} for nanocrack generation in the Ni-graphene layered composite on the parameter λ are shown in Fig. 7, for the cases illustrated in Figs. 6(a), 6(b) and 6(c). The two upper curves in Fig. 7 correspond to the formation of a nanocrack in the Ni layer (Fig. 6(a)), for $\alpha = 70^{\circ}$, $h = 1.7$ nm and 0.3 nm (curves *1* and *2*, respectively). Curve *3* corresponds to the formation of a nanocrack at the Ni–graphene interface (Fig. 6(b)). Curve *4* corresponds to the formation of a nanocrack within the multilayer graphene platelet at one interatomic distance from the Ni–graphene interface terminating the dislocation pileup (Fig. 6(c)). As it is seen in Fig. 7, the critical stress τ_{fr} is the lowest for the case of nanocrack formation inside a multilayer graphene interface. At the same time, Fig. 7 demonstrates that if the graphene interface represents a monolayer graphene sheet, the nanocrack is the easiest to form along the Ni–graphene interface. Thus, the formation of nanocracks in metal-graphene layered composites is least likely if the graphene interfaces represent monolayer graphene sheets and the metal layers adhere well with graphene.

4 CONCLUSIONS

To summarize, we have theoretically examined fracture of polycrystalline graphene and the competition between plastic deformation and fracture processes in metal-graphene layered composites. In considering polycrystalline graphene, we have shown that individual disclinations and their dipoles at GBs can be responsible for the experimentally observed [8,9] dramatic decrease of fracture strength of polycrystalline graphene compared to its pristine counterpart. In consideration of metal-graphene layered composites, we have demonstrated that the critical fracture stress τ_{fr} for Ni-graphene nanolayered composites with multilayer graphene interfaces is always lower than the critical stresses τ_{pl} and τ_{fr} characterizing Ni-graphene nanolayered composites containing monolayer graphene interfaces, for the same values of the metal layer thickness λ. Therefore, Ni-graphene nanolayered composites containing monolayer graphene interfaces are specified by higher strength than their counterparts with multilayer graphene interfaces. At the same time, in a Ni-graphene nanolayered composite with monolayer graphene interfaces, for any values of the metal layer thickness λ, the critical fracture stress τ_{fr} is close to the critical stress τ_{pl} for the transfer of plastic deformation across a graphene interface. As a corollary, in the case of monolayer graphene interfaces in Ni-graphene nanolayered composite, the processes of plastic deformation and interface fracture compete and can occur concurrently.

5 ACKNOWLEDGEMENTS

The work was supported by St. Petersburg State University research grant 6.37.671.2013 and the Russian Ministry of Education and Science (Grants 14.B25.31.0017 and MD-2893.2015.1).

6 REFERENCES

[1] A.K. Geim, K.S. Novoselov, The Rise of Graphene, Nature Materials, 6, 183–191, 2007.

[2] A.K. Geim, Graphene: Status and Prospects, Science, 324, 1530–1534, 2009.

[3] A.H. Castro Nero, F. Guinea, N.M.R. Peres, K.S. Novoselov, A.K. Geim, The Electronic Properties of Graphene, Reviews on Modern Physics, 81, 109–162, 2009.

[4] A.A. Balandin, Thermal Properties of Graphene and Nanostructured Carbon Materials, Nature Materials, 10, 569–581, 2011.

[5] I.A. Ovid'ko, Mechanical Properties of Graphene, Reviews on Advanced Materials Science, 34, 1–11**,** 2013.

[6] T. Yamada, J. Kim, M. Ishihara, M. Hasegawa, Low-Temperature Graphene Synthesis Using Microwave Plasma CVD, Journal of Physics D: Applied Physics, 46, 063001, 2013.

[7] C. Lee, X. Wei, J.W. Kysar, J. Hone, Measurement of the Elastic Properties and Intrinsic Strength of Monolayer Graphene, Science, 321, 385–388, 2008.

[8] P.Y. Huang, C.S. Ruiz-Vargas, A.M. van der Zande, W.S. Whitney, M.P. Levendorf, J.W. Kevek, S. Garg, J.S. Alden, C.J. Hustedt, Y. Zhu, J. Park, P.L. McEuen, D.A. Muller, Grains and Grain Boundaries in Single-Layer Graphene Atomic Patchwork Quilts, Nature, 469, 389–392, 2011.

[9] C.S. Ruiz-Vargas, H.L. Zhuang, P.Y. Huang, A.M. van der Zande, S. Garg, P.L. McEuen, D.A. Muller, R.C. Hennig, J. Park, Softened Elastic Response And Unzipping in CVD Graphene Membranes, Nano Letters, 11, 2259–2263, 2011.

[10] Y. Kim, J. Lee, M.S. Yeom, J.W. Shin, H. Kim, Y. Cui, J.W. Kysar, J. Hone, Y. Jung, S. Jeon, S.M. Yan, Strengthening Effect of Single-Atomic-Layer Graphene in Metal–Graphene Nanolayered Composites, Nature Communications, 4, 2114, 2013.

[11] I.A. Ovid'ko, Review on Grain Boundaries in Graphene. Curved Nano- and Polycrystalline Graphene Structures as New Carbon Allotropes*, Reviews on Advanced Materials Science,* 30, 201–224, 2012.

[12] G.R. Irwin, Analysis of Stresses and Strains near the End of Crack Traversing a Plate. Journal of Applied Mechanics, 24, 361–364, 1957.

[13] S. Arghavan, A.V. Singh, Effects of van der Waals Interactions on the Nonlinear Vibration of Multi-layered Graphene Sheets, Journal of Physics D: Applies Physics, 45, 455305, 2012.

[14] K. Kim, V.I. Artyukhov, W. Regan, Y. Liu, M.F. Crommie, B.I. Yakobson, A. Zettl, Ripping Graphene: Preferred Directions, Nano Letters, 12, 293–297, 2012.

[15] A. Cao, Y Yuan, Atomistic Study on the Strength of Symmetric Tilt Grain Boundaries in Graphene, Applied Physics Letters, 100, 211912, 2012.

Proceedings of the 4th International Conference on
Fracture Fatigue and Wear, pp. 78-83, 2015

FRETTING FATIGUE OF DEEP ROLLED SHRINK FITTED SAMPLES

C. Santus

University of Pisa, Department of Civil and Industrial Engineering, Italy

Abstract: The shrink fitted shaft to hub connection, loaded under bending, experiences Fretting Fatigue at the end of the contact where both stress concentration and microslip are acting. Shrink fitted testing is not standard and common as the bridge type test, however, the round geometry implies no edge effect, the shrinkage and the bending loads can be carefully controlled with strain gages, and the stress distribution easily calculated with finite element analyses. Though the shrink fit compressive state, the cyclic bending introduces tensile stresses, hence the introduction of compressive residual stresses can play a significant role to prevent the initiation and the propagation of the fretting fatigue cracks. Experimental results are reported in the paper where the fretting fatigue strength was remarkably improved after a deep rolling treatment. Numerical analyses even predicted the complete mode I closure of potential fretting fatigue cracks by taking into account the compressive residual stresses. SEM investigation showed how the crack pattern was significantly different with deep rolling, having multiple crack initiation sites and then either coalescence or crack branching. From the modelling point of view, the paper shows that the self-arrest theory cannot be used to assess the fretting fatigue strength, for deep rolled specimens, where the crack remains closed. A better prediction can be obtained with a critical plane multiaxial fatigue criterion, based on the shear stress amplitude, which under a compressive stress state can be more effectively assumed as the driving force of the crack. Consistently the orientation of the plane experiencing the maximum shear stress amplitude was found in agreement with the observed initial crack direction.

Keywords: Fretting fatigue; Deep rolling; Residual stresses; Crack initiation direction

1 INTRODUCTION

The Fretting Fatigue (FF) damage can be experienced in several applications, typically the dovetail interface of turbomachinery [1,2] and also the so called shrink-fitted (tubular or cylindrical) connection [3,4]. Experimental fretting fatigue testing approaches can be categorized as [5,6]: (1) full/small scale simulation of the real fretting problem and (2) idealized fretting fatigue testing where the contact conditions are properly controlled. Fretting tests are well summarized in the book by Hills and Nowell [5], and usually are according to the “bridge” type testing, where bridge means a two sided contact pad indenter. Many examples of this kind of testing are reported in the literature, e.g. the book by Attia and Waterhouse [7] and many other papers. A main limitation of the of the bridge type testing is that the displacement can never be equal at the two sides of the contact, in turn leading to different actual local fretting configurations. This problem can be solved by fixing one side of the contact bridge to the rigid part of the testing frame. This solution is reported in several contributions, e.g. Rossino et al. [8]. The contact configuration in bridge type testing usually is “Hertzian” contact, i.e. cylindrical-to-flat or sphere-to-flat contacts. The “flat and rounded contact” edge problem was tested, under the bridge configuration, by Namjoshi et al. [9]. The lateral edge contact effect was investigated by Kim and Mall [10] along with the issue of plane strain at mid width and plane stress at the sides. Another problem is the misalignment, a tilting angle can cause edge stress concentrations. Moreover the flat contact (either rounded or not) can experience tilting during the load thus producing a not well controlled stress distribution at the contact region. This latter problem is not the case with Hertzian contact, having a rounded geometry, but can be not well controlled in flat and rounded contact. The round geometry proposed in the present paper has no edges and the tilt due to the bending is well considered in the related FE model. The present paper shows fretting tests with a specific shrink-fitted assembly that resembles a tubular connection component, it is also based on the half bridge concept, and it eliminates geometry misalignments and any other edge effects.

The most common approaches to fretting are the analogies either with a crack or a notch [11] and the approach according to Kitagawa-Takahashi (KT) diagram, where the short crack arrest can be evaluated and the size effect is inherently considered [12]. This approach naturally assumes that the fretting is a tensile driven fatigue fracture since small crack propagation is caused by mode I. Another approach is multiaxial fatigue critical plane as reported by Araújo et al. [13] and others, where the shear stress amplitude is predominant. The test results presented in this paper are critically considered with the available approaches and a discussion provided specifically about the initiation crack direction.

2 EXPERIMENTAL ACTIVITY

2.1 Bending setup of fretting fatigue tests

Fig. 1 illustrates the setup of the proposed fretting fatigue testing. The specimen, at the fretting interface, is conical in order to allow a calibration of the shrinkage imposed by means of an adjusting nut. The fretting load is applied according to a bending scheme with of a controlled hydraulic actuator. Two strain gages were used. One strain gage is on the shaft, with axial direction, at a certain distance with respect to the fretting point, for monitoring the actual bending load applied during the test. The other strain gage is applied at the outer periphery of the hub component, along the hoop direction, and it is used to calibrate the interference generated during the nut tightening before starting the fatigue loading.

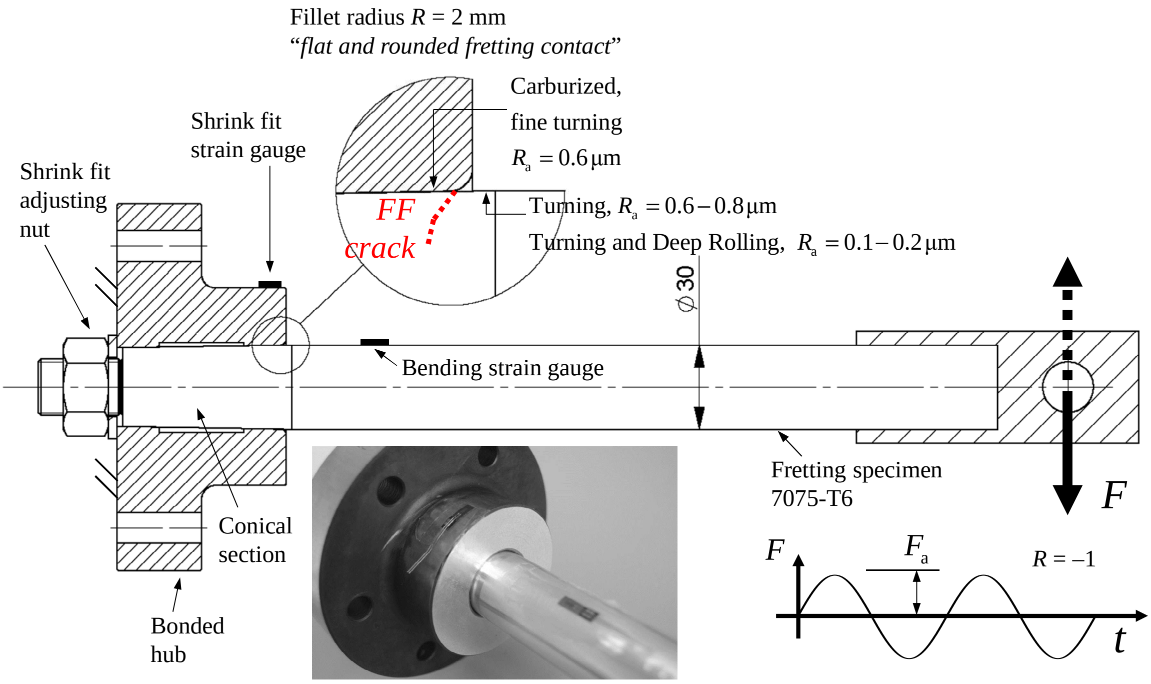

Fig. 1 Test setup, bending load and machining details at the fretting interface.

2.2 Deep rolling surface treatment

Some specimens were Deep Rolled, at the fretting interface (the conical section) to provide a comparison with the untreated specimens. Fig. 2 illustrates the deep rolling process and the residual stresses along the principal directions. More details can be retrieved in Ref. [14] describing both the parameter dependencies and the residual stresses measurements, preliminarily performed on flat samples and then on the shafts.

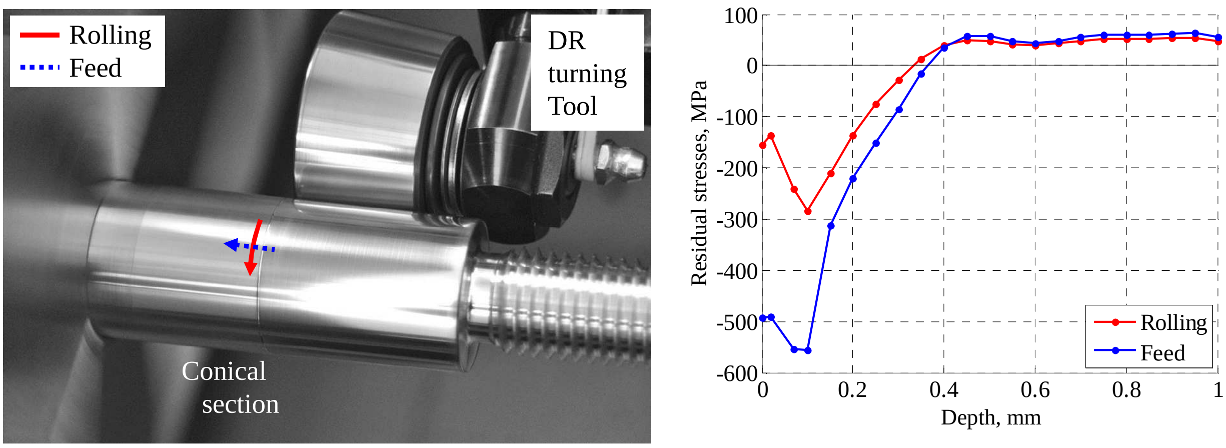

(a) (b)

Fig. 2 Deep Rolling treatment on the shaft specimen: (a) process, (b) residual stress distribution.

A conical edge contact roller was used and the treatment was performed just by means of a CNC turning machine tool. The treatment is not isotropic, indeed along the shaft axis direction the (compressive) residual stress is quite higher than the other direction, and it is approximately equal to the material yield stress, so introducing the maximum possible beneficial effect.

2.3 Test results

The Fretting Fatigue test results are reported in Fig. 3. Four test series were performed combining both the application of the deep rolling and a lubrication to be initially applied before the interference preload. The test trends are evident and according to as expected: the lubrication reduced the local stresses (the friction shear component) and the residual stresses also increased the strength by hindering the crack initiation and propagation, as usual under fatigue. The highest strength was therefore obtained with both lubrication and deep rolling (series C). Some of the deep rolled tests reported failure outside the expected fretting ‘hotspot’ since the failure was at the deep rolling edge where the indenter tool was removed. All other tests reported a fretting fatigue crack initiated at the edge of the contact, either at the upper or the lower sides that nominally experienced the same local load, indeed the bending load was reversal. A few tests showed fretting crack both sides, however, just a single crack among the two was predominant and propagated up to the specimen final fracture.

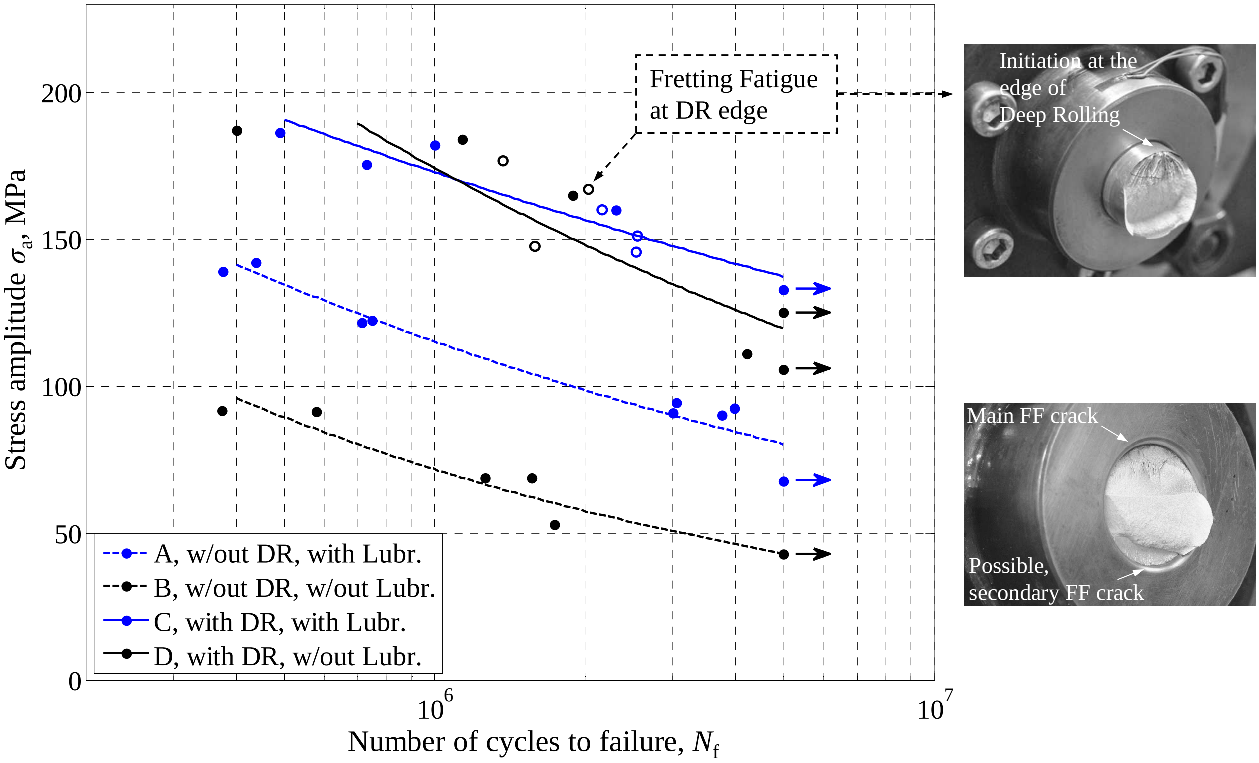

Fig. 3 Test results and fretting fatigue fracture sections.

2.4 SEM investigation of the fretting fatigue crack

After the fretting tests, SEM investigation were performed on the runouts. Fig. 4 illustrates the crack formation for each series. Multiple cracks were observed especially about the deep rolled specimens. The main evidence is that these cracks show a shallow angle with respect to the horizontal line. Obviously the leading crack would continue following a path more perpendicular to the specimen axis (mode I) but this happened only after a quite large size of the crack, in the order of 1 mm. Among the four series, those without lubrication (B and D), showed a preliminary very shallow path and then a slightly deviated path, while the others were more inclined to remain shallow or at least branch. This shallow direction is usual under fretting, and many literature examples can be cited. The general understanding of the problem is that a crack initiates along a shallow path which is consistent with the direction of the maximum shear stress amplitude, and then the crack kinks into the direction where the tangential stress is at a maximum in the mixed mode stress field, as Mutoh and Xu reports [15]. Alternatively the crack path can be immediately of mode I if the normal stress is prevailing as recently stated by Giner et al. [16].

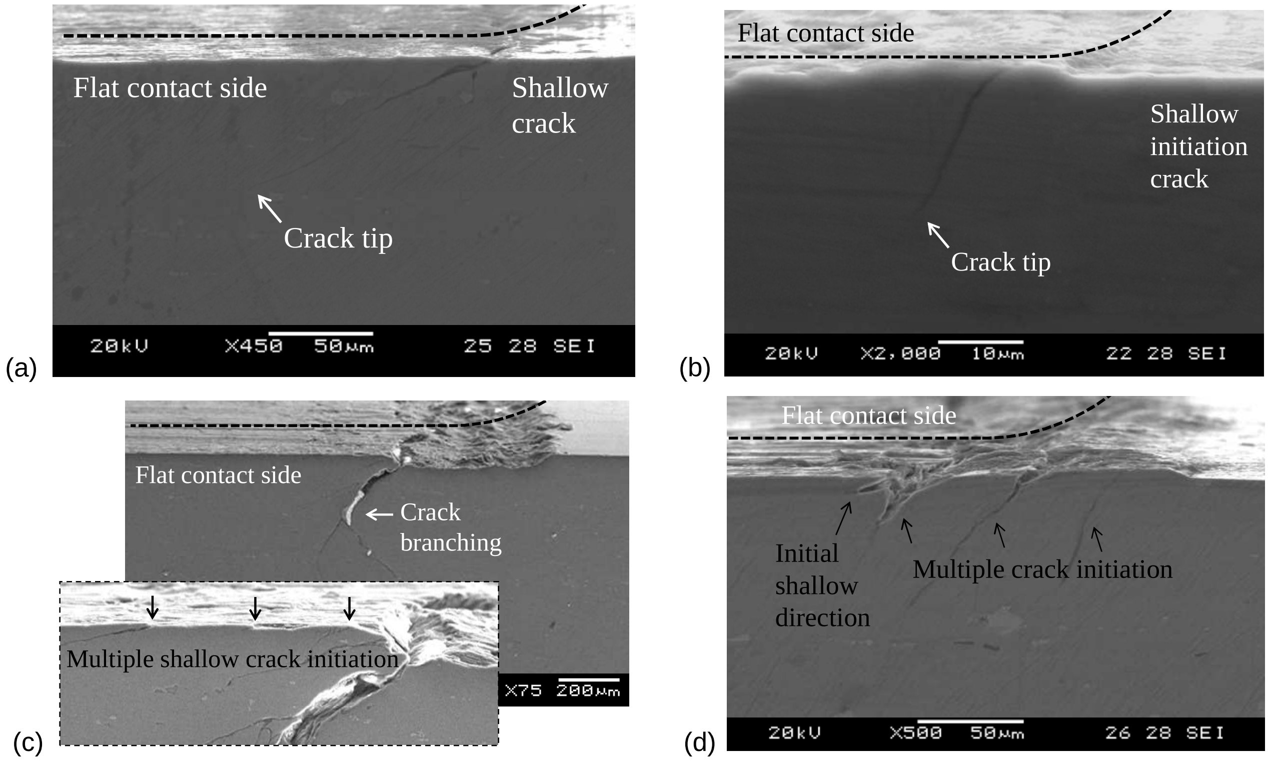

Fig. 4 SEM investigations on fretting fatigue cracks: (a), (b), (c), (d) for A, B, C, D series respectively.

3 NUMERICAL RESULTS

3.1 Direction of crack initiation

Numerical analysis allowed obtaining the local stress distribution at the fretting region. The first investigation was then devoted to the crack initiation angle prediction. The shear stress amplitude was calculated at the half the material size a_0 along with the maximum normal stress, Fig. 5.

$$a_0 = \frac{1}{\pi}\left(\frac{\Delta K_{th}}{\Delta \sigma_0}\right)^2 \tag{1}$$

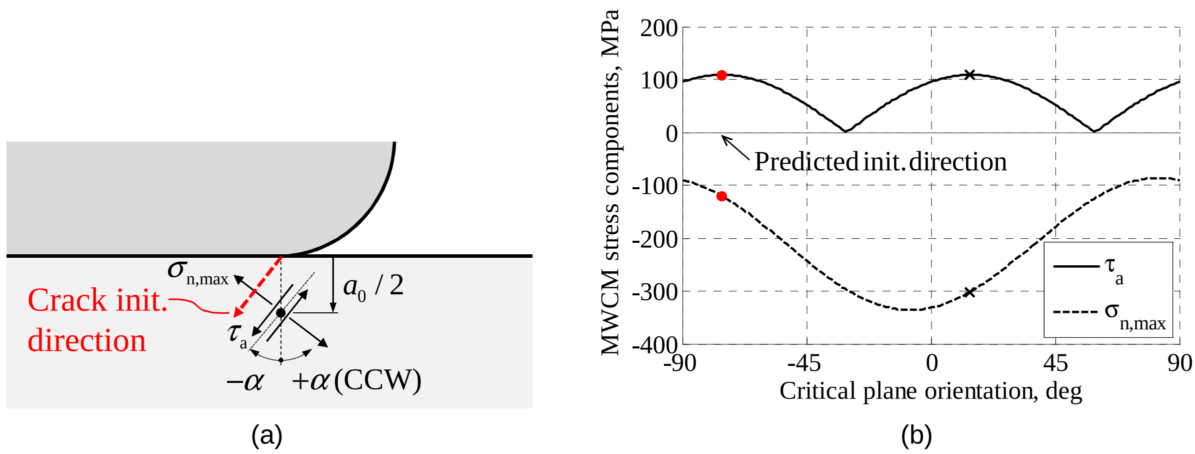

Fig. 5 Prediction of the initiation crack direction for the deep rolled specimens.

It is very important to mention that the shear stress amplitude is a 90° periodic function, indeed the shear is equal by comparing any two perpendicular directions [16,17]. Consequently, there are two shear amplitude maxima in the half plane range from -90° to 90°. Nevertheless, the maximum normal stress is a 180° periodic function, hence just one single plane direction is identified if the combined max shear stress amplitude and most tensile normal stress criteria are applied. By following this plane selection, a shallow negative angle is identified, that is coherent with the experimental evidence, Fig. 5. Actually, this consistent prediction just happened only for the deep rolled specimens (C and D series). Not rolled specimens showed a similar shear stress amplitude trend, but the most tensile plane was at the other max shear amplitude angle. The predicted direction was therefore to be corrected by considering a different combining parameter. Instead of the max normal stress, the mode II stress intensity factor range showed remarkably higher values within the a_0 range, Fig. 6. After introducing this correction, the initial shallow orientation was again captured. The direction toward the inner flat contact side was preferential despite the positive mode I stress intensity factor that would have experienced the crack along the complementary direction, Fig. 6.

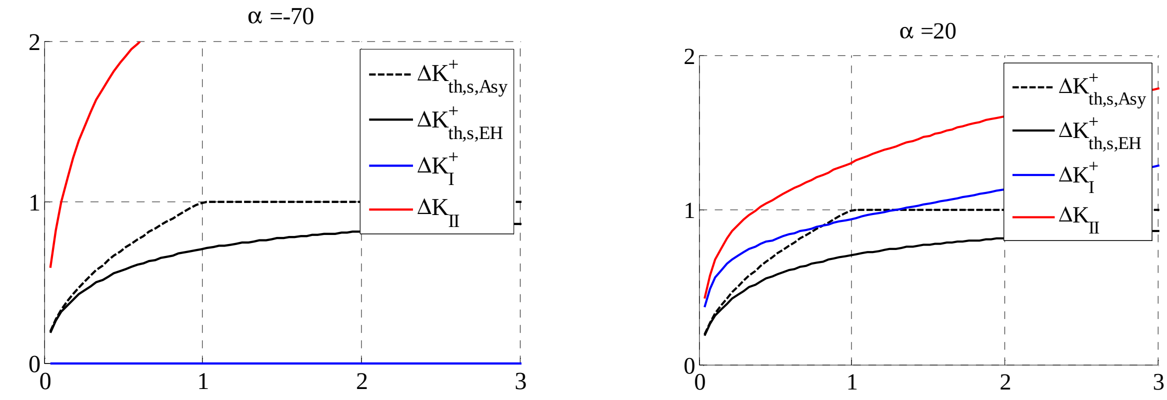

(a) (b)

Fig. 6 Mode I and II stress int. factor ranges along the complementary directions, not rolled specimens.

3.2 Strength prediction based on a shear stress parameter

According to the appropriate crack direction, shear stress amplitude and maximum normal stresses were considered and a multiaxial parameter evaluated at the half the material length, according to Refs. [8, 13]:

$$\tau_{\mathrm{a,eq}} = \tau_{\mathrm{a}} + \kappa\left(\frac{\sigma_{\mathrm{n,max}}}{\tau_{\mathrm{a}}}\right),\ \ \tau_{\mathrm{a,eq}}\ \text{to be compared to}\ \lambda \tag{2}$$

The results based on this equivalent shear stress amplitude are reported in Tab. 1. An accurate prediction is evident confirming the driving role of the shear stress for this specific configuration of fretting tests.

Table 1 Multiaxial fatigue criterion results, ratio $\tau_{\mathrm{a,eq}} / \lambda$.

Series A	Series B	Series C	Series D
0.99	0.80	0.90	1.23

4 CONCLUSIONS

- A bending device for fretting has been presented along with four test series on aluminium alloy 7075-T6 combining different surface conditions: lubrication and deep rolling treatment.
- Fretting strength was increased both by the introduction of a lubricant, that reduced the coefficient of friction, and in turn the shear stresses at the fretting interface, and by the deep rolling that induced highly compressive residual stresses.
- The angle of the initial direction of the crack was found to be in accordance with the SEM experimental evidence for the deep rolled specimens, while for the untreated tests the normal stress suggested the complementary plane. The introduction of a further parameter as the mode II stress intensity factor range was required to retrieve the correct prediction.
- The critical plane multiaxial predictive stress, suggested in the literature, was found to be quite accurate for the tests presented in the paper, confirming the shear stress as the driving parameter.

5 ACKNOWLEDGEMENTS

This work was carried out as part of the Italian research program PRIN 2009Z55NWC. The Authors would like to express their gratitude for the funding. Brusa Meccaniche company (Livorno, Italy) is also acknowledged for performing the deep rolling treatments. Finally, the authors are very grateful to Peen Service company (Bologna, Italy) for the X-ray diffraction residual stresses measurements.

6 REFERENCES

[1] P.A. McVeigh, G. Harish, T.N. Farris, M.P. Szolwinski, Modeling interfacial conditions in nominally flat contacts for application to fretting fatigue of turbine engine components, International Journal of Fatigue, 21(Suppl.1), S157–S165, 1999.

[2] B.J. Carter, E.C. Schenck, P.A. Wawrzynek, A.R. Ingraffea, K.W. Barlow, Three-dimensional simulation of fretting crack nucleation and growth, Engineering Fracture Mechanics, 96, 447–460, 2012.

[3] T. Juuma, Torsional fretting fatigue strength of a shrink-fitted shaft, Wear, 231(2), 310–318, 1999.

[4] C. Santus, Fretting fatigue of aluminum alloy in contact with steel in oil drill pipe connections, modeling to interpret test results, International Journal of Fatigue, 30(4), 677–688, 2008.

[5] D.A. Hills, D. Nowell, Mechanics of Fretting Fatigue, Kluwer Academic Publishers, 1994.

[6] J. De Pauw, P. De Baets, W. De Waele, Review and classification of fretting fatigue test rigs, Sustainable Construction and Design, 2(1), 41–52, 2011.

[7] M.H. Attia, R.B. Waterhouse, Standardization of Fretting Fatigue Test Methods and Equipments, ASTM, STP 1159-EB, 1992.

[8] L.S. Rossino, F.C. Castro, W.W. Bose Filho, J.A. Araújo, Issues on the mean stress effect in fretting fatigue of a 7050-T7451 Al alloy posed by new experimental data, International Journal of Fatigue, 31(11-12), 2041–2048, 2009.

[9] S.A. Namjoshi, S. Mall, V.K. Jain, O. Jin, Fretting fatigue crack initiation mechanism in Ti-6Al-4V, Fatigue and Fracture of Engineering Materials and Structures, 25(10), 955–964, 2002.

[10] H.S. Kim, S. Mall, Investigation into three-dimensional effects of finite contact width on fretting fatigue, Finite Elements in Analysis and Design, 41(11-12), 1140–1159, 2005.

[11] D. Dini and D.A. Hills, Bounded asymptotic solutions for incomplete contacts in partial slip, International Journal of Solids and Structures, 41(24-25), 7049–7062, 2004.

[12] J.A. Araújo, D. Nowell, Analysis of pad size effects in fretting fatigue using short crack arrest methodologies, International Journal of Fatigue, 21(9), 947–956, 1999.

[13] J.A. Araújo, L. Susmel, D. Taylor, J.C.T. Ferro, E.N. Mamiya, On the use of the Theory of Critical Distances and the Modified Wöhler Curve Method to estimate fretting fatigue strength of cylindrical contacts, International Journal of Fatigue, 29(1), 95–107, 2007.

[14] M. Beghini, L. Bertini, B.D. Monelli, C. Santus, M. Bandini, Experimental parameter sensitivity analysis of residual stresses induced by deep rolling on 7075-T6 aluminium alloy, Surface and Coatings Technology, 254, 175–186, 2014.

[15] Y. Mutoh and J.-Q. Xu, Fracture mechanics approach to fretting fatigue and problems to be solved, Tribology International, 36(2), 99–107, 2003.

[16] E. Giner, M. Sabsabi, J.J. Ródenas, F. Javier Fuenmayor, Direction of crack propagation in a complete contact fretting-fatigue problem, International Journal of Fatigue, 58, 172–180, 2014.

[17] V. Lamacq, M.-C. Dubourg, Modelling of initial fatigue crack growth and crack branching under fretting conditions, Fatigue and Fracture of Engineering Materials and Structures, 22(6), 535–542, 1999.

International Journal of Fracture Fatigue and Wear, Volume 3
Proceedings of the 4th International Conference on
Fracture Fatigue and Wear, pp. 84-89, 2015

FATIGUE RESISTANCE OF MOTOR COMPONENTS: ROLE OF RESIDUAL STRESSES

A. Roth and A. Galtier

ASCO Industries CREAS, BP 70045, 57301 Hagondance Cedex, France

Abstract: Fatigue resistance is an important issue for carmakers, especially concerning motor components as crankshafts or diesel injection rails. These high technical components show geometrical singularities (crankshaft fillets and injection holes in common rails) which are subjected to stress concentration and so highly sensitive to fatigue damages. One way to prevent fracture is to control and stop crack propagation. In a first approach the study was focused on crankshafts fillets fatigue resistance. To resist to fatigue, this part of crankshaft is generally deep-rolled to induce a field of high compressive residual stresses in depth. Results from fatigue bending tests correlated to a first modeling effort based on fracture mechanics show that fatigue strength is governed by crack arrest mechanism. Increasing the fatigue strength therefore requires developing grades with high stress intensity factor threshold or with a capacity to introduce high level of residual stresses. The importance of controlling the residual stresses distribution during specific processes as deep-rolling (for crankshaft) or autofrettage (expanding operation for common rails) is shown. Their determination goes through the knowledge of the behavior law of materials thanks to tension-compression tests results and appropriate simulations.

Keywords: fatigue tests; residual stresses; stress intensity factor; simulation; crack arrest

1. INTRODUCTION

Fatigue is an unavoidable weakening of materials due to cyclic applied loads. The main challenges about fatigue consist in understanding its mechanisms to predict and delay it, insuring a longer lifetime to the material. Motor components as crankshafts or common rails have specific geometrical shapes that make certain pieces of them particularly sensitive to fatigue damages. Indeed these geometrical singularities (crankshaft fillets and rail intersection holes) are the place of intense stress concentration resulting from a high stress concentration factor. As a consequence, theses parts of the components are the first to be concerned by the increase of loads resulting to cost reduction and downsizing trends in automotive industry. All these constraints have to be taken into account by Asco Industries when developing special steels with high mechanical properties. To ensure the component to better resist to fatigue, a specific treatment is applied. Concerning crankshafts, the most used process is deep-rolling [1]: the crankshaft fillets are cold worked with rollers; the first part of this article will be thus dedicated to our fatigue approach concerning this process. Common rails will be the object of a second part. There are subjected to an operation of autofrettage which consists in applying a high pressure inside the holes to plastify their surface. Both processes induce a field of high residual stresses in depth that can stop cracks initiated from the surface.

The development of new grades of steel requires the control of stress level: voluntary residual stresses induced by the processes mentioned above as undesirable residual stresses resulting from some operation like straightening or quenching. From experimental data and simulation, the necessity to give a good description of the material behavior in order to have an appropriate estimation of residual stresses induced during autofrettage and their evolution during fatigue will be enhanced.

2. FATIGUE BEHAVIOR OF CRANKSHAFTS

2.1. Experimental Approach

In service the main loading of crankshaft and particularly crankshaft fillets is bending. At low regime, the load ratio defined by $R = M_{min}/M_{max}$ is as $R = 0$ whereas $R = -1$ for high motor regime due to inertia effects. To understand the fatigue behavior of deep-rolled crankshafts, a bending test has been developed (see Fig. 1) in collaboration with PSA [2] at the Asco Industries research and development center CREAS with a special specimen whose fillets can be deep-rolled with industrial Hegenscheidt head [3], exactly like industrial crankshafts.

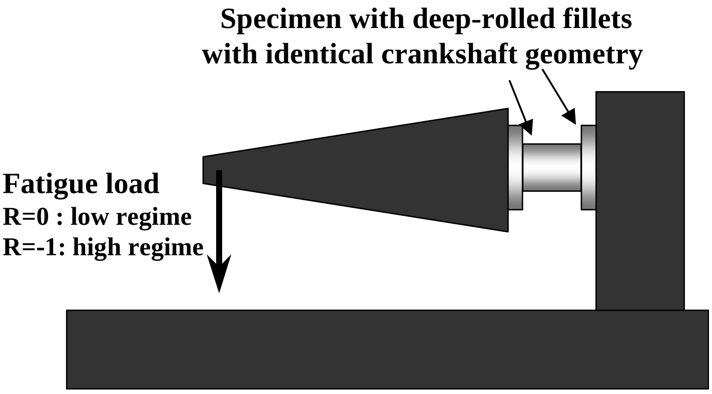

Fig. 1 Deep-rolled crankshaft bending test.

Load controlled tests with different amplitudes allow finding the fatigue strength at 2 million cycles by the iterative method, which is based on the sample failure or no-failure. As it can be seen in Fig. 2, cracks have been observed on unfailed specimen at 2 million cycles. Further observation of these specimens showed a maximum crack length of 1,3mm. It implies that, even if cracks are initiated, they do not propagate to lead to fracture.

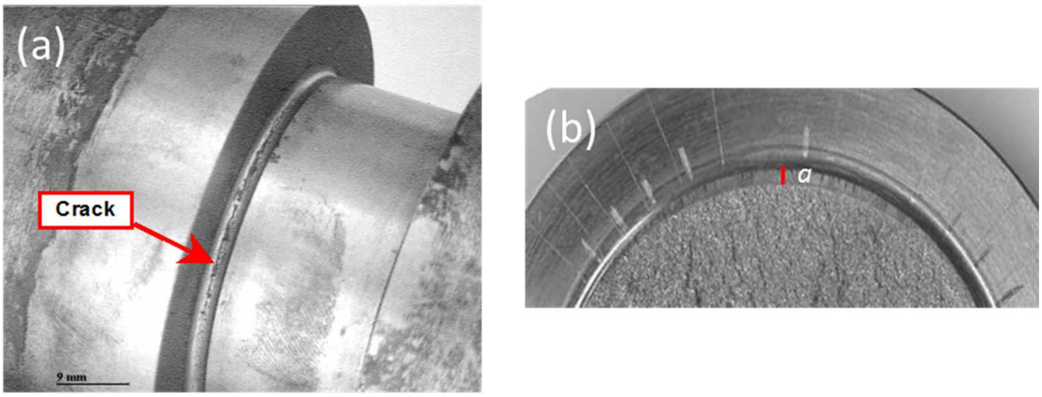

Fig. 2 Example of crack on unfailed specimen at 2 million cycles: (a) crack on the surface of the specimen groove; (b) observation of the crack (length a) in the cross section after forced fracture.

From fracture mechanics theory, the arrest mechanism may be governed by the stress intensity factor (ΔK for cyclic loading with $\Delta K = K_{max} - K_{min}$) according to the following relationship :

$$\Delta K = K_{max} = f(a).\left(\sigma_{app}^{max}(a) + \sigma_{res}(a)\right).\sqrt{\pi a}$$

In the case of R = -1, with $K_{min} = 0\ MPa.m^{1/2}$

Where: a is the crack length
$f(a)$ is a shape factor
$\sigma_{app}^{max}(a)$ refers to the applied stress, depending on *a*
$\sigma_{res}(a)$ are the residual stresses, depending on *a*

If $\Delta K > \Delta K_{Th}$, where ΔK_{Th} in an intrinsic material constant, then the crack propagates. Based on these considerations, a first modeling effort is made to give an estimation of ΔK and its evolution with the crack length.

2.2. Crack propagation modeling

The adopted method is based on previous work on crankshaft fatigue resistance made by Taylor [4]. It allows estimating the applied stress σ_{app}^{max} thanks to linear-elastic finite elements modeling. This has been realized at the CREAS on FORGE ® software. The prediction of fatigue failure requires to know the material fatigue limit and the stress intensity threshold ΔK_{Th}. To complete the calculation of ΔK according to the above equation, it is also necessary to evaluate $\sigma_{res}(a)$. Since the residual stresses cannot be evaluated by the proposed method which only consider linear-elastic fracture mechanics, a complementary cyclic plastic modeling is realized, based on the calculation of cumulated plastic strain. If in metal forming simulations, the strain hardening is generally supposed isotropic because strains are large enough (greater than 10%), for these operation of cold deformation and then in the case of cyclic loading, the strain level remains too low to ignore kinematic hardening. A non-linear part of the hardening is therefore introduced in isotropic hardening through memory effects that represent the change of loading direction during fatigue cycles. More details about this analytical model named CLIEME (for Combined Linear Kinematic Hardening and Isotropic strengthening or softening with Evanescent Memory Effect) are given in [5]. The simulation of circumferential residual stresses after deep-rolling shows a good correlation with X-Ray measurements performed on the material.

Thanks to the combination of finite elements and the analytical model, ΔK can be calculated taking a shape factor of 1, and its evolution along the crack length is described in Fig. 3 for different loading levels. As seen in this figure, a threshold of ΔK_{Th}.≈ 6 MPa.m$^{1/2}$ is chosen, which is a typical value for steels. The ΔK curve shows a valley that corresponds to 1-2 mm depth; this observation is in good agreement with the maximum crack length of 1,3 mm. For example, a bending moment of 5300 Nm will induce a crack that stops at 1 mm depth.

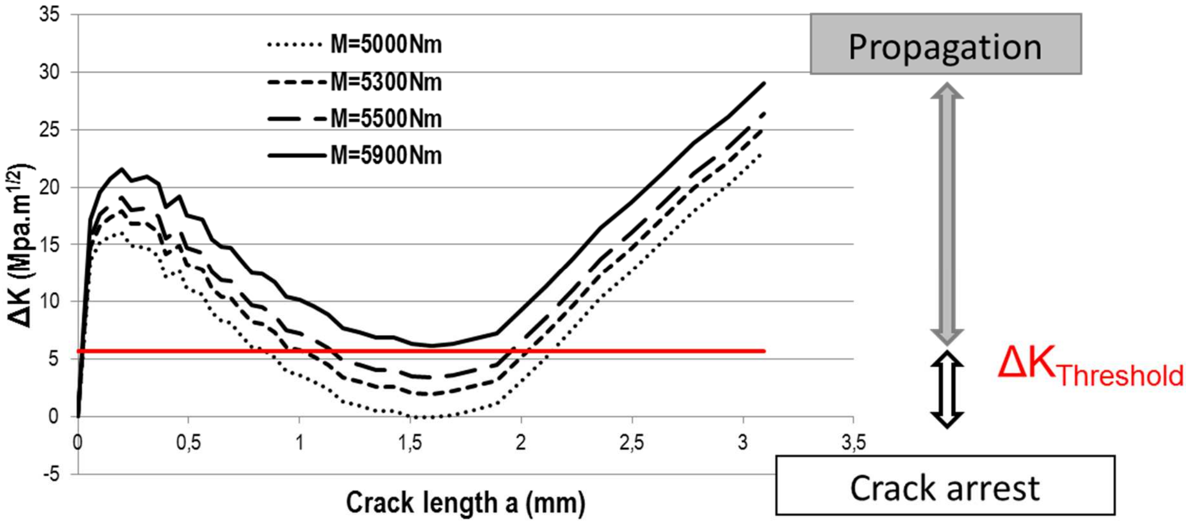

Fig. 3 Evolution of ΔK with crack depth for different loading levels.

Further finite element simulations are expected to show great performances in fatigue of grades displaying a high ΔK_{Th} and handling a high level of residual stresses during the deep-rolling operation. These expectations are motivated by the results presented in Fig. 4. A comparison is made between different grades and two different deep-rolling loads. In a general manner, bainitic steels show a higher fatigue resistance than other grades. This result is supposed to be due to a higher ΔK_{Th} of the material. Moreover, increasing the deep-rolling load from 900 daN to 1100 daN still increases the fatigue resistance for bainitic steels. This feature is expected to be related to a higher level of residual stresses induced by deep-rolling.

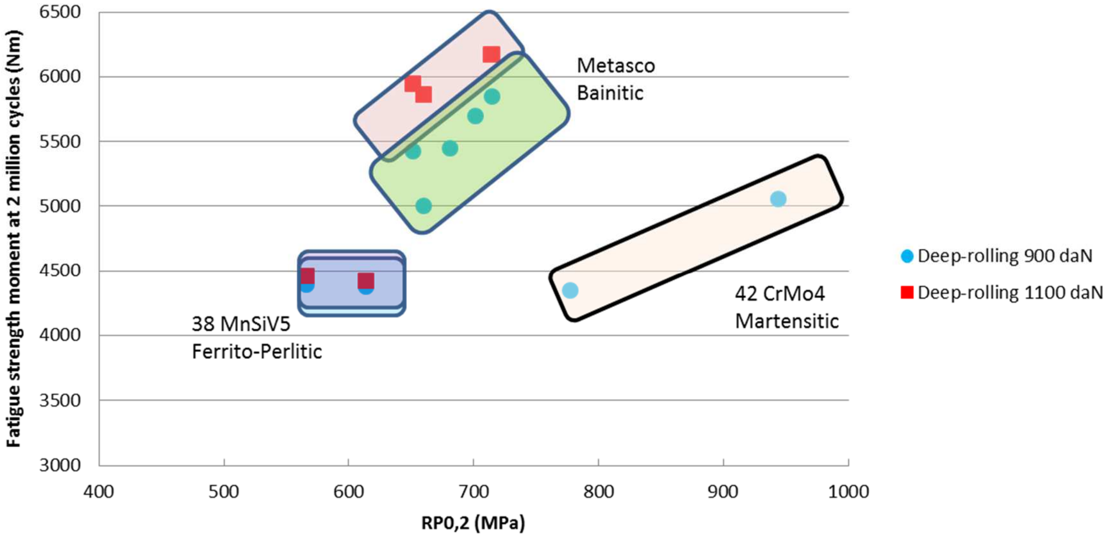

Fig. 4 Comparison of the fatigue resistance of different grades subjected to different deep-rolling loads.

3. FATIGUE BEHAVIOR OF COMMON RAILS

The current European anti-pollution standards require increasing in-use injection pressures, reaching 2200 bars in 2017. This pressure increase is associated with downsizing which implies geometry modifications of common rails, in particular holes diameter reductions. With such high pressure conditions, it is necessary to enhance the fatigue resistance of the component especially at the holes intersections. The operation of “autofrettage” allows introducing residual compressive stresses inside the material by applying a high overload pressure of typically 7000 b. The increasing injection pressures will require increasing autofrettage pressure too.

Finite element simulation is used to evaluate the stress fields in the holes intersection (see Fig. 5) where the cracks are seen to be located. Since the real load applied to the common rail is multiaxial, a 2D simulation is not adequate to appropriately describe the stress field and 3D effects must be taken into account. The stress profile at the hole intersection (see Fig. 6) shows an important stresses concentration with $K_T \approx 2.5$ and is very similar to what can be found for crankshafts fillets [5]. The reflection made on crack arrest mechanism on crankshafts should also be valid for common rails and complementary with the present study carried on behavior laws. Determining an appropriate elastoplastic behavior law of the material is of great importance to know the level of residual stresses induced by the autofrettage operation.

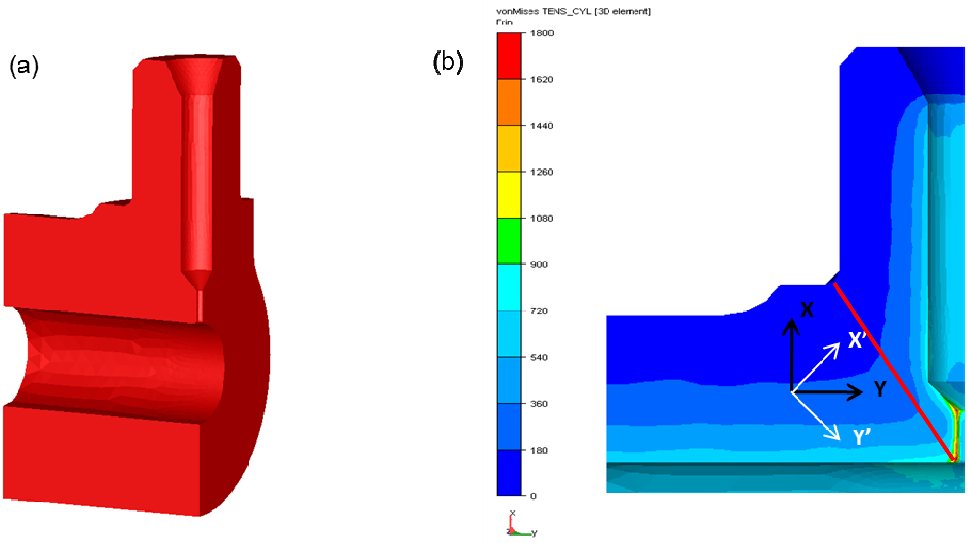

Fig. 5 (a) Effective part of the common rail modeled by finite elements on FORGE ®; **(b)** Focus on the intersection holes: Von Mises stresses at 4000 bars (elastic behavior) in the (X’Y’) space (fracture plane) oriented toward 45° from (XY) along the red path.

To obtain this information, a first 3D simulation is in progress based on cyclic tension-compression tests results of the materials which will be used to design the common rails. By this way, the behavior law will be identified considering a combination of kinematic and isotropic hardening. It has been shown [6] that a linear model is not sufficient for a good description of the behavior; non-linearity must be thus introduced in the formulation. The chosen formulation is based on the non-linear Lemaître-Chaboche kinematic model [7].

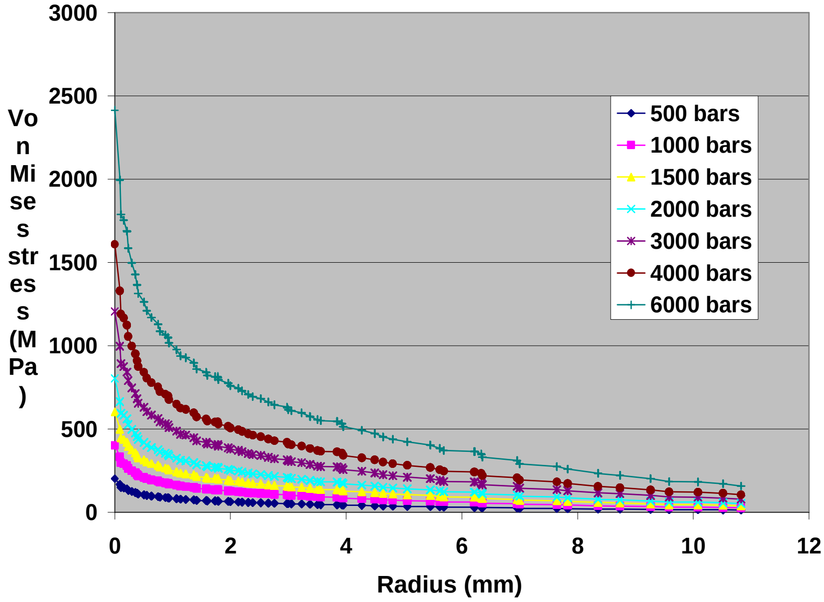

Fig. 6 Von Mises stresses profile along the red path of Fig. 5 (b) near the hole intersection of common rails where cracks are typically found.

4. CONCLUSIONS AND FUTURE WORK

The constraints required by European standards always necessitate the carmakers to adapt the design of the automotive components and as a consequence the steelmakers to propose new grades of steel able to handle the pre-use and in service conditions, as in the case of crankshafts and common rails. An analysis of cyclic stress intensity factors has been realized for the application of deep-rolling on crankshafts fillets. The simulated evolution of this parameter as a function of the crack length correlated to the experimental results can explain the crack arrest mechanism observed after fatigue bending tests. It has been shown that the residual stresses induced by deep-rolling processes act as barrier to crack propagation, delaying the moment where the threshold ΔK_{Th} will be reached. It is thus challenging to develop grades with high enough stress intensity factor threshold in order to increase the fatigue strength.

The second example deals with the operation of autofrettage on common rails. Like deep-rolling, this process induces beneficial residual stresses at the surface of injections holes that make them more resistant to fatigue due to cyclic in service high pressure conditions. An important work on behavior laws is in progress in order to determine suitable material parameters for an implementation in a 3D elastoplastic finite element model for common rail as well as for crankshafts. Coupled with fracture simulation, this model should give a better description of the applied and residual stresses profiles around the interest points for each application and will constitute a basis for the CREAS to compare the fatigue performances of different grades of steel.

5. REFERENCES

[1] A. Benamar, J.F. Flavenot, J. Lu, C. Sardine, G. Chalant, G. Inglebert “ Galeter pour tenir en fatigue ” / CETIM-Information N°129 octobre 1992.

[2] H. Michaud, M. Blanc, P. Dierickx, X. Roy, B. Quinet, D. Forest “ Analyse du mécanisme de renforcement de la tenue en fatigue des aciers par galetage : exemple du vilebrequin ” ATTT 2002- 31ème congrès du traitement thermique et de l’ingénierie des surfaces / ATTT Grenoble 19, 20 et 21 juin 2002.

[3] G. Felgentreu, C. ReuB (société Hegenscheidt) “ Le galetage aujourd’hui dans le bureau d’études et dans l’usine ” Publication CETIM du 7/11/1991 “ Les contraintes résiduelles et le bureau d’études ” p. 100-125.

[4] D. Taylor “Crack modelling: a novel technique for the prediction of fatigue failure in the presence of stress concentrations » Computational Mechanics 20 (1997) 176-180.

[5] H. Michaud, J.M. Sprauel “Analytical and experimental approach of residual stress on deep-rolled crankshafts and auto-fretted Diesel injection rails. Effect on fatigue resistances in service.” Materials Science Forum vol. 681 (2011) 261-266.

[6] J. Demurger, R. Forestier, B. Kieber, P. Lasne “Deep-rolling process simulation, impact of kinematic hardening on residual stresses“ Proc.& ESAFORM 2006.

[7] J. Lemaître, J.L. Chaboche “Mécanique des matériaux solides” *Dunod*, Paris 1988.

Proceedings of the 4th International Conference on
Fracture Fatigue and Wear, pp. 90-96, 2015

CRITICAL PLANE METHOD FOR MULTIAXIAL FATIGUE LIFE ASSESSMENT OF COMPONENTS UNDER COMBINED BENDING-TORSION LOADING

S.T. Kyaw, A.B. Azahari and W.Sun

Materials, Mechanics & Structures Research Division, Faculty of Engineering
The University of Nottingham, Nottingham NG7 2RD, UK

Abstract: This paper presents some results of multiaxial fatigue life assessment of components under combined bending-torsion loading. The loading cycle is assumed as completely reversed and in-phase loading. Critical plane damage models (Smith-Watson-Topper and Fatemi-Socie) are used to estimate the lifetime based on stress and strain results from finite element analysis of components under loading. The predicted lifetime (number of load cycles) represents the time required to initiate a meso crack of a few mm. To benchmark the method, lifetime assessment of a notched specimen that has identical dimensions and loading conditions to the experiment from the open literature is carried out. The lifetime deviation from the experimental results is within a factor of five. The crack initiation sites and orientation of crack planes are also compared against experimental results. Crack initiates at the root of the specimen notch where stress concentration occurs. Finally, the correlation between the directions of principal stresses and maximum shear strain and crack plane orientation is analysed to understand the effect of combined loading on crack plane orientation.

Keywords: multiaxial fatigue lifetime; critical plane model; notched analysis; FEA

1 INTRODUCTION

In reality, many engineering components are subjected to multiaxial loadings under service conditions. Even if uniaxial loading is applied remotely, the stress and strain states at the stress concentration features such as notches will be multiaxial. The stress state becomes more complicated when the loading applied is fatigue loading. This paper focuses on predicting the lifetime of a notched specimen under multiaxial fatigue loading. Despite the actual multiaxial loads expected at notched regions of components under service conditions, most fatigue tests, in order to extract parameters for fatigue lifetime models such as fatigue ductility coefficient, are carried out using smooth specimen using uniaxial loading. Hence, it is important to have the ability to predict multiaxial fatigue life from existing uniaxial fatigue properties.

Early theories existed for multiaxial fatigue life prediction. Most notably, equivalent stress approaches (von Mises, Tresca) and maximum principal stress criteria [1, 2] are examples of the earliest approaches. To study the role of plasticity in low cycle fatigue, strain based approaches [3, 4] were also proposed by modifying static yield theories in terms of strain parameters. In this paper, the critical plane approach is used to predict multiaxial fatigue life time. The method is based on the physical nature of fatigue crack initiation and propagation on a specific plane within a component. The concept was introduced in [5]. The orientation of this plane is determined by material type, applied strain amplitude and state of stress and strain within the component. Maximum normal stress on the critical plane and maximum shear stress play an important role in life prediction depending on the type of crack. Two damage models are applied in this paper. The first one is proposed by Smith, Watson and Topper [6] and the method is suitable for damage analysis where the crack development is tensile dominant. An alternative method by Fatemi and Socie [7] is found to be superior when the damage is driven by shear strain amplitude and modified by direct stresses.

To justify the lifetime prediction models presented in this paper, the predictions were made for the notched specimen which has identical dimension to multiaxial fatigue experiment carried out by Fash [8]. To obtain the stress/strain state at the notch of the specimen, finite element analysis (FEA) was carried out for completely reversed fatigue loading. Mixed mode loading condition is considered by applying in-phase bending and torsion loads. The resultant fatigue lifetime, crack locations and its orientations are compared to experimental results from [8]. Additionally, the effect of mixed mode loading on orientations of principal plane and crack initiation direction are also investigated.

2 FINITE ELEMENT MODEL

To obtain stress/strain state of the notched specimen, FEA is carried out. The model has the dimensions shown in Fig. 1 (i). Fash [8] used two linear servo-hydraulic actuators to apply constant amplitude bending and torsion moments at 150mm from the notch. To mimic this experiment while saving computation time, only a portion of the specimen is used for FEA as shown in Fig. 1 (ii). The elements used are three dimensional general purpose brick elements with reduced integration (C3D8R) within Abaqus. Mesh and boundary conditions of the model can be found in Fig. 1 (ii). Encastre condition is applied to the clamped end of the specimen to restrict all displacement degrees of freedom (d.o.f). The other end is constrained by kinematic coupling constraints to the reference point (RP) where loadings will be applied. A vertical force (V) is applied so that the bending moment at the notch is I×V. Torsion moment (T) is also applied at the RP. The material used for FEA is SAE-1045 steel and its behaviour is elastic-plastic with isotropic hardening with the parameters from [8]. To study the mixed mode loading effect, bending moment to torsion (M/T) ratio of about 0.71 with different magnitudes of each loading were used and they are tabulated in Table 1. At the end of each time step of FEA, stress and strain results of elements around the notched region are written into the data file and the results are post-processed in Matlab [9] to obtain multiaxial fatigue life.

Table 1 Constant amplitude mixed mode loadings applied to FE model of notched shaft

Case	Bending moment (Nm)	Torsion (Nm)
1	1475	0
2	2600	0
3	1730	0
4	1220	1710
5	990	1390
6	1850	2550

3 CRITICAL PLANE MODELS FOR MULTIAXIAL FATIGUE

The critical plane technique assesses fatigue lifetime by using hypothetical damage parameter D. The parameter is based on maximum direct stress and shear strain amplitudes obtained after transforming stress and strain outputs at each time step into local arbitrary material planes. Two types of critical plane models are applied here. The damage parameter (D) for Smith-Watson-Topper (SWT) model and Fatemi-Socie (F-S) model can be expressed as Eq (1) and Eq (2) respectively. In the earlier work, critical plane was assumed as the plane experiencing maximum normal strain amplitude (ε_a) or maximum shear strain amplitude (γ_a). In this work, a modified version proposed in [10, 11] is used where critical plane is the plane experiencing maximum D. Once D is known for a candidate plane, fatigue lifetime (N_f) can be evaluated by using empirical parameters such as $\sigma_f^{'}$, $\varepsilon_f^{'}$ as shown in Eq (1) and Eq (2).

$$\varepsilon_a \sigma_{\max} = \frac{\left(\sigma_f^{'}\right)^2}{E}\left(2N_f\right)^{2b} + \varepsilon_f^{'}\sigma_f^{'}\left(2N_f\right)^{b+c} \tag{1}$$

$$\gamma_a\left(1+\left(\sigma_{\max}/\sigma_y\right)\right) = \frac{\tau_f^{'}}{G}\left(2N_f\right)^{b} + \gamma_f^{'}\left(2N_f\right)^{c} \tag{2}$$

where, E is elastic modulus, b and c are fatigue strength and ductility exponents, $\sigma_f^{'}$ is tensile fatigue strength coefficient, $\varepsilon_f^{'}$ is fatigue ductility exponent, $\tau_f^{'}$ and $\gamma_f^{'}$ are shear fatigue strength and torsional ductility coefficients, ε_a and γ_a are direct and shear strain amplitudes, G is modulus of rigidity, $\sigma_{\max}$ is the maximum direct stress at the candidate material plane, σ_y is yield stress and N_f is number of cycles to failure. These material properties for SAE-1045 steel are taken from [12].

To use the critical plane models, stress and strain must be transformed into the coordinate system of a candidate plane. This can be done if the direction cosines of a candidate plane to the original coordinate system are known. The direction cosines of a candidate plane can be illustrated by Fig. 2 where θ is z direction cosine and θ_R is y direction cosine to the projected normal vector (n) onto X-Y plane. Using θ and θ_R, direction cosines can be expressed as Eq (3). The angles vary from zero to 180° with 1° increments to create possible candidate planes. For each time step of FEA and for every candidate plane, normal strain (ε), shear strain (γ) and normal stress (σ) to a candidate plane can be calculated as shown in Eqs (4) to (6). Once these are known for a whole cycle, the normal and shear strain amplitudes and maximum normal stress can be found. Finally fatigue life time (N_f) is calculated by either Eq (1) and Eq (2) using the Newton-Raphson method. If the loading is more complicated than the completely reversed fatigue loading applied here, accumulated damage must be calculated using rainflow counting method as mentioned in [13].

$$\begin{aligned} n_z &= \cos\theta \\ n_y &= \sin\theta(-\cos\theta_R) \\ n_x &= \sin\theta\sin\theta_R \end{aligned} \tag{3}$$

$$\varepsilon = \varepsilon_x n_x^2 + \varepsilon_y n_y^2 + \varepsilon_z n_z^2 + \gamma_{xy} n_x n_y + \gamma_{yz} n_y n_z + \gamma_{xz} n_x n_z \tag{4}$$

$\gamma = 2\left(\varepsilon_R^2 - \varepsilon^2\right)^{0.5}$, where ε_R can be obtained from Eq (7) (5)

$$\sigma = \sigma_x n_x^2 + \sigma_y n_y^2 + \sigma_z n_z^2 + 2\tau_{xy} n_x n_y + 2\tau_{yz} n_y n_z + 2\tau_{xz} n_x n_z \tag{6}$$

$\varepsilon_R = \left(\varepsilon_{Rx}^2 + \varepsilon_{Ry}^2 + \varepsilon_{Rz}^2\right)^{0.5}$, where

$$\begin{aligned} \varepsilon_{Rx} &= \varepsilon_x n_x + 0.5(\gamma_{xy} n_y + \gamma_{xz} n_z) \\ \varepsilon_{Ry} &= \varepsilon_y n_y + 0.5(\gamma_{xy} n_x + \gamma_{yz} n_z) \\ \varepsilon_{Rz} &= \varepsilon_z n_z + 0.5(\gamma_{xz} n_x + \gamma_{yz} n_y) \end{aligned} \tag{7}$$

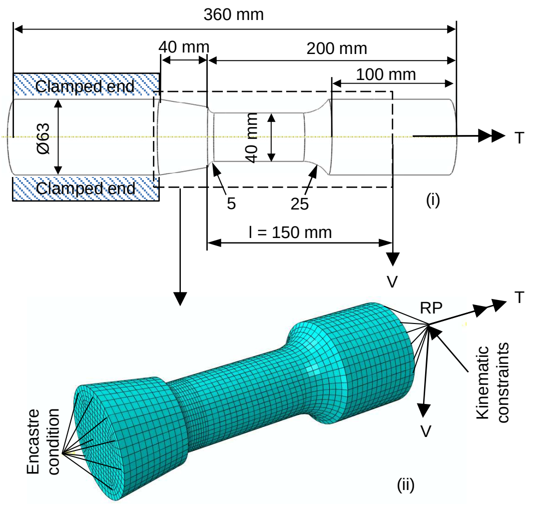

Fig. 1 (i) Geometry of the notched specimen, and (ii) the portion of the specimen used for FEA and geometry and mesh of FEA model

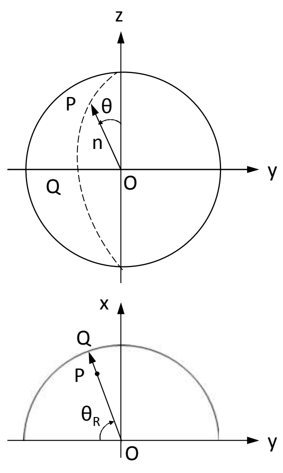

Fig. 2 Orientation of unit normal (n) to candidate material planes and its direction cosines from global coordinate system

4 RESULTS AND DISCUSSION

Cracks tend to initiate at the area where von Mises stresses are concentrated due to higher plastic strains. Stress contours are studied at the peak of fatigue loading within a cycle. For pure bending cases, stress concentration occurs in the vicinity of the notch of the specimen shown as site 1 in Fig. 3 (i). Additional area of stress concentration (site 2) is expected for combined loading cases especially when a very high torsion load is applied such as case 6 as shown in Fig. 3 (ii). The locations of stress concentration sites in comparisons to loading directions are illustrated in Fig. 4.

With information of stress and strain data from FE analysis and using Eqs (1) to (7), fatigue lifetimes of the specimen for loading cases 1-6 are estimated. The results are compared to experimental results from [8] in Table 2. The scatters in experimental results can be found and this is due to difficulty in detecting the time when crack has grown 1mm (assumed this is a crack length for fatigue damage initiation) is observed. Nevertheless, apart from the outliners for case 2 failure estimation by F-S method, both SWT and F-S methods predict the lifetime within the factor of 5. The lack of implementation of stress redistribution by damage process could be the reason of inaccuracy in the lifetime prediction results. However, the current method can be used as a quick estimation tool for multiaxial fatigue lifetime.

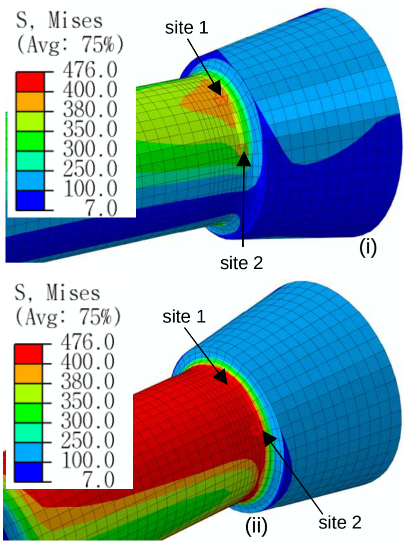

Fig. 3 von Mises stress contours for (i) case 1, and (ii) case 6 at the peak of loading

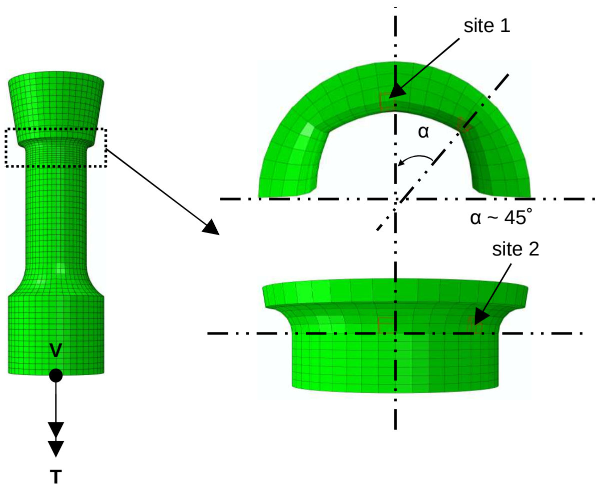

Fig. 4 Sites of the notched specimen where crack initiation is expected

Table 2 Fatigue lifetime as estimated by SWT and F-S methods, and experiments [8]

	Experimental lifetime (N_{exp}) [8]						
Case	Test 1	Test 2	Test 3	Numerical life by SWT (N_{SWT})	Numerical life by F-S ($N_{F\text{-}S}$)	N_{exp}/ N_{SWT}	N_{exp}/ $N_{F\text{-}S}$
1	230, 000	463, 976	-	125, 867	206,412	1.83, 3.69	1.11, 2.25
2	7930	3000	8111	3427	664	2.31, 0.88, 2.37	11.94, 4.52, 12.22
3	60, 000	130, 000	30,000	48, 227	50,247	1.24, 2.7, 0.62	1.19, 2.59, 0.6
4	107, 460	72, 000	-	83, 764 (site 1)	113,183 (site 1)	1.28, 0.86	0.95, 0.64
				84, 697 (site 2)	115, 375 (site 2)	1.27, 0.85	0.93, 0.62
5	933, 000	350, 000	-	352, 355 (site 1)	959,213 (site 1)	2.65, 0.99	0.97, 0.36
				355, 751 (site 2)	971, 383 (site 2)	2.62, 0.98	0.96, 0.36
6	5113	-	-	9034 (site 1)	1573 (site 1)	0.57	3.25
				7115 (site 2)	1641 (site 2)	0.72	3.12

Another important result which can be extracted from stress-strain results of FE analyses with multiaxial fatigue loading is the influence of direction of principal axes on the directions of crack initiation and propagation. The orientation of the crack initiation plane is represented by direction cosines as shown in Fig. 2. As described in [8], the crack growth can be divided into two stages; the crack initially grows along the maximum shear strain plane during Stage I and then propagates orthogonally to the maximum principal stress during Stage II. There are two types of maximum shear plane depending on the direction of principal axes as shown in Fig. 5 (i). If the shaded area represents the surface of the material, the shear plane of type B shear illustrates that crack grows towards the thickness of the material during Stage I whereas cracks grows around the surface for Type A shear plane. Therefore, it can be said that Type B shear is more damaging than Type A and it will shorten the fatigue lifetime.

For the notched specimen, the global coordinate system at the crack initiation site is shown in Fig. 5 (ii). Relative to the global coordinate system, the orientations of principal axes for pure bending loading cases (cases 1-3) are also shown in Fig. 5 (ii). It can be clearly seen that the shear plane is Type B for pure bending cases. The maximum shear plane intersects the maximum principal plane at the circumferential direction of the notch. Since the stress level around the site 1 is increased if higher amplitude of bending is applied, more cracks are expected at the initiation stage. Moreover, maximum principal stress direction is nearly along the Y-axis of the global coordinate which can cause subsequent propagation of cracks and failure. The results from experiment as shown in Fig. 6 agree well with the numerical prediction. More crack initiation sites are observed for case 3 with higher amplitude of bending compared to case 1. The fracture surface is shown to be perpendicular to the axis of the specimen indicating that the maximum principal stress direction is along the Y-axis of the specimen.

Cases 4, 5 and 6 have nearly identical loading ratio but different directions of principal axes are expected due to the differences in amplitudes of bending and torsion. The principal axes directions for cases 4-6 are illustrated in Fig. 5 (iii) to (v). Type A shear plane is expected for cases 4 and 5. In contrast, the maximum shear plane is Type B for case 6 and cracks are expected to grow into specimen thickness during Stage I growth. This might be one of the reasons of significantly lower fatigue life for case 6 (**Table 2**) compared to cases 4 and 5 despite having the same loading ratio. Experiment carried out by Fash [8] nonetheless showed that cracks initiate circumferentially at the notch rather than in the maximum shear plane direction. The macroscopic failure is shown to be driven by the maximum principal stress and the crack plane is perpendicular to the direction of the maximum principal plane.

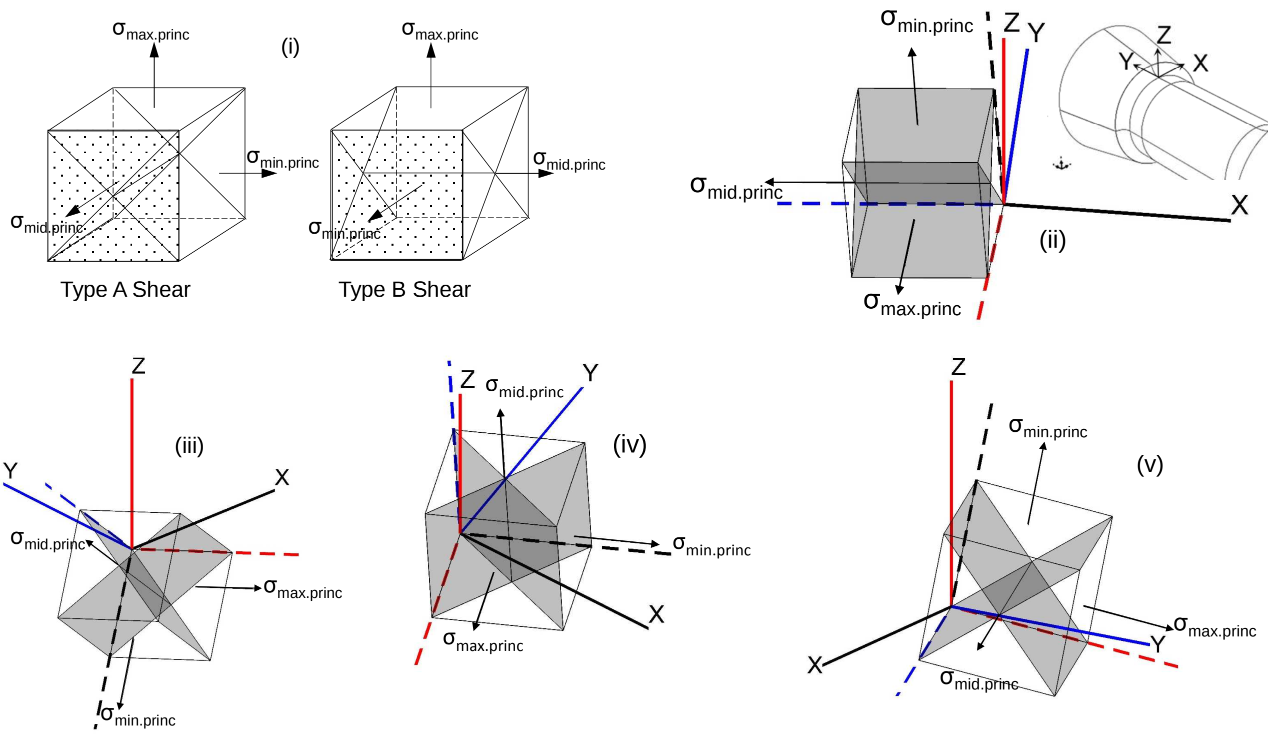

Fig. 5 (i) Two types of maximum shear plane, maximum principal stress and shear planes for (ii) cases 1-3, (iii) case 4, (iv) case 5, and (v) case 6 at the peak of loading; note plotted principal directions for cases 4-6 are at failure site 1

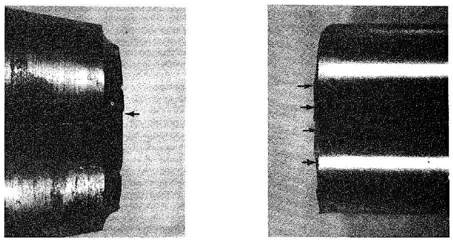

Case 1 Case 3

Fig. 6 Macroscopic crack growth behaviours of notched specimen for pure bending loading cases from experiment [8]; the arrows represents crack initiation sites

5 CONCLUSIONS

In this work, multiaxial lifetime of a notched specimen under a combined bending-torsion load mode is estimated using two different types of critical plane methods. The methods make use of stress and strain results from FE analyses of the notched specimen and the associated empirical fatigue parameters. The lifetimes predicted are compared to the experimental findings from [8] and the error is within a factor of 5. Additionally, orientations of crack initiation plane are predicted from different types of the maximum shear plane, which depends on principal axes directions. For pure bending cases, crack initiation sites and fracture plane of macroscopic failure agree with numerical predictions. For the mixed mode loading with identical loading ratio, the magnitude of bending and torsion determines the orientation of the maximum shear plane. Higher damage and shorter fatigue life are expected for the case when the maximum shear plane is Type B.

ACKNOWLEDGEMENT

The authors would like to acknowledge the financial support of The Engineering and Physical Science Research Councils (EPSRC) UK (Grants EP/K021095/1).

6 REFERENCES

[1] E. Krempl. The Influence of State of Stress on Low-Cycle Fatigue of Structural Materials: A Literature Survey and Interpretive Report. American society for materials and testing. (1974).

[2] S.M. Tipton. Fatigue Behavior Under Multiaxial Loading in the Presence of a Notch: Methodologies for the Prediction of Life to Crack Initiation PhD thesis (Stanford University). (1984).

[3] T. Yokobori, H. Yamanouchi, S. Yamamoto. Low cycle fatigue of thin-walled cylindrical specimens of mild-steel in uni-axial and torsional tests at constant strain amplitude. INT J FRACTURE. 1-2 (1966) 3-13.

[4] G.Z. LIBERTINY. SHORT-LIFE FATIGUE UNDER COMBINED STRESSES Journal of strain analysis. 2 (1967) 91-5.

[5] A. Nadia. Plasticity: A Mechanics of the Plastic State of Matter, McGraw-Hill Book Compnay, Inc. (1931.).

[6] R.N. Smith, P. Watson, T.H. Topper. A stress-strain function for the fatigue of metals. Journal of Materials. 5 (1970) 767-78.

[7] A. Fatemi, D.F. Socie. A critical plane approach to multiaxial fatigue damage including out-of-phase loading. Fatigue and Fracture of Engineering Materials and Structures. 11 (1988) 149-65.

[8] W. Fash. An Evaluation of Damage Development During Multiaxial Fatigue of Smooth and Notched Specimens. PhD thesis (University of Illinois). (1985).

[9] MATLAB and Statistics Toolbox Release 2013, The MathWorks, Inc., Natick, Massachusetts, United States.

[10] J.A. Bannantine, D.F. Socie. A multiaxial fatigue life estimation technique. In: Mitchell MR, Landgraf RW, editors. Advances in fatigue lifetime predictive techniques, ASTM STP 1122, Philadelphia: American Society for Testing and Materials (1992) pp. 249-75.

[11] D. Socie. Critical plane approaches for multiaxial fatigue damage assessment. In: McDowell DL, Ellis R, editors. Advances in multiaxial fatigue, ASTM STP 1191, Philadelphia: American Society for Testing and Materials (1993) pp. 7-36.

[12] S.M. Tipton, J.W. Fash. Multiaxial fatigue life predictions of the SAE specimen using strain based approaches, multiaxial fatigue: analysis and experiments, SAE AE-14. Society of automotive engineers, Warrendale, PA. (1989) pp. 67-80.

[13] S. Gupta, I. Rychlik. Rain-flow fatigue damage due to nonlinear combination of vector Gaussian loads. Probabilistic engineering mechanics. 22 (2007) 231-49.

Proceedings of the 4th International Conference on
Fracture Fatigue and Wear, pp. 97-102, 2015

MODELLING OF FULL LIFE CYCLIC VISCO-PLASTIC BEHAVIOUR OF A P91 STEEL AT 600^{O}C

Jiawa Lu[1], Wei Sun[1], Adib Becker[1] and Abdullah Aziz Saad[2]

[1]Faculty of Engineering, University of Nottingham, Nottingham, NG7 2RD, UK
[2]School of Mechanical Engineering, Universiti Sains Malaysia

Abstract: A damage variable was coupled to the constitutive equations of the Chaboche elasto-visco-plastic model to describe the cyclic material behaviour of a P91 steel at 600 ^{o}C, which allows the full life cyclic softening behaviour to be accurately predicted. A UMAT subroutine in ABAQUS was produced to implement the Chaboche model. A stress partition method is introduced to understand the fatigue softening behaviour of P91 at 600 ^{0}C, and is used to give an initial estimate of the material constants in the Chaboche model. Further optimisation procedures with plastic strain range dependency of the material constants were introduced in the optimisation procedure in order to accurately predict the material behaviour, especially after damage initiation.

Keywords: Cyclic plasticity; Chaboche visco-plasticity model; Continuum damage mechanics; P91 Steel

1 INTRODUCTION

Martensitic steel P91 is widely used in power generation plants for steam piping systems, which may be subject to long term steady and cyclic loading conditions at high temperatures. Due to the intermittent nature of renewable energy generation, conventional power plants are now subject to a higher frequency of thermo-mechanical cycling, demanded by 'flexible' operation. Due to this reason, the study of visco-plasticity behaviour of advanced power plant steels has become increasingly important.

A continuum damage mechanics (CDM) approach is coupled to the constitutive equations of the cyclic plasticity model in this study to investigate the influence of the damage variable on the Chaboche model behaviour of the P91steel. The plastic and creep deformations were analysed in combination, and plasticity formulations were considered as special cases of viscoplasticity formulations. Damage refers to the presence of discontinuities in the microscopic view, including micro-cavities and cracks. The damage value is also described in a continuum mechanics way, where it is assumed that heterogeneous behaviour can be averaged through a homogeneous representative volume element [1].

2 THEORETICAL BACKGROUND

Within the framework of visco-plasticity, the total strain $\boldsymbol{\varepsilon}$ is decomposed into two internal variables, the elastic strain $\boldsymbol{\varepsilon^e}$ and the irreversible visco-plastic strain $\boldsymbol{\varepsilon^p}$. The elastic strain is calculated using the linear elastic law, as follows:

$$\boldsymbol{\varepsilon}^{\boldsymbol{e}} = \frac{1+v}{E}\widetilde{\boldsymbol{\sigma}} - \frac{v}{E}Tr(\widetilde{\boldsymbol{\sigma}})\boldsymbol{I} \quad (1)$$

where the effective stress $\widetilde{\boldsymbol{\sigma}} = \boldsymbol{\sigma}/(1-D)$ defined under the concept of CDM, where the damage parameter D ranges from $D = 0$ (no damage) to a critical damage value D_c . The internal variables, including kinematic hardening $\boldsymbol{X}$, isotropic hardening R and initial yield stress σ_y are introduced to describe the yield function fy [2]:

$$fy = J(\widetilde{\boldsymbol{\sigma}}^D - \boldsymbol{X}) - R - \sigma_y \quad (2)$$

where the function J represents the second invariant of the tensor in the bracket, and $\widetilde{\boldsymbol{\sigma}}^D$ is the effective stress deviator. The isotropic hardening R represents the size of the elastic domain, and is formulated as follows:

$$R = R_s[1 - exp(-bp)] + Hp \quad (3)$$

where p is the accumulated plastic strain, b is the coefficient controlling the changing rate, and R_s is the saturated value of isotropic hardening or softening. The kinematic hardening variable tensor $\boldsymbol{X}$, related to the internal micro-stress, represents schematically the centre of the elastic domain. The kinematic hardening starts from an initial value X_0 [3], and the nonlinear evolution law of the kinematic hardening proposed by Armstrong and Frederick [4] is employed, such that

$$\dot{\boldsymbol{X}} = \gamma\left(\frac{2}{3}X_s\dot{\boldsymbol{\varepsilon}}^{\boldsymbol{p}} - \boldsymbol{X}\dot{p}\right) \tag{4}$$

where X_s is the saturation value of kinematic hardening and the coefficient γ controls the rate of change. The yield stress σ_y in visco-plasticity formulations is slightly different from the concept in static tests at room temperature, since plastic flow occurs at a much lower stress than the normal yield stress. The flow rule for the plastic strain obeys the normality rule, such that the rate of plastic deformation is the product of the normal direction $\boldsymbol{n}$ and the accumulated plastic strain rate $\dot{p}$:

$$\dot{\varepsilon}_{ij}^{p} = \boldsymbol{n}\dot{p} = \frac{3}{2}\frac{\tilde{\boldsymbol{\sigma}}^{D}-\boldsymbol{X}}{J(\tilde{\boldsymbol{\sigma}}^{D}-\boldsymbol{X})}\dot{p} \tag{5}$$

The value of the accumulated plastic strain rate $\dot{p}$ defined as $\dot{p} = \left(\frac{2}{3}\dot{\boldsymbol{\varepsilon}}^{p}:\dot{\boldsymbol{\varepsilon}}^{p}\right)^{\frac{1}{2}}$ is calculated from Norton's law for the visco-plastic material behaviour such that

$$\dot{p} = (\sigma_v/S_k)^n \tag{6}$$

The rate exponent n controls the material sensitivity to plastic deformation, while the drag force S_k controls the resistance to plastic deformation. Plasticity is the limiting case when the yield surface $fy = 0$, and the value of the accumulated plastic strain rate $\dot{p}$ can be obtained by solving the equation $fy = 0$.

3 EXPERIMENTAL RESULTS

Several strain-controlled isothermal fatigue tests were conducted by Saad [5] at 600 ºC to investigate the stress-strain relationship. The tests were performed at a strain rate of 0.1%/s and with strain ranges of $\pm0.5\%$, $\pm0.4\%$, $\pm0.25\%$ and $\pm0.2\%$ respectively. The failure criterion defined for the continuously softening materials is defined when there is 10% force drop from the projected straight line locus of peak tensile stress versus cycles. The obtained number of cycles to failure N_f were 608, 1467, 3614 and 10659 respectively. They were related to the plastic strain range by the Manson-Coffin relationship as

$$N_f = (\Delta\varepsilon^p/2c_F)^{\gamma_F} = (\Delta\varepsilon^p/58.806)^{0.57} \tag{7}$$

in which $\Delta\varepsilon^p$ is the steady state plastic strain range, γ_F and c_F are both material constants. From the evolution of the stress amplitude($\Delta\sigma/2$) for all these strain ranges shown in Fig. 1a, it could be observed that there is a fast initial decrease of stress amplitude before about 0.2N_f, followed by a steady linear decrease during cycle numbers between approximately 0.2N_f and 0.8N_f. Finally, there is a sudden decrease of stress amplitude after about 0.8N_f.

The detailed stress-strain loops for cycle numbers 1, 101, 201, 301, 401, 501 and 601, 655 (final cycle number) for the strain range of $\pm0.5\%$ test are plotted in Fig. 1b, and the cycle number could be identified easily by the decreasing maximum stress. These stress-strain curves are smooth without a sudden change at yielding, which is caused by the viscous effect. There is a clear change of slope in the elastic region when the number of cycles is 601 or 655 (N_f), but not much of a clear change before the cycle number 501 (0.8N_f). Since damage could also be regarded as the degradation of Young's modulus, it is reasonable to postulate that the final decrease of stress amplitude was caused by the acceleration of damage propagation, which could be observed macroscopically after about 501 cycles.

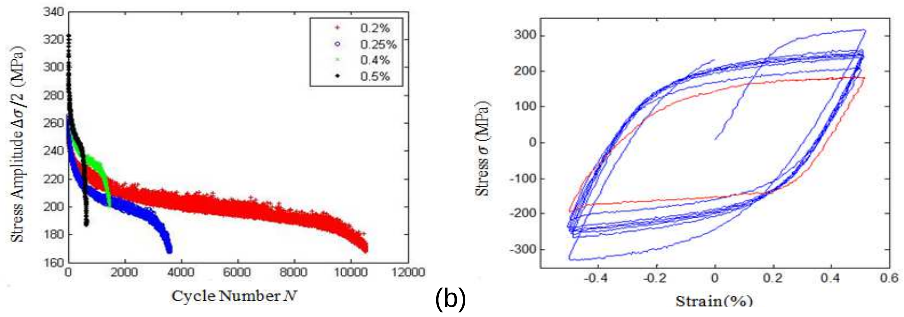

(a) (b)

Fig.1 (a) Stress amplitude $\Delta\sigma/2$ against cycle number for strain ranges of $\pm0.5\%$, $\pm0.4\%$, $\pm0.25\%$ and $\pm0.2\%$. [5] (b) Stress-strain curves for strain range at $\pm0.5\%$ at the cycle number 1, 101, 201, 301,401, 501 and 601, 655 (the final loop)

Using a continuum approach, damage could be viewed as the degradation of the effective Young's modulus $\tilde{E}$. Therefore, a typical method to obtain damage evolution is to determine the effective Young's modulus $\tilde{E}$ by the following equation:

$$\tilde{E} = \Delta\sigma/(\Delta\varepsilon - \Delta\varepsilon_p) \quad (8)$$

The damage parameter then can be determined via the following equation:

$$\mathrm{D} = 1 - \tilde{E}/E \quad (9)$$

The result is shown in Fig. 2a. Damage starts from 0 and progress to a critical damage value D_c=*0.1*, determined by failure criterion set during experiment .The damage evolutions for the strain ranges of $\pm0.5\%$, $\pm0.4\%$, $\pm0.25\%$ and $\pm0.2\%$ are also consistent against the life portion $L = N/N_f$. The evolution curves are fitted to the *sinh* function of the life portion gives $D = sinh(10.6L)/187667$ and $dL/dN = 1/N_f(\Delta\varepsilon^p) = (58.806/\Delta\varepsilon^p)^{0.57}$.

The microstructural mechanics responsible for the cyclic softening mechanics were examined by SEM and TEM for the as-received specimen, the interrupted specimens at cycle numbers 200 (0.33N_f) and 400 (0.66 N_f), and the specimen at failure, for the strain range of ±0.5%. It is observed from the SEM results that there is no obvious microstructure change before the 200th cycles (not shown here). A crack initiates before the 400th cycle at the specimen's surface at two locations, and many microcracks with a length of about a grain size were observed at the 400th cycle (Fig. 3b). When the force drops by over 10% at failure, the crack lengths are about 10 grain sizes (Fig. 3c). Bright field images in Fig. 4 exhibit features including the martenstic lath and dislocations, which act as obstacles in producing slip. The martenstic lath are small angle subgrain boundaries, regarded as arrays of edge and screw type dislocations. Dislocations inside the subgrains could be observed as short straight lines pinned at subgrain boundaries. A small fraction of dislocations inside and at the subgrain boundaries is regarded as mobile dislocations contributing to plastic deformation, whereas the majority of dislocations hinder plastic deformation [6].

Both subgrain size and dislocation density could be roughly calculated by the line intercept method and the result is shown in Fig. 2b. The as-received sample exhibits small and inconsistent subgrain sizes, and high dislocation density. As cycles increase to cycle number 200 when the stress amplitude softens initially, the lath structure becomes longer, and the subgrain size increases by around 33%. There are thus less low angle boundaries, and a lower dislocation density. Dislocation annihilation occurs since dislocations located inside the subgrain tend to move towards the low angle boundaries of the opposite sign until the distance is less than a critical dislocation annihilation value. Slower evolutions of the subgrain size and dislocations density were observed after cycle number 200 to failure.

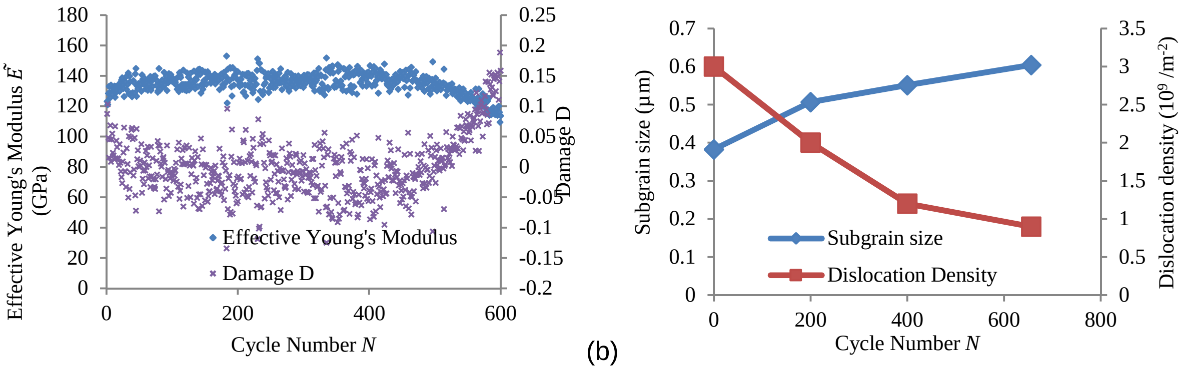

(a) (b)

Fig. 2 (a) Subgrain size and dislocation density evolution based on the TEM results for the strain range of $\pm0.5\%$;(b) Evolution of the effective Young's modulus $\tilde{E}$ and damage D against cycle number N

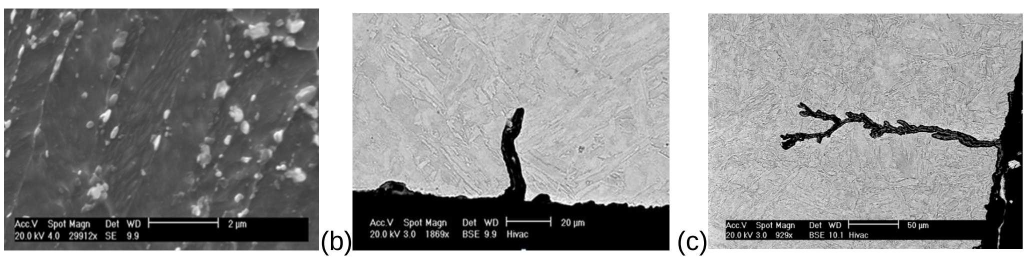

(a) (b) (c)

Fig. 3 SEM results at the surface of the P91 specimen in a fatigue test at strain range of ±0.5%: (a) the as-received material; (b) Microcracks observed at the 400th cycles; (c) Mesocracks observed at failure

4 FINITE ELEMENT IMPLEMENTATION

4.1 UMAT subroutine

The commercially available finite element software ABAQUS is used to conduct the stress analysis. A UMAT subroutine is the alternative for the user to code the material behaviour, by updating stresses and the Jacobian matrix (change of stress increment with respect to strain increment) based on the previous material condition at every strain increment. An elastic predictor-plastic corrector method is used to update the stress in the coding [7].

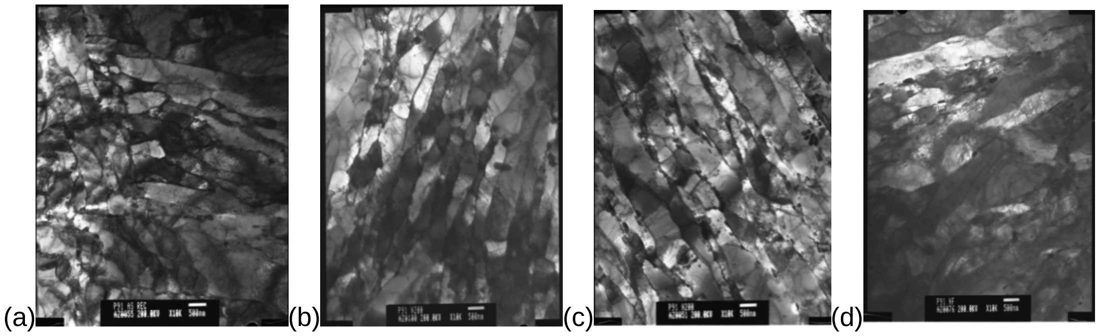

Fig. 4 Bright field TEM results of the P91 specimen in a fatigue test at strain range of ±0.5% (a) the as-received material and (b) at the 200th cycles (0.33N_f); (c) at the 400th cycles (0.66 N_f); (d) at failure

The first step is to assume that there is no plastic deformation ($\Delta p = 0$), and the stress increment is caused by elastic deformation only, and thus there is no change in isotropic and kinematic hardening, as follows:

$$\tilde{\boldsymbol{\sigma}}^{pr} = \tilde{\boldsymbol{\sigma}}_n + \tilde{\boldsymbol{J}}^e d\boldsymbol{\varepsilon} \tag{10}$$

where $\tilde{\boldsymbol{J}}^{\boldsymbol{e}}$ is the effective elastic Jacobian matrix, and the passed-in variable $\tilde{\boldsymbol{\sigma}}_n$ is the effective stress for the last increment. If the material behaviour in the specific increment *n* is unable to accommodate the excessive stress, when the elastic predictor brings the yield function *fy* out of the yield surface, such that

$$fy = J(\tilde{\boldsymbol{\sigma}}^{pr} - \boldsymbol{X}_n) - R_n - \sigma_y > 0 \tag{11}$$

the plastic corrector is used to correct the accumulated plastic deformation and thus stress by using Newton-Raphson iterations to minimise the objective residual function f_{res}

$$f_{res} = \phi(\Delta \mathrm{p}, \boldsymbol{X}, R) - \Delta p/\Delta t \tag{12}$$

where

$$\phi(\Delta \mathrm{p}, \boldsymbol{X}, R) = \dot{p}_{n+1} = \left[(J(\tilde{\boldsymbol{\sigma}}^{pr} - \boldsymbol{X}_n) - R_n - \sigma_y)/K_s \right]^n \tag{13}$$

Expanding Equ.(12) by Taloy's expansion,

$$f_{res} + \frac{\partial f_{res}}{\partial \Delta \mathrm{p}} \delta \Delta \mathrm{p} + \frac{\partial f_{res}}{\partial \mathrm{R}} \delta R + \frac{\partial f_{res}}{\partial \boldsymbol{X}} \delta \boldsymbol{X} = 0 \tag{14}$$

Rearranging Equ.(14), gives

$$\delta \Delta \mathrm{p} = f_{res}/(-\frac{\partial f_{res}}{\partial \Delta \mathrm{p}} - \frac{\partial f_{res}}{\partial R}\frac{\partial R}{\partial \Delta \mathrm{p}} - \frac{\partial f_{res}}{\partial \boldsymbol{X}}\frac{\partial \boldsymbol{X}}{\partial \Delta \mathrm{p}}) \tag{15}$$

The accumulated plastic deformation Δp is updated by $\Delta p + \delta \Delta \mathrm{p}$. The final step is to update the isotropic hardening, kinematic hardening and stress as follows:

$$R_{n+1} = R_n + b(R_S - R_{n+1})\Delta p + H(1 + bp)\Delta p \tag{16}$$

$$\boldsymbol{X}_{n+1} = (\boldsymbol{X}_n + \tfrac{2}{3}\gamma X_S n \Delta p)/(1 + \gamma \Delta p) \tag{17}$$

$$\boldsymbol{\sigma} = \tilde{\boldsymbol{J}}^e(\Delta \boldsymbol{\varepsilon} - \Delta \boldsymbol{\varepsilon}^p) \tag{18}$$

The Jacobian matrix to be updated in the UMAT subroutine is the same as the elastic Jabobian matrix $\tilde{\boldsymbol{J}}^{\boldsymbol{e}}$ to simplify the coding, since it mainly accounts for the convergence rate of the ABAQUS FE solver, rather than improvement of the accuracy.

4.2 Uniaxial simulation results

The size and centre of the elastic domain and the viscous stress values could be obtained based on the Cottrell's stress partition method [8] shown in Fig. 5a.

$$X = (\sigma_e^{max} + \sigma_e^{min})/2 \tag{19}$$

$$\sigma_v = \sigma^{max} - \sigma_e^{max} \tag{20}$$

$$R + \sigma_y = (\sigma_e^{max} - \sigma_e^{min})/2 \tag{21}$$

The method coded was applied to the stress-strain curve for the strain range of $\pm 0.5\%$. The radius and centre of the elastic domain are plotted against the number of cycles *N* in Fig. 5b, as well as the viscous stress σ_v. The obtained stress components are quite noisy due to the scatterings in the original fatigue data; however, the general trend can be easily observed. The initial softening of the stress amplitude is attributed to the initial fast decrease of both isotropic and kinematic hardening. The linear decrease of the stress amplitude is caused by the steady decrease of isotropic hardening, when the kinematic hardening is already saturated with regard to the accumulated plastic deformation. The final decrease of stress amplitude is caused by Young's modulus degradation, which also results in the decrease of the size of the elastic domain. Throughout the fatigue life, not much change was observed for the viscous stress.

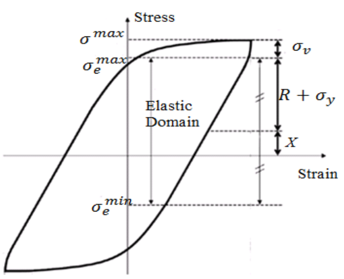

(a)

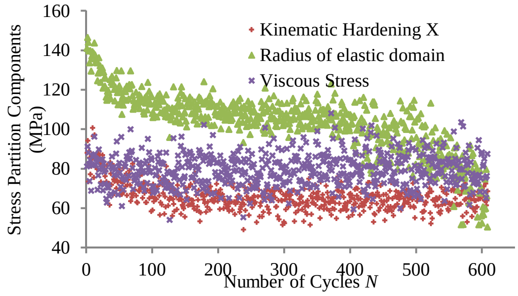

(b)

Fig. 5 (a) Stress partition method [9]; (b) Evolution of the stress components by the stress partition method, including radius of elastic domain $R + \sigma_y$, kinematic hardening *X* and viscous stress σ_v

A series of fatigue tests were simulated using the UMAT subroutine with a cubic geometry, under the same uniaxial cyclic loading condition. The objective of the fatigue test simulation is to check the validity and capability of the damage term in the model. Only one element is used in the current study and the element type is eight-node continuum brick element with full integration (C3D8 in ABAQUS).

In order to accurately predict the value of the drag force and the exponent in the Norton's law, another set of experiments with the same testing temperature at 600 ^{0}C with a dwell holding time of 120s at the maximum strain were conducted. The material constants were obtained by the inverse method to give the best curve fitting of the fatigue and stress partition results. The obtained material constants for the strain range of $\pm 0.5\%$ are shown in Table 1 . The stress-strain curves obtained from the FE simulation at cycles 1, 300 and 600 are compared to the experimental results in Fig. 6a. The figure shows that the FE simulation is able to accurately capture the main features of the cyclic plasticity behaviour, such as the size change and shift of the centres of elastic domain, the hysteresis loop, as well as the degradation of Young's modulus. The maximum stress evolutions in both FE simulation and experiment are plotted in Fig. 6b, as well as the damage evolution from both FE simulation and experimental post-processing results. They show good prediction of the full life behaviour, including initial fast softening, steady linear softening, as well as the damage propagation.

Table 1 Material constants for P91 at temperature of 600 ^{o}C and for the strain range of $\pm 0.5\%$

	E (MPa)	ν	σ_y (MPa)	K_s (MPa s$^{1/n}$)	n	b	R_s (MPa)	X_0 (MPa)	X_s (MPa)	γ	H
Optimised result	125000	0.3	120	6339	2.02	10	-66	0.24	-10	1.29	-1.73

The material constants H, R_s and b are strain range dependent, and the optimised values at the strain ranges of $\pm 0.4\%$, $\pm 0.25\%$ and $\pm 0.2\%$ are plotted in Fig. 7a. The evolutions of maximum stress σ_{max} against cycle number *N* are plotted in Fig. 7b. They give good approximations of the peak stress evolution, especially after the initial fast softening period.

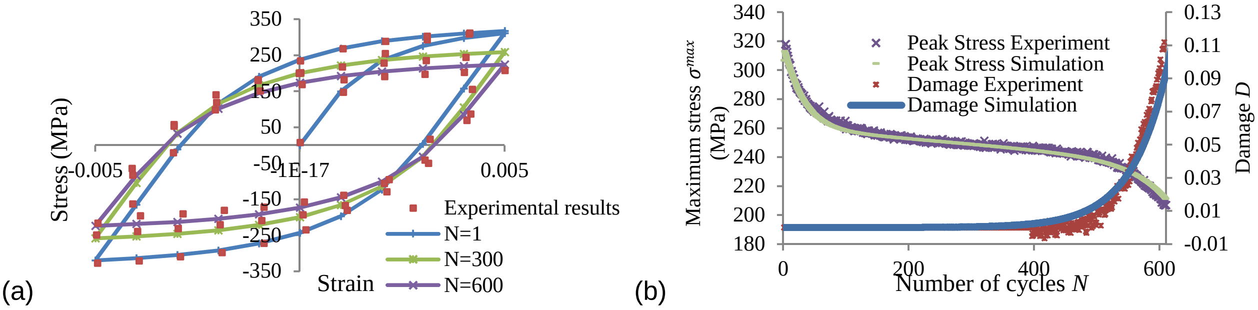

Fig. 6 (a) Experiment and FE simulation of stress-strain curve at cycle number 1, 300 and 600 for the strain range of $\pm 0.5\%$; (b)Experiment and FE simulation of the maximum stress σ^{max} and damage D evolution against cycle number for the strain range of $\pm 0.5\%$

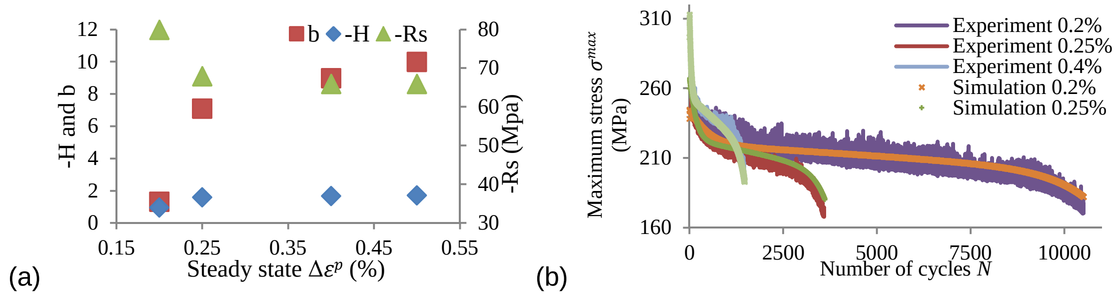

Fig. 7 (a) Steady state plastic strain range $\Delta\varepsilon^p$ dependency of the material constants of isotropic hardening; (b) Experiment and FE simulation of the maximum stress σ^{max} against cycle number for the strain range of $\pm 0.4\%$, $\pm 0.25\%$ and $\pm 0.2\%$

5 CONCLUSIONS

A damage variable is coupled to the constitutive equations of the Chaboche elasto-visco-plastic model to describe the full life cyclic plasticity behaviour of a P91 steel at 600 ºC under low cycle fatigue conditions. A stress partition method is introduced to understand the fatigue softening behaviour of P91 at the high temperature of 600 ºC, and gives an initial estimate of the material constants in the Chaboche model. Further optimisation procedures with plastic strain range dependency of the material constants are introduced in the optimisation procedure in order to accurately predict the material behaviour, especially in the failure stage. Good approximations are achieved for the maximum stress evolution, especially in the linear softening stage and the damage propagation stage.

ACKNOWLEDGEMENT

The authors would like to acknowledge the financial support of The Engineering and Physical Science Research Councils (EPSRC) UK (Grants EP/K021095/1).

6 REFERENCES

[1] Chaboche, J.L., *Continuum Damage Mechanics: Part I---General Concepts.* Journal of Applied Mechanics, 1988. **55**(1): p. 59-64.
[2] Chaboche, J.L., *A review of some plasticity and viscoplasticity constitutive theories.* International Journal of Plasticity, 2008. **24**(10): p. 1642-1693.
[3] Ucak, A. and P. Tsopelas, *Constitutive Model for Cyclic Response of Structural Steels with Yield Plateau.* Journal of Structural Engineering, 2011. **137**(2): p. 195-206.
[4] Frederick, C.O. and P.J. Armstrong, *A mathematical representation of the multiaxial Bauschinger effect.* Materials at High Temperatures, 2007. **24**(1): p. 1-26.
[5] Saad, A.A., *Cyclic plasticity and creep of power plant materials, PhD thesis*. 2012, University of Nottingham: Nottingham.
[6] Ma, A., F. Roters, and D. Raabe, *A dislocation density based constitutive model for crystal plasticity FEM including geometrically necessary dislocations.* Acta Materialia, 2006. **54**(8): p. 2169-2179.
[7] Dunne, F. and N. Petrinic, *Introduction to computational plasticity* 2005: Oxford University Press.
[8] Cottrell, A.H., *Dislocations and plastic flow in crystals*. 1953, UK: Oxford University Press.
[9] Giroux, P.F., *Experimental study and simulation of cyclic softening of tempered martensite ferritic steels. PhD thesis*. 2011, Ecole Nationale Superieure des Mines de Paris

International Journal of Fracture Fatigue and Wear, Volume 3

Proceedings of the 4th International Conference on
Fracture Fatigue and Wear, pp. 103-108, 2015

THE EFFECT OF LOW-CYCLIC FATIGUE ON FRACTURE MECHANICS PARAMETERS BY LOCAL DISPLACEMENT MEASUREMENTS

Yu.G. Matvienko [1], V.S. Pisarev [2] and S.I. Eleonsky [2]

[1] Mechanical Engineering Research Institute of the Russian Academy of Sciences (IMASH RAN), Russia
[2] Central Aero-Hydrodynamics Institute named after Prof. N.E. Zhukovsky (TsAGI), Russia

Abstract: Crack tip opening, singular stress intensity factor (SIF) and non-singular T-stress values are determined for cracks of different length at different stages of low-cyclic fatigue loading ($\Delta\sigma$ = 333.3 MPa, R= – 0.33). Narrow notches of 0.2 mm width are used for cracks modelling. Initial points of all symmetrical notches belong to the edge of central open holes of 3.0 mm diameter in rectangular plane specimens with dimensions 180x30x4 mm3. The specimens are made from aluminium alloy of 2024 type. Experimental approach employs optical interferometric measurements of local deformation response on small notch length increment. Initial experimental data represent in-plane displacement component values measured by electronic speckle-pattern interferometry at some specific points located in a vicinity of the notch tip. The availability of high-quality interference fringe patterns, which are free from rigid-body motions, serves as the reliable indicator of real stress state caused by the crack existence. The SIF and T-stress values are calculated by a determination of the first four coefficients of the Williams series solution. All experimentally obtained values correspond to a tension of each specimen by nominal stresses σ_0 = 53.1 MPa and three successive crack length increments. Measurements are performed for six different specimens after applying N_C = 0, 100, 1000, 1800, 2500 and 3300 loading cycles. The fracture of analogous specimen occurred after N_{CF} = 3800 cycles. The dependencies of fracture mechanics parameters for cracks of the fixed length from the number of loading cycles, which reveal a process of fatigue damage accumulation, are constructed.

Keywords: Low-cyclic fatigue loading; Stress intensity factor; T-stress; Crack length increment; Electronic speckle-pattern interferometry.

1 INTRODUCTION

The need for various experimental investigations of local elastic-plastic strain fields in irregular structure's areas for ensuring a detailed description of the low-cyclic fatigue process is based on the local fracture criterion (e.g. [1-3]). An analysis of the above publications and numerous others revealed that there is a deficiency of experimental data about local elastic-plastic strain fields in a vicinity of stress concentrators, when a structure is subjected to both static and cyclic loading. Implementing various optical interferometric techniques is one of the most effective approaches for the investigation of local elastic-plastic strains. This work presents the study of the influence of fatigue damage accumulation on singular and non-singular fracture mechanics parameters for symmetrical cracks propagated from a central through hole in thin rectangular plate. The specimens are subjected to one-axis cyclic tension-compression with the cycle parameters are $\Delta\sigma$ = 333.3 МПа, R = – 0.33. This loading range leads to arising high-level plastic strains at the hole vicinity. The values of the crack mouth opening displacement (CMOD), SIF and T-stress are obtained for the number of loading cycles N_C = 0, 100, 1000, 1800, 2500 и 3300 under the same loading conditions.

2 MEASUREMENT PRINCIPALS

Narrow notches of 0.2 mm width are used for cracks modelling. Initial experimental information is the values of in-plane displacement components, which are measured at some points belonging to crack borders by electronic speckle-pattern interferometry [7-8]. Modified version of the crack compliance method serves for a transition from in-plane displacement components to the values of the stress intensity factor (SIF) K_I and T-stress [8]. The essence of this approach resides in recording interference fringe patterns, which correspond to a difference between two in-plane displacement component fields. Each field is referred to a crack of close but different length. The first exposure is made for a crack of initial length a_{n-1}.

Then initial crack length is increased by small increment Δa_n so that new total crack length becomes equal to $a_n = a_{n-1} + \Delta a_n$ and the second exposure is performed. Required interference fringe patterns are visualized by numerical subtraction of two images recorded for two cracks. Two interferograms, which are obtained by this way for the tension of thin plate with symmetrical central crack under one-axis, are shown in Figure 1. The direction of *x*-axis in Figure 1 coincides with the direction of the crack propagation.

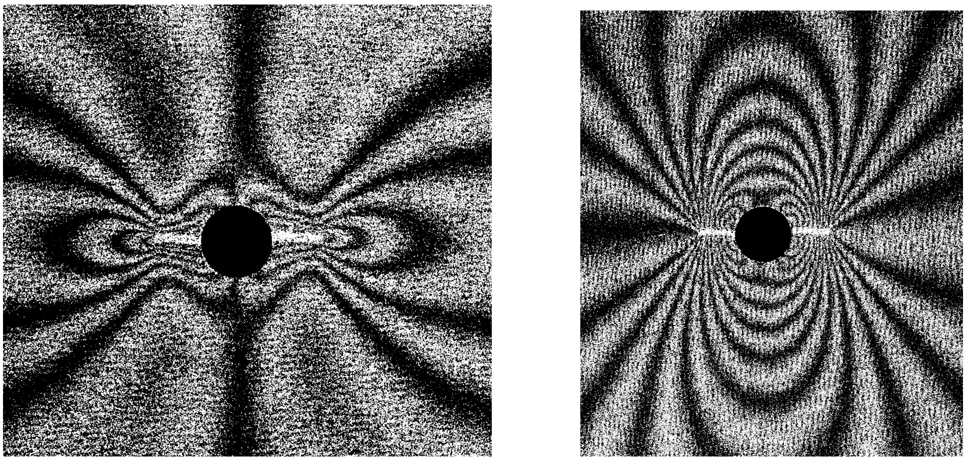

a b

Fig. 1 Specimen T4_08. Interference fringe pattern, obtained in terms of in-plane displacement component *u* (a) and *v* (b). Initial crack length $a_0 = 0$ with increment $\Delta a_1^- = 1.90$ mm (left) и $\Delta a_1^+ = 2.11$ mm (right)

Developed procedure of deriving required fracture mechanics parameters from interference fringe patterns is based on Williams' formulation [9]. Displacement components near a crack tip are expressed as infinite series for each in-plane displacement component. When *x*-direction coincides with the crack line, as it is shown in Figure 1, these series for mode I condition have the following form:

$$u = \sum_{\mathrm{m}=1}^{\infty} \frac{r^{\frac{\mathrm{m}}{2}}(1+\mu)}{E} A_{\mathrm{m}} \left\{ \left[k + \frac{m}{2} + (-1)^{\mathrm{m}} \right] \cos\frac{m\,\theta}{2} - \frac{m}{2}\cos\frac{(m-4)\,\theta}{2} \right\},$$
$$v = \sum_{\mathrm{m}=1}^{\infty} \frac{r^{\frac{\mathrm{m}}{2}}(1+\mu)}{E} A_{\mathrm{m}} \left\{ \left[k - \frac{m}{2} - (-1)^{\mathrm{m}} \right] \sin\frac{m\,\theta}{2} + \frac{m}{2}\sin\frac{(m-4)\,\theta}{2} \right\}, \tag{1}$$

where *u* and *v* are in-plane displacement component in direction of *x* and *y* axis, respectively; μ is the Poisson's ratio; *E* is the elasticity modulus; $k = (3–\mu)/(1+\mu)$ for plane stress and $k=(3–4\mu)$ for plane strain conditions; A_m are constants to be determined; *r* and θ are radial and angular distance from the crack tip.

The values of stress intensity factor K_I and T-stress are connected with coefficients of infinite series (1) by the following way [10]:

$$K_I^n = A_1^n \sqrt{2\pi}\,,\ T^n = 4A_2^n\,, \tag{2}$$

where superscript *n* shows that SIF and T-stress values are related to a crack of Δa_n length. The value of coefficient A_1^n is defined by the solution of linear algebraic equations system that includes two unknown parameters, namely A_1^n and A_3^n. This solution has the following form [8]:

$$K_{\mathrm{I}}^{\mathrm{n}} = \frac{E\sqrt{2\pi}}{8\sqrt{\Delta a_{\mathrm{n}}}} \left\{ 2\sqrt{2}\Delta v_{\mathrm{n}-0.5} - \Delta v_{\mathrm{n}-1} \right\}, \tag{3}$$

where Δv_{n-1} and $\Delta v_{n-0.5}$ are crack opening values at point with coordinates ($r = \Delta a_n$, $\theta = \pi$) and ($r=\Delta a_n/2$, $\theta = \pi$), respectively. The values Δv_{n-1} and $\Delta v_{n-0.5}$ are experimentally derived from interference fringe pattern of type shown in Fig. 1b.

The value of coefficient A_2^n is defined in analogous way by using two unknown parameters, namely A_2^n and A_4^n. Two required experimental parameters, which are essential for the solution of linear algebraic equations system, represent by itself in-plane displacement components *u*. These components are measured at two points coinciding with crack tip for cracks of Δa_n and Δa_{n+1} length. This procedure based on interference fringe patterns of type shown in Fig. 1a is described in details in Ref. [8].

3 EXPERIMENTAL PROCEDURE

Plane specimens with dimensions 180x30x4 mm^3 made from aluminum alloy of 2024 type are the objects of the investigation. All specimens have a central through hole of diameter $2R$ = 3.0 mm. Two points of the intersection of the hole edge and horizontal symmetry axis of each specimen, which is perpendicular to load direction, are the crack starting points. One from the specimens (T4_08) serves for the determination of fracture mechanics parameters for cracks propagating in the material that is not undergone to local elastic-plastic deformations due to cyclic loading. Before performing the first symmetrical notch the specimen is subjected to constant one-axis tensile load that correspond to nominal stress σ_0 = 53.1 MPa. The results of SIF values determination for specimen T4_08 coincide with analogous theoretical data within 8 per cent [11]. Cyclic loading ($\Delta\sigma$ = 333.3 MПa, R = – 0.33, f = 0.8 Hz) of the specimen-witness up to fracture is the second stage of performed investigations. The fracture occurred after applying N_{CF} = 3800 cycles.

Table 1 Nomenclature of the Specimens

Specimen's number	T4_08	T4_06	T4_02	T4_05	T4_03	T4_07
The number of loading cycles, N_C	0	100	1000	1800	2500	3300

Five other specimens are subjected to periodical tension-compression with the same cycle parameters. The number of loading cycles for each investigated specimen is listed in Table 1. The final point of the study (specimen T4_07) is chosen because after applying N_C = 3300 cycles a short surface crack is clearly seen at the hole vicinity. After finishing of cyclic loading, the deformation and force fracture mechanics parameter are determined for cracks propagating in the material that is undergone to the influence of local elastic-plastic strains. Before performing the first symmetrical notch all specimens are subjected to constant one-axis tensile load that correspond to nominal stress σ_0 = 53.1 MPa. Three successive symmetrical notches are used for modeling the process of the crack growth. Averaged total lengths of these notches counted from the hole edge in one direction are $\tilde{a}_1$=2.0 mm, $\tilde{a}_2$ = 4.0 mm and $\tilde{a}_3$= 6.0 mm. Measured values are in-plane displacement components related to some specific points, which are located at the crack borders. Interference fringe patterns obtained for specimen T4_08 with the material in initial state are shown in Fig. 1. These images correspond to the first crack length increment. Interference fringe patterns obtained for specimen T4_05 after applying N_C = 1800 cycles are shown in Fig. 2 and Fig 3 for the first and the second crack length increment, respectively.

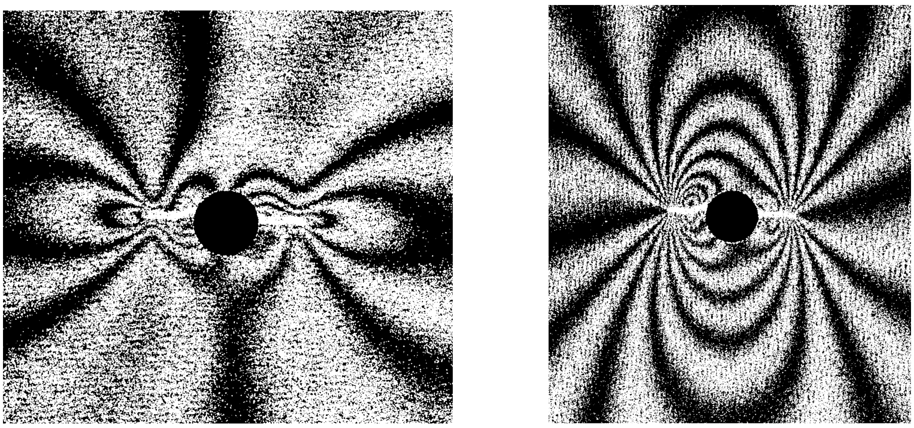

a b

Fig. 2 Specimen T4_05. Interference fringe pattern for in-plane displacement component *u* (a) and *v* (b). Initial crack length a_0 = 0 with increment Δa_1^- = 2.24 mm (left) and Δa_1^+ = 2.18 mm (right)

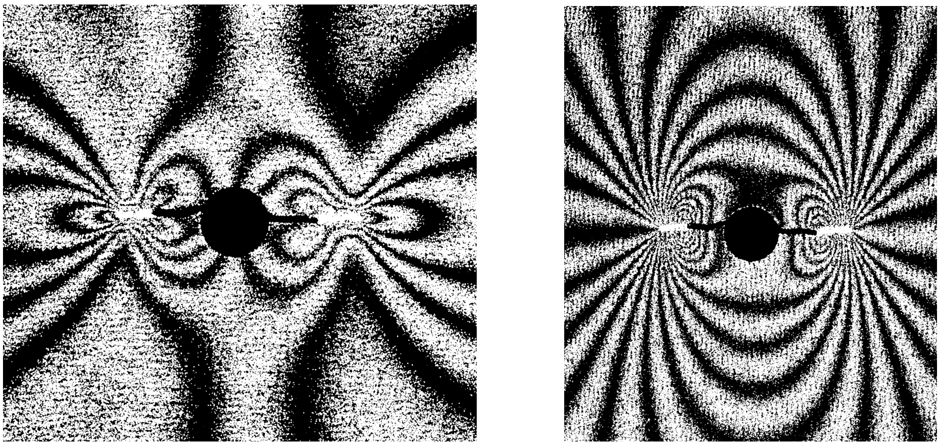

a b

Fig. 3 Specimen T4_05. Interference fringe pattern, obtained in terms of in-plane displacement component *u* (a) and *v* (b). Initial crack length a_1^- = 2.44 mm with increment Δa_2^- = 1.56 mm (left); initial crack length with increment Δa_2^+ = 1.97 mm (right)

4 MAIN RESULTS

The dependencies of relative crack opening values for the first left (a_1^+) and the first right (a_1^-) cracks from the loading cycle number N_C are shown in Fig. 4. The main feature of these distributions is the availability of the detectable splash that corresponds to N_C = 1800 cycles. This fact is of considerable interest in the course of the formulation and verification of deformation fracture criteria.

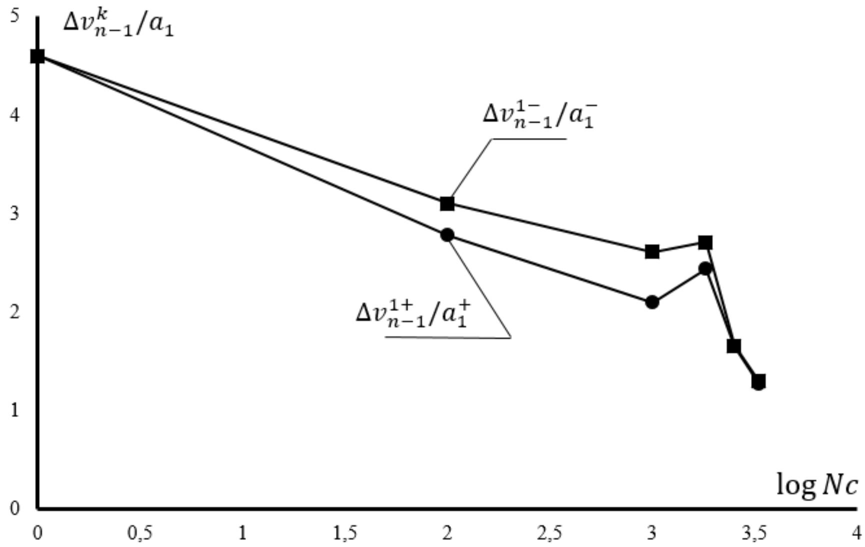

Fig. 4 Dependencies of relative crack opening values for the first left (a_1^+) and the first right (a_1^-) cracks from the loading cycle number

The dependencies of SIF values K_I^n against the crack length, which are obtained at different stage of local elastic-plastic deformation process due to low-cyclic fatigue loading, are shown in Fig. 5. The transfer from measured in-plane displacement components to SIF and T-stress values is performed by modified version of the crack compliance method [8]. Careful understanding of presented information, which is obtained for the first time, needs some additional efforts. It should be however noted that the differences between K_I^n-values, which correspond to the different loading cycle number N_C, is quite detectable. Developed approach is capable of fast obtaining experimental data for any cycle of interest under the same cycle parameters. Moreover, such investigations could be performed in analogous way for loading cycles with various parameters. The latter fact is of great importance from the standpoint of the formulation of force fracture criteria.

The dependencies of non-singular T-stress values T^n from the crack length, which are obtained at different stage of local elastic-plastic deformation process due to low-cyclic fatigue loading, are shown in Fig. 6. A difference between T^n values that are related to the different numbers of loading cycles N_C is quite detectable. The comparison of the dependencies shown in Fig. 5 and Fig. 6 are of specific interest.

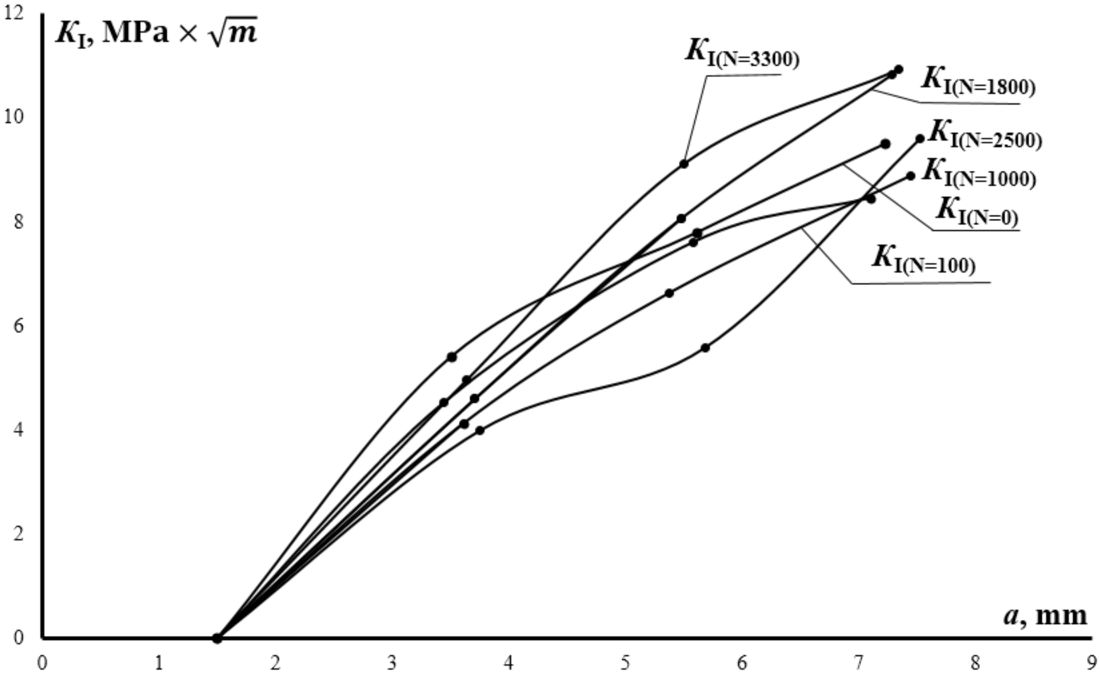

Fig. 5 Dependencies of K_I^n-values from the crack length for different stages of cyclic loading

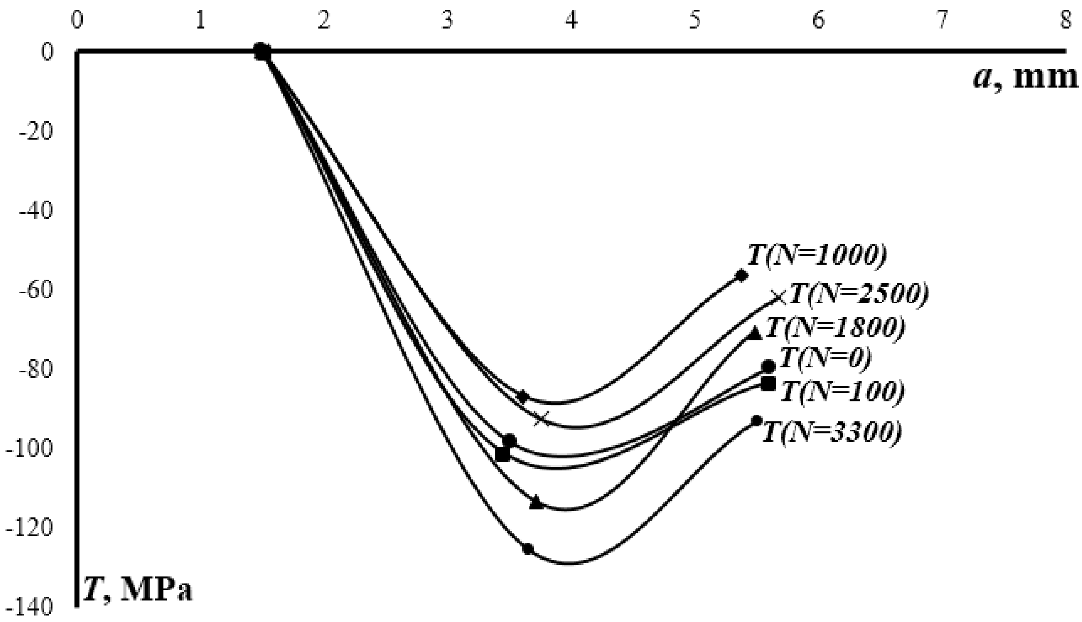

Fig. 6 Dependencies of T^n-values from the crack length for different stages of cyclic loading

The dependencies of singular and non-singular fracture mechanics parameters from the loading cycle number are shown in Fig. 7a and Fig. 7b. These dependencies are constructed for fixed crack length. Presented distributions have pulsing feature corresponding to N_C = 1800 loading cycles that has been revealed for relative crack opening (see Fig. 4).

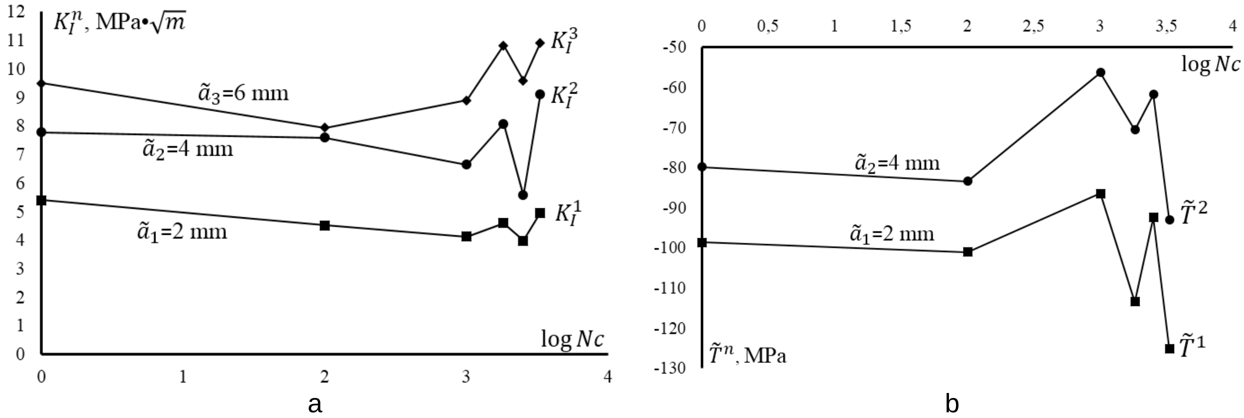

Fig. 7 Dependencies of K_I^n (a) and T^n (b) values from the loading cycle number N_C for fixed crack lengths

5 CONCLUSION

The novel method for obtaining experimental data, which reveal real deformation processes near the crack tip at different stages of cyclic loading, is developed and implemented. The measurements of local in-plane displacement components immediately along borders of the notch used for the crack modeling are the main feature of the developed technique. The transfer from measured in-plane displacement components to SIF and T-stress values is performed by modified version of the crack compliance method. First, the dependencies of SIF and T-stress values from the crack length for the fixed loading cycle number are obtained by this approach. Second, the dependencies of K_I^n and T^n values from the loading cycle number N_C for fixed crack lengths are constructed. Obtained information, which describes the influence of fatigue damage accumulation on the value of singular and non-singular fracture mechanics parameters, is essential for the formulation and verification of fracture criteria.

6 ACKNOWLEDGEMENTS

This study is performed in the framework of the Program of Joint Investigations of TsAGI and IMASH RAN.

7 REFERENCES

[1] C. Osgood, Fatigue Design, 2nd edition, Oxford, U.K.: Pergamon Press, 1982.

[2] N. Makhutov, Yu. Matvienko, S. Chernyakov, A unified methodological approach to calculation analysis of the stages of nucleation and growth of low-cycle fatigue cracks, Materials Science, 29 (2), 109-114, 1993.

[3] J. Collins, Failure of Materials in Mechanical Design: Analysis, Prediction, Prevention, 2nd edition, NY, Chichester, Brisbane, Toronto, Singapure, John Wiley & Sons, 1993.

[4] F. Chiang, Moiré and speckle methods applied to elastic-plastic fracture studies, In: Experimental Techniques in Fracture mechanics, 3rd edition, Edited by J.S. Epstein, NY: VCH, 1993, pp. 291 – 325.

[5] D. Post, B. Han, P. Ifju, High Sensitivity Moiré, Experimental Analysis for Mechanics and Materials, Berlin: Springer Verlag, 1994.

[6] V. Shchepinov, V. Pisarev, S. Novikov, V. Balalov, I. Odintsev, M. Bondarenko, Strain and Stress Analysis by Holographic and Speckle Interferometry, Chichester: John Wiley, 1996.

[7] P. Rastogi, Digital Speckle Pattern Interferometry and Related Techniques, West Sussex: John Wiley, 2001.

[8] Y. Matvienko, V. Pisarev, S. Eleonsky, A. Chernov, Determination of fracture mechanics parameters by measurements of local displacements due to crack length increment, Fatigue & Fracture of Engineering Materials & Structures, 37(12), 1306–1318, 2014.

[9] M. Williams, On the stress distribution at the base of a stationary crack, ASME Journal of Applied Mechanics, 24(1), 109–114, 1957.

[10] J. Yates, M. Zanganeh, Y.Tai, Quantifying crack tip displacement fields with DIC, Engineering Fracture Mechanics, 77 (11), 2063–2076, 2010.

[11] Y. Murakami, Stress Intensity Factors Handbook. Oxford: Pergamon Press, 1987.

Proceedings of the 4th International Conference on
Fracture Fatigue and Wear, pp. 109-115, 2015

ADVANTAGES OF LARGE PIEZOELECTRIC ACTUATORS AND HIGH POWER DRIVERS FOR FATIGUE AND FRETTING TEST

A. Kras, O. Sosnicki, A. Riquer, S. Rowe and F. Claeyssen

Cedrat Technologies, France
e-mails: aleksander.kras; olivier.sosnicki ; aurelien.riquer ; frank.claeyssen@cedrat-tec.com

Abstract: Constant expansion of new materials requires fretting or fatigue machines in order to test their failure. In many cases tests must be performed in severe conditions and at high frequency. These requirements come from the use of the materials in highly demanding applications. At the same time it is expected to reduce the time required to characterise such materials. Piezoelectric actuators are more and more common in testing machines, but they still reach limitations in terms of maximum displacement, cycling frequency or power. In order to cope with these issues, Cedrat Technologies has been investigating solutions. In this paper long stroke and high frequency actuators, coupled with powerful driving control are introduced. These actuators are based on piezoelectric materials and can be easily integrated into the fatigue machines. In order to improve precision of these tests, two of the most common displacement sensors used in smart actuators are also presented in this paper.

Keywords: Piezoelectric actuator; ECS sensor; Switching amplifier; Heat management

1 INTRODUCTION

Most common systems used these days for fatigue machines are based on servohydraulics actuators. Although these systems provide high force and long stroke they are limited in terms of frequency, speed or acceleration. Due to these limitations fatigue machines based on smart actuators have the advantage over the hydraulic systems in terms of response time and cost. Especially piezoelectric actuators are good candidates [1, 2]. This type of propulsion presents many advantages over the conventional systems. It can provide good accelerations with high amounts of force. At the same time integrated displacement sensors allow precise measurement for closed loop control system. Recently, Cedrat Technologies has developed new actuators and a dedicated high power supply that are adapted to testing machines.

First development was concentrated on improving the actuator maximum displacement. Typically available piezoelectric actuators reach stroke limitation above 1mm. In order to extend this boundary Cedrat Technologies has developed a new actuator that doubles this limitation. A second development concerned increasing the actuator maximum driving frequency. The frequency limitation derives from self overheating of the piezoelectric ceramics, which is a huge problem. Sufficient cooling systems allow increasing the driving frequency and at the same time prevent overheating. However a higher driving frequency requires sufficient power supply for the piezoelectric components. The current need increases linearly with the driven frequency. Development of the power supply for piezoelectric actuators is presented in this paper. Final improvement was concentrated on the displacement sensors used for precise control and possible closed loop systems. Current position measurement is based on strain gauges. A new option for displacement measurement is an eddy current sensor integrated in the actuator. Both systems are presented and described in this paper.

2 LONG STROKE ACTUATOR

Maximum stroke increase of piezoelectric actuators is subject to extensive research. Typically the maximum displacement generated by piezoelectric ceramics is limited to a 0.1% elongation. This value depends on the type of the ceramics. With mechanical amplification this value can be increased 10 times. For many years Cedrat Technologies has been producing mechanically amplified actuators within the most compact volume. This patented mechanism used with piezoelectric ceramics is called amplified piezoelectric actuator (APA®). Up till now the maximum displacement of these actuators was 1mm.

Over the last year intensive research was performed in order to double the available stroke of an APA®. The research was based on the standard actuator APA1000L, which provides nearly a 1mm stroke and uses stack of 6 (10x10x20mm³) piezoelectric ceramics to generate displacement. The idea was to keep the same number of the ceramics and to increase the amplification ratio of the mechanism.

Based on simulations work an increase of amplification ratio was shown to be possible, in order to reach the required displacement. First measurements with standard ceramics showed that the displacement of the actuator was doubled compared to previews products. The new actuator provides a 1967µm stroke. The amplification ratio is now multiplied by 15. It is the biggest amplification ratio obtained so far with this type of an actuator. Furthermore the maximum force obtained with this actuator is 60N. Based on blocked force value and displacement measurements this actuator generates 15mJ of energy. The developed actuator was named APA2000L (Fig. 1). A derivate called the APA1500L has also been design, which produces a stroke of 1480µm and a blocked force of 121N. When more force is needed, two identical actuators may be set up in parallel to double the available force, with the same stroke.

Maximum speed and acceleration of the actuator depends on the driven frequency. With piezoelectric actuators, there are two configurations in which they can be used. The first configuration is called Blocked – Free. In this condition one extremity of the actuator is attached to a rigid base while the other one is free. The second configuration called Free – Free is when both actuator extremities are not rigidly fixed. Due to these two configurations the resonance frequency varies and changes the maximum driving frequency. The APA2000L can be driven up to 30Hz in Blocked – Free condition and up to 150Hz in Free – Free condition. The generated acceleration is quite huge regarding to the offered displacement. For the Blocked – Free condition the actuator can reach acceleration of 37m/s² and in Free – Free condition it can reach 1740m/s².

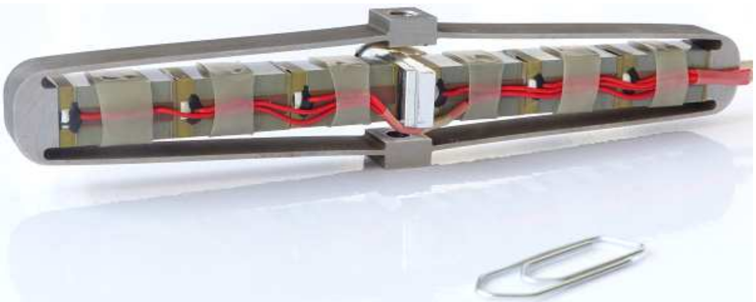

Fig. 1 Long stroke amplified piezoelectric actuator APA2000L.

The developed actuator, has a compact dimensions of 140x10x28mm³ (length x width x height), and can be easily integrated in fatigue mechanisms. The increase of maximum displacement, improved performance and doubled the stroke of typical actuators, together with high generated energy can be sufficient in fatigue of fretting testing.

3 HIGH FREQUENCY ACTUATOR

Due to excessive overheating of the piezoelectric ceramics, the use of piezoelectric actuators in high dynamic conditions is limited. In many cases the maximum operating temperature is limited to 85°C. With this limitation the actuators can be used only for a few moments at maximum frequency, typically one or two minutes, depending on the driven frequency. In order to overcome this issue it was decided to develop an actuator that could work at high frequency for a long period of time.

Development of an actuator with a sufficient cooling system was investigated at Cedrat Technologies. Some precautions are needed: A piezo actuator has to be encapsulated in order to use a cooling system and the cooling fluid must be compatible with piezo ceramics.

(a) (b) (c)

Fig. 2 Regular PPA80L (a), Encapsulated PPA80L-E (b) and thermal image at high frequency (c).

Two-stage architecture was made with internal cooling system that is used to extract the heat from the ceramic to the encapsulation, and an external system that employs compressed air and radiator fins in the encapsulation to improve heat extraction. A developed prototype was based on a standard parallel pre-stressed actuator PPA80L, renamed PPA80L-E for identifying the encapsulation (Fig. 2). This actuator has been tested in order to verify both cooling systems. Significant improvement of the actuator in terms of maximum driving frequency has been observed.

In the first test the internal cooling system was tested alone. Based on this test it was observed that the PPA80L-E can be driven at 230Hz constantly. Monitored temperature of the ceramics stayed below the critical temperature value. During long cycling test the actuator has performed 170 million cycles during 8 days. During this period the actuator was turned off and on couple of times. These activities allowed to obtain heat up and cooling graphs of the actuator. The heats up curves of the regular and encapsulated actuators were compared (Fig. 3). Working at 230Hz, regular actuator reaches 81°C in 1:07minute and should then been stopped to prevent damages. At the same time the encapsulated actuator can work constantly at that frequency.

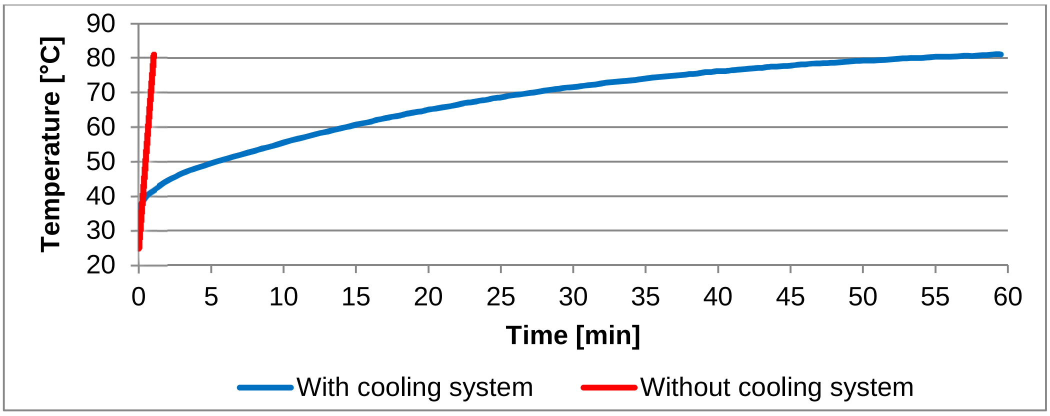

Fig. 3 Heat up curves of the PPA actuators with and without cooling system driven at 230Hz.

Promising results led to testing the external cooling system, this just requires plugging the actuator into a compressed air supply. The air pressure was set to 0.25bar. With both cooling systems working, the maximum driving frequency was increased up to 1000Hz in continuous running. The external system, based on optimised flow of compressed air, allows an increase in the driving frequency by a factor of 4 compared to using the cooling fluid only.

The developed actuator with cooling system can be used at high frequency in many different applications. One of these applications can be integration in the fatigue mechanism, where using higher frequencies reduces testing time and increases efficiency of the machines.

4 SENSOR INTEGRATION

The most common sensors integrated in the piezoelectric actuators are strain gauges. This type of sensor presents many advantages which include good reliability, conditioning and accuracy. The strain gauge is directly glued to the ceramics and measures strains on the piezoelectric component, which is then converted by the conditioner into a standard ±10V signal. Calibrated output signal is proportional to the displacement of the whole actuator with a specific gain value.

Although this sensor presents many advantages, the measured displacement in APA® actuator is indirect due to mechanical amplification. This means that displacement of the actuator is measured on the base of the ceramics displacement. This solution works well, as long as the actuator is not subject to dominant external forces. Unfortunately, it is often the case in fatigue or wear test benches.

The possibility of a direct measurement of the displacement in APA® has been investigated. A solution was developed with an eddy current technology probe. This sensor allows for a contactless and direct measurement of the actuator displacement.

Promising results of the prototype introduced in previous publications [3, 4] induced further investigation of ECS sensor integration in standard actuators. The integration of the sensor in the APA® actuators was initiated by designing support that could be integrated in the actuator. Three supports were manufactured and tested in order to choose the best configuration. First two supports were measuring displacement of the actuator between two extremities. Third version was attached at ceramics level and measured displacement of the actuator extremity relatively to the position of the ceramics.

Evaluation of designed supports was based on thermal testing and measurements at low and high frequencies. Measurements at different frequencies showed which support type gives the best sensitivity with narrow hysteresis. Thermal tests clarified the actuator stroke measurement error caused by temperature variation. It was observed that one of the supports extinguish with good results from two others (Fig. 4). This type of support due to small dimensions provides the best sensitivity at different frequencies with small signal error coming from temperature variation.

The ECS probe mounted inside the APA® shape allows direct measurement of the actuator extremity displacement. The compact dimensions of the probe and the fixing method do not increase the total volume of the actuator. At the same time the hysteresis correction and thermal behaviour presented the best conditions with the selected support.

Fig. 4 ECS with special support integrated in the APA.

Both presented sensors can be easily used and integrated in fatigue test benches. Signals coming from the sensor can be used for monitoring and controlling the actuator. Displacement measurement can provide information about fatigue or fracture propagation in the tested samples. Based on this data the closed loop control system can adjust testing parameters in real time.

5 HIGH POWER AMPLIFIER

One advantage of piezoelectric actuator for fatigue testing machines is the opportunity to work at high frequency. But with big actuators, this requires high power amplifier, as the current need is proportional to the frequency. The most common amplifiers used for driving capacitive loads are linear amplifiers. Although this type of amplifier provides smooth supply signals with low output noise (THD), their configuration causes huge power losses. At the same time power and current values require large components and heat sinks that make this amplifier massive. Due to this disadvantage the maximum current value is limited (Fig. 5).

It became necessary to develop a new amplifier for overtaking the limitation in current. In order to get an amplifier capable to generate more power, a new configuration based on switching topology was investigated. This configuration enables to obtain much more power with negligible losses that makes this amplifier very efficient. Developed portfolio of switching amplifiers obtained the name SA75.

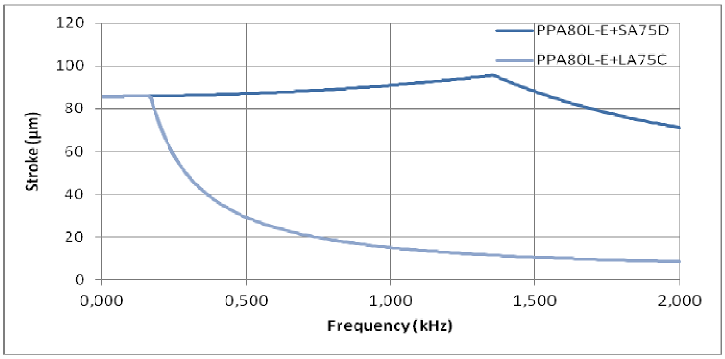

Fig. 5 Power capabilities comparison of a switching amplifier (SA) and linear amplifier (LA) on a PPA80L actuator

The design of the amplifier has concentrated on driving capacitive loads, particularly piezoelectric actuators. The low voltage piezoelectric materials require a driving range between -20 and 150V (170Vpp). At the same time, driving these actuators at high frequency requires high current values. Following the requirements, the developed amplifier can provide up to 20A continuously, in the SA75D version. This value is sufficient enough to drive one large actuator (like actuators from the L or XL range from Cedrat Technologies) at high frequency or couple actuators in parallel.

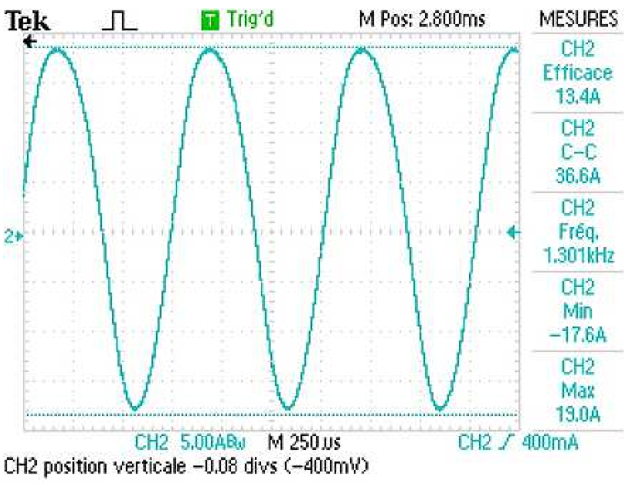

Fig. 6 Current measurement of the PPA80L-E driven with SA75D at 1300Hz.

Tests with the SA75D and PPA80L-E showed that this amplifier can easily provide 18.3A peak value while driving the actuator at 1300Hz (Fig. 6). In these conditions, the PPA80L provides 3500N and a stroke of 94µm. At 1300Hz, the mechanical reactive power stored in the actuator is 1.3kVA, whereas the maximum electric reactive power provided by the amplifier is 1.5kVA [5]. Power consumption gets a benefit from the low losses of switching technology. Moreover, an energy recovery system has been included for driving capacitive loads. Finally, at maximum driving parameters (20A and 170Vpp) the required active power is less than 100W.

Low power consumption and recovery system allowed using smaller and less massive components. The mass of the core amplifier is less than 850g with total volume of 100x100x100mm^3. The power ratio of the amplifier is 1.75kVA/kg.

6 APPLICATION NOTES

Piezo actuators are easily controllable, this makes them versatile for test machines or for particular methodologies. Due to the proportional relation between voltage order and actuator displacement the fatigue excitation or fretting stroke on the sample can be easily set up. Additionally the signal shape can be adjusted to the requirements. A large variety of signals can be applied to the actuators: from the most common continuous sin, square, sawtooth, triangle signals to a personally-created signal that can vary in amplitude or over time.

In fretting test benches, which are used to produce the wear of two surfaces, the amplitude of the relative sliding motion is in the order of magnitude of a few microns to millimeters. Piezoelectric actuators are a good choice for this application, offering easy control and high speeds. Their intrinsic mechanical stiffness is an additional advantage for the application.

For fatigue machines a piezoelectric actuator may be coupled with a hydraulic actuator to get the benefit of both technologies. This is the choice that Fraunhofer LBF (DE) has made. They developed a hybrid high cycle fatigue (HCF) testing machine used to investigate the high frequency properties of different materials, with a low-frequency hydraulic actuator for a frequency band between static to 50 Hz and a high frequency piezo actuator system for frequencies up to 1000Hz (Fig. 7).

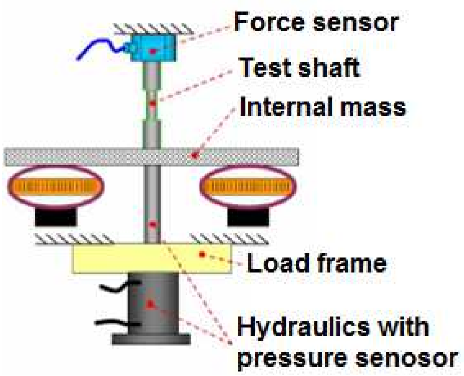

Fig. 7 Hybrid high cycle fatigue (HCF) testing machine using 4 APA230L (Courtesy of Fraunhofer LBF)

Since the introduction of our devices in that field, laboratories such as LAMCOS (Fig. 8) or LMT and industrial such as AIRBUS or EPT (Electronics Precision Technology) have tested and approved our technology for fretting.

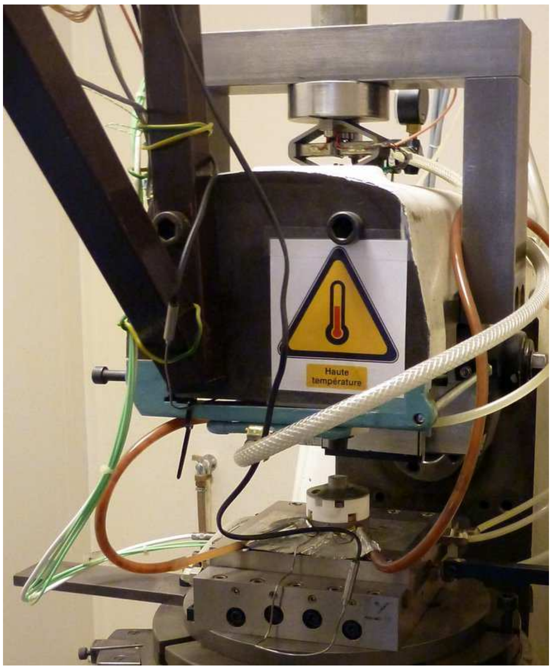

Application: Impact or sliding testing

Temperature: up to 500°C

Horizontal mouvement:
- Shaker Gearing Watson V 100 SS 600
- Sinusoidal Force peak 778N
- Maximum Acceleration Peak 981m/s²
- Maximum Velocity Peak 1.65m/s
- Maximum Displacement pk-pk 12.7mm

Vertical Mouvement:
- Piezoelectric actuator APA 120 ML
- Sinusoidal stroke 0 to 70µm
- Bloqued force 1400N
- Maximum frequencu Blocked-free 1750Hz

Forces sensor
- KISTLER 9251A
- Measurement of impact forces and tangential rubbing forces

Fig. 8 IMPACT II: APA120ML actuator for impact or normal force control (Courtesy of LAMCOS)

7 CONCLUSIONS

Presented development of the new piezoelectric actuators can bring advantages in fatigue and fretting testing machines. Encapsulated actuator with integrated cooling systems (PPA80L-E) allows performing tests at high frequency, up to 1000Hz. This parameter reduces time and/or improves efficiency of testing machines. The switching amplifier range SA75 provides sufficient power to drive big piezoelectric actuators at high frequency. Presented test results shows that this amplifier can drive the encapsulated actuator at up to 1300Hz. At the same time real power consumption stays below 100W. Long stroke actuators (APA2000L) generate two times larger displacement compared to standard actuators, with maintained dynamic capacities. For complete mechanism, a displacement sensor can be integrated in the piezoelectric actuators. Displacement sensor based on the eddy current effect (ECS) can be used for monitoring and controlling the actuator.

8 ACKNOWLEDGEMENTS

The research leading to these results has received funding from the European Union's Seventh Framework Programme (FP7/2007-2013) for the Clean Sky Joint Technology Initiative under grant agreement n° [632604].

9 REFERENCES

[1] M. Matthias, T. Melz, R. Wagener, C. Lanz, High dynamic testing machines based on piezo-ceramic actuators for the experimental characterization of materials and components, Actuator2014, A5.3, 138–143, 2014 Bremen.

[2] C. Fischer, R. Wagener, T. Melz, H. Kaufmann, Piezo based testing facilities to discover new areas in material characterization", SAE international, 2014

[3] A Kras, F. Bourgain, F. Claeyssen, Amplified piezo actuator APA® with viscoelastic material for machine tool semi active damping system, Journal of machine engineering Vol. 14 No.3 2014, Wrocław, 2014.

[4] A Kras, M. Brahim, T. Porchez, C. Bouchet, F. Claeyssen, Compact, Lightweight, and Efficient Piezo-Actuation Chain for Aeronautical Applications, Actuator2014, B6.5, 305–308, 2014 Bremen.

[5] M. Fournier, M. Brahim, T. Porchez, O. Sosnicki, New design of high switching power amplifier for driving piezoelectric actuators in aeronautic applications, EPE'14 ECCE conference, 2014.

Proceedings of the 4th International Conference on
Fracture Fatigue and Wear, pp. 116-121, 2015

FATIGUE LIFE ESTIMATION METHOD USING CRITICAL DISTANCE STRESS THEORY

T. Hattori[1], M. A. Bin Ab Wahab[2], Niu Jie [2] and S. Ikeya[3]

[1]Department of Mechanical Engineering, Shizuoka Institute of Science and Technology, Fukuroi, Japan
[2]Graduate student, Gifu University, 1-1 Yanagito, Gifu, Japan
[3]Graduate student, Shizuoka Institute of Science and Technology, Fukuroi,Japan

Abstract: Generally the critical distance stress theory was applied for the fatigue limit estimation of general structures using fatigue limit of smooth specimen (σ_{w0}), and threshold stress intensity factor range (ΔK_{th}). In this paper we extended this method for the estimation of low cycle fatigue life too. In this method we define the critical distance (r_c') on static strength conditions, which is calculated using ultimate tensile strength (σ_B) and fracture toughness (K_{IC}), in addition to the critical distance on fatigue limit condition (r_c). Then the critical distances of any low cycle fatigue conditions can be calculated by interpolation of critical distance on fatigue limit (r_c) with critical distance on static strength (r_c'). By unifying these low cycle fatigue life estimation method with high cycle fatigue limit estimation method we can estimate the full range fatigue life easily. And to confirm the availability of this estimation method we perform the fatigue test for any stress concentration specimens and some actual industrial structures such as fretting structures and shaft couplings.

Keywords: Low cycle fatigue, Stress intensity factors. Critical distance stress theory. Fretting fatigue, Contact edge, Oldham's shaft coupling

1 INTRODUCTION

In general the critical distance stress theory (point method and line method) were used for estimation of fatigue limit with any shape structures. In this method the fatigue limit can be obtained using typical material strength parameters such as the fatigue limit of smooth specimen's σ_{w0} and the threshold stress intensity factor range ΔK_{th} of the cracked specimens. In the case of point method, the fatigue failure supposed to occur when the stress range at specific length r_c from maximum stress point reach $\Delta\sigma_{w0}$. This r_c can be derived as follows.

$$r_c=(\Delta K_{th}/\Delta\sigma_{wo})^2/2\pi \quad (1)$$

In this paper we extended this method to the low cycle fatigue regions. Then I will explain this development in detail. Firstly the critical distance in low cycle fatigue region is derived by interpolating between critical distance in fatigue limit as shown in above and critical distance in static strength. This static strength critical distance can be derived using ultimate strength of smooth specimen σ_B and the fracture toughness K_{IC} of the cracked specimen as follows.

$$r_c'=(K_{IC}/\sigma_B)^2/2\pi \quad (2)$$

The critical distance in each stress level is calculated by interpolation of critical distance on fatigue limit (r_c) with critical distance on static strength (r_c') as shown by chain line in Fig. 1(right). The critical distance on objective conditions (structure, load) can be estimated by reflecting the stress distributions of objective structure as shown by dotted line in Fig. 1(right). The low cycle fatigue life in this objective condition can be estimated by applying this reference stress σ at critical distance r on S-N curve of smooth specimens as shown in Fig. 1(left upper).

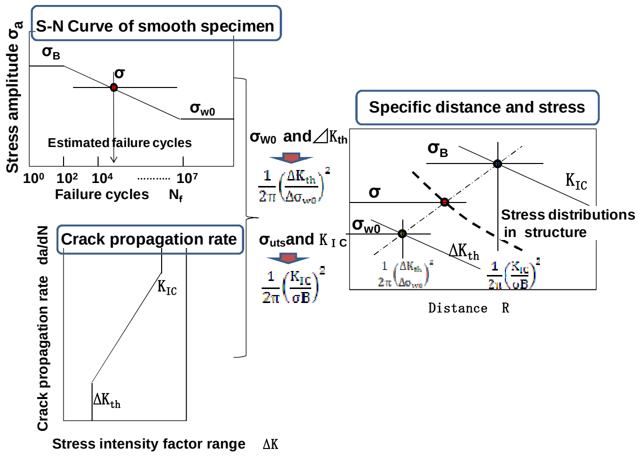

Fig.1 Derivation of specific distance in low cycle fatigue region and estimation of low cycle fatigue life

2 APPLICATION ON GENERAL STRESS CONCENTRATION SPECIMENS

To confirm the validity of this critical distance approach we applied this method on low cycle fatigue life estimation of circle hole specimens. Smooth specimen and circle hole specimen used on this test are shown in Fig. 2, and material properties of SS400 steel are shown in Table 1. S-N curve of the smooth specimens is shown in Fig. 3. And Critical distance on fatigue limit r_c and on static strength r_c' are estimated using Eq.(1),(1)' and (2),(2)' as 0.077mm and 1.24mm respectively, and shown in Figs.4,5 by ●points.

$$r_c = \frac{1}{2\pi}\left(\frac{\Delta K_{th}}{\Delta\sigma_{wo}}\right)^2 = \frac{1}{2\pi}\left(\frac{6.7\times10^6}{305\times10^6}\right)^2 = 0.077 \quad \text{(mm)} \tag{1'}$$

$$r'_c = \frac{1}{2\pi}\left(\frac{\Delta K_c}{\Delta\sigma_b}\right)^2 = \frac{1}{2\pi}\left(\frac{39.5\times10^6}{448\times10^6}\right)^2 = 1.24 \quad \text{(mm)} \tag{2'}$$

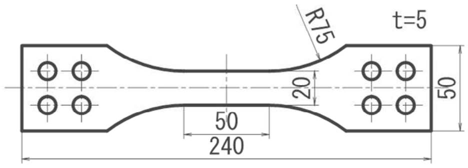

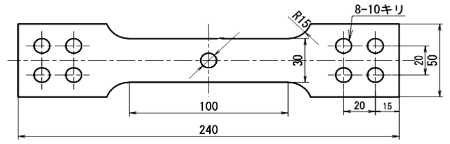

(a) Smooth specimen (b) Circle hole specimen

Fig. 2 Dimensions of smooth and circle hole specimens

Table 1 Mechanical properties of SS400 steel

$\Delta\sigma_{w0}$ [MPa]	ΔK_{th} [MPa·m$^{1/2}$]	σ_B [MPa]	K_{IC} [MPa·m$^{1/2}$]
305	6.7	448	39.5

By interpolating these two points the critical distances on arbitrary conditions are estimated as solid line(predict line) in Fig. 4,5. The critical distance of circle hole specimens on each loading condition can be estimated as the cross point of these stress distributions lines on each loading conditions with interpolation line (predict line) as shown in Fig. 4,5. And by reflecting the stress σ on this cross point on S-N curve of smooth specimens we can estimate the fatigue life of each loading condition of each circle hole specimen.

By repeating this estimation we can estimate the S-N curve of each circle hole specimen as shown in Fig. 8,9 by solid line. These estimated results coincided well with the experimental results shown as symbol ■ in each Figures.

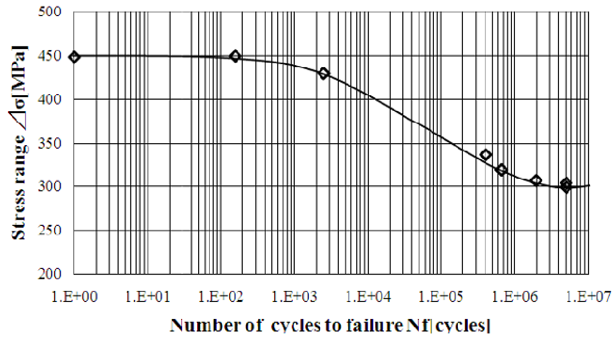

Fig. 3 S-N curve of smooth specimens (SS400)

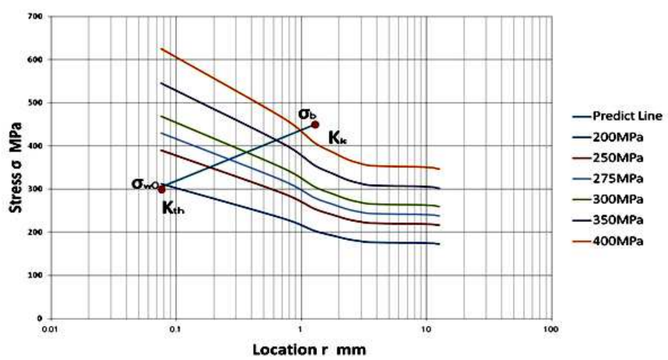

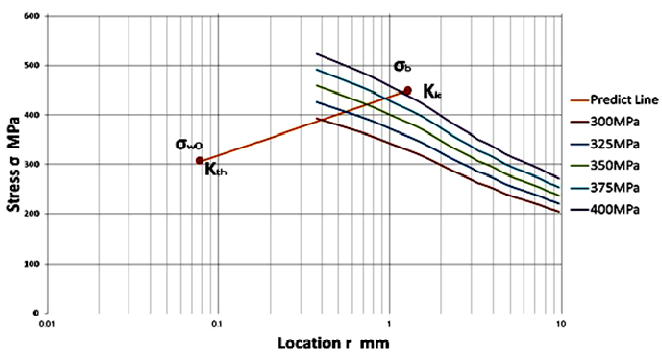

Fig. 4 Stress distributions in circle hole specimen with circle diameter 4mm on each nominal stress

Fig. 5 Stress distributions in circle hole specimen with circle diameter 10mm on each nominal stress

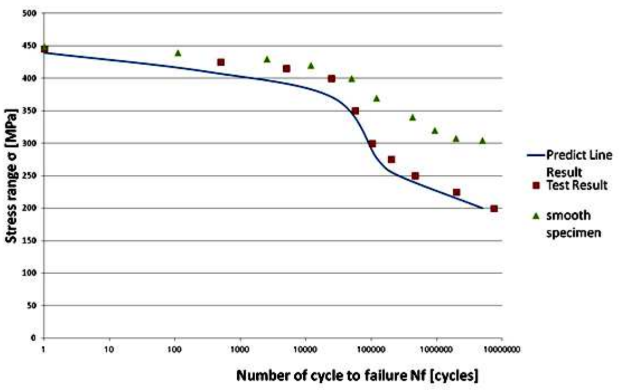

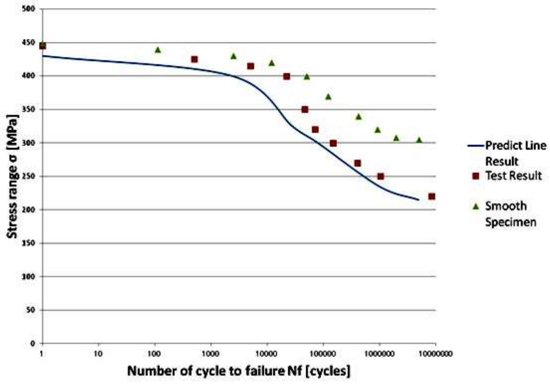

Fig. 6 Estimated and experimental S-N curves of circle 4mm specimens

Fig. 7 Estimated and experimental S-N curves of circle 10mm specimens

3 APPLICATION ON FRETTING FATIGUE STRUCTURES

Then we will apply this extended critical distance theory on the fretting fatigue life prediction. In Fig. 8 (left upper) the S-N curve of Ni-Mo-V steel smooth specimen in complete reversed loading conditions (R=-1), and in Fig. 8 (left under) the crack propagation characteristic of cracked specimen is shown. From these material characteristics we can obtain the critical distance r_C is 0.011mm and r_C' is 2.13mm as shown in Fig. 8 (right). The stress distributions in fretting conditions were calculated using FEM model as shown in Fig. 9. The calculated example of stress distribution near the contact edge is shown in Fig. 10. The mean contact pressure σ_p and mean axial stress σ_a in this case are 200MPa and 100MPa respectively.

The critical distance on each loading conditions can be estimated by reflecting these stress distributions on Fig. 8 (right) as shown by dotted line. The low cycle fretting fatigue life in this loading condition (σ_a is 200MPa) can be estimated by applying this stress level at critical distance (490MPa) on S-N curve of smooth specimens as shown in Fig. 8(left upper). By connecting these fretting fatigue life on each stress level we can estimate the fretting fatigue S-N curve as shown in solid line in Fig. 11. These estimated S-N curve coincided well with experimental results as shown by symbol ○.

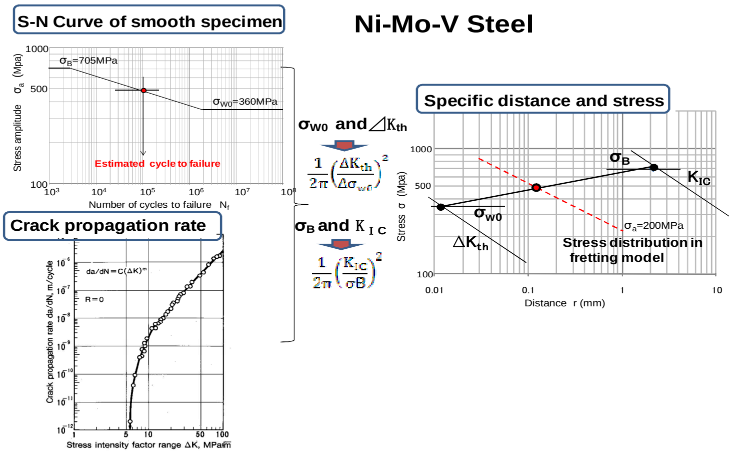

Fig. 8 Derivation of specific distance in low cycle fatigue region and estimation of fretting fatigue life

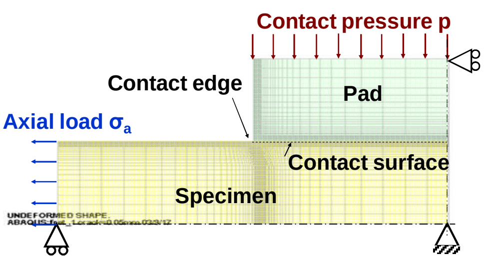

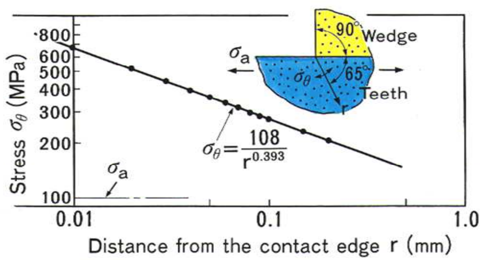

Fig. 9 FEM Fretting model

Fig. 10 Calculated result of stress distributions

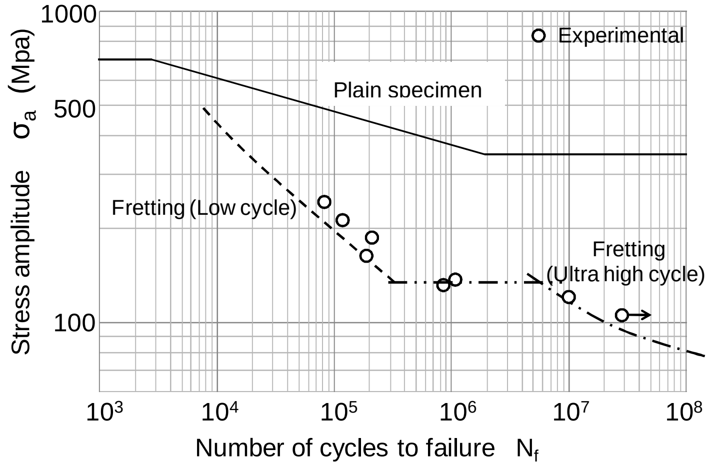

Fig. 11 Estimated and experimental fretting fatigue S-N curves

4 APPLICATION ON OLDHAM'S SHAFT COUPLINGS

Finally we applied this fatigue strength and life estimation methods on the general machine elements such as Oldham's shaft couplings as shown in Fig. 12. This shaft coupling composed of drive and follow hub made in aluminium alloy (A2017) and disk made in PEEK. Mechanical properties of both materials are shown in Table 2. And also the critical length r_C and r_C' calculated from these material properties and Eq.(1),(2) are shown in Table 2. And S-N curves of smooth specimens made from A2017 and PEEK are shown in Fig. 13 and Fig. 14 respectively. FEM stress analysis for each elements under operating torque of T=160N-m are shown in Fig. 15, and16 respectively.

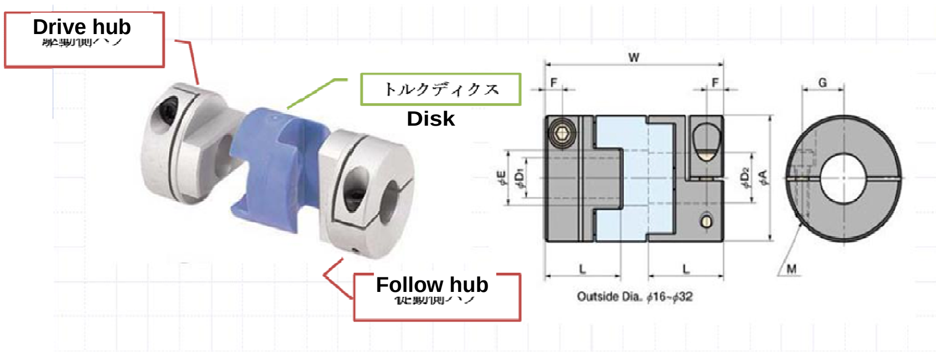

Fig. 12 Schematic figures of Oldham's shaft coupling

Table 2 Mechanical properties and critical length of each materials

	$\Delta\sigma_{w0}$ (MPa)	ΔK_{th} (MPa√m)	σ_B (MPa)	K_{IC} (MPa√m)	r_C (mm)	r_C' (mm)
PEEK	88	3.0	118	14.0	0.33	1.93
2017	134	8.0	430	29.3	0.568	0.74

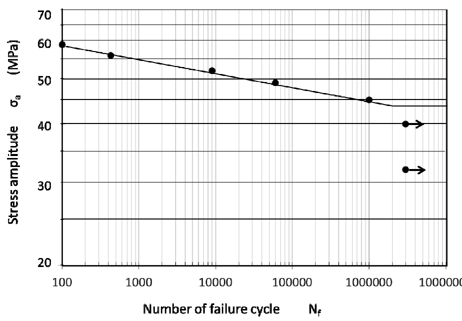

Fig. 13 S-N curve of PEEK smooth specimens

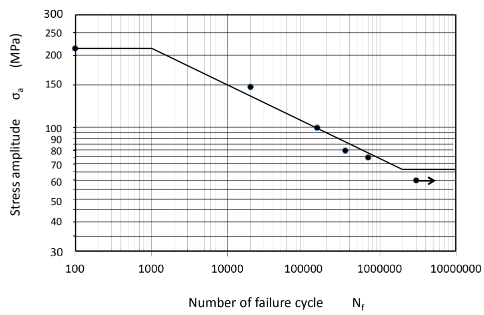

Fig. 14 S-N curve of A2017 smooth specimens

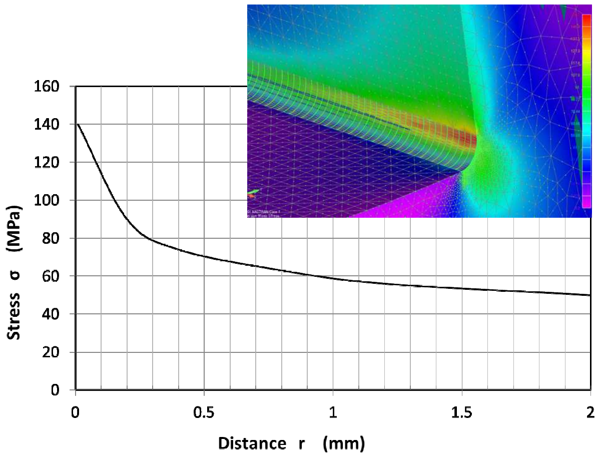

Fig. 15 FEM stress analysis of PEEK Disk (T=160N-m)

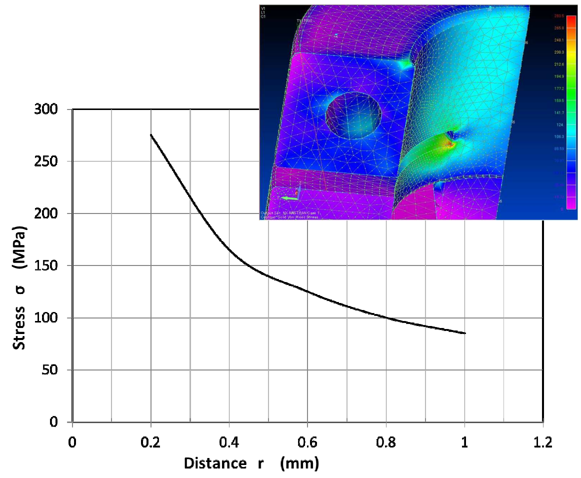

Fig. 16 FEM stress analysis of A2017 Hub (T=160N-m)

By plotting these stress distributions on the critical distances graphs we can obtain the fatigue life of these elements under each loading torques. Application result of these methods on PEEK Disk element is shown in Fig. 16, and we can get the estimated S-N curve of PEEK Disk element as shown by solid line in Fig. 17.

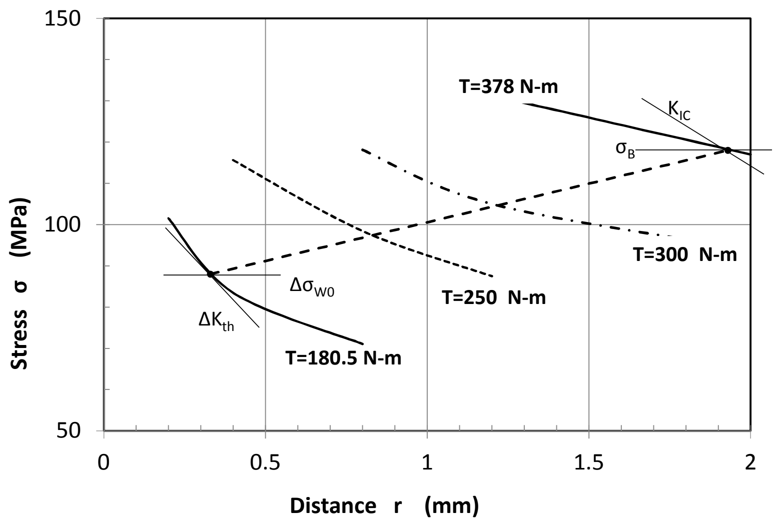

Fig. 17 Critical distances and stress distributions in PEEK Disk under each loading torque

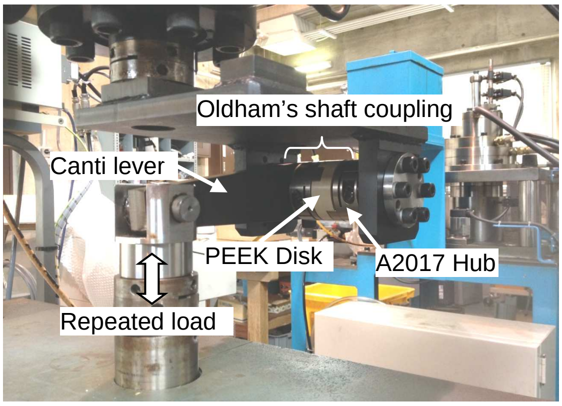

Fig. 18 Fatigue test apparatus for Oldham's shaft coupling

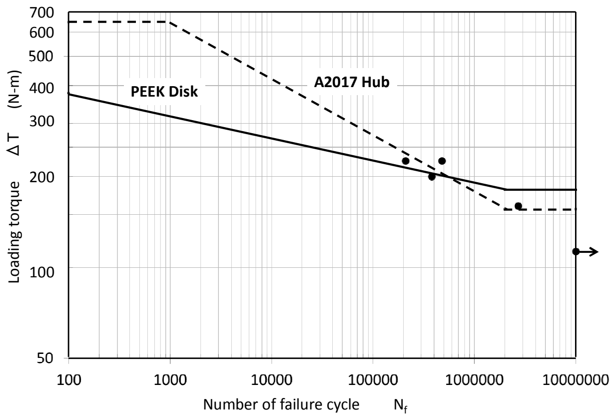

Fig. 19 Estimated and experimental S-N curves of Oldham's shaft coupling

By the same way we get the estimated S-N curve of A2017 Hub element as shown by dashed line in Fig. 19.

To confirm the validity of these methods we perform the fatigue test of Oldham's shaft couplings. The fatigue test apparatus is shown in Fig. 18. In this fatigue test apparatus the repeated torque is loaded by the canti lever. The Experimental results are shown in Fig. 19 by the symbol ●, in whole cases the fatigue failure occur in the PEEK Disk elements. These experimental results coincided well with the estimated results shown by solid line, and we can confirm the validity of these fatigue life estimation method using critical stress theory.

5 CONCLUSIONS

(1) We present new fatigue life estimation method using critical distance stress theory. In this method the critical distances of any low cycle fatigue conditions can be calculated by interpolation of critical distance on fatigue limit (r_c) with critical distance on static strength (r_c'), and here (r_c) can be calculated using fatigue limit (σ_{w0}), and threshold stress intensity factor range (ΔK_{th}) and (r_c') can be calculated using ultimate tensile strength (σ_B) and fracture toughness (K_{IC}).

(2) Firstly we applied this method to the central circle hole specimens made by SS400 steel, and we confirm the good agreement with experimental results.

(3) Then we applied this method to the fretting fatigue structures made by Ni-Mo-V steel, and we confirm the good agreement with experimental results.

(4) Finally we applied this method to the Oldham's shaft couplings made by PEEK Disk and A2017 Hub, and we confirm the good agreement with experimental results.

6 ACKNOWLEDGEMENTS

The authors would like to acknowledge the overwhelming support of FUJI HENSOKUKI CO., LTD. (TACHIKAWA Group). They present us the research fund and Oldham's shaft couplings.

7 REFERENCES

[1] Taylor, D., "Geometrical Effects in Fatigue: A Unifying Theoretical Model," Int. J. Fatigue, **21**, 413-420 (1999).

[2] Toshio Hattori, Muhammad Amiruddin Bin Ab Wahab, Takuya Ishida and Minoru Yamashita, "Fretting Fatigue Life Estimations Based on the Critical Distance Stress Theory", Engineering Procedia, **10** pp 3134-3139 (2011)

[3] Muhammad Amiruddin Bin Ab Wahab, Niu Jie, Toshio Hattori and Minoru Yamashita, "Fatigue Strength and Life Estimation Methods Using Critical Distance Stress Theory", Advanced Materials Research, Vol. **694-697** pp 853-863 (2013)

[4] Toshio Hattori ,Muhammad Amiruddin Bin Ab Wahab and Minoru Yamashita, "Low Cycle Fatigue Life Estimations Based on the Critical Distance Stress Theory", Advanced Materials Research Vol. **891-892** pp 1773-1778 (2014)

Proceedings of the 4th International Conference on
Fracture Fatigue and Wear, pp. 122-127, 2015

FATIGUE DAMAGE EVOLUTION IN CFRP USING DIC

S. Venkatachalam, S.M. Khaja Mohiddin and H. Murthy

Department of Aerospace Engineering, Indian Institute of Technology Madras, Chennai, India

Abstract: Damage evolution has been studied in carbon fiber reinforced plastic (CFRP) specimens subjected to fatigue loading under various conditions (tension-tension, tension-compression and compression-compression). Digital image correlation (DIC) has been adopted to obtain full field surface strains. Since delamination initiation is a local phenomenon, its effect on global parameters is not significant. Further, the delamination affects transverse strain more than the longitudinal strain. Consequently, local transverse strain was found to be a better indicator of delamination. Ratio of transverse strain to applied stress near the initiated delamination was tracked with number of fatigue cycles. Plot of variation of this transverse stiffness had scatter and waviness due to large displacements and lag between load data and images used for DIC respectively. Scatter was eliminated using different reference images and waviness was avoided using sine curve fit to obtain maximum transverse strain in a cycle. Variation of the local transverse stiffness with number of fatigue cycles indicates that the damage evolution occurs over 2-3 stages. In each stage, there was a stable crack growth with drastic increase in damage between the stages. Preliminary studies seem to indicate that these stages correspond to different damage mechanisms (matrix cracking, fiber matrix debonding, fiber breakage) over different periods during the fatigue life. Fatigue life curves were generated for different R-ratios and run-out lives were determined.

Keywords: CFRP; fatigue; damage evolution; DIC; transverse strain

1 INTRODUCTION

Fibre reinforced composite materials are widely used for last few decades as an alternative material to the conventional metallic materials in a variety of applications. This is mainly due to their high strength to weight ratio as well as high toughness. Application in various critical areas necessitates the understanding of the damage and failure mechanism of the fibre composites under cyclic loading. General features in the damage of composite materials subjected to fatigue loading are attributed to the matrix cracking in the off axis plies, fibre/matrix debonding, delamination and fiber fracture. However, the failure behaviour of laminated composites is complex and mainly depends on the properties and the volume fraction of the individual constituents, fibre orientation, lay-up sequence and the fabrication process [1]. The damage developed in composite materials subjected to cyclic loading has little or no effect in reducing the longitudinal modulus, but has a significant reduction in Poisson's ratio [2,3,4]. Hence, the reduction in global stiffness in the longitudinal direction is not significant to characterize the fatigue behaviour [2,5]. There exist many experimental techniques such as replication technique, X-ray radiography, eddy current, acoustic emission etc., for detecting different damage modes that occur during the fatigue of composites [6]. In the present study, it is proposed that the reduction in local transverse stiffness of a specimen can be a parameter to estimate the fatigue damage in composite materials. This reduction in local transverse stiffness is measured in terms of local transverse strain. This local transverse strain has been obtained from the full field surface strain measured using DIC technique. Further, local transverse strain is used to map the damage evolution in CFRP. Certain issues in synchronised acquisition of images and subsequent DIC have been discussed and solutions have been suggested.

2 FATIGUE TESTING OF CFRP

In this work, elaborate well-controlled experiments have been conducted to understand fatigue damage in CFRP composites. Fatigue tests have been conducted at three different stress ratios (R=0.5, 2 & -1). The specimens used for fatigue test are 17 layered carbon fiber (HS Carbon UD Fabric G0827-B1040-HP03-1F) and epoxy resin (Epolam 2063) composites with the stacking sequence of $[+45/90/-45/0/+45/0/-45/0/\overline{90}]_s$. The gripping sections of the specimens are strengthened by adding glass fibre reinforced plastic tabs to avoid failure at the gripping portion. The dimensional details of the specimen used for tension-tension, compression-compression and tension-compression fatigue tests are shown in Fig. 1(a) and 1(b).

Specimens used for compression mode fatigue tests have shorter gage length to avoid buckling. The specimens were supplied by National Aerospace Laboratory, Bangalore.

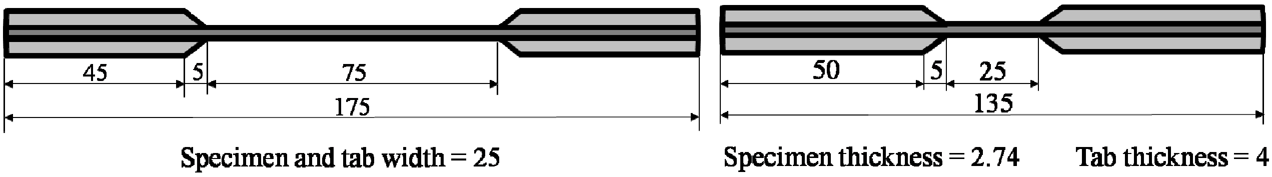

(a) (b)

Fig. 1 Schematics of the specimens used for (a) tension-tension; (b) compression-compression and tension-compression fatigue tests (all dimensions are in mm)

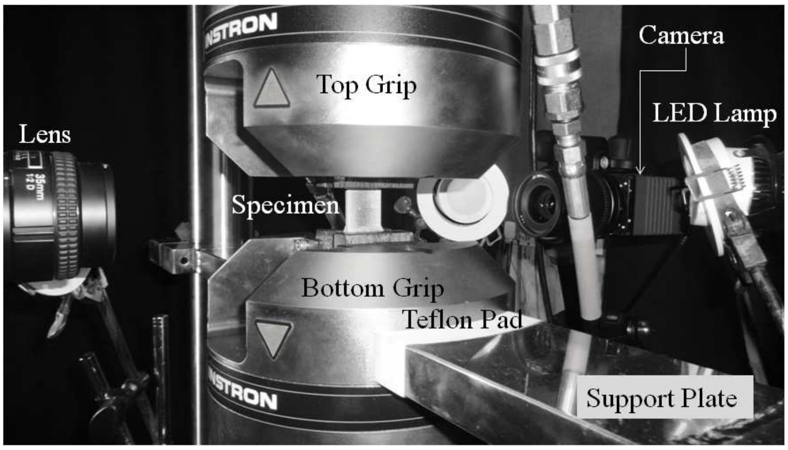

Fig. 2 Experimental set-up

Fatigue tests have been conducted using a 100 kN INSTRON 8801 fatigue testing machine. The experimental setup (photograph shown in Fig. 2) consists of two cameras, one on either side of the specimen, to acquire images of the speckle pattern introduced on the specimen and 4 light sources (LED lamps) to illuminate the specimen surface. In addition, two support plates with teflon pads are mounted on either sides of the actuator to ensure alignment of loading axis during fatigue tests in compression mode. The specimen is gripped between hydraulic wedge grips of size 50 mm x 50 mm with flat carbide coated surf alloy jaw faces.

Speckles are introduced on the specimen through spray painting and these speckle patterns are tracked with time to obtain strains on the surface using digital image correlation (DIC). DIC is a non-contact full field image analysis technique for measuring displacement and strain from relative motion of the speckle patterns. This technique correlates the gray values on digital images captured before and after the deformation of the specimen to obtain the full field strain. For unique correlation, the technique compares the gray intensity over a small square region of pixels called subset instead of a pixel. By tracking the subset on the digital images, the system measures the average surface displacement and strain of a pixel at subset centre. In similar fashion, all the subsets of the digital images can be tracked to find the full field surface displacement and strain [7].

3 DAMAGE MONITORING THROUGH TRANSVERSE STRAIN MEASUREMENT

During preliminary tension-tension fatigue tests, it was found that there is less than 2% reduction in the global longitudinal stiffness even after considerable visible delamination in the specimen. This may be because, damage initiates locally and may not modify global longitudinal stiffness significantly until it is critical. Moreover, it is observed that plies do bend locally in transverse direction after delamination. Hence, it has been assumed that change in local transverse stiffness along the thickness direction is a better indicator of delamination. To evaluate the local transverse stiffness, it is required to measure the local transverse strain in the specimen. Since the location of damage initiation is not known *a priori*, DIC technique has been used to get the full field strain data. This strain data would lead to the identification of damage zone on the free surface along the thickness direction, over the gage length of the specimen.

3.1 Digital imaging and damage zone detection

For strain measurement using DIC, images of speckled lateral faces along the thickness direction of the composite specimen have been captured at specified frame rate using two charge-coupled device (CCD) cameras during fatigue tests. For fatigue experiments with f = 1 Hz, 10 images of each lateral surface are captured per cycle with a dwell period of 99 cycles. For fatigue experiments with f = 5 Hz, 6 images of the each lateral surface are captured per cycle for two cycles with a dwell period of 198 cycles. These images of speckled patterns are then correlated with image of the speckle pattern on the specimen in undeformed condition. From this correlation, transverse strain contour plots are obtained. Any significant local damage in the specimen would reflect in these contour plots. The damage zone/area on the lateral faces along the thickness direction of the composite specimen were identified by observing these transverse strain contour plots and then the transverse strain at the location was tracked as a function of number of cycles to understand the damage evolution with number of cycles.

3.2 Evolution of maximum local transverse strain

Fig. 3a shows the transverse strain contour plot for a typical tension-tension experiment (R = 0.5, σ_{max} = 600 MPa and f = 1 Hz). After identifying the damage zone from this plot, a point (i.e., a pixel) close to the damage zone is considered as a critical point for finding strain variation with cycles. The local transverse strain of this critical point has been extracted from the first image of each cycle (10 images captured/cycle) for the entire test. The variation of this local transverse strain divided by the longitudinal stress is plotted against the number of cycles (Fig. 3b). Small waviness and large scatter beyond 40,000 cycles can be observed in the shown plot. The large scatter is observed only after visible delamination, which in turn leads to large local transverse strain [8]. The waviness may be due to the time lag between the load data acquisition and image captured. To avoid this lag, peak strain was estimated by fitting a sinusoidal curve to the strains obtained from DIC of images and peak load was obtained from the data acquired during each cycle. Ratios of these peaks were used for plotting instead of loads and strains at any random instant of time. For obtaining the best fit sine curve, the strain variation for each cycle was assumed as follows:

$$Y = A + \lambda \sin(\omega t + \phi) = A + B\sin(\omega t) + C\cos(\omega t) \quad (1)$$

where A is mean strain, λ is strain amplitude, ω is the frequency of strain data acquired and ϕ is phase angle. Linearization of the equation with respect to A, B and C as shown gives B = λcos(ϕ) and C = λsin(ϕ). The values of A, B and C can be obtained from linear fit using least square method for different ω. Value of ω could be obtained by minimizing the error using these fitted parameters for different chosen values of ω.
The variation of ratio of maximum local transverse strain to maximum applied longitudinal stress is as shown in Fig. 3c. It can be observed that the waviness has been eliminated by plotting the maximum local transverse strain variation with cycles. The change of slope in strain variation is indicated as different stages in the plot. These stages may correspond to different damage modes/mechanisms in the composites during fatigue. Further, the cycle at which the visible delamination, as observed from the images, occurs was found to correlate with the onset of scatter in the plot. It can be concluded that the variation of local maximum transverse strain in the specimen during fatigue cycling clearly indicates the loss of stiffness even before the visible delamination occurs. The method of elimination of scatter in the strain plot after the initiation of visible delamination has been explained in the result section.

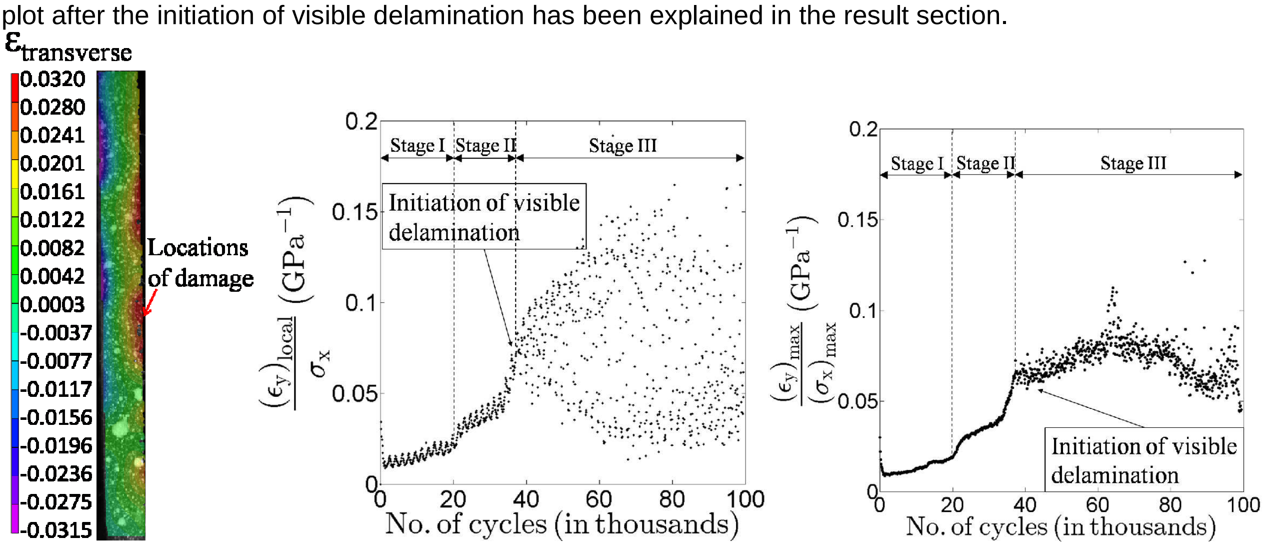

Fig. 3 (a) Transverse strain contours of the specimen at 37000 cycles; Variation of (b) $(\epsilon_y)_{local}/\sigma_x$; (c) $(\epsilon_y)_{max}/(\sigma_x)_{max}$ with number of cycles for the fatigue test with R = 0.5, σ_{max} = 600 MPa and f = 1 Hz with undeformed state as reference image

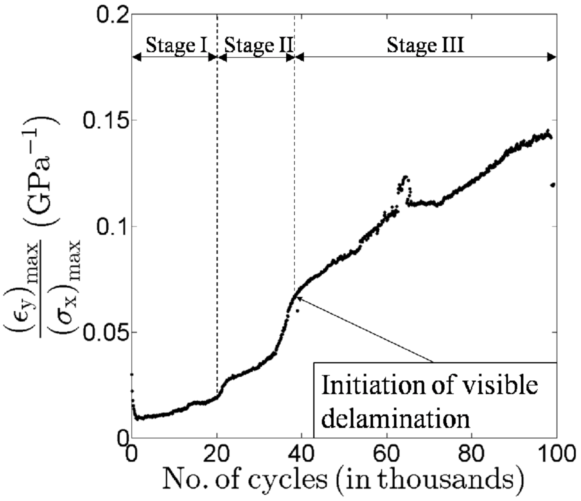

Fig. 4 Variation $(\epsilon_y)_{max}/(\sigma_x)_{max}$ with number of cycles for the fatigue test with R = 0.5, σ_{max} = 600 MPa and f = 1 Hz

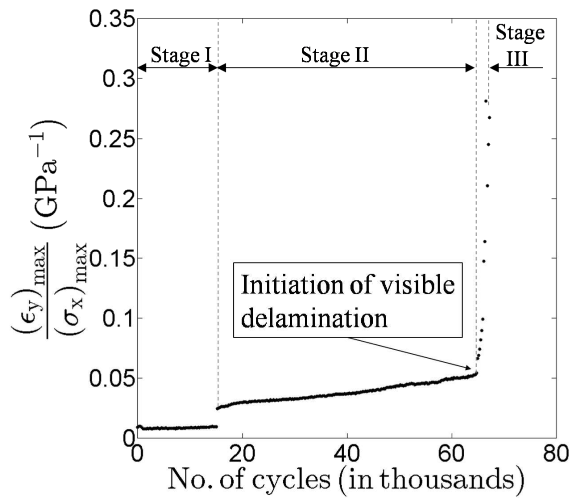

Fig. 5 Variation $(\epsilon_y)_{max}/(\sigma_x)_{max}$ with number of cycles for the fatigue test with R = 2, σ_{max} = 424 MPa and f = 5 Hz

4 EXPERIMENTAL RESULTS AND DISCUSSION

To confirm the method of monitoring the damage by measuring the local maximum transverse strain, further fatigue tests have been conducted with other R-ratios (R = 2 for compression-compression and R = -1 for tension-compression fatigue tests). Results of all these fatigue tests are discussed below.

4.1 Tension-tension fatigue test

Though the waviness has been eliminated in the plot, still there is scatter beyond 40,000 cycles. This could be due to large relative displacement between the speckle patterns in the underformed configuration and the deformed configuration. To remove the scatter in the plot, the images have been correlated again using DIC software with different reference images to obtain the relative strains. In this analysis, three stages have been considered. Image of the undeformed specimen was used as reference image for stage I (0 to 20,000 cycles). For other two stages (20,000 to 37,000 cycles and 37,000 cycles to end of the experiment), last image of the previous stage was used as the reference image. The absolute strain values at each stage have been obtained by adding the relative strains of that stage to the absolute strain value of the reference image already obtained from the analysis of images in the previous stage. From these absolute strains, maximum transverse strains in each cycle have been obtained using sine curve fit. Fig. 4 shows the variation of ratio of maximum local transverse strain to maximum applied longitudinal stress with cycles. It can be observed that this strain plot has smooth variation and the scatter is eliminated as well.

4.2 Compression- compression fatigue test

The variation of ratio of maximum transverse strain to maximum applied longitudinal stress versus the number of cycles for the fatigue test at R = 2 and σ_{max} = 424 MPa and f = 5 Hz is shown in Fig. 5. The initiation of visible delamination and catastrophic failure of the specimen occurs at about 67,000 cycles. From these experiments, it was also observed that there is no significant difference between the cycles corresponding to initiation of visible delamination and final failure of the material unlike the tension-tension fatigue experiments, where the specimen was capable of carrying the load for very high number of cycles even after the initiation of visible delamination. This may be mainly due to the fact that the composites are fiber controlled and hence have low load carrying capability in compression mode after the initiation of visible delamination.

4.3 Tension- compression fatigue test

Fig. 6 shows the variation of ratio of maximum transverse strain to maximum applied longitudinal stress versus the number of cycles for the fatigue test conducted at R = -1 and σ_{max} = 285 MPa and f = 5 Hz. The specimen failed after 9000 cycles of loading. It was observed that the variation of these parameters clearly indicates the three stages of damage evolution during fatigue cycling.

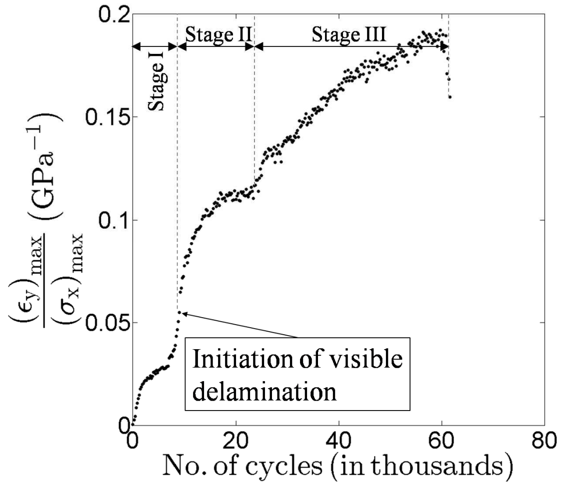

Fig. 6 Variation $(\epsilon_y)_{max}/(\sigma_x)_{max}$ with number of cycles for the fatigue test with R = -1, σ_{max} = 285 MPa and f = 5 Hz

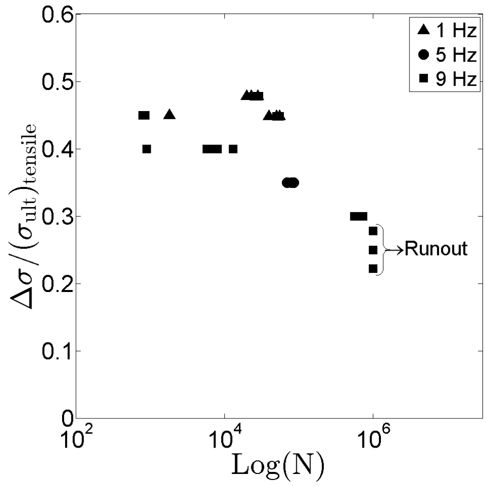

Fig. 7 Fatigue life curve at R = 0.5

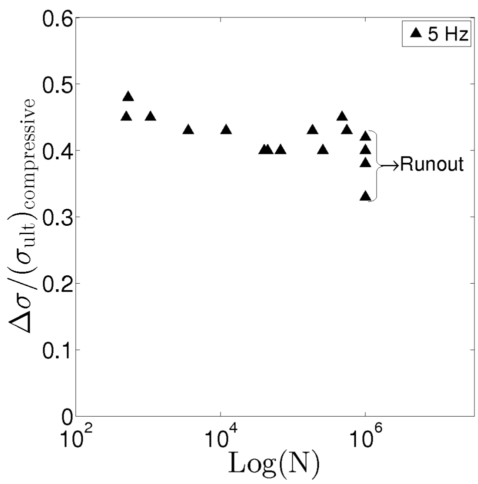

Fig. 8 Fatigue life curve at R = 2

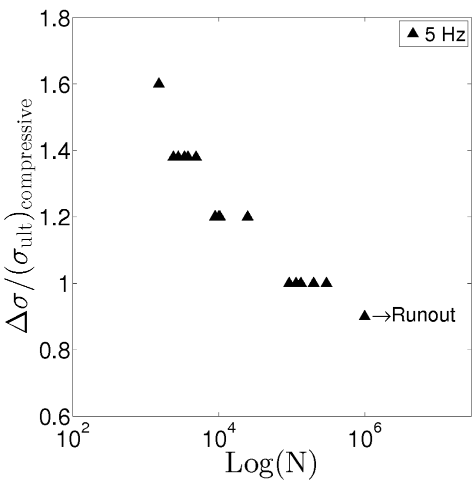

Fig. 9 Fatigue life curve at R = -1

4.4 Fatigue life curve

The fatigue life curves for the experiments with different R ratios are shown in Figs. 7 to 9. The ordinate in the fatigue life curve is the stress range normalized with the corresponding tensile/compressive strength of the specimen. Since the frequencies between 1 and 9 Hz has no effect on the fatigue life of the CFRP specimens [8], the tension-tension fatigue tests conducted at frequencies 1, 5 and 9 Hz were considered for plotting the fatigue life curve. For the tension-tension tests, the stress amplitude for run-out of the composite laminate is 125 MPa which corresponds to the σ_{max} = 500 MPa (55% of tensile strength). For compression-compression tests, the stress amplitude for run-out is 100 MPa which corresponds to the σ_{max} = 400 MPa (75% of compressive strength) and for tension-compression fatigue tests, the stress amplitude for run-out is 214 MPa (45% of compressive strength).

5 CONCLUSIONS

Damage evolution in CFRP materials subjected to fatigue loading has been studied using DIC. The variation of local transverse strain with number of cycles was found to be a better indicator of loss in stiffness in the CFRP material due to delamination and related damage mechanisms. The waviness and scatter in the plot of ratio of transverse strain to applied stress with number of cycles were avoided using sine curve fit to obtain maximum transverse strain in a cycle and different reference images for DIC respectively. Variation of the local transverse stiffness with number of fatigue cycles indicates that the damage evolution occurs over 2-3 stages. The run-out for the CFRP material was found to be at σ_{max} = 500 MPa (55% of tensile strength), 400 MPa (75% of compressive strength) and 214 MPa (45% of compressive strength) for tension-tension (R = 0.5), compression-compression (R = 2) and tension-compression (R = -1) fatigue loading respectively.

6 NOMENCLATURE

ϵ_y	Transverse strain	
σ_x	Longitudinal stress	MPa
σ_{max}	Maximum stress	MPa
$\Delta\sigma$	Longitudinal stress range	MPa

7 ACKNOWLEDGEMENTS

Authors would like to thank Dr. Sankara Subramanian for introducing us to the digital image correlation technique.

8 REFERENCES

[1] M.R. Bhat, C.R.L. Murthy, Fatigue damage stages in unidirectional glass-fibre-epoxy composites: identification through acoustic emission technique. International Journal of Fatigue, (5), 401–405, 1993.

[2] P. A. Smith, J. R. Wood, Poisson’s ratio as a damage parameter in the static tensile loading of simple crossply laminates. Composites Science and Technology, (38), 85–93, 1990.

[3] M. Surgeon, E. Vanswijgenhoven, M.Wevers, O. Van Der Biest, Transverse cracking and Poisson’s ratio reduction in cross-ply carbon fibre-reinforced polymers. Journal of Materials Science, (34), 5513–5517, 1999.

[4] W. Van Paepegem, I. De Baere, E. Lamkanfi, J. Degrieck, Poisson’s ratio as a sensitive indicator of (fatigue) damage in fibre-reinforced plastic. Fatigue & Fracture of Engineering Materials & Structures, (30), 269–276, 2007.

[5] M. Bourchak, I.R. Farrow, I.P. Bond, C.W. Rowland, F. Menan, Acoustic emission energy as a fatigue damage parameter for CFRP composites. International Journal of Fatigue, (29), 457–470, 2007.

[6] W. W. Stinchcomb, Nondestructive evaluation of damage accumulation processes in composite laminates. Composites Science and Technology, (25), 103–118, 1986.

[7] M. A. Sutton, J.-J. Orteu, H. W. Schreier, Image correlation for shape, motion and deformation measurements. Springer, New York, 2009.

[8] S.M. Khaja Mohiddin, S.J. Subramanian, H. Murthy, Study of damage evolution during fatigue of composites using DIC, Proc SEM XII International Congress & Exposition on Experimental & Applied Mechanics Conference,Costa Mesa, USA, CD-ROM, 2012.

International Journal of Fracture Fatigue and Wear, Volume 3
Proceedings of the 4th International Conference On
Fracture Fatigue and Wear, pp. 128-134, 2015

THE EFFECT OF FRETTING ON THE ROLLING CONTACT FATIGUE PERFORMANCE OF TAPERED ROLLER BEARINGS

G.Carvajal, J. Kowal, T. Nixon and P.J. Bouchard

The Open University - Materials Engineering Group - UK

Abstract: The progress achieved in manufacturing rolling bearing steel has led to an ever increasing level of steel cleanliness which has consequently resulted in an improvement of the classic subsurface rolling contact fatigue life of rolling element bearings. This in turn emphasizes the role that other modes of failure, such as surface initiated rolling contact fatigue, may play in limiting the life of clean steel rolling bearings. In this paper the effect of fretting as a precursor of surface initiated rolling contact fatigue is studied and for this, pre-damaged tapered roller bearings, made of through hardened SAE 52100 steel, are tested in a purpose built rig at an accelerated but realistic configuration characterized by a contact pressure of 2.2 GPa, a speed of 3000 rpm and a temperature of 80°C. Different levels of fretting are studied as obtained by varying the pre-load used during the fretting experiment and, for each case, the material response to both the fretting process and the subsequent rolling contact fatigue is evaluated and presented in details.

Keywords: Rolling contact fatigue, fretting, tapered roller bearing, wear, false brinelling

1 INTRODUCTION

The present study is part of a larger endeavor that seeks to find out the root cause of a phenomenon leading to the unexpected premature failure of a well-defined type of tapered roller bearing (illustrated in Fig. **1**) when used in particular application within a drivetrain system. The forensic studies conducted in field-used and damaged bearings led to a partial conclusion that the damage, which resembles Rolling Contact Fatigue (RCF) induced damage, follows a characteristic pattern defined by sets of damaged areas uniformly distributed around the inner ring raceway. Furthermore, it was found that the regular angular spacing between these damaged areas matches, within a certain tolerance, the roller pitch associated with this particular tapered roller bearing.

Fretting in non-rotating bearings, also referred to as false brinelling or vibration corrosion, is known for inducing regularly spaced flutes in the raceways which after subsequent running of the rolling bearing may lead to surface initiated RCF [1, 2]. This phenomenon has been proven and studied mainly for cylindrical roller bearings and ball bearings where fretting is said to be more likely to occur, but it has been less explored for tapered roller bearings for which the presence of the always necessary pre-load is thought to be the main contributor in reducing the effects of fretting.

The mechanics of fretting is in essence simple, as it is a small amplitude oscillatory movement between two contacting surfaces. But from the wear point of view, fretting is a complex phenomenon. It involves corrosion, adhesion and abrasion as main wear mechanisms in proportions and combinations that are highly influenced by the fretting conditions: oscillation amplitude, normal load and lubrication among others [3–5].

In the present study, the effect of fretting in a tapered roller bearing made of through-hardened 52100 type steel is evaluated not only in terms of the damage it induces onto the raceways but also the impact this damage has on the RCF performance of the bearing.

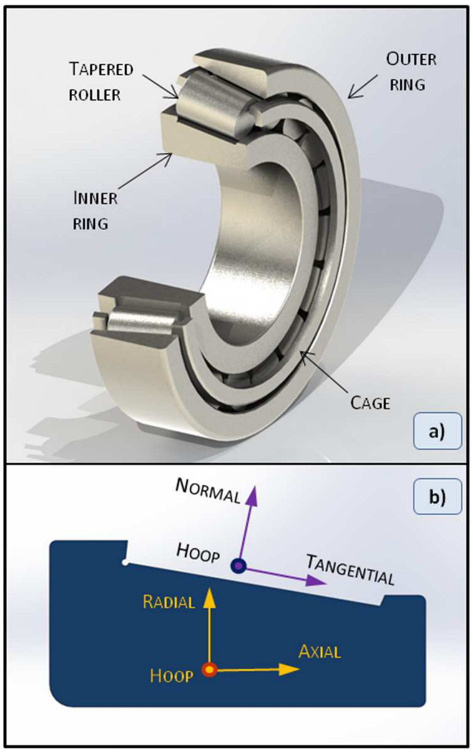

Fig. 1 a) 3D model of a 30206 type tapered roller bearing indicating its main components. b) 2D representation of an inner ring cross section defining the two sets of orthogonal axes used throughout the present study

2 TEST METHOD/OVERVIEW

As far as the relative motion between contacting surfaces is concerned, at least four different modes of fretting are defined: tangential (also known as classic), radial, torsional and rotational [5]. For the case of tapered roller bearings, due to the fact that the rollers are distributed in a conic arrangement between the rings, fretting will tend to occur as a combination of two or more of these fretting modes.

For the purpose of this study, tapered roller bearings were fretted in combined tangential and radial modes which are associated with displacements in the tangential and normal direction respectively according to the definition of axes presented in Fig. **1**b. In order to generate such a fretting condition, test bearings were mounted in a housing (as shown in Fig. 2a) and by means of a servo hydraulic cylinder, a high frequency and low amplitude axial displacement was introduced between the outer and inner rings.

A general view of the set up used for the fretting experiments is presented in Fig. 2b while a summary of the test parameters is given in Table 1.

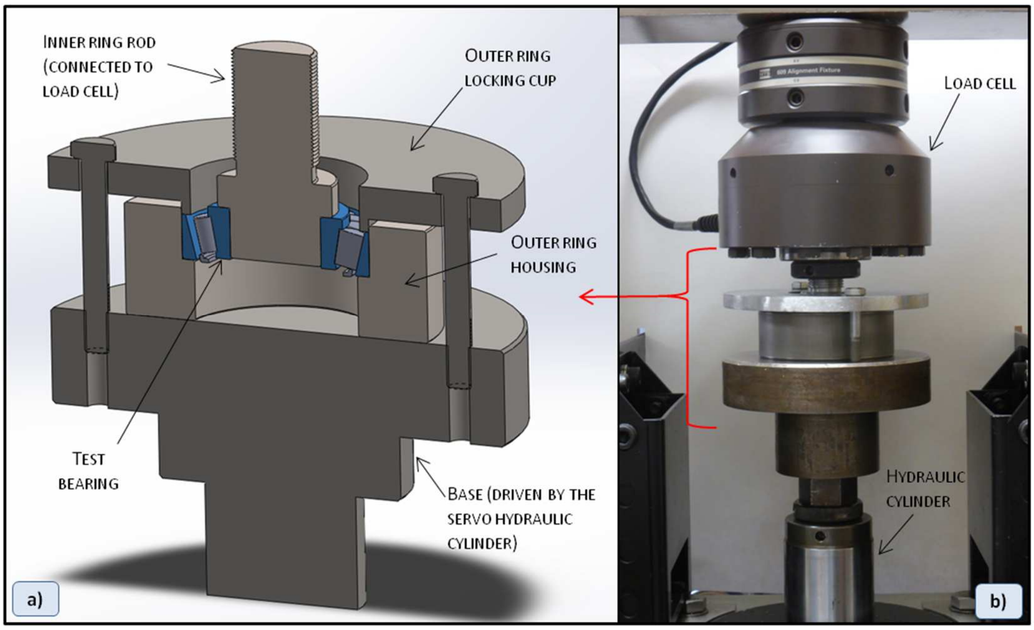

Fig. 2 a) Cut section of a 3D model of the fretting rig indicating its main components. b) Picture of the set-up used for the fretting experiments

By adjusting the compressive axial pre-load used during the fretting experiments, three different kinds of fretted samples were generated as follows:

- A1: bearings having a pre-load equal to the nominal in-service pre-load (i.e. -5 kN) were fretted by applying an axial sinusoidal displacement such that the maximum axial load gets as close to zero as possible but remains in the compressive zone.
- B1: using the same oscillation parameters as for A1 but having a pre-load of -7.2 kN, which corresponds to the maximum compressive pre-load that is acceptable in in-service bearings.
- C1: the test would start in the condition described for A1 and the pre-load would be gradually reduced (in absolute values), aiming for a state characterised by a total air gap of the order of 10µm between the rings and rollers when the hydraulic cylinder is at its lowest position. In order to achieve and maintain this configuration, it was necessary to instrument a real time monitoring system for the load and displacement that would allow for small corrections in the pre-load in order to maintain the air gap as constant as possible throughout the test.

All the fretting experiments were conducted at a frequency of 50 Hz and for a total of $1x10^5$ cycles in commercially available bearings. Prior to testing, the bearings were ultrasonically cleaned in isopropanol followed by acetone.

Table 1 Summary of the basic fretting testing parameters

Parameter	Value or range
Oscillation amplitude	10-40 µm
Compressive axial load	0 - (-14.5) kN
Roller inner ring contact pressure	0-2.3 GPa
Frequency	50 Hz
Lubricant	none
Cycles	$1x10^5$
Control system	Displacement controlled
Ambient temperature	22 ±1.5°C
Relative humidity	75 ±5 %

To assess the damage introduced during fretting, the raceways of inner rings from each of the fretting types mentioned above (i.e. A1, B1 and C1) were inspected using the following techniques:

- Optical microscopy: for morphological analysis and general observation.
- Confocal microscopy: for topographical analysis and roughness survey.
- Scanning electron microscopy (SEM): Crack survey and general microscopic examination.
- Energy dispersion spectroscopy (EDS): Chemical characterisation of the debris.

For the RCF study, fretted bearings were run in a purpose built rig, designed to test two bearings simultaneously, in a back to back configuration under accelerated conditions. To reduce the testing time, a pure axial load was chosen as the loading configuration leading to a calculated contact pressure of the order of 2.2 GPa between each roller and the inner ring. The basic testing parameters are summarised in Table 2.

Table 2 Summary of the basic RCF testing parameters

Parameter	Value or range
Contact pressure	2.2 GPa
Speed	3000 rpm
Temperature in the proximity of outer ring	80±2.5°C
Lubricant-(viscosity at 40°C and 100°C)	Transmission oil – (98 and 11.3 mm^2/s)
Lubrication regimen	Full elastohydrodynamic lubrication
Lubricant temperature	73±1.5°C
Loading condition	Axial only

3 RESULTS/DISCUSSION

For the fretting experiments conducted in the A1 and B1 fretting conditions, the time-dependent load readings showed a consistent smooth sinusoidal response as a result of the sinusoidal displacement wave used as input for the test control. This led to a quasi-elliptical load vs. displacement cycles in both cases (Fig. 3) which denotes that fretting took place in a so-called partial slip regime exhibiting an elasto-plastic deformation behavior of the contacting surfaces. This is typical for radial fretting [5, 6] where the total response is a combination of the macro elastic deformation of the contacting bodies and an elasto-plastic micro deformation occurring within the contacting area.

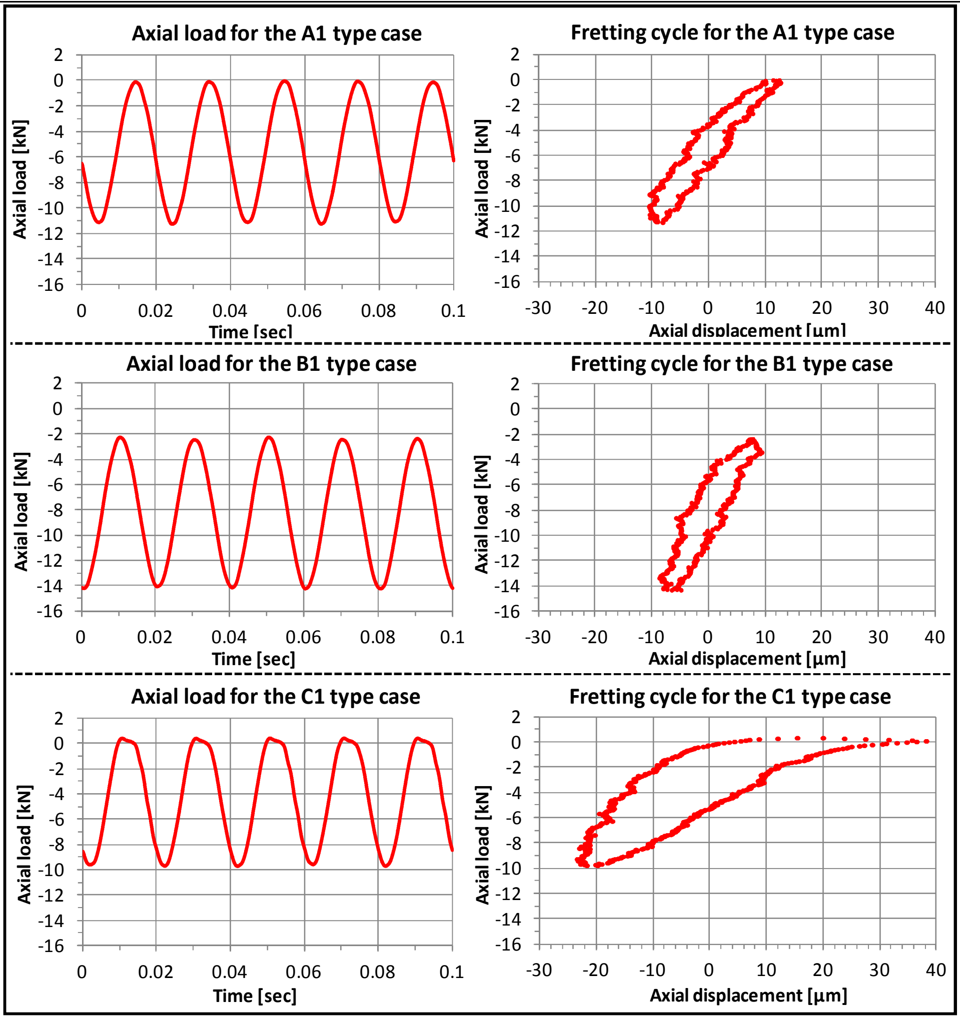

Fig. 3 Axial load vs. time and axial load vs. axial displacements as measured during testing under the A1, B1 and C1 fretting modes

In agreement with the partial slip regime proposed for the A1 and B1 fretting cases, the observation of the fretting scars by both SEM and optical microscopy (Fig. 4) reveals: a) the existence of a stick zone with marginal surface damage at the center of the contact and b) a rim surrounding the stick zone for which fretting corrosion seems to have been the main acting mechanism. The width of the stick zone, as measured in the center of the raceway in the hoop direction, is considerably larger for the B1 case (about 135µm) than for A1 (of the order of 39µm), which is consistent with the fact that the lowest compressive load (in absolute values) for B1 is several times larger than the corresponding load in the A1 case (of the order of 2.3kN and 0.05kN respectively). This in turn, leads to a larger minimum contact area for B1 than for A1. Indeed, the contact width, as calculated by the Hertzian theory for a line contact [7] results in 119µm and 23µm for the B1 and A1 cases, respectively.

On the other hand, the analysis of the roughness parameters Ra and Rq, as obtained from traces taken in the tangential direction for both within the stick zone and in undamaged areas of the raceways shows the presence of a smoothing effect taking place in the A1 and B1 cases. This is not a common feature of radial fretting [6] but is consistent with the fact that the fretting experiment studied here is a combination of radial and tangential fretting.

For the C1 case, the fretting experiment behaved differently when compared to the A1 and B1 tests. First, after a few initial cycles in the C1 testing condition, there was a tendency for the rollers to bond to the raceways. Consequently, an axial tension load between the rings was needed in order to achieve the required air gap between rollers and rings. This effect can be observed in the load vs. time curve shown in Fig. 3, where the tensile load increases up to a point (around 0.4 kN) after which, de-bonding manifests as a consequent drop in the tensile load. The bonding effect was physically verified in a test that was interrupted after 1,000 cycles.

The energy per cycle reported for C1 is almost 3 and 3.4 times larger, as compared to the B1 and A1 tests respectively (54.3 mJ, 60.3 mJ and 179.4 mJ for A1, B1 and C1 respectively), which is thought to be directly linked to the intensive wear process observed in the C1 test. A combination of fretting corrosion, abrasion and adhesion is believed to have worn the surface, causing:

1. Deeper and wider scars as compared to the A1 and B1 tests. In fact, the average fretting scar width for C1 is of the order of 3 to 4 times larger than the corresponding values for the A1 and B1 cases respectively (Fig. 4) while the mean depth is found to be about 6 times larger for C1 than for A1 (Fig. 5).
2. Significant liberation of fine ferritic oxide powder, some of which agglomerated to form a coating layer in the vicinity of the fretting scars (Fig. 4).
3. Marked increase of the roughness parameters Ra and Rq in the tangential direction.
4. Surface micro-cracking in the hoop direction.

Also, the analysis of the fretting scar profiles in the hoop direction (Fig. 5) shows a pile-up of material on either side of the fretting scar for the C1 fretting test. This effect could either be associated with plastic deformation, in which case the finding would be consistent with previous results from literature [2], or it could be related to the layer of oxide particles in the vicinity of the scars (Fig. 4). Further investigation by X-ray diffraction is being carried out to evaluate the extent of plastic deformation (if any).

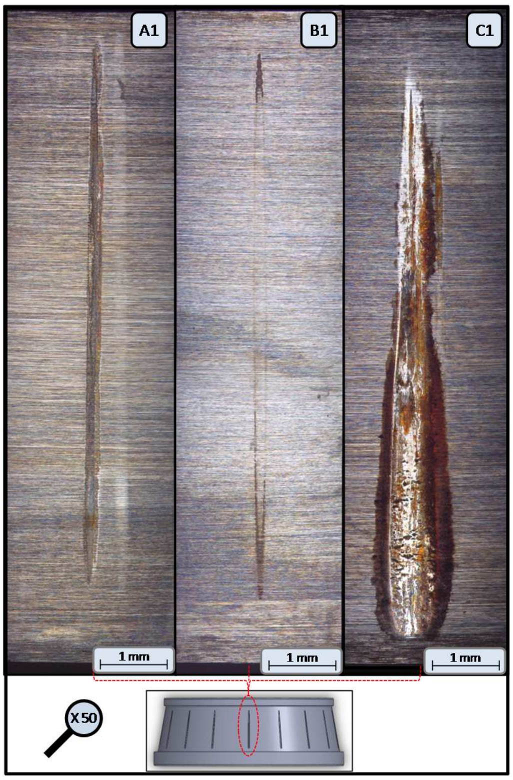

Fig. 4 Low magnification images of the scars left in the inner ring raceways of tapered roller bearings after been fretting tested under the A1, B1 and C1 fretting modes. At the bottom of the figure, an after fretting inner ring representation shows the distribution and orientation of such scars

For the RCF assessment, samples generated for each fretting mode have been run, in a two-at-a-time scheme under the testing conditions summarised in Table 2. Although the number of tested bearings does not allow for a quantitative assessment of the RCF life, valuable qualitative information can be withdrawn from the analysis of the tested units, as follows:

- The test conducted for the A1 and B1 cases showed similar characteristics in terms of:
  - The initial vibration level (see Table 3).
  - RCF-like damage distributed in an irregular pattern in the inner ring raceway.
  - In the raceways there are visible traces associated to the fretting conducted prior to RCF testing.
  - There is no direct link between the fretting scars and the RCF damaged areas.
- The test conducted in samples corresponding to the C1 fretting case also developed RCF-like damage but in this case it was distributed in a regular pattern where the RCF damage is located immediately after the fretting scar.

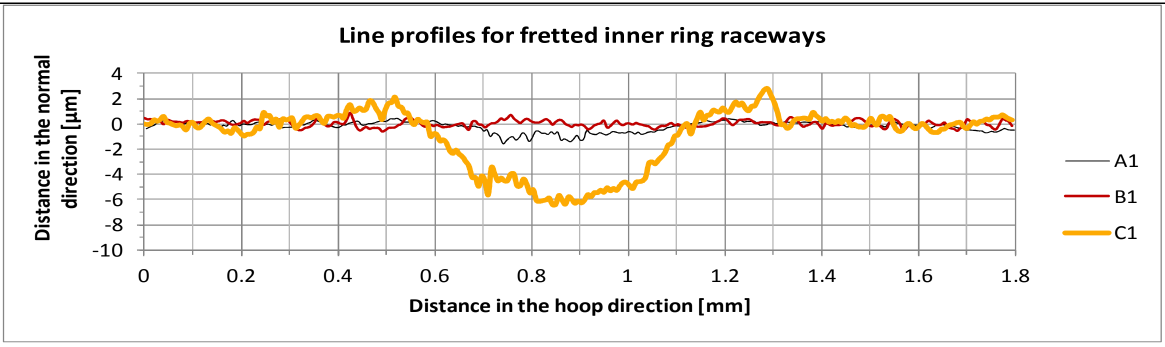

Fig. 5 Inner ring raceway profiles for the A1, B1 and C1 fretting cases as taken in the middle of the raceways in the hoop direction

Table 3 Basic information from the RCF tests conducted in fretting pre-damaged bearings

Fretting case	Number of test conducted	Total number of samples tested	Vibration level at the beginning [mg]	Testing time [h:mm]
A1	2	4	9 ; 17	64:32 ; 113:46
B1	1	2	8	128:53
C1	1	2	686	41:09

4 CONCLUSIONS

A fretting test rig and methodology was successfully designed and implemented in order to generate different levels of fretting damage in tapered roller bearings based on the pre-load adopted for testing.

Three different levels of fretting damage have been qualitatively and quantitatively analysed leading to the conclusion that: when the axial pre-load is large enough to guarantee a full compressive contact between rollers and rings, the fretting-induced surface damage is low (marginal in some cases) and thought to be driven by fretting corrosion as wear mechanism. On the other hand, if the axial pre-load is not able to secure a full compressive contact between rollers and ring and consequently an air gap is present between these elements, then significant fretting-induced surface damage is found in the rings raceways. The latter is believed to be driven by fretting corrosion, abrasion and adhesion as main wear mechanisms and is characterised by a significant loss of material, corrosion and surface micro-cracking.

The RCF performance of tapered roller bearings, having different levels of fretting damage, was qualitatively evaluated by means of a bespoke rig, allowing the following conclusion to be drawn: fretting-induced damage has been found to be a precursor of surface-initiated RCF only when the surface damage introduced by the fretting process is severe, such as when there has been a significant loss of material, accompanied by corrosion and surface micro-cracking.

5 ACKNOWLEDGEMENTS

The author is sincerely thankful to his PhD supervision team for their guidance and support; to the technical staff at the material engineering group of The Open University for all the help in commissioning the testing equipments and to the whole material engineering group at The Open University for creating this fruitful and enjoyable working environment.

6 REFERENCES

[1] ISO-15243:2004, “Rolling bearings - Damage and failures - Terms , characteristics and causes,” vol. 3, 2004.

[2] H. Pittroff, “Fretting Corrosion Caused by Vibration With Rolling Bearings Stationary,” *J. Fluids Eng.*, vol. 87, no. 3, pp. 713–723, Sep. 1965.

[3] N. Ohmae and T. Tsukizoe, “The effect of slip amplitude on fretting,” *Wear*, vol. 27, no. 3, pp. 281–294, 1974.

[4] A. Warhadpande, B. Leonard, and F. Sadeghi, “Effects of fretting wear on rolling contact fatigue life of M50 bearing steel,” *Proc. Inst. Mech. Eng. Part J J. Eng. Tribol.*, vol. 222, no. 2, pp. 69–80, 2008.
[5] M. H. Zhu and Z. R. Zhou, “On the mechanisms of various fretting wear modes,” in *Tribology International*, 2011.
[6] M. H. Zhu and Z. R. Zhou, “An experimental study on radial fretting behaviour,” *Tribol. Int.*, vol. 34, pp. 321–326, 2001.
[7] K. L. Johnson and K. L. Johnson, *Contact mechanics*. Cambridge university press, 1987.

International Journal of Fracture Fatigue and Wear, Volume 3
Proceedings of the 4th International Conference on
Fracture Fatigue and Wear, pp. 135-142, 2015

FINITE ELEMENT ANALYSIS OF FRETTING FATIGUE OF FRETTED WIRES

D.G. Wang [a, b, c e, *], M. Abdel Wahab[c], L.L Wang[d], X.W. Li[a], Z.C. Zhu[a], D.K. Zhang[a], X.B. Mao[e]

[a]School of Mechatronic Engineering, China University of Mining and Technology, Xuzhou 221116, China
[b]State Key Laboratory of Solid Lubrication, Lanzhou Institute of Chemical Physics, Chinese Academy of Sciences, Lanzhou 730000, China
[c]Faculty of Engineering and Architecture, Soete Laboratory, Ghent University, B-9052 Zwijnaarde, Belgium
[d]Low Carbon Energy Institute, China University of Mining and Technology, Xuzhou 221116, China
[e]State Key Laboratory of Geomechanics & Deep Underground Engineering, China University of Mining and Technology, Xuzhou 221116, China

Abstract: Finite element analysis of fretting fatigue of fretted wires is presented in thist study. Effects of fretting wear depth and contact load on stress distributions and crack initiation characteristics on fretting conact surfaces of fretted wires are analyzed using the finite element method, which was validated by fretting fatigue tests. The results show that increasing wear depth and contact load induces distinct stress distributions and accelerates crack initiation on fretting surfaces.

Keywords: Finite element analysis; fretting fatigue; fretted wires

1 INTRODUCTION

In mine hoisting systems, hoisting ropes connecting the mine hoist and the conveyance have played a vital role because their endurance strength and fatigue life have great effect on the mine production and the safety of miners [1-3]. During mine production, the hoisting rope winding around the friction wheel lifts and releases the hoisting container cyclically, and is always subject to axial tensile load and bending load. Those loads lead to microscopic motion of individual wires relative to their neighbouring wires in the rope and tangential force (induced by contact load). The interaction between contact load, relative displacement and cyclic load causes fretting fatigue of steel wires, which accelerates the rope failure [4-7]. During the fretting fatigue process, contacting wires present different wear depths of wear sars at distinct fatigue cycles. Therefore, it is significant to explore the fretting fatigue failure of wires during bending fatigue of the rope and fretting fatigue behaviors of fretted wires.

Over the last years, several advances have been made in the understanding of the fretting fatigue damage of steel wires. Hobbs and Raoof [8] explored different fretting fatigue mechanisms of steel wire ropes under different cyclic loading modes. Zhang et al. [9] investigated fatigue fracture behaviors of fretted wires. Dieng et al. [10] revealed the impact of lubrication and zinc coating on the fretting fatigue behavior of high strength steel wires. Périera et al. [11,12] studied the impact of water and sodium chloride on fretting fatigue behaviors of bridge cable wires and pointed out the lubrication effect of water and corrosive effect of sodium chloride in fretting fatigue. Wang et al. [13, 14] conducted fretting fatigue tests of steel wires in low cycle fatigue and explored crack initiation characteristics of steel wires in Hertz contact during the initial fretting-fatigue. From literature studies mentioned above, it is found that previous efforts have been focused on fretting fatigue behaviors under distinct fretting parameters and different environments, and crack initiations of wires in Hertz contact. Unlike previous studies, stress distributions and crack initiation properties of fretted wires during fretting fatigue employing finite element analyses are explored in this study.

The objective of the present study is to conduct finite element analyses of fretted wires under the action of fretting fatigue loading conditions. Section 2 presented the finite element model of fretting fatigue of fretted wires to explore the roles of fretting wear depth and contact load on stress distributions and crack initiation characteristics on fretting contact surfaces. In Section 3, in order to validate the finite element model, fretting fatigue tests of steel wires at different fatigue cycles (distinct fretting wear depths) to examine crack initiation characteristics on contacting surfaces of fretted wires are presented.

2 FINITE ELEMENT ANALYSIS OF FRETTING-FATIGUE OF FRETTED WIRES

2.1 Finite element model

Figure 1 shows that the wear scar takes place at the plane in the central section and arc-shaped transitional sections near both trailing edges. Therefore, fretting fatigue of fretted wires can be simplified as shown in Figure 2. During fretting fatigue of steel wires, assuming that the wear width of loading wire at a certain time is W and relative displacement between steel wires is RD, the length of wear scar of a fatigue wire is RD+W. An increase of fretting time induces increases in wear width of the loading wire and wear length of the fatigue wire, respectively. Assuming that wear depths of loading and fatigue wires are the same at the same time for simplicity, the finite element model of fretted wires is established to analyze stress distributions, and crack initiation and propagation characteristics in fretting contact zones during fretting-fatigue.

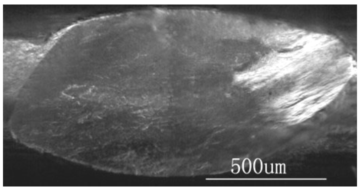

Fig. 1 Morphology of fretting wear scar of steel wire

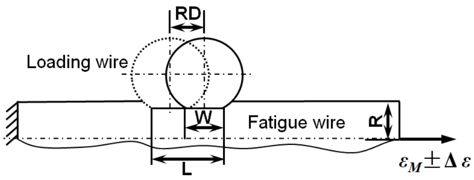

Fig. 2 Schematic of fretting-fatigue of fretted wires

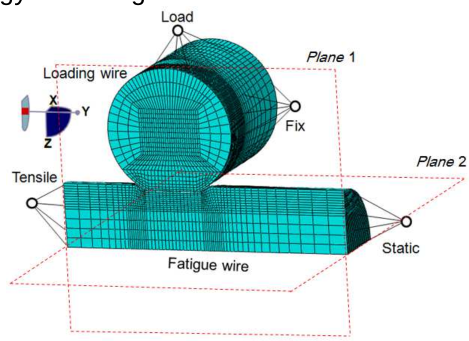

Fig. 3 Finite element model of fretted contacting wires

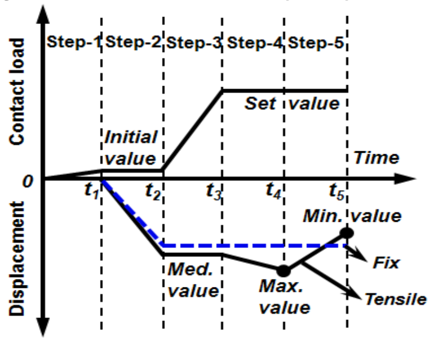

Fig. 4 Schematic of the loading process

Due to symmetry, only one quarter of the configuration is chosen to establish the finite element model of perpendicularly crossed fretted wires employing ABAQUS/CAE as shown in Figure 3. Both wires have a Young' s modulus of 203 GPa, a Poisson ratio of 0.3 and a diameter of 0.8 mm. The relationship of true stress versus plastic strain for wire material after yielding is shown in Table 1, which was obtained by a uniaxial tension test. Three-dimensional, eight nodes, solid linear brick elements with reduced integration (C3D8R) were used for the structural discretization. The master-slave contact algorithm on contact surfaces between wires was used to transfer loads. The penalty algorithm was employed to deal with local contacts between contact surfaces (penalty, friction of coefficient = 0.5 [9, 13, 14]). Reference points, *Load* and *Fix*, were established to couple the nodes on upper and side surfaces of the loading wire through the kinematic coupling constraint, respectively. The nodes on fixed and tensile end surfaces were coupled by reference points *Static* and *Tensile*, respectively, using distributing coupling constraint [15-17]. Symmetric boundary conditions, i.e. *XSYMM* ($U_X=UR_Y=UR_Z=0$) and *ZSYMM* ($U_Z=UR_X=UR_Y=0$), were applied to the planes of symmetry perpendicular to X and Z directions (Planes 1 and 2 in Figure 3), respectively. All degrees of freedom of *Fix* and *Tensil*e except U_Z, and all degrees of freedom of *Static* were constrained. A half of the total contact load was applied at *Load*, and cyclic displacement of fatigue wire was applied at *Tensile* along *Z* direction.

Table 2 shows fretting fatigue parameters used in the finite element analysis. The loading process consists of four steps: 1) applying the initial contact load at *Load* along the *Z* direction to ensure the contact between contacting surfaces; 2) with the constant initial contact load, applying the medium displacement at *Tensile* along the *Y* direction at first and then applying the displacement of central point of contact surface of stretched fatigue wire at *Fix*; 3) increasing the contact load at *Load* to the preset value with constant displacements of points, *Tensile* and *Fix* and 4) applying maximum and minimum displacements at *Tensile* with a constant contact load and displacement of point *Fix*. The loading diagram is shown in Figure 4.

Table 1 Data for wire material after yielding

True stress (MPa)	1450	1498.61	1570.51	1634.2	1657.56	1680.94	1690.94	1696.52
Plastic strain	0	0.000107	0.000739	0.00158	0.00228	0.00290	0.00359	0.00429

Table 2. Fretting fatigue parameters in finite element analysis

Wear depth (μm)	Contact load (N)	Fretting amplitude (μm)	Cyclic strain range ($\times 10^{-3}$)
20-60	10-40	60	4-5

2.2 Stress distributions of the wire contact zone under the typical condition

Figures 5 shows the stress distributions on the contact surface of fatigue wire with the wear depth of 40 μm for the fretting fatigue condition of contact load of 20 N at the relative displacement of 60 μm. It is clearly seen from Figure 5a that the contact pressure leads to a high stress distribution having a square ring-shaped on the fretting surface and the stress level increases with increasing distance to the center of contact. Figure 5b shows that the tensile stress leads to higher stress near the left trailing edge of fretting surface. Figure 5c shows the square ring-shaped high stress distribution of shear stress on the fretting surface..

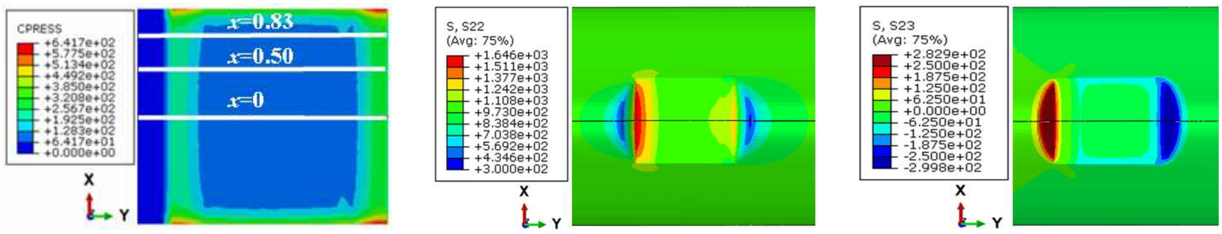

(a) Contact pressure (b) Tensile stress (c) Shear stress

Fig. 5 Stress distributions on the contact surface of fretted fatigue wire at t_4

2.3 Effect of fretting wear depth on stress distributions on the wire fretting surface

Figure 6a shows that the contact pressure presents the parabolic distribution along the path at every *x* location on the fretting surface (*x*=0, 0.5 and 0.83, Figure 5a) and abrupt changes of stress near trailing edges revealing severe stress concentration [14, 18, 19]. The contact pressure and abrupt change amplitude of stress present higher values near the leading edges at t_4 and t_5. An increase of fretting wear depth induces an overall decrease in contact pressure attributed to the constant contact load and increase in fretting contact area. The distance between the location of abrupt change and center of contact increases with increasing fretting wear depth, which indicates that stress concentration induced fatigue crack initiation location moves away from center of contact. The amplitude of abrupt change of contact pressure at the trailing edge decreases with increasing fretting wear depth as compared to the decrease at first and then an increase in the amplitude at the leading trailing edge as shown in Fig. 6a and b. Along the paths *x*=0, 0.5 and 0.8, an increase of fretting wear depth from 20 μm to 60 μm induces the ranges of contact pressure in the central contact region varying from 40.3-132.3 MPa to 60.9-213.2 MPa (Figure 6a) as compared to the ranges changing from 41-132.5 MPa to 65.1-214.9 MPa (Figure 6b).

Figure 6c-f shows that maximum values and abrupt changes of tensile and shear stresses are all located near trailing edges of the fretting surface, which reveals accelerated crack initiation and early crack propagation due to the cyclic plastic deformation and plastic cumulative damage on the fretting surface [14, 19]. An increase of fretting wear depth induces an overall increase in tensile stress and a decrease in shear stress along the path at every *x* location. Amplitudes of abrupt changes of stresses increase at trailing edges as shown in Figure 6c and e, and decrease at leading edges in Figure 6d and f, with increasing fretting wear depth, which reveals increased and reduced possibilty of the crack initiation. Along the paths *x*=0, 0.5 and

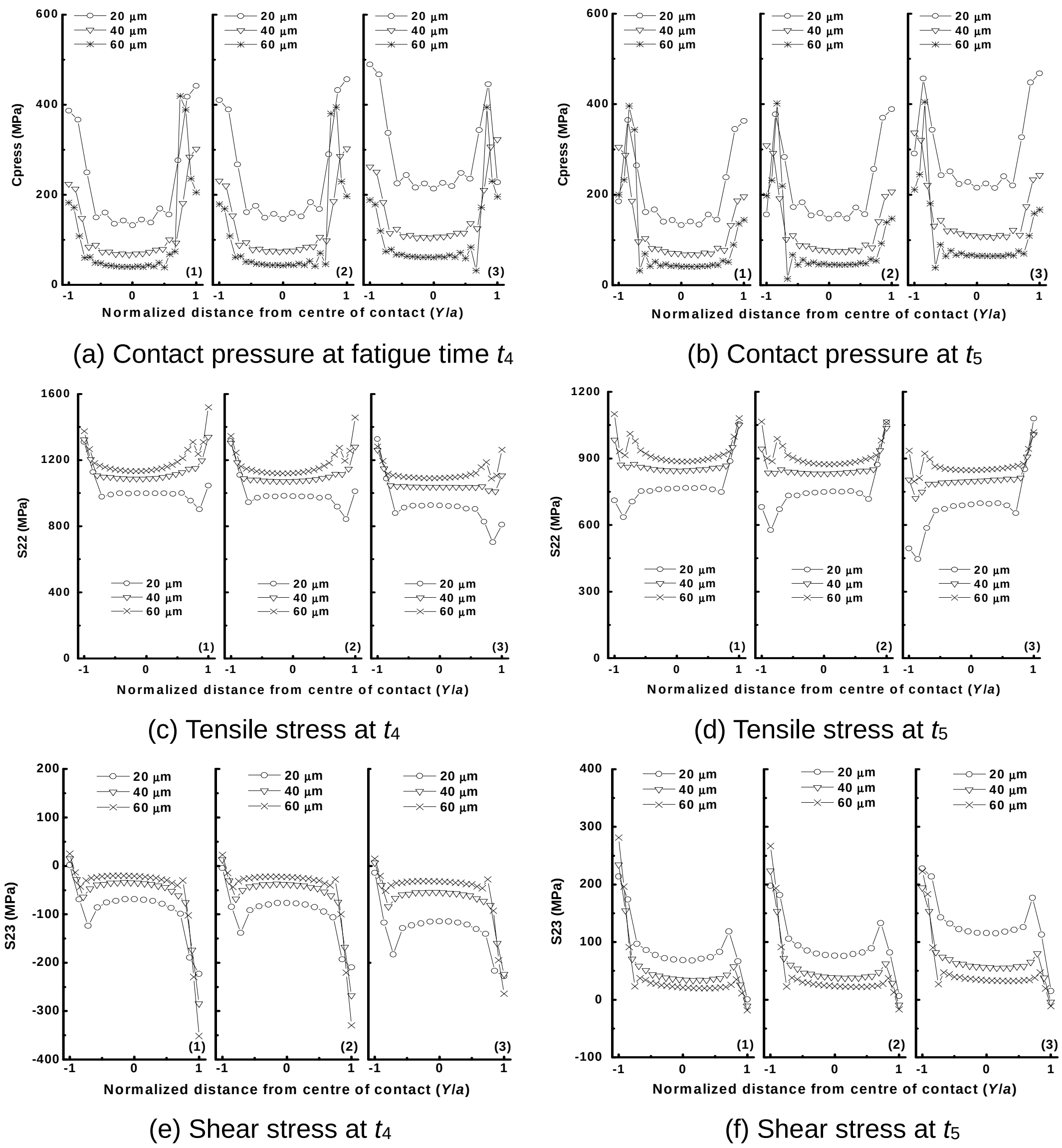

(a) Contact pressure at fatigue time t_4 (b) Contact pressure at t_5

(c) Tensile stress at t_4 (d) Tensile stress at t_5

(e) Shear stress at t_4 (f) Shear stress at t_5

Fig. 6 Stress distributions along paths at distinct *x* locations of fatigue wire surfaces at different fretting wear depths

0.8, an increase of fretting wear depth from 20 μm to 60 μm induces the range of tensile stress in the central contact region varying from 998.5-1135.9 MPa to 924.6-1091.3 MPa in Figure 6c as compared to the range changing from 764.7-886.6 MPa to 692.6-847.3 MPa in Figure 6d, as well as the range of shear stress varying from -69.1- -21 MPa to -114.9- -32.1 MPa in Figure 6e in comparision to the range changing from 68.5-21.2 MPa to 115.5-33.6 MPa in Figure 6f.

2.4 Effect of contact load on stress distributions on the wire fretting surface

Figure 7a and b shows that an increase of contact load induces overall increases in contact pressure and the amplitudes of abrupt changes near trailing edges, which accelerates the stress concentration and thereby faster crack initiation. An increase of contact load causes the decrease in the tensile stress along the path at every *x* location, and increases of shear stress and amplitudes of abrupt changes at both leading and trailing edges, which indicates more easier crack initiation [14, 16]. Along paths *x*=0, 0.5 and 0.8, an increase of contact load from 20 N to 80 N results in contact pressure in the central contact region ranging from 63.9-274.9 MPa to 99-437.4 MPa (Figure 7a) as compared to that varying from 67.5-286.4 MPa to 102.6-457 MPa (Figure 7b), and induces the tensile stress changing from -140.8- -33.9 MPa to -229.4- -52.5 MPa (Figure 7c) in comparision to that varying from 34.2-138.1 MPa to 53-226.3 MPa (Figure 7d).

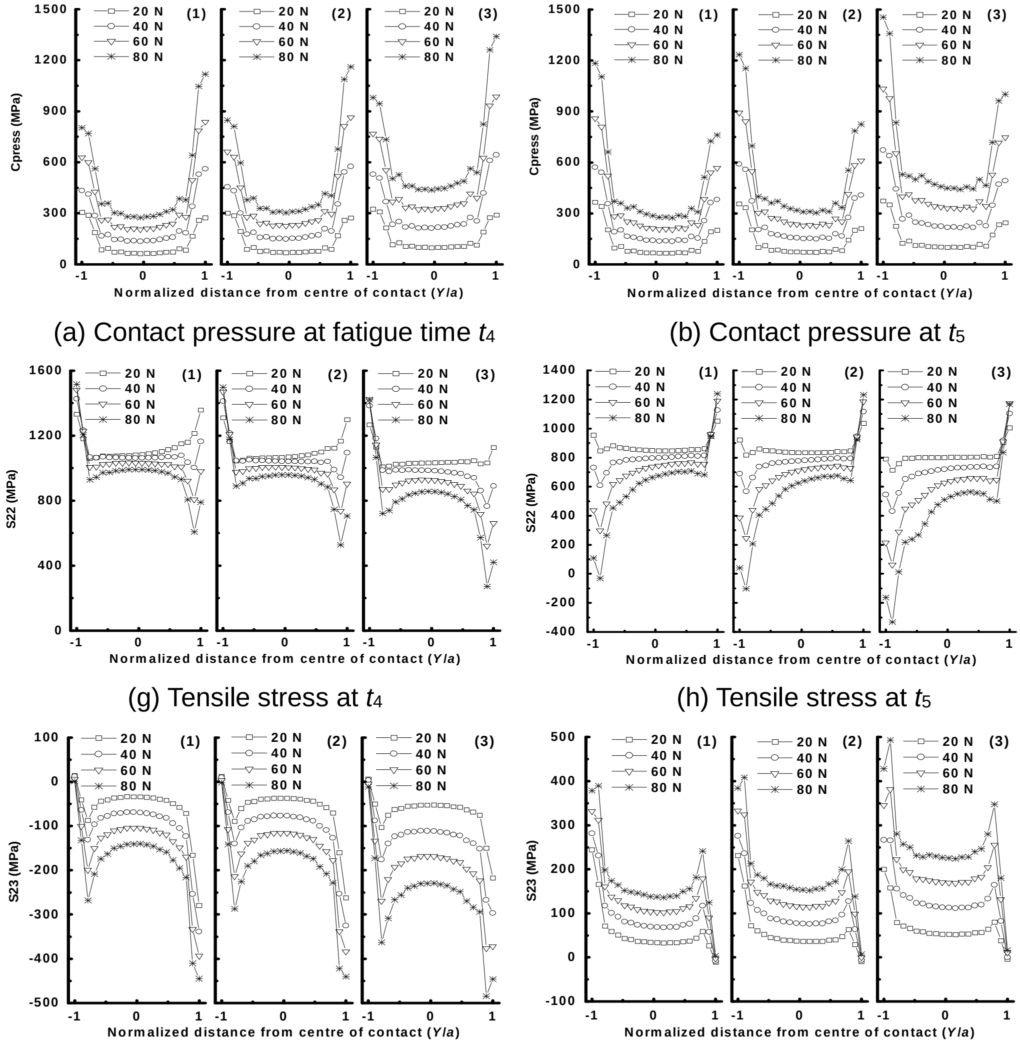

(a) Contact pressure at fatigue time t_4

(b) Contact pressure at t_5

(g) Tensile stress at t_4

(h) Tensile stress at t_5

(i) Shear stress at t_5

(j) Shear stress at t_4

Fig. 7 Stress distributions along paths at distinct *x* locations of fatigue wire surfaces at distinct loads

3 VALIDATION OF THE FINITE ELEMENT MODEL

In order to validate the finite element model, fretting fatigue tests of steel wires were carried out under the fretting fatigue condition of cyclic strain ranging from 4×10^{-3} to 5×10^{-3} and contact load of 20 N at the relative displacement of 60 μm employing the fretting fatigue test rig introduced in details in Ref. [20]. Morphologies of fretting contact scars of wire specimens at different fatigue cycles (corresponding to distinct wear depths) were observed by the scanning electron microscopy to examine wear mechanisms.

It is clearly seen from Figure 8 that loading and fatigue wires present circular and elliptical wear scars on contacting surfaces during fretting fatigue at different fatigue cycles. The wear scar exhibits two regions in all cases, i.e. the fretting plane and arc-shaped transition regions. Boundaries of two regions are not obvious in Figure 8a.1 and a.4 due to small fretting wear depth. As the fretting wear depth increases to 61.3 μm, obvious boundaries are observed as shown in Figures 8b.1 and b.4, i.e. A and A' representing the arc-shaped transition regions, and B and B' indicating the fretting planes. Slight fretting damages at the arc-shaped transition regions and severe damge on the fretting plane with adhesion near the center of contact of fretting plane (overlap region between contacting wires) are clearly seen, which validates the simplified finite element model of fretting-fatigue in Section 2.1.

It is obviously observed from Figure 8a that the fretting contact surface presents plastic deformation, material adhesion and pits, which indicates that the wear mechanism is adhesive wear. It is clearly seen from Figures 8a.2 and a.3 that the leading and trailing edges exhibit many micro fatigue cracks characterizing the fatigue wear. The ploughing as shown in Figure 8a.4 reveals the abrasive wear between contacting wires. Therefore, wear mechanisms are adhesive wear, abrasive wear and fatigue wear in the case of fretting wear depth of 20 μm. Figure 8b shows the material adhesion in the central region of wear scar of fatigue wire, obvious ploughing and delaminating in the wear scar of loading wire, and lots of micro cracks at trailing edges and in the central region of fatigue wire. These characteristic results indicate that wear mechanisms are adhesive wear, abrasive wear and fatigue wear.

Therefore, lots of micro cracks are present at trailing edges of the wear scars in fretting fatigue tests of steel wires at different fretting wear depths, which coincides with locations of crack initiation induced by abrupt changes of stresses in finite element analyses in Sections 2.2 and 2.3. An increase of fretting wear depth increases the number of micro cracks, which coincides with conclusions in Section 2.3, and indicates that tensile stress distribution mainly affects the crack initiation and propagation characteristics on the fretting contact surface of steel wire. Meanwhile, small fretting wear depth induces severe plastic deformation in the wear scar of steel wire; an increase of fretting wear depth induces the decrease in plastic deformation in the wear scar, which is attributed to larger contact pressure and shear stress between contacting wires at smaller fretting wear depth and the decreases in contact pressure and shear stress with increasing fretting wear depth. These results coincide with conclusions from finite element analyses in Section 2.3.

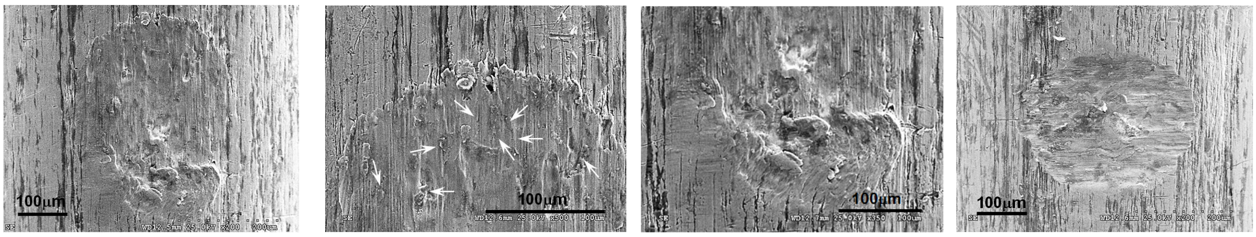

(1) (2) (3) (4)

(a) 9000 cycles (1)-(3) Fatigue wire surface and its partial views; (4) loading wire surface

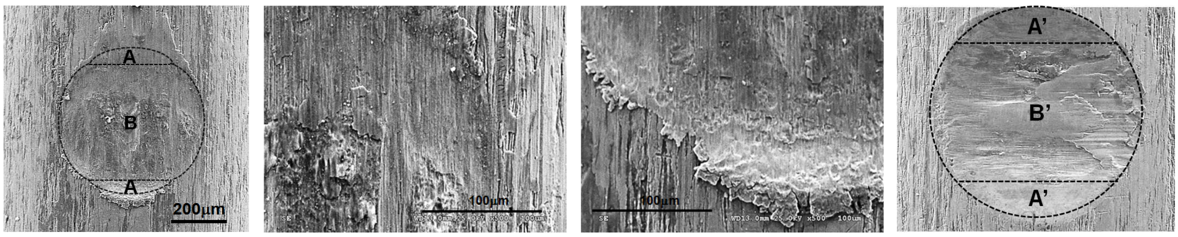

(1) (2) (3) (4)

(b) 90000 cycles (1)-(3) Fatigue wire surface and its partial views; (4) loading wire surface

Fig. 8 Wear morphologies of loading and fatigue wires after fretting fatigue tests conducted at different fatigue cycles (a and b corresponds to wear depths of 20 μm and 61.3 μm)

4 CONCLUSIONS

The finite element model of fretted wires under fretting fatigue loading condition was given to explore stress distributions and crack initiation characteristics on fretting contact surfaces. The contact pressure leads to square ring-shaped stress distributions on the fretting surface. Abrupt changes of stresses near both leading and trailing edges are clealy seen, which reveals faster crack initiation. An increase of fretting wear depth induces overall decreases in contact pressure and shear stress, and an overall increase in the tensile stress along the path at every x location. As the fretting wear depth increases, the fretting contact surface presents distinct abrupt changes of stress near trailing edges and increased possibility of crack initiations on fretting contact surfaces. An increase of contact load induces overall increases in the contact pressure and shear stress, but a decrease in the tensile stress. As the contact load increases, the amplitudes of abrupt changes of three stresses near both leading and trailing edges of fretting surfaces increase, which indicates faster crack initiation.

In order to validate the finite element model, fretting fatigue tests of steel wires at different fatigue cycles and different fretting wear depths are conducted. In those tests, lots of micro cracks are present at trailing edges of the wear scars. An increase of fretting wear depth increases the number of micro cracks, and decreases the plastic deformation in the wear scar. Those results agree with those obtained using finite element analysis.

5 ACKNOWLEDGEMENTS

The research was supported by National Nature Science Foundation of China (Grant No.51405489; Grant No. 51375479), Postdoctoral Science Foundation of China (2013M540474), Tribology Science Fund of State Key Laboratory of Solid Lubrication (LSL-1305), Fundamental Research Funds for the Central Universities (2014QNA42), and Priority Academic Program Development of Jiangsu Higher Education Institutions. The second author wishes to thank the Ghent University for the financial support received by the Special Funding, BOF (Bijzonder Onderzoeksfonds), in the framework of project (BOF 01N02410). The first author thanks CWO (Commissie Wetenschappelijk Onderzoek), Faculty of Engineering and Architecture, Ghent University for providing financial suypport for a research stay at Soete Laboratory.

6 REFERENCES

[1] Wang DG, Zhang DK, Zhang ZF, Ge SR. Effect of various kinematic parameters of mine hoist on fretting parameters of hoisting rope and a new fretting fatigue test apparatus of steel wires. Eng Fail Anal, 2012;22:92-112.

[2] Chaplin CR. Interactive fatigue in wire rope applications. In: Symposium on mechanics of slender structures (MoSS 2008), Keynote lecture, 2008 July 23-25, Baltimore, USA.

[3] Liu Y, Chen GD, Li JH, Xue YJ. Dynamics Simulation of the hoisting cable of single cable winding hoisting device. Mech Sci Technol Aerospace Eng 2009;28(9):1225-9.

[4] McColl IR, Waterhouse RB, Harris SJ. Lubricated fretting wear of a high-strength eutectoid steel rope wire. Wear 1995;185(1-2):203-12.

[5] Attia MH, Waterhouse RB. Standardization of fretting fatigue test methods and equipment, ASTM STP 1159. Philadelphia: ASTM; 1992.

[6] Araújo JA, Nowell D. Mixed high low fretting fatigue of Ti6Al4V: Tests and modeling. Tribol Int 2009;42:1276–85.

[7] Cai ZB, Zhu MH, Yu HY, Shen HM, Huang Q, Zhou ZR. Radial fretting damage behavior of human femur cortical bone and fem analysis. J Biotechnol 2008;136:S410.

[8] Hobbs RE, Raoof M. Mechanism of fretting fatigue in steel cables. Int J Fatigue 1994;16(4):273-80.

[9] Zhang DK, Ge SR, Qiang YH. Research on the fatigue and fracture behavior due to the fretting wear of steel wire in hoisting rope. Wear 2003;255(7-12):1233-7.

[10] Dieng L, Urvoy JR, Siegert D, Brevet P, Périer V, Tessier C. Assessment of lubrication and zinc coating on the high cycle fretting fatigue behavior of high strength steel wires. In: Ridge IML, editor. How to get the most out of your ropes: rope-machine interaction, rope maintenance and lubrication. OIPEEC conference 2007, 2007 September 12-14, Johannesburg, South Africa. Int J Rope Sci Technol; 2007. p. 85-97.

[11] Périera V, Dienga L, Gaillet L, Tessier C, Fouvry S. Fretting–fatigue behavior of bridge engineering cables in a solution of sodium chloride. Wear 2009;267(1-4):308-14.

[12] Périera V, Dienga L, Gaillet L, Fouvry S. Influence of an aqueous environment on the fretting behavior of steel wires used in civil engineering cables. Wear 2011;271(9-10):1585-93.

[13] Wang DG, Zhang DK, Ge SR. Fretting–fatigue behavior of steel wires in low cycle fatigue. Mater Des 2011;32:4896–993.

[14] Wang DG, Zhang DK, Ge SR. Finite element analysis of fretting fatigue behavior of steel wires and crack initiation characteristics. Eng Fail Anal 2013;28: 47–62.

[15] Erdonmez C, Imrak CE. A finite element model for independent wire rope core with double helical geometry subjected to axial loads. Sadhana 2011;36(6):995–1008.

[16] Shi YP, Zhou YR. Examples of ABAQUS finite element analysis. Beijing: Mechanical Industrial Press; 2006.

[17] Shibu G, Mohankumar KV, Devendiran S. Analysis of a three layered straight wire rope strand using finite element method. In: proceedings of the world congress on engineering (WCE 2011), 2011 July 6–8, London, UK.

[18] Xu YJ, Yuan H. Computational analysis and characterization of fretting stress fields. Comp Mater Sci 2009; 45:674-9.

[19] Talemi HR, Wahab AM, Baets DP. Numerical investigation into effect of contact geometry on fretting fatigue crack propagation lifetime. Tribol T 2012;55(3):365–75.

[20] Wang DG, Zhang DK, Wang SQ, Ge SR. Finite element analysis of hoisting rope and fretting wear evolution and fatigue life estimation of steel wires. Eng Fail Anal 2013;27:173–93.

Proceedings of the 4th International Conference on
Fracture Fatigue and Wear, pp. 143-147, 2015

EXPERIMENTAL ANALYSIS OF MODE I FATIGUE CRACK GROWTH IN LARGE SCALE YIELDING CONDITIONS

W. Zhang[1&2], S. Pommier[1], F. Curtit[2] and G. Léopold[2]

[1]LMT, ENS-Cachan, CNRS, Université Paris Saclay, France
[2] EDF R&D /MMC, France

Abstract: Mode I crack propagation under cyclic loading in large scale yielding conditions (LSY) is a phenomenon commonly encountered in certain industrial components. However it is rarely studied neither experimentally nor numerically. Moreover, the traditional methods in the prediction of fatigue crack growth which are based on linear fracture mechanics could no longer be available in this case. In this paper, an experimental set-up is built which allows the experimental studies of crack growth in LSY conditions for 316L stainless steel. Experimental results show that the mechanism of fatigue striation plays a significant role in crack propagation in LSY conditions as in small scale yielding conditions (SSY) except for the large striation spacing observed in LSY condition. A history effect in LSY condition is observed as well.

Keywords: Fatigue, Crack growth, Large Scale yielding

1 INTRODUCTION

Mode I fatigue crack growth in large scale yielding (LSY) conditions is encountered in certain industrial components subjected to cyclic thermal loadings as shown in the structure in Fig 1. Cold water at room temperature is injected periodically in the tunnel where hot water flows. As a consequence, stress is introduced resulting from different thermal expansion caused by temperature variations, moreover the stress is so important that a large part of the structure could not remain in its elastic domain. So if there was a hypothetical defect in the plasticized part, it could probably propagate with great speed due to the high cyclic loading and cause important loss. Therefore, it is of importance and necessity to be capable of predicting fatigue crack growth in this case namely in large scale yielding conditions. However, little study has been conducted neither experimentally nor numerically. The existing methods based on linear elastic fracture mechanics cannot be used to predict fatigue crack growth in LSY conditions [1]. There is a lack of fatigue crack growth data in LSY conditions and the mechanisms of fatigue crack growth in 316L are not well documented in LSY conditions.

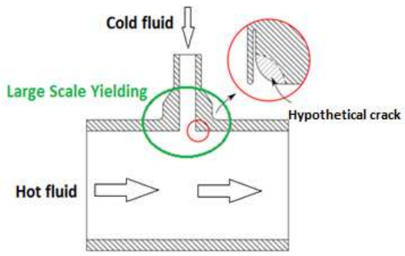

Fig. 1 Industrial structure under high cyclic thermo-mechanical loading

It is in this background that EDF has developed an experimental set-up named PACIFIC which allows performing fatigue crack propagation tests in LSY conditions under thermo-mechanical loading [2]. Its working principles are illustrated in Fig 2. The specimen is composed of a central part made of the studied material and an external part. Once the specimen is placed in the set-up, the four independent circuits allow applying different temperatures to the upper and lower surfaces of the central and external parts of the specimen and as a result, thermal gradients could be obtained along radial direction or/and thickness direction. In this way, the phenomenon observed in the industrial component is well simulated and reproduced by the PACIFIC set-up in laboratory.

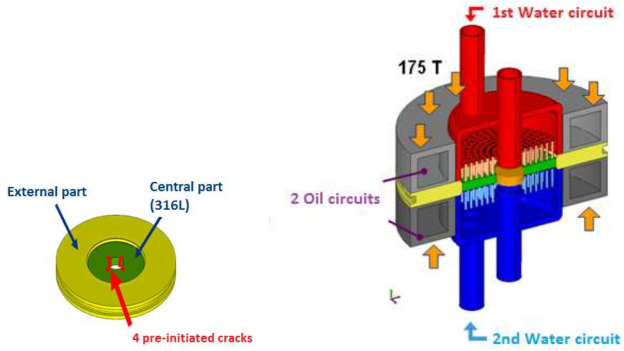

Fig. 2 Illustration of PAFICIF set-up

A finite element simulation of PACIFIC test under isothermal condition is realised. The isothermal condition is obtained by keeping the temperature of central part of specimen constant at 50°C while the external part of specimen experiencing a cyclic temperature varied from 50°C to 220°C. The plastic strain in angular direction in a zone of 20 mm's radius from the central part is plotted in Fig 3: the red line represents the angular evolution of plastic strain at mid-thickness of the central part when the external part of the specimen is at 220°C while the blue line is for the temperature of external part at 50°C. A few conclusions could be drawn: firstly the central part of the specimen is largely plasticized under the load condition. Secondly, the plastic strain decreases along the radial direction which results in stable crack propagation. And most importantly, a cyclic plastic strain is obtained in a region of about 10 mm, which shows the existence of cyclic large scale yielding in PACIFIC specimen. In other words, the plasticity which causes crack growth is not confined in a small-size zone around the crack tip but in a relatively very important region compared to the structural size.

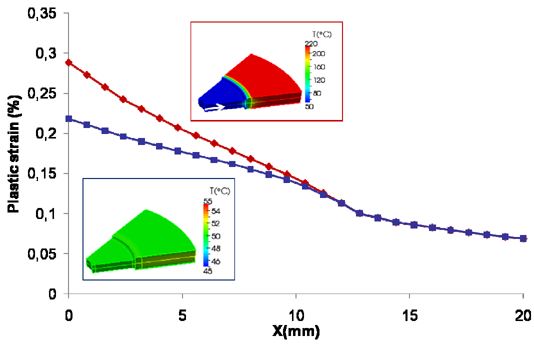

Fig. 3 Illustration of cyclic LSY conditions

2 DEFINITION OF MECHANICAL SPECIMEN

Lack of knowledge of fatigue crack growth in LSY conditions requires experimental studies. Unfortunately the existing specimens are designed for the study of fatigue crack growth in SSY conditions and the overload of LSY conditions on these specimens may cause instable crack propagation. So in order to perform mechanical fatigue crack growth test in LSY conditions, such geometry of a specimen derived from the SENT specimen is proposed with the central part as the useful part (Fig 4). Thickness modification between head and central part of the specimen ensures cyclic plasticity in the central part under cyclic loading. The misalignment of the vertical axis of the central part allows imposing a decreasing stress, strain and plastic strain gradient along the crack propagation plane as observed in the specimen of PACIFIC.

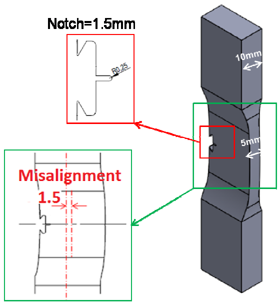

Fig. 4 Geometry of the specimen designed for fatigue crack growth in LSY conditions test

Strain field in central part of specimen is recorded during test under cyclic loading with the help of digital image correlation technique. As shown in Fig 5 on the left the strain field at maximum loading, more than 2/3 of the specimen experiencing plasticity given that 316L begins to plasticize with deformation of 0.1%. In addition, global cyclic plasticity is observed by the force—strain behavior of two points located far from crack tip (indicated by triangles in Fig 5 on the left) in Fig 5 on the right. These observations show that this geometry definitely meets our requirements.

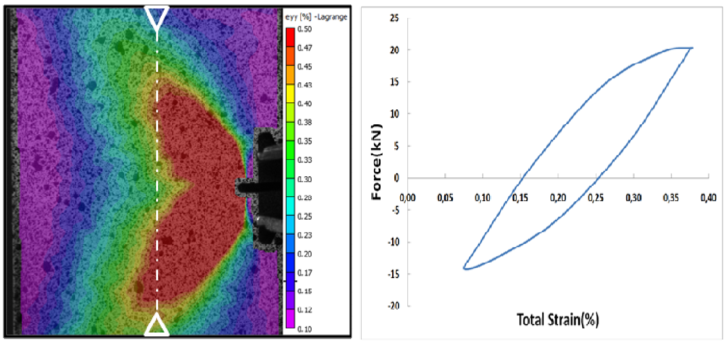

Fig. 5 Cyclic plasticity in specimen under loading

3 FATIGUE CRACK GROWTH EXPERIMENT CONDITIONS

The experiment is conducted with a MTS hydraulic machine with capacity of 25 kN. A strain-controlled loading is applied via an extensometer to ensure global plasticity as shown in Fig 6. An optic technique is employed for the crack length measurement by a photo post-treatment process which allows identifying crack tip with the photos taken by a numeric camera at maximum crack opening. Experiments are conducted under constant strain controlled amplitude as well as variable strain controlled amplitude with a frequency of 0.1Hz and loading ratio ($R\varepsilon$) of 0.2 on pre-cracked specimen. The results will be presented in the following paragraphs.

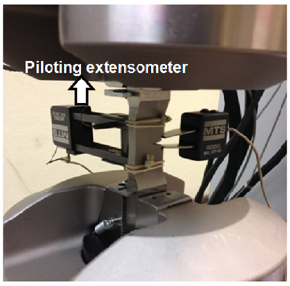

Fig. 6 Experimental set-up

4 EXPERIMENTAL RESULTS

A series of experiments is performed under different loading conditions as listed in Table 1. Stable crack propagation with decreasing crack growth speed is observed during the tests and a crack length large enough is obtained with a few thousands of cycles.

Table 1 LSY experiment

Specimen number	Maximum load(ε_{max})	N_{cycle}	Crack length(mm)
1884-4A	0.3%	4950	8.06
1884-7A	0.5%	1800	9.84
1884-3A	0.5%	1950	9.12
1884-5A	0.7%	1320	11.65
1884-2A	0.7%	1220	10.77
1884-13A	0.3% with overload of 0.7%	2050	5.43

4.1 Experiment under constant loading conditions

Experiments under constant loading condition of three different amplitudes were performed. The fracture surfaces were observed using a scanning electron microscope. When constant amplitude fatigue cycles are applied, the crack growth is planar and fatigue striation are clearly visible (Fig 7). In addition, the local crack growth rate determined by the striation spacing from SEM image is found in good consistency with macroscopic crack propagation rate per cycle for each test (Fig 8). It is therefore important to recognize that the mechanism of fatigue striation plays a significant role in LSY fatigue crack growth as well as in SSY fatigue crack propagation. However, large striation up to 10 microns is obtained which is quite unusual against that in SSY conditions [2].

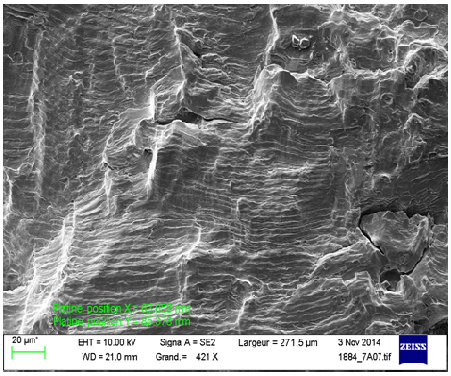

Fig. 7 SEM image taken for a constant amplitude fatigue test (ε_{max} = 0.5%)

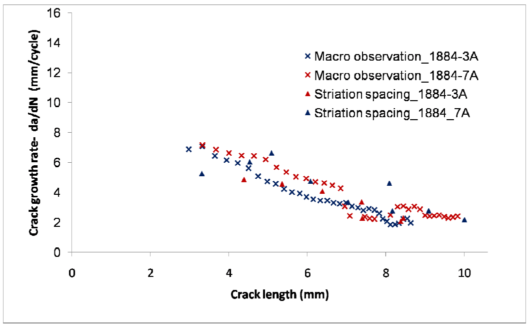

Fig. 8 Comparison of crack growth rate between striation spacing and macroscopic observation (ε_{max} = 0.5%)

4.2 Experiment under variable loading conditions

In order to evaluate history effect in LSY fatigue crack propagation in 316L, a variable amplitude fatigue crack growth experiment is carried out. For this purpose, 100 cycles of overloads are applied before the constant amplitude fatigue cycles, both the deformation ratio of overload and that of the constant load are fixed at $R\varepsilon$=0.2. It is observed that the application of the overload decrease significantly the crack growth rate. A retardation effect of about a factor 2.5 is found in this case (Fig 9). In conclusion, even in LSY condition, the plasticity is not confined in crack tip region, the retardation effect should be considered in the prediction of crack growth as well.

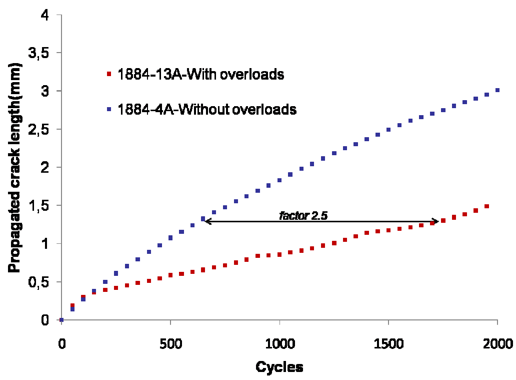

Fig. 9 Evolution of the LSY fatigue crack length with or without overloads in 316L

5 CONCLUSIONS AND FUTURE WORKS

The mechanism of fatigue crack propagation in cyclic LSY conditions is explored in this work through a series of mechanical experiments realised on a special designed specimen. Striation observed on fatigue fracture surfaces indicates the mechanism of fatigue striation on crack growth in cyclic LSY conditions. This conclusion is also confirmed by the coherence between striation spacing and microscopic crack growth rate per cycle. Besides, history effect is found as well in this case even through plasticity is not confined in near crack tip region. According to these observations, it is possible to develop an existing condensed model based on fatigue striation mechanism in the prediction of fatigue crack propagation in constant/variable cyclic LSY condition [3-4].

In the next future, the enrichment of the condensed model should be done by finite element simulation method in consideration of generalised plasticity. Various points should be treated. Firstly the modification of the model in accounting for LSY conditions will be studied with constitutive model for 316L from perfect elastic perfectly plastic law to constitutive law including non-linear kinematic and non-linear isotropic hardening. Secondly, the generalised plasticity caused by uni-axial loading as well as multi-axial loading will also be studied.

6 ACKNOWLEDGEMENTS

This work is supported by Electricity of France through the Project COFAT and by Areva the word-leading company in nuclear energy.

7 REFERENCES

[1] P.C. Paris, F.Erdogan, A critical analysis of crack propagation laws. Journal of Basic Engineering 85, 528-534, 1963

[2] C. Vallet, T. H. Chau, J-M. Stéphan , Crack propagation under high thermal amplitude cycles in a ductile material. Proceedings of the ASME 2012 Pressure Vessels and Piping Conference, 2012.

[3] F. Fremy, S. Pommier, A scaling approch to model history effects in fatigue crack growth under mixed mode I+II+III loading conditions for a 316L stainless steel. International Journal of Fatigue, 42(2012), 207-216, 2012

[4] S. Pommier, R. Hamam, Incremental model for fatigue crack growth based on a displacement partitioning hypothesis of mode I elastic-plastic displacement fields. Fatigue & Fracture of Engneering Materials & Structures, 30(2007), 582-598, 2007

[5] W. Zhang, S. Pommier, Mode I crack propagation under high cyclic loading in 316L stainless steel, Procedia Material Science, 3(2014) 1197-1203, 2014

Proceedings of the 4th International Conference on
Fracture Fatigue and Wear, pp. 148-154, 2015

HETEROGENOUS FATIGUE BEHAVIOR OF A FRICTION STIR WELDED TITANIUM ALLOY IN RELATION TO MICROSTRUCTURAL AND RESIDUAL STRESS GRADATION

M. Muzvidziwa*[1], M. Okazaki[1], S. Hirano[2] and M. Sekihara[2]

[1]Nagaoka University of Technology 1603-1 Kamitomioka-machi, Nagaoka-shi, Niigata 940-2188, Japan
[2]Hitachi Research Lab., Hitachi 319-1292, Japan

Abstract: Monotonic mechanical properties and local fatigue behaviour of a Ti-6Al-4V titanium alloy friction stir welded butt-joint were investigated. In fatigue crack propagation tests on CT specimens with initial notches parallel to the weld direction; cracks propagating in the stirred zone showed lower growth rates than those in the base metal. Also, the cracks with initial notches in the stirred zone showed a tendency to deflect towards the thermos-mechanically affected zone on the retreating side of the joint whereas those in the base metal remained normal to the loading direction. These differences were discussed with relation to the local interaction of the crack with the different microstructural phases and their intrinsic fracture behaviours and variation of the residual stresses across the weld affected area. From the residual stress measurements through the X-ray diffraction method, it was found that the residual stresses had graded, significant shear stress components which could also play a role in the differences in FCP behaviour of the base metal, stirred zone and the advancing and retreating sides of the weld.

Keywords: Friction stir welding, 6-4 titanium alloy, microstructural gradation, residual stress, fatigue crack propagation

1 INTRODUCTION

Development of tools applicable to friction stir welding (FSW) and friction stir processing (FSP) of materials with high softening temperatures has recently promoted research in processing of titanium alloys via these techniques. The FSW technology is relatively new and offers a number of advantages over conventional welding techniques namely higher process speeds, elimination of filler materials and minimal shrinkage and post weld distortion [1]. As such, a considerable amount of work has been done to optimise and understand the damage behaviour of friction stir welded (FSWed) aluminium alloys [2-4]. The roles of microstructure gradation, hardness distribution and residual stresses have been articulated by a number of researchers working on aluminium alloys [5-7]. Tra et al. [5] reported more significant influence of the microstructure than the residual stress on the fatigue crack propagation (FCP) behaviour in a FSWed 6063-T5 aluminium alloy, whereas Bussu and Irving [7] found dominant effect of residual stress in the FCP of a FSWed 2024 aluminium alloy. Similarly, in the limited work carried out on FCP behaviour of titanium alloys, the roles of the microstructure and the residual stresses have not been fully understood. John et al. [8] and Pasta and Reynolds [9] showed residual stress effects in the FCP behaviour longitudinal and transverse to the weld in Ti-6Al-4V friction stir welds, respectively. Limited focus was put on the influence of microstructure by both groups. Pao et al. [10], however, considered the influence both the crack tip microstructure and the residual stress in their work on the FCP in FSWed Ti-5111. Through comparison of the FCP behaviour in specimens prepared at different FSW conditions and also some exposed to post-weld stress relief annealing, they deduced that residual stress played a more significant role than the microstructure except near ΔK threshold levels where the influence of the microstructure was predominant. However, the residual stress distribution was not obtained in that work. The growing interest and potential application of FSW in fabricating titanium components in aerospace and space vehicle components entails further work be carried to understand the damage tolerance properties of FSWed joints.

In this work, the role of the microstructure and residual stresses on the FCP of a FSWed 6-4 titanium alloy were investigated. Initially, the microstructural development in the weld was studied and correlated to the measured monotonic properties of the weld. FCP tests on CT specimens containing initial notches in the stirred zone (SZ) and parallel to weld direction were carried out with subsequent analysis based on the microstructure and residual stresses obtained through the X-ray diffraction (XRD) method. The residual stresses were measured in the base metal (BM), SZ, advancing side (AS) and also on the retreating side (RS) of the weld.

2 EXPERIMENTAL METHODS

The starting material in this work was a 5mm FSWed plate of a titanium alloy joined through a single pass in a butt joint configuration. The cross section of the weld area was analysed using an optical microscope after metallographic preparation and etching. The etching was carried out in two stages by swabbing the specimen with Kroll's reagent for 10 seconds, rinsing in water and alcohol and then immersing it into a solution made up of 2% HF, 5% H_2O_2 and 93% water for 5 seconds to enable phase contrast and grain boundary viewing.

2.1 Hardness and Tensile Tests

The hardness distribution and tensile strengths were measured through micro-indentation hardness tests and traction tensile tests on miniature specimens respectively. To characterize the hardness distribution along the weld width and thickness, multiple indentations were made on the weld cross section along two lines, at 0.3mm and 1mm from the top surface, using a Vickers indenter under a 500g force for 10seconds. Due to the limited thickness of the welded area, miniature tensile test specimens with a thickness of 500µm, Fig. 1 (a), were extracted by electro-discharge machining (EDM) transverse to the weld direction such that the gage length contained the stirred zone as illustrated in Fig. 1 (c). Base metal specimens of the same dimensions were also extracted. The tensile tests were carried out using a 5KN Yonekura testing machine tailored for miniature specimens.

2.2 Fatigue Crack Propagation Tests

The fatigue crack growth rates in the base metal and welded area were measured on compact tension (CT) specimens with initial notches in the base metal and the stirred zone respectively. The CT specimens of dimensions shown in Fig. 1 (b) were precisely extracted from a depth of 0.4mm from the top surface by EDM from both the welded area; Fig. 1 (c). The fatigue crack propagation (FCP) tests were carried out under ambient conditions, a load ratio, R, of 0.6 and loading frequency of 20Hz. The crack length was monitored and measured through a travelling digital microscope continuously focused on the specimen surface.

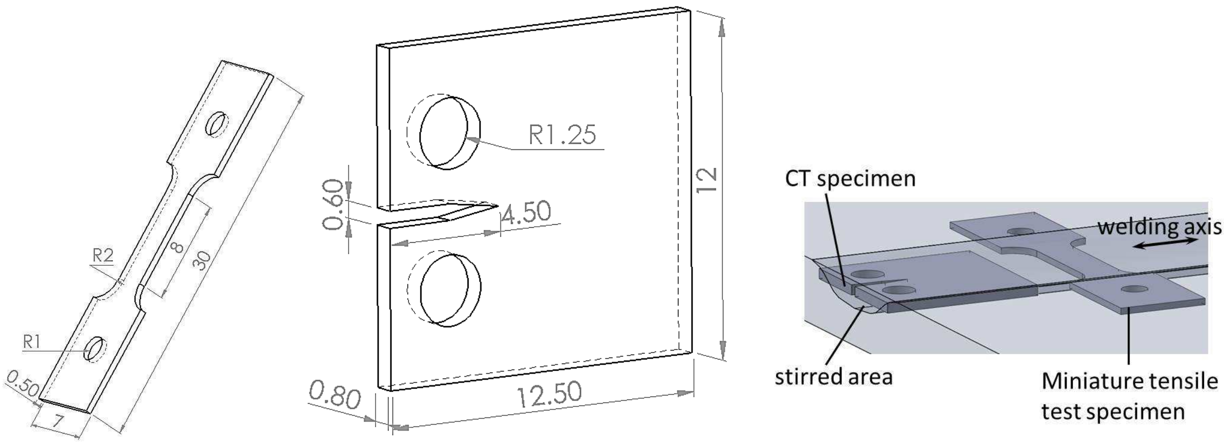

Fig. 1 (a) Dimensions of the miniature tensile test specimen, (b) Dimensions of the CT specimen and (c) Extraction of the tensile test and CT specimens

Table 1 XRD Parameters and Conditions

	BM	**FSW**
Target	Cu-Kα	Cu-Kα
Crystallographic plane	{21.3}	{30.2}
Tube voltage, KV	30KV	30KV
Tube Current, mA	30mA	30mA
Irradiation area, mm	4x4mm	4x4mm
Stress Constant K, MPa/deg.	-274	-205
Peak determination	FWHM	FWHM

2.3 Residual stress measurement

The residual stresses in the base metal and the welded area were measured through the $Sin^2\psi$ method of the X-ray diffraction (XRD) technique. Square-faced plates with dimensions of 30mm x 30mm x 4mm were extracted from a depth of 0.4mm from the top surface of the weld (from the same depth as the CT specimens) using EDM and exposed as-machined. The parameters and conditions used for the measurement and calculations are shown in Table 1. Noteworthy is that the diffraction planes employed for the BM and FSW areas were different as dictated by empirically obtained intensity peaks upon initial 2-theta scanning. Measurements were carried out along three in-plane directions; longitudinal and transverse to weld direction and their mid-point line, 45°. The obtained residual stresses were then used to calculate the principal stress components and their directions.

3 RESULTS AND DISCUSSIONS

3.1 Microstructure, Hardness Distribution and Tensile Strengths

It is worth noting that despite the use of 5mm plates, welding was deliberately effected to a depth of about 1.8mm as observable from the macrograph presented in Fig. 2. Within the stirred area, some defects related to incomplete root penetration were observed near the weld root. Based on these observations, specimens for subsequent tests were therefore extracted within a 1mm thickness in the mid-thickness region of the weld; 0.4mm from the top and root of the weld. Optical microscopy not only revealed significant refinement of the grains in the stirred zone (SZ) but also showed grain size variation through the weld thickness. The microstructure within a depth of 0.3mm from the crown, the surface in contact with the tool shoulder during the FSW, had the smallest grains in the stirred area. This grain refinement could be related to the high lattice strain and temperatures achieved in the material in contact with the tool shoulder. This could lead to rapid nuclei formation during recrystallization and combined with high cooling rates at the surface, this would result in the fine structure. At a depth of 0.5mm from the surface, the grain sizes were found to be the largest within the SZ; larger than those at the weld root. This variation has also been discussed with regards to the differences in the thermomechanical processes at these depths [11]. The reported [12] relatively low temperatures at the tool pin tip near the weld root would result in high strains promoting nuclei formation with limited grain growth [13]. Whereas in the mid-thickness of the weld, the rate of nucleus growth could be higher due to higher temperatures and less thermomechanical work thereby giving larger grains. This through-the-thickness gradation is unlike in aluminium alloys and could therefore be related to the low thermal conductivity of titanium alloys. Furthermore, the region surrounding the SZ, which has been characterized as the TMAZ and the HAZ in FSWed aluminium alloys, did not show distinct features as those observed in the aluminium alloys. This could also be attributed to the low thermal conductivity and high strength of the material. The heat dissipated to the zone outside the tool pin shoulder is not sufficient to facilitate plastic deformation of the surrounding material thus limiting the size of the TMAZ.

Vickers hardness profiles at different depths across the weld are presented in Fig. 3. The hardness peak in the SZ is related to the grain refinement observed there.

The tensile properties of the BM and the transverse FSW specimens are shown in Table 2. The tensile strength of the FSW specimen gave a joint strength of 90% and half the elongation of the BM. Rapture of the FSW specimen was about 2mm from the weld centre towards the interfacial area between the SZ and the BM.

3.2 Fatigue Crack Propagation

The FCP curves in Fig. 4 (a), which are plotted on the basis of traditional fracture mechanics, show that the FCP rate in the FSW was lower than that in the BM. This improvement in the fatigue crack propagation resistance after FSW could be attributed to the microstructure refinement. The recrystallized equiaxed microstructure in the SZ has been observed to contain significantly refined prior β grains with α colony sizes of one quarter to half the prior β grain size [14]. In the current work, the prior β was refined from 13μm in the BM to approximately 5μm thus α colony sizes and related slip lengths could be in the 1μm range. This significant reduction in the slip length is reported to improve the high cycle fatigue properties in bimodal titanium alloys [15]. Meanwhile, the cracks in the FSW specimens also showed significant kinking towards the retreating side of the weld whereas in the BM specimens the cracks propagated perpendicular to the loading direction, Fig. 4 (b). The kink angle in both of the FSW specimens was about 40° and the kinking occurred after normal propagation of approximately 1mm. The propagation in the vicinity of the notch is known to be influenced by the notch such that the initial propagation perpendicular to the loading direction could be related to this effect. Considering that the stress intensity factor (SIF) range, ΔK_I, used in Fig. 4 (a)

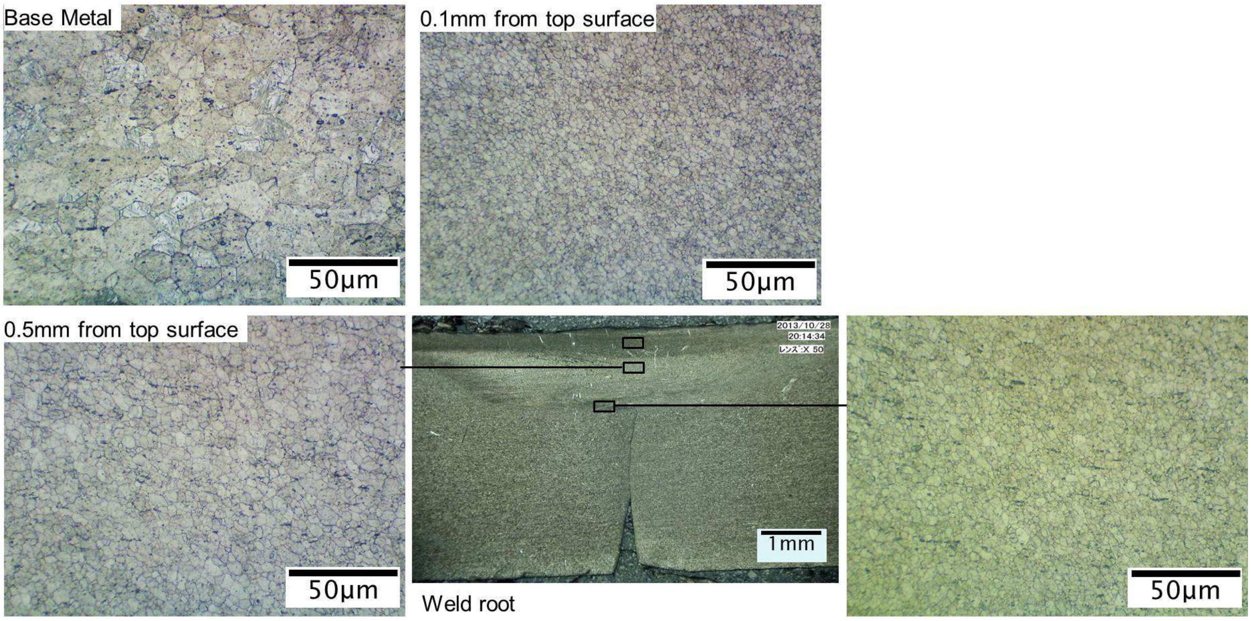

Fig. 2 Microstructural gradation in the FSWed area

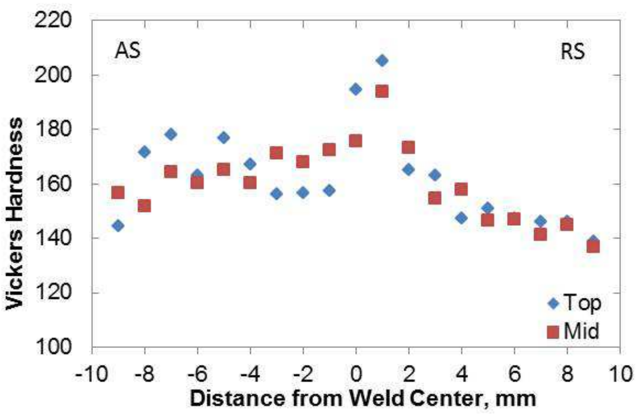

Fig. 3 Hardness distribution across the FSWed area

Table 2 Tensile Properties

	UTS, MPa	Elongation, %	Specimen
BM	378	19	
FSW	335	8	

assumed pure Mode I loading where the crack length was based on the horizontal increment, it is worthy to discuss the role of crack deflection in the effective stress intensity factor. As a first approximation this is possible in terms of the coplanar maximum strain energy release rate theory [16]. Where the effective stress intensity factor, ΔK_{eff}, for a finite kink length is given by:

$$\Delta K_{eff} = \Delta K_I \left\{ \left[\cos^3(\theta/2)\right]^2 + \left[\sin(\theta/2)\cos^2(\theta/2)\right]^2 \right\}^{1/2}, \tag{1}$$

where θ is the kink angle. A plot of the ΔK_{eff} and the FCP rate in Fig 4 (c) shows the curves of the FSW approaching those of the BM but not enough to cover the whole band. The remaining difference could thus be attributed to the discussed microstructural refinement. To get a better insight on the preference of the crack to deflect towards the RS, and not the AS, residual stresses were measured across the weld and are presented in the next section.

3.3 Residual Stress Distribution

The residual stresses obtained by the XRD method in the three in-plane directions, Fig. 5 (b), are shown in Fig. 5 (a). A wide distribution of the residual stresses was observed in all the 3 direction with peaks in the weld centre. Within the weld affected areas the residual stresses were tensile in all directions except in the transverse and 45° directions on the AS. This profile generally resembles that obtained in conventional welds [17]. However, there has been a paucity of data on the residual stresses in FSWed titanium alloys. In work on a FSWed Ti-6Al-4V alloy, John et al. [8] measured transverse residual stresses through XRD and reported a similar profile with peak stresses in the weld centre and variations through the weld thickness.

Pasta and Reynolds [9], on the other hand, used the cut compliance technique to measure the longitudinal residual stresses in a Ti-6Al-4V FSW and also reported peak tensile stresses in the SZ flanked by compressive residual stresses on the both the AS and RS. In the current work, since the loading direction in the FCP test was transverse to the welding direction, a consideration of the transverse residual stresses would indicate preferred FCP on the RS than on the AS. However, this cannot adequately explain the crack deflection because the SZ which has the highest tensile residual stresses would be more preferable for FCP than the RS. Based on the tensile residual stresses in the SZ, the FCP rate in the FSW specimens would be expected to be higher than that in the BM which had marginal compressive transverse residual stresses of -57 MPa. This discrepancy could indicate that the microstructure had higher influence on the FCP rate in the SZ than the residual stresses. In the work by Pao et al. [10] on the FCP in Ti-5111 FSWed at different conditions, they showed through stress relief annealing that the influence of the microstructure and residual stresses could depend on the FSW conditions and the ΔK level. As such, the observations made in this work cannot be expected to be the general relationship.

Further calculations were also made for the present work to evaluate the principal and maximum shear stresses and their directions. Fig. 6 shows a representation of these stresses and their directions schematically imposed on macrographs of the cracked FSW CT specimen. The shear stresses were found to be heterogeneous in both magnitude and direction where the shear stresses of 96 MPa on the AS were found to cause rotation that is counter to that caused by the 82.7 MPa shear stresses in the SZ. Whereas the shear stresses on the RS were oriented for co-rotation with those in the SZ. Factoring in the misalignment of just 32° in their directions, the co-rotation between the SZ and the RS would have a resultant shear stress component to cause Mode II loading that could result in the crack deflection. This observed heterogeneity in the residual stresses suggests that the maximum shear stress components could play a major role in the FCP behaviour in the welded area.

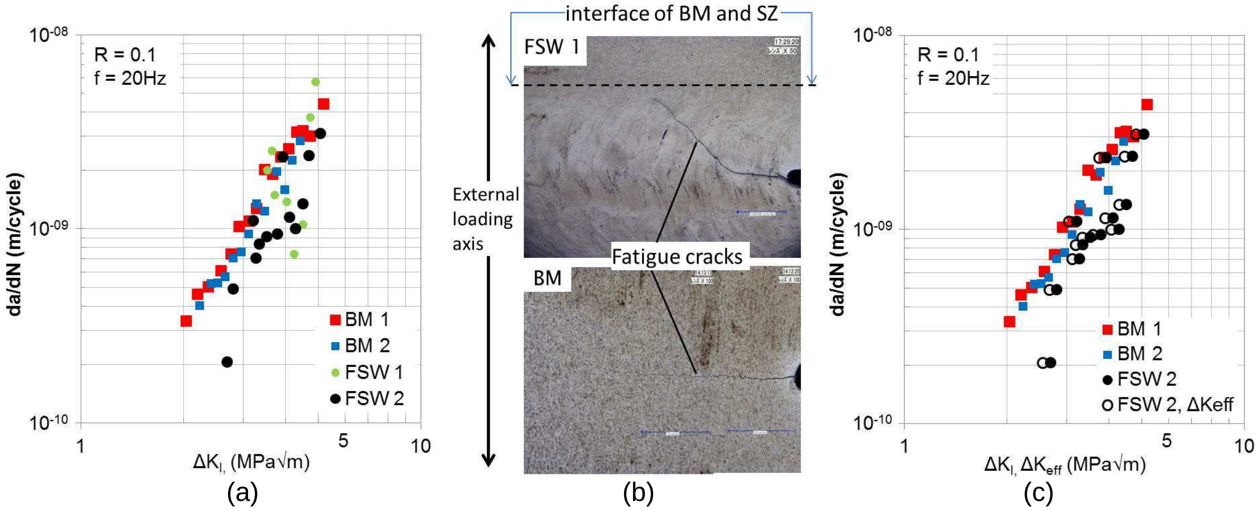

Fig. 4 (a) FCP rates in the BM and the FSW, (b) Crack appearance showing kinking in the FSW specimen and (c) FCP rates with respect to ΔK_{eff} calculated using Eq. 1

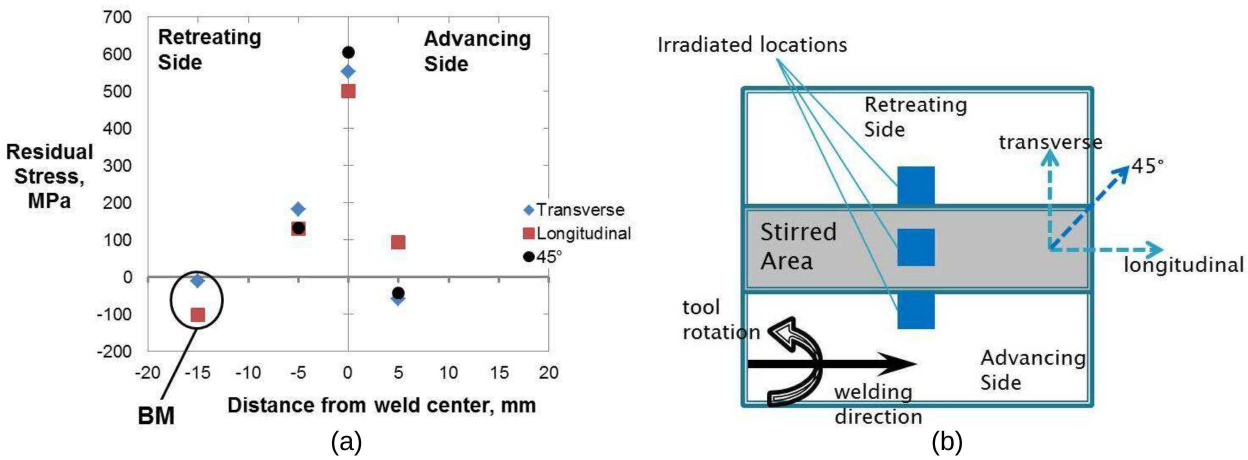

Fig. 5 (a) Residual stress distribution in 3 in-plane directions (b) Illustration of the directions and measurement locations

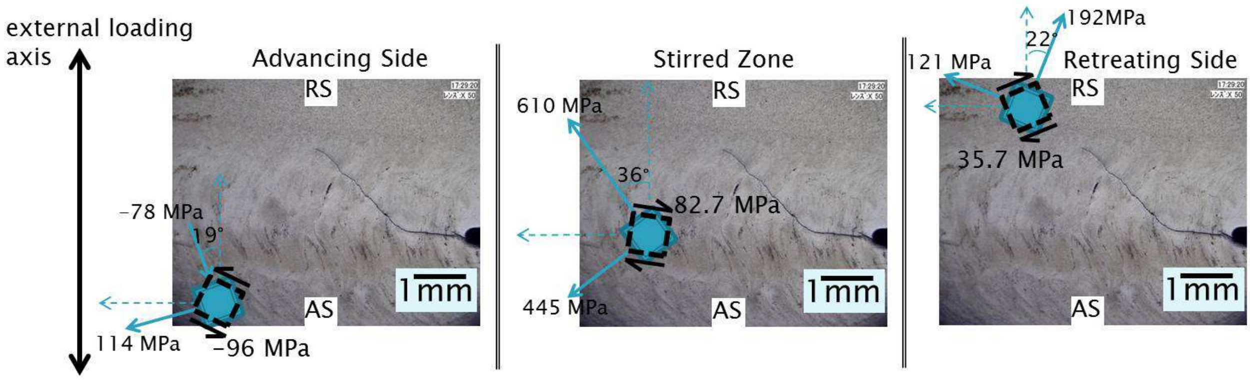

Fig. 6 Illustration of the principal and maximum shear stresses and their directions with respect to the fatigue crack on the FSWed specimen

4 SUMMARY

In this work, the role of the microstructure and residual stresses on the FCP of a FSWed titanium alloy were investigated. Observation of the microstructure on the weld cross section showed refinement of the prior β grain size from 13μm in the base metal to approximately 5μm in the SZ due to the thermomechanical effect of the stirring. Considerable gradation in the grain sizes across the weld thickness was also observed where the mid-thickness area of the weld had the largest grain sizes within the SZ. This was discussed with regards to the differences in the thermomechanical processes at these depths and the low thermal conductivity of the material. The hardness distribution showed a peak in the SZ concomitant with the refined microstructure and miniature specimens used for tensile testing fractured with 90% joint efficiency near the interface of the SZ and the BM indicating competence of the SZ. FCP tests using CT specimens with initial notches in the SZ and parallel to the weld direction showed lower propagation rates in FSW specimens than the BM. Significant kinking of the cracks towards the retreating side was also observed in FSW specimens but not in the BM. The effect of the kinking on the effective crack driving force, ΔK_{eff}, at the crack tip was factored in using the coplanar maximum strain energy release rate theory, after which a small reduction in the differences between the FCP rates of the BM and the FSW was obtained. The difference in the FCP rate between the BM and the FSW after application of the ΔK_{eff} was discussed with regards to the microstructural evolution; refinement of the microstructure gives small sized α colonies and slip lengths which could result in the lower FCP rates. Residual stresses obtained through XRD could also be used to understand the FCP behaviour in the FSW specimens. The in-plane residual stresses were found to be predominantly tensile but with significant variations across the weld. Considering the tensile residual stresses in the SZ and the lower FCP rates, it was postulated that for the current material, the influence of microstructure on the FCP was predominant over that of the residual stress. It was also shown through considerations of the heterogeneity in maximum shear stress components that these variations could play a role in the crack kinking and thus the FCP behaviour in the FSW.

4 ACKNOWLEDGEMENTS

M. Muzvidziwa would like to acknowledge support from the Ministry of Education, Culture, Sports, Science and Technology (MEXT) provided through the MEXT scholarship. M. Okazaki would like to thank the Japan Society for the Promotion of Science (JSPS) for financial support through grant-in-aid #25249003. Gratitude is also extended to Hitachi Research Laboratories, Japan for supplying the friction stir welded materials used in this research.

5 REFERENCES

[1] R. S Mishra, M. W. Mahoney (Eds.), Friction Stir Welding and Processing, ASM International, 2007, pp. 1-5.

[2] R. Nandan, T. DebRoy and H.K.D.H Bhadeshia, Recent advances in friction-stir welding – Process, weldment structure and properties, Progress in Materials Science 53, 2008, pp. 980–1023.

[3] Y. Sato, H. Kokawa, M. Enomoto, and S. Jogan, Microstructural evolution of 6063 aluminum during friction-stir welding, Metallurgical and Materials Transactions A, Vol.30, 1999, pp. 2429-2437.

[4] R. Brown, Wei Tang and A.P Reynolds., Multi-pass friction stir welding in alloy 7050-T7451: Effects on weld response variables and on weld properties, Materials Science and Engineering A513–514, 2009, pp. 115–121.

[5] T. H Tra, M. Okazaki and K. Suzuki, Fatigue crack propagation behavior in friction stir welding of AA6063-T5: Roles of residual stress and microstructure, International Journal of Fatigue 43, 2012, pp. 23–29.

[6] KV. Jata, KK. Sankaran, JJ. Ruschau, Friction-stir welding effect on microstructure and fatigue of aluminum alloy 7050–T7451, Metallurgical and Material Transactions 31A, 2000, pp.2181–92.

[7] G. Busu and PE. Irving, The role of residual stress and heat affected zone properties on fatigue crack propagation in friction stir welded 2024–T351 aluminum joints, International Journal of Fatigue 25, 2003, pp. 77–88.

[8] R. John, K. V. Jata, and K. Sadananda, Residual stress effects on near threshold fatigue crack growth in friction stir welds in aerospace alloys, International Journal of Fatigue 25, 2003, pp. 939-948.

[9] S. Pasta and P. Reynolds, Residual stress effects on fatigue crack growth in a Ti-6Al-4V friction stir weld, Fatigue and Fracture of Engineering Materials & Structure 31, 2008, pp. 569-580.

[10] P. S. Pao, R.W. Fonda, H.N. Jones, C.R. Feng, and D.W. Moon, fatigue crack growth in friction stir welded Ti-5111, in: Friction Stir Welding and Processing V, R. S. Mishra, M. W. Mahoney (Eds.), TMS, 2009, pp. 29-38.

[11] P.D. Edwards and M. Ramulu, Investigation of microstructure, surface and subsurface characteristics in titanium alloy friction stir welds of varied thicknesses, Science and Technology of Welding and Joining vol. 14 no. 5, 2009, pp. 476-483.

[12] J.A. Schneider, Temperature Distribution and Resulting Metal Flow, in: Friction Stir Welding and Processing V, R. S. Mishra, M. W. Mahoney (Eds.), ASM international, 2007, pp. 37-49.

[13] R. E. Reed-Hill, Physical Metallurgy Principles, second ed., D. Van Nostrand Company, 1973, pp. 284-297.

[14] A.L Pilchak and J.C. Williams, The effect of friction stir processing on the mechanical properties of investment cast and hot isostatically pressed Ti-6Al-4V, Metallurgical Transactions 42A, 2011, pp. 1630-1645.

[15] G. Lutjering, Influence of processing on microstructure and mechanical properties of (α + β) titanium alloys, Mat. Sci. and Eng. A243, 1998, pp. 32-45.

[16] S. Suresh, Crack Deflection: Implications for the Growth of Long and Short Fatigue Cracks, Met. Trans. Vol. 14A, 1983, pp. 2375-2385.

[17] A. J. McEvily, Metal Failures: mechanisms, analysis, prevention, John Wiley & Sons, Inc., New York, 2002, pp. 150.

International Journal of Fracture Fatigue and Wear, Volume 3

Proceedings of the 4th International Conference on
Fracture Fatigue and Wear, pp. 155-160, 2015

IMPROVEMENT OF TIGHTENING CHARACTERISTICS OF ALUMINUM BOLTS AND TITANIUM BOLTS

Shinji Hashimura[1], Takefumi Otsu[2] and Kyoichi Komatsu[3]

[1]Department of Engineering Science and Mechanics, Shibaura Institute of Technology, Tokyo, JAPAN
[2]Department of Mechanical Engineering, Kurume National College of Technology, Fukuoka, JAPAN
[3] Tohnichi Manufacturing Co. ltd., Tokyo, JAPAN

Abstract: It is well-known that coefficients of friction between mating surfaces of aluminum parts and titanium parts are significantly higher than those of steel. In bolted joints, the tightening strength of the bolt decreases with an increase in the coefficient of friction between thread surfaces because the twisting torque generates by the thread friction to the bolt increases. In our previous study, we confirmed the tightening strength of A5056 aluminum alloy bolts and TW340 pure titanium bolts decreased until approximately a half of the tensile strength. Therefore to maintain the tightening strength of the nonferrous bolts, we need to propose the appropriate lubricant to reduce the coefficients of friction between thread surfaces. In this study, tightening tests for A5056 aluminum alloy bolts and TW340 pure titanium bolts were conducted using four kinds of lubricants, machine oil ISO VG46, MoS_2 grease and two polyisobuthylenes with different kinetic viscosity. The results showed that the tightening strengths of A5056 aluminum alloy bolts were greatly improved if the bolted joints were lubricated by MoS_2 grease or two polyisobuthylenes during a tightening. The tightening strengths of TW340 pure titanium alloy bolts could not enough be improved even if MoS2 grease and polyisobuthylenes were used. However if the polyisobuthylene with high kinetic viscosity was used for the lubricant, the tightening strength of TW340 pure titanium bolt was improved 10 % against the other lubricated conditions.

Keywords: Bolt Tightening, Aluminium Alloy Bolt, Pure Titanium Bolt, Lubricant, Tightening Strength

1 INTRODUCTION

Lightweight technology is demanded in various vehicles to improve the efficiency. Hence we have to reduce weight of not only structural members and frames but also machine elements such as bolts and nuts at present [1]. In general, it is well-known that the coefficients of friction between mating surfaces of aluminium parts and titanium parts are greatly higher than those of steel [2-6]. Bolted joints have two contacting surfaces, thread surface and bearing surface, in usual. The tightening strengths of bolts decrease with an increase in the coefficient of friction between thread surfaces because the twisting torque generates by the thread friction to the bolt increases [7,8]. Hence if the bolted joints are made of aluminium or titanium, the tightening strengths of the bolts decrease against the tensile strengths. In our previous study, it was confirmed that the tightening strength of aluminium alloy bolts and pure titanium bolts decreased until a half of the tensile strengths [9]. Therefore appropriate lubricants, which can stably decrease the coefficient of friction between thread surfaces for aluminium bolts and titanium bolts, must be proposed to improve the strength of the bolted joints.

In this study, tightening tests have been conducted using aluminium alloy bolts and pure titanium bolts to find out the appropriate lubricants for the tightening. The test bolts made of A5056 aluminium alloy and made of TW340 pure titanium were used. A clamped part material and a nut material were also the same as the bolts. The lubricants in the experiments were used machine oil ISO VG46, MoS_2 grease and two polyisobuthylenes with different kinetic viscosity. The relationships between torque coefficients corresponding to the frictional characteristics in bolted joints and the tightening strengths have been investigated under each lubricated condition. And then the appropriate lubricants for the tightening have been selected.

2 TEST BOLTS, TEST NUTS AND BOLT/NUT ASSEMBLY

Figure 1 shows a schematic illustrations of a test bolt, a test nut and a tightening situation of tightening tests. The test bolt was used a commercial hexagon head bolt M8 made of A5056 aluminum alloy and

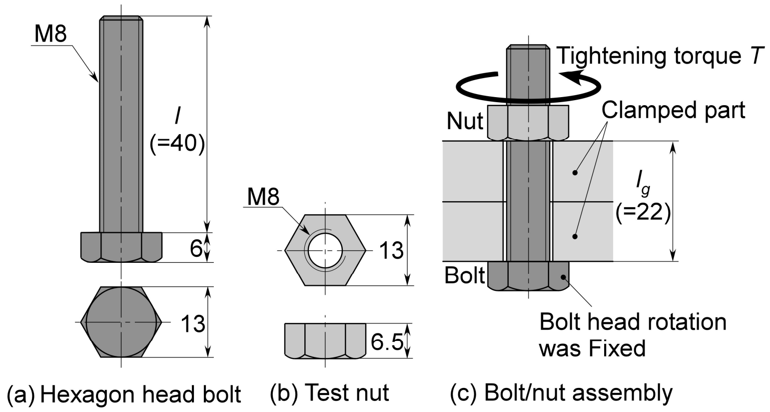

Fig. 1 Test bolt, test nut and bolt/nut assembly

TB340 pure titanium. Table 1 shows the mechanical properties of the test bolts published by the manufacturers. Table 2 shows the chemical composition of the bolt materials. The thread portion of the bolts were processed with cold thread rolling.

The test nut shown in Fig. 1(b) was the commercial hexagon nut M8 made of the same material as the each bolt. The clamped part contacting the nut bearing surface was also made of the same material as the each bolt. When the bolt/nut assembly was tightened as shown in Fig. 1(c), the bolt head rotation was fixed and the nut was rotated during the tightening test. The grip length of the bolt/nut assembly was l_g=22 mm and the engaging thread length was l_e=6.5 mm (the nut height).

Table 1 Mechanical properties of the test bolts

Material	Ultimate strength σ_u	0.2% proof stress $\sigma_{0.2}$
A5056	310 MPa	205 MPa
TW340	392 MPa	245 MPa

Table 2 Chemical composition of the test bolts

Material	Cu	Fe	Si	Mn	Cr	Zn	N	O	H	Mg	Al	Ti
A5056	0.01	0.12	0.07	0.07	0.07	0.00	-	-	-	4.58	RE.	0.03
TW340	0.04	0.037	-	-	-	-	0.002	0.043	0.0024	-	-	RE.

3 EXPERIMENT

Figure 2 shows an experimental apparatus for the tightening tests. Fig. 2(a) shows the schematic experimental apparatus and Fig. 2(b) shows the bolt/nut assembly including a load cell. In Fig. 2(a), the tightening device including a wrench, a torque transducer and an induction motor can move in a perpendicular direction by a manual jack. The tightening torque T was measured with the torque transducer and the nut rotation (Tightening angle θ) was measured by a rotary encoder attached to the motor. The nut rotation speed at the tightening test was set at ω=5 rpm.

In the bolt/nut assembly shown in Fig. 2(b), the load cell to measure the thread torque T_t and the clamping force F was set on the base plate. The bolt head was fixed at the load cell. The upper clamped part was fixed on the upper plate. At that time, we could measure the thread torque T_t independently by maintaining a space between the lower clamped part and the upper clamped part. The bolt/nut assembly was tightened rotating the nut.

Four kinds of lubricants were used in the tightening experiments. The first one is a machine oil ISO VG46 (VG46), the second one is a MoS_2 grease (MoS_2). The third lubricant is a polyisobuthylene (PIB) which is sold as the special lubricant for bolt tightening. The fourth lubricant is polyisobuthylene (PIB-H) with higher kinetic viscosity than PIB. Table 3 shows the characteristics of two types of polyisobuthylene.

Table 3 Kinetic viscosities, viscosities and densities of the lubricants

Lubricant	Kinetic viscosity, mm^2/s at 20°C	Viscosity, Pa-s at 20°C	Density kg/m^3 at 20°C
PIB	24324	21.6	890
PIB-H	261384	235	900

In this study, we investigate the relationships between the frictional characteristics under the different lubricated conditions and the tightening strengths of the bolt/nut assemblies. And then we propose the appropriate lubricant for the bolt tightening. Parameters which was used in discussion of the frictional characteristics are explained.

In the tightening process, the tightening torque T is divided into the thread torque T_t and the bearing surface torque T_w, and the relationship between the tightening torque T and the clamping force F is also expressed as a following equation.

$$T = T_t + T_w = K \cdot d \cdot F \tag{1}$$

where K is defined as a torque coefficient, and d is bolt size. The tightening torque T was measured by the torque transducer shown in Fig. 2(a). And the thread torque T_t and the clamping force F was measured by the load cell shown in Fig. 2(b).

K is expressed by a following equation.

$$K = \frac{1}{2 \cdot d}\left\{d_2 \cdot \mu_s \cdot \sec\alpha' + D_w \cdot \mu_w + \frac{P}{\pi}\right\} \tag{2}$$

where d_2 is pitch diameter. μ_s is the coefficient of friction between thread surfaces, and μ_w is the coefficient of friction between bearing surfaces. α is flank angle of the bolt thread. P is the thread pitch. D_w is the equivalent torque diameter of the bearing surface, which is expressed as a middle diameter between the outer diameter of the contacting bearing surface D_o and the inner diameter of the contacting bearing surfaces D_i.

We also defined the thread torque coefficient K_t as the coefficient of the thread torque T_t to reveal influences of the friction characteristic between thread surfaces on the tightening strengths of the bolt/nut assemblies. The thread torque coefficient K_t is defined by a following equation.

$$K_t = \frac{1}{2 \cdot d}\left\{d_2 \cdot \mu_s \cdot \sec\alpha' + \frac{P}{\pi}\right\} \tag{3}$$

T_t is expressed by a following equation.

$$T_t = K_t \cdot d \cdot F \tag{4}$$

In the tightening experiments, after the test bolt and the nut were set to the experimental apparatus as shown in Fig. 2(b), the nut was tightened until the clamping force F reached 3 kN. After the wrench was removed once from the nut, the wrench was set to the nut again. Then the nut was tightened until the bolt breaks. The tightening torque T, the thread torque T_t, the clamping force F and the tightening angle θ were measured in the tightening experiments. After experiments, we calculated the torque coefficient K and the thread torque coefficient K_t. The proof clamping force $F_{0.2}$ and the ultimate clamping force F_u were also

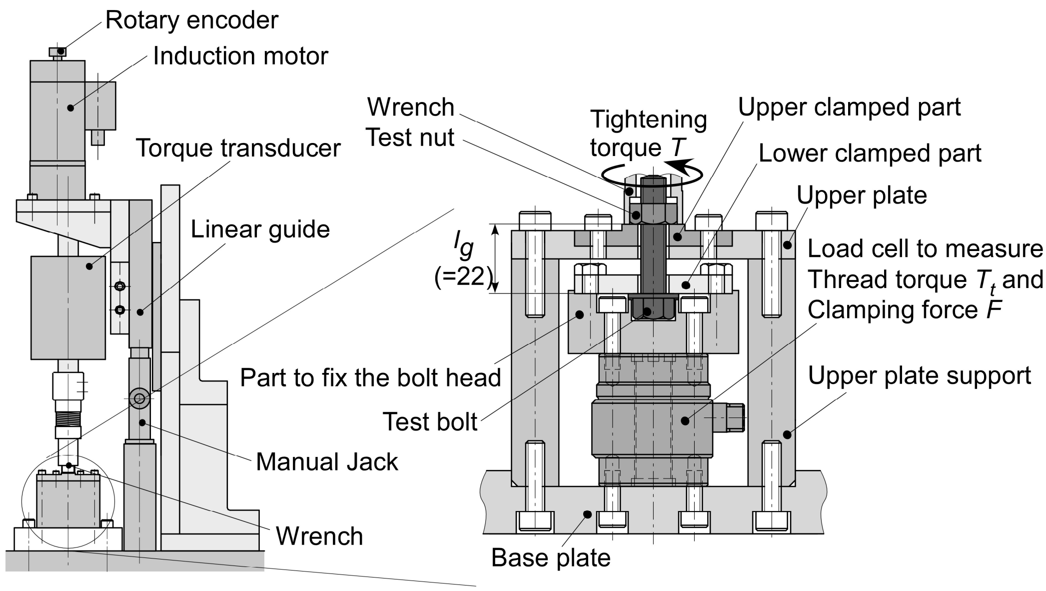

(a) Whole of experimental apparatus (b) Detail of a bolt/nut assembly

Fig. 2 Experimental apparatus

measured. The tightening experiments were also performed under no lubricated condition (NL) in addition to the tightening experiments under the lubricated condition by four lubricants. The each tightening experiment was performed five times. The test bolt and the test nut was replaced a new bolt and nut in each experiment. The bearing surface of the upper clamped part was also polished by a sand paper #600 in each experiment.

4 EXPERIMENTAL RESULTS AND DISCUSSIONS

Figure 3 shows examples of relationships between the tightening torque T and the clamping force F in the tightening tests for A5056 aluminum alloy bolts. In Fig. 3, the abscissa is the clamping force F. The ordinate is the tightening torque T. The black solid line shows a result under no lubricated condition. The gray solid line shows a result for the lubricated condition by machine oil ISO VG46. The gray dotted line shows a result for the lubricated condition by MoS_2 grease, and the black dotted line shows a result for the lubricated condition by PIB.

It could be seen in Fig. 3 that an inclination of T against F for NL was significantly larger than others. But we cannot find the obvious difference in between the behaviours of T in the tightening test under the four lubricated conditions. The results shows that the coefficient of friction under no lubricated condition for A5056 aluminum alloy bolt was significantly higher than others.

Figure 4 shows examples of relationships between the clamping force F against the tightening angle θ in the tightening tests for A5056 aluminum alloy bolts. In Fig. 4, the abscissa is the tightening angle θ. The ordinate is the clamping force F. The black solid line shows a result of the tightening test lubricated by machine oil ISO VG46. The gray solid line shows a result of the tightening test under no lubricated condition. In Fig. 4, the proof clamping force $F_{0.2}$ was defined as the clamping force F at which the bolt was elongated 0.2 % against the grip length l_g=22 mm. The ultimate clamping force F_u was defined as the maximum clamping force F.

The proof clamping force $F_{0.2}$ and the ultimate clamping force F_u in the tightening test of VG46 were obviously higher than those of NL. In the tightening test of NL, the elongation until the bolt breaks also decreased drastically. It could be seen that the bolt under no lubricated condition had already occurred plastic deformation at F=3 kN although the experiments were once stopped at F=3 kN.

Figure 5 shows the proof clamping forces $F_{0.2}$ and the ultimate clamping forces F_u of A5056 aluminum alloy bolts under each lubricated condition. Figure 6 also shows $F_{0.2}$ and F_u of TW340 pure titanium bolts. In Fig. 5 and Fig. 6, the abscissa is $F_{0.2}$ and F_u. The ordinate indicates the lubricated conditions. The black error bars show the scatter bands of F_u and the black circles show the average of F_u. The gray error bars show the scatter bands of $F_{0.2}$ and the gray circles show the average of $F_{0.2}$. The results of tensile tests were also showed in the left side in Fig. 5 and Fig. 6.

Figure 5 shows that the tightening strengths, F_u and $F_{0.2}$, of A5056 were obviously lower than the tensile strengths, P_u and $P_{0.2}$. It can be seen that the tightening strengths remarkably depend on the lubricated conditions. The tightening strengths under no lubricated condition were lower than the half of the tensile strength, and the tightening strengths under the lubricated condition by machine oil ISO VG46 were almost the half of the tensile strength. The tightening strengths under the lubricated condition by MoS_2 grease, PIB and PIB-H were about 80 % of the tensile strength. The results indicate that MoS_2 grease, PIB and PIB-H

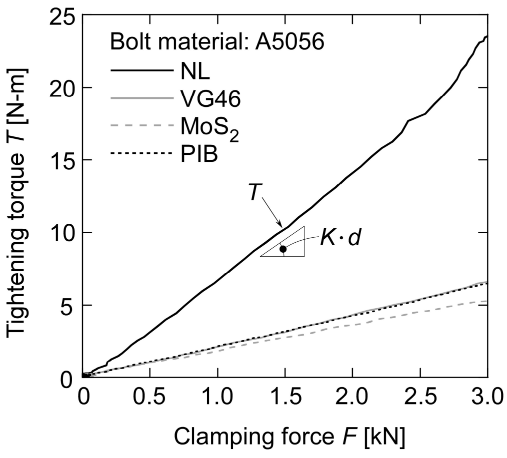

Fig. 3 Behaviours of the tightening torque T against the clamping force F during tightening tests for A5056 aluminum alloy bolts.

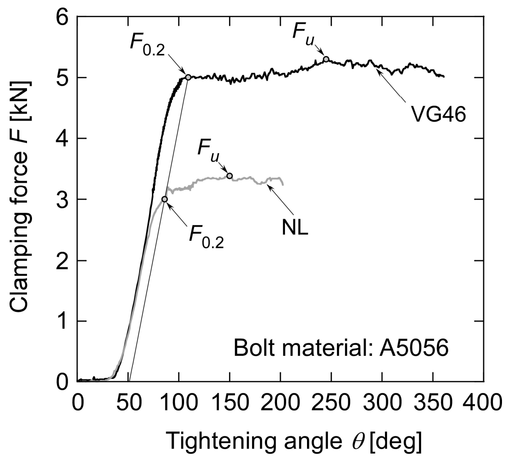

Fig. 4 Behaviours of the clamping force F against the tightening angle θ during tightening tests for A5056 aluminum alloy bolts.

are the appropriate lubricants for A5056 aluminum alloy bolts to maintain their strengths.

Figure 6 also shows that F_u and $F_{0.2}$ of TW340 obviously decreased until half of P_u and $P_{0.2}$. However the tightening strengths were almost the same regardless of the lubricated condition except for PIB-H. The tightening strengths under the lubricated condition by PIB-H were about 10 % higher than others. The results indicate that PIB-H are better lubricants for TW340 pure titanium bolts than others.

In bolt tightening process, the relationship between the tightening torque T and the clamping force F is not almost constant although the relationship is usually considered as a constant in general. This is because the frictional characteristics between thread surfaces and between bearing surfaces frequently change during tightening process. Hence the torque coefficient K and the thread torque coefficient K_t were devided into two parts. The first torque coefficient K and the first thread torque coefficient K_t were calculated averaging these value at the early tightening process stage, F=0 kN ~ 3 kN. The second torque coefficient K and the second thread torque coefficient K_t were also calculated averaging these value at the final tightening process stage, F=4 kN ~ 6 kN. K and K_t in the final stage roughly correspond to K and K_t in plastic region. Fig. 7 shows the scatter bands of the two torque coefficients K and the two thread torque coefficients K_t in the early stage and the final stage for A5056 aluminum alloy bolts on the each lubricated

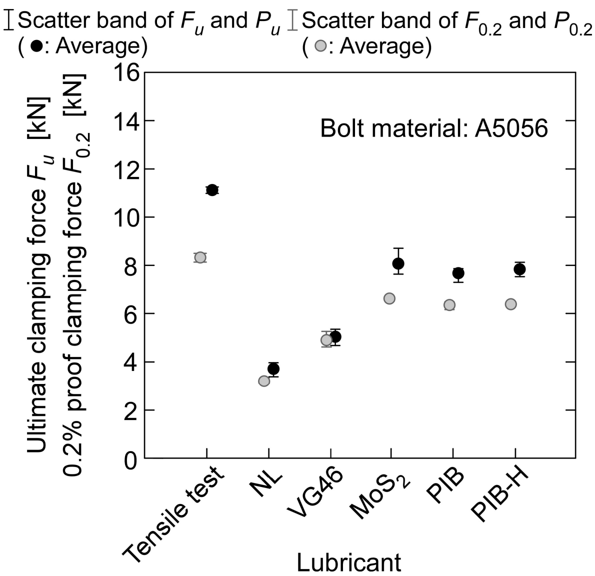

Fig. 5 Ultimate clamping force F_u and 0.2 % proof clamping force $F_{0.2}$ of A5056 bolts tightened under each lubricated condition.

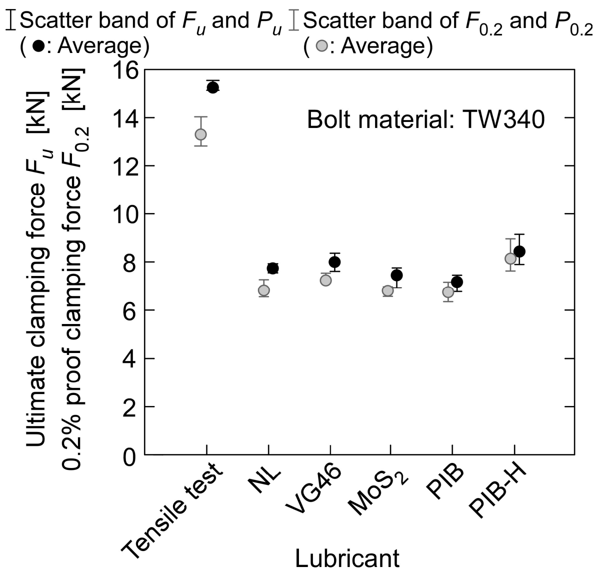

Fig. 6 Ultimate clamping force F_u and 0.2 % proof clamping force $F_{0.2}$ of TW340 bolts tightened under each lubricated condition.

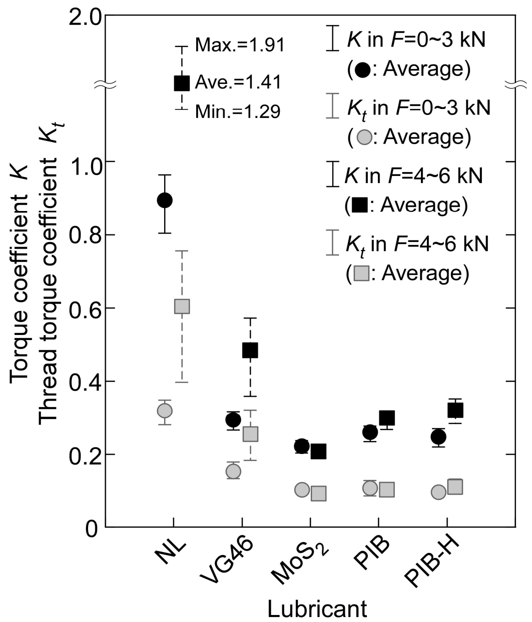

Fig. 7 Torque coefficients K and thread torque coefficient K_t of A5056 bolts

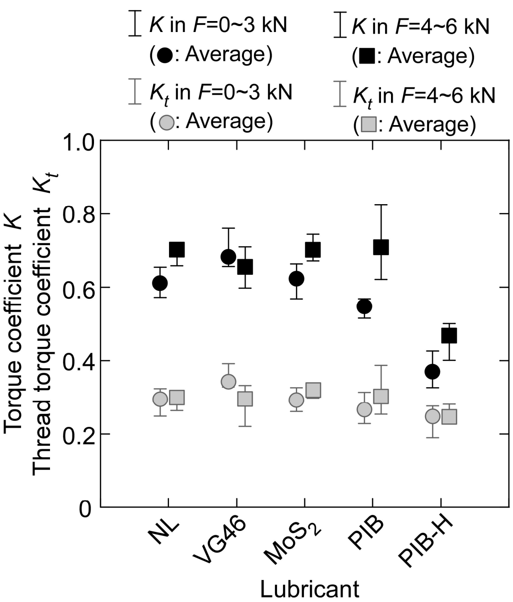

Fig. 8 Torque coefficients K and thread torque coefficient K_t of TW340 bolts

condition. Fig. 8 also shows the scatter bands of K and K_t in the early stage and the final stage for TW340 pure titanium bolts on the each lubricated condition. In Fig. 7 and 8, the black solid lines show the scatter bands of K in the early stage, and the black circle shows these averages. The black dotted lines show the scatter bands of K in the final stage, and the black square shows these averages. The grey solid lines show the scatter bands of K_t in the early stage, and the grey circle shows these averages. The grey dotted lines show the scatter bands of K_t in the final stage, the grey square shows these averages.

It can be seen from Fig. 7 and 8 that the tightening strengths F_u and $F_{0.2}$ became low, if the torque coefficients K and K_t were high regardless of the stages. We can confirm that there are good correlations in the both bolts. It can be also seen that the correlations between the torque coefficients K and K_t and the tightening strengths in the final stage were stronger than the correlations between the torque coefficients K and K_t and the tightening strengths in the early stage. The reason is considered as the follows. When the bolts reach the tightening strengths, F_u and $F_{0.2}$, the bolts have already exceeded the yield stress. Therefore it is considered that the torque coefficients K and K_t at the final region, which is the torque coefficients in the plastic region, have a strong correlation.

5 CONCLUSIONS

The tightening tests under the several lubricated conditions for A5056 aluminum alloy bolt and TW340 pure titanium bolts were conducted in order to propose the appropriate lubricants for the tightening. The results obtained in this study are summarised as follows.

1. The tightening strength of A5056 aluminum alloy bolt, the proof clamping force and the ultimate clamping force, in the tightening tests under the lubricated conditions by MoS2 grease and polyisobuthylene were about 20 % lower than the tensile strength. The tightening strength in the tightening tests under the lubricated by machine oil decreased about 50 %, and the tightening strength under no lubricated condition decreased over 50 %. As the results, it was considered that MoS2 grease and polyisobuthylene are the appropriate lubricants for A5056 aluminum alloy bolts to maintain the tightening strengths.
2. The tightening strength of TW340 pure titanium bolts decreased until half of the tensile strength approximately. The tightening strengths did not almost depend on the lubricated condition except for polyisobuthylene with high kinetic viscosity. The tightening strengths under the lubricated condition by the polyisobuthylene with high kinetic viscosity were about 10 % higher than others. As the results, it was considered that polyisobuthylene with high kinetic viscosity are better lubricants for TW340 pure titanium bolts.

6 REFERENCES

[1] K. Westphal, et al., Joining of Magnesium Components Using Al Fasteners, Journal of Light Metal Age, pp.2-3, 2005.

[2] D. Croccolo, M. D. Agostinis, N. Vincenzi, Influence of Tightening Procedures And Lubrication Conditions on Titanium Screw Joints for Lightweight Applications, Tribology International, Vol.55, pp.68-76, 2012.

[3] D. Jörn, P. Kohorst, S. Besdo, M. Rücher, M. Stiesch and L. Borchers, Influence of Lubricant on Screw Preload And Stresses In A Finite Element Model For A Dental Implant, The Journal of Prosthetic Dentistry, Vol. 112, Issue 2, pp.340-348, 2014.

[4] G. Gerstmayr, G. Mori, H. Leitner, W. Eichlseder, On the Applicability of High Strength Self-tapping Aluminum Bolts in Magnesium Nut Materials for Automotive Applications, Journal of Material Corrosion, Vol.61, No.5, pp.379-387, 2010.

[5] E. Leidich, S. Schuller, D. Grober, H. Lang and B. Bruzek, Investigation into Friction Coefficients of Matched EN AW-6082 Specimens Including Qualitative Reliability And Applicability of Bolted Connections, Materialwiss Werkstofftech, Vol.41 No.9 Page.776-783, 2010.

[6] V. E. Oliker, et al., Tribological Properties of Detonation Coatings Based on Titanium Aluminides and Aluminium Titanate, Powder Metall. Met. Ceram., Vol.44 No.11−12 Page.531-536, 2005.

[7] W. Eccles, I. Sherrington, and R.D. Arnell, Frictional Changes During Repeated Tightening of Zinc Plated Threaded Fasteners, Tribology International, Vol.43, pp.700-707, 2010.

[8] B. Walters, A New Approach to Tightening Bolts, Sealing Technology October 2005, pp.6-8, 2005.

[9] S. Hashimura, Yu Kurakake, Yukio Miyashita, Shigeru Yamanaka and Genki Hibi, The Tightening Characteristics of Magnesium Alloy Bolts, Transaction of the JSME, Journal of Solid Mechanics and Materials Engineering, Vol.5, No.12, pp.732-741.

Proceedings of the 4th International Conference on
Fracture Fatigue and Wear, pp. 161-166, 2015

FRETTING WEAR PERFORMANCE OF W460 HIGH STRENGTH STEEL UNDER UNLUBRICATED SLIDING CONDITIONS

N. Arun Prakash[1], T.T. Zhu[2] and C.J. Bennett[2]

[1]University Technology Centre in Gas Turbine Transmission Systems, The University of Nottingham, United Kingdom
[2]Department of Mechanical, Materials and Manufacturing Engineering, The University of Nottingham, United Kingdom

Abstract: Fretting wear performance of the homogenous specimen pairs of high strength alloy steel, BÖHLER W460 under normal laboratory conditions was investigated. Fretting wear studies were conducted under an applied normal load of 250 and 650 N with displacement amplitudes of 25 and 100 µm in a cylinder-on-flat configuration. The hardness of the heated treated W460 specimen was in the range of 605 ± 15 HV30. The average values of the surface roughness (R_a) of the flat and cylindrical specimen are 0.40 ± 0.08 µm and 0.43 ± 0.10 µm respectively. Steady state tangential force coefficient increases with an increase in displacement amplitude and decreases with an increase in applied normal loads for the conditions examined. At low displacement amplitude, the total dissipated energy and wear volume decreases with increase in applied normal load which may be attributed to the change in the shape of the friction loops from quasi-static rectangular shape to elliptical shape i.e., from gross slip regime to mixed slip regime. At high displacement amplitude, the total dissipated energy increases with an increase in applied normal load and there is no appreciable change in wear volume for same displacement amplitude with an increase in applied normal load. The worn surface morphology of the fretted specimen examined by scanning electron microscope shows the presence of loose wear debris in the wear track, delamination cracks, delamination with large discontinuities, plate-like wear debris, oxide patches and formation of large cavities.

Keywords: Fretting wear; high strength steel; wear mechanism

1 INTRODUCTION

Fretting is a tribological mechanism of surface degradation occurring between two normally loaded contacting members as a result of cyclic loading, sustained for a large number of cycles, causing reciprocating slip typically in the order of a few tens of microns. The probability of encountering fretting in machine elements and engineering structures such as splines, bearing races, keys and keyways, clamped connections and mechanically fastened joints is extremely high during service due to vibration of the total system or variation in loads which may lead to damage of the contacting surfaces and can dramatically reduce the operating life of the components [1]. Fretting wear has been investigated for more than five decades by researchers and it has been reported that fretting damage can be influenced by more than fifty parameters [2]. Although the form of fretting wear is complicated in nature, the displacement amplitude and the applied normal load are considered as the two most important factors affecting the process of fretting action [3]. In fretting wear the role of wear debris is critical; as the wear debris gets accumulated between the mating surfaces it forms a compacted oxide bed, often resulting in the wear rate dropping significantly. The absence of an all-embracing wear law due to the complex relationship between fretting wear, slip regime and the evolution of wear debris in, or release from, the contacting interface makes the quantitative modelling of fretting wear phenomenon as a challenging topic. The effect of contact geometry on the fretting wear rate of the high strength alloy steel, SCMV, were studied by Warmuth et al. [4], who reported that less conforming contact resulted in higher wear rates and more conforming contact was associated with lower wear rates due to the fact that in more conforming contacts, higher levels of adhesive transfer and beds of metallic debris particles are observed. They also stated that the variation in the contact geometry does not affect the wear rate and wear mechanism due to the differences in contact pressure, but it is influenced by the amount of oxygen in the fretting contact zone and the amount of debris flowing out of the fretting contacts. Pearson et al. [5] studied the effect of temperature on the fretting wear behaviour of SCMV steel; they found that the wear rate and coefficient of friction of SCMV in contact with itself decreases with an increase in temperature and proposed this was due to the fact that oxide particles sintered at the contact interface surface to form a protective debris bed.

BÖHLER W460 is a newly developed, ultra high strength steel for motorsport and advanced engineering applications. The double vacuum melted production route leads to an ultra clean steel with excellent mechanical properties. Suggested applications for this steel are highly fatigue-loaded components such as camshaft, gears, bolts and drive shafts, all of which are susceptible to fretting wear where contact conditions exist. In this work, the fretting wear behaviour of BÖHLER W460 (i.e., W460 against W460), was investigated using a cylinder-on-flat configuration under various applied normal loads and displacement under dry sliding conditions.

2 TEST MATERIAL AND EXPERIMENT DETAILS

A series of fretting wear tests were conducted on the BÖHLER W460 (4.55 Cr, 3 Mo, 0.75 V, 0.5 C, 0.2 Si, 0.45 Mn and balance Fe by wt. %) high strength alloy steel at ambient temperature using a crossed cylinder-on-flat configuration, which results in a 10 mm line contact. The test material was initially cut into specimen blanks with a heat treatment allowance on all the sides. After the heat treatment process was performed, the raw material blanks were further machined into the final dimensions of the flat and cylindrical specimens ensuring that the decarburised layer formed by the heat treatment was completely removed from the specimen surface area. Figure 1 shows the cylinder-on-flat configuration of the specimen pair assembled for the fretting tests. The Vickers hardness of the heat treated W460 material machined surface was found to be in the range of 605 ± 15 HV30. The room temperature yield strength and ultimate tensile strength of the W460 material is 1800 and 2250 MPa respectively. The surface roughness of the flat and cylindrical specimen was measured using surface profilometer on six specimens with three repeats on each specimen. The average values of the surface roughness of the flat and cylindrical specimens were found to be 0.40 ± 0.08 µm and 0.43 ± 0.10 µm respectively.

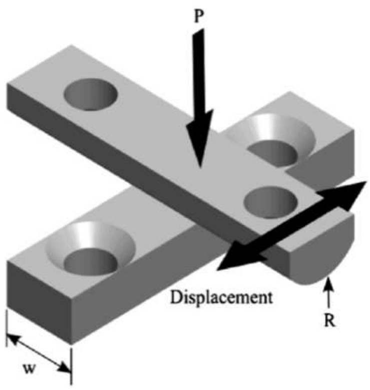

Fig. 1 Cylinder-on-flat specimen configuration used in the fretting experiments, where W = 10 mm, R = 6 mm, P is the normal load applied

The flat specimens were manufactured with a width of 10 mm while the cylindrical specimens have a radius of 6 mm. The full details of the fretting wear setup are given elsewhere [5] although a brief description of the test rig is presented here for ease of understanding. Prior to the experiment, all specimens were demagnetised, thoroughly degreased using detergent, rinsed with industrial methylated spirit (IMS) and acetone and finally dried using a hot air dryer. The flat specimen was mounted on a stationary lower specimen mounting block (LSMB) while the cylindrical specimen was mounted on a moving upper specimen mounting block (USMB). Fretting experiments were performed with displacement amplitudes of 25 and 100 µm and a constant frequency of 20 Hz with relative humidity of 35 ± 5 %. Fretting wear test conditions used in the present investigation are listed in Table 1. An electromagnetic vibrator generates a force, which is axially guided by a leaf spring, which produces the relative displacement between the flat and cylindrical specimens which was measured between the upper and lower specimen mounting block using a linear variable differential transformer (LVDT) and piezoelectric load cell was used to measure the tangential force at the contact interfaces. Dead weights were used to apply the normal loads using the lever arm to the USMB. The tangential force (Q) and relative displacement (Δ), were continuously measured using the control and data acquisition system programmed in LabVIEW. Both displacement and load sensors were calibrated (both externally and in-situ) under static conditions. The important quantitative fretting parameters such as the tangential force, displacement amplitude and dissipated energy were obtained by post processing the acquired raw data. The load and displacement signals were sampled at a rate of two hundred measurements per fretting cycle and the value of the tangential force coefficient per fretting cycle was calculated by dividing the maximum tangential force values obtained in a friction loop by the corresponding normal load applied. The behaviour of the contact throughout the experiment can be monitored by observing the fretting loops and frictional loops were obtained by plotting the friction force against the imposed displacement during the entire fretting cycle. Energy dissipation at the contact interface was estimated by calculating the area enclosed within a friction loop and the summation of energy dissipated throughout the fretting cycle gives the total dissipated energy for that individual fretting experiment. To evaluate the topography, the wear scar on both the flat and cylindrical specimens were scanned individually using a Taylor-Hobson Talysurf CL1 1000 tactile profilometer with a fine diamond stylus of 90° and 2 µm radius. Prior to scanning, the specimens were rinsed with acetone to remove the wear debris that is not adhered to the surface. In flat specimens, as the wear scars extend over the full width of the specimen, profiles were taken only on the central 8 mm of the scars at 0.25 mm spacing between the traces. For cylindrical specimens, the profiles were taken over an area covering the wear scar with 0.25 mm spacing between the traces. The specific wear rate were calculated using the empirical equation [4] as given below

$$\text{Specific wear rate } \dot{\mathrm{V}}^{-} = \frac{\mathrm{V}^{-}}{4\delta \mathrm{PC}}$$

where, V^{-} is the total wear volume of the flat and cylindrical specimens (mm^3), *δ* is the displacement amplitude (mm), *P* is the applied normal load (N), *C* is the number of cycles elapsed. The worn surface morphology of the fretted surfaces were characterised by using a Philips XL 30 SEM scanning electron microscope.

Table 1 Summary of the fretting test conditions

Normal load, P (N)	250 and 650
Displacement amplitude, Δ (µm)	25 and 100
Number of cycles (C)	100 x 10^3
Radius of the cylindrical specimen, R (mm)	6
Frequency, f (Hz)	20
Temperature (°C)	Ambient

3 RESULTS AND DISCUSSIONS

The tangential force coefficient under fretting sliding conditions is defined as the ratio of the tangential force amplitude and the applied normal load. The variation of tangential force coefficient with cycles elapsed for W460 steel fretted against W460 steel at different applied normal loads and displacement amplitude is shown in Figure 2. At the fretting contact region, the tangential force is considered to be produced through either trapping of the oxide debris in between the surface asperities, or by direct interlocking of surface asperities. At the beginning of fretting, the tangential force coefficient is low and after the completion of a few hundred cycles, the tangential force coefficient increases rapidly for all the conditions investigated. During the fretting process, the tangential force coefficient decreases/increases with increasing fretting cycles and reaches a more steady state value. The initial increase is attributed to the rapid removal of the natural lubricant layer on the contacting surface, which is a weak oxide and provides minimal protection to wear; this initial case is a two-body wear system [6]. As the fretting cycles progress, more and more wear debris are generated at the contact interface due to the repeated sliding action and these debris may remain stuck between the two contacting interfaces thereby forming a three-body wear system. This third-body (wear debris) acts as a natural barrier by separating the direct interaction between the two contacting interfaces, subsequently the local stress field is lowered, which prevents further crack nucleation and propagation and thereby the tangential force coefficient reaches a steady state value. Formation of the wear debris within the fretting contact interface normally specifies that fretting wear phenomenon has reached the steady state when the third-body dynamics will determine the fretting wear performance [7]. The tangential force coefficient decreases with an increase in applied normal loads under fretting for same displacement amplitude; this behaviour is similar to that reported by previous researchers [8, 9]. At low applied normal loads the presence of loose wear debris in the contact interfaces and low surface contact stresses makes the asperities interlock each other at the mating interfaces and results in high a tangential force coefficient irrespective of the displacement amplitude. As the displacement amplitude increases the tangential force coefficient increases for the same amount of the applied normal load. Surface contact stresses increase with an increase in the applied normal loads and the surface asperities at the contact interface are deformed resulting in a low tangential force coefficient [1]. To enable further comparison between the different parameters, the average values of the tangential force coefficient between 25 x 10^3 to 100 x 10^3 cycles was calculated and is presented in Figure 3 for the different fretting conditions investigated. The data shows that the steady state tangential force coefficient increases with an increase in displacement amplitude and decreases with an increase in applied normal loads.

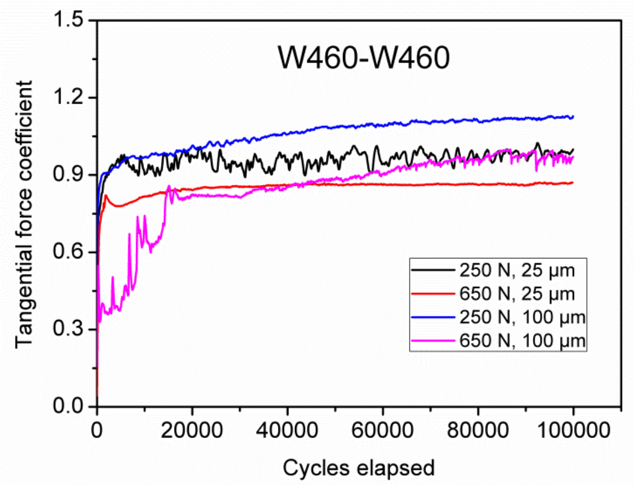

Fig. 2 Variation of the tangential force coefficient with elapsed cycles for W460 steel fretted against W460 steel at different applied normal loads and displacement amplitude

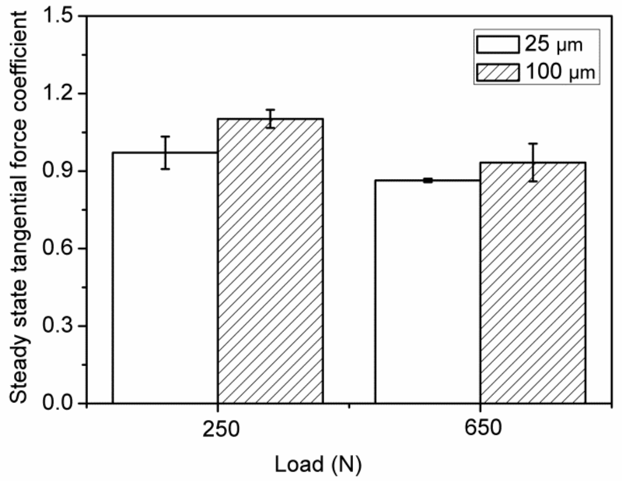

Fig. 3 Steady state tangential force coefficient plotted for the conditions

The friction force and relative displacement of the sample provides evidence about the nature of the contact that occurs between the contacting interfaces during fretting. Figure 4(a) represents the friction log, or cycle varying history of the force-displacement loops of the test carried out at a load of 250 N and displacement amplitude of 100 µm; from the figure it is clear that under these conditions, the contact interface is in the gross slip regime. The change in the slip regime is identified by the change in the shape of the friction loops from trapezoidal to a near elliptical shape. Figure 4(b) shows the characteristic, steady state friction loops at 50,000 cycles under the different conditions investigated. The quasi-rectangular shape of the force-displacement loop at low applied normal loads indicates the gross slip regime where the slip is spread over the entire contact area with a significant amount of dissipated energy. Under the gross slip condition, all the work done by fretting is irreversibly dissipated by displacement as friction; the condition is associated with severe wear. In the gross slip condition, the energy spent to move the specimen is dissipated in the form of heat at the contacting interfaces and the actual relative displacement may be considered as almost equal to the applied stroke [10]. Under gross slip, the shear stress is a maximum at the centre of the contact region while under partial slip conditions, the maximum shear stress occurs at the boundary of stick and slip zone. Figure 5 shows the graphical representation of the various fretting regime that occurred during fretting action for the different applied normal loads and displacement amplitudes carried out as part of this testing. It is observed that partial slip is present at 650 N load and 25 µm displacement, whereas at other displacement amplitudes and applied normal loads a gross slip condition exists.

As the displacement amplitude increases the area enclosed by the force-displacement curve increases, indicating that the energy required for the fretting action increases. Figures 6(a) and 6(b) show the influence of applied normal load and displacement amplitude on total energy dissipated and specific wear rate respectively. At low displacement amplitudes, the total dissipated energy and wear volume decreases with increase in applied normal load which may be attributed to the change in the shape of the friction loops from a quasi-static rectangular shape to an elliptical shape i.e., from gross slip regime to mixed / partial slip regime. At high displacement amplitude, the total dissipated energy increases with an increase in applied normal load and there is no appreciable change in the wear volume for the same displacement amplitude. Figure 7 shows the scanning electron microscope images of the W460 steel fretted against W460 steel at 250 N applied normal load and 25 µm displacement amplitude. During fretting action oxidized wear debris was formed within the contact and substantial amounts of loose dark brown wear debris are piled up on both the edges of the fretted specimen wear scar irrespective of the test conditions, which indicates that it is primarily composed of Fe_2O_3 particles with a small amount of un-oxidized metal. For all the conditions investigated, the surface of the wear scar is primarily metallic with small amount of oxidized debris on the outer edge of the wear scar. Figures 7(a) and 7(b) show the scanning electron microscope and back scattering electron microscope image showing the presence of metallic wear and oxide debris with loose wear debris. Figures 7(c) and 7(d) show the presence of delamination cavities and plate-like debris with loose wear particles on the contact surfaces respectively. For all the conditions tested the scanning electron microscope analysis shows the presence of loose wear debris in the wear track, delamination cracks, plate-like wear debris, oxide patches and the formation of large delamination cavities. The most predominant mechanism of failure in W460 steel fretted against W460 steel under these conditions is abrasive wear.

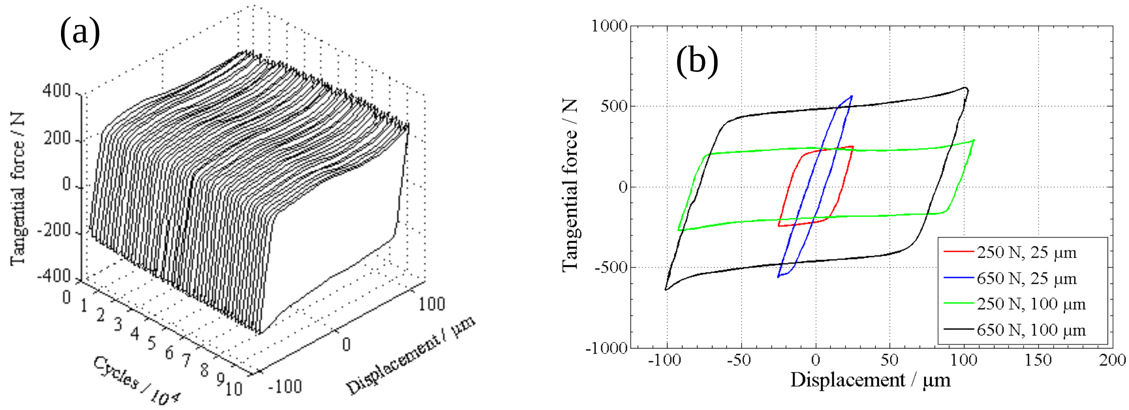

Fig. 4 W460 steel fretted against W460 steel (a) friction logs at 250 N, 100 µm (b) friction loop at 50,000 cycles

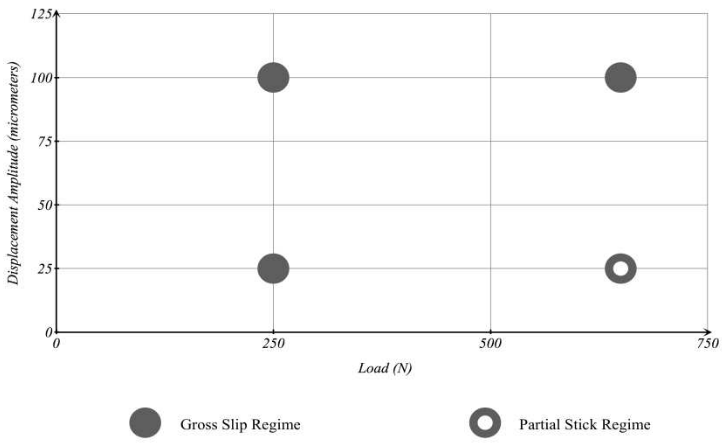

Fig. 5 Graphical representation of the fretting regime for the test condition investigated

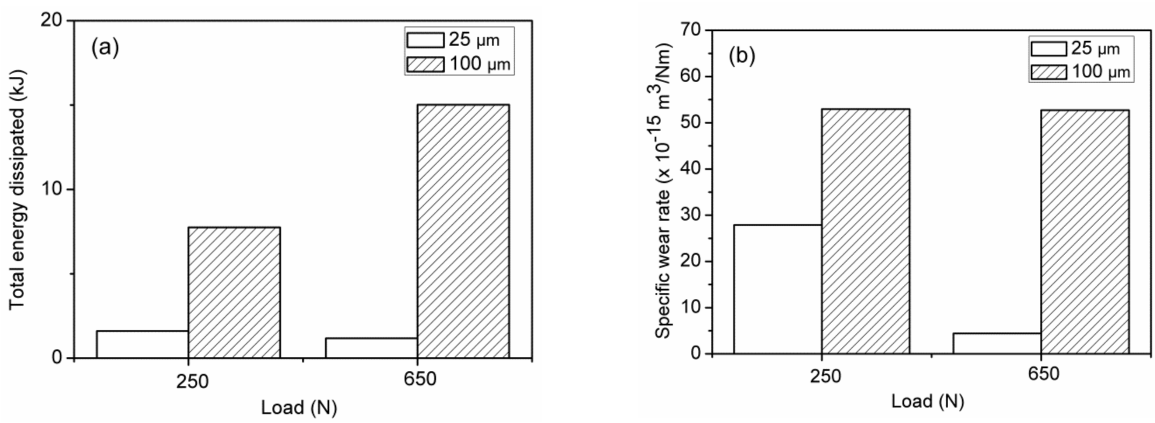

Fig. 6 Influence of applied normal load and displacement amplitude on (a) total energy dissipated and (b) specific wear rate

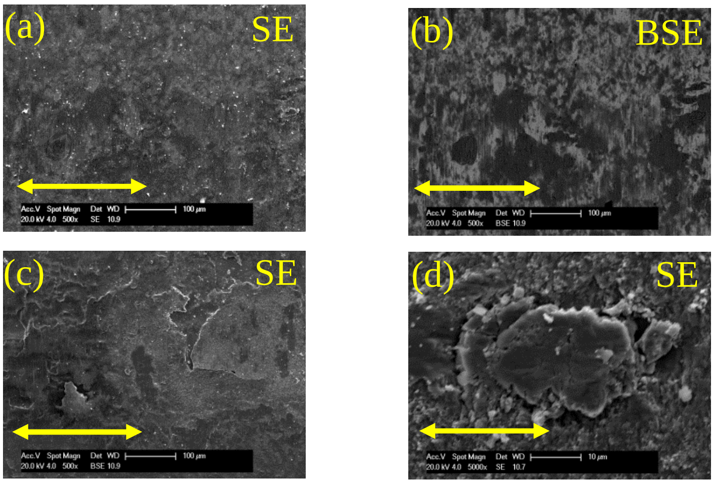

Fig. 7 SEM images of the W460 steel against W460 steel at 250 N, 25 µm (a & b) oxide debris with loose wear debris, (c) delamination with large discontinuities and (d) plate-like debris with loose wear particles

4 CONCLUSIONS

The fretting wear performance of W460 steel against W460 steel was examined using a cylinder-on-flat configuration. For the conditions studied, the steady state tangential force coefficient decreases with an increase in applied normal loads and increases with an increase in displacement amplitude. The total dissipated energy and wear volume decreases with increase in applied normal load for low displacement amplitude, which may be attributed to a change in the slip regime. At high displacement amplitude, the total dissipated energy increases with an increase in applied normal load, however with an increase in applied normal load for the same displacement amplitude, there is no appreciable change in wear volume. Abrasion was found to be the most predominant mechanism of failure in W460 under the fretting conditions investigated.

5 ACKNOWLEDGEMENTS

This work is part of a Collaborative R&T Project, SILOET II Project 6 High Temperature Capability - Compressor and Discs supported by the Technology Strategy Board and carried out by The University of Nottingham and Rolls-Royce plc.

6 REFERENCES

[1] N. Arun Prakash, R. Gnanamoorthy, M. Kamaraj, Fretting Wear Behaviour of Controlled Ball Impact Treated Aluminium Alloy Under Dry Sliding Condition, Surface and Coatings Technology, 207, 450–460, 2012.

[2] J. M. Dobromirski, Variables of fretting process: are there 50 of them? in M. Helmi Attia and R. B. Waterhouse (Eds.), Standardization of Fretting Fatigue Test Methods and Equipment, ASTM STP 1159, American Society for Testing and Materials, Philadelphia, 1992, pp. 60-66.

[3] O. Vingsbo, S. Soderberg, On Fretting Maps, Wear, 126(2) 131–147, 1988.

[4] A. R. Warmuth, S. R. Pearson, P. H. Shipway, W. Sun, The Effect of Contact Geometry on Fretting Wear Rates and Mechanisms for a High Strength Steel, Wear, 301(1-2), 491-500, 2013.

[5] S. R. Pearson, P. H. Shipway, J. O. Abere, R. A. A. Hewitt, The Effect of Temperature on Wear and Friction of a High Strength Steel in fretting, Wear, 303(1-2), 622-631, 2013.

[6] A. D. Sarkar, Friction and Wear, Academic Press, London, 1980.

[7] H. Mohrbacher, B. Blanpain, J. P. Celis, J. R. Roos, The Influence of Humidity on the Fretting Behaviour of PVD TiN Coatings, Wear, 180(1-2), 43-52, 1995.

[8] R. Ramesh, R. Gnanamoorthy, Effect of Hardness on Fretting Wear Behaviour of Structural Steel, En 24, Against Bearing Steel, En 31, Materials and Design, 28(5), 1447-1452, 2007.

[9] D. K. Zhang, S. R. Ge, Y. H. Qiang, Research on the fatigue and fracture behaviour due to the fretting wear of steel wire in hoisting rope. Wear, 255(7-12), 1233-1237, 2003.

[10] R. D. J. Mindlin, Compliance of Elastic Bodies in Contact, Applied Mechanics, 16, 259-268, 1949.

International Journal of Fracture Fatigue and Wear, Volume 3
Proceedings of the 4th International Conference on
Fracture Fatigue and Wear, pp. 167-173, 2015

WEAR AND CAVITATION EFFECT IN AN EPOXY FILLED WITH BORON AND SILICON NANOCARBIDES

J. Abenojar[1], J. Tutor[2], Y.Ballesteros[2], J.C. del Real[2] and M.A. Martínez[1]

[1] University Carlos III of Madrid, Spain
[2] University Pontificia Comillas, Madrid, Spain

Abstract: Cavitation is a complex process that includes the steps of nucleation, growth, coalescence, collapse and successive rebound of bubbles and/or clusters of vapour and/or gas in a liquid when varying its thermodynamic and hydrodynamic conditions during short periods of time. When cavitation occurs close to the surface of a solid, it causes localized damage due to the high impact pressures that exceed the yield strength of the material and/or as a consequence of the fluctuating stresses that promote surface fatigue. In many systems like hydraulic equipment, fluid pump impellers, ship propellers and steam turbines, etc. mechanical erosion can be a great problem. For this reason, a growing interest in polymer coatings for tribological applications has emerged in the last years, being epoxy resins are good candidates. This work focused on the analysis of surface damage of nanocomposites as epoxy-based coating. The epoxy resin used was a commercial resin, the fillers were boron and silicon carbides with particle size of 60 and 100 nm respectively, and they were used in two percentage (6 and 12 wt.%). Pin on disk test were carried out to evaluate wear. Cavitation test were performed on aluminium specimens coated with the nanoparticles/epoxy composites, to evaluate their effectiveness as wear-resistance coating. Wear tracks and cavitation samples were studied by Scanning Electron Microscopy (SEM). The results showed higher wear resistance of nanocomposites than clear epoxy resin, and also better cavitation resistance.

Keywords: Wear; Cavitation, Nanocomposites, Coatings.

1. INTRODUCTION

In many systems like hydraulic equipment, fluid pump impellers, ship propellers, hydrodynamic bearings, fluid seals, inlets to heat-exchanger tubes, diesel engine wet cylinder liners, hydrofoils, liquid metal power plants, steam turbines, etc., mechanical erosion could be a great problem, induced by the pulse pressure exerted by the collapse of vapour bubbles, causing surface damage [1,2]. Such process of the formation of vapour bubbles in low pressure regions within a fluid (when the hydrostatic pressure acquires a value lower than the saturation vapour pressure) is called cavitation. The mechanical erosion brought about by the cavitation is called cavitation erosion [3]. A great variety of materials and many different surface engineering processes have been applied to increase the cavitation resistance [1,3,4]. Many metallic and intermetallic compounds have been used as coatings due to their good cavitation erosion resistance by their high work hardening rate, high hardness, good oxidation and corrosion resistance [1]; also, many ceramics compounds have been used by their excellent wear resistance and high hardness and they are considered to be potencial candidates for applications needing high resistance to cavitation erosion [4]. Some authors [5,6] have provided useful data related to erosion rates for many materials, including polymers, but there is still a lack of specific information related to polymer coatings for potential use in tribological applications. Epoxy resins have shown been good results when used as coating on stainless steels by Garcia et al. [7].

The aim of this work is the use of nanocomposites as coatings with high resistance to wear and cavitation erosion. An epoxy resin filled with nanocarbides has been used by the high hardness of carbides. Silicon and boron carbides are widely used for abrasion applications. In other works composites with microparticles of silicon and boron carbides have been studied under wear conditions [8,9], showing problems due to lack of anchorage lack between particles and resin. However the composite with nano SiC showed better wear resistance that unreinforced resin [8].

2 EXPERIMENTAL PROCEDURE

2.1 Materials and fabrication of nano-composites

The used epoxy was a bi-component, with Epofer Ex 401 resin and Epofer E432 hardener (Feroca Composites, Madrid, Spain). It has low viscosity (1300 cps) at 25 ºC, and it cures at room temperature for 24 h. The resin-hardener mass ratio is 100:32.

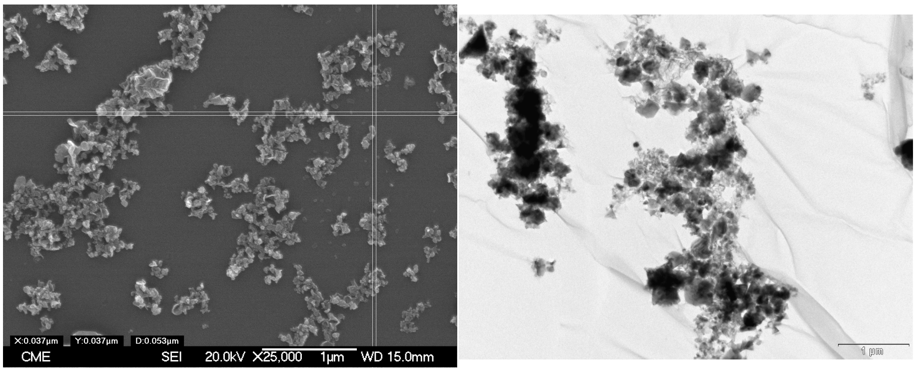

Fig. 1 Carbides used micrographs: (Left) B_4C; (Right) SiC.

The nanoparticles used in this work were: nano SiC (Bioker Research S.L., Oviedo, Spain) with average particle size 80-120 nm (Fig. 1 right), and nano B_4C (PlasmaChem GmbH Berlin, Germany) with average particle size 30-60 nm and its morphology shown in Fig. 1 left. The nanoparticles were added in two different percentages 6 and 12 wt.%. Among the methods used to disperse nanoparticles in a polymer, an extrusion method was selected in this work, with a previous deaeration of the resin. The mixture was poured into silicon moulds with shapes adequate for the different tests.

In the text and figures, the nomenclature will be: E (for the clear resin, Epofer), ESC (for nanocomposite with nano silicon carbide), EBC (for nanocomposite with nano boron carbide), and including 6 or 12 according to filler amount.

2.2 Wear test

Dry wear tests were carried out at room temperature using a pin-on-disk tribometer (Microtest, Madrid, Spain). A 6 mm diameter alumina ball was used for the pin. Test conditions were a speed of 120 rpm, with an applied load of 15 N, relative humidity below 30% and friction radius was 8 mm. The sliding distance was 1000 m.

For the wear test the bulk composites were used. The wear tracks were studied by scanning electron microscopy (SEM) Philips X-30, Philips Electronic Instruments, Mahwah, NJ, USA), in order to determine the mechanism of wear.

The wear resistance was calculated by weight loss according to ASTM G99 standard. Also coefficient of friction was measured following the same standard.

2.3 Cavitation erosion test

For cavitation tests, clear resin and nano-composites were used in form of coatings. Aluminium tips were cleaned with MEK (methylethylketone), and silanized with γ-GPS (3-Glicidoxypropyl-trimetoxysilane, Sigma Aldrich, Saint Louis, USA) to improve coating adhesion, and finally coatings were casted on them. The 1% solution of silane was hydrolysed for one hour in MilliQ water at pH 5 and dried in oven for 1 h at 100 ºC.

The cavitation tests were done according the ASTM G32 standard, with a Digital sonifier model S-450 (Branson Ultrasonic, Dambury, USA). The vibratory apparatus used for these tests produce axial oscillations of a test specimen inserted to a specified depth in the test liquid (water in the present experiments).

The conditions of cavitation test were a frequency of 20 kHz and amplitude of 25 microns. The tests were carried out in intervals of 5 min. Every 5 min the tips were dried and weighed, to determine the cumulative mass loss and the erosion rate. The tests were carried out until the stabilization the mass loss. As-manufactured samples were used for cavitation tests, as flat surfaces were obtained from casting. It is well known that roughness influences erosion cavitation [10], and processed surfaces have less roughness than the one obtained if samples were sanded.

Surfaces after cavitation test were evaluated by SEM. Before the analysis, the samples were gold coated using a sputtering system.

3 RESULTS

3.1 Wear

In the wear test, nanocomposites have higher wear resistance than clear resin, except for E12SC (Fig. 2). E6SC has the highest wear resistance. The EBCs present similar wear resistance than clear resin for both amounts of nanoparticles. Friction coefficients are also observed in Fig. 2. Only 6% nanocomposites have friction coefficients lower than clear resin.

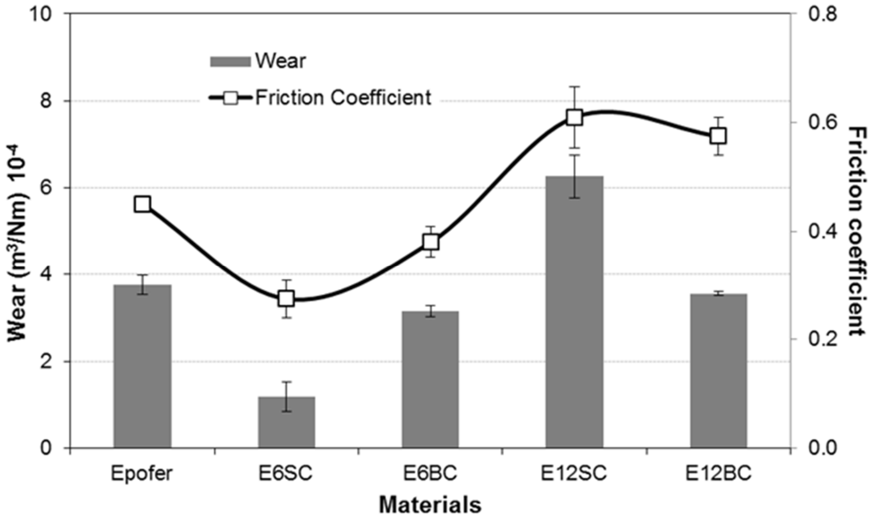

Fig. 2 Wear resistance and friction coefficient for clear resin and its nanocomposites.

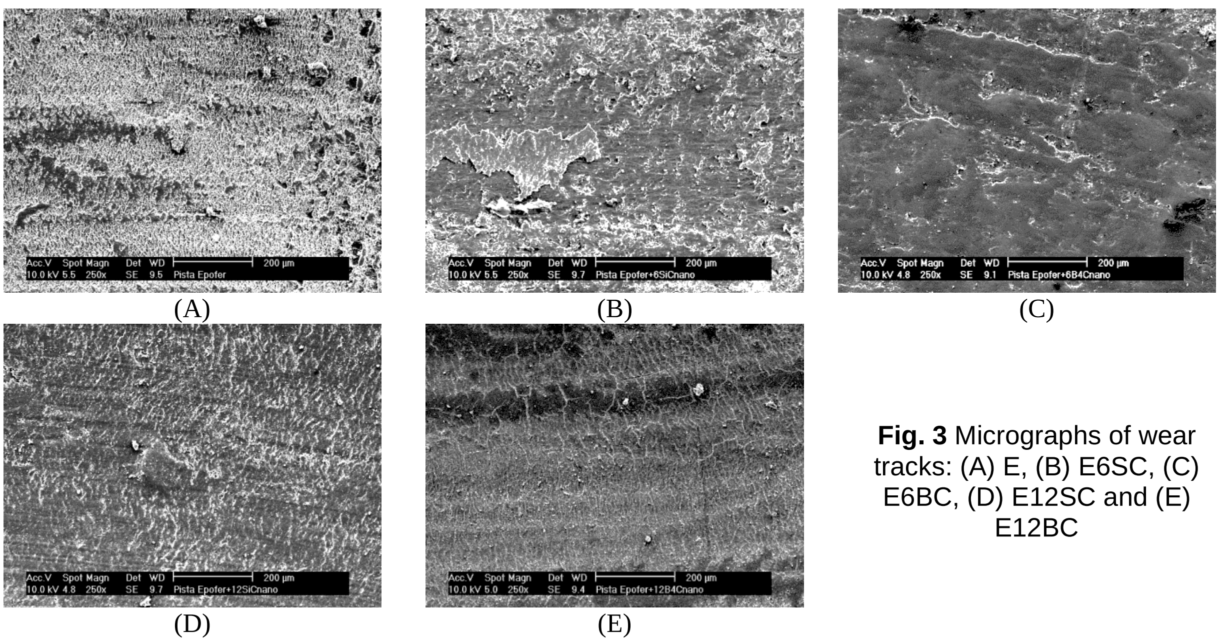

Fig. 3 Micrographs of wear tracks: (A) E, (B) E6SC, (C) E6BC, (D) E12SC and (E) E12BC

This behaviour can be explained in terms of wear mechanisms, as anchoring between nanoparticles and resin plays a very important role. In general wear tracks present abrasive wear, as it is observed in Fig. 3, where abrasion lines are found. These abrasion lines are defined more clearly in clear resin and nanocomposites with 12% of particles, which derives in high friction coefficients. Small cracks (produced by fatigue) are also found in clear resin and 12%-addition nanocomposites (Fig. 3 A, D and E). However in nanocomposites with 6% of filler, adhesive wear also takes place. Therefore they have low wear and friction coefficient (Fig. 2). The difference found between E12SC and E12BC is due to anchoring of nanoparticles (Fig. 3 D and E). The B_4C nanoparticles have some hydroxyls groups in their surface; these groups come from the manufacturing process. The OH groups can join better to the clear resin and they can not get loose so easily, as occurs in E12SC. In E12SC the nanoparticles can exert as third body and increase abrasive wear (Fig. 3 D).

3.2 Cavitation

Fig. 4 shows mass loss rate produced in cavitation tests for clear resin and the nanocomposites. Clear resin (E) shows a higher mass loss rate than the nanocomposites. Fig. 5, plotting cumulative mass loss vs time for materials, clearly shows that mass loss is higher for clear resin than for nanocomposites. Maximum values of mass loss are delayed for the clear resin.

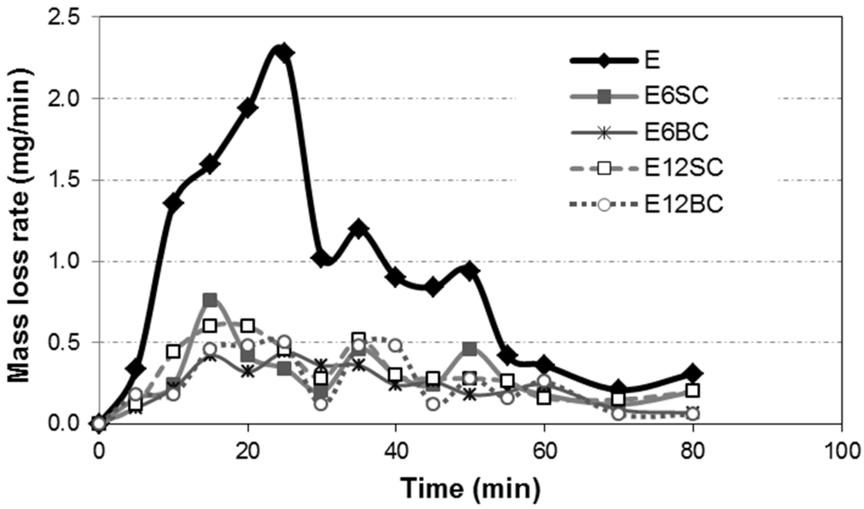

Fig. 4 Mass loss rate obtained by cavitation test for clear resin and nanocomposites.

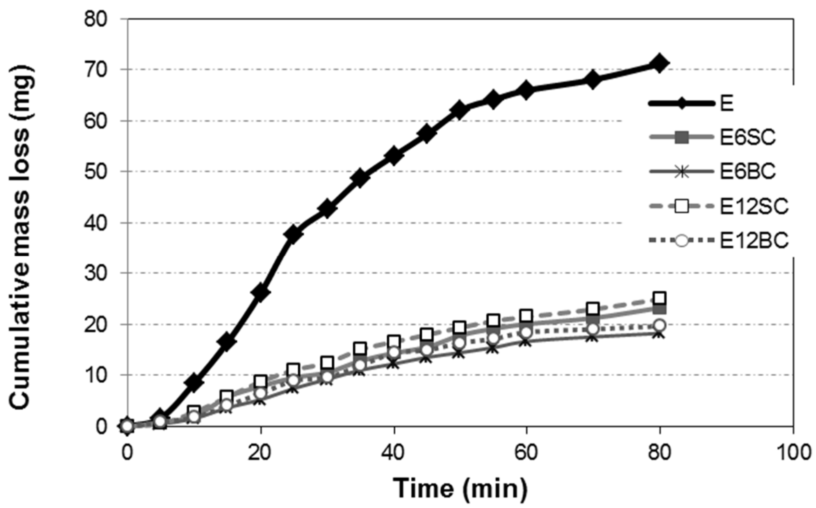

Fig. 5 Cumulative mass loss obtained by cavitation test for clear resin and nanocomposites.

The solid material absorbs the impact energy as elastic deformation, plastic deformation or fracture; the last two processes lead to the erosion of material. The more elastic or plastic deformation energy a material can absorb, the higher its resistance to cavitation erosion. Erosion is generally associated with mass loss of the surface, and it takes place after an incubation time. During this time, the materials are deformed elastically or plastically [11]. According to ASTM 32 standard, maximum and terminal erosion rate and incubation time (Table 1) can be calculated from Fig. 5.

Table 1 shows that maximum and terminal erosion rate in nanocomposites are smaller than in the clear resin. Among nanocomposites, slight differences are also found. In ESC, maximum and terminal erosion rates are similar (their values are inside measurement error, ±0.02); while in EBC maximum erosion is lower than in E12BC. This can be explained because of the lower density of E12BC than that of E6BC (Table 1), as porosity has a considerable influence on incubation time and on rate of erosion [12]. The incubation time is similar for all materials (clear resin and nanocomposites). The slight differences found can be due to measurement error (±1 min). Anyway, these times are very low when they are compared to metals, but the easy replacement of these coatings against metal repair allows its industrial use.

Mean depth of erosion (MDE) is obtained from mass loss, density and sample area by Eq. 1. The sample area was 2.778 cm^2 and density was calculated measuring volume and mass (Table 1). MDE is according to the data of mass loss, so depth of erosion is lower for nanocomposites than for clear resin. In EBC, MDE values lower than in ESC are found, being measurement error ±5 μm. Moreover the higher depth always corresponds to nanocomposites with 12% load.

$$MDE = \frac{\text{Mass loss}}{\text{Area} * \text{density}} \tag{1}$$

Table 1 Maximum and finish erosion rate, incubation time, density and mean depth of erosion at 60 min for clear resin and nanocomposites.

Materials	Maximum erosion rate (mg/min)	Terminal erosion rate (mg/min)	Incubation time (min)	Density (g/cm^3)	Relative density (%)	Mean depth of erosion at 60 min (μm)
E	2.11	0.26	7.3	1.07	99.07	222
E6SC	0.59	0.16	6.1	1.10	97.35	65.5
E6BC	0.39	0.08	5.8	1.10	98.21	54.7
E12SC	0.56	0.18	4.7	1.11	94.87	69.5
E12BC	0.48	0.06	6.4	1.12	96.55	59.2

The micrographs of cavitation samples show generalized cavitation in clear resin (Fig. 6 A); however in nanocomposites the cavitation is more localized in areas with defects, as porosity. This porosity is according with density lower than clear resin. In all nanocomposites, it is observed an outer ring without cavitation (Fig. 6 B, C, D and E) and also interior areas without cavitation (Fig. 6 B).

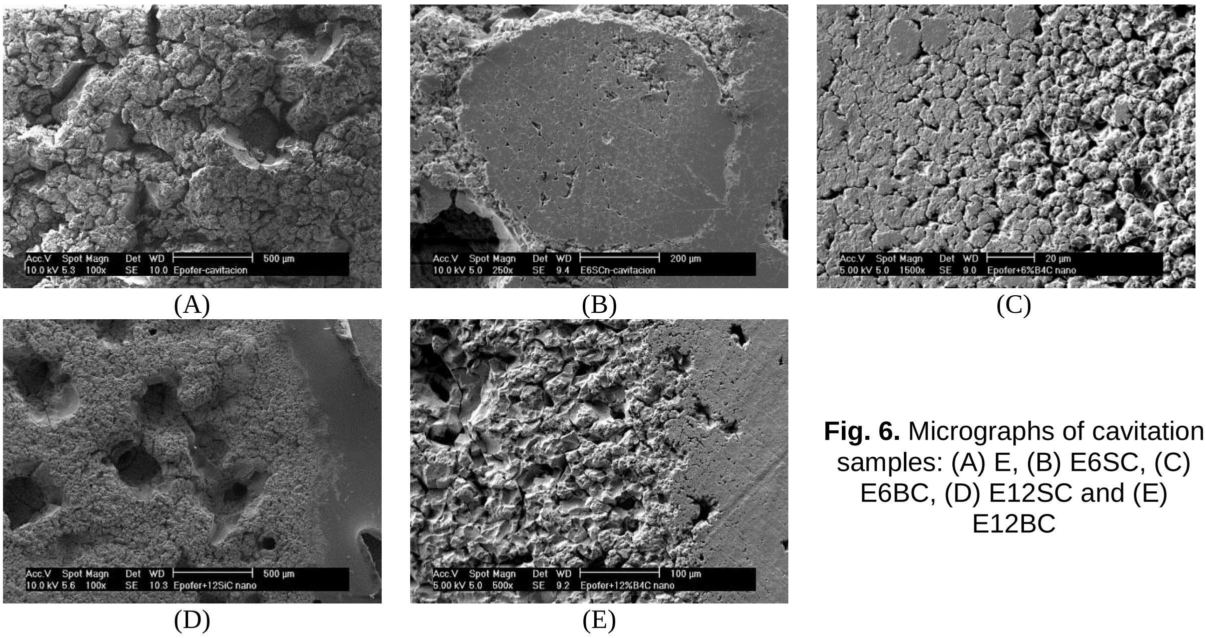

Fig. 6. Micrographs of cavitation samples: (A) E, (B) E6SC, (C) E6BC, (D) E12SC and (E) E12BC

4 CONCLUSIONS

In this study it has been proved possible to use epoxy matrix nanocomposites as coatings against cavitation erosion. The percentage of load (filler) and its anchoring with matrix and a good mixture are key aspect to increase the resistance to cavitation and erosion wear.

Nanocomposites with 6% fillers present better behaviour than nanocomposites with 12%. Between E6BC and E6SC, the results have demonstrated better properties in the E6BC, for its best anchoring with the matrix.

The manufacturing of these nanocomposites as paints could allow fast repairs industrially.

5 ACKNOWLEDGEMENTS

The authors would like to acknowledge to Fernando Pérez (laboratory technic of Mechanical Department of University Pontificia Comillas) his help in the performing of this work.

6 REFERENCES

[1] C.E. Brennen, Cavitation and Bubble Dynamics, Oxford University Press, New York, 1995.

[2] J.T Chang, C.H. Yeh, J.L. He, K.C. Chen, Cavitation Erosion and Corrosion Behavior of Ni–Al Intermetallic Coatings, Wear 255, 162-169, 2003.

[3] G. Bregliozzi, A. Dischino, H. Haefke, J.M. Kenny, Cavitation Erosion Resistance of a High Nitrogen Austenitic Stainless Steel as a Function of iIts Grain Size, Journal of Materials Science Letters, 22, 981-983, 2003.

[4] C.T. Kwok, H.C. Man, F.T. Cheng, Cavitation Erosion and Pitting Corrosion of Laser Surface Melted Stainless Steels, Surface and Coatings Technology, 99, 295-304, 1998

[5] T. Okada, Y. Iwai, K. Awazua, A Study of Cavitation Bubble Collapse Pressures Erosion part 2: Estimation of Erosion from the Distribution of Bubble Collapse Pressures, Wear 133, 233-243, 1989

[6] S. Hattori, T. Itoh, Cavitation Erosion Resistance of Plastics, Wear 271, 1103–1108, 2011.

[7] G.L. García, V. López-Ríos, A. Espinosa, J. Abenojar, F. Velasco, A. Toro, Cavitation Resistance of Epoxy-based Multilayer Coatings: Surface Damage and Crack Growth Kinetics during the Incubation Stage, Wear 316, 124–132, 2014

[8] J. Abenojar, M. A. Martinez, M. Pantoja, F. Velasco, J. C. del Real, Epoxy Composite Reinforced with Nano and Micro SiC Particles: Curing Kinetics and Mechanical Properties, The Journal of Adhesion. 88, 1-18, 2012.

[9] J. Abenojar, M. A. Martínez, F. Velasco, V. Pascual-Sánchez, J. M. Martín-Martínez, Effect of Boron Carbide Filler on the Curing and Mechanical Properties of an Epoxy Resin. The Journal of Adhesion 85, 216–238, 2009

[10] M. Pohl, J. Stella, Quantitative CLSM Roughness Study on Early Cavitation-Erosion Damage, Wear 252, 501–511, 2002

[11] ASM International, Friction, Lubrication and Wear Technology, in: ASM Handbook, 1992

[12] L. Boccanera, S. Rodrigues, A.J. Almeida Buschinelli, C.R. Rodrigues De Freitas, J. Valença dos Santos, Influência do Acabamento Superficial, Porosidade e Diluição sobre a Resistência à Cavitação de Revestimentos Soldados, XXIV ENTS, Fortaleza. 15 (1998) 1–14.

International Journal of Fracture Fatigue and Wear, Volume 3
Proceedings of the 4th International Conference on
Fracture Fatigue and Wear, pp. 174-179, 2015

EFFECT OF ATMOSPHERIC PLASMA TORCH ON BALLISTIC UHMWPE COMPOSITE

M.A. Martínez, J. Abenoja and B. Enciso

University Carlos III of Madrid, Spain

Abstract: Ultra high molecular weight polyethylene (UHMWPE) is a thermoplastic polymer. It is synthesized from ethylene monomer by a process based on metallocene catalysts. As a result is obtained the UHMWPE polymer with macro-molecules between 100000 to 250000 monomer units. Fibers are formed by oriented filament and have a yield strength of 2.4 GPa and a density of 0.97 (Dyneema SK75 for example). Several layers of unidirectional fibres or taffeta type cloths are used for personnel and vehicles armor.
The atmospheric plasma torch (APPT) is a cold plasma technique. Polymeric materials surfaces can be treated in a fast and environmentally correct way with it. APPT treatment modifies topography and chemistry of surfaces. This process also presents the industrial advantage of avoiding the vacuum step, thus an in-line procedure can be implemented. Contact angle measurements were used to determine wettability properties and to calculate the surface energy values using the Owens–Wendt–Rabel–Kaelble (OWRK) calculus method.
Dynamic tests were conducted according to ASTM D 5430 standard and using a drop-tower impact system. Composites were performed by five-layer of 78x78 mm (with and without APPT treatment). The matrices were made of EP (epoxy) and LDPE (polyethylene) and the samples were set between two clamps with an open surface of 55 mm diameter.

Keywords: Ultra high molecular weight polyethylene; Wettability; Atmospheric pressure plasma; T-peel test, Adhesion tensile test; Impact test.

1 INTRODUCTION

Ultra-high-molecular-weight polyethylene (UHMWPE) is a subset of the thermoplastic polyethylene. The sintering is performed from ethylene monomers, which are joined together to form the basis of polyethylene. Ultra-high-molecular-weight polyethylene molecules are several orders of magnitude greater than high-density polyethylene (HDPE) molecules. This is due to a synthesis process based on metallocene catalysts. As a result, UHMWPE molecules typically have 100000 to 250000 monomer units per each molecule compared to HDPE molecules which have 700 to 1800 monomers. The longer chain serves to transfer load more effectively to the polymer backbone by strengthening intermolecular interactions [1]. It is known that the UHMWPE fiber, as main constituent of the laminate, shows only rate-sensitivity in the creep regime but hardly at quasi-static strain rates in ballistic. These results are obtained in a very tough material, with the highest impact strength of any thermoplastic nowadays manufactured [2,3]. Additionally, fibres are chemically inert and the bonding strength to other materials like resins is weak. Moreover, friction coefficient is very low, so the fibre is extremely slippery [4].

The energy of the projectile is absorbed by breaking the strong fibres while perforation of layers occurs [5]. During that process, the localized kinetic energy of the impactor is spread out to an increasing volume of the target. Besides this, permanent plastic deformation and delamination absorb also energy. It has been reported that laminated shields made of a resin, exhibit higher penetration resistance both working at low and high impact speed. This resistance is expected to be as a function of the grade of penetration and humectation of the adhesive between the woven fibres [6].

They are mainly used in ballistic fabrics for both flexible and rigid light shield applications. The UHMWPE materials with rigid characteristics are formed by several layers of fabrics fibres bonded by a polymeric matrix, such as low-density polyethylene, rubber, epoxy, etc. In order to increase the protection ability against the impact of high energy projectiles, high density ceramic components could be bonded to the surface (fig. 1). However, the adhesion of these materials to the composite surface is hindered by the low fibre wettability properties. The wettability characteristics of fibres as a reinforcement have received great interest due to the strong relationship between the mechanical behaviour of composite material and the fibre matrix-adhesion [7].

Polyethylene fibres are chemically inert, which is considered to be a positive factor, allowing excellent sunlight resistance and little degradation in aqueous environment, as compared to other organic and inorganic fibres. However, their chemical inertness does not allow sufficient interactions in order to produce a high interfacial bond with most polymer resins. Significant efforts have been proposed to improve fibre-resin adhesion by introducing the functionalities at the fibre surface that could interact with organic resins [8].

Three methods have been explored for polyethylene fibres, chemical etching, plasma treatment and coupling agents. The treatment at low pressure chamber plasma [9,10] of polyethylene fibres in an atmosphere of oxygen is the most effective among the many techniques studied. Plasma technology is an active medium consisting of energetic neutral. Ions and electrons act on a surface modifying its physicochemical nature without affecting bulk properties. Atmospheric pressure plasma torch (APPT) main effects are cleaning, decomposition of pollutants, surface etching and activation due to the introduction of polar nature radicals (-OH, - COOH, -CO, -NH). For this reason, surface energy is significantly increase and therefore, the adhesion properties of the polymers will be improved [11,12]. This process also presents the industrial advantage of avoiding the vacuum step, thus an in-line procedure can be implemented.

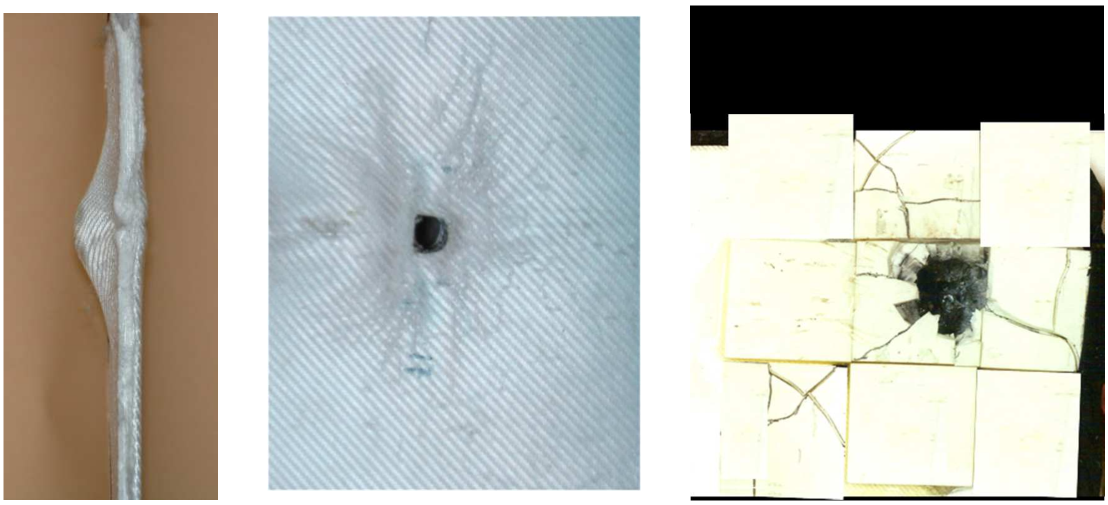

A B

Fig. 1 (A): Trauma and fracture of fibers after the impact of a projectile on ballistic fabrics for rigid light shield. B) Impact of a projectile on a ceramic-rigid layer shield [6].

2 EXPERIMENTAL PROCEDURE

2.1 Materials

Several fabrics can be used for the manufacture of materials with high impact resistance [13]. The main characteristics of the fabrics are shown in table 1. In fig. 2 can be observed the appearance of the two fabrics used.

Table 1 Tested fabrics

Fabric	Shape
BT	SK66 fibers are woven and laminated forming a continuous roll. The fibers are arranged in a woven structure of 0º/90º
UD	HB50 fibers 0°/90° cross-plied uni-directional fibre composites from yarns and rubber matrices

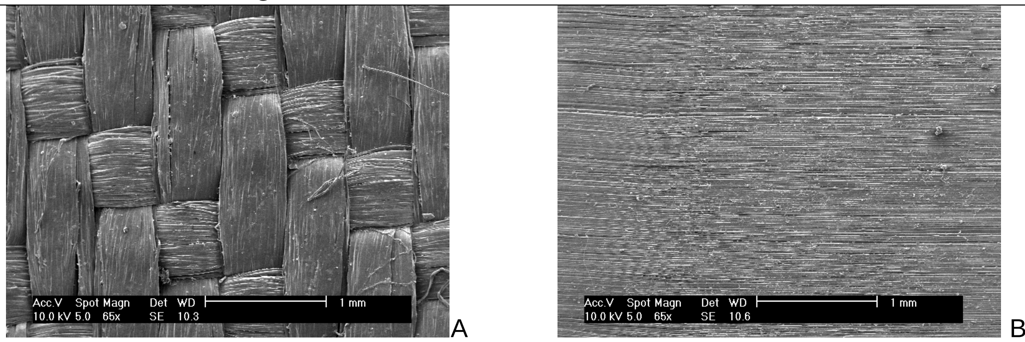

Fig. 2 UHMWPE fabrics with A) BT and B) UD

The employed adhesives are elastic polyurethane (SIKAFLEX-252, provided by SIKA S.A.U. Spain), a rigid epoxy (ARALDITE RAPID provided by Ciba-Geigy, S.A. Spain) and low density polyethylene compacted for 20 minutes at 120 °C under a pressure of 250 N/cm^3.

2.2 Atmospheric pressure plasma treatment (APPT)

Material was treated with an atmospheric pressure plasma device which operating conditions are frequency of 50/60 Hz, 230 voltage and 16 A (PLASMATREAT GMBH, mod. FG 3001, Steinhagen, Germany). High energy condition (13 mm, 0.5 mm/s) was tested, without observing a change in colour of the material, which would be indicative of UV radiation degradation (fig. 3).

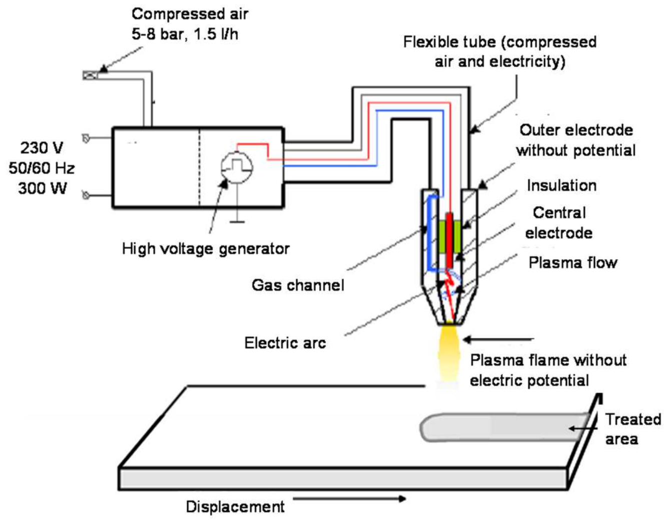

Fig. 3 Atmospheric plasma torch scheme

2.3 Contact angle and surface energy calculations

Diiodomethane, distilled water and glycerol were the test liquids selected for contact angle measurements. They cover a wide range of polar and disperse fractions. Contact angle measurements have been performed on the untreated and APPT treated samples. For the contact angle measurements a goniometer Dataphysics Contact angle system OCA 30-2 from Data Physics Instruments (GmbH, Filderstadt, Germany) was used. The model is able to measure in a range of 1 to 180º with an accuracy of ± 0.5º. The instrument contains a 3x zoom and a software SCA 202 V.3.11.13 build 162.

The surface energy is calculated according to Owens-Wendt-Rabel-Kaeble method.

2.4 Mechanical tests

The quasi-static tests were carried out with a Microtest (Microtest, Madrid, Spain) machine provided with a 1 kN load cell. Adhesion tensile tests were performed in order to ensure that APPT treatment improves the adhesion strength of rigid materials used for shielding steel or ceramic materials. On the other hand, tensile test method is used to determine the force required to separate a steel dolly (20 mm diameter) fixed to a specific area of the material. The test was performed following the ASTM D 4541 standard. The standard procedure was developed for metal substrates, but it may also be suitable for other rigid substrates such as some type of polymers and wood. Woven specimens of 50x50 mm were previously bonded with a rigid adhesive to an aluminium sheet to maintain its rigidity as shown in fig 4A. Once the bonding had been cured, the system was tested with the tensile test (relative to the plane of the adhesive bond) at a speed of 1mm/min.

The T-peel test was used to prove the resistance variation of the adhesive bonding after plasma treatment. Fabric specimens (formed by two pieces) of 30x80 mm were also used, bonded by adhesive (fig. 4B), according to the standard ASTM D1876-08

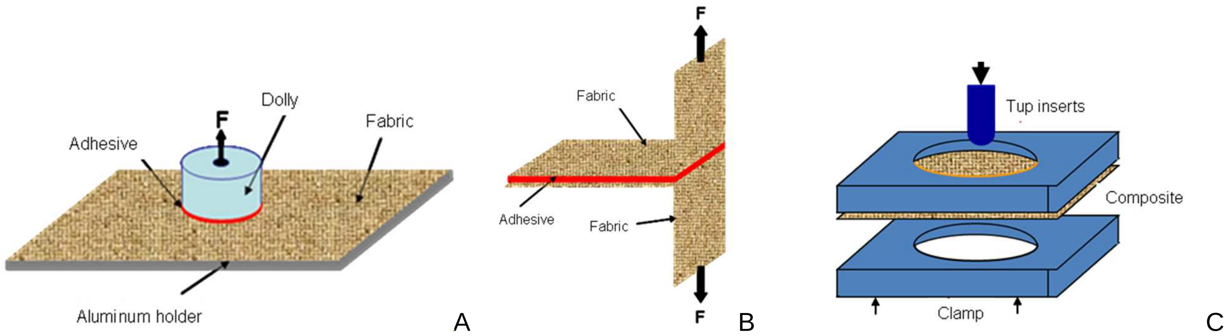

Fig. 4 A) Adhesion tensile test, B) T-peel test, C) Impact test

Dynamic tests were conducted in accordance with ASTM D 5430 98 standard and a drop-tower impact system (CEAST 9350, Instron Barcelona, Spain). Using suitable instrumentation, the load on the specimen is continuously recorded as a function of time and/or specimen prior to the fracture. A semi-spherical tip of 3220 g and 20 mm diameter was used. Specimens of 70x70 mm five-layer-fabric composites (with and without APPT treatment) were prepared. Matrices were made of EP (epoxy) and LDPE (low density polyethylene) and the samples were set between two clamps with an open surface of 55 mm diameter (fig. 4C).

3 RESULTS AND DISCUSSION

Untreated samples show high contact angle values (above 100º), which is due to a significant hydrophobic behaviour. After APPT treatment, all data decrease because of the surfaces functionalization. The creation of oxidized groups give rise to the polar fraction of surface energy, so water and glycerol contact angles decrease in a higher extent than diiodomethane which is almost pure disperse.

According to table 2, the results of surface energy for untreated samples have low levels and dispersed behaviour. When the fibres are modified by APPT, the polar component of the surface energy reaches values above 40 mJ/m^2. This great increase is based on a more polar character of the fibres.

Table 2 Variations of surface energy fraction of fabric samples untreated and treated with APPT. (mJ/m^2)

	BT		UD	
Surface energy fraction	**Untreated**	**Treated**	**Untreated**	**Treated**
E_{total}	22.78	42.70	45.57	49.25
E_{polar}	0.04	42.42	12.32	43.42
E_{disp}	22.74	0.28	33.26	5.83

As explained above, this improvement in polarity is caused by two main effects on the UHMWPE fibres surface.

A) Surface chemistry is changed by functionalization with oxygen and/or nitrogen containing groups exhibiting a polar character.

B) SEM micrographs of fibres before and after APPT are observed in fig. 5 and 6. Fibres treated with APPT show a smoothening at a micro-scale. An improvement in roughness in some fibres was produced thanks to the creation of grooves as a consequence of the plasma flux impact [14]. In the UD material it is also observed the binder elimination of the material surface, so fibres are cleaner (fig. 6).

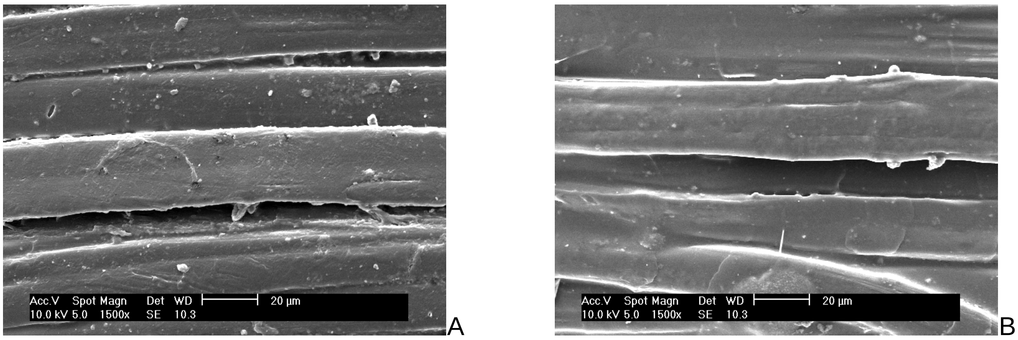

Fig. 5: BT fibres untreated (A) and plasma modified (B)

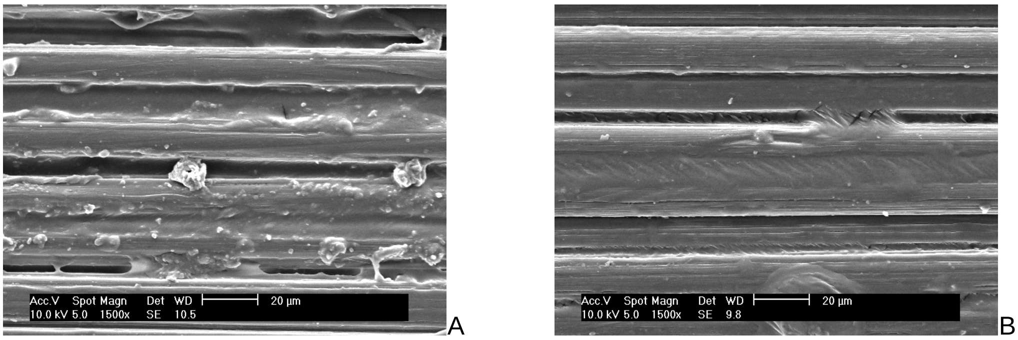

Fig. 6 UD fibres untreated (A) and plasma modified (B)

The average values obtained in the T-peel test and trauma values are presented in table 3.

Table 3 The mean values obtained in T-peel test and impact test trauma

Fabric	Adhesive	Untreated		Treated	
		T peel test (N/cm)	**Trauma (mm)**	**T peel test (N/cm)**	**Trauma (mm)**
BT	**EP**	6.5	12.50	7.1	12.73
	LDPE	2.3	6.73	2.2	7.02
UD	**EP**	6.8	7.07	2.0	5.37
	LDPE	>0.1	5.62	1.5	12.63

In these tests it is observed that plasma treatment does not substantially improve the adhesion with the adhesives used. Only can be remarked that trauma value is reduced in UD material bonded with EP.

Due to the fact that on these composites, layers of shielding of other materials will be added, the adhesion between this fabric and other elements was studied by tensile adhesion test. In table 4 the obtained results are shown. As it is observed, plasma treated composites have a higher tensile strength. It is important to highlight that in the cases of UD material, the delamination breakage of the composite occurs before the adhesive bonding failure (*).

Table 4 Adhesion tensile test results (kPa).

Adhesive	Untreated	Treated
BT	76	310
UD	37	45(*)

4 CONCLUSIONS

UHMWPE fibres modification with APPT treatment provides a polar component increase of the fibres surface energy which means that their wettability improves with certain adhesives. Contrary to what might be expected regarding aramid results [15], in this kind of reinforcements, APPT treatment does not improve bond strength between composite layers when adhesives, such as LDPE or EP, are used. In these cases T-peel tests results are low, which involves very deep and extensive traumas.

The adhesion tensile tests show that after APPT treatment, joint mechanical resistance between each fabric and the aluminium dolly has increase significantly. This improvement in resistance is lower for the UD material because, as already mentioned, the material fails by delamination before the adhesive joint breakage occurs. Therefore, this treatment improves the fabric union with other materials, such as metals or ceramics.

5 REFERENCES

[1] H. L. Stein. Ultrahigh molecular weight polyethylenes (UHMWPE). Engineered Materials Handbook Volume 2: Engineering Plastics. Cyril A. Dostal (Ed.). ASM, USA 1988. pp 167–171

[2] J. Rodriguez, I.S. Chocron, M.A. Martinez, V. Sánchez-Gálvez. High strain rate properties of aramid and polyethylene woven fabric composites. Composites Part B: Engineering. 27, 147-154, 1996

[3] I.S. Chocron, J. Rodriguez, M.A. Martinez, V. Sánchez-Gálvez. Dynamic tensile testing of aramid and polyethylene fiber composites. International Journal of Impact Engineering 19, 135-146, 1997

[4] R. Marisse. Design with Ultra Strong Polyethylene Fibers Materials Sciences and Applications. 2, 319-330 2011. doi:10.4236/msa.2011.25042

[5] M.B. Mukasey. J. L. Sedgwick D. W. Hagy, "Ballistic resistance of body armor", NIJ 0101.06, US Department of Justice, Office of Justice Programs, Washington, DC, US, July 2008

[6] C. Navarro, M.A. Martinez, R. Cortes, V. Sanchez, Some observations on the normal impact on ceramic faced armours backed by composite plates, International Journal of Impact Engineering, 13,145-156, 1993

[7] G. Dorey, The Fibre-Matrix Interface and Composite Strength in Composite Materials in Aircraft Structures, D. H. Middleton (Ed.). Longman Scientific and Technical, New York, 1990, pp. 50-68

[8] J.K. Kim, Y. W. Mai. Engineered Interfaces in Fiber Reinforced Composites. Elsevier Science. Nederland 1998 pp 201-205.

[9] N.H. Ladizesky, I.M. Ward. A study of the adhesion of drawn polyethylene fiber/polymer resin systems. Journal of Materials Science. 18, 533-544, 1983

[10] I.M. Ward. A review of recent developments in the processing and properties of oriented polyethylene. Plastics, Rubber and Composites Processing and Applications. 19, 7-13, 1993

[11] N. Encinas, B. Díaz-Benito, J. Abenojar, M.A. Martínez. Extreme durability of wettability changes on polyolefin surfaces by atmospheric pressure plasma torch. Surface Coatings Technology 205, 396-402, 2010.

[12] F. Caiazzo, P. Canonico, R. Nigro, V. Tagliaferri, Electrode discharge for plasma surface treatment of polymeric materials, Journal of Materials Processing Technology, 58, 96-99, 1996

[13] Lightweight Ballistic Composites. Military and Law-Enforcement Applications A. Bhatnagar Ed, Honeywell International Inc., Elsevier, USA 2006

[14] S. Manolache, H. Jiang, F. Denes, Generation of nanotopographies on polymeric substrates by cold plasmas Polymer Surface Modification: Relevance to adhesion vol. 5. K.L. Mittal (Ed.). Koninklijke Brill NV, 2009, pp. 45-62

[15] M.A. Martínez, J. Abenojar. Effect of atmospheric plasma torch on ballistic woven aramid. 3rd International Conference on Fracture Fatigue and Wear. FFW2014. International Journal of Fracture Fatigue and Wear: Conference Series proceedings, 2, 34-39, 2014.

Proceedings of the 4th International Conference on
Fracture Fatigue and Wear, pp. 180-188, 2015

EFFECT OF CARBON CONTENT ON TRIBOLOGICAL BEHAVIOR OF AUSTENITIC MANGANESE STEELS UNDER IMPACT LOAD

F. Delgado[1,2], S.A. Rodriguez[1] and J.J. Coronado[1]

[1] Research Group of Fatigue and Surfaces, Mechanical Engineering School, Universidad del Valle, Cali, Colombia
[2] Military Aviation School, Colombian Air Force, Cali, Colombia

Abstract: Austenitic manganese steels are commonly used in applications which involve high contact pressure and impact between surfaces such as in mining machines, railroads, or in fragmentation of metals and plastics for recycling processes. This research analyses the wear behavior of austenitic manganese steels with two different chemical compositions, which were exposed to impact wear using a swing hammers tribometer. The highest peripheral speed of the hammers was 37 m/s and homogeneous metallic parts were used as processed material in the tribometer. Wear mechanisms such as adhesion between processed material and base material of the specimens as well as micro-cutting, micro-fracture and plastic deformation were identified. Specimens that contained 1.45 % C, 2.2% Cr, and 14.9% Mn presented lower mass loss and more noticeable strain hardening than those which contained 0.62 % C, 2.6% Cr, and 13.8 % Mn. The influence of hammer position inside the mill was neutralized by a suitable experiment design method. The running-in period was approximately 5 minutes for every set of hammers for both materials.

Keywords: Austenitic manganese steels; impact wear; running-in; wear mechanisms; strain hardening.

1 INTRODUCTION

Austenitic manganese steels are known for their remarkable high strain hardening and toughness. Those mechanical properties are a consequence of a manganese content which helps to stabilize austenitic matrix in the microstructure. Steels with the original composition (1.2% C and 12% Mn) were named Hadfield steels, although the term is used for other austenitic manganese steels with different carbon and manganese contents which can also include Cr, Ni or Mo. Fragmentation of metallic parts are among the most common applications of Hadfield steels. Curves which show the influence of carbon content on tensile strength and yield strength of austenitic manganese steels are presented by Higuera and Tristancho [1]. The results for Hadfield steels with 12.2 – 13.8% Mn show a stable value for tensile strength (830 MPa) when the carbon content is in the range of 1% -1.8% C, but this value decreases gradually for the range 1 - 0.4% C (522 MPa for 0.4% C). Results for yield strength show a stable value (410 MPa) for carbon contents in the range of 0.9 -1.8% C, but also show a gradual decrease for 0.9-0.4% C (175 MPa for 0.4% C). The results also show the effect of Cr, Ni and Mo additions which causes a decrease on the tensile strength in a 1.15% C Hadfield steel. Garcia and Varela [2] have studied the influence of manganese content on wear resistance (pin on disk test) in four austenitic manganese steels (1-1.5% C, 4-6% Mn). The highest wear resistance was found on steel with 6% Mn (the highest Mn content among the four steels) and 1.5%C (the highest C content among the four steels). The austenitic manganese steel with the highest initial hardness had the highest mass loss among the four materials tested. Bayraktar and Khalid [3] examined the strain hardening behaviour of thin metallic sheets (1.1 mm thickness) made of Hadfield steel by means of uniaxial tensile tests and stress-strain curves. They found that a fast strain rate (2 s^{-1}) during tensile test caused less strain hardening compared with strain hardening at slow strain rate (7.5 x 10^{-4} s^{-1}). Crack initiation on a swing hammer has been analysed by Brusa and Morsut [4]. They studied the dynamical behaviour of a hammer which belongs to a scrap shredding machine by means of finite element method and multi body dynamics and related the results with wear and crack initiation caused on the hole where the hammer is supported by a shaft. Nevertheless the research did not focus on the tribological behaviour caused by the recurrent impacts between hammer and scrap, nor the hammer material was austenitic manganese steel. Some studies have been done to stablish the abrasion resistance of Hadfield steels or other austenitic steels, or the mechanical behaviour of components under dynamical impact load, but there is few information about a quantitative tribological study of different austenitic manganese steels under impact load and the role of carbon content.

2 METHODOLOGY

2.1 Manufacturing of specimens

Blocks (hammers) of austenitic manganese steel produced by casting were cut using electro-discharge machining. The dimensions of a hammer are detailed on Fig.1. Chemical analysis was carried out via a Spectrophotometer Angstrom S-1000. Two sets of hammers with different chemical compositions named H1 and H2 were used and the chemical compositions are shown on Table 1.

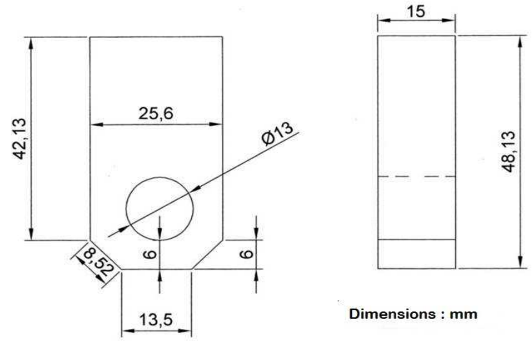

Fig. 1 Dimensions of a hammer

Table 1 Chemical composition of specimens

Material	%C	%Si	%Mn	%P	%S	%Ni	%Cr	%Mo
H1	0.619	0.596	13.88	0.047	0.063	0.94	2.613	0.82
H2	1.453	0.409	14.928	0.062	0.062	0.068	2.277	0.031

2.2 Swing hammers tribometer and processed material

The tribometer (hammer mill) used to perform the test has 10 hammers supported on four shafts (two shafts support two hammers and two shafts support three hammers) symmetrically distributed. The tribometer is driven by a 1 HP motor via pulleys. The rotational speed measured on the driving shaft was 4750 RPM. The positions of shafts are shown in Fig. 2. Metallic angles (30 mm x 13mm x2 mm) were fed as material to be processed by the mill and 120 gr/min were processed (twelve angles/min).

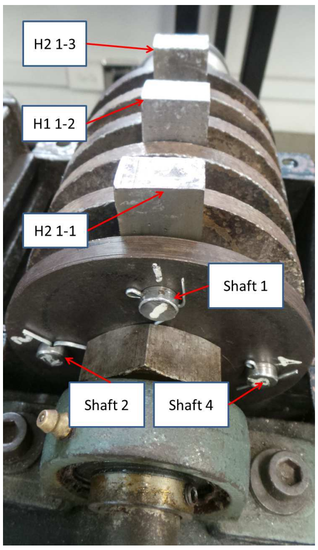

Fig. 2 Location of four shafts and its hammers

2.3 Experiment design

A set of five hammers of each steel were mounted on the hammer mill. To avoid an influence of hammer position on the comparison between the materials, the position of hammers was determined by an aleatory method. It was guaranteed that for each set of five hammers, three of them were mounted on shafts for three hammers and two of them on shafts for two hammers. Nevertheless, the influence of position on each material was also analysed. Hammers with a carbon content of 0.62 % were named H1 and those with carbon content of 1.45% were named H2. The other numbers define the position of the hammer inside the mill as show Fig. 2 and Fig. 3.

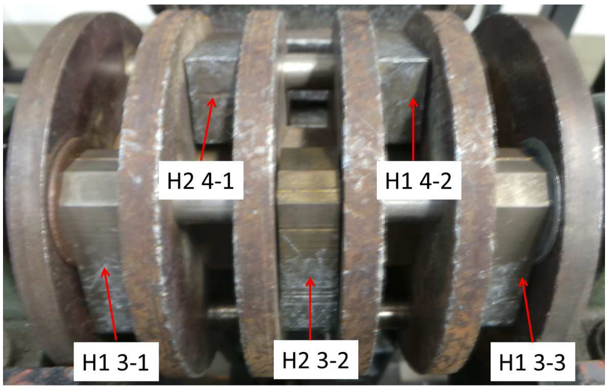

Fig. 3 Location of 5 hammers on shafts 3 and 4

Vickers Microhardness and mass loss of each hammer were measured using a Microhardness Tester FUTURE TECH FM-700, and a VIBRA AF-220E scale with a resolution of 0.0001g respectively. Fifteen measures of micro hardness were realized on each hammer for each step of the test to obtain an error of 3-8% on the global microhardness per material. A stereo microscope ADVANCED OPTICAL SE-2200 was used to examine effects of impact loads on the hammer surfaces. The microstructure of each material was observed using an ADVANCED OPTICAL XJL-17 microscope.

3 RESULTS

A coarse microstructure of austenitic grains is clearly observed on both materials. The grains have different forms and a very large size. Some of the smallest grains on each material are showed on Fig.4.

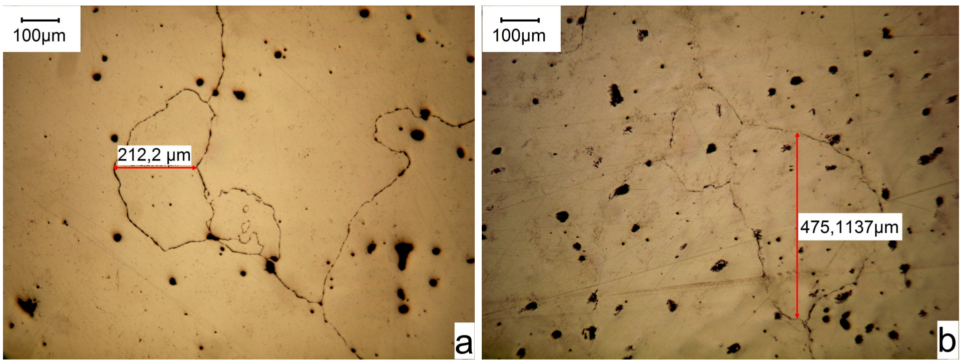

Fig. 4 Austenitic grains. a) H1 austenitic matrix. b) H2 austenitic matrix

Material H2 presents lower mass loss than material H1 through the test. Fig.5 shows, in two colours, a clear difference in mass loss between material H1 and H2.The highest mass loss on H2 hammers (H2 4-1) is slight lower than the lowest loss on H1 hammers (H1 1-2).The highest mass losses in material H1 were measured on hammers H1 2-1 and H1 4-2 both located on shafts of two positions and lowest mass loss was measured in hammers H1 1-2 and H1 3-3 both located on shafts of three positions The same trend was observed in H2 set. Hammers H2 4-1 and H2 2-2 located on shafts 4 and 2 (two positions) presented the highest mass loss, while hammers H2 1-3 and H2 3-3 located on shafts 1 and 3 had the lowest mass loss as can be seen on Fig.5. The shafts and the hammers on the shafts are symmetrically distributed. Distance between hammers on the shaft 1 is the same on the other 3 shafts. The central hammers on shafts 1 and 3 are located exactly in the middle of the shaft length. The processed material was fed manually at a constant rate, sequence and direction along the whole length of the hopper. Each single angle was fed on pre- determined points of the hopper inlet which were regularly distributed along the hopper inlet to avoid a higher feeding on a determined hammer. The load caused by the fed angles is movable and dynamic but has a regular distribution and motion pattern if it is analysed for long times. It is some kind of "live load" described on structural analysis. Ochshorn [5] states, "Since it is not possible to measure these loads absolutely, a probabilistic approach is used, taking into consideration actual observed loading conditions". The impact load caused by the fed angles could be considered as a uniform distributed impact load (live load) acting on the shaft which approaches the hopper inlet. Therefore, this uniform distributed impact load acts instantly on each shaft and on its hammers when they approach the hopper inlet. The symmetric distribution of hammers on each shaft causes a load effect on each hammer similar to the effect presented on arrays of columns which support a uniform vertical distributed load [6]. Arrays of columns with regular distribution take a proportional percent of the vertical uniform load in a similar way the hammers take the impact load on the present research. Therefore hammers on shafts 2 and 4 support more impact load because it is distributed on two hammers while shafts 1 and 3 have three hammers which receive a lower percent of the impact load per hammer. However, it is clear that the mass loss is not distributed proportionally on the hammers but the above explained analogy is probably the cause for higher mass loss of hammers located on shafts 2 and 4.

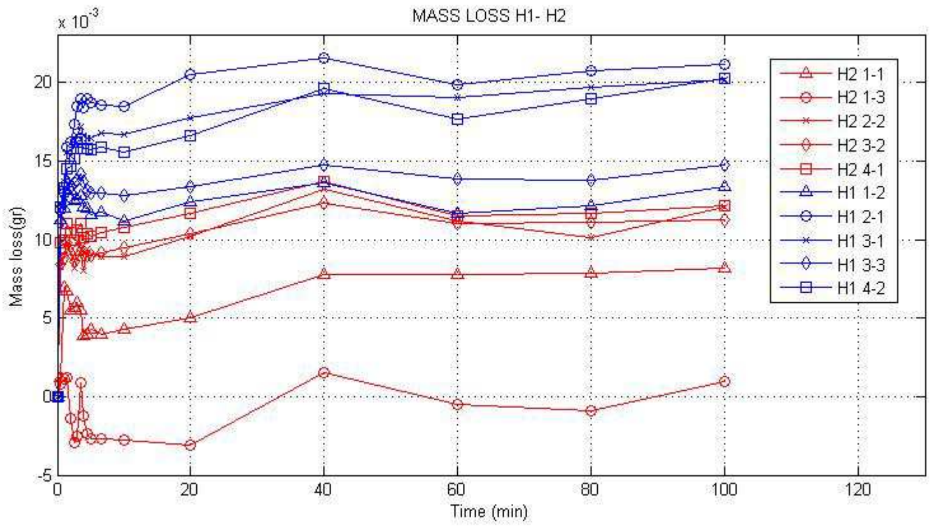

Fig. 5 Mass loss of ten hammers during the test

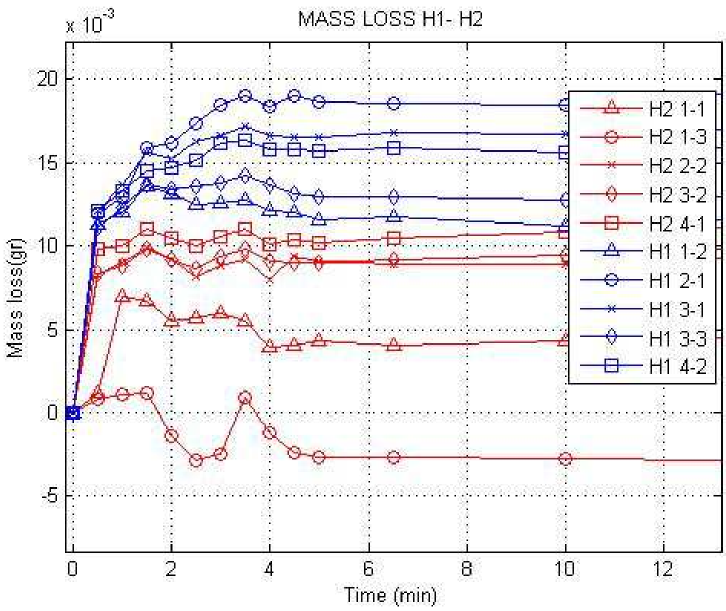

Fig. 6 Mass loss during running-in period for ten hammers

Mass loss rate (slope of the curves) is much lower after 5 minutes for all hammers, therefore running-in period duration is approximately 5 minutes (Fig. 6).During this period hammers H2 1-3 and H2 1-1 had remarkable descents on their mass loss. The difference between both sets of hammers was only their chemical composition. Both sets had the same peripheral velocity and dimensions. The processed material was the same (homogeneous chemical composition, weight and shape) and mass consumption was constant through the test.

Mass loss values also show some descents during the rest of the test for both materials especially between 40 and 60 minutes as can be seen on Fig.5. This is caused by adhesion between the processed material and the hammers (Fig.7 a). The noticeable descent on mass loss between 40 and 60 minutes is influenced by a higher temperature on each hammer because the periods between each mass loss measurement are longer than for the first minutes of test. Impacts and friction cause easy visible sparks that heat the hammers. Under this condition and a longer time between measurements, metallic angles are prone to present more adhesion on the hammers surface because the temperature of them is higher. Processed material had a high surface content of zinc which was observed by EDS. Evidence of micro-cutting can be seen in a H1 specimen on Fig. 7b. Fig.7b shows also transferred material which has a combined composition (iron, manganese, zinc) which was consequence of adhesion of zinc (surface component of processed particles) on hammer surface and subsequent micro-cutting of the mixed layer which contains also manganese (component of hammer steel). Plastic deformation on both materials is also observed on the hammers edges that are more exposed to impact load as well as a micro-crack which can be seen on Fig. 8. This characteristics were carefully observed on hammers H1 4-2 and H2 4-1 which presented a relative high mass loss. Fig. 8 and 9 show plastic deformation on each material. A crack is visible on H1 4-2 specimen (Fig. 8), which originated just below a high deformed zone of an edge. Although these micro mechanisms are present on both materials more noticeable fractures were observed on specimen H1 4-2 as can be seen on Fig.10. This is consistent with a higher mass loss on material H1. Microcracks are observed on the surfaces of both materials although it is not clear if they are the cause of subsequent mass loss or if they are transitory cracks which disappear when a new impact load deforms the material.

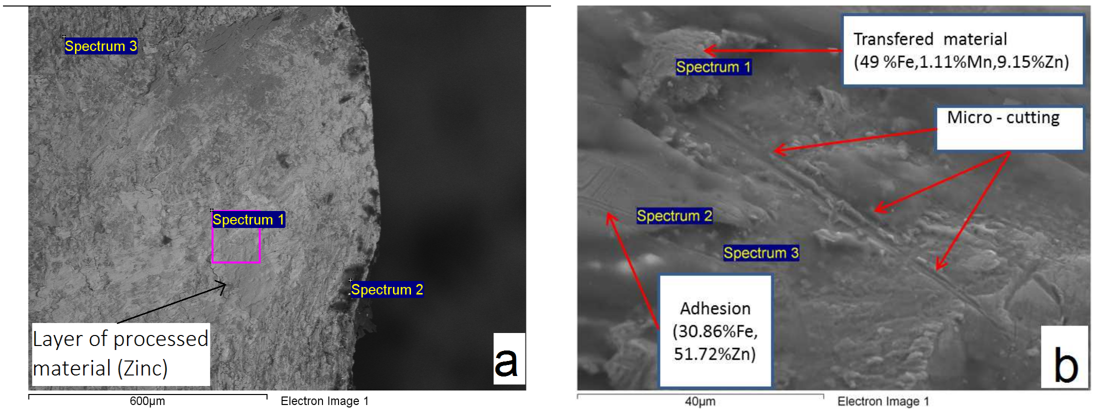

Fig. 7 SEM of wear surfaces a) Highlighted adhesion zone which contains 41% zinc on H2 1-3 hammer at 3.5 minutes (100X). b) Micro - cutting and adhesion on H1 1-2 hammer at 60 minutes (1500X)

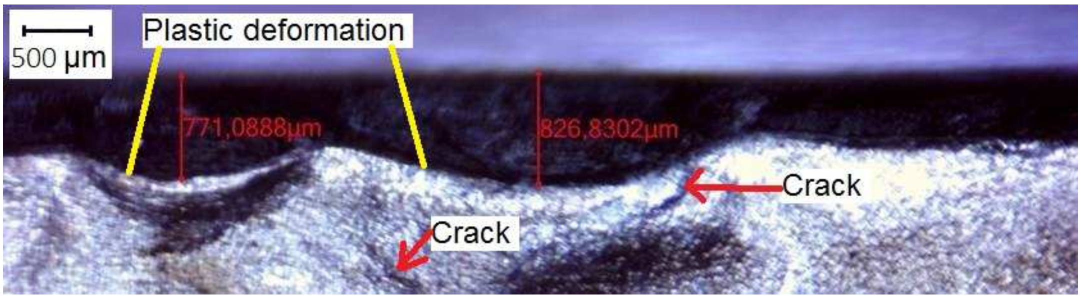

Fig. 8 Deformed impact edge on H1 4-2 at 60 minutes (20X)

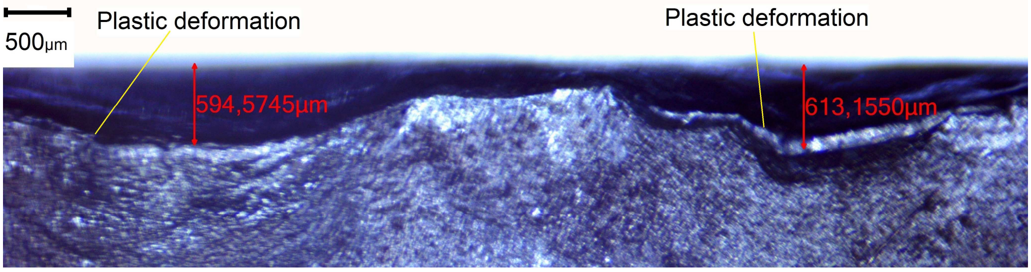

Fig. 9 Deformed impact edge on H2 4-1 at 60 minutes (20X)

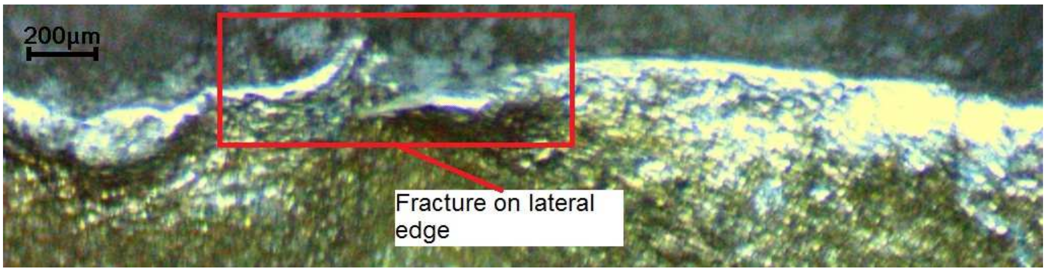

Fig. 10 Fracture on lateral edge. H1 4-2 at 100 minutes (50X)

Micro hardness HV with load of 300 g was measured on each time interval of the test. The global micro-hardness of each material (75 measures per set) was registered in Fig 11. Material H1 presents fluctuations during the test. Initial average value is 279.84 HV and final average value is 349.14 HV, this material strain hardens 24.76% . Material H2 exhibits fewer fluctuations during the test. Initial average value is 264.55 HV and final value is 362.92 HV. This material strain hardens 37.18% and its average microhardness was higher than H1 material at the end of the test. Nevertheless, the materials didn´t have a very high strain hardening. Yan and Fang [7] measured surface hardness of Hadfield steel samples (1.2% C,12.86 % Mn ,0.87 % Si,0.05% S,0.09% P) with surface dimensions 40mm x 75mm that were treated using shot peening (constant and uniform impact of cast steel billiards of 0.2 mm diameter). Initial micro hardness was 256 HV. After 120 minutes of uniform shot peening treatment on the whole surface, hardness value was 774 HV. Micro hardness increment was 202%. Heredia [8] studied changes in Brinell hardness, for 6 austenitic manganese steels (1.14%C, 12.78% Mn, 0.069% Ni, 0.19% Cr, 0.85% Mo) with 6 different thermal treatments. Hardness was measured after 100 impacts of a steel sphere (12,5 cm diameter , 58RC) used in ball mills .The sphere hit the Hadfield samples from 1 meter height which represent 68.67 J of kinetic energy. The results showed an initial hardness in the range of 156-178 HB and a final value between 518-526 HB. The increment was also near 200%. Differences in hardness increments between the present research and the above cited researches could be caused by differences on load application and on materials which impact the Hadfield samples. Each metallic angle hits the hammers on localized small impact zones which cover slowly the surface of the hammer as the number of impacts increases during the test. On the other hand shot peening applies a uniformly distributed constant compressive load on the whole surface during the surface treatment. The angles used as processed mass are thin and more easily deformable than the mill ball used by Heredia [8]. The kinetic energy transmitted by the hammers (43.16 J) is partially absorbed by the angles but the ball mill sphere transmits 68.67 J and doesn't deform due to its higher stiffness and hardness. Therefore Hadfield samples are forced to absorb the energy causing their deformation and hardening. A more speculative reason is that under high strain velocity the hardening potential of Hadfield steel can be lower than for slow strain velocities applied to the whole mass of steel [3]. Highest impact velocity of hammers is 37 m/s while highest velocity of the ball used by Heredia was 4.42 m/s, these differences could influence the strain hardening. Velocity of billiards for shot peening couldn´t be calculated with the parameters cited by the authors. On the other hand, adhesion layers and mixed layers located on the surface most probably have lower hardness than original base material which was deformed and this fact also affects the hardness values.

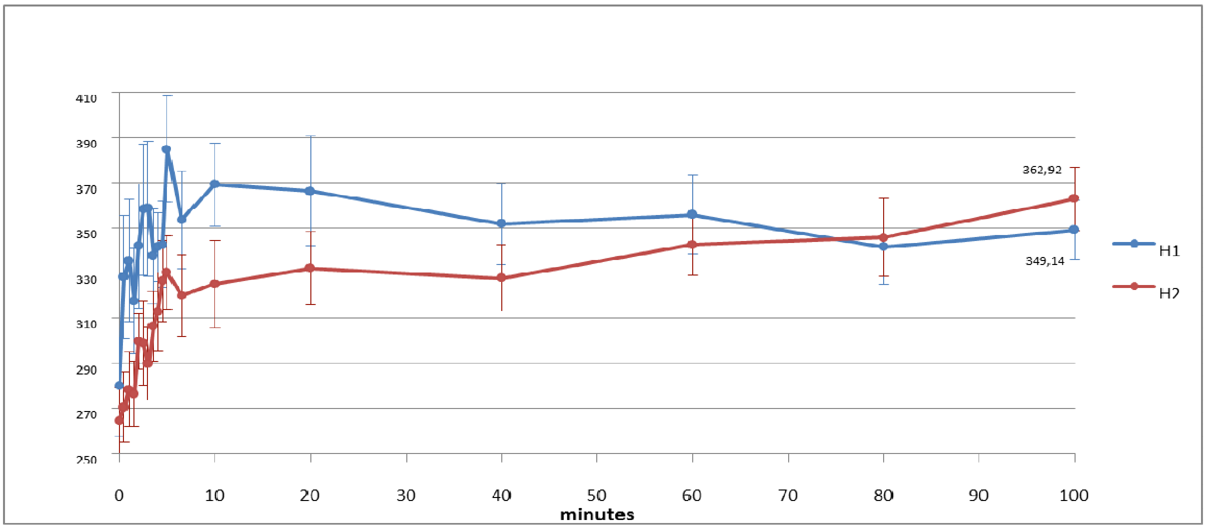

Fig. 11 Microhardness HV for materials H1 and H2. Duration of test was 100 minutes

The different compositions caused a clear difference on the mass loss of H1 and H2. Material H1 which contains less carbon, but more chromium and nickel presented more mass loss than material H2 which contains more carbon, and less chromium. This difference on chemical composition was clearly correlated with mass loss behaviour.

Pribulová, and Babic [9], studied 16 notched samples of Hadfield steel with 16 different chemical compositions (0.94-1.32% C, 12.4-13.4% Mn, 0.01-0.88% Cr, 0.03-0.92% Ni). The samples were tested with three repetitive impact loads. Seven steels with higher chromium and nickel content were among the group which presented fracture just with two impacts. Although, the carbon content was not the focus of the cited research 8 steels with a carbon content of less than 1.19 %C didn´t resist three impacts and presented fracture on the cross section or very visible cracks. Seven of the remaining 8 steels resisted three impacts and all of them had more than 1.19 % C. The same phenomena but in a microscopic scale could occur on the present research. Impact loads affect small areas localized on edges and surfaces of the hammers and micro-cracks can appear on edges and surfaces of them. On this scale, H2 with more carbon and less chromium and nickel contents, had a lower mass loss than material H1 which presented less carbon content and more chromium content.

Differences on initial micro hardness values could not have a direct influence on wear of Hadfield steels during service. Higuera and Moreno [10] examined the wear behaviour of a Hadfield steel ASTM A-128 C (1.05-1.35% C,11.5-14% Mn, 1.5-2.5% Cr) under different thermal treatments and din´t find a clear correlation between hardness after thermal treatment and behavior of Hadfield steel under wear on crossed cylinder apparatus. On the present research, hardness was not related with initial mass loss until running-in period, but after this period H2 became harder than H1 and its mass loss values remained lower than H1. A higher mass loss on H1 seems to be related with micro-cutting that was observed clearly on hammer H1 1-2. Fracture and cracks were observed on hammer H1 4-2 on one of its lateral edges with a magnification of 50X (Fig.10). Other cracks are observed with SEM on both materials but with a higher magnification (1000X). H2 4-1 shows a single crack as can be observed on Fig. 12. Hammer H1 4-2 shows two cracks with shorter secondary cracks (Fig. 13).

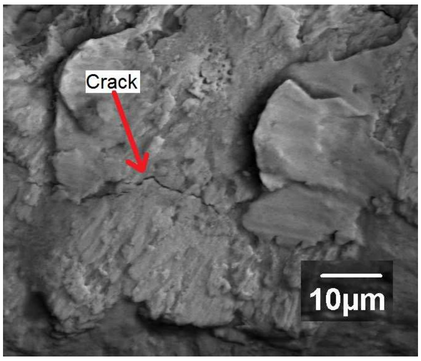

Fig. 12 Crack on H2 4-1 at 100 minutes (1000X)

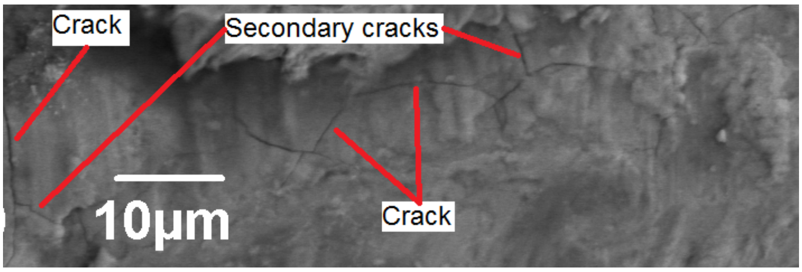

Fig. 13 Net of cracks on H1 4-2 at 100 minutes (1000X)

Adhesion on material H2 is higher than on H1 as the results on Fig. 6 show. Hammers H2 1-3 and H2 1-1 present the most noticeable descent in mass loss among all ten hammers. Plastic deformation is clearly observed on both materials. It is higher on H1 4-2 than in H2 4-1 for 60 minutes test. Nevertheless, the larger plastic deformation (2257 µm) was measured on hammer H2 4-1 at the end of the test on its frontal edge which receives the impact load directly as is shown on Fig.14.

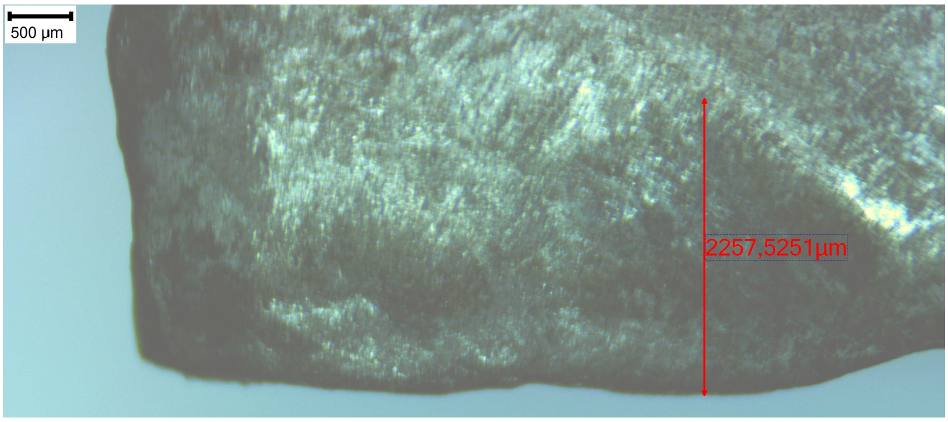

Fig. 14 Largest plastic deformation on edge of H2 4-1 after 100 minutes (20X)

4 CONCLUSIONS

Running-in period shows the same duration for each hammer with no apparent influence of material or position of the hammer. This suggests that other variables influence the running-in duration, such as chemical composition of processed material, size and shape of the hammers, and peripheral velocity.

The results obtained in this research and previous studies by other authors suggest that a carbon content lower than 1 % causes an increase in mass loss under recurrent impact loads, but also affects negatively the strain hardening capacity of Hadfield steels which is a crucial property for good performance under wear.

Wear of austenitic manganese steels under impact load involves wear mechanisms such as adhesion, micro-cutting, and micro - cracking which were observed on the present research and seem to determine the higher mass loss in H1 due to slight more micro-cutting and micro-cracking and a lower mass loss on H2 due to more adhesion and slight higher plastic deformation.

Strain hardening was not very high on this test because each impact load of a metallic angle affected hammers on a very small area, the shape of the angle and its low thickness allows a plastic deformation which absorbs energy and only after numerous impacts on each face or edge the Hadfield steel increases its hardness.

A comparison with other researches suggest that a compressive constant uniform load applied on the whole surface causes more strain hardening than localized higher impact loads which also tend to cause mass loss on already strain hardened layers.

The evidence shows that a higher number of hammers per shaft causes a decrease in mass loss for the conditions of this research (homogeneous processed material, uniform distributed feeding and symmetrical distribution of hammers inside the tribometer) and suggests that concepts applied to static load distribution analysis are also valid for analysis of swing hammers mills although there are other complex dynamical phenomena involved in this application.

5 ACKNOWLEDGMENTS

The authors would like to acknowledge Universidad del Valle for its support through the project CI 2711, as well as Colombian Air Force for the use of Materials Laboratory Facilities at Military Aviation School “Marco Fidel Suarez”. Professor Fernando Delgado Gómez thanks Colombian Air Force for the financial support of his magister studies.

6 REFERENCES

[1] O. Higuera, J. Tristancho, L. Florez, Fundamentos teoricos de los aceros austeniticos al manganeso (aceros hadfield), Sciencia et Technica vol.XIII 034,231-236, 2007.

[2] A. Garcia, A. Varela, J.L. Mier, C. Camba, F. Barbadillo. Estudio tribológico de aceros austeniticos tipo Hadfield: influencia del manganeso en su respuesta frente al desgaste. Revista de Metalurgia, Vol. 46 numero extraordinario, 47-52, 2010.

[3] E. Bayraktar, F. Khalid, C. Levaillant, Deformation and fracture behavior of high manganese austenitic steel, Journal of Materials Processing Technology 147, 145–154, 2004.

[4] E. Brusa, S. Morsut, N. Bosso, Dynamic behavior and prevention of the damage of material of the massive hammer of the scrap shredding machine. Meccanica 49, 575-586, 2014.

[5] J. Ochshorn, Loads, in: J. Ochshorn, Structural Elements for Architects and Builders .Butter Worth Heinemann, Oxford 2009, pp. 39-60

[6] J. Ochshorn, Columns, in: J. Ochshorn, Structural Elements for Architects and Builders .ButterWorth Heinemann, Oxford, 2009, pp. 107-127

[7] W. Yan, L. Fang, K. Sun, Y. Xu, Effect of surface work hardening on wear behaviour of hadfield steel, Materials Science and Engineering A 460-461,542-549, 2007.

[8] J. Heredia, Estabilidad de la fase austenitica ,variación de la dureza en los aceros al manganeso afectados por el calor y sometidos a impactos, Revista del instituto de investigación (RIIGEO).FIGMMG-UNMSM vol 15 No. 29,99-108, 2012.

[9] A. Pribulová, J. Babic, D Baricová, Influence of Hadfield´s Steel Chemical Composition on Its Mechanical Properties, Chem. Listy 105, 430-432, 2011.

[10] O. Higuera, C. Moreno, C. Ramírez, Efecto del Precalentamiento y de la severidad del temple en la resistencia al desgaste adhesivo del acero austenítico al manganeso. Dyna, vol 77, num 164, 76-87, 2010.

International Journal of Fracture Fatigue and Wear, Volume 3
Proceedings of the 4th International Conference on
Fracture Fatigue and Wear, pp. 189-194, 2015

FRETTING CORROSION RESPONSE AT THE INTERFACE OF AISI 4340 STEEL PIN AND BRASS BUSH IN 3.5% NACL SOLUTION

Sumit Kumar and Raghu V Prakash

Machine Design Section, Department of Mechanical Engineering, Indian Institute of Technology Madras. Chennai 600036, Tamilnadu, INDIA.

Abstract: Fretting wear studies under corrosion environment (3.5% NaCl solution) were performed using a in-house developed fretting wear test rig to understand the fretting corrosion behavior of AISI 4340 steel (EN 24 steel) hemispherical pin (nominal diameter of 18 mm) mating with a brass bush (nominal ID of 18.05 mm) having conformal contacts. Experiments were carried out at varying fretting amplitudes, frequencies, and normal loads for pre-defined number of cycles and results compared with baseline data obtained under standard lab air conditions. Wear loss in corrosive environment is higher than that in standard lab air conditions, which can be attributed to the presence of Na^+ and Cl^- ions percentage in the medium. Wear loss and fretting damage rate increases with the increase in sliding amplitude and decreased with increase in test frequency. Based on the results, one can conclude that there is synergistic effect of fretting wear and corrosive environment, which results in accelerated damage due to fretting.

Keywords: Fretting corrosion; damage rate; salt solution; conformal contact; synergy.

1 INTRODUCTION

Fretting is a particular form of wear occurring between two surfaces having small amplitude oscillatory relative motion. Fretting corrosion is a degradation process resulting from the combined action of oscillatory relative motion of small amplitudes between contacting parts and the corrosivity of the environment. Usually, the condition exists in machine components that are considered fixed and not expected to wear. Hurricks explained the mechanism of fretting which involves two major processes, viz., adhesion and metal transfer, and material separation [1]. Oxidation is the most common element in the fretting process. In an oxidizing system, fine metal particles removed by adhesive wear are oxidized and trapped between the fretting surfaces. The oxides act like an abrasives and increase the rate of material removal. This type of fretting in materials is easily recognized by the formation of fine powder material oozing from between the contacting surfaces [2].

The destructive effect of fretting corrosion is more serious than individual corrosion or fretting wear, which can accelerate the failure process of components. Fretting corrosion results in metal degradation due to the simultaneous action of mechanical wear and of chemical oxidation. Here corrosion is accelerated by wear and similarly wear may be affected by corrosion phenomenon. Thus wear corrosion involves mechanical and chemical mechanism, the combination of which often results in significant mutual effects because of the complicated synergy, and both will accelerate the surface damage of materials [3, 4].

Fretting corrosion is a complex phenomena and is influenced by various factors such as fretting amplitudes, frequency, normal load, fretting cycles, debris between the contacting surfaces, corrosivity of the medium. The specimen configurations widely used include crossed cylinder geometry, cylinder-on-flat surface, and sphere-on-flat surface [6-8]. The widely used material for bearing applications, viz., brass is fretted with a AISI 4340 steel (EN 24) pin of hemispherical shape with conformal contacts in simulated 3.5% sodium chloride salt solution is considered for fretting corrosion studies. Wear difference and damage rate is analyzed for a set of fretting parameters like fretting amplitudes, frequencies and normal load. These experiments were also performed in standard lab air conditions and synergism of corrosion on wear as well as synergism of wear on corrosion were studied.

2 EXPERIMENTAL PROCEDURES

2.1 Design Requirement

The fretting wear test set up should be capable of measuring the different fretting parameters such as fretting amplitude, frequency of reciprocating motion, normal load etc. Fretting action actuated at very low amplitudes which is of the order of tens to hundreds of microns. The test set-up is capable of applying very low amplitudes (relative motion) and this is main requirement of design. For obtaining low amplitudes an electro-dynamic shaker used; the displacement range of this set-up is calibrated with non-contact type displacement sensor (micro-epsilon opto NCDT1400) with the help of an oscilloscope (Agilent DSO1014A type). The test set-up is capable of generating frequency in the range of 10 to 30 Hz. The normal contact load is applied by means of dead weights placed at the top of oscillatory movement using a knife edge pin. Simulated sodium chloride salt solution (3.5% NaCl) is poured drop by drop between the conformal contacts of the specimens throughout the experiment.

2.2 Experimental set up

The fretting wear behavior of brass and AISI 4340 steel (EN 24) steel is studied using a fretting set-up in which the relative motion between the fretted contacts is provided by a variable amplitude power oscillator. The schematic of the fretting test set-up used in this study is given in Fig. 1. A power oscillator (1) is connected to transfer the reciprocating motion to the specimen holder (3), through reciprocating rod (2). The reciprocating motion amplitudes and frequencies are controlled by means of voltage. Moving specimen holder (4) which contains AISI 4340 steel pin is mounted at the other end of oscillating rod. The test specimen which is inside another holder is mounted on the other side of test set-up and balanced by counter weight (7). The normal load is applied by the dead weights (5) which are placed on a plate above the test specimen holder by means of a point (6) load. Cylinder inside a hollow cylinder geometry, which makes a conformal geometry results in a line contact, is used in the study of fretting tests.

2.3 Test Procedure

The displacement of fretting specimen is measured using a non contact laser displacement sensor with an accuracy of 3 µm. The fretting amplitude, frequency and normal load were continuously monitored throughout the experiment and recorded using a data acquisition software and a personal computer. The test rig permits fretting tests at different fretting amplitudes ranging from 1 to 200 µm and test frequency ranges from 10 to 30 Hz. All tests were carried out in a dry laboratory air environment and simulated sodium chloride salt solution without any external lubrication. Tests parameters are shown in table 1.

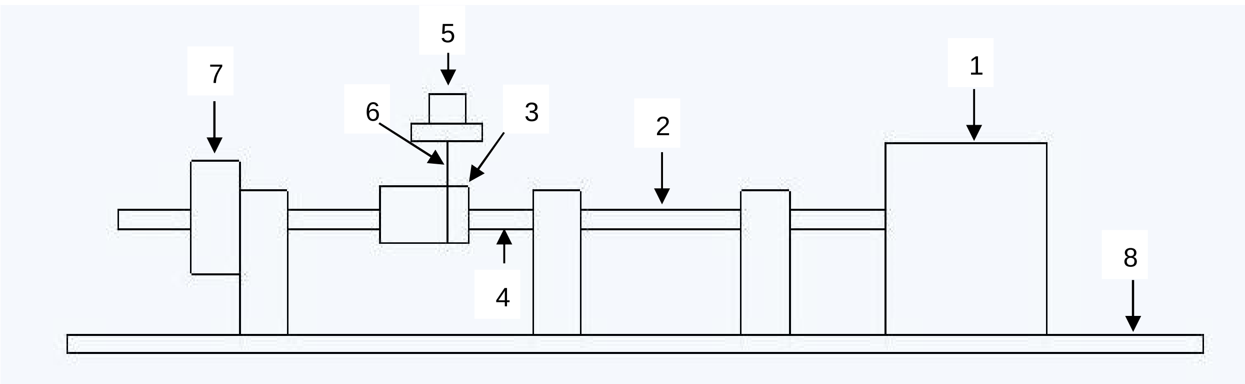

1. Power oscillator
2. Reciprocating rod
3. Test specimen holder
4. Pin holder
5. Dead weight.
6. Knife edge pin for normal load
7. Counter weight
8. Base

Fig. 1 Schematic diagram of fretting test rig.

Table 1 Test parameters used to study the fretting wear and fretting corrosion

Test parameters	Values
Fretting Amplitudes (µm)	50-200
Frequency (Hz)	10-30
Normal force (N)	10
No. of fretting cycles	1,000,000
Medium conditions	Dry lab air, Simulated salt solution

3 RESULTS AND DISCUSSION

3.1 Weight difference at different fretting amplitudes and frequencies

The weight difference in dry lab air can be calculated by taking the difference of specimen's weight before and after the completion of experiment; whereas, the weight difference in salt solution can be calculated as weight difference of specimen due to immersion in salt solution subtracted to weight difference of specimen which has undergone fretting corrosion test. The weight is measured by semi-micro balance with resolution of 0.01 mg with built-in internal calibration. The variation of weight difference vs. fretting amplitude at different frequency is shown in Fig. 2; results are compared with data obtained under dry lab air and salt medium conditions. The weight of specimen after fretting corrosion wear test increased in salt medium so it is represented on negative axis of the curve.

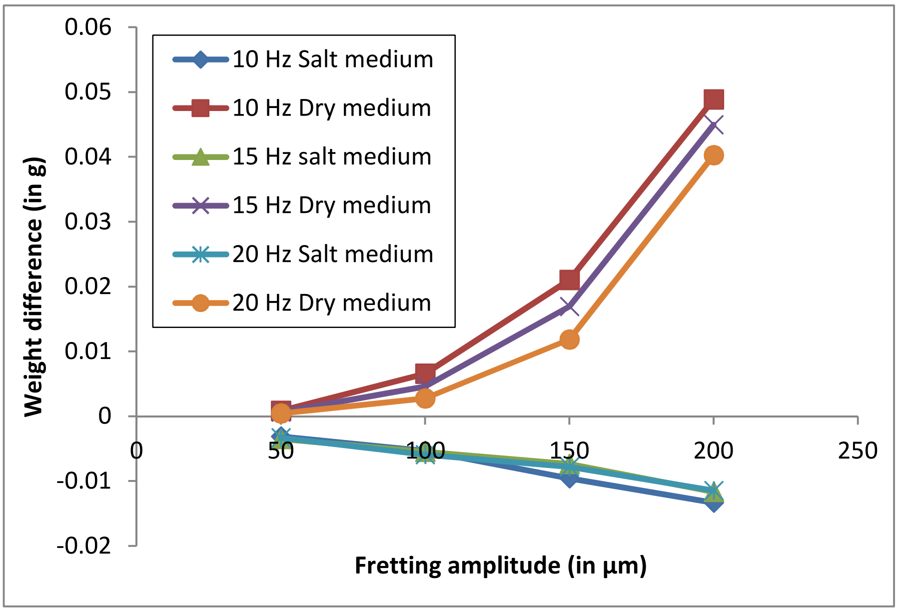

Fig. 2 Variation of weight difference vs. fretting amplitude at different frequency and its comparison between dry lab air and salt medium.

The immersion time of specimens in salt solution whose experiments were conducted at different frequencies up to 10^6 cycles are given in table 2 and shown in Fig. 3.

Table 2 Immersion time of specimens in salt solution

Immersion time (in min)	Frequency of test (in Hz)	No. of cycles
833	20	1,000,000
1111	15	1,000,000
1666	10	1,000,000

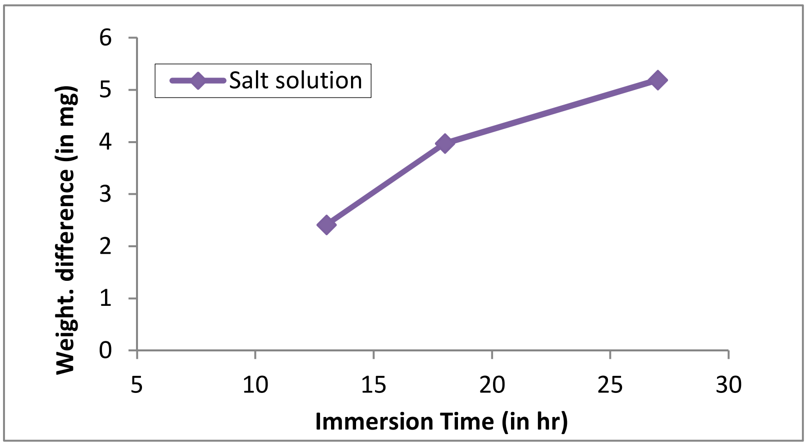

Fig. 3 Weight difference of specimen at different immersion time

3.2 Damage rate at different fretting amplitudes and frequencies

The ratio of weight difference to unit fretting stroke is used to describe the fretting damage rate. Average damage rate, *K* can be given as,

$$K = \frac{\Delta m}{2DN} \tag{1}$$

where *K* is the average damage rate (in mg/m), Δ*m* is weight difference (in g), *D* is displacement amplitude (in μm) and *N* is no of fretting cycles. The variation of damage rate vs. fretting amplitude at different frequencies is shown in Fig. 4; results are compared with those obtained under dry lab air and salt medium conditions. The weight difference of specimen whose test is conducted in salt medium is negative therefore there is a negative value of damage rate for the same.

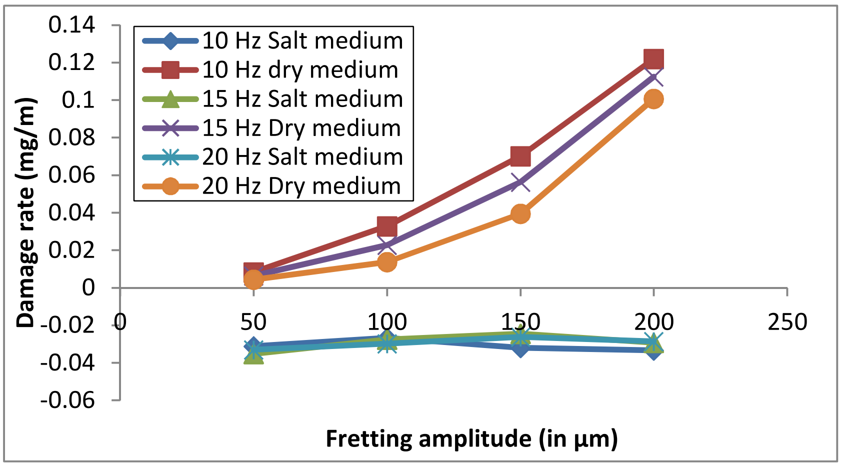

Fig. 4 Variation of Damage rate vs. fretting amplitude at different frequency and its comparison between dry lab air and salt medium.

3.3 Wear scar morphology

Figure 5 shows SEM micrographs wear scar of brass bush for frequency of 20 Hz and normal load of 10 N for fretting amplitude of 50 µm and 100 µm whose fretting test conducted in NaCl solution; the surfaces were cleaned with acetone. The worn surface form porous corrosion products with Na^{+} and Cl^{-} ions present in salt solution because the passive film is not dense. This surface got damaged continuousy by the fretting movement between the fretted surfaces, which results in the formation of small amount of debris on the wear scar area.

At higher fretting amplitudes,salt solution can freely enter the contact zone and the flow of salt medium makes it easier for the debris to escape from the interface. Corrosion products are loose structures and have a weak bonding force with the substrate so they are easily removed from the surface during fretting. Subsequently a fresh surface is exposed to the salt solution making it the region for corrosion to occur, hence wear accelerates the process of corrosion.

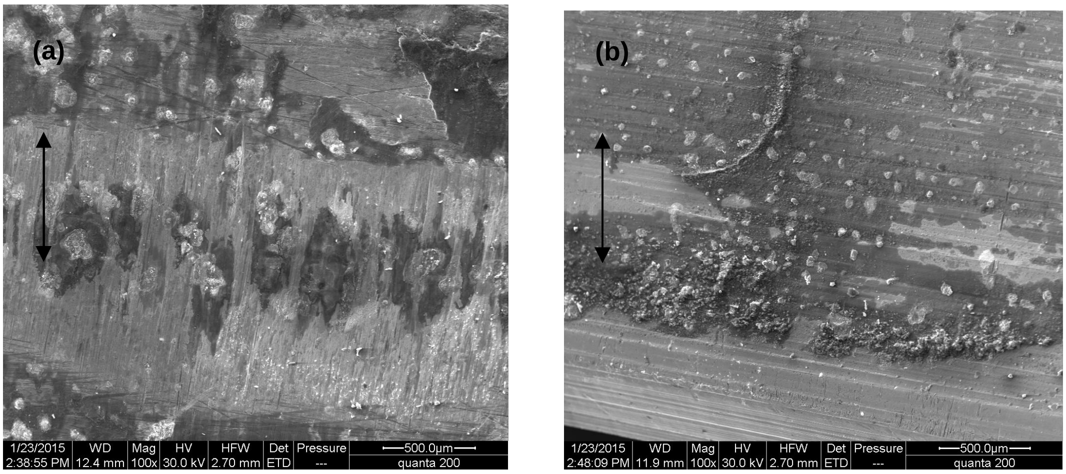

Fig. 5 SEM micrographs of Brass bush wear scar in NaCl solution conducted at the frequency of 20 Hz and normal load of 10 N up to 10^6 cycles (a) fretting amplitude of 50 µm (b) fretting amplitude of 100 µm.

4 CONCLUSIONS

The fretting wear and fretting corrosion of AISI 4340 structural steel (EN 24 steel) and brass bush is investigated under constant load wear condition and compared with dry lab air and simulated sodium chloride salt solution. Weight difference and damage rate depends on contact conditions like fretting amplitude, frequency, normal load between contact surfaces and experimental environment conditions. With the increase in fretting amplitudes, the wear loss increases and the damage rate increased with the increase in fretting amplitude. The interaction of corrosion and fretting wear is crucial for material loss of fretting corrosion in salt solution. The corrosion is accelerated by wear and similarly wear is accelerated by corrosion.

5 REFERENCES

[1] P. L. Hurricks, The Mechanism of Fretting - A review, Wear 15 (1970) 389-409.

[2] William Glaeser, Ian G. Wright, Forms of Mechanically Assisted Degradation in: ASM Metals Handbook, Vol 13A - Corrosion: Fundamentals, Testing, and Protection, ASM international, 2003, pp. 322-330.

[3] H. Y. Ding, G. H. Zhou, and D. Hui, Friction and wear performance of an aluminium alloy in artificial seawater, Proc. IMechE Part J: Journal of Engineering Tribology, Vol. 225, 2011, pp. 43-49.

[4] D. Zhang, S. Wang, Y. Shen and S. Ge, Interactive mechanisms of fretting wear and corrosion of steel wires in alkaline corrosion medium, Proc. IMechE Part J: Journal of Engineering Tribology, Vol. 226(9), 2012, pp. 738–747.

[5] R. B. Waterhouse, Fretting Corrosion, Pergamon press, 1972, pp. 36-43.

[6] R. Ramesh, R. Gnanamoorthy, Fretting wear behavior of liquid nitrided structural steel, En24 and bearing steel, En31, Journal of Materials Processing Technology 171 (2006) 61-67.

[7] S. Fouvry, Shakedown analysis and fretting wear response under gross slip condition, Wear 251 (2001) 1320–1331.

[8] Etsuo Marui, Hiraki Endo, Norihiko Hasegawa, Hidetoshi Mizuno, Prototype fretting wear testing machine and some experimental results, Wear 214 (1998) 221-230.

[9] V. Chaudhry, Satish V.Kailas, Fretting studies on self-mated stainless steel and chromium carbide coated surfaces under controlled environment conditions, Wear 301 (2013) 524–539.

[10] D. E. Taylor, R. B. Waterhouse, An electrochemical investigation of fretting corrosion of a number of pure metals in 0·5M sodium chloride, Corrosion Science, 1974, vol. 14, pp. 111-122.

Proceedings of the 4th International Conference on
Fracture Fatigue and Wear, pp. 195-199, 2015

INVESTIGATION ON COMING OUT PHENOMENON OF THE SHAFT FROM THE SLEEVE BY 2-D PLATE MODEL APPROACH

Dedi Suryadi[1], Nao-Aki Noda[1], Yoshikazu Sano[1],Yuanming Xu [1] and Chengwei Wu[2]

[1] Kyushu Institute of Technology, Kitakyushu, Japan
[2]Dalian university of Technology, Dalian, China

Abstract: The ceramics roller can to be used in the heating furnace because of high temperature resistance. The roller consists of ceramics sleeve and steel shaft connected by shrink fitting. Since ceramics is brittle, it should be noted that only low shrink fitting ratio can be applied for the connection. Therefore, coming out of the shaft from the sleeve during rotation should be investigated in this study. In this study, the finite element analysis is applied to simulate this phenomenon. In the previous study, mechanism of coming out has been considered by using 3-D model. However, since 3-D model analysis needs large computational time, only small number of cycle can be considered, and therefore, the coming out phenomenon cannot be predicted easily. In this research, the 2-D plate model approach is proposed in order to reduce computational time, considering the upper and lower alternate load, repeatedly. Then, the effects of the magnitude of the load and shrink fitting ratio are investigated systematically. Finally, the simulation of the coming out phenomenon can be carried out for much larger number of cycles.

Keywords: Ceramics Roller, Coming Out, Shrink Fitting, 2-D Plate Model, Finite Element Method

1 INTRODUCTION

Steel conveying rollers are used in the heating furnace for producing high-quality steel plates for automobiles. Recently, the conventional roller has been used in the heating furnace which consists of sleeve and shaft. They are connected by shrink fitting. The roller material is steel with ceramics spray coating on the outside of sleeve. The coated sleeve and shaft are bonded by welding. To reduce the temperature, inside of the roller is cooled by water. However the thermal expansion mismatch may exceed the adhesion strength of the ceramics layer and causes failure on the roller surface such as crack, peeling [1], wearing, and shortens the life of the roller.

A new ceramics roller consists of steel shaft at both ends and ceramics sleeve having high heat resistance, corrosion resistance and wear resistance [2]. The ceramics sleeve may prevent defects caused by coating, and therefore, the roller life can be extended significantly. The shrink fitting may be the most suitable joining method for cylindrical ceramics as discussed in Refs. [3,4]. By using shrink fitting connection, the maintenance cost and replacement time of the shaft can be reduced. On the other hand, the thermal expansion coefficient of steel is about four times larger than that of ceramics. Since the fracture toughness of ceramics is lower than the value of steel, attention should be paid to the ceramics sleeve at joint portion.

In the previous study, the influence of the shrink fitting ratio and the friction coefficient upon the coming out behavior of the shaft was analyzed by using 3-D model [5]. And the mechanism of coming out has also been considered by using 3-D model. However, since the 3-D model analysis takes very large computational time. It is nearly impossible to calculate when cycle number N larger than 10.

In this paper, the 2-D model has been used instead of the 3-D model, so that the computational time can be greatly reduced and the model can be calculated until a large cycle number N (N=40). In this way, the coming out behavior of the shaft can be accurately evaluated by using the result of a large cycle number N 2-D model rather than a small cycle number N 3-D model. The finite element method is applied to simulate the behavior. Then, several mechanical factors will be considered to understand the coming out of the shaft.

2 ANALYISIS CONDITIONS

2.1 Analysis Model

Figure 1 shows dimensions of the real roller. In this paper, in order to reduce computational time, the 3-D model is simplified to a 2-D model. Here, the sleeve is modeled by rigid body, while hollow shaft is modeled by a composite shaft as shown in Fig.2.

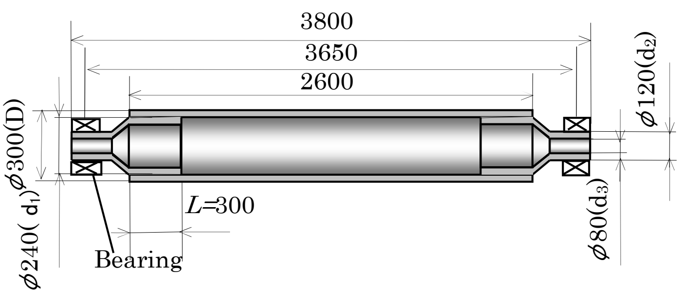

Fig. 1 Structure and dimensions of a real ceramic roller (mm).

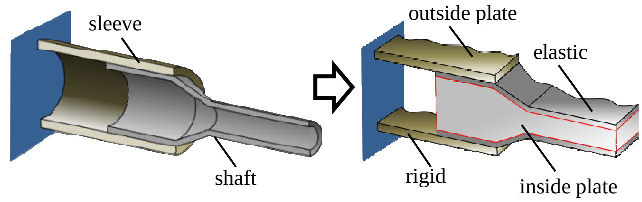

Fig. 2 Simplification from 3-D model to 2-D model

The rule of mixture is applied to obtain the average Young's modulus of the hollow shaft. Then, the average Young’s modulus is given by using following equation.

$$E_{comp} = E_1 \frac{A_1}{A_1+A_2} + E_2 \frac{A_2}{A_1+A_2}$$

$$= E_1 \frac{A_1}{A_1+A_2} = 51.55MPa$$

Here, E_1 devotes the Young's modulus of the shaft, E_2 devotes the Young's modulus of the hollow portion of the shaft (E_2=0), A_1 devotes the cross-sectional area of the peripheral portion shaft and A_2 devotes the cross-sectional area of the hollow portion of the shaft (see Fig.3).

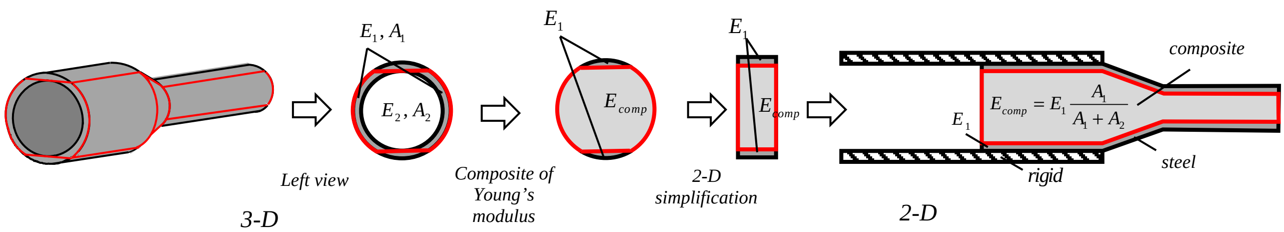

Fig. 3 Simplification from 3-D shaft to 2-D inside plate

2.2 Analysis Method and Boundary Conditions

In this study, the coming out of the inside plate in Fig.2, will be realized by the simulation. Then, the fundamental several important factors will be discussed. First, the coming out at room temperature is considered because the coming out easily occurs. Here, the shrink fitting ratio between outside and inside plates is defined as δ/d, where δ is the width difference (see Fig. 7.a) and d is the width of the inside plate d=240 mm. In this study, the shrink fitting ratio is considered in the range δ/d=0.01x10^{-3}-0.4x10^{-3}.

In this study, three models will be considered, that is, the 3-D real model (a), 3-D alternate load model (b) and 2-D alternate load model (c). In the previous studies, the half model of roller was used in the simulation. The roller is subjected to distributed load w=30N/mm due to the weight of the conveyed steel. In order to simulate the rotational behavior of the model, the distributed load on the sleeve part *w* is shifted repeatedly at certain time interval of the rotational angle θ_0 in circumferential direction in Figure 4.

In the first place, as shown in Fig.5, in this paper, in order to reduce the computational time, the 3-D rotation load is simplified as an alternate load model. The ceramic sleeve is simplified as a rigid sleeve and the left end of the sleeve has been completely fixed. And the load changes as shown in Figure 5.

Figure 6 shows the loading condition of the 2-D alternate load model. The distributed load is determined to satisfy the effectiveness of concentrated load applied upon per millimeter diameter length of the shaft. And the distributed load changes alternatively as shows in figure 6. Plane strain assumption is used.

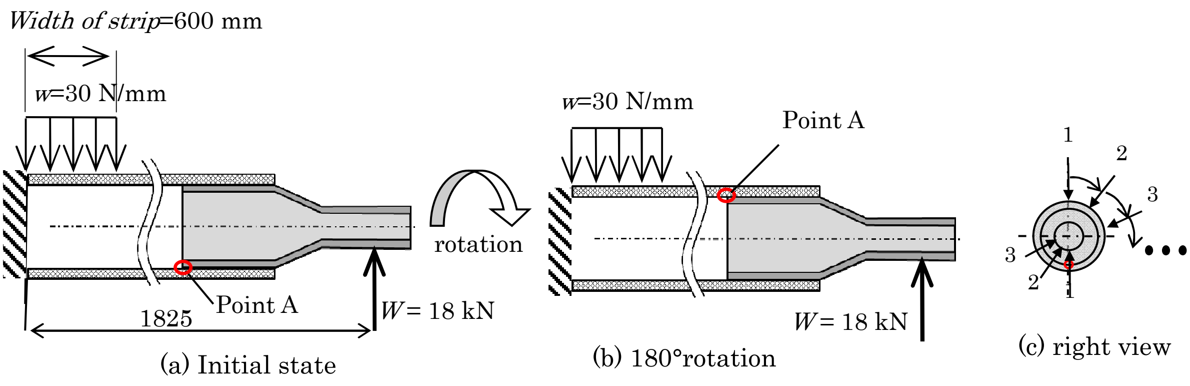

Fig. 4 Three-dimensional real roller model

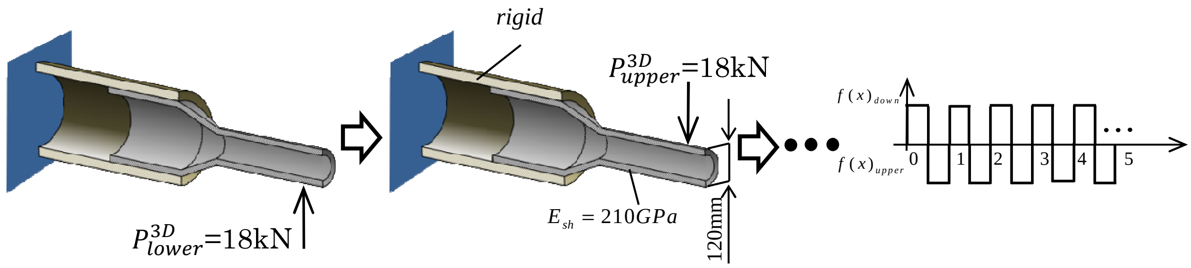

Fig. 5 Three-dimensional alternate loading model

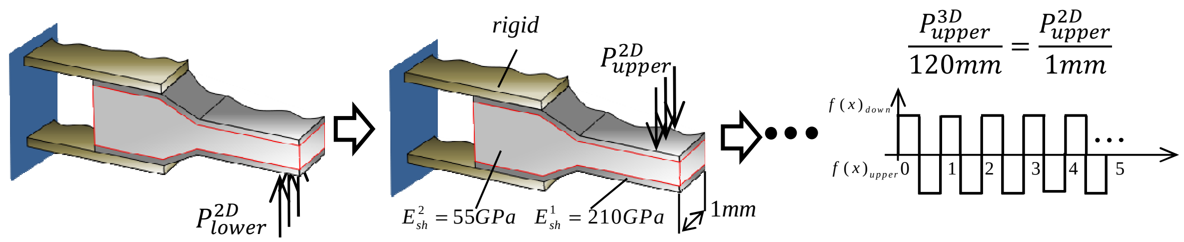

Fig. 6 Two-dimensional alternate loading model

3 EVALUATION METHOD FOR THE COMING OUT AND DEFLECTION OF THE SHAFT DUE TO THE DISTRIBUTED LOAD AND SHRINK FITTING RATIO

Deformation of the shaft due to initial load is considered. Figure 7(a) shows definition of coordinates (r,z) on the position of the shaft at before shrink fitting. Here, the relative displacement u_{zC} from initial position is focused. The displacement direction $u_{zC}^{N=0}$ (>0> u_{zC}^{sh}) at point C initiates coming out by initial load as shown in Figure 7(b). The displacement of the inner plate goes to negative direction by shrink fitting and it goes to positive direction due to the load. Moreover, point C is focused. The $u_{zC}^{N=0}$ is put as the initial displacement at number of cycle N=0.

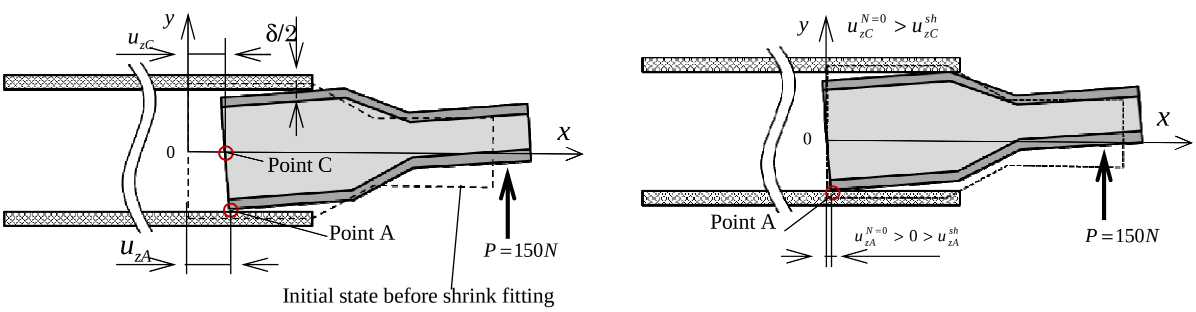

(a) Definition of displacement u_{zC}, u_{zA} (b) Definition due to shrink fitting and initial load (N=0)

Fig. 7 Displacement of the shaft due to bending

4 COMPARISON OF THE RESULTS OF THREE MODELS

To confirm the usefulness of simplified 2-D model, three models are compared under the shrink fitting ratio δ/d=0.2×10^{-3} in Fig.8. The results for 3-D real roller (model A), 3-D alternate load model (model B) and 2-D alternate load model (model C) are compared focusing on u_{zC}. It is seen that the u_{zC} of model A increases at N=0~2. Then, it becomes constant at N=2~3. Since 3-D real model (model B) needs very large computational time, the simulation is carried out only until N=3. Therefore, it is hard to judge whether the coming out of the shaft occurs or not from this model. Further, the u_{zC} of the model B increases at N=1~6. However, the speed of the coming out of the shaft decreases gradually, therefore, the possibility of coming out of the model B looks very small. For the model C, the number of cycle can be reached until N=40. Here, the u_{zC} increases with increasing number of cycle N=0~5 and becomes constant after N=5, therefore, the coming out of Model C does not occur. From Fig.8, it is seen that model C is useful to judge whether the coming out occurs or not.

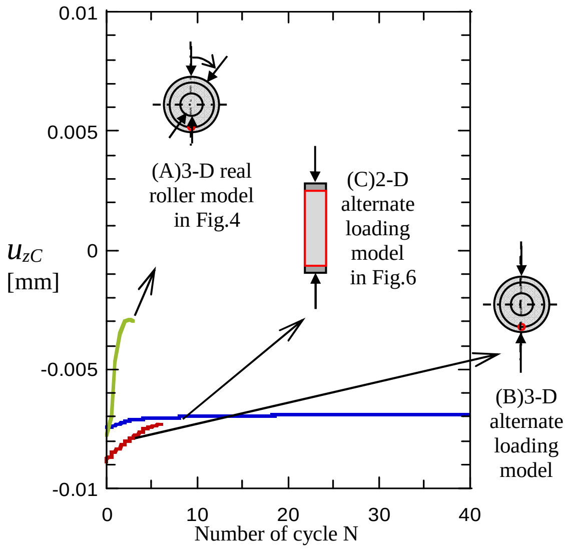

Fig. 8 The displacement u_{zC} vs. number of cycle N for 3-D real roller model, 3-D alternate loading model and 2-D alternate loading model with δ/d =0.2×10^{-3}

5 THE COMING OUT CONDITIONS DUE TO LOAD AND SHRINK FITTING RATIO

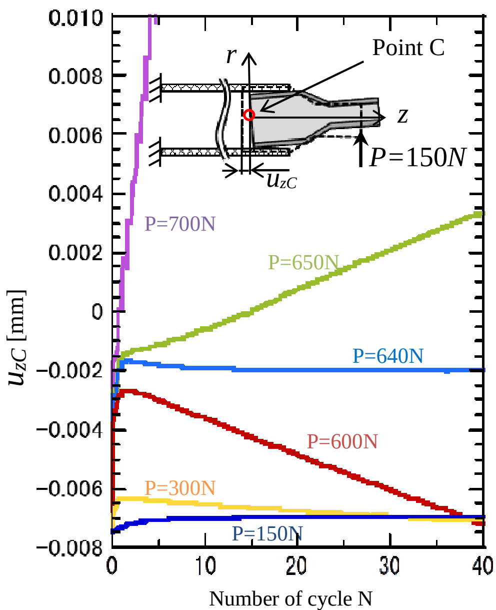

Fig. 9 The displacement u_{zC} vs. number of cycle N for different load P when δ/d =0.2×10^{-3}

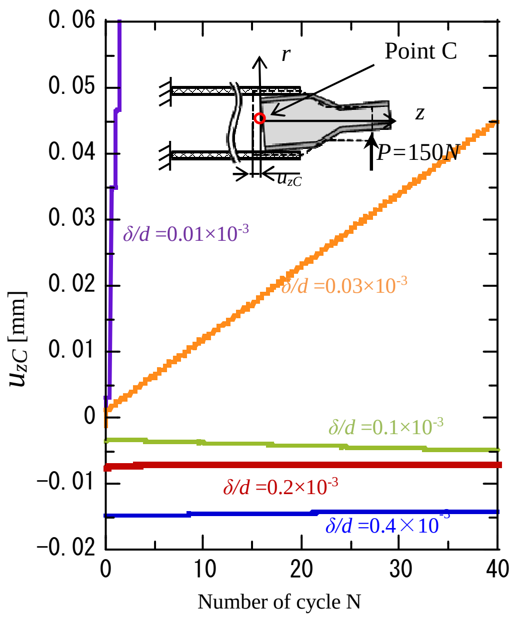

Fig. 10 The displacement u_{zC} vs. number of cycle N for different load δ/d when P=150N

Figure 9 shows the effect of the magnitude of alternative load upon u_{zC} under the shrink fitting ratio δ/d=0.2×10^{-3}. From the graph, the large load P causes large z-displacement u_{zC}. The u_{zC} tends to increase at N=0-4 independent of the magnitude P. Then, after N=4, it is seen that for P≥650N, the u_{zC} increases significantly, and the coming out occurs. After N=4, it is seen that for P≤640N, the u_{zC} becomes constant, which means that the coming out does not occur.

Figure 10 shows the effect of the shrink fitting ratio upon the u_{zC}. The large shrink fitting ratio causes negative u_{zC} at N=0 due to compressive stress. For N=0~40, the u_{zC} increases significantly with increasing N under the low shrink fitting ratio δ/d =0.01×10^{-3} and δ/d =0.03×10^{-3}, therefore, the coming out of the shaft occurs easily. On the other hand, the u_{zC} becomes constant under the shrink fitting ratio $\delta/d = 0.1\times10^{-3}$, $\delta/d = 0.2\times10^{-3}$ and $\delta/d = 0.4\times10^{-3}$, therefore, the coming out of the shaft does not occur. Fig.9 and 10 show the usefulness of the 2-D alternate load model because the results for large N can be obtained easily.

6 REFERENCES

[1] Fujii, M. Yoshida, A. Ishimaru, J. Shigemura, S. and Tani, K., Influence of sprayed layer thickness on rolling contact fatigue of ceramics sprayed roller, Transactions of the JSME Series C, Vol. 72, No. 716, pp. 1354-1360 (in Japanese), 2006.

[2] Ono, T., Current status and future prospect of the development of high performance ceramics, Journal of the Japan Society of Mechanical Engineers, Vol.86, No.774, pp.470-475 (in Japanese), 1983.

[3] Li, W. Noda, N.A. Sakai, H. and Takase, Y., Analysis of Separation Conditions for Shrink Fitting System Used for Ceramics Conveying Rollers, Journal of Solid Mechanics and Materials Engineering, Vol.5, No.1, pp.14-24, 2011.

[4] Li, W. Noda, N.A. Sakai, H. and Takase, Y., Thermal Stress Analysis for Shrink fitting System used for Ceramics Conveying Rollers in the Process of Separation, Key Engineering Materials, Vols.452-453, pp.241-244, 2011

[5] Noda, N.A., Suryadi, D., Sano, Y., Takase, Y., Kumasaki, S., Xu, Y., Coming out mechanism of the shaft from the sleeve for the shrink fitted ceramics roller, Proceedings of ACMFMS2014, pp. 159-162, 2014.

Proceedings of the 4th International Conference on
Fracture Fatigue and Wear, pp. 200-207, 2015

THE INFLUENCE OF COATING THICKNESS ON LINEAR WEAR RATE IN SILVER COATED CONTACTS

Jian Song, Vitali Schinow and Haomiao Yuan

Ostwestfalen-Lippe University of Applied Sciences
Liebigstr. 87, 32657 Lemgo, Germany

Abstract: The base material in an electrical contact is generally protected by a coating layer. The basis for determining the protection effect requires sufficient investigation of coating layer. In this paper, the influence of silver coating thickness on the lifetime of silver coated contacts and the wear rate is studied respectively. The silver coating thicknesses range from 0.5 to 9 µm, with a sphere/flat geometry. Based on fretting wear and corrosion tests the correlation, between lifetime as well as wear rate and the coating thickness is determined. A theoretical model to predict the wear depth at a given sliding distance is proposed and then validated using sphere samples with a 6µm silver coating thickness.

Keywords: electrical contact, fretting corrosion, lifetime, wear rate, wear depth, silver, coating thickness

1 INTRODUCTION

Silver, as a metal, possesses the highest electrical conductivity and is therefore widely used as the coating material of contacts in industry [1]. The electrical conductivity of the contacts can be reduced by corrosion and fretting corrosion. Since silver is a noble metal, corrosion and fretting corrosion do not initially make a difference, although the relative motions have already occurred. As those generated relative motions develop, the corrosion and fretting corrosion start to affect the property of the contact and must be taken into consideration. The motions between electrical contacts are produced by the close and open of the electrical connectors, vibration and/or diverse thermal expansion. When the surface layer is worn through, the motion causes the fretting corrosion of the base material, which subsequently leads to the electrical failure.

This study therefore focuses on the fretting wear of silver coated contacts with different coating thicknesses.

1.1 Fretting Corrosion and Tribological Measurement

Fretting corrosion is one of the most common reasons leading to failure in electrical connectors. It occurs wherever the contact material is non-noble and relative motions take place.

The high specific electrical resistance of oxides, as a result of the relative motions, increases the total resistance of the electrical contacts and after a certain period the electrical contacts fail. Two time periods (Lifetime I and Lifetime II) are defined for characterizing the failure of the electrical contacts, following a current test method [2, 3]. In Fig. 1, a typical resistance diagram for fretting corrosion is shown. Lifetime I is defined as the number of cycles when the resistance is 5 mΩ higher than the initial resistant. In this study the initial resistance is from 1 to 3 mΩ, while Lifetime II is the number of cycles when the resistance is higher than 300 mΩ.

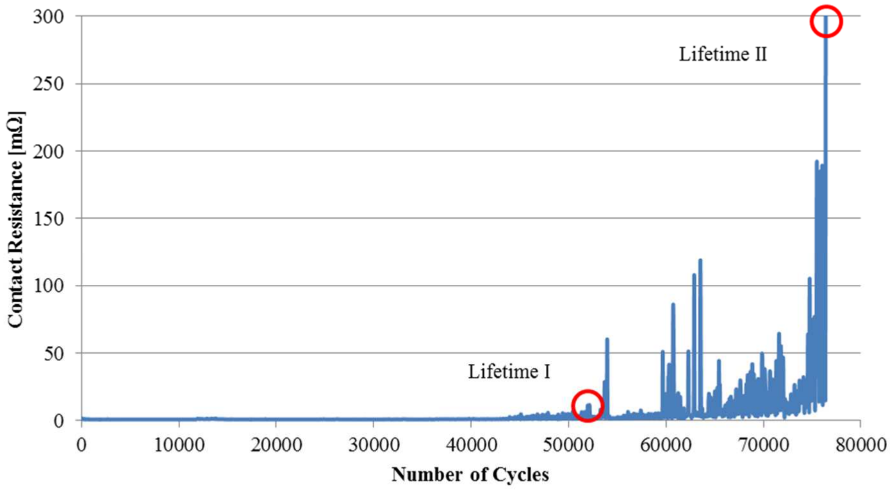

Fig. 1 Lifetime in the fretting test

Fretting wear and corrosion tests were used to measure the wear of electrical contacts. The volumetric wear is the amount of removed materials [mm³], however, it is more convenient to use the linear wear W_L:

$$W_L = \frac{W_V}{A} \tag{1}$$

where W_V is the volumetric wear and A is the apparent contact surface.

According to Archard's wear law, the volumetric wear is:

$$W_V = V_{wear} = k_V \cdot F \cdot s \tag{2}$$

where F is the normal force, s is the sliding distance and k_V is the volume wear coefficient.

The sliding distance s can be calculated as:

$$s = 2N \cdot s_0 \tag{3}$$

s_0 is the amplitude of the motion. The wear follows a fixed principle, as shown in Fig. 2. The removal rate (initial phase) in Phase I is relatively high, representing the high wear resulting from the microscopical unevenness at surface. Phase II starts when the bearing surface is increased by wear and plastic deformation. This phase is recognized by lower wear. The focus of this study is on phase II i.e. the steady state wear. The severe wear in Phase III usually attracts less interest due to the fact that at that moment the wear through of the coating material has already occurred.

Fig. 3 shows an example for the wear measurement. During this measurement, the focus is placed on the first two phases in wear process.

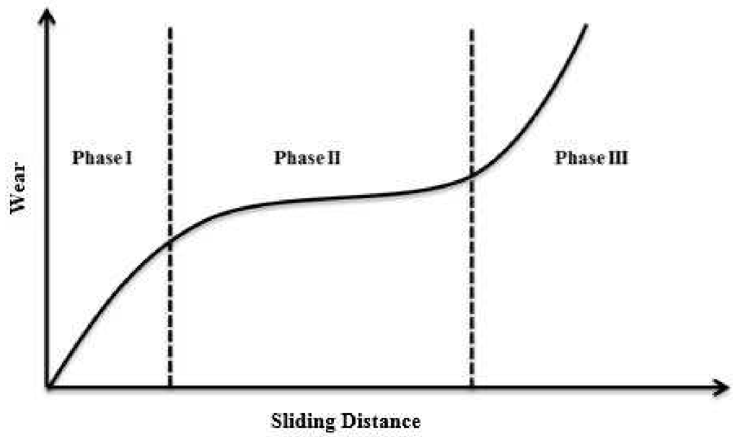

Fig. 2 Principle diagram of the wear process [4, 5]

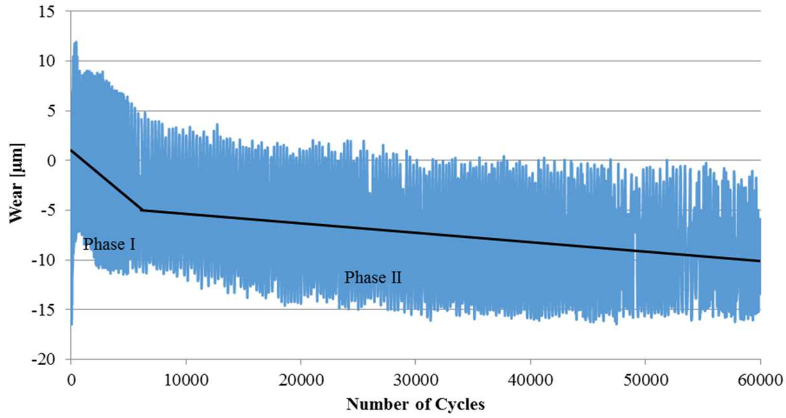

Fig. 3 First two phases of the wear

2 SAMPLES USED IN MEASUREMENTS

The contact samples used in these experiments were a sphere part on a flat part, in which the radius at contact point was 4.5 mm (in Fig. 4). The base material of the samples was bronze (CuSn4) and the samples were electrochemically galvanized with silver to different thicknesses, namely 0.5, 3, 6, 9 µm in sphere and flat respectively.

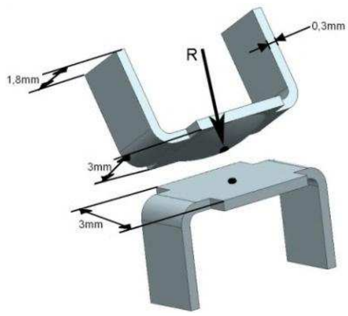

Fig. 4 Geometry of the contact samples: sphere/flat with radius 4.5 mm at contact point

3 METHOD OF MEASUREMENTS

A fretting wear and corrosion test rig was used for the tests (see Fig. 5). Various test parameters such as amplitude of travel, normal contact force, frequency of the motion and temperature can be set up in these tests. The ranges of the parameters are as follows: the amplitude of travel from 1 to 350 µm, the normal contact force from 0.5 to 5 N, frequency from 0.1 to 10 Hz and temperature from ambient temperature to 80 °C [6]. The testing parameters used in this study are amplitude 200 µm, contact force 3 N, frequency 1 Hz and room temperature. During the experiments, contact resistance, wear, normal force, friction force and friction coefficient were recorded continually along with the measuring cycles. In order to verify the wear curves, the tests were terminated at different cycles, and then the remaining silver thickness was measured using an X-ray fluorescence device (Fischerscope X-ray produced by HELMUT FISCHER GmbH&Co.KG).

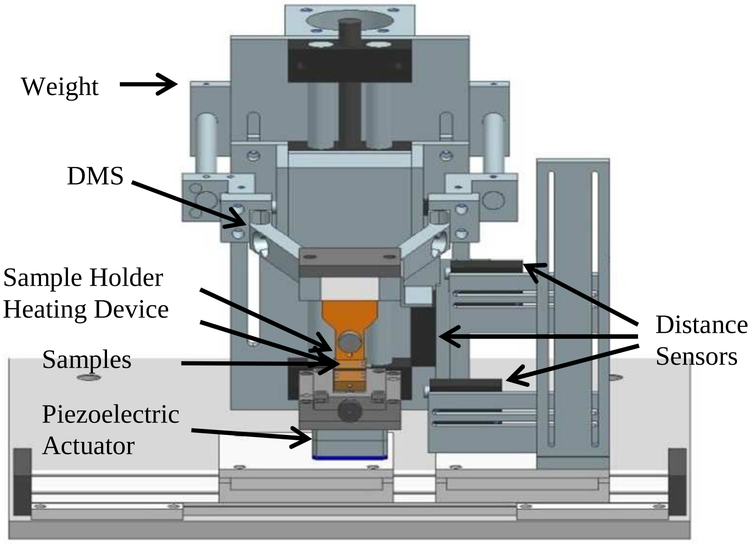

Fig. 5 Measurement device for wear and fretting corrosion tests

4 RESULTS AND DISCUSSIONS

4.1 Lifetime

In this section the correlation between Lifetime II and silver coating thickness will be discussed. Fig. 6 illustrates an instance for the contact resistance versus number of cycles with the four silver coating thicknesses. Obviously, the relationship between Lifetime II and the silver coating thickness is non-linear (Fig. 7) however, it follows an exponential tendency.

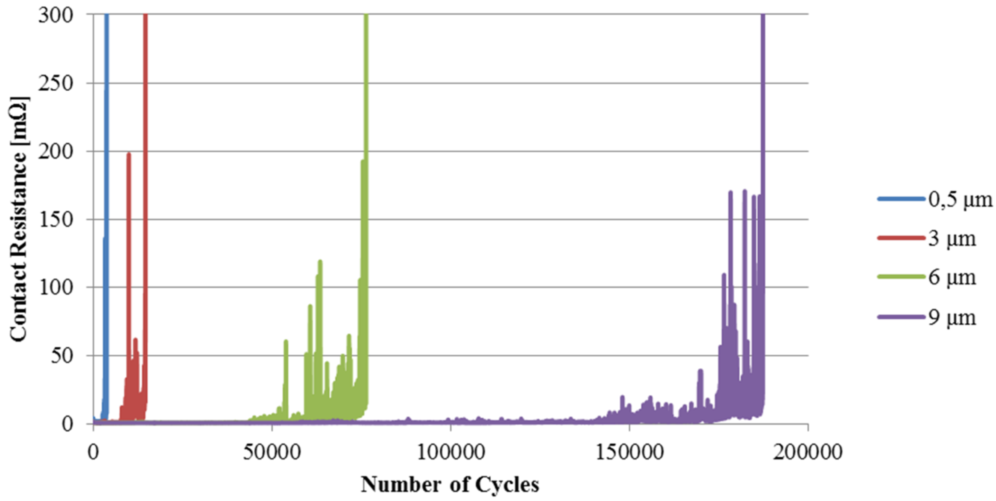

Fig. 6 Lifetime with different silver coating thicknesses

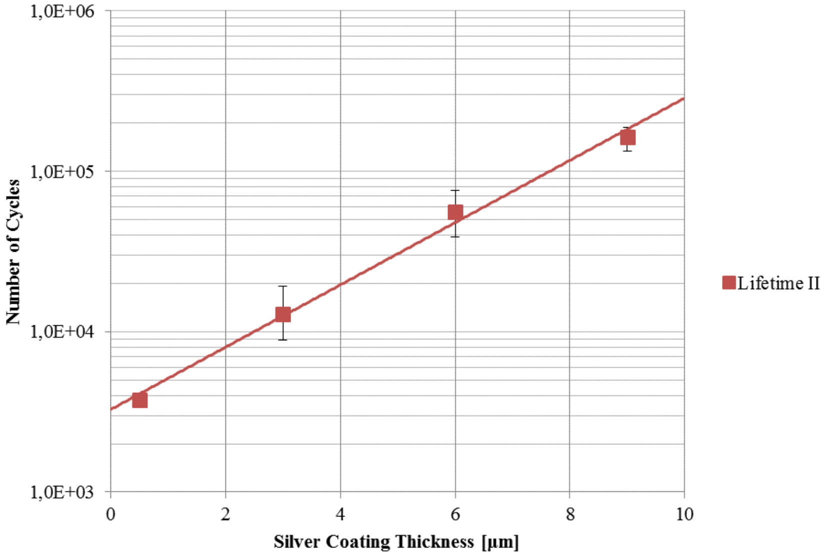

Fig. 7 Correlation between Lifetime II and silver coating thickness

4.2 Wear Rate

The analysis of the linear wear rate was carried out in both the phase I and the phase II (Fig. 3). The linear wear rate I from Phase I describes the wear at the functional layer close to the surface, while the linear wear rate II refers to the real silver-silver combination. As shown in Fig. 8, both the linear wear rate I and II decrease with increasing coating thickness.

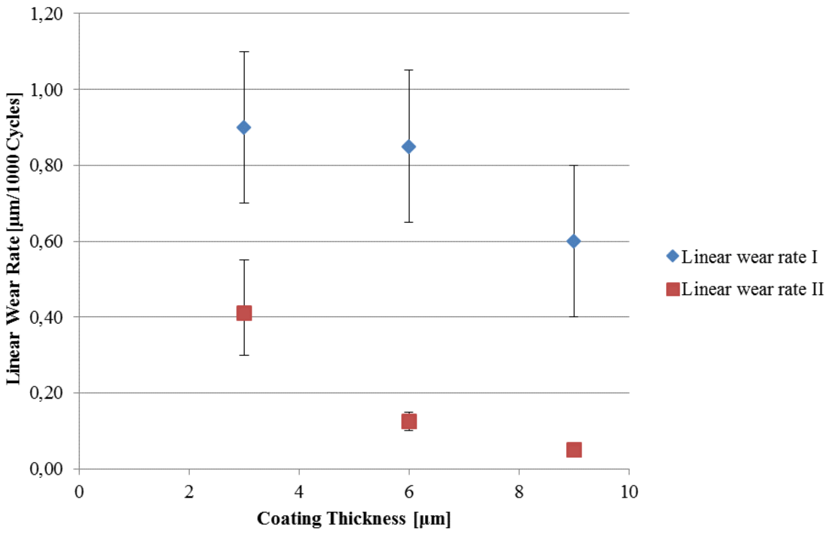

Fig. 8 Correlation between the Linear wear rate (I, II) and the coating thickness

4.3 Wear Curves

The difference between the linear wear rate I and II implies that in the initial phase the silver removal is much faster than the following period in silver coated contacts. In order to examine this, fretting wear analysis was conducted using the following method: several parallel experiments (with the same experimental conditions) were terminated at different cycles with subsequent characterization of the silver coating layer. For each measurement a new sample was used. The results from the 6 µm silver coated contacts with sphere geometry are shown in Fig. 9.

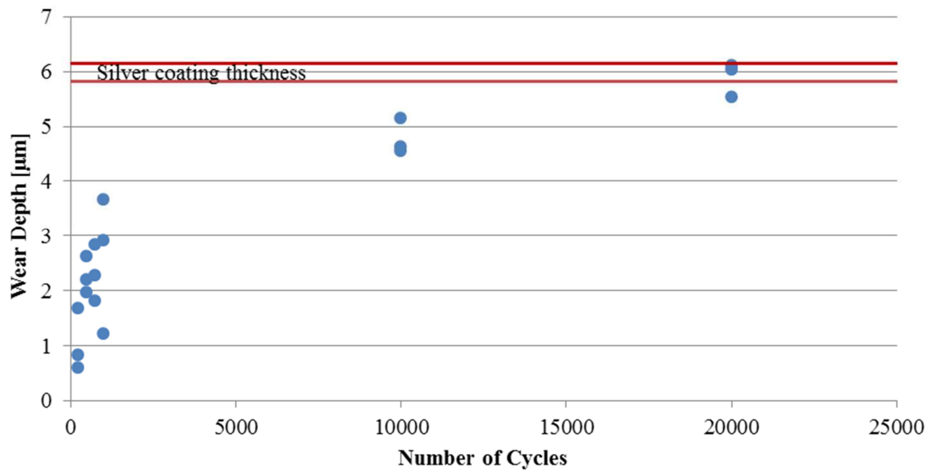

Fig. 9 Depth of wear in correlation with the number of cycles using the sphere geometry samples with 6 µm silver coating thickness

In Fig. 9, during the initial period, namely around the first 1000 cycles, nearly half of the silver layer was removed, however the left half part required around 19000 cycles. This would imply that the linear wear rate decreases dramatically with increasing tests cycles.

Two reasons for the phenomenon are as follows. Firstly, according to Archard's wear law (Equation (2)), at a predefined normal force and amplitude, the volumetric wear at the same sliding distance increment remains constant. Since the contact area at the contact point increases progressively in the tests, the linear wear must decrease along with the measurement cycles. Secondly, the initial running-in period is an unsteady state (Fig. 2) and the removal rate is relatively high due to many complex factors, such as the unevenness and different roughness at the surface.

A theoretical model is proposed in the following section in order to characterize the relationship between wear depth and sliding distance in Phase II, using a mathematic formula.

4.4 A Theoretical Model of Wear of the Sphere Part at Sphere/Flat Contact

In this study, the second phase (Fig. 2) attracts more interest. In order to predict the wear depth referring to the number of cycles, or more generally to the sliding distance, a theoretical model and calculation method are developed in this section of the paper.

According to Archard, the volumetric wear was proposed as Equation (2) in Section 1.1:

$$V_{wear} = k_V \cdot F \cdot s$$

where F is the normal force, s is the sliding distance, and k_V is the volume wear coefficient.

Due to the elastic and plastic deformation, the sphere is at the initial stage slightly flattened and this creates an initial contact area A_0, which can be determined with an FEA computation. The radius of the contact area r_0 and the reduced thickness h_0 (Fig. 10) can, as a result, be easily calculated. According to Archard's wear law (Equation (2)), the volumetric wear is linearly proportional to the sliding distance and consequently to the number of cycles at a given amplitude (Equation (3)), if the other parameters remain constant. Therefore the instant linear wear rate k_L at the given wear depth h (Fig. 10) can be calculated with the equations:

$$k_L = k_V / A = k_V / \pi r^2 \qquad (4)$$

with

$$r^2 = R^2 - (R - h - h_0)^2 = -h^2 + 2(R - h_0)h + 2Rh_0 - {h_0}^2 \qquad (5)$$

where A is the instant apparent contact surface. With the increasing wear depth, the instant apparent contact surface increases progressively. Therefore the linear wear rate must decrease along with the increasing sliding distance.

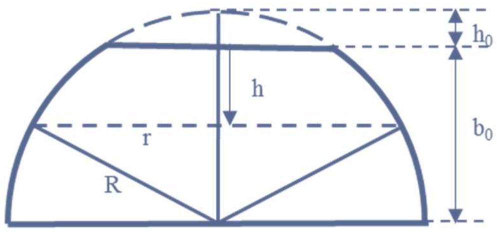

Fig. 10 Sketch of the values used in calculation

For a given depth of wear h, the sliding distance s is:

$$s = \frac{\pi}{k_V \cdot F}\left[-\frac{1}{3}h^3 + (R - h_0)h^2 + \left(2Rh_0 - {h_0}^2\right)h\right] \tag{6}$$

From FEA computation, the initial contact area A_0 is 0.0086 mm^2 and thus the initial radius of the contact area is around 0.05 mm with the initial reduced thickness h_0 at around 0.0003 mm.

Based on the removed volume from Cycle 1000 to Cycle 2000, the volume wear coefficient can be determined and a curve of wear depth in the phase II can be calculated. The comparison between the calculated curve and the test results is illustrated in Fig. 11.

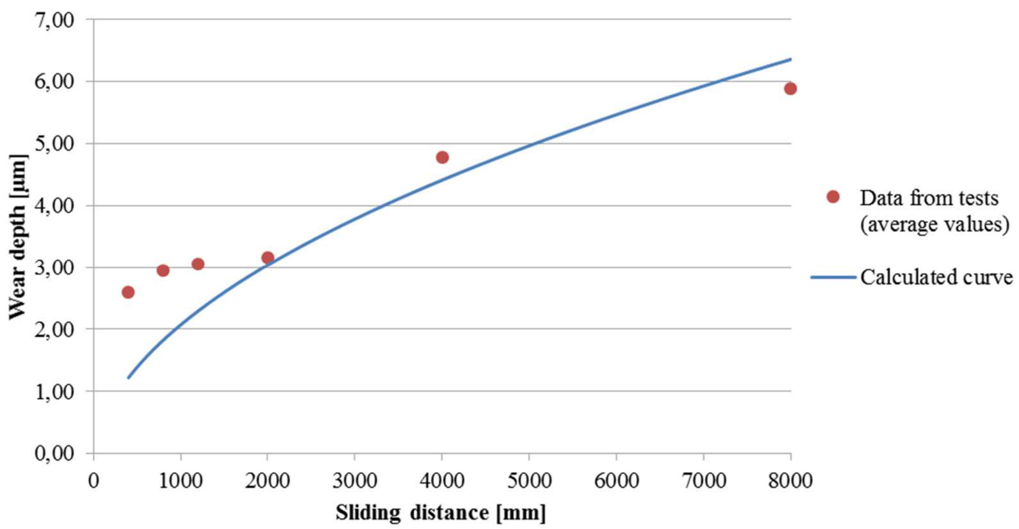

Fig. 11 Comparison between the calculated curve and the test results

The calculated wear curve is in good agreement with the data from tests at the steady state i.e. at 8000 mm sliding distance, namely 20000 cycles. Consequently the theoretical model is a reliable tool which can be used to predict the wear depth at a given sliding distance.

5 CONCLUSIONS

The analyses demonstrate a good correlation between lifetime, wear rate and coating thickness in silver coated contacts. The linear wear rate at the initial running-in phase is relatively high, compared to the second phase which is steady. In both of the two phases, the linear wear rates decrease progressively and thus the required number of cycles to wear through increases disproportionately with the increasing coating thickness at a contact with sphere/flat geometry. The proposed theoretical model represents a rough approach to characterize the relationship between wear depth and sliding distance. A more precise and generalized model, to describe the wear of the coated contact between a spherical and a flat surface, is currently being investigated.

6 ACKNOWLEDGEMENT

The authors would like to express their appreciation to their colleagues Liangliang Wang and Johannes Kösters in the Precision Engineering Laboratory for their support in conducting the experimental tests and their evaluation.

7 REFERENCES

[1] R.C. Weast, CRC Handbook of Chemistry and Physics, CRC Press, 58 Edition, 1977, pp. E84

[2] E. Hornbogen: Trockene Reibung, in K.-H. Zum Gahr, DGM-Informationsgesellschaft, Oberursel 1989, pp. 50-56

[3] N.N.: Prüfrichtline für Kfz.- Steckverbinder, AK PR 01-1996-04, 1994

[4] N.N.: Entwurf Prüfrichtline für KFZ-Steckverbinder, AK 432 2009-11-12, 2009

[5] J. Song, et al., Wear of Electrically Conductive Surfaces, Proceeding of Fracture Fatigue and Wear (FFW) conference, Kitakyushu, Japan, 2014

[6] N.N., Surfaces, Interfaces, and their Applications II - Introduction to Wear, ETH, Zurich, Switzerland, 2014

[7] F. Sawitzki: Einflussparameter von Reibkorrosionsuntersuchungen, Masterarbeit an Hochschule OWL, Lemgo, 2009, pp. 25-40

[8] D. Luther: Entwicklung, Bau und Erprobung eines Tribo- und Reibkorrosionsprüfstandes für elektrische Kontakte, Bachelorarbeit an Hochschule OWL, Lemgo, pp. 16-17, 2012I

Proceedings of the 4th International Conference on
Fracture Fatigue and Wear, pp. 208-214, 2015

FUNCTIONAL OBSOLESCENCE OF BOUNDARY LUBRICATED METALLIC FRICTIONAL PAIRS: SCUFFING CASE

L. Wojciechowski[1] and T.G. Mathia[2]

[1]Institute of Machines & Motor Vehicles, Poznan University of Technology, Poland
(T: +48 61 6652376, F: +48 61 6652736, E: lukasz.wojciechowski@put.poznan.pl)
[2]Laboratoire de Tribologie et Dynamique des Systèmes, Ecole Centrale de Lyon, France

Abstract: Motivated by rapid marketing and technological evolutions, new materials, novel components, innovating engineering solutions are developed and launched on the marketplace with ever-increasing rush. One of consequences is a dramatic change in manufacturing methods of all machinery and their market accessibility. An increasing production sector is in front of issues where and when life of products no longer interconnects with life cycles of required components. In case of frictional components this issue is functional obsolescence, may become when they do not function in the manner that they did when they were designed and created. This may be due to "natural" wear, or due to some specific phenomena, therefore wear monitoring and attempt of wear modelling are ambitious but necessary solutions. Presented study is focused on specific, still not very well known boundary lubricated regime with pure and additivated of well-known metallic materials (cast iron, steel and brass). Besides scuffing investigations, 3D morphologies of surfaces as well as micro hardness of rubbing surfaces are characterized before and post scuffing tribological qualifications. The series of elucidated conclusions are presented from fundamental as well as technological point of view.

Keywords: scuffing, boundary lubrication, pV limits

1 INTRODUCTION

Scuffing process (SP) is the catastrophic form of wear and due to its rapid and disaster character may lead to a functional obsolescence or definitive destruction of frictional operating parts of machines. According to the ASTM G40 standard, scuffing can be defined as a form of wear occurring in inadequately-lubricated tribosystems that is characterized by macroscopically observable changes in texture with features related to the direction of relative sliding. It should be underlined the macroscopic consequences of (SP) which activated generates a surface damage (adhesive by nature) to such a degree that subsequent service life of parts is significantly shortened or stopped. Curiously, there is a little knowledge of (SP) under lubricated conditions especially for metallic alloys; however a great number of parts which are submitted to severe tribological conditions are at risk, for instance cylinder liner, crankshafts, gearbox, camshafts, linear bearings and many others. Several theories concerning mechanism of (SP) activation [1] have been suggested in the literature but none of them unequivocally determine the initiation and evolution of that process. The most relevant of them connect the initiation of scuffing under boundary lubrication (BL) with: some critical temperature-pressure combination [2], debris generation size or a kinetic of their accumulation in interface [3], plastic deformation of asperities [4], formation and destruction of protective oxide films [5], desorption of polar constituents of lubricant from metallic surfaces [1,6], a lubricant structure decomposition [7], an energetic activation of surfaces [8], adiabatic shear instability [9] and some minor others. In practice, all of mentioned mechanisms of (SP) activation can occur in depending on some individual friction conditions or in the mutual combination with each other. On the other side, industrial approach to this problem requires determination of maximum values of some operational parameters which not exceeded secure against (SP) occurring. The example of such parameters most commonly used in industry (especially by bearing producers) is pV criteria. The pV (pressure x velocity) of contacting bodies limits have enormous practical importance offering possibility of calculation the limitations in friction nodes working in different kinetic configuration of materials and tribological conditions. Another practical use for pV limits is the selection of polymers for tribological applications. Thanks to that it is possible to evaluate conditions where the sudden, catastrophic wear or overheating of polymers may occur. Beside the polymer and bearing industry the pV limit is a useful parameter to define a maximum performance of gear boxes. In its classic sight it assumes that during (SP), the maximum value along the gear contact path of the product normal Hertzian pressure by the sliding speed remains constant. Of course this simplification does not take into account some parameters like: transitional regime, type of lubricant, its viscosity and temperature, gears' materials and geometry etc. That is why, in the case of gear boxes, their performance determination should be based also on some lubricant criterion (ex. on critical lubricant film thickness [10]).

Irrespective of that (BL) cannot provide a long-term protection against scuffing. For this reason it is fundamental to recognize the role of breaking point of the boundary layer activating (SP). Authors present the topological paradigmatic approach to this problem in which the key role plays the interaction between rheological, morphological and physicochemical properties of contacting surface layers [1, 11, 12]. In order to understand better the fundamentals of scuffing process (SP) under (BL) conditions, the series of systematic tribological double-blind trial are carried out with different more (ZDDP and olefin sulphide) or less (paraffin) active lubricants poorly lubricated cylinder/plan interface. (SP) is analyzed at the final phase under (BL) conditions particularly for finally ground or burnished steel cylinders (AISI 1045, AISI 4140) and finely polished planes from cast iron (EN-GJN 300), steel (AISI 1045) and brass (C37700). The role and the influence of rheological, morphological and physical-chemical previous characterizations of dynamics interfaces are discussed c.f. infra.

2 METHODOLOGY OF SURFACES CONDITIONING AND TRIBOMETRY

The surfaces investigated in the tribological experiments were manufactured from AISI 4130 and AISI 1045 steel in the shape of cylinders of 45mm external diameter and of 12mm width. The cylinders were ground consequently offering anisotropic morphologies of surfaces; therefore profile roughness is relevant to their characterizations. Grinding process offered Ra of approx. 0.5μm.

I AISI 4130 cylindrical surfaces were submitted to burnishing with six values of pressure of two symmetrical spherical sector-shaped rolls of 50 mm in diameter described in details elsewhere [1]. Selected load conditions comply with the following values of burnishing pressures : 1st: 1,3 GPa, 2nd:1,64 GPa, 3rd: 1,87 GPa, 4th: 2,06 GPa, 5th: 2,22 GPa, 6th: 2,36 GPa. Kinematic conditions for burnishing are: speed – 100m/min, burnishing feed – 0.08mm/rev, number of passes – 2, lubricated by a 1:1 mixture of mineral oil and kerosene.

II AISI 1045 cylindrical surfaces were divided into four batches when first of them remained ground (as a reference) and others were burnished with three levels of pressure: 1st: 1,64 GPa, 2nd: 2,06 GPa and 3rd: 2,36 GPa. Kinematic burnishing conditions were as for of AISI 4130 cylinders.

Systematic areal morphological analyses were performed thanks to optical interferometer on milimetric region relevant to contact surface during experimental tribological investigations. The area of 1,2 mm x 0,9mm in five parts of cylindrical surfaces every 72º were performed. Metrological analyses have been done very carefully and consciously taking into consideration calibration as well as transfer function and measurement limitations of selected topometric device.

The μhardness investigations of ground (AISI 1045 cylinders) and burnished (AISI 1045 and AISI 4130 cylinders) surfaces were carried out using Vickers test respecting EN-ISO 6507-1 standard. In order to satisfy statistical requirements the μhardness measurements was performed five times for each type of cylinders.

The criterion for determination of scuffing is increasing of friction coefficient under constant load (Fig. 1). The experiments were performed under single drop lubrication using gear oil with ca. 5% olefin sulphide as an extreme pressure additive. Therefore, scuffing activation period is measured by the time it took for scuffing to occur which is equivalent to the situation of poor lubrication in the friction node. The scuffing kinetics were performed at sliding speed of 0.5 m/s between rotating cylinder (AISI 4130 or AISI 1045) and the stationary block (EN-GJL-300 cast iron with flake graphite). Load applying incrementally to the friction pair is also presented in Fig. 1. In order to satisfy the statistical requirements the scuffing investigation was performed four times for each pair of cylinders and flat blocks.

3 RESULTS ANALYSIS AND DISCUSSION

Changes of 3D ISO 25178 (in the case of AISI4130/EN-GJN 300 pair) or 2D ISO 4287 (in the cases of AISI1045/EN-GJN 300 and AISI1045/AISI1045 pairs) morphological parameters indicate their role in the scuffing performance. Fig. 2 presents the relationship between morphology (Ssk/Rsk parameters) versus scuffing process (time to scuffing activation (t_{SC})). Cylinders burnished with the maximum pressure were excluded from the subsequent analysis because the most morphological, rheological and physical-chemical parameters are subject to meaningful worsening due to the critical cold work achievement. The level of crystallites packing of the material is so high that further plastic deformation does not cause any further strengthening of the surface layer and its destruction begins. It can be observed from the Fig. 2 that a tendency of areal skewness (Ssk) changes in the (SP) context is different in nature in all cases. However, cast irons' pairs are linked by one common and important feature – the best scuffing resistance was obtained for similar values of Ssk. For AISI4130/EN-GJN 300 pair, the longest t_{SC} corresponds to Ssk=–0,752 (Fig. 2a). The similar situation characterizes the case of AISI1045/EN-GJN 300 pair when the greatest t_{SC} responds to Rsk value equal – 0,786 (Fig. 2b). Values of Ssk/Rsk parameters are negative what indicates that a majority of material is localized near peaks due to grinding or burnishing process. However, it is worth noting that the optimum resistance to (SP) does not correspond to the most "flat" surface morphology. The most probable reason of this fact is too small volume of valleys when the surface is too flat. Surface valleys may operate as some specific lubricant's pocket which assures an adequate supply of oil into the contact area. If the volume of valleys is too small, the limited amount of oil located in them may make difficult long-lasting remaining of the full HD or EHD conditions.

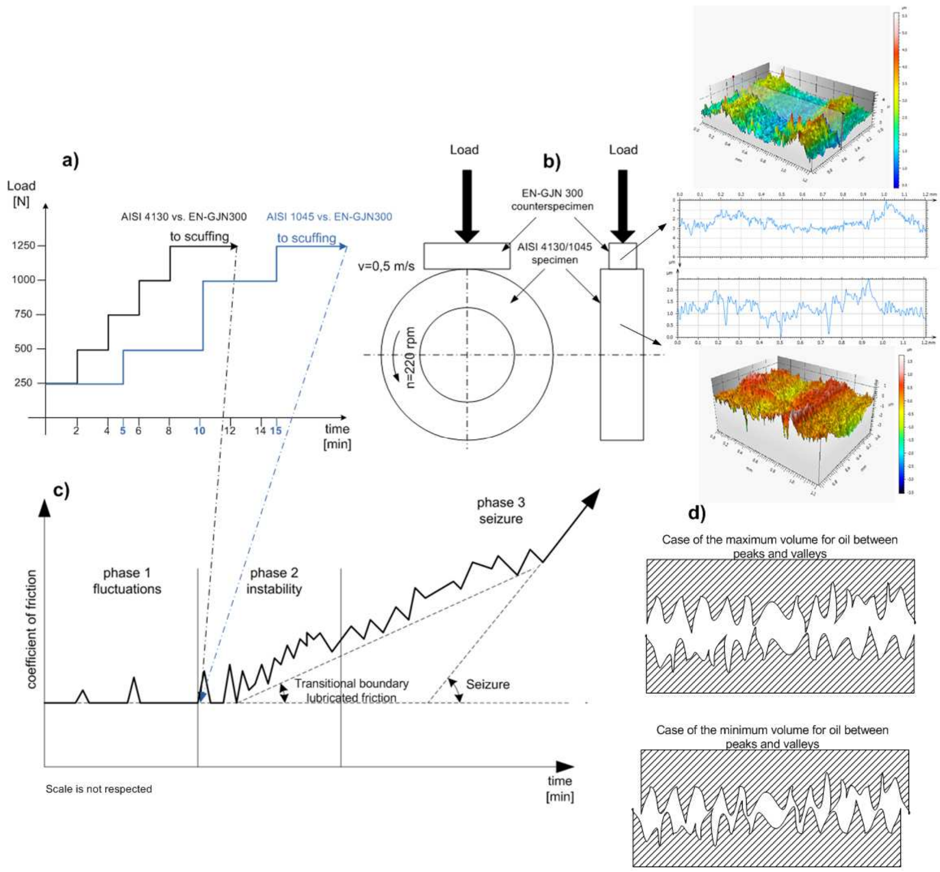

Fig. 1 Schematic view of scuffing experimental procedure, (a) load application kinematics, (b) micro (morphology) and geometry of contacting bodies, (c) recurrent typical coefficient of friction versus time and (d) relevant morphologies orientation of peaks and valleys in the context of oil volume reservoirs in the areal real contact.

Some confirmation of this conjecture can be an analysis of Sv and Sp/St for the AISI4130/EN-GJN300 pair (Fig. 3a). It can be observed that the best scuffing performance ensures the lowest value of the max valley depth Sk and the highest value of Sp/St ratio (max peak height/max height of surface roughness). Irrespective of that all values of Sk are relatively small what points flattening of the surface to such a level in which the optimal relationship between critical pressures and volume of oil in the real contact area can be recognized. Similar explanation can be applied to Sp/St variations (the longest time to scuffing corresponds to the highest value of this ratio). Ratios of Sp/St less than 0.5 offer favourable morphology for wear performance. Additionally, on the basis of measured scuffed areas of blocks (EN-GJN 300 counter-specimens), the pV limits for analysed friction pair (Fig. 1) were calculated and obtained results are presented at Fig. 3b. Changes of pV limits in the function of skewness bears a resemblance to the case of its relationship with time to scuffing (Fig. 2b).

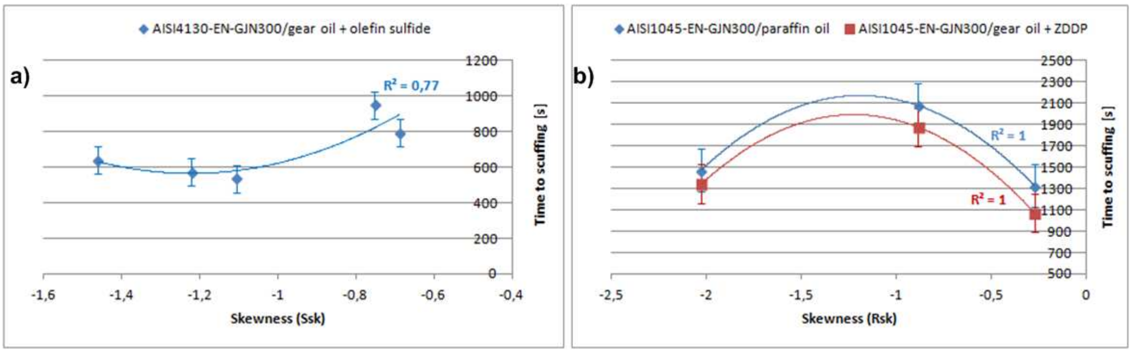

Fig. 2 Scuffing resistance versus morphological parameters (Skewness) for different lubricants: AISI4130/EN-GJN300 pair (a), AISI1045/EN-GJN300 pair (b).

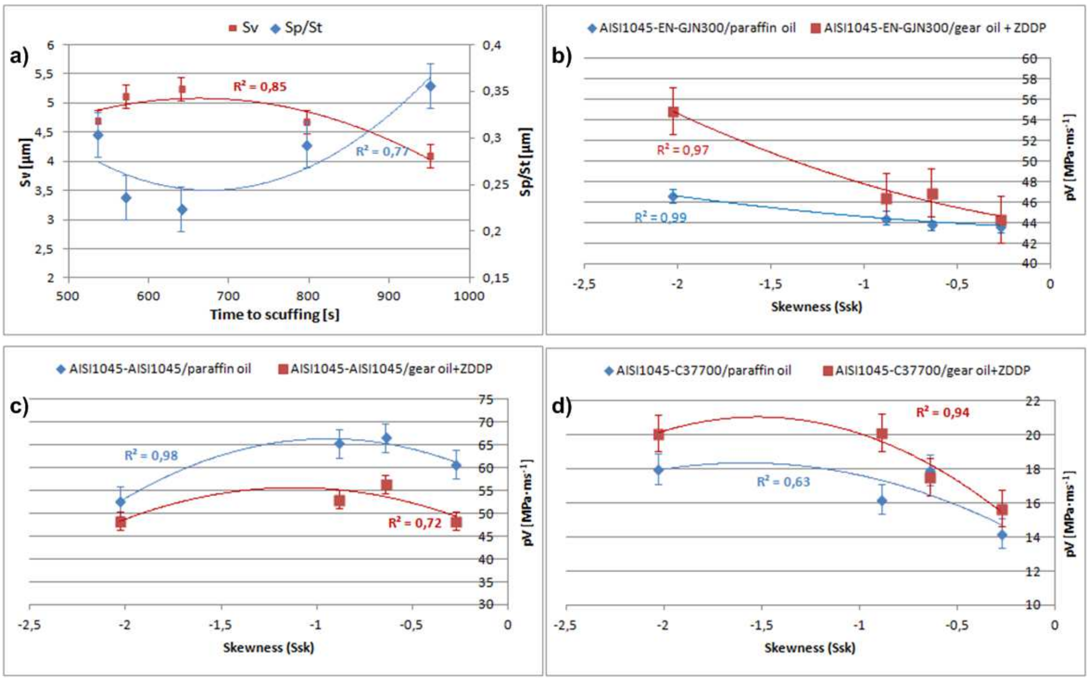

Fig. 3 Scuffing resistance for different lubricants versus morphological parameters (Sv&Sp/St) (a) pV limits versus Skewness of AISI4130/EN-GJN300 (b), AISI1045/AISI1045 (c), AISI1045/C37700 (d).

Thanks to tribometry it has been stated the small influence of morphology (relatively big differences in Skewness) on pV limits for most material associations (some exception is AISI1045-EN-GJN300 pair lubricated by oil with ZDDP). For comparison purposes, Fig. 3c and 3d show pV limits dependence of skewness for the pair of AISI1045-AISI1045 and AISI1045-C37700). Both cases present the same character as in the steel-cast iron configuration. Therefore, it seems that Ssk may be considered as the morphological precursor to a technological plastic forming and scuffing performance of lubricated friction pairs.

The additional assumption of the Ssk application as a technological precursor of scuffing performance can be the analysis of the peak and valleys' shapes and areas presented at Fig. 4. Cylinders distinguished by the longest time to scuffing are characterized by the ratio of mean area of peak and valleys close to 1 (0.92 for t_{SC}=950 s and 0,99 for t_{SC}=796 s). Therefore, it can be conjectured that in these cases the optimal relationship between pressures on asperities and oil capacity of valleys was obtained. Of course, such kind of conjecture should be confronted with other types of materials and their treatment methods.

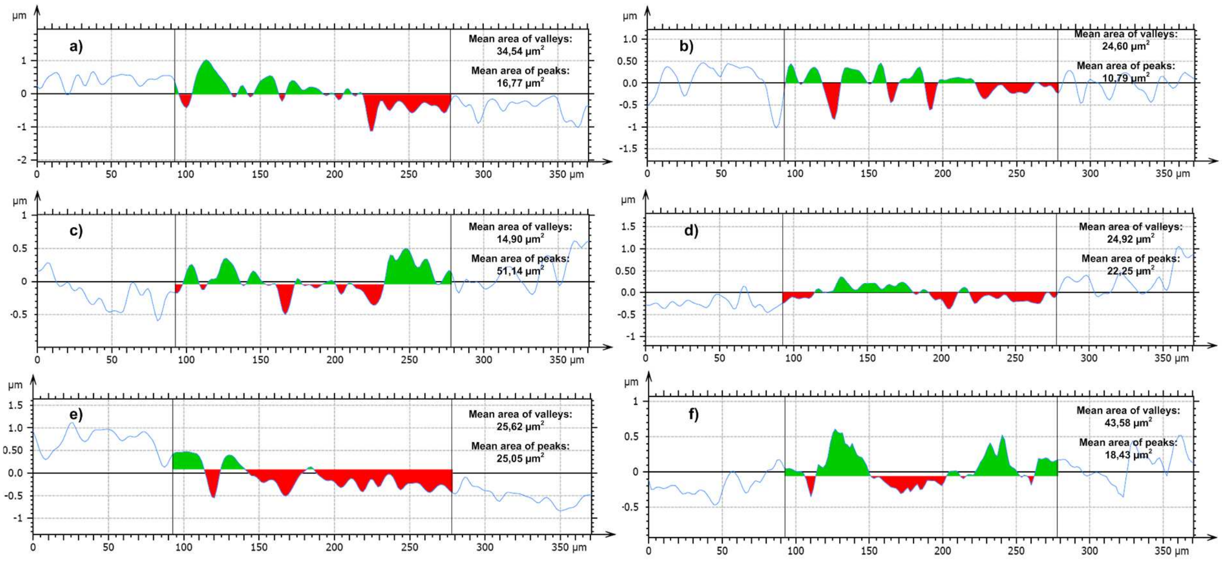

Fig. 4 Mean section of valleys and peaks of AISI4130 cylinders differently burnished: 1st (a), 2nd (b), 3rd (c), 4th (d), 5th (e) and 6th (f) level of burnishing pressure.

Obtained results of morphological analysis are compatible with prior investigations of authors (ex. [13]). Referring to them, there are some morphology invariants connected with the (SP) activations. Apart from the starting values they stabilize at up-close level which is characteristic for the (SP) initiation. Mean numbers of motifs and their mean height and volume are at the certain level due to scuffing. It may indicate the shaping of real contact area of particularly favorable characteristics for scuffing activation. The next morphological invariant identified in scuffing investigations is Vvv (Void volume of the valleys) parameter characterized by similar values for all types of scuffed cylinders. It may indicate that a critical volume of oil is reached and scuffing can be activated. This assumption has a similar denotation as the changes of Ssk, Sv and Sp/St characterized in this study. Topological approach to the (SP) requires the analysis of other parameters than morphological ones. The best representative of surface rheological parameters can be residual stresses. Generally, the increases of the compressive residual stresses cause the increase of the scuffing performance [1,13]. The measurement of this parameter needs specialized and expensive equipment increasing the difficulties of its application in engineering practice. A surface hardness is a quantity strongly correlated with residual stresses and relatively easy to measure. Generally dominated opinion, the higher hardness corresponds to the better scuffing performance [14] is confirmed in present study too. The relationship between cylinders µhardness and scuffing performance is concurrent to the literature information. Fig. 5 presents the influence of HV0,1 µhardness of cylinders on time to (SP) activation for AISI4130-EN-GJN300 and AISI1045-EN-GJN300 friction pairs.

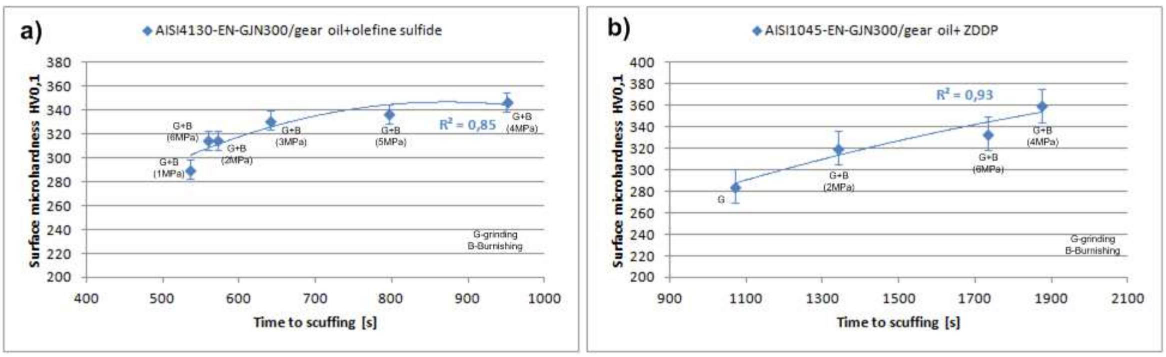

Fig. 5 Scuffing resistance for different (time to scuffing) versus HV0,1 µhardness (different burnishing): AISI4130/EN-GJN300 pair (a), AISI1045/EN-GJN300 pair (b).

Additionally, it is worth to note that the increase of surface hardness by work hardening is more beneficial in preventing scuffing than is a change in carbon content or heat treatment [14]. It can be observed that (as in the case of morphological parameters [1, 13] the achievement of critical cold work has a negative impact on µhardness (5, 6 MPa – Fig. 5a and 6 MPa – Fig. 5b). The surface of AISI 4130 and AISI 1045 cylinders damaged by too high pressures of burnishing can be described by a clear decrease of all analyzed characteristics. However, it should be stated that in the case of rheological parameters (µhardness, residual stresses [13]) this effect is not evident one as in the relationship between levels of burnishing pressure and surface morphology and physical chemistry (ex. polar component of surface free energy [1, 15]).

4 CONCLUSIONS

On the basis of experimental observations under (BL) conditions, following conclusions can be stated.

- It has been measured the clear relationship between some morphological parameters of AISI 4130 and AISI 1045 cylinders (Ssk/Rsk, Sv, Sp/St) and their scuffing performance. The negative values of Ssk & Rsk parameters indicate the concentration of material localized near large summits of surface due to grinding machining process. However, the optimum resistance to (SP) does not correspond to the "smooth flat summits" surfaces. A probable reason of that tribological behaviour is coming from too small volume of valleys limiting the amount of oil located in. This assumption was confirmed by the analysis of mean areas and shapes of cylinders' valleys and peaks (Fig. 4). Cylinders distinguished by the best scuffing performance are characterized by the ratio of mean area of peak and valleys close to 1. Therefore, it can be conjectured that in such cases the optimal relationship between pressures on asperities and oil capacity of valleys was obtained.
- The large range in Ssk does not offer significant changes in pV limits for most materials associations. That is why Ssk may be considered as the morphological precursor to the technological forming of scuffing performance of lubricated friction pairs (but not as a precursor to their operating performance- Fig. 3).
- It can be observed the clear relationship between HV0,1 micro hardness of AISI 4130 and AISI 1045 cylinders and their scuffing performance (Fig. 5). Generally, higher hardness of surfaces, the better their scuffing performance.
- In the case of metallic surfaces morphology (Ssk) and rheology (hardness), may be considered as magnitudes for preliminary valuation of scuffing resistance without the application of expensive measurement equipment [16]. That is why they may be recommended for correct metrological use in engineering practice as some precursors for the catastrophic, functional obsolescence of friction pairs.

5 NOMENCLATURE

Abbreviations	
BL	Boundary lubrication
HD	Hydrodynamic lubrication
EHD	Elastohydrodynamic lubrication
HV0,1	Vickers micro hardness
SP	Scuffing process
ZDDP	Zinc dialkyldithiophosphates
Topographical Parameters:	
Sp	Maximum peak height, height between the highest peak and mean line [μm]
Ssk/Rsk	Skewness of the surface/profile height distribution
Sv	Maximum pit height, depth between mean line and the deepest valley [μm]
St	Maximum height between the highest peak and the deepest valley [μm]
Vvv	Void volume of the valleys [ml/mm^2]
Tribological Parameters:	
t_{SC}	Time to scuffing [s]

6 REFERENCES

[1] Ł. Wojciechowski, T.G. Mathia, Conjecture and paradigm on limits of boundary lubrication, Tribology International, 82 (Part B), 577-585, 2015.

[2] S.C. Lee, H.S. Cheng, Experimental validation of critical temperature-pressure theory of scuffing, Tribology Transactions, 38 (3), 738-742, 1995.

[3] J. Enthoven, H.A. Spikes, Infrared and visual study of the mechanisms of scuffing, Tribology Transactions, 39 (2), 441-447, 1996.

[4] L. Jiajun, L. Zhigiang, C. Yingian, The study of scuffing and pitting failure of cam-tappet rubbing pair, Wear, 140 (1), 135-147, 1990.

[5] A.W. Batchelor, G.W. Stachowiak, Some kinetic aspects of extreme pressure lubrication, Wear, 108 (2), 185-199, 1986.

[6] H.A. Spikes, A. Cameron, Scuffing as a desorption process – an explanation of the Borshoff effect, ASLE Transactions, 17 (2), 92-96, 1974.

[7] S.M. Hsu, M.C. Shen, E.E. Klaus, H.S. Cheng, P.I. Lacey, Mechano-chemical model: reaction temperatures in a concentrated contact, Wear, 175 (1-2), 209-218, 1994.

[8] A.P. Semenov, The phenomenon of seizure and its investigation, Wear, 4 (1), 1-9, 1961.

[9] J. Hershberger, O.O. Ajayi, J. Zhang, H. Yoon, G.R. Fenske, Evidence of scuffing initiation by adiabatic shear instability, Wear 258 (10), 1471-1478, 2005.

[10] J. Castro, J. Seabra, Scuffing and lubricant film breakdown in FZG gears. Part II: New PV scuffing criteria, lubricant and temperature dependent, Wear, 215 (1-2), 114-122, 1998.

[11] T.G. Mathia, F. Louis, G. Maeder, D. Mairey, Relationship between surface states, finishing processes and engineering properties, Wear, 83 (2), 241-250, 1982.

[12] K.J. Kubiak, M.T.C. Wilson, T.G. Mathia, Ph. Carval, Wettability versus roughness of engineering surfaces, Wear, 271 (3-4), 523-528, 2011.

[13] Ł. Wojciechowski, T.G. Mathia, Proposal of invariant precursors for boundary lubricated scuffing, Proceedings of 16th Nordic Symposium on Tribology, Aarhus, Denmark, 10-13 June 2014, 134-139.

[14] Y. Yamamoto, F. Hirano, Relation between scuffing resistance and the increase in surface hardness during tests under conditions of rolling/sliding, Wear, 63 (1), 165-173, 1980.

[15] Ł. Wojciechowski, S. Nosal, The application of surface free energy measurement to valuation of adhesive scuffing, Eksploatacja i Niezawodność - Maintenance and Reliability, 45 (1), 83-90, 2010.

[16] T.G. Mathia, P. Pawlus, M. Wieczorowski, Recent trends in surface metrology, Wear, 271 (3-4), 494-508, 2011.

Proceedings of the 4th International Conference on
Fracture Fatigue and Wear, pp. 215-220, 2015

FRICTION AND WEAR PROPERTIES OF HEAT-TREATED Cr-Mo STEEL DURING RECIPROCATING SLIDING CONTACT WITH SMALL RELATIVE MOTION

M. Endo[1], T. Saito[1], S. Moriyama[1], S. Okazaki[2] and H. Matsunaga[2]

[1]Fukuoka University, Fukuoka, Japan
[2]Kyushu University, Fukuoka, Japan

Abstract: Effects of the reciprocating sliding contact with the micrometer level of relative movement on the dry friction and wear properties were investigated. A novel ring-on-ring test was developed by making use of a tension-torsion fatigue-testing machine. The material investigated was a heat-treated JIS SCM435 (Cr-Mo steel) with a Vickers hardness of 330. The tests were conducted under a wide range of the testing conditions with the relative sliding displacement of 10-250 μm, the contact stress of 10-300 MPa, the sinusoidal frequency of 0.05-20 Hz, and with the number of reciprocating sliding cycles of 10-10^4 cycles. The time variations of tangential force and relative sliding displacement between contact surfaces were monitored during testing. The worn surfaces and the wear progress inside the specimen were microscopically observed. The relationship between friction force and displacement exhibited a quasi-rectangular hysteresis loop. The coefficient of kinetic friction was within a range of 0.6 to 0.8 independently of the above test conditions. The thin layer of contact surfaces locally underwent a severe cyclic plastic deformation and thereby the grain refinement took place, which formed a very hard layer. Wear particles, such as very fine powder and metallic fragments, were formed between the contact surfaces. Microscopic cracking was also observed on the worn surfaces.

Keywords: Ring-on-ring test; micrometer scale sliding displacement; coefficient of friction; fretting wear; Cr-Mo steel

1 INTRODUCTION

A number of failure problems emerged in engineering applications are associated with repeated sliding motion between the contact surfaces. Fretting-wear, -corrosion and -fatigue are typical examples of this type of failure. It is known that the amplitude of the motion is in a range of 1 to 100 μm [1], but the amplitude is not uniform on the contact surface and at the boundary of the area where slip motion occurs and the area where it does not occur, eventually, the amplitude falls asymptotically to zero.

The rolling-contact fatigue failures, such as the flaking-type failure in bearings, are intimately related to shear-mode (mode II and III) fatigue crack growth [2-5], which is also involved in the repeated sliding contact. The growth rate and the threshold condition for propagation are influenced by the interaction of opposing crack faces [5-7]. In this case, the relative displacement along the faces of a crack in a specimen can be in the order of several micrometers or more but it approaches to zero at the crack tip.

All the above phenomena are closely related to the micro-nano level of cyclic reciprocating slip. To make a quantitative analysis for this type of engineering problems, it is quite important to know about the mechanisms of friction and wear, including those of coefficient of friction, formation of contact surface topography, change of subsurface microstructure, formation of debris and microscopic fracture, occurred in the regime of micro-nano level sliding motion. However, the experimental technique that enables to systematically investigate these complex mechanisms is still in a nascent stage of development. Although extensive researches have been made on frictional processes in the micro- and nano-Newton range, for instance, with an atomic force microscopy (AFM) [8-10], there is a gap between classical tribology and nanotribology and the gap has yet to be closed [11].

In this study, a novel testing method was developed to explore the properties of the sliding contact, on the micrometer level of relative displacement, for the contact area with an engineering size of tens mm^2. Then the reciprocating sliding contact tests were conducted to investigate the coefficient of friction and the damage mechanism of contact surfaces.

2 EXPERIMENTAL PROCEDURES

The material investigated was a JIS SCM435 (Cr-Mo steel), which was quenched from 860ºC followed by tempering at 550ºC for 1 hour. The chemical composition in mass% was: 0.36C, 0.30Si, 0.77Mn, 0.027P, 0.015S, 0.02Cu, 0.02Ni, 1.06Cr, 0.18Mo and bal. Fe. The Vickers hardness, *HV*, measured with a load of 9.8 N was 330. Tensile strength was 950 MPa.

Fig. 1 shows the shape and dimensions of the specimen with a hollow cylinder. The end faces of hollow cylinders were finished by polishing with an emery paper and then by buffing with an alumina paste. As shown in Fig. 2, reciprocating sliding contact test was performed by contacting the end faces of two hollow cylinders one another and by applying reversed angular displacement to the specimens. The test based on such a configuration is known as a ring-on-ring test, which is, though, usually performed in unidirectional rotation. This testing method has an advantage that there is no edge effect and consequently the coefficient of friction can be defined as the ratio of tangential to normal forces acting on the contact surface based on the assumption of an identically-distributed force.

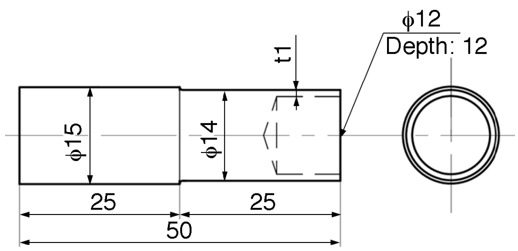

Fig. 1 Shape and dimensions of specimen

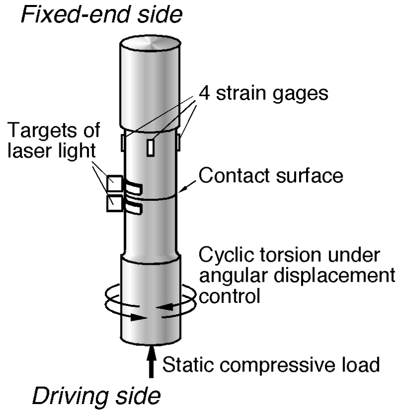

Fig. 2 Configuration of specimens and measurement devices

An MTS servo-hydraulic fatigue testing machine, which was custom-designed for conducting the combined tension and torsion fatigue tests at an operating speed of ~0 to 50 Hz, was utilized to perform the ring-on-ring test. This testing machine has a high stiffness and can accurately control the twisting moment and angle, and independently, the axial load and displacement. The capacities are 100 kN in axial load and 1000 Nm in twisting moment. The sine-wave displacement was applied by rotating the specimen at the driving side under the control of angular displacement, cf. Fig. 2. Therefore, the sliding velocity is not constant during the test; i.e., it reaches to zero at the switching point of sliding direction and to the maximum at the neutral point of displacement.

A laser displacement meter was used to measure the sliding displacement between the contact surfaces. A small light plastic plate, on which a well-polished tinfoil was pasted, was glued to the specimen surface at a distance of 5 mm from the edge of hollow cylinder as a target of laser light. The relative sliding displacement, *S*, was defined as the value computed by subtracting the displacement measured for the fixed-end side target from that for the driving side target, cf. Fig. 2.

To attain the condition of uniform contact over the whole contact surface, the contacted specimens was, before starting the test, rubbed with each other with a large sliding displacement of more than 10 mm under a contact stress of 10 MPa until the difference of the values in four strain gages measured on the specimen was sufficiently minimized, cf. Fig. 2. Therefore, it must be noted that the contact surfaces are not damage-free but have been initially worn by rubbing.

In the present experiments, the apparent contact stress, *p*, was defined by

$$p = W/A \tag{1}$$

where *W* is the normal compressive load measured by a load cell equipped in the testing machine. Further, *A* is the apparent area of contact and a nominal value of 40.8 mm^2 for the cross-sectional area of specimen's hollow cylinder was used for the calculation in this study, cf. Fig. 1. The gross value of frictional force, *F*, tangent to the contact surface was defined by

$$F = T/r \tag{2}$$

where T is the twisting moment measured by a load cell, and r is the mean radius (i.e., half the mean value of inner and outer diameters of hollow cylinder), for which a nominal value of 6.5 mm was used for the calculation throughout this study. During testing, the tangential force, F, and the relative sliding displacement, S, were simultaneously monitored as a function of time, t.

3 RESULTS AND DISCUSSION

3.1 Coefficient of friction

Fig. 3(a) shows the friction force, F, and the relative displacement, S, as a function of the time, t, which were measured under a contact stress, p, of 50 MPa, at a test frequency, f, of 1 Hz and at a number of reciprocating cycles, N, of around 10 cycles after the beginning of test. A rectangle hysteresis loop shown in Fig. 3(b) represents the relationship between F and S for the data in the part surrounded by the dotted line in Fig. 3(a).

The time variation of S exhibited approximately a sine waveform, while that of F was approximately of a square waveform. Vertical quick change of F corresponds to an interval that slippage between contact surfaces does not occur. It is considered that the elastic deformation of hollow cylinders between targets may account for the displacement in this interval. After the value of F reached the maximum static friction force, slippage occurred macroscopically. The kinetic friction force, F_k, during slipping, which was somewhat less than the maximum static friction force, remained nearly constant. When examined closely, however, it was seen that F_k, only slightly, decreased initially with increase of sliding velocity and subsequently increased with decrease of sliding velocity. The above results may merely exhibit almost the same properties of dry friction that have been recognized well [1]. Acute increases of F were frequently appeared in the middle of horizontal part as seen in Figs. 3 (a) and (b). These may presumably be an indication of stick-slip movement.

The relation of F and S observed at N = 2000 is shown in Fig. 4, in which the result for N = 10 is also shown for comparison. The kinetic friction force, F_k, at N = 2000 was somewhat larger than that at N = 10. In addition, F_k was not constant but increased gradually with increase of slipping distance. This difference of friction properties between N = 10 and 2000 is simply attribute to the repetition of reciprocating sliding movement. Wear debris was observed on the contact surfaces after 2000 cycles. The specific wear rate was 6.6×10^{-7} mm^2/N. This value corresponds to the transition regime of mild wear and severe wear.

After the debris was removed from the contact surfaces at N = 2000, the test was continued for 10 cycles until N = 2010. As a result, as shown in Fig. 4, the value of F_k dropped overall but a tendency of gradual increase was remained. Thus, the presence of debris plays a partial role in the increase of F_k but for the gradual increase of F_k, other factors, such as the increasing effects of adhesion, mechanical interlocking of asperities, etc., may be involved

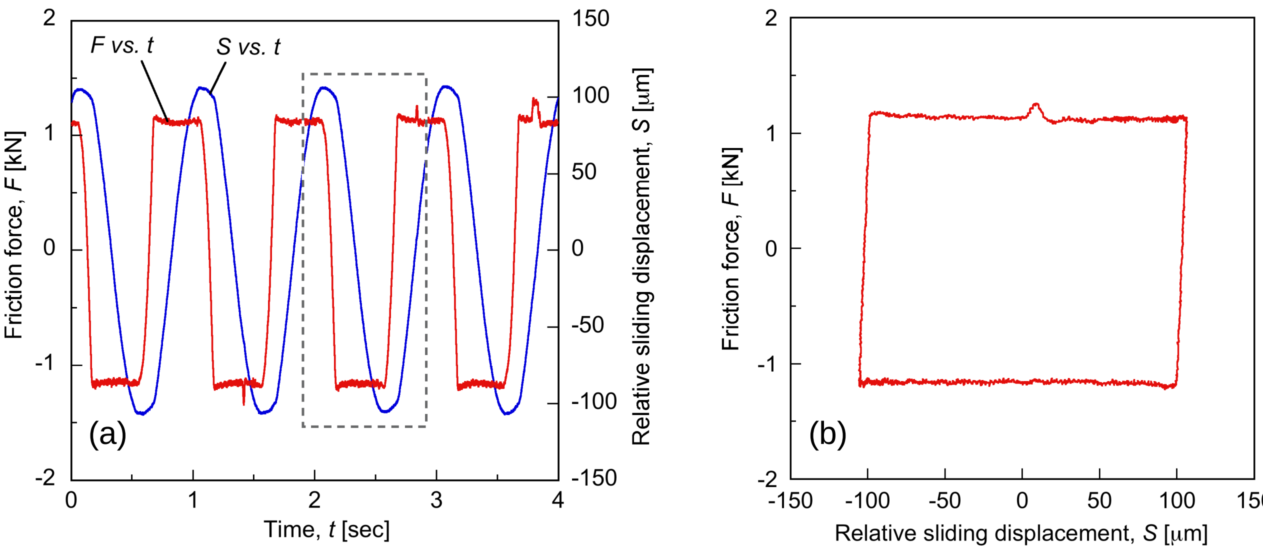

Fig. 3 (a) Time-variation of friction force, F, and relative sliding displacement, S; and (b) relationship between F and S, which were observed at N = 10 under the conditions with ΔS = 200 μm, p = 50 MPa, and f = 1 Hz.

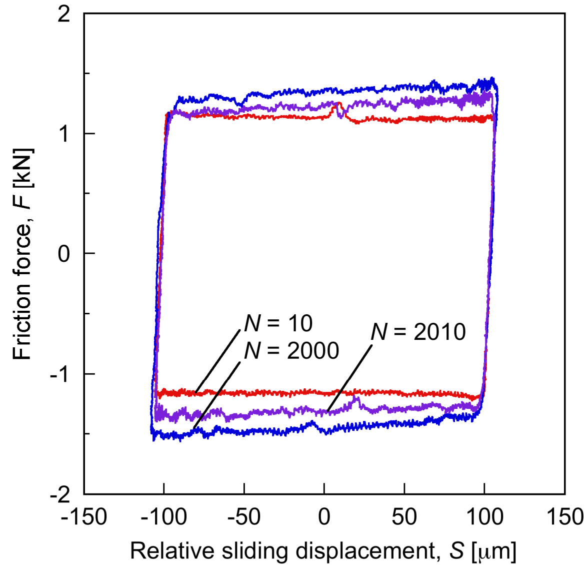

Fig. 4 Relationship between F and S for N = 10, 2000 and 2010 cycles under the testing condition: ΔS = 200 μm, p = 50 MPa, and f = 1 Hz; Debris was removed at N = 2000 and thereafter the test was continued until N = 2010.

The coefficient of kinetic friction, μ, was defined by the following equation:

$$\mu = F_k/W \tag{3}$$

A half of the range of upper and lower values of F_k at the neutral point of S in a hysteresis loop, cf. Fig. 4, was used as a representative value for F_k. The values of μ was measured under the conditions with the range of relative sliding displacement, ΔS, of 10-250 μm, the contact stress, p, of 10-300 MPa, the sinusoidal frequency, f, of 0.05-20 Hz, and with the number of cycles, N, of 10-10^4 cycles. Fig. 5 shows the values of μ as a function of the above factors. The detailed information about the data in this figure is

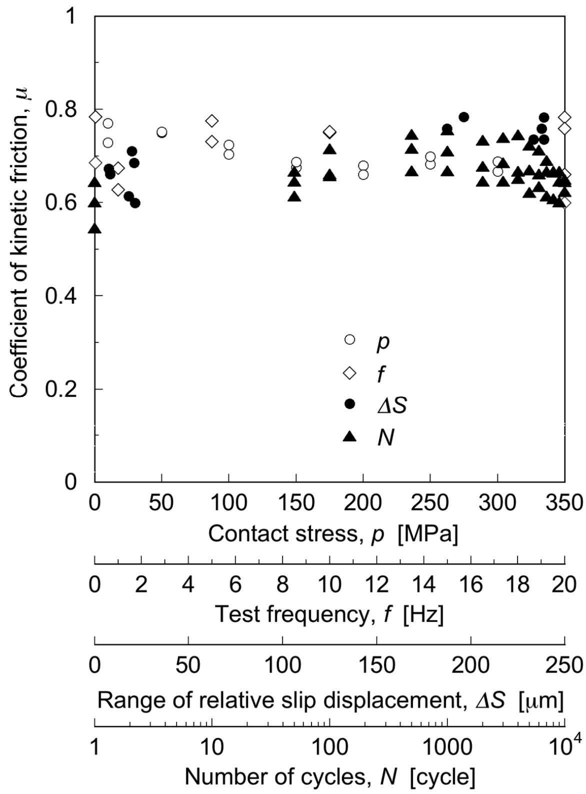

Fig. 5 Coefficient of kinetic friction, μ, as a function of p, f, ΔS and N

provided in [12]. The value of μ was evenly scattered from 0.6 to 0.8, independently of a wide range of the testing conditions, giving the average value of about 0.7.

3.2 Damage of surfaces in contact

Fig. 6 shows the contact surface after the test cycled until $N = 10^4$ under the conditions of $\Delta S = 180$ µm, $p = 100$ MPa, and $f = 1$ Hz. The debris was removed before taking this picture. The damaged surface was characterized by a rough surface composed of the plowing wear scars, smeared metal prows and the depressions, which were all aligned parallel to the sliding direction. Fig. 7 shows a microscopic crack emanated from the bottom of depression, which was observed on the cross section of worn surface. Flaking induced by subsurface cracking may play a role for the formation of depressions.

To investigate what happened inside the specimen, the testing machine was paused in the process of sliding wear and then the specimens were fixed with two halved steel-pipes and an epoxy-bonding agent to keep the specimens contacted with each other. Fig. 8 shows a state of the contact surfaces obtained on the cross section of such fixed-specimens. The microstructure just below the surfaces exhibits the extensive plastic flow and the grain refinement. The Vickers hardness of the fine-grained microstructure reached *HV*720, which is much larger than that of gross microstructure (*HV*330). The sliding contact, eventually, does not take place between the surfaces of original material but mostly between those of hardened materials. In addition, different types of wear debris existed between the contact surfaces, such as small wear particles, relatively large fragments and plate-like aggregates of fine wear powder elongated in the sliding direction. The delamination of the fine-grained surface layer is also seen as shown by an arrow in Fig. 8, where the nucleation of subsurface crack and its propagation parallel to the surface are involved. This seems to be one of the mechanisms that accounts for the formation of rough surface and metal fragments.

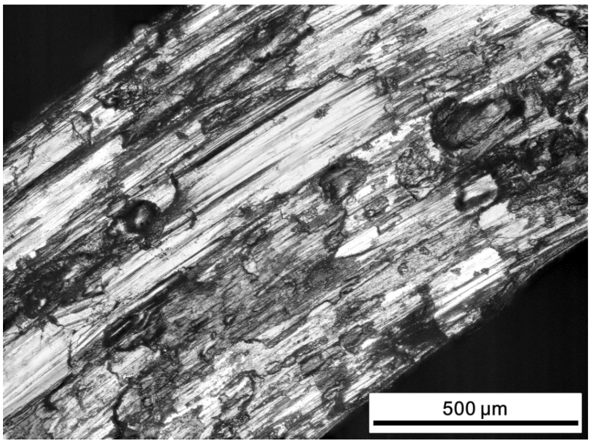

Fig. 6 Worn surface observed after the test cycled until $N = 10^4$ under the conditions with $\Delta S = 180$ µm, $p = 100$ MPa, and $f = 1$ Hz

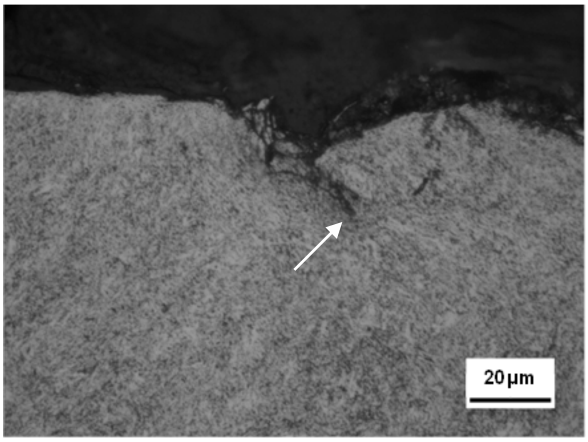

Fig. 7 Microscopic crack emanated from the bottom of depression; the crack tip is indicated by an arrow.

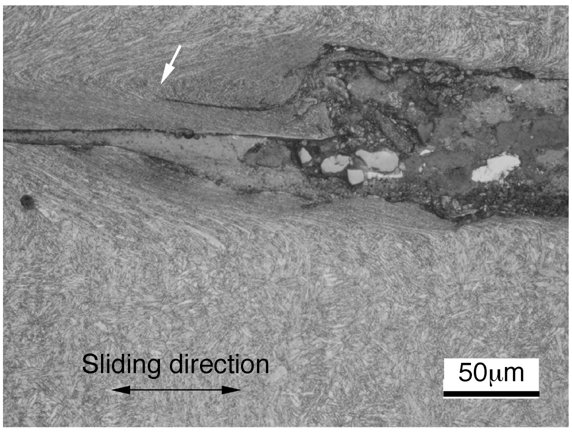

Fig. 8 State of contact surfaces in the process of sliding observed inside specimen at $N = 2000$ under testing condition with $\Delta S = 200$ µm, $p = 50$ MPa, and $f = 1$ Hz; The crack tip is indicated by an arrow.

4 CONCLUSIONS

The characteristics of friction and wear associated with micrometer-level reciprocating sliding contact were investigated in the novel ring-on-ring testing method for heat-treated Cr-Mo steel. The obtained results are summarized as follows:

- The relationship between friction force and displacement exhibited a quasi-rectangular hysteresis loop.
- The property of friction at the beginning of test was almost the same as that of well-known dry friction. As the number of cycles of reciprocating sliding increased, the kinetic friction force somewhat increased. This is partly because of the debris generated by a number of sliding repetitions.
- The coefficient of kinetic friction was within a range of 0.6 to 0.8 independently of a wide range of testing conditions.
- The cyclically worn surface was rough and different types of debris existed between the contact surfaces. A thin layer of the surfaces underwent locally a severe cyclic plastic deformation and thereby the grain refinement took place forming a very hard layer. Microscopic cracking was also observed on the contact surfaces.

5 REFERENCES

[1] I. M. Hutchings, Tribology: Friction and Wear of Engineering Materials, Edward Arnold, London, 1992.

[2] A. Otsuka, Y. Fujii and K. Maeda, A New Testing Method to Obtain Mode II Fatigue Crack Growth Characteristics of Hard Materials, Fatigue & Fracture of Engineering Materials & Structures, 27, 203-212, 2004

[3] S. Beretta, M. Boniardi, M. Carboni and H. Desimone, Mode II Fatigue Failures at Rail Butt-welds, Engineering Failure Analysis, 12, 157-165, 2005.

[4] M. W. J. Lewis and B. Tomkins, A Fracture Mechanics Interpretation of Rolling Bearing Fatigue, Journal of Engineering Tribology, 226, 389-405, 2012.

[5] H. Matsunaga, N. Shomura, S. Muramoto and M. Endo, Shear Mode Threshold for a Small Fatigue Crack in a Bearing Steel, Fatigue & Fracture of Engineering Materials & Structures, 34, 72-82, 2010.

[6] E. K. Tschegg, Mode III and Mode I Fatigue Crack Propagation Behavior under Torsional Loading, Journal of Materials Science, 18, 1604-1614, 1983.

[7] S. Okazaki, H. Matsunaga, T. Ueda, H. Komata and M. Endo, A Practical Expression for Evaluating the Small Shear-mode Fatigue Crack Threshold in Bearing Steel, Theoretical and Applied Mechanics, 73, 161-169, 2014.

[8] B. Bhushan and S. Sundararajan, Micro/Nanoscale Friction and Wear Mechanisms of Ultrathin Hard Amorphous Carbon Coatings Using Atomic Force Microscopy, Wear, 225-229, 678-689, 1998.

[9] E.-S. Yoon, S. H. Yang, H.-G. Han and H. Kong, An Experimental Study on the Adhesion at a Nano-contact, Wear, 254, 974-980, 2003.

[10] S. Achanta, D. Drees and J.-P Celis, Friction and Nanowear of Hard Coatings in Reciprocating Sliding at Milli-Newton Loads, Wear, 259, 719-729, 2005.

[11] V. L. Popov, Contact Mechanics and Friction: Physical Principles and Applications, Springer, Heidelberg, 2010.

[12] T. Saito, A study on the characteristics of cyclic reciprocating sliding friction (In Japanese), Master Thesis, Fukuoka University, 2015.

International Journal of Fracture Fatigue and Wear, Volume 3

Proceedings of the 4th International Conference on
Fracture Fatigue and Wear, pp. 221-226, 2015

COMPARISON OF TWO FINITE ELEMENT MODELS OF BRISTLES OF GUTTER BRUSHES FOR STREET SWEEPING

M.M. Abdel-Wahab[1], L.V. Vanegas-Useche[2], and G.A. Parker[3]

[1] Ghent University, Laboratory Soete, Belgium
[2] Universidad Tecnológica de Pereira, Facultad de Ingeniería Mecánica, Colombia
[3] University of Surrey, Faculty of Engineering and Physical Sciences, United Kingdom

Abstract: This paper models a bristle of a gutter brush for road sweeping, by means of two finite element models. In one of the models, displacement and rotation boundary conditions are applied to an end of the bristle, so that it follows a certain circular path under a given function of time. In the other model, the same end of the bristle is totally constrained, and inertia loads are applied so that they simulate the motion given by the path and function of the first model. The results of both models are validated, analysed, and compared. They indicate that their accuracy with respect to the degree of freedom results is acceptable. However, regarding force and moment results, the accuracy of the first model strongly depends on the number of straight lines used to approximate the circular path. The accuracy may be very low, mainly due to the modelling of damping. Appropriate values for the time step and integration time step are found so that both models produce reliable results. When these values are used, they provide practically the same results. It is concluded that the model that applies inertia loads may be more appropriate, because the modelling of damping may be more realistic and because much less computational resources are required.

Keywords: dynamic FEM; damping; inertia loads; displacement boundary conditions; friction

1 INTRODUCTION

This work is related to a research into the characteristics and performance of gutter brushes. These are cup-shaped brushes of road sweepers that sweep the debris that is located in the gutter of the road. The study of this brush is of certain interest, as about 80% of the road debris is found in the gutter [1,2]. Fig. 1 depicts a gutter brush of a street sweeper. It comprises one or more rows of clusters of bristles attached at an angle ϕ (bristle mount angle) relative to the mounting board normal.

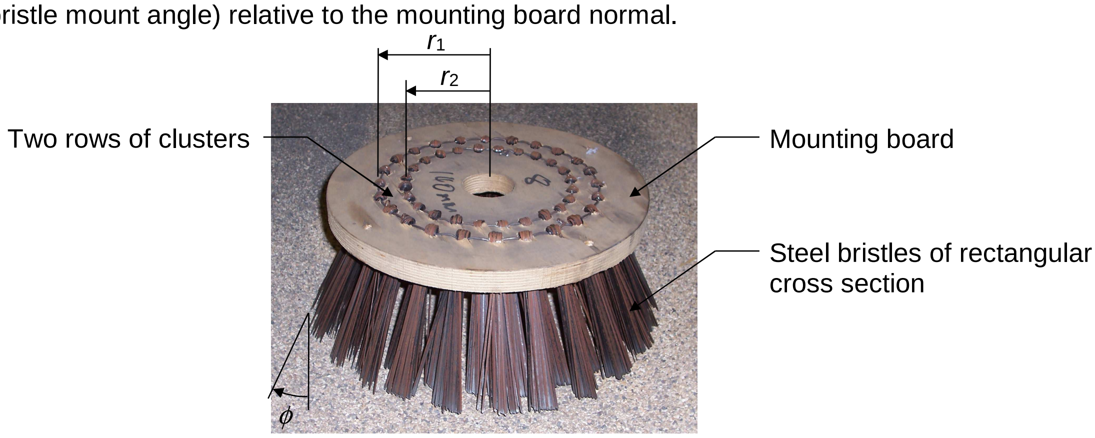

Fig. 1 Gutter brush of a street sweeper

In particular, the research is concerned with the novel idea of analysing whether oscillations superimposed onto the rotation of the gutter brush are of any value for increasing sweeping effectiveness. Therefore, in order to study brush characteristics, a *dynamic* Finite Element Model (FEM) is considered. A dynamic model of a cup-like, oscillatory brush has been developed; this model entails a transient nonlinear structural 3-D analysis involving contact, and it is described in a previous work [3]. In this model, the clamped ends of the bristles are fixed (the brush mounting board is modelled as a stationary body); therefore, in order to simulate brush motion, inertia loads are applied. In conjunction to this, the road surface has to be rotated and translated to obtain the relative movement between brush and road.

In this paper, the results of applying the model referred to above are compared with those a FEM in which the clamped end of the bristle is rotated about the brush axis. The circular path followed by the bristle top end is approximated by a large number of straight lines.

The outline of the paper is as follows. Section 2 presents the main parameters and characteristics of the model. Section 3 provides the results of the validation of the model; this process enabled to obtain the friction coefficients for concrete surface-road interaction. Section 4 presents the comparison of the results of the two models; the results of sensitivity analyses and the validation of the models are also included. Finally, Section 5 concludes the paper.

2 DESCRIPTION OF THE MODEL AND METHODOLOGY

The model that applies inertia loads has been described in detail in a previous work [3]; therefore, only the basic characteristics and the main parameters are provided here. The geometric parameters of the gutter brush that is modelled are given in Table 1. Some of these parameters are illustrated in Fig. 1. Regarding the bristle mount orientation angle, it controls the deflection of the bristle. If $\gamma = 0$ (cutting brush), the bristle cross section is orientated such that the bristle mainly deflects in the brush radial direction. If $\gamma = 90°$ (flicking brush), it deflects backwards, i.e., tangentially and opposite to the bristle sweeping direction.

Table 1 Brush geometric parameters used in the models

Geometric parameter	Symbol	Value
Bristle mount orientation angle	γ	0 (cutting brush)
Bristle length	l_b	240 mm
Mount radius	r	112.5 mm
Bristle breadth	t_1	2 mm
Bristle width	t_2	0.5 mm
Bristle mount angle	ϕ	26°
Number of mount radii	n_r	1

The bristles are modelled as 3-D quadratic beams. For bristle-road interaction, rigid-to-flexible contact is assumed: a contact element is attached to the bristle tip (flexible) and a target element to the road surface (rigid). Regarding friction modelling, an exponential friction function is used [4]:

$$\mu = \mu_k + (\mu_s - \mu_k)e^{-c_v|v|}, \tag{1}$$

where μ_k is the kinetic friction coefficient, μ_s is the static friction coefficient, v is the relative velocity, and c_v is the decay coefficient.

As the modelling of an oscillatory brush requires a dynamic analysis, load steps (loads and boundary conditions) are applied every Time Step (TS), δt. Through these steps, the motions of the brush and the surface are modelled. Two load cases are studied in this work. In the first case, the displacement load case (DispLC), nodal displacements and rotations are prescribed to the top (clamped) nodes, to simulate brush rotation, and displacements are applied to the surface, to simulate sweeper speed. In the second case, the inertia load case (InerLC), the motion of the brush is simulated by applying inertia forces, but the bristle top remains fixed, and the surface is translated and rotated. For the DispLC, this is illustrated in Fig. 2(a), where, Δs and $\Delta\theta$ are the clamped node displacement and rotation, respectively, and Δx is the surface displacement (see also Fig. 6). For the InerLC (Fig. 2(b)), the surface is rotated and displaced through a pilot node in order to model the relative motion between bristle and surface (see also Fig. 7). The inertia forces applied are the centrifugal and tangential forces, related to the variable rotational speed, as well as the Coriolis effects. A disadvantage of the DispLC is that the circular path followed by the clamped end is approximated by a polygon of many sides (each side corresponds to a ramped function); this approximation may lead to inaccuracies, as discussed later; therefore, δt has to be sufficiently small (see sensitivity analyses in Section 4). Similarly, the TSs are divided into integration time steps (ITSs), δt_{ITS}; the ITS has to be sufficiently small to obtain the required accuracy when applying the dynamic equilibrium equations. In both models, gravity is applied as an inertial force.

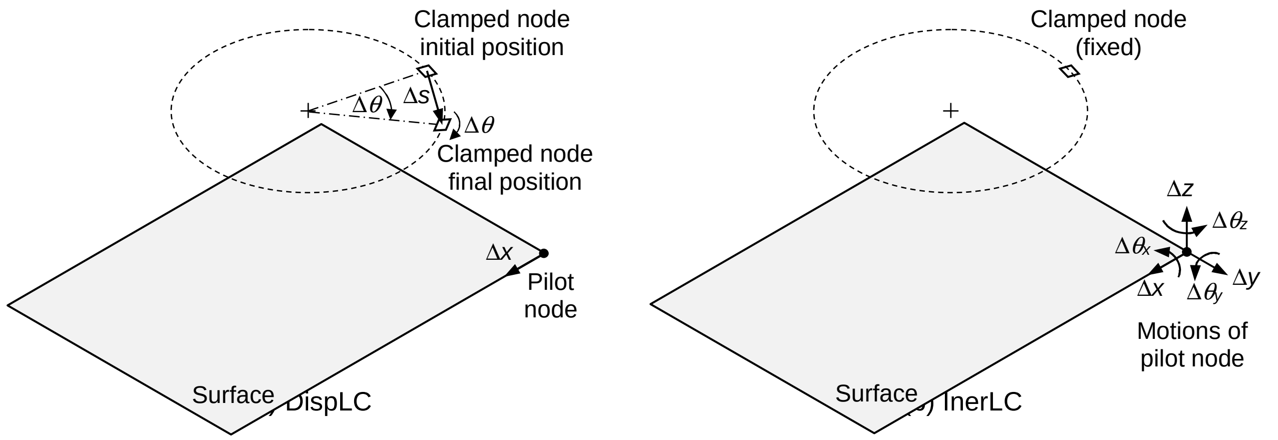

Fig. 2 Displacements and rotations prescribed to the clamped node and the surface pilot node

An oscillatory brush rotates at a variable angular speed $\omega(t)$. Two $\omega(t)$ functions are considered. The VAP function, which was devised by the authors to produce small brush angular accelerations and is given by [5]

$$\omega(t) = \omega_m + \frac{2\omega_a}{1-b} h_1(t) \left(1 - b\, e^{\frac{1-b}{b}[2h_2(t)-1]} \right), \tag{2}$$

where

$$h_1(t) = \frac{1}{\pi} \arcsin\left(\sin\left(2\pi f t\right)\right) \tag{3}$$

and

$$h_2(t) = \frac{1}{\pi} \arcsin\left\{\sin\left[\arccos\left(\cos\left(2\pi f t\right)\right)\right]\right\}. \tag{4}$$

In these equations, ω_m and ω_a are the mean angular speed and alternating angular speed, respectively, f is the frequency of speed oscillation, t is time, and b is a number between 0 and 1 that controls the shape of the angular speed curve; the closer the parameter to zero, the smaller the maximum angular acceleration, but the speed curve becomes less smooth.

The second function is a sinusoidal function

$$\omega(t) = \omega_m + \omega_a \sin 2\pi f t\,. \tag{5}$$

As mentioned before, the variable angular speed produces centrifugal and tangential forces. For the InerLC, these are applied by means of the ANSYS commands ‘‘OMEGA’’ and ‘‘DOMEGA,’’ respectively. Besides, the Coriolis effects are applied through the command ‘‘CORIOLIS’’; further details are given in Ref. [3]. In the DispLC, $\omega(t)$ is integrated in order to obtain the angular function $\theta(t)$; this is used to prescribe the nodal displacements ($r\cdot\Delta\theta(t)$) and rotations ($\Delta\theta(t)$).

Regarding damping, Rayleigh damping is assumed; this is a form of viscous damping, which leads to linear equations of motion. In this damping model, damping forces are proportional to the velocity of the element, and the damping matrix **C** is in turn proportional to a linear combination of mass and stiffness dependent damping:

$$\mathbf{C} = \alpha_D \mathbf{M} + \beta_D \mathbf{K}\,, \tag{6}$$

where **M** is the mass matrix, **K** is the stiffness matrix, α_D is the mass proportional damping coefficient, and β_D is the stiffness proportional damping coefficient.

3 VALIDATION OF THE MODEL AND FRICTION COEFFICIENTS

The FEMs have been validated by comparing the results of the two load cases dealt with (see Section 4) and by comparing the modelling results with those obtained experimentally by Peel [6] for a horizontal brush (i.e., a brush with its mounting board parallel to the surface). The comparison with experimental data enabled to obtain the friction parameters (Eq. 1) for road-bristle interaction.

As reported by Peel [6], the contact between a bristle and a rough surface exhibits stick-slip friction cycles. This is because an irregularity of the road surface may stop the tip for some time until it climbs up the irregularity. However, in the Finite Element (FE) analyses performed, no stick-slip friction cycles are exhibited, because the surface is modelled as a totally flat surface; therefore, equivalent friction coefficients are determined. This is not entirely satisfactory, but the complexities of modelling a rough surface are avoided.

The validation and process of determining the friction coefficients are provided in a previous work; the results suggest that the FEM is valid, as the experimental points are fitted appropriately by the FE results [7]. The validation process yields: μ_k = 0.27, μ_s = 0.70, and c_v = 0.40 s/m for the cutting brush (γ = 0) [7]. These values are obtained by a best fit (Eq. 1) of three points (see Fig. 3), which were obtained by finding suitable values of the friction coefficients for three brush rotational speeds (60, 100, and 140 rpm).

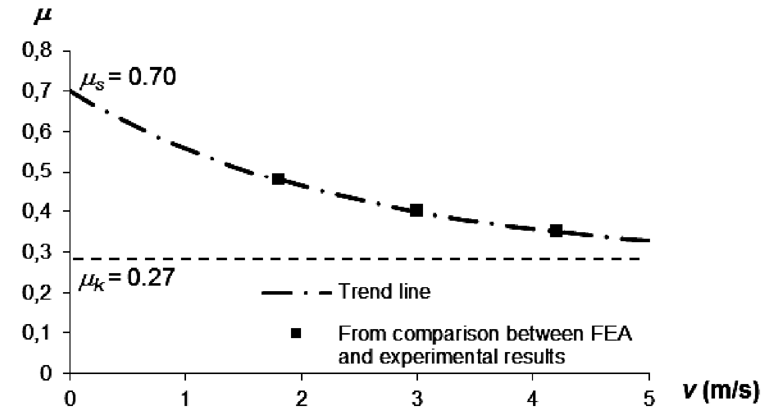

Fig. 3 Friction coefficient curve [7]

4 RESULTS

The effects of the Integration Time Step (ITS), Time Step (TS), and the number of beam elements are studied. Because in the case of a bristle impacting a surface, the contact times are minute, the ITS has to be very small. The results suggest that an appropriate maximum limit for the ITS is 5 to 10 μs. With regard to the number of beam elements in the bristle, the results indicate that 12 beam elements is an appropriate number.

Regarding the TS, δt, an appropriate value depends critically on the type of load case used. In the DispLC, the top node of the bristle follows a circular path. However, this circumference is approximated by a polygon with many sides. Due to this approximation, the velocity of the top nodes undergoes abrupt changes of direction at the intersections of the sides of the polygon. Consequently, the accelerations at those points are, in theory, infinite. Then, very high accelerations, as well as forces and moments, may be produced.

Analyses with various TS values, which affect the size of the sides of the polygon, are performed. The data for these analyses are: brush angle of attack (angle between the mounting board normal and the normal to the road surface), β = 0; the speed function is the VAP function with ω_m = 100 rpm, ω_a = 5 rpm, f = 9 Hz, and b = 0.08; mass proportional damping coefficient, α_D = 0.1 s^{-1} and stiffness proportional damping coefficient, β_D = 21 ms. The analyses reveal that the approximation of the circular path tends to produce errors relatively small in the Degree of Freedom (DOF) results, but it may produce huge errors in the forces and moments, particularly the damping components. Fig. 4 presents an example that suggests that the damping forces should be positive and less than 0.05 N. However, when δt = 1 ms, damping forces of the order of -140 N are generated. The static and inertia components of the forces and moments are also affected by the approximation of the circular path; nevertheless, their values are much smaller than the damping components. In general, the results suggest that convergence is achieved when $\delta t \lessapprox 0.01$ ms. The small value required for δt is a reason for preferring the InerLC to the DispLC, because this would require very large computing times. It is noted that for the InerLC, convergence is practically achieved at least when $\delta t \lessapprox 1$ ms.

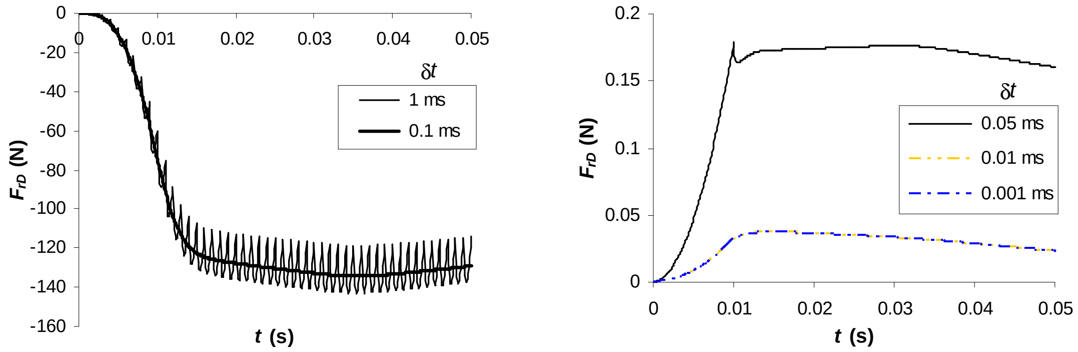

(a) δt = 1 and 0.1 ms (b) δt = 0.05, 0.01, and 0.001 ms

Fig. 4 Damping force at the clamped end in the brush radial direction vs. time for a number of time steps

In order to validate the two load cases, a comparison of results from both of them is carried out. The data for these analyses are: $\mu_s = \mu_k = 0.5$, brush angle of attack, $\beta = 10°$, brush penetration (i.e., vertical distance between the road surface and the tip of the bristle that withstands the greatest deflection if it could penetrate the road without deflection), $\Delta = 0.04$ mm, brush translational speed (sweeper speed), $v = 1.5$ m/s. The oscillatory function is the sinusoidal function with $\omega_m = 150$ rpm, $\omega_a = 4$ rpm, and $f = 5$ Hz. No damping was considered in this analysis. Examples of the results of both models are shown in Fig. 5 to 7. It is noted that the curve for the DispLC in Fig. 5(b) is an equivalent curve, so that it can be compared with the InerLC curve. The small differences that are exhibited in Fig. 5 may be partly due to the different TS used (δt = 1 ms in the InerLC and δt = 0.01 ms in the DispLC) and the differences in the way in which high frequency vibrations are modelled in both cases. The DispLC tends to be very sensitive to δt, and high accelerations tend to be developed due to the abrupt changes in the velocity of the top node. The InerLC tends to produce smoother values of accelerations and forces.

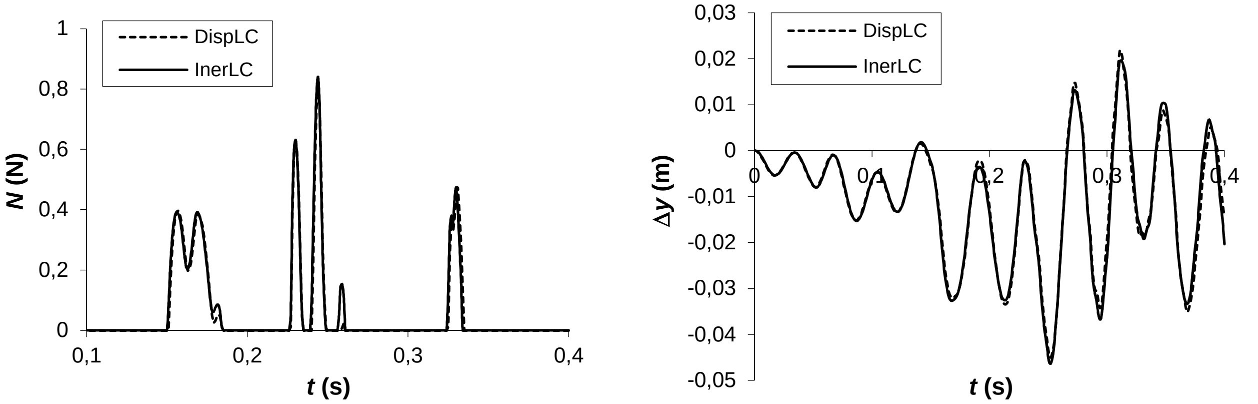

(a) Normal tip-road contact force vs. time (b) Tip displacement in the radial direction vs. time

Fig. 5 Comparison between inertia and displacement load cases

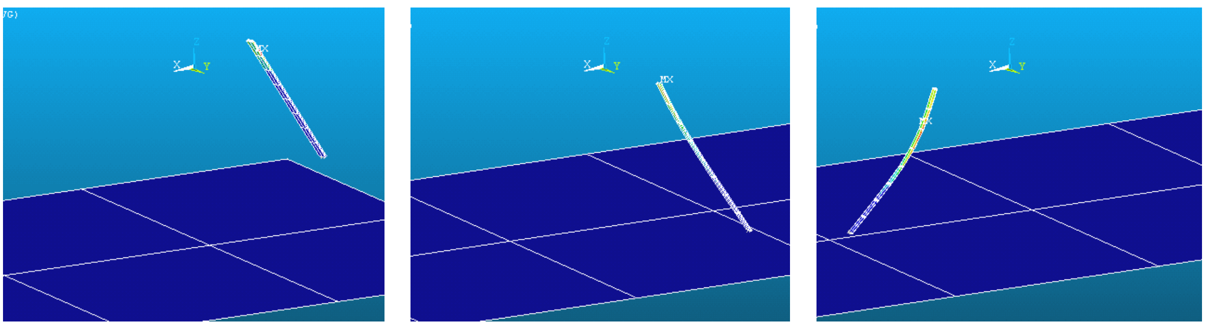

(a) t = 0 s (b) t = 0.125 s (c) t = 0.25 s

Fig. 6 Application of the displacement-load-case model

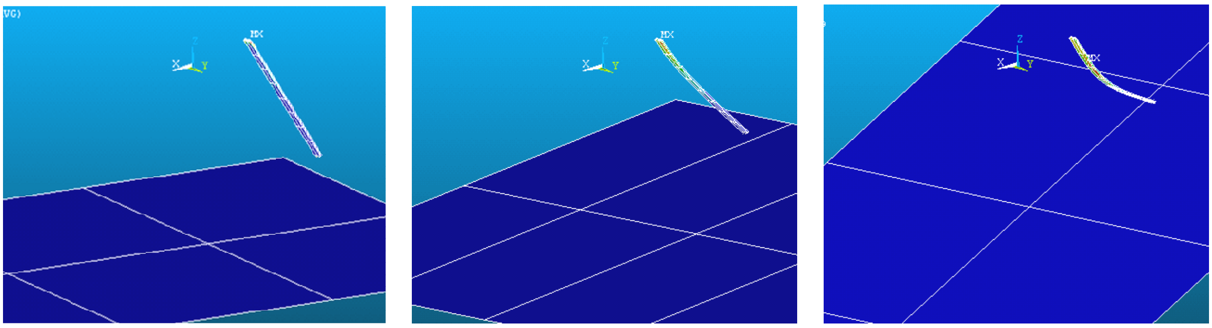

(a) t = 0 s (b) t = 0.125 s (c) t = 0.25 s

Fig. 7 Application of the inertia-load-case model

5 CONCLUSIONS

In this paper, two finite element models of a bristle of an oscillatory gutter brush were presented and compared. In the first model (DispLC), displacements and rotations were applied to the clamped end of the bristle, so that it rotates about the brush axis following a circular path. However, this path was approximated by a certain number of straight lines. In the second model (InerLC), the clamped end is fixed, and inertia loads were applied. Sensitivity analyses, validation, and comparison of the models were carried out. The results indicate that both models are valid and may provide accurate results. However, with regard to forces and moments, the accuracy of the model that applies displacements and rotations critically depends on the number of straight lines that approximate the circular trajectory. If the number of lines is not sufficiently large, the accuracy is very low, mainly due to the damping forces. Suitable values for the time step and integration time step were determined so that the DispLC model produces reliable results. When these values are used, both models provide practically the same results. It is concluded that applying inertia loads may be more suitable for modelling and oscillatory gutter brush, because much less computational resources are needed.

6 ACKNOWLEDGEMENTS

The authors acknowledge the support of the Universidad Tecnológica de Pereira (Colombia), the University of Surrey (UK), and the Programme Alβan, European Union Programme of High Level Scholarships for Latin America, identification number (*E03D04976CO*).

7 REFERENCES

[1] M. Michielen, G.A. Parker, Detecting Debris using Forward Looking Sensors Mounted on Road Sweeping Vehicles, Proceedings of Mechatronics 2000, paper number: M2000-094, 2000.

[2] G. Peel, M. Michielen, G. Parker, Some Aspects of Road Sweeping Vehicle Automation, 2001 IEEE/ASME Int. Conf. Adv. Intelligent Mechatronics Proc., I-II, Como, Italy, 337-342, 2001.

[3] L.V. Vanegas-Useche, M.M. Abdel-Wahab, G.A. Parker, Dynamic Finite Element Model of Oscillatory Brushes, Finite Elements in Analysis and Design, 47(7), 771-783, 2011.

[4] SAS IP, Inc., Release 10.0 Documentation for ANSYS, 2005.

[5] L.V. Vanegas-Useche, M.M. Abdel-Wahab, G.A. Parker, Dynamics of a Freely Rotating Cutting Brush Subjected to Variable Speed, International Journal of Mechanical Sciences, 50(4), 804-816, 2008.

[6] G. Peel, A General Theory for Channel Brush Design for Street Sweeping, PhD Thesis, University of Surrey, UK, 2002.

[7] L.V. Vanegas-Useche, M.M. Abdel-Wahab, G.A. Parker, Determination of Friction Coefficients for Cutting Brush - Road Surface Interaction through FEM, Proc. of the IEEE SoutheastCon 2010, Charlotte-Concord, U.S.A., March 18-21, 77-80, 2010.

Proceedings of the 4th International Conference on
Fracture Fatigue and Wear, pp. 227-232, 2015

DEBRIS MODELS USED FOR WEAR SIMULATIONS

Tongyan Yue and Magd Abdel Wahab

Ghent University, Laboratory Soete, Belgium

Abstract: In fretting wear, debris is usually trapped between contact surfaces due to the micro relative slip. Therefore, debris plays an important role in fretting wear, which can protect or harm interfaces according to different dominant wear mechanisms. Experimental methods for investigating debris, however, are time consuming and difficult to provide the instantaneous information during the wear process. Getting contact information by numerical modelling method is therefore necessary. Meanwhile, a suitable debris model is an indispensable part of a complete prediction tool for fretting wear. This paper reviewed the experiments of fretting wear and the numerical models of debris in wear, especially in fretting wear conditions.

Keywords: Debris, Fretting wear; Numerical modelling

1 INTRODUCTION

Fretting wear is a surface damage between two contact surfaces, with oscillated micro relative slip under contact pressure. The index e, which is the ratio of relative slip δ to half contact width a between interfaces, is used for identifying the transition from fretting to reciprocating wear [1]. If $e > 1$, the contact surface is exposed to the surroundings, and thus the debris created from matrix material can eject from interface easily. While if $e < 1$, there is an unexposed area that the debris could stay in since the magnitude of applied normal load is sufficiently high and the amplitude of displacement is small [2]. Therefore one important characteristic of fretting wear is debris staying in the contact surfaces during the process of wear.

In real applications, fretting wear may happen in every tribo-system suffered from cyclic load, such as stem/cement contact of hip joint [3], blade/disk contact of dovetail joint in turbine [4], interface between strands in hosting ropes [5], or surfaces between electrical connectors [6]. For cemented total hip joint authors of reference [7] found that cement surface was severely damaged in contact with stem surface by doing in-vitro simulation. Moreover the cement debris trapped in the micro-pores may cause aseptic loosening of the femoral component. In the electrical connectors aspect, research of [8] showed that, in Au coated copper electrical contacts, the contact resistance increased significantly when the oxide debris covering the contact surface as a result of fretting wear.

Due to the important role debris playing in the practical application, researchers tried to explain the process of fretting wear from debris aspect. The motivation of present work is to review the research of wear debris in both experimental and numerical modelling aspects. This paper is divided 4 parts; after the introduction section, the experimental research of debris is reviewed. Then, the numerical methods employed for debris modelling is presented in section 3. Finally, a conclusion is presented.

2 EXPERIMENTAL RESEARCH FOR DEBRIS

According to the research by Hurricks [9] in 1970, the process of fretting wear between metal could be divided into three stages: (a) initial adhesion and metal transfer (b) generation of debris and (c) the steady-state wear. In 1973, the delamination theory of wear was presented by Suh [10]. This theory was also based on three points: (a) the behavior of dislocations at the surface, (b) sub-surface crack and void formation, and (c) subsequent joining of cracks by shear deformation of the surface. It took actual micro-mechanism based failure and damage processes into consideration, which was more close to practical situation. The next year Waterhouse and Taylor [11] studied fretted surfaces of 0.7 carbon steel, commercially pure titanium, and Al-Zn-Mg alloy, which showed that loose wear debris caused by the propagation of sub-surface cracks was similar to that postulated in the delamination theory of wear. Thus, delamination wear was proved as one of wear mechanisms happens in the fretting wear. Later on, C. Colombié et al [12] studied fretting wear tests of different materials, i.e. steel on steel and chalk on glass, and found that the generation and maintenance of debris layer with abrasion of debris layer governed the wear of matrix material, which means abrasion wear also could be a wear mechanism for fretting wear.

Varenberg et al. [13] investigated the role of oxide debris in fretting wear in tribo-systems of steel on bronze and steel on steel. They found that the wear mechanisms are different according to different types of friction pairs. For the combination of steel and bronze, the adhesive wear mechanism was dominant and the debris acted as a kind of lubricant, which could reduce damage of fretting wear, while for the pair of steel on steel the abrasive mechanism was prevailing, the debris could accelerate the damage. The same year M.Z. Huq et al [14] found that the normal load and relative humidity of the ambient air also had influence on the movement of debris in fretting wear of coatings. The recent paper of J. D. Lemm [15] presented findings that for contact pairs of steel where they had different hardnesses, a critical hardness differential threshold existed. Above this threshold, the wear was predominantly related to the harder specimen, which meant the surface hardness of steel impacted on the debris retention in fretting wear process. Furthermore, even for the same fretting coupling, an aluminum alloy (A357) on 52100 steel which studied by K. Elleuch and S. Fouvry [16], the form and composition of debris were various relating a displacement amplitude threshold that is independent of sliding velocity and temperature effect.

Based on the experimental results above, it could be concluded that fretting wear is a very complex phenomenon of surface damage and that debris plays various role, which depend on the materials of tribo-system (types, hardness), loading conditions (normal load and displacement amplitude applied) and environment conditions. However due to the micro range of displacement between interfaces and micro or even nano scale of debris, doing experiment is difficult to capture the movement of debris during the process of wear synchronous, hence researchers turn to numerical modelling to analyse the role debris playing during wear process.

3 NUMERICAL MODELLING OF DEBRIS

3.1 Numerical modelling of debris

Authors of reference [17] developed the dry contact model with debris for the heavily loaded rolling and sliding contacts as shown in Fig. 1, which could predict elastic-plastic debris denting process when the debris passes through the contact area.

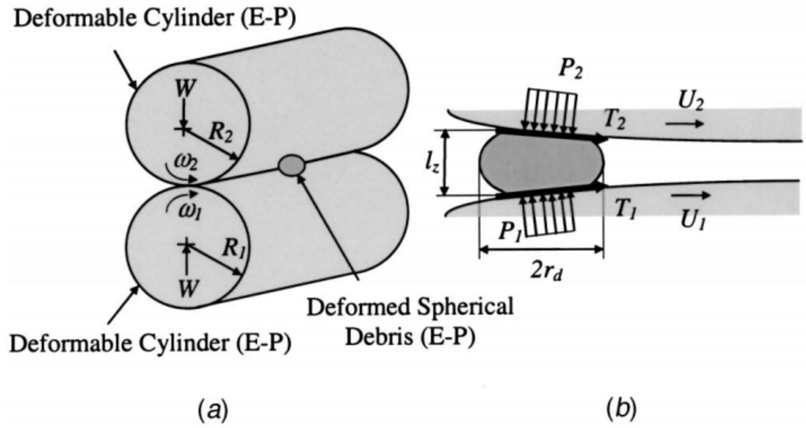

Fig. 1 Dry contact model with debris: (a) two cylinders in contact; and (b) debris forces [17]

According to the dry contact model, the relationship of surface profile and deformation of mating surface is given by:

$$\boldsymbol{H(X,Y) = H_0(X,Y) + \frac{X^2}{2} + \frac{2R_xP_h}{\pi E'}\iint \frac{P(X'-Y')}{(X-X')^2-(Y-Y')^2} dX'dY'} \tag{1}$$

Where $\boldsymbol{H}$ and $\boldsymbol{H_0}$ are the dimensionless mating surface curvature and the constant used for calculating $\boldsymbol{H_0}$, respectively. $\boldsymbol{X}$ and $\boldsymbol{Y}$ are the dimensionless coordinates in rolling direction and cross rolling direction, respectively. $\boldsymbol{P_h}$ and $\boldsymbol{P}$ are the maximum Hertzian pressure (Pa) and dimensionless pressure, respectively. Also $\boldsymbol{R_x}$ is the reduced radius of curvature in rolling direction, which can be calculated as:

$$R_x{}^{-1} = R_1{}^{-1} + R_2{}^{-1} \tag{2}$$

Where R_1 and R_2 are the radius of contacting cylinders. And E' is the equivalent modulus of elasticity:

$$\frac{2}{E'} = \frac{1-v_1{}^2}{E_1} + \frac{1-v_2{}^2}{E_2} \tag{3}$$

Where E_1 and E_2 are young's modulus of the cylinders. The debris shape when it goes along the contact is given by:

$$D_S = \frac{L_Z}{2}\sqrt{1 - \frac{(X-X_C)^2}{R_d^2} - \frac{(Y-Y_C)^2}{R_d^2}} \tag{4}$$

Where L_Z is the dimensionless debris height, R_d is the dimensionless radius of the deformed debris, X_c, Y_c are the dimensionless center coordinate of the debris in the rolling and cross rolling directions, respectively.

By finite element method (FEM) and fast fourier transform method, authors [17] studied the debris material properties, location and the friction between the debris and matching surfaces and they found that these parameters played important role in the debris size and that high contact pressure between debris and contact surface can cause plastic deformation.

Jinbin Han et al. [18] proposed an irreversible cohesive zone model based on cohesive zone model to simulate delamination wear in a coating system. The proposed modelling approach had the advantage that details of the delamination wear process can numerically be studied, and that a unified framework from delamination initiation and propagation was provided. Based on this model, the influence of displacement amplitude, normal load and hardness on sliding wear were studied and the wear rate obtained had good agreement with the Archard model. However the main difficulty of this model is obtaining the exact values of parameters used in this model by experiments, such as cohesive strength, cohesive length and cohesive energy.

Fillot and co-authors [19] presented an analytical wear model based on particle detachment mechanism and mass equilibrium. They used the mass equilibrium equation to link the detachment and ejection of debris based on third body concept to investigate the process of wear. In article [20], the same author presented a numerical model based on the same idea, i.e. detachment of particles and flow of debris. Instead of FEM, the discrete element method was employed since FEM was not yet suitable to model the detachment and movement of the discontinuous particles. In this paper, authors studied the role played by adhesion in wear, and found that if the particle adhesion was less, the detached particles ejected the interface easily, which brought more wear, while wear was reduced when the particle adhesion increased since the flow of detached and ejected particles decreased during the process, as shown in Fig. 2 (a) and (b), respectively.

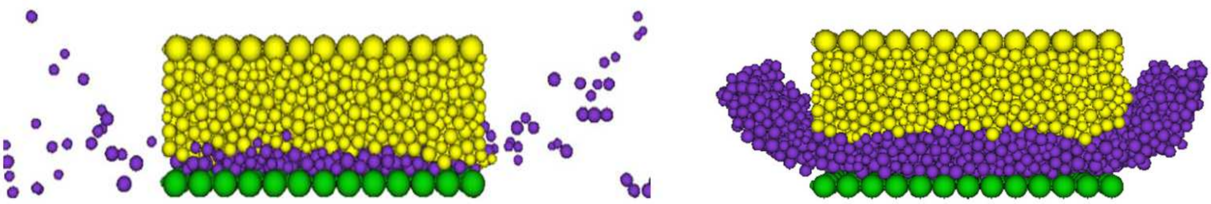

(a) *(b)*

Fig. 2 The contact interface when a stable layer of third body is obtain.
(a) the particles are not adhesive, (b) the particles are highly adhesive [20]

3.2 Fretting wear modelling with debris

Due to the critical impact of debris in fretting wear process, some researchers developed models of debris in fretting wear. Elleuch and Fouvry found [21] that the debris ejection controlled fretting wear and developed a debris flow chart approach, shown in Fig. 3, which illustrated that the total wear kinetics could be described as a function of debris generation and ejection rates. And by increasing the sliding amplitude, the flow of debris trapped in the interface increased, which meant that the debris flow velocity should have a relation with the applied displacement amplitude.

Based on the FE tools of fretting wear presented by McColl in [22], researchers of this group revised this model to simulate the debris as a layer structure accumulated on the contact surface [23] in 2007. In Fig. 4, two contact interfaces exist in this model. In the interface between bottom of debris and $\mathbf{\Gamma_1}$ the contact constraint was assumed rigid connection, while for the interface between $\mathbf{\Gamma_2}$ and $\mathbf{\Gamma_3}$ the basic Coulomb friction model was applied for the contact property. During simulation of fretting wear, the evolution behaviour of debris, such as thickness and width, and the normal movement of debris layer was investigated. This simulation tool predicted debris effects on wear damage by redistributing the contact pressure and relative slip between contact surfaces based on Archard wear model and Hill's yield model.

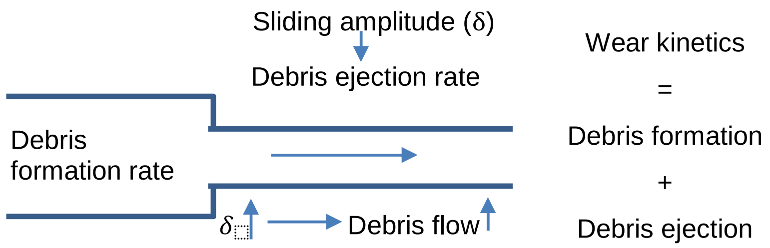

Fig. 3 The debris flow chart approach of wear kinetics under gross slip fretting wear conditions [21]

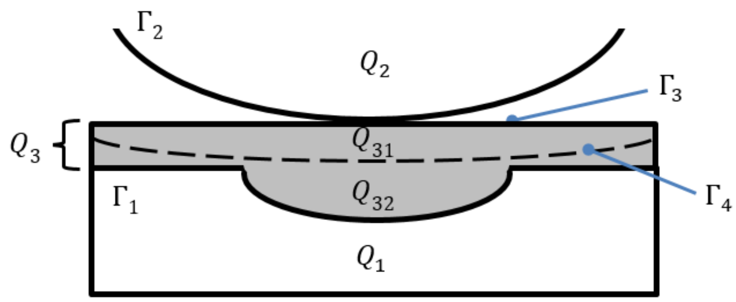

Fig. 4 The simplified fretting wear contact model with a debris layer, $\boldsymbol{Q_1}$ and $\boldsymbol{Q_2}$: the contacting bodies, $\boldsymbol{Q_3}$: debris, $\boldsymbol{Q_{31}}$: loose debris layer and $\boldsymbol{Q_{32}}$: compacted debris layer. $\boldsymbol{\Gamma_1}$: top surface of $\boldsymbol{Q_1}$, $\boldsymbol{\Gamma_2}$: bottom surface of $\boldsymbol{Q_2}$, $\boldsymbol{\Gamma_3}$: top surface of debris, $\boldsymbol{\Gamma_4}$: boundary between $\boldsymbol{Q_{31}}$ and $\boldsymbol{Q_{32}}$ [23]

Two years later, the authors presented a multi-scale modelling method for fretting wear simulation [24]. The macro model is wear simulation based on Archard wear model, and the micro model is asperity contact model based on the roughness characteristics, shown in Fig. 5. $\boldsymbol{\lambda}$ is the wavelength of the asperity spacing which is estimated by the roughness information of the contacting surfaces. $\boldsymbol{d_{sub}}$ is the instantaneous thickness of the debris layer. Both normal load $\boldsymbol{p^{sub}}$ and displacement with amplitude $\boldsymbol{\lambda/2}$ were applied to the micro model. Micro model was used to determine the local plastic deformation under debris layer and furthermore to gain the insightful understanding of fretting wear mechanics. Though some assumptions were made, i.e. a) asperities were distributed uniformly, b) asperities were spherical with uniform radius which were determined by the roughness information, and c) asperities were rigid, this multi-scale model successfully predicted the fretting wear simulation with evolution of interface between debris and substrate, which is closer to the realistic situation.

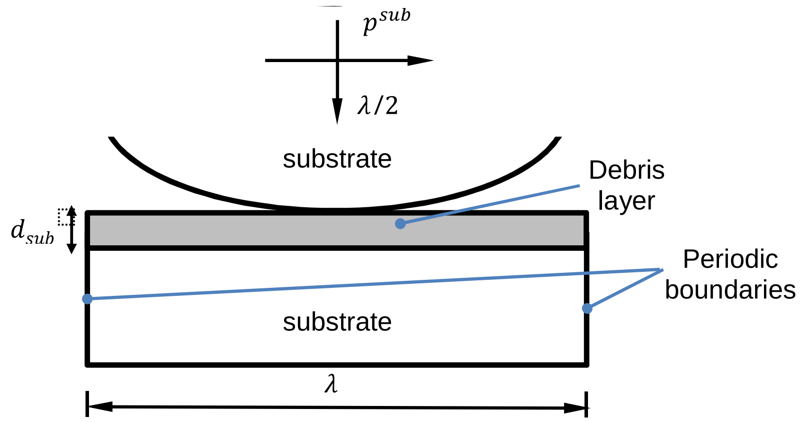

Fig. 5 The asperity model used in [24]

In 2011, Basseville et al. [25] presented a fretting wear model which explicitly included the rectangular particles of fixed number as the third body, shown as Fig. 6. The wear model for both substrate and particles was from dissipated energy method, and the link between substrate and particles was based on the conservation of matter, i.e. the amount of matter lost due to wear was added to the debris. Though authors simplified fretting wear process for this model, such as neglecting the oxidation, choosing the fixed number of particles, the simulation showed that debris may be trapped in the contact interface in partial slip condition while they ejected from the interface when gross sliding or mixed slip occurred, which provide debris movement information of fretting wear from physical aspect.

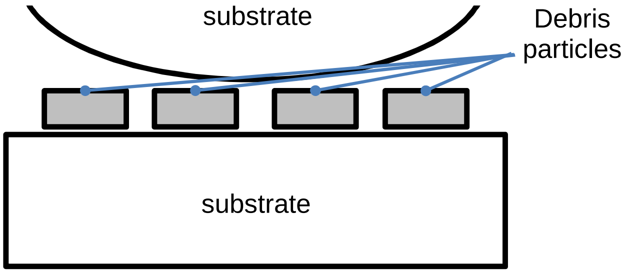

Fig. 6 Schematic of the fretting wear model applied in [25]

More recently, Benjamin D. Leonard et al. [26] developed a fretting wear modelling with the effect of the third body by the combined finite-discrete element method. In this model, FEM was employed for the calculation of substrate bodies, while the debris and contact interactions between debris and substrates was simulated by the discrete element method. In this article they presented two models, i.e. a) the flow of the third body between flat rigid plates for analysing the viscous properties, b) a worn Hertzian contact due to partial slip with third body for studying contact variables of the interfaces. Though the third body of this model was just imported in the worn surface but without attending the process of fretting wear, by modelling of contact between substrates, contact between substrate and the debris, and contact between debris particles themselves. This model studied influence of wear particles on the stress distribution in the contact surface from particle shapes, number of cycles, etc. aspects.

4 CONCLUSIONS

Debris of wear, especially of fretting wear, plays various role in the wear process. By experiments, it is found that debris can reduce the damage of fretting wear or bring aggravation. Several wear mechanisms could exist in fretting wear process according to different tribo-systems, loading conditions, or the surrounding conditions. Given to the importance and complexity of debris, researchers also applied numerical modelling method, i.e. analytical method, FEM, multi-scale techniques and finite-discrete method, to predict the movement of debris in wear or fretting wear. Though a significant progress has been achieved in modelling the debris in wear process, improvement would be realised in the mechanical property definition of debris, the contact property between debris and substrate, modelling the evolution behaviour of debris etc. in the future.

5 ACKNOWLEDGEMENTS

The authors would like to acknowledge the support of China Scholarship Council.

6 REFERENCES

[1] S. Fouvry, P. Kapsa and L. Vincent, Quantification of fretting damage, Wear, 200 (1–2), 186-205, 1996.

[2] N. Arun Prakash, R. Gnanamoorthy and M. Kamaraj, Fretting wear behavior of controlled ball impact treated aluminium alloy under dry sliding condition, Surface and Coatings Technology, 207 450-460, 2012.

[3] P. Herberts and H. Malchau, Long-term registration has improved the quality of hip replacement: a review of the Swedish THR Register comparing 160,000 cases, Acta Orthopaedica, 71 (2), 111-121, 2000.

[4] K. Anandavel and R. V. Prakash, Effect of three-dimensional loading on macroscopic fretting aspects of an aero-engine blade–disc dovetail interface, Tribology International, 44 (11), 1544-1555, 2011.

[5] D. Wang, D. Zhang, S. Wang and S. Ge, Finite element analysis of hoisting rope and fretting wear evolution and fatigue life estimation of steel wires, Engineering Failure Analysis, 27 (0), 173-193, 2013.

[6] M. Antler, Electrical effects of fretting connector contact materials: A review, Wear, 106 (1–3), 5-33, 1985.

[7] S. Barrans, L. Blunt, H. Zhang and L. Brown, Reproduction of fretting wear at the stem—cement interface in total hip replacement, Proceedings of the Institution of Mechanical Engineers, Part H: Journal of Engineering in Medicine, 221 (8), 963-971, 2007.

[8] W. Ren, P. Wang, J. Song and G. Zhai, Effects of current load on wear and fretting corrosion of gold-plated electrical contacts, Tribology International, 70 (0), 75-82, 2014.

[9] P. L. Hurricks, The mechanism of fretting — A review, Wear, 15 (6), 389-409, 1970.

[10] N. P. Suh, The delamination theory of wear, Wear, 25 (1), 111-124, 1973.

[11] R. Waterhouse and D. Taylor, Fretting debris and the delamination theory of wear, Wear, 29 (3), 337-344, 1974.

[12] C. Colombié, L. Vincent, M. Godet, Y. Berthier and A. Floquet, Fretting: Load Carrying Capacity of Wear Debris, Journal of Tribology, 106 (2), 194-201, 1984.

[13] M. Varenberg, G. Halperin and I. Etsion, Different aspects of the role of wear debris in fretting wear, Wear, 252 (11), 902-910, 2002.

[14] M. Huq and J.-P. Celis, Expressing wear rate in sliding contacts based on dissipated energy, Wear, 252 (5), 375-383, 2002.

[15] J. D. Lemm, A. R. Warmuth, S. R. Pearson and P. H. Shipway, The influence of surface hardness on the fretting wear of steel pairs—Its role in debris retention in the contact, Tribology International, 81 (0), 258-266, 2015.

[16] K. Elleuch and S. Fouvry, Wear analysis of A357 aluminium alloy under fretting, Wear, 253 (5), 662-672, 2002.

[17] Y. S. Kang, F. Sadeghi and M. R. Hoeprich, A Finite Element Model for Spherical Debris Denting in Heavily Loaded Contacts, Journal of Tribology, 126 (1), 71, 2004.

[18] J. Han and T. Siegmund, Computational simulations of delamination wear in a coating system, Wear, 267 (9-10), 1680-1687, 2009.

[19] N. Fillot, I. Iordanoff and Y. Berthier, Wear modeling and the third body concept, Wear, 262 (7-8), 949-957, 2007.

[20] N. Fillot, I. Iordanoff and Y. Berthier, Modelling third body flows with a discrete element method—a tool for understanding wear with adhesive particles, Tribology International, 40 (6), 973-981, 2007.

[21] K. Elleuch and S. Fouvry, Experimental and modelling aspects of abrasive wear of a A357 aluminium alloy under gross slip fretting conditions, Wear, 258 (1-4), 40-49, 2005.

[22] I. R. McColl, J. Ding and S. B. Leen, Finite element simulation and experimental validation of fretting wear, Wear, 256 (11-12), 1114-1127, 2004.

[23] J. Ding, I. R. McColl, S. B. Leen and P. H. Shipway, A finite element based approach to simulating the effects of debris on fretting wear, Wear, 263 (1-6), 481-491, 2007.

[24] P. H. Shipway, E. J. Williams, S. B. Leen and J. Ding, A multi-scale model for fretting wear with oxidation-debris effects, Proceedings of the Institution of Mechanical Engineers, Part J: Journal of Engineering Tribology, 223 (7), 1019-1031, 2009.

[25] S. Basseville, E. Héripré and G. Cailletaud, Numerical simulation of the third body in fretting problems, Wear, 270 (11-12), 876-887, 2011.

[26] B. D. Leonard, A. Ghosh, F. Sadeghi, S. Shinde and M. Mittelbach, Third body modeling in fretting using the combined finite-discrete element method, International Journal of Solids and Structures, 51 (6), 1375-1389, 2014.

International Journal of Fracture Fatigue and Wear, Volume 3

Proceedings of the 4th International Conference On
Fracture Fatigue and Wear, pp. 233-234, 2015

ELASTOPLASTIC MODELLING OF CERAMIC MATERIALS AT HIGH TEMPERATURE

D. Bigoni[1], F. Dal Corso[1], M. Penasa[1,2] S. Gregoire[2] and S. Romero Baivier[2]

[1] Trento University, Via Mesiano 77, 38123 Povo, Italy
[2] Vesuvius Group S.A., Rue de Douvrain 17, 7011 Ghlin, Belgium

Abstract: Elastoplastic constitutive modelling is an effective tool in the design of ceramic pieces exposed to a high temperature environment, such as that typical of liquid steel technologies. In this situation ceramics exhibit inelastic deformation and strongly nonlinear mechanical behaviour, which are shown to be correctly represented within a proposed elastoplastic constitutive framework. A mechanical model is proposed, calibrated on a specifically designed experimental protocol, and validated through numerical simulations compared with the mechanical behaviour of ceramic structural elements.

Keywords: Ceramics; High temperature; Elastoplasticity; Thermoplasticity

1 INTRODUCTION

Ceramics are usually considered brittle materials evidencing only traces of inelastic deformation prior to failure, so that elastoplastic modelling has not been developed for these materials. However, even for these materials there are situations in which inelastic strain strongly determines the mechanical behaviour. One of these situations is when a ceramic powder is compacted to obtain a green piece, a context where coupled elastoplastic modelling has been shown to represent the key to engineering modelling and design [1]-[3]. Another important situation is when a ceramic structural element is exposed to a high temperature environment, as is the case of the liquid steel technology. Indeed in metal casting, refractories are used in ladle/tundish slide gate systems, and for nozzles, moulds, and tubes (Fig. 1), so that their mechanical performances at high temperature have to be optimized to improve safety, as well as thermal efficiency.

Fig. 1 Left: a subentry nozzle in working conditions, at 1500 °C. Right: the same piece after use.

Thermoelastoplasticity is the reference framework for this modelling, since inelastic deformation cannot be neglected at high temperature (see Fig. 2, where samples are shown after a four-point bending test at different values of temperature).

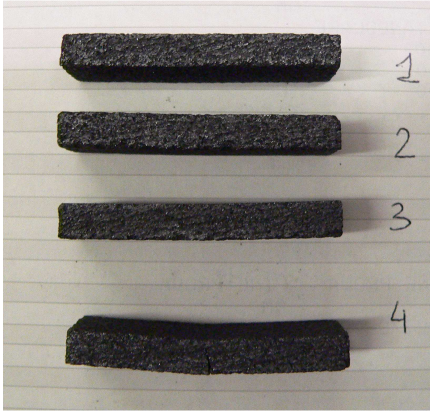

Fig. 2 Ceramic samples after four point bending test at high temperature. Sample n. 1 is undeformed, while samples 2, 3, and 4 have been deformed at controlled displacement at a temperature of 20 °C, 200 °C, and 800 °C, respectively, until the load was decreased to 95% of the value reached at the peak. Permanent deformation is visible at naked eye.

2 CONCLUSIONS

An inelastic mechanical model has been developed for the high-temperature response of refractories to be employed in the liquid steel technology. The model is based on experimental evidence and allows a rational design of pieces to be optimized to satisfy strict safety requirements.

3 ACKNOWLEDGEMENTS

The authors would like to acknowledge the support from European Union FP7 project under contract number PIAPP-GA-2013-609758-HOTBRICKS.

4 REFERENCES

[1] Stupkiewicz, S., Denzer, R.P., Piccolroaz, A. and Bigoni, D. Implicit yield function formulation for granular and rock-like materials. *Computational Mechanics*, DOI 10.1007/s00466-014-1047-8, 2014.

[2] Penasa, M., Piccolroaz, A., Argani, L., Bigoni, D. Integration algorithms of elastoplasticity for ceramic powder compaction. *J. European Ceramic Soc.* 34, 2775-2788, 2014.

[3] Stupkiewicz, S., Piccolroaz, A., Bigoni, D. Elastoplastic coupling to model cold ceramic powder compaction. *J. European Ceramic Soc.* 34, 2839-2848, 2014.

Proceedings of the 4th International Conference On
Fracture Fatigue and Wear, pp. 235-240, 2015

CYCLE COUNTING CHARACTERIZATION FOR ASSESSING FATIGUE DAMAGE USING STRESS-STRAIN-DAMAGE DISTRIBUTION

S.S.K. Singh[1], S. Abdullah[1] and N.M. Nikabdullah[2]

[1]Department of Mechanical and Materials Engineering, Faculty of Engineering and Built Environment, Universiti Kebangsaan Malaysia, Malaysia
[2] Department of Mechanical Engineering, Universiti Malaysia Pahang, Malaysia

Abstract: This paper presents the cycle counting characterization in assessing fatigue damage using the stress-strain-damage distribution. The objective of this study is to computationally assess the fatigue damage by synthetically generating the random loading sequence using the stochastic process. For this objective, the cycle counting characterization was reviewed by transforming the time series sequence to the cycle by cycle definition with consideration of the local maxima and minimum values. The strain-life (ε-N) method was suggested to model and quantify the effects of the various mean stress correction factor models on fatigue behaviour of the material for low cycle fatigue. Then, the statistical comparison for the fatigue behaviour was performed to verify the accuracy of the calculated stochastic algorithm against the ductile cast iron Grade ASTM 100-70-03 results. The computational algorithm provides an accurate and efficient prediction of the fatigue damage assessment when compared with the experimental methods.

Keywords: fatigue assessment; cycle counting; Markov Chain; mean stress correction factor; crankshaft.

1 INTRODUCTION

The fatigue failure of components and structures are considered to be stochastic in nature because of the uncertainties arising from the randomness in the structural materials and the applied loads that lead towards the failure of the component. The fatigue damage for the mechanical components is unavoidable even though it is designed to last a lifetime with a significant safety limit, as mentioned by Sander et al. [1]. Likewise, the fatigue failure of the mechanical component is due to the service loading experienced by the component and it is categorized as a non-deterministic failure. Besides that, a major concern of fatigue failure in the automotive industry is the damage of the crankshaft where fatigue failure occurring on the crankshaft will lead towards severe failure of the engine block and its connecting subcomponents as shown by Jung et al. [2] in his review. Likewise, Ktari et al. [3] illustrated that the fatigue damage occurs from the high cycle and low stress of bending and torsion loads that act on the component. By understanding the physics of failure for the component, the fatigue damage can be analysed although components or structures that are subjected to stresses less than yield, do not experience plastic deformation and have relatively long lives.

Therefore the local stress–strain approach considering both low-cycle fatigue and high energy impact loads using the mean stress correction factor for fatigue damage assessment was suggested by Hongxia et al. [4]. Likewise, with the presence of a non-zero normal stress would influence the fatigue behaviour of the materials, where the mean stress levels are relatively low compared to the cyclic yield stress. Moreover, the mean stresses can significantly increase or decrease the life of a component or structure which includes the crack initiation as well as the crack propagation in fatigue loading in assessing fatigue damage, and the selection of an appropriate model should be based on comparisons of the test data from the experimental analysis of the fatigue failure in understanding the damage assessment of a component as illustrated by Borodii et al. [5]. Hence, the presence of a mean stress correction influences the fatigue behaviour of the material. Therefore, the damage assessment under service loading is calculated using the total strain characterization where the load cycle is obtained from the cycle counting characterization. Hence, to model the fatigue damage analysis during its life cycle, the stochastic process is suggested by Rychlik [6] through the pairing of the local minima and local maxima to obtain the equivalent load cycles.

Hence, the purpose of this paper is to assess fatigue damage of the automobile crankshaft using the stress-strain-damage distribution by synthetically generating the service loading through the stochastic process. In many studies performed before this, it was seen that the fatigue failure of the crankshaft is generally due to the service loading experienced by the component and is generally categorized as a deterministic failure. However, in this study, the authors aim to assess the fatigue damage though the stochastic process under a random loading sequence whereby this process has the capability of assessing the stress-strain-damage based on the structural integrity of the component. Furthermore, the mean stress correction factor is considered in this paper because the fatigue behaviour of the material is influenced by the non-zero mean normal stress. More poignantly, the stress-strain-damage approach using the mean stress correction factor is a more effective method in predicting the fatigue damage where it provides an understanding of the durability of the crankshaft.

2 METHODOLOGY

The suggested framework this paper proposes is the development of a damage assessment algorithm for the automobile crankshaft during its life cycle using the cycle counting characterization through the mean stress correction models as shown in Fig. 1. The proposed framework uses the Markov Chain as a stochastic process to illustrate the physics of failure for the component in the stated condition, where in general the combination of the states will lead towards the failure of the crankshaft.

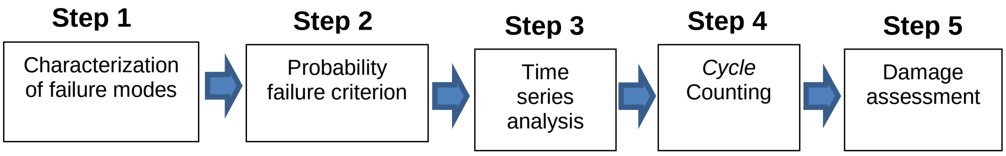

Fig. 1 Schematic algorithm development for damage analysis using stochastic process

The physics of failure of the crankshaft is mathematically modelled through a Discrete Markov Chain using the mean stress correction method by defining the failure state condition during its life cycle with the understanding that the current state condition is independent of the past state condition as shown in Eq. 1.

$$P[X_t = j|X_{t-1} = i, X_{t-2} = n, ..., X_0 = m] = P_r[X_t = j|X_{t-1} = i] = p_{ij_t}$$

$$\begin{aligned} &= \mathrm{P}[\mathrm{X}_t = j, X_{t-1} i_1, X_{k-2} = i_2, X_0 = i_t] \\ &= \mathrm{P}[\mathrm{X}_t = j|Xk - 1 = i_1]P[X_{k-1} = i_1, X_{k-2} = i_2, ..., X_0 = i_k] \\ &= \mathrm{P}[\mathrm{X}_t = j|Xk - 1 = i_1]P[X_{k-1} = i_1|X_{k-2} = i_2]P[X_{k-2} = i_2, ..., X_0 = i_0] \\ &= \mathrm{p}_{i_1 j} p_{i_2 i_1} p_{i_3 i_2} ... p i_t i_{t-1} P[X_0 = i_k] \end{aligned} \tag{1}$$

where $X_t, t = 0, 1, 2, ...$,*n+1* with i and j as the state transitions.

Hence, the discrete Markov Chain is expressed as a generalized term, with the introduction of the probability vector μ to avoid confusion over the failure state condition that occurs on the crankshaft as shown in Eq. 2.

$$E(t) = \begin{pmatrix} \mu_{11} & . & . & . & \mu_{1b} \end{pmatrix} X \begin{pmatrix} P_{11} & . & . & P_{1b} \\ . & . & . & . \\ . & . & . & . \\ P_{a1} & . & . & P_{ab} \end{pmatrix}^n X \begin{pmatrix} L_{max} \\ L_{random1} \\ L_{random2} \\ L_{min} \end{pmatrix} \tag{2}$$

where *a* and *b* represent the probability of each state condition over a given period of *n*.

From the generalized term of Eq. 2, the service loading acting on the crankshaft is generated and counted using the cycle counting characterization to convert the time series to a cycle counting series. This is done by reaching the same level of the local minima and maxima with a small downward or upward excursion by moving forward or backward for each cycle with a minimum less than i and a maximum greater than *j* providing a rise of the interval [*i,j*] as shown in Eq. 3. Therefore, the main idea is to model the fatigue damage using a concept of linear damage accumulation based on the subjected cyclic loading as shown in Eq. 4.

$$N_K^{rfc}(i,j) = \# \begin{Bmatrix} rainflow & cycle & with \\ minimum < i & and & maximum > j \\ for & x_k & t = 0, 1, ..., K \end{Bmatrix} \tag{3}$$

$$D = \sum_{i=1}^{k} \frac{n_i}{N_i} \tag{4}$$

Hence, the damage parameter is calculated using the total strain based on the load cycle obtained from the cycle analysis using the Ramberg-Osgood equation as shown in Eq. 5 to calculate the strain based fatigue through the mean stress correction models of Coffin Manson and Morrow and of Smith, Watson and Topper as shown from Eq. 6 to Eq.8. This is to quantify the effects of the mean stresses on the fatigue behaviour of the crankshaft and to determine the suitable mean stress model to represent the fatigue damage for the component.

$$\varepsilon_t = \tfrac{\sigma}{E} + (\tfrac{\sigma}{K'})^{\frac{1}{n'}} \tag{5}$$

$$\varepsilon_{CM} = \tfrac{\sigma'_f}{E}(\tfrac{2}{D})^b + \varepsilon'(\tfrac{2}{D})^c \tag{6}$$

$$\varepsilon_{morrow} = \tfrac{\sigma'_f - \sigma_m}{E}(\tfrac{2}{D})^b + \varepsilon'_f(\tfrac{2}{D})^c \tag{7}$$

$$\sigma_{max}\varepsilon_{SWT} = \tfrac{(\sigma'_f)^2}{E}(\tfrac{2}{D})^{2b} + \sigma'_f\varepsilon'_f(\tfrac{2}{D})^{b+c} \tag{8}$$

where b = fatigue strength exponent, c = fatigue ductility exponent, σ'_f = fatigue strength coefficient, ε'_f = fatigue ductility coefficient, and N_f = cycle life.

3 RESULTS AND DISCUSSION

The cycle counting characterization required a variable load sequence for the strain based fatigue analysis, where the variable load sequence was obtained through the proposed Discrete Markov Chain model. This is because of the variable amplitude loading fatigue test consisting of the complete load cycles would take several years considering its specimen size as mentioned by Bisping et al. [7]. Therefore, in assessing the fatigue damage based on the strain signals, the load has been transformed into the strain domain using the Ramberg-Osgood equation as shown in Eq. 5 which provides a more feasible cycle by cycle analysis with consideration of the material properties for the crankshaft as shown in Fig. 2.

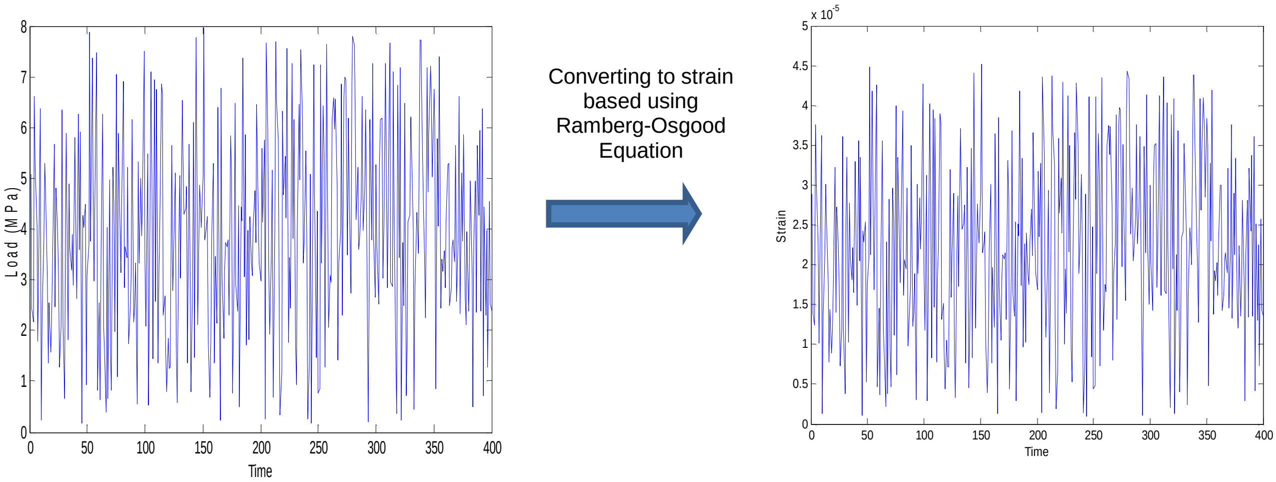

Fig. 2 Markov Chain loading signal converted to strain signal using Ramberg-Osgood Equation

The damage assessment obtained from the cycle counting characterization is compared against the experimental fatigue data that that was performed by Tartaglia [8] for the ductile cast iron Grade ASTM 100-70-03. The accuracy of the stochastic algorithm was performed under a 95% confidence level in order to observe the prediction accuracy of the developed stochastic algorithm as shown in Fig. 3. The figures illustrate the relationship of strain and fatigue life where the higher the strain the higher the damage occurrence at a lower cycle life for the material. This is because of the presence of the oil seal on the journal of the crankshaft which indicates that the oil seal acts as a notch resulting in cyclic plastic deformation. Even though there are minimal differences between the mean stress correction factor models, the SWT model is the most suitable model to be used in fatigue damage assessments because the SWT models fatigue damage when the maximum tensile stress becomes a positive maximum tensile stress.

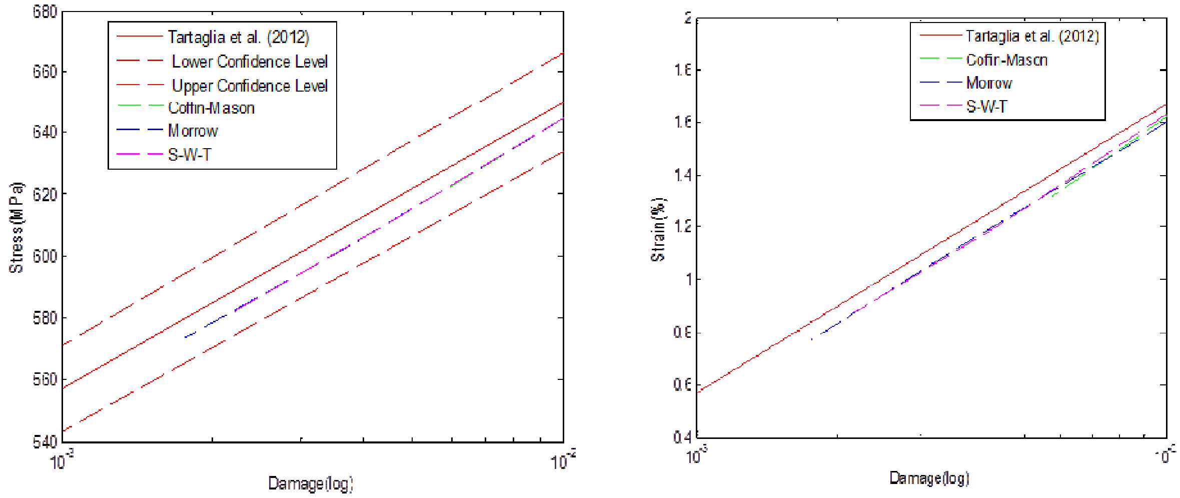

(a) (b)

Fig. 3 Statistical analysis of the stochastic process in damage assessment (a) Stress-Damage plot (b) Strain-Damage plot

The damage assessment is for the durability of the crankshaft during its life cycle, where it provides an influential understanding of fatigue behaviour of the material. The failure due to the fatigue damage was assessed to be at the highest for the crankshaft at RPM3500 during its operating condition. An illustration of the damage assessment of the crankshaft that is calculated by the inversion of the linear damage accumulation through the cycle counting characterization as mentioned earlier is shown in Fig. 4.

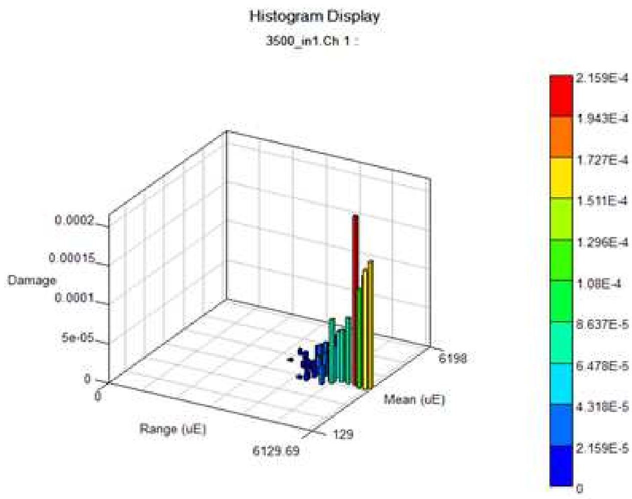

Fig. 4 Damage assessment of the crankshaft at RPM 3500

The damage assessment using the mean stress correction method as shown in Fig. 5 illustrates the surface contour plot for the damage assessment by considering the mapping of the stress-strain plane. The graphical illustration indicates that the elastic-plastic strain is dominant with regards to the damage assessment of the crankshaft when the mean stress life is relatively low and the behaviour of the fatigue is in a long-life regime due to the cyclic loading occurring on the component. This is observed through the yield strength and the ultimate tensile strength values of the ductile cast iron Grade ASTM 100-70-03 obtained from the strain life fatigue database. It is known that the failure of this component will lead to a significant damage in the engine itself and to the other connecting subcomponents. This provides adequate information regarding the effects of stress-strain-damage during the loading sequence which in turn could be used for the durability analysis of the structure.

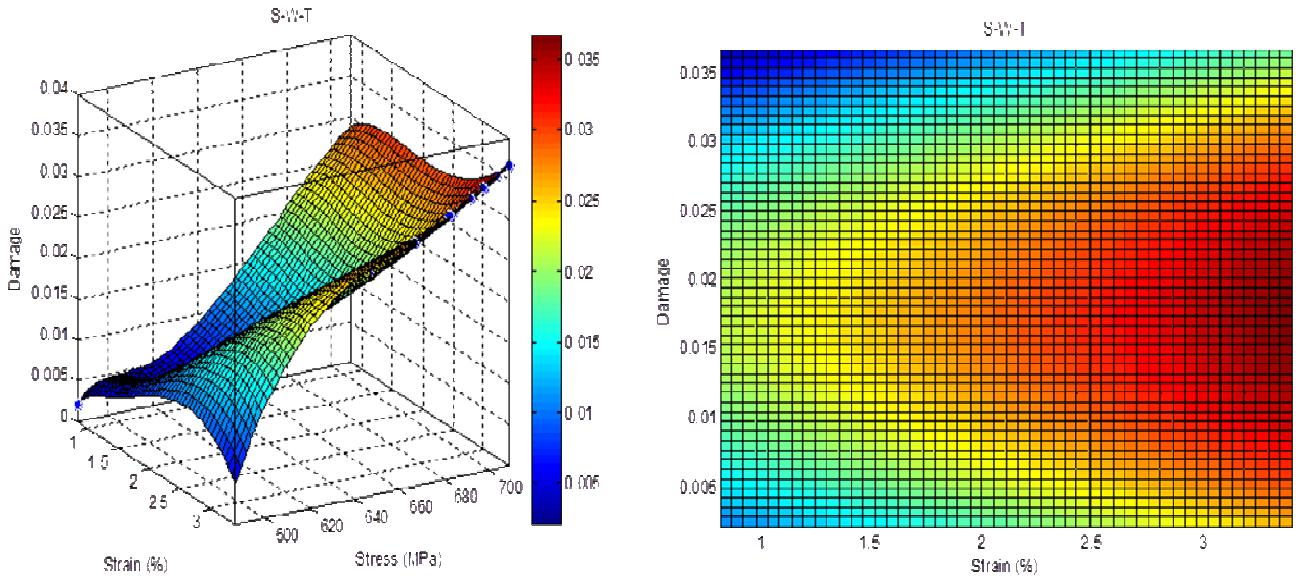

(a) (b)

Fig. 5 The stress-strain-damage distribution plot (a) Stress-strain-damage plot; (b) Damage-strain mapping using SWT mean stress correction factor

4 CONCLUSION

In this paper, the assessment for the fatigue damage using a strain based analysis is presented through the cycle counting distribution. The developed failure probability criterion is used to model the mechanisms and physics of the failure the crankshaft through the failure state condition using the Discrete Markov Chain . Likewise, the Discrete Markov Chain is used to model the failure in terms of the state condition for the crankshaft through the cycle counting characterization by synthetically generating random loads. Hence, the loading sequence obtained from the synthetically generating random loads was converted to the local strains using the Ramberg-Osgood method in order to assess the fatigue damage through the life cycle calculation using the cycle counting characterization. It this study, the damage assessment calculated from the cycle counting characterization is compared against the experimental analysis data as mentioned earlier for the ductile cast iron Grade ASTM 100-70-03 with consideration of the mean stress correction models. The proposed stochastic algorithm for the Markov Chain model showed a high accuracy where the predicted fatigue damage was within the given 95% confidence level of the material. Therefore, the authors propose the use of the Smith, Watson and Topper (SWT) mean stress correction method to model the fatigue damage assessment of the crankshaft for this study. This is because the SWT was selected to model fatigue damage when the maximum tensile stress becomes a positive maximum tensile stress. The SWT has been successfully applied to grey cast iron as this is the equivalent material used for the crankshaft. The SWT is suitable in describing the fatigue damage of the automotive components though the mean stress model under a low cycle fatigue damage.

5 ACKNOWLEDGEMENT

The authors would like to acknowledge the support of the Sector of Higher Education Malaysia, Ministry of Education Malaysia for funding this study and also the national automobile industry for providing the necessary information pertaining to the success of this study.

6 REFERENCES

[1] M. Sander, T. Müller, J. Lebahn, Influence of mean stress and variable amplitude loading on the fatigue behaviour of a high-strength steel in VHCF regime, International Journal of Fatigue 62,10-20, 2014.

[2] D. H. Jung, H. K. Kim, Y. S. Pyoun, A. Gafurov, G. C. Choi, J. M. Ahn, Reliability prediction of the fatigue life of a crankshaft, Journal of Mechanical Science and Technology, 23, 1071-1074, 2009.

[3] A. Ktari, N. Haddar, H. F. Ayedi, Fatigue Fracture Expertise of Train Engine Crankshafts, Engineering Failure Analysis, 18(3), 1085-1093, 2011.

[4] C. Hongxia, C. Yunxia, Y. Zhao, Coupling Damage and Reliability Model of Low-Cycle Fatigue and High Energy Impact Based on the Local Stress–Strain Approach, Chinese Journal of Aeronautics 27(4), 846–855, 2014.

[5] M. V. Borodii, M. P. Adamchuk, Life Assessment for Metallic Materials with the Use of the Strain Criterion for Low Cycle Fatigue, International Journal of Fatigue, 31, 1579-1587, 2009.

[6] I. Rychlik, M. Frendahl, Rainflow Analysis: Markov Method, International Journal of Fatigue, 15(4), 265-272, 1993.

[7] J.R. Bisping, B. Peterweth, C. Bleicher, R. Wagener, T. Melz, Fatigue life assessment for large components based on rainflow counted local strains using damage domain, International Journal of Fatigue, 2014). (article in press, http://dx.doi.org/10.1016/j.ijfatigue.2014.05.008).

[8] J.M Tartaglia, Comparison of Monotonic and Cyclic Properties of Ductile Irons in the AFS/DOE Strain-Life Fatigue Database for Cast Iron, Element Wixom Michigan, American Foundry Society 2012.

Proceedings of the 4th International Conference On
Fracture Fatigue and Wear, pp. 241-246, 2015

Detection of Biaxial Fatigue Stress Concentration Zone under Magnetic Flux Leakage Signals by using Wavelet Transform

S. A. N. Mohamed, S. Abdullah, A. Arifin, A. K. Ariffin, M. M. Padzi, M. F. M. Yunoh

Department of Mechanical and Materials Engineering, University Kebangsaan Malaysia, 43600 Bangi, Selangor, Malaysia

Abstract: Accumulation of fatigue damage is difficult to assess in components and structures under biaxial loading. Although several types of effective non-destructive methods have been developed, various factor interferences restrict their implementation. In the present study, biaxial fatigue damage was diagnosed and evaluated on medium carbon steel through metal magnetic memory method. This method has been adopted for early detection of flaws and considered as an accessible and accurate technique for ferromagnetic materials. Testing was performed under different levels of stress loading to study the trend of fatigued magnetic memory signals. Analysis of the magnetic memory signal showed that the internal magnetic field changes with the appearance of fatigue cracks. Hence, fluctuations in the magnetic signal increase with initiation of the cracks.

Keywords: biaxial fatigue; ferromagnetic materials; magnetic signal; metal magnetic method; non-destructive test

1 INTRODUCTION

Engineering applications of various structural materials involve various operating conditions. Most critical automotive components are subjected to repetitive and complex loading. Fatigue failure under multi-axial loading is a complex phenomenon that occurs when more than one principal stresses act on the critical plane. The most common approach for dealing with multi-axial loading is transformation with von Mises yield criterion. The static values of the principal stress are replaced by amplitudes, and yield strength is replaced by uniaxial fatigue strength. The correlation among these parameters was established by Jordan and Garud [1] for multi-axial data under proportional loading. Ellyin and Golos [2] proposed that the durability of components should be characterized by the amount of energy that a material can absorb, but this approach has been criticized by few researchers. Brown and Miller [3] suggested the use of multi-axial data analysis in the critical plane to explain fatigue behavior. In this concept, fracture parameters are defined as the combination of the maximum shear strain (or stress) and the normal strain (or stress) on the plane.

In consideration of these studies, several safety assessments during service inspection in multi-axial systems have been applied in non-destructive tests to comply with the developing technology. Metal magnetic memory (MMM) testing was proposed by Russian researchers in the late 1990s; this unique and non-destructive tool utilizes the self-magnetic leakage field, which occurs in the zones of stable dislocation slip bands caused by the working load effect. MMM method is used to monitor fatigue damage because of its capacity for early diagnosis of harmful ferromagnetic pieces and parts, which is important for precise characterization of stress concentration. Nevertheless, the magnetic sensing signal is very weak and influenced by noise, interference, and undesired ambient magnetic signals [4]. Thus, data filtering techniques are applied to extract complicated signals into several easy features and remove erroneous data. For processing of non-stationary signals, discrete wavelet transform (DWT) provides satisfactory performance and outstanding results. The formula is based on recurrence relationship and used to generate progressively finer discrete samplings of an implicate mother wavelet function; this function was discovered by Daubechies [5] in a family of wavelet transform.

Wavelet denoising approach is widely used in noise and vibration research but rarely applied in fatigue modeling, particularly in time-series analysis. In this research, magnetic flux leakage signals were processed to define defects attributed to biaxial fatigue loading. Ferromagnetic material was diagnosed through MMM testing. The denoising process of DWT was also performed to remove noise, as well as filter and eliminate outlier points in the MMM signal. The location of the stress concentration zone (SCZ) can be clearly detected at a certain level of implementation.

2 METHODOLOGY

A specimen fabricated from medium carbon steel with a smooth surface (Fig. 1) was selected for the experiment because of its monotonic mechanical properties and applications in the automotive industry. The specimen was fabricated according to ASTM E-08, and its chemical composition as received included 0.42% C, 0.5% Mn, 0.025% S, 0.15% Si, and 0.025% P [6]. Tensile testing was then conducted at ambient temperature with a universal testing machine in compliance with ASTM E466. A cyclic biaxial fatigue experiment combined with tension–torsion loading was performed on a servohydraulic machine with a capacity of 25 kN (Fig. 2). During fatigue design, constant loading was applied for 50% and 90% from the equivalent von Mises stress to compare high and low loading values based on their finite life [7].

The magnetic flux leakage signals were captured by a magnetic-based data logger apparatus (Fig. 3). During loading and unloading, the signals were recorded at logarithmic intervals in cycles of 10 and 20 and continued until the specimen was completely broken, as specified in ASTM E2207 [8]. Data recording arrangement is shown in Fig. 4. Thereafter, the captured signals were transmitted to the designated software package for further analysis.

Fig. 1 Smooth medium carbon steel

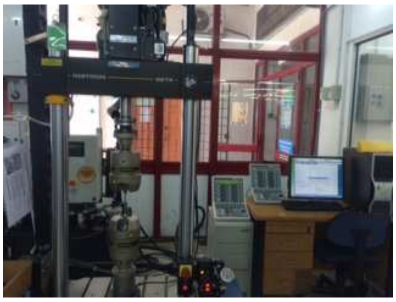

Fig. 2 Servo hydraulic machine

Fig. 3 Metal magnetic memory

Fig. 4 Signal recording

2.1 Equivalent von Mises stress

With the von Mises criterion, the axial and shear stresses can be combined to obtain the equivalent stress amplitude. The applied tension load and torque were also combined to obtain the equivalent stress ($\bar{\sigma}$), which was calculated with Eq. 1.

$$\bar{\sigma} = \sqrt{\sigma^2 + 3\tau^2} \tag{1}$$

where σ is maximum axial stress amplitude and τ is the maximum shear stress amplitude. The octahedral shear stress criterion (von Mises) is the most widely used equivalent criterion for multi-axial fatigue of a ductile material.

2.2 Signal filtering

Mechanical signals in real applications can be classified into stationary and non-stationary. The statistical property value that remains constant with time is the stationary signal, and the statistical parameter value is dependent on time [10]. The randomness of the signals can be improved using signal processing methods to determine the pattern of signal data. DWT is used for filtering engineering signals and is defined in Eq. 2.

$$W_{\psi}(m,n) = \int_{-\infty}^{\infty} x(t)\, a_0^{\frac{-m}{2}}\, \psi^*(a_0{}^{-m}, t - nb_0)\, dt \qquad (2)$$

After the signal was transformed into the wavelet domain, the resulting wavelet filter coefficient must be modified to achieve the denoising effect. In this process, the class includes members ranging from highly localized to highly smooth; hence, some large coefficients were maintained and the others were reduced or even set to zero. The corrected signal was then inversely transformed back into the time domain.

3 RESULTS AND DISCUSSION

Tensile test was performed in our laboratory to determine the monotonic properties of the specimen. The ultimate tensile strength, modulus of elasticity, and yield strength are listed in Table 1.

Table 1 Monotonic properties of medium carbon steel.

Properties	Value
Ultimate tensile stress, σ_u	623 MPa
Yield stress, σ_y	608 MPa
Young modulus, *E*	220 GPa

The original magnetic flux signals for $0.5\bar{\sigma}$ and $0.9\bar{\sigma}$ are transmitted as shown in Fig. 5. The magnetic signals for 805 and 887 MPa were analyzed according to DWT. The random pattern represents the self-magnetization of the ferromagnetic structures, which act in the ambient fields. The parameter signal was captured where Hp(*x*) exhibits its peak field strength and Hp(*y*) changes its polarity around SCZs or macroscopic defects. Hence, Hp(*x*) is the magnetic flux leakage component parallel to the material surface and Hp(*y*) is the component perpendicular to the material surface given the coefficient of intensity *K* [11]. Magnetic field leakage was produced in the stress concentration position because of the irreversible changes in the magnetic domain orientation; these changes can be attributed to operating stress affected by the magnetic field. The *K* values were then plotted in graphs and reprocessed with DWT.

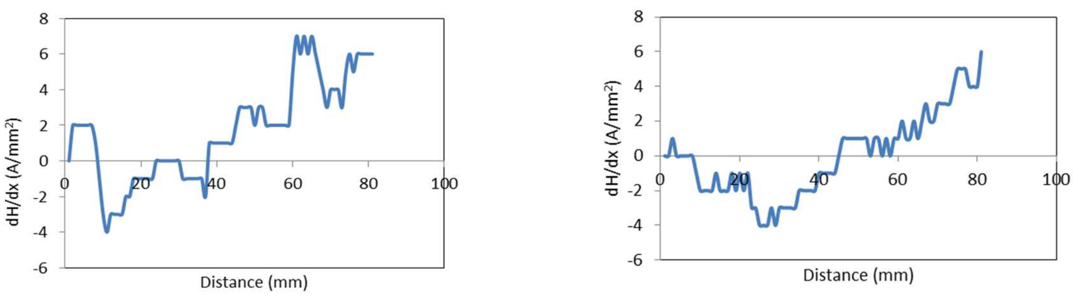

(a) (b)

Fig. 5 Original magnetic flux signal for, (a) $0.5\bar{\sigma}$ and (b) $0.9\bar{\sigma}$

Figs. 6 and 7 illustrate DWT in a time-scale domain function. In the denoising procedure, the wavelet transform decomposed a signal, which overlaps in terms of time and frequency [12]. The signal was reconstructed from the mother signals to detect SCZ, which is the potential failure location of the specimen. The signals for 805 MPa decomposed until the fourth order of the wavelet transform, whereas those for 887 MPa required the fifth order wavelet transform to show the location of failure. The signal decomposes into two parts, namely, approximations and details. These parameters reveal the interference that occurred in the magnetic signal. Low-pass filters generated the approximation, and high-pass filters produced the details. The decomposition process is restricted to different resolutions to fulfill the rules of wavelet levels. When $N = 2^n$, the $n + 1$ generated wavelet levels are deformed. Therefore, the largest gradient in the graph is approximately the value of K, which is the stress concentration location. The potential failure of the magnetic signals for 805 and 887 MPa occurred within 70–80 mm and 60–70 mm, respectively (Fig. 8).

4 CONCLUSION

In this research, magnetic flux leakage signals were processed using DWT. The results showed that decomposition can be applied for research on fatigue damage and is a suitable approach for smoothing the random pattern of the original magnetic flux signal. This process also removes the outliers captured in the raw signal from the MMM. Although the process includes removal and filtering at high amplitudes, the graph pattern on the SCZ (defect area) exhibits the highest changes in terms of the K values. The developed signal processing technique can also be implemented during the early stages to diagnose ferromagnetic fatigue failure, particularly during service life inspection. Hence, MMM method can be used to determine the possible locations of defects even if defect characteristics are not quantitatively defined. These wavelets can also be used to perform local analysis and thus can analyze a localized area of a large signal.

5 ACKNOWLEDGEMENTS

The authors would like to express their gratitude to National University of Malaysia through the fund of AP-2012-015 for supporting this project research.

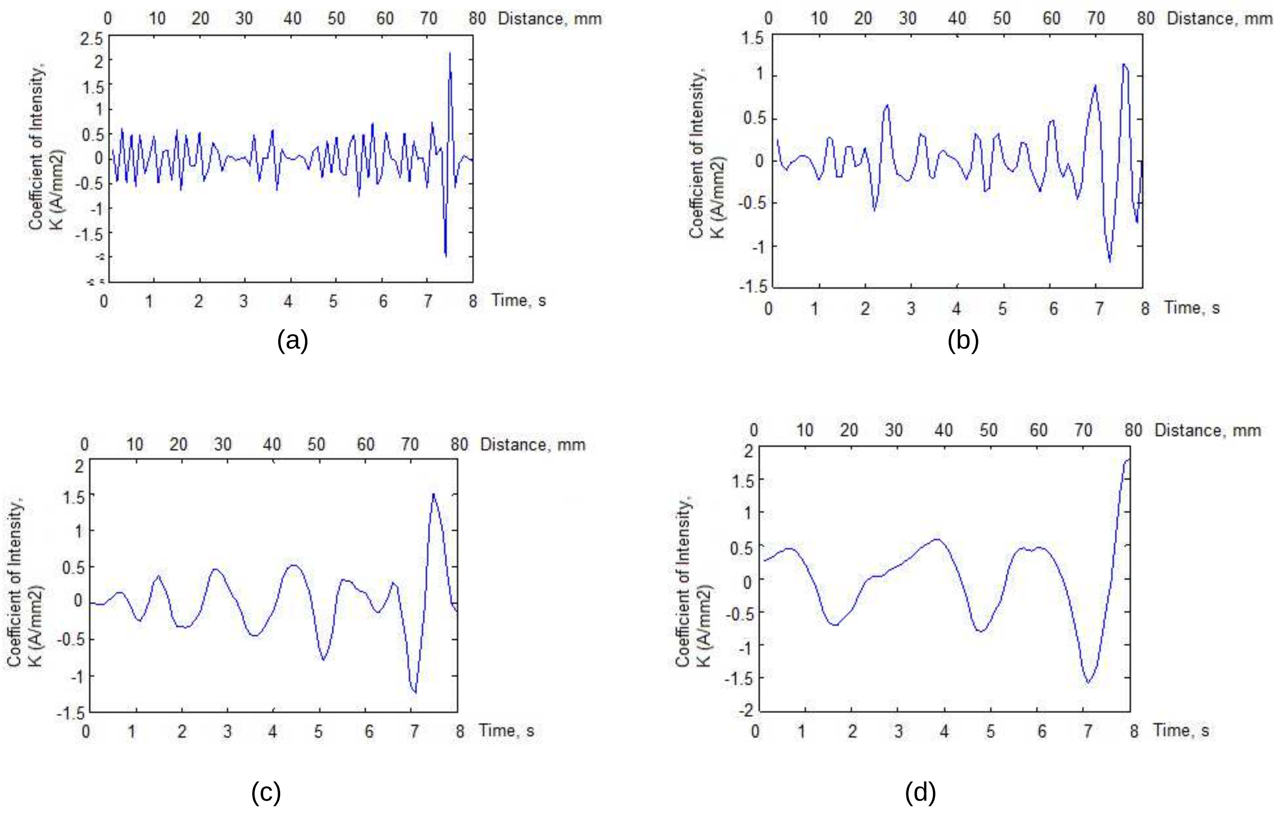

Fig. 6 Decomposition of DWTs for 805 MPa. (a) First order, (b) second order, (c) third order, and (d) fourth order wavelet transforms.

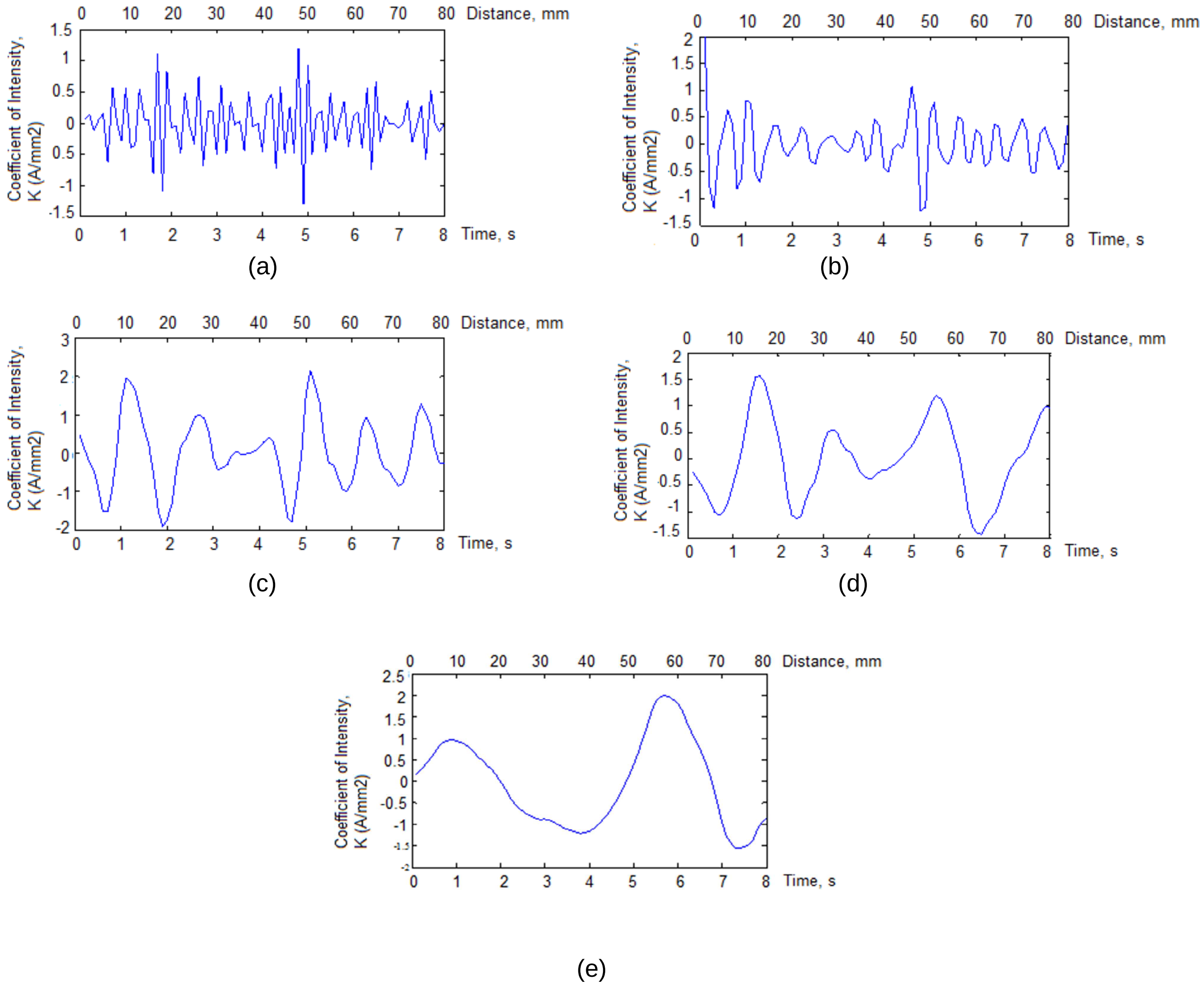

Fig. 7 Decomposition of DWTs for 887 MPa. (a) First order, (b) second order, (c) third order, (d) fourth order, and (e) fifth order wavelet transforms.

Fig. 8 Specimen failure location for (a) 805 and (b) 887 MPa.

6 REFERENCES

[1] Y. S. Garud, Multiaxial Fatigue: A survey of the state of the art, Journal of Testing and Evaluation, 9, 165-178, 1981.

[2] E. Macha and C.M.Sonsino, Fatigue Fracture Engineering Material Structure, Blackwell Science Ltd, Germany, 1053-1077, 1999.

[3] A. Varvani-Farahani, A new energy-critical plane parameter for fatigue life assessment of various metallic materials subjected to in-phase and out-of-phase multiaxial fatigue loading conditions, J. Fatigue 22 (2000) 295–305.

[4] D. Yang, Z. Hu, Y. Yang, and X. He, Weak Magnetic Memory Signal Denoising Based on Cascaded Singular Value Decomposition, Chemical Engineering Transaction, 33, 37-42, 2013.

[6] B. Li, L. Reis, and M. de Freitas, Simulation of cyclic stress/strain evolutions for multiaxial fatigue life prediction, International Journal of Fatigue, 28, 451-458, 2006.

[7] S. M. Tipton, Mechanical Design Handbook, McGraw-Hill, 2006.

[8] A. Lennie, S. Abdullah, Z.M. Nopiah, and M.N. Baharin, Behavioural Investigation of Fatigue Time Series using Statistical Approach, Journal of Applied Science, 10 (16), 1714-1722, 2010.

[9] N.M. Zarroug, R. Padmanabhan, B.J. MacDonald, P. Young, M.S.J. Hashmi, Mild steel (En8) rod tests under combined tension–torsion loading, Journal of Materials Processing Technology, 143–144, 807–813, 2003.

[10] ASTM E2207-08 e1, Standard Practice for Strain-Controlled Axial-Torsional Fatigue Testing with Thin-Walled Tubular Specimens, 2013.

[11] Information on http://dx.doi.org/10.1155/2014/902304.

[12] S. Abdullah, S.N. Sahadan, M.Z. Nuawi, A. Zaharim, and Z.M. Nopiah, On the Need of the 4th Order of Daubechies Wavelet Transforms to Denoise a Nonstationary Fatigue Loading, Proceedings of the 7th WSEAS International Conference on Signal Processing, Robotics, and Automation, 20-22, 2008.

International Journal of Fracture Fatigue and Wear, Volume 3

Proceedings of the 4th International Conference On
Fracture Fatigue and Wear, pp. 247-253, 2015

CLASSIFICATION OF FATIGUE FEATURES EXTRACTION USING ARTIFICIAL NEURAL NETWORKS

M. F. M. Yunoh, S. Abdullah, M. H. M. Saad, Z. M. Nopiah, M. Z. Nuawi and S. S. K. Singh

Department of Mechanical and Materials Engineering, Faculty of Engineering and Built Enviroment, Universiti Kebangsaan Malaysia, 43600 UKM Bangi, Selangor, MALAYSIA

Abstract: This paper focuses on the classification of the fatigue features extraction datasets associated with the measurement of Variable Amplitude Loadings (VAL) of strain signals from the coil springs of an automobile during road tests. The wavelet transform was used to extract high amplitude segments of the fatigue strain signals. The parameters of the kurtosis, wavelet-based energy coefficients, and fatigue damages were then calculated for every segment. All the parameters were used as an input for the classification analysis using Artificial Neural Networks (ANN). Using the back-propagation trained ANN, the corresponding fatigue damage level were classified. It was observed that the classification method was able to give more than 90% accuracy on the classifications based on the features that were extracted from the training and the validation datasets.

Keywords: Artificial Neural Network, Classification, Fatigue features extraction, Segment, Wavelet Transform

1 INTRODUCTION

Durability deals with the material fatigue and it depends on three important parameters: design geometry, materials properties, and loading environment [1]. In the real world, vehicle components such as the coil spring in suspension systems are subjected to Variable Amplitude Loading (VAL) due to the unevenness of road surfaces. These loading histories often contain a large of percentage of low and high amplitude cycles, which contribute to the fatigue failure. In the design phase, the assessment of component durability needs to be considered. The experimental assessment is time consuming and expensive to perform [2]. Therefore, in several cases, the fatigue time histories that consisted of VALs were edited by removing the low amplitudes cycles in order to produce a well-represented and meaningful yet economical testing [3].

In fatigue research, especially for fatigue life assessment, many researchers developed techniques and tools, such as laboratory tests, data collection, and software, in order to identify and prevent fatigue damage [4]. Recently in fatigue research, not many works were done in finding the index category of the structure failures in automotive components especially for suspension systems. Most of the studies were in development of the safety index related to industrial structures such as marine structures, building structures and oil and the gas industry [5]. A possible method can be applied to the development of the index by employing clustering and classification approaches. The classifier has been extensively tested on larger data sets acquired from fatigue experiments. The Artificial Neural Network (ANN) has been widely researched during the last decades, resulting in vast amounts of network structure types [6].

Very few analysis methods have been developed in connection with the clustering and classification of fatigue data for detecting the levels of fatigue damage in automotive components. The objective of this study is to detect the different levels of fatigue damage based on road conditions by using the ANN classification. In general, high fatigue damage is represented by a lower level and higher fatigue damage is represented by a higher level in the classification results. Thus, the features extraction is classified using ANN algorithm and it is divided into several different levels of the fatigue damage.

2 THEORETICAL BACKGROUND

2.1 Features Extraction

Features extraction is the process of creating a representation or transformation from the original strain signal data. Generally, there are several approaches used in signal processing to describe or determine the information of the signal. In this study, three types of analysis have been chosen in order to extract and select the features, i.e. global signal statistical analysis, Wavelet Transform and fatigue damage calculation.

2.2 Signal Peakedness Indication of the Data

A time series contains a set of information for the variable that was taken at equally spaced intervals of time. Kurtosis is the 4th order of statistical moment in the global statistical approach. Kurtosis is very sensitive to the spike of the data or signal. Kurtosis is commonly used to measure non-gaussianity for the detection of fault symptoms because of its sensitivity to the spike or outlier signals among the instantaneous values.

$$K = \frac{1}{n(r.m.s)^4} \sum_{j-1}^{n} \left(x_j - \bar{x}\right)^4 \quad (1)$$

In some definitions of the kurtosis, a deduction of 3.0 is added to the definition in order to maintain the kurtosis of the Gaussian distribution to be equal to zero. Therefore, a kurtosis value of higher than 3.0 indicates the presence of more extreme values than that which should be found in a Gaussian distribution. The increase of fatigue damage across all frequencies with the increased kurtosis levels causes faster component failure.

2.3 Wavelet Transform Analysis

A wavelet transform can be classified as either a Continuous Wavelet Transform (CWT) or a Discrete Wavelet Transform (DWT) depending on the discretisation of the scale parameter of the analysing wavelet. Orthogonal wavelet transforms are normally applied for the compression and feature selection of signals. DWT is derived from discrete CWT, and it is shown as the following expression:

$$W_{\psi}(m,n) = \int_{-\infty}^{\infty} x(t) a_0^{-m/2} \psi * (a_0^{-m}, t - nb_0) dt \quad (2)$$

Where *a* and *b* are the scale factors and *Ψ* is the mother wavelet. The Wavelet-based energy coefficient enables the detection of fatigue damage significantly before the component is exposed to fatigue failure

2.4 Fatigue Strain-Life approach

In the automotive industry, the components imposed under service loadings are commonly evaluated using the strain-life approach. The strain-life approach consists of converting the loading history, geometry and material properties input into a fatigue life prediction. Nowadays, Coffin-Manson, Morrow, and Smith Watson Topper (SWT) are the most famous approaches in strain-life analysis for life assessments. The Coffin-Manson strain-life model is mathematically defined as:

$$\varepsilon_a = \frac{\sigma'_f}{E}(2N_f)^b + \varepsilon'_f (2N_f)^c \quad (3)$$

Where ε_a is the total strain amplitude, *σ'f* is the fatigue ductility coefficient, *c* is the fatigue ductility exponent, and *E* is the modulus of elasticity. Nevertheless, the Coffin-Manson relationship only considers the damage calculation at zero mean stress. The damage parameters are usually developed to consider the mean stress effects on fatigue behaviour, such as the Morrow and Smith-Watson-Topper (SWT) models. The Morrow strain-life model is mathematically defined as:

$$\varepsilon_a = \frac{\sigma'_f}{E}\left(1 - \frac{\sigma_m}{\sigma'_f}\right)(2N_f)^b + \varepsilon'_f (2N_f)^c \quad (4)$$

In addition, the SWT strain-life model is defined according to this formula:

$$\varepsilon_a \sigma_{mak} = \frac{\sigma'^2_f}{E}(2N_f)^{2b} + \sigma'_f \varepsilon'_f (2N_f)^{b+c} \quad (5)$$

The strain-life approach is often applied in the analysis of ductile materials with the low fatigue life and for materials with some plasticity at high fatigue life. Therefore, this approach is a general method that can be used as a replacement for the stress-life approach.

3 METHODOLOGIES

3.1 Vehicle Road Test

The fatigue strain signal from various road surface conditions is important for fatigue analysis especially for automotive components. The reason for performing the VAL testing is to extract the information of fatigue strain signals under complex loadings based on rough rural road conditions. Therefore, to extract the fatigue features of the VAL, there is a need to conduct actual road tests. The VAL testing procedure is shown in Figure 1. The strain gauge is attached at the critical region of the coil spring during the service loading. This is to ensure the strain signal is accurate; the attachment point was polished to a mirror reflection. Then, the strain gauge was connected to the data acquisition and computer for signal measurement and monitoring. A sampling rate of 500 Hz was considered so that the essential components of the signal were not lost during measurement.

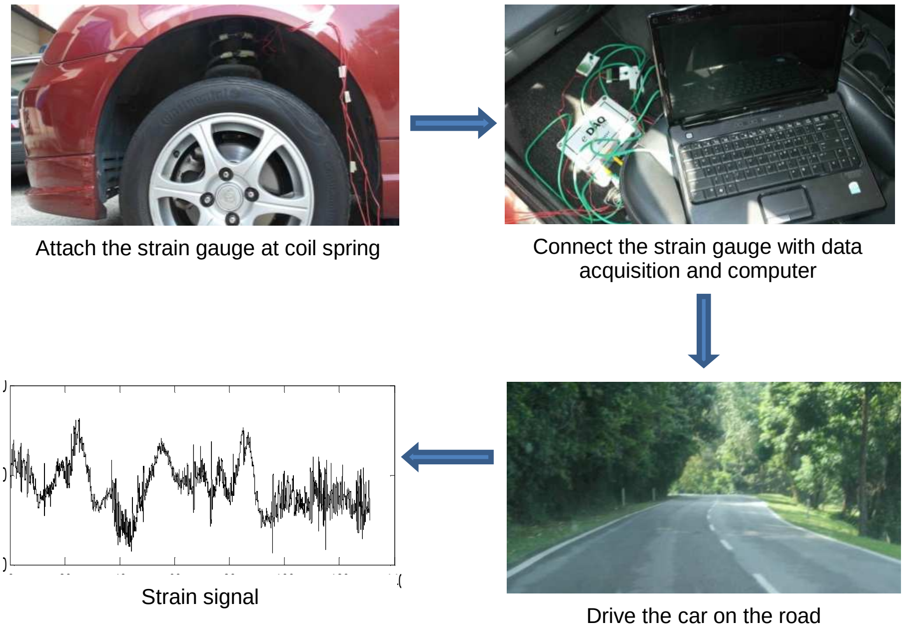

Fig. 1 A diagrammatic process flow for fatigue strain signal collection

3.2 Fatigue Data Extraction and Features Extraction

Data segmentation of the processes divides the data into certain sections or segments after the extraction process, using a wavelet transform analysis. The obtained strain signals from the data were analysed with the wavelet coefficient plot using the time-scale representation. The wavelet coefficient is associated with the energy coefficient plot for the input values in the fatigue data extraction. The segment extraction was done using the wavelet transform analysis in order to divide the data into segments after the low amplitude was removed. The features extraction for every segment was analysed and calculated the Kurtosis, wavelet-based energy coefficient and fatigue damage. All the values of these parameters were then normalised and served as the input in the classification process.

3.3 Classification of Features Extraction Using Artificial Neural Network

Classification is an application of machine learning; which is creates the classifier based on observing the examples and supervised learning. The artificial neural network is a huge class of similar processing structures that are useful in specific categories of complex problems. The Multi Layered Perceptron (MLP) with back-propagation for training was used in the classification. The ANN has a number of neurons that are connected by weight links that pass the signals from one neuron to another neuron.

Figure 2 shows a schematic diagram of a simple perceptron with 3 input nodes, 5 output node, and a hidden layer. Back propagation, which is the one of the famous training algorithm for MLP, is a gradient descent technique to minimize the errors for a particular training pattern. The back propagation trainingalgorithm has some drawbacks, but this method was used because it is simple and reliable.

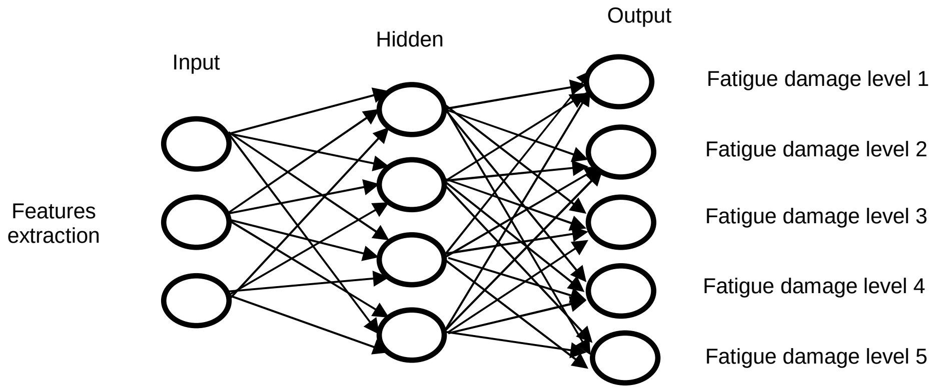

Fig. 2 A simple perceptron with 3 input nodes, 5 output node, and a hidden layer.

For the ANN classification, the input layers have 3 nodes comprising of the features consisting of kurtosis, wavelet-based energy, and fatigue damage that were extracted from the high amplitude segments of the strain signal. An algorithm with momentum is used to train the neural networks during the training process. A selection of the number of epochs is provided prior to training which the training is expected to converge. The outputs are then compared to what they should actually be, and the error is factored into adjusting the condition criteria that future inputs need to meet. The output layers have 5 nodes denoting the different classes of fatigue damage. Each node gives the level of the classification. The lower class represents lower fatigue damage and the higher class represents higher fatigue damage. The verification is initiated during training by comparing the predicted output with different datasets of strain signals. Once the verification is matched, then the classification is verified.

4 RESULTS AND DISCUSSION

The Examples of VAL strain signals from the road test are shown in Figure 3. Figure 3(a) represents the data from SAESUS [7] and Figure 4(b) from the rough rural area. SAESUS is used to validate the measurement data. Basically, the road test consists of rough rural road in order to classify the fatigue damage. For this overall VAL strain signal, the SAESUS data created the highest range of strain amplitude values compared to rough rural road. This may due to the numerous potholes on the road and the rough road surface. For the rough rural road, the range of amplitude values of the strain generated was much smaller than SAESUS as this road was mostly of good surface compared to SAESUS.

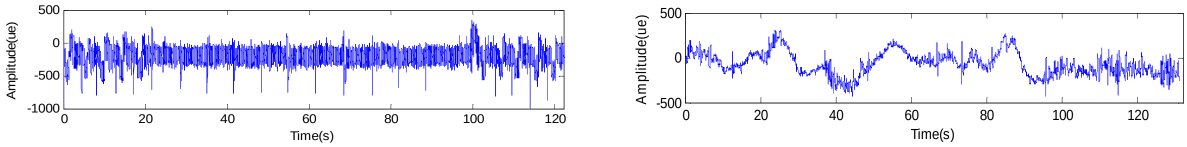

(a) (b)

Fig. 3 Strain time history collected based on road conditions (a) SAESUS (b) Rough rural area road

Statistical analysis is concerned with reducing a long time signal into a few numerical values that describe it behaviour. In order to find the spikiness of the data, the kurtosis values are calculated. The kurtosis value for SAESUS was found to be at 4.28 and for rough rural area at 3.07. Based on these results, these two data are non-stationary because a kurtosis value of higher than 3.0 indicates the presence of more extreme values than that which should be found in a Gaussian distribution. The difference of the kurtosis value on the SAESUS data is higher than the rough rural road because the road surface represented a noisier and higher range of strain amplitude.

Subsequently, the strain signal was used to conduct the damage analysis based on the fatigue strain-life model and wavelet transform analysis. Figures 4 (a) and (b) show the fatigue damage magnitude, damage distribution, cycle range and wavelet-based energy plots for the SAESUS and rough rural road data. Based on the fatigue damage magnitude and distribution, the SAESUS data contributed higher fatigue damage, with damage values at 4.80 x 10^{-3} compared to the rough rural road data at 2.48 x 10^{-4}.

According to the Wavelet-based energy coefficient plots, a lower scale at higher frequency and small amplitude means that the cycles of the signal had a lower energy and gave a small or no fatigue damage potential. A large scale was indicative of low frequency, and higher amplitude indicates that the cycles had higher energy i.e. able to cause fatigue damage. Obviously, the lower frequency indicates a higher magnitude of distribution and the lower magnitude of distribution presents a higher frequency of events. The high amplitudes then were extracted into segments and the feature extraction was calculated for classification. The distribution of the features extraction data as shows in Figure 5.

Figures 6 (a) and (b) show the plots of the ANN classification for the SAESUS and rough rural road datasets. The classifications for these two data have been done based on the generated level of 1 to 5. Table 1 shows the results for the classification of SAESUS and rough rural road. The SAESUS data consists of 21 samples with 98% accuracy and the rough rural road data consists of 25 samples with 96% accuracy. The validation is done by data from the SAESUS as a SAE standard data.

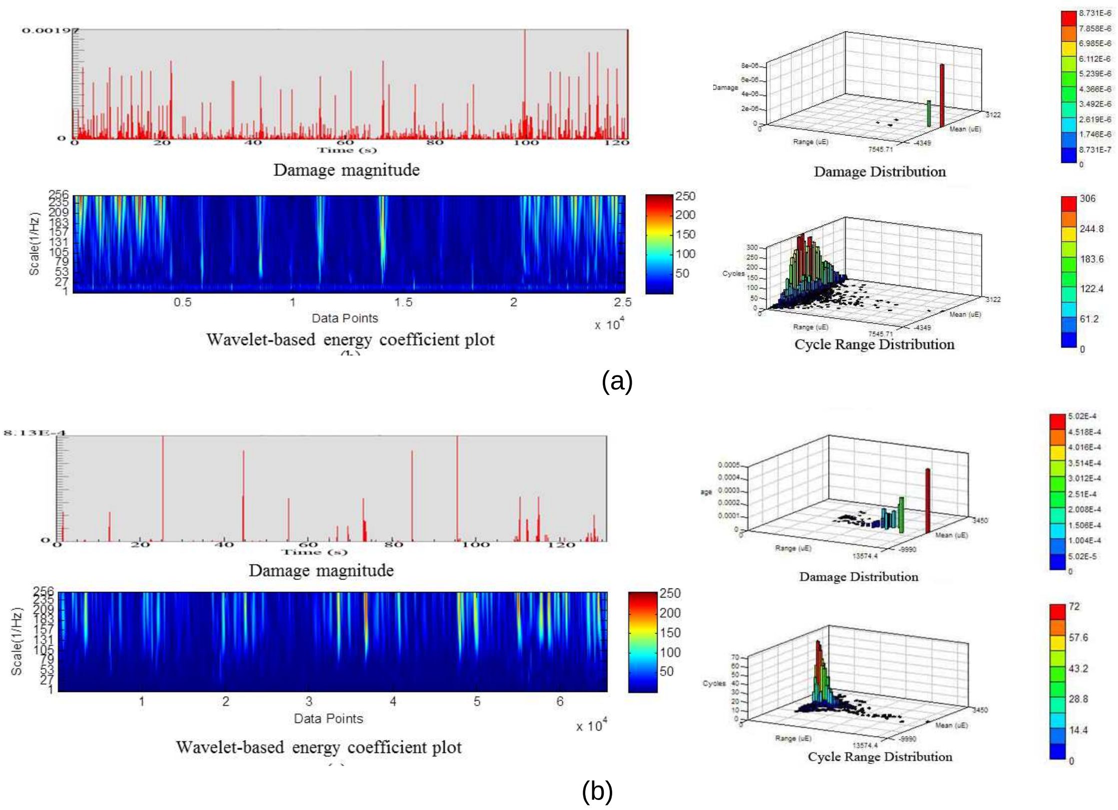

Fig. 4 The damage magnitude and Wavelet-based energy coefficient (a) SAESUS, (b) rough rural road

Based on the plots, the data for SAESUS is scattered at all level from level 1 to level 5. Meanwhile, the data for rough rural road was only scattered at level 1 to level 2. According to their classification, it can be suggested that SAESUS contributed higher fatigue damage compared to the rough rural road and was more inclined to the fatigue failure. This is due to the VAL strain signal, whereby the SAESUS data created the highest range of strain amplitude compared to the rough rural road. This is because of the numerous potholes on the road and the rough road surface. For the rough rural road, the range of the strain amplitude values generated was much smaller than SAESUS because this road was mostly of good surface conditions compared to SAESUS as shows in Figure 4.

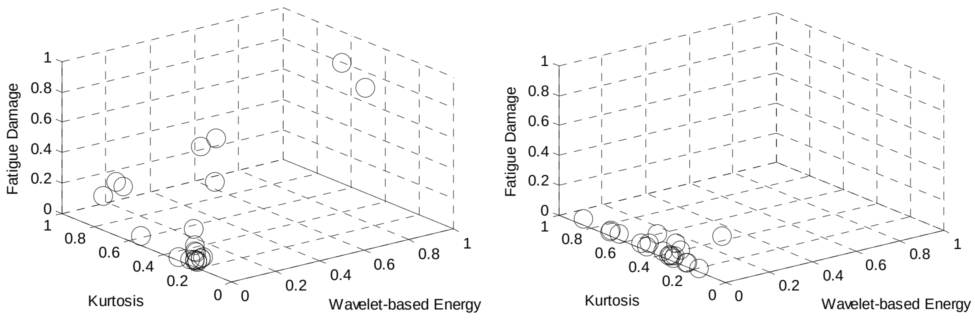

(a) (b)

Fig. 5 Plot of ANN classification (a) SAESUS, (b) Rough rural road

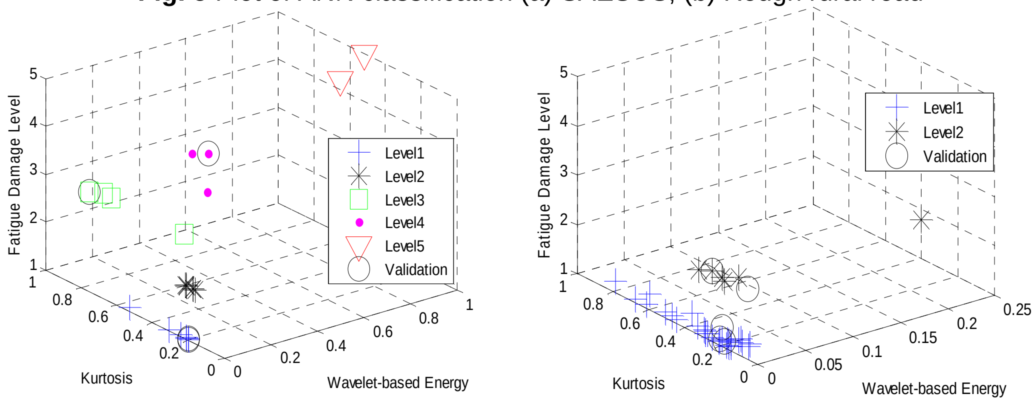

(a) (b)

Fig. 6 Plot of ANN classification (a) SAESUS, (b) Rough rural road

Table 1. Classification results for SAESUS and Rough rural road

Data	No. of Samples	Training Samples	Validation Samples	Accuracy %
SAESUS	21	16	5	98
Rough Rural Road	24	21	5	96

5 CONCLUSION

The present study demonstrated that ANN can be used to classify the fatigue damage of coil springs. The classification can classify level of low fatigue damages to higher fatigue damages into five levels. Based on the classification, the level of fatigue damage for SAESUS and rough rural road datasets were determined. SAESUS data scattered all in five level compared to the rough rural road, which only had scattered data in level 1 and 2. It is suggested that the fatigue damage for SAESUS is more Highers compared to rough rural road.

6 ACKNOWLEDGEMENTS

The authors would like to express their gratitude to Universiti Kebangsaan Malaysia (Research funding: UKM-GUP-2011-069 and UKM-AP-2011-13, for supporting this research.

7 REFERENCES

[1] A. S. Sener, Determination Of Vehicle Components Fatigue Life Based On FEA Method And Experimental Analysis, Intenational Journal of Electronics Mechanical and Mechatronics Eng. 2, 133-145, 2011.

[2] A. Morel, A. Bignonnet, G. Germain, F. Morel, Teaching Durability In Automotive Applications Using A Reliability Approach, International Journal on Interactive Design and Manufacturing 4, 281-287, 2010.

[3] R. I. Stephens, P. M. Dindinger, J. E Gunger, Fatigue Damage Editing For Accelerated Durability Testing Using Strain Range And SWT Parameter Criteria, International Journal of Fatigue 19, 599-606, 1997.

[4] D. C. Lee, C. S. Han, CAE (Computer Aid Engineering) Driven Durability Model Verification For The Automotive Structure Development, Finite Elements in Analysis and Design, 45(5), 324-332, 2009.

[5] W. Mao, I Rychlik, G. Storhaug, Safety Index Of Fatigue Failure For Ship Structure Details, Journal of Ship Research, 54(3), 97-208, 2010.

[6] Z. Dworakowski, L. Ambrozinski, P. Packo, K. Dragan, T. Stepinski, T. Uhl, Application Of Artificial Neural Networks For Damage Indices Classification With The Use Of Lamb Waves For The Aerospace Structures, Key Engineering Materials,588, 12-21, 2014

[7] C. S. Oh, Application Of Wavelet Transform In Fatigue History Editing, International Journal of Fatigue, 23, 241-250, 2001.

Proceedings of the 4th International Conference On
Fracture Fatigue and Wear, pp. 254-259, 2015

DAMAGE DETECTION BY TRANSMISSIBILITY CONCEPTION IN BEAM-LIKE STRUCTURES

Yun-Lai Zhou[1], Magd Abdel Wahab[2] and Ricardo Perera[1]

[1] Department of Mechanical Engineering, Technical University of Madrid
Jose Gutierrez Abascal 2, 28006 Madrid, Spain
[2] Faculty of Engineering and Architecture, Ghent University
Technologiepark Zwijnaarde 903, B-9052 Zwijnaarde, Belgium

Abstract: Even though lots of methods for detecting damage have been developed, early and global output-based damage detection still have difficulty. In this study, a global indicator is constructed for detecting the structural damage from a global aspect. And a simulated clamped-clamped steel beam is analyzed to check the applicability of the proposed approach. The results show the well performance of the proposed approach, and further investigation of experiment validation will be conducted.

Keywords: Transmissibility; Damage detection; Structural health monitoring

1 INTRODUCTION

Structural health monitoring (SHM) has become a global trend since the damage problems in big structures like oil pipes, tall buildings and so on attracted a lot of attention from engineering field and research field as well. The damage detection problems in real engineering put forward the research in scientific field. However, in the beginning, damage detection is based on the measurement of real structures or experimented models. For the purpose of saving cost, numerical analysis has been raised and processed a booming development in the past decades for almost all engineering fields, for instance, joint analysis, crack propagation [1-2], and it has also been widely used in SHM, for instance, in [3], single side damage is simulated with three different finite element models – solid, shell, and beam model, and the beam modal analysis is conducted entirely with numerical analysis.

In SHM, lots of different methods have been developed, from measurement aspect, oil penetrating based, magnetic based, impedance based, vibration based, ultrasonic, acoustic emission, and so on. With the development of high technology, X-ray, acoustic emission and other high technology integrated instruments like optical fibre have also been introduced to SHM.

On the other hand, data analysis is another aspect, a large quantity of algorithms have also been developed like curve fitting, Poly-Max, Rational fractional Polynomial (RFP) and so on.

However, the aforementioned algorithms are based on the excitation and response; and this restricted the application in large civil infrastructures like long-span bridges. Then, researchers tend to find some output based methods for SHM. Transmissibility is one of the pursuit results in this period.

Transmissibility, due to its own characteristic depending on output data only [4, 5], gives the possibility in a better use in real engineering. And it has been developed for damage detection [6, 9], localization [11], and quantification [7, 8], and response reconstruction [10], and so on. But difficulty still exists as damage can be caused by a lot of changes, and environmental varieties will also add more hardship in real engineering.

In this study, a new transmissibility based damage detection methodology is proposed with assuming that damage will change the structural stiffness, no matter the damage is caused by any form of damage. Later, transmissibility based damage detection procedure is constructed, and then a simulated beam is used for testing the proposed approach.

2 TRANSMISSIBILITY

Considering a linear multiple-degree-of-freedom system, the dynamic equilibrium equation can be written by the well-known second order differential equation:

$$\mathbf{M}\ddot{\mathbf{x}}(\mathrm{t}) + \mathbf{C}\dot{\mathbf{x}}(\mathrm{t}) + \mathbf{K}\mathbf{x}(\mathrm{t}) = \mathbf{f}(\mathrm{t}) \tag{1}$$

Where $\mathbf{M}$, $\mathbf{C}$ and $\mathbf{K}$ are the mass, damping and stiffness matrices of the system, respectively, f(t) is the input force vector, x(t) contains the responses of each degree-of-freedom of the system.

Herein, for a harmonic applied force at a given coordinate, the transmissibility between point i and a reference point j can be defined as

$$T_{(i,j)} = \frac{X_i(\omega)}{X_i(\omega)} \tag{2}$$

where $X_i(\omega)$ and $X_j(\omega)$ are the complex amplitudes of the system responses $x_i(t)$ and $x_j(t)$, respectively, and ω is the frequency.

For calculating transmissibility, it might be calculated in some manners; amongst them to use the frequency response function (FRF) is one easy and convenient way in early damage detection analysis,

$$T_{(i,j)} = \frac{X_i(\omega)/F_t(\omega)}{X_j(\omega)/F_t(\omega)} = \frac{H_{it}(\omega)}{H_{jt}(\omega)} \tag{3}$$

where t is the excitation point, and H represents the FRF.

From Equation (3), one can see that transmissibility can be estimated by ratio of two FRFs, and since FRF change can be used for detecting damage, logically speaking, transmissibility change might also be used for detecting damage.

On the other hand, modal assurance criterion (MAC) might also be used to estimate the change of transmissibility before and after damage. Note that considering the imperfect of the response along the entire frequency domain, one might only choose one segment within the frequency band of interest. Then it might be expressed as:

$$MAC(T^d_{(i,j)}, T^u_{(i,j)}) = \frac{((T^d_{(i,j)})^T (T^d_{(i,j)}))^2}{((T^d_{(i,j)})^T (T^d_{(i,j)}))((T^u_{(i,j)})^T (T^u_{(i,j)}))} \tag{4}$$

where $T^d_{(i,j)}$ represents transmissibility under damaged condition, while $T^u_{(i,j)}$ means the transmissibility under intact condition, $()^T$ means transpose.

For Equation (4) above, threshold should be set to each equation, while this depends on the engineering experience of each user. Note that the threshold will directly determine the predicting results of the structural damages. In this study, the value under intact condition is set as threshold.

For detecting the structural damage, procedures can be set as follows:

Step 1: To extract the structural dynamic response, Fourier transform is used to analyze the data in frequency domain with deriving the transmissibility;

Step 2: To calculate the damage indicator with Equation (4);

Step 3: With the threshold set before, one might predict whether the structure is damaged or not.

3 NUMERICAL STUDY

For checking the feasibility of the aforementioned damage detection procedure, numerical analysis is carried out with a clamped-clamped steel beam shown in Fig. 1. And the physical properties are shown in Table 1. The beam is divided into 20 elements on average, and each element is named as shown in Fig. 1. Then the excitation is loaded at node nine (right boundary of element eight) with a unit impulse in frequency domain. And the beam is considered as Euler-Bernoulli beam with one dimension model. And a constant damping ratio of 0.2% is taken into account for simulating a slight damping.

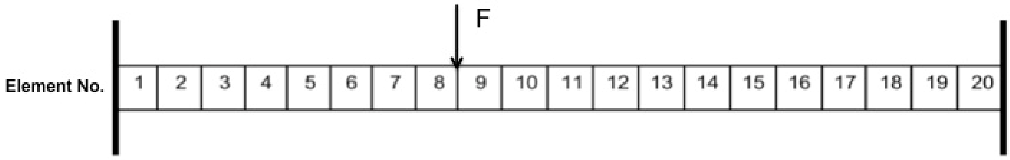

Fig. 1 Numerical simulation with 50 elements

Table 1 Beam properties

Beam properties	Value
Young's modulus (GPa)	210
Poison's ratio	0.3
Density (Kg/m^3)	7800
Length (m)	1.0
Width (m)	0.05
Thickness (m)	0.006

For examining the proposed damage detection procedure, various simulations are conducted and analysed by considering single damage in element three. Damage has been introduced with four levels, which are shown in Table 2.

Note that in this study herein presented, the damage is introduced by stiffness reduction into the distinct element, where only the element will be influenced, in an attempt to simulate the structural damage in real engineering. Then, the vertical acceleration response of each node was derived and analysed.

Table 2 Damage scenarios

Scenario	Value
D0	Intact state
D1	5% stiffness reduction
D2	15% stiffness reduction
D3	40% stiffness reduction

4 RESULTS AND DISCUSSION

In order to validate and illustrate the applicability of the proposed approach, the aforementioned damage detection procedure is conducted and the results are as follows:

Fig. 2 and Fig. 3 show transmissibility T(15, 4) and T(11, 3) under D1-D3 along with intact condition D0, respectively.

From the figures, one can find that:

(i) The difference between D1, D2, D3 and D0 is clear in the entire frequency domain, which suggests that the transmissibility might be used to detect the damage. This can be also found in Fig. 3.

(ii) The peaks and anti-peaks in Fig. 2 all move forward to the left part, this might suggest the structural resonant frequencies decrease as the damage enlarges. This can also be confirmed in Fig. 3 in part, however, one can find in Fig. 3 that one anti-peak does not move to the left part. This might be resulted from the chosen transmissibility.

Note that to choose a proper transmissibility for identifying structural damage is a key issue during the whole SHM process, while until now no exact rules have been drawn out, one need to choose according to his own experience.

To summarize, using the transmissibility change, if the transmissibility is well chosen, it can successfully detect structural damage.

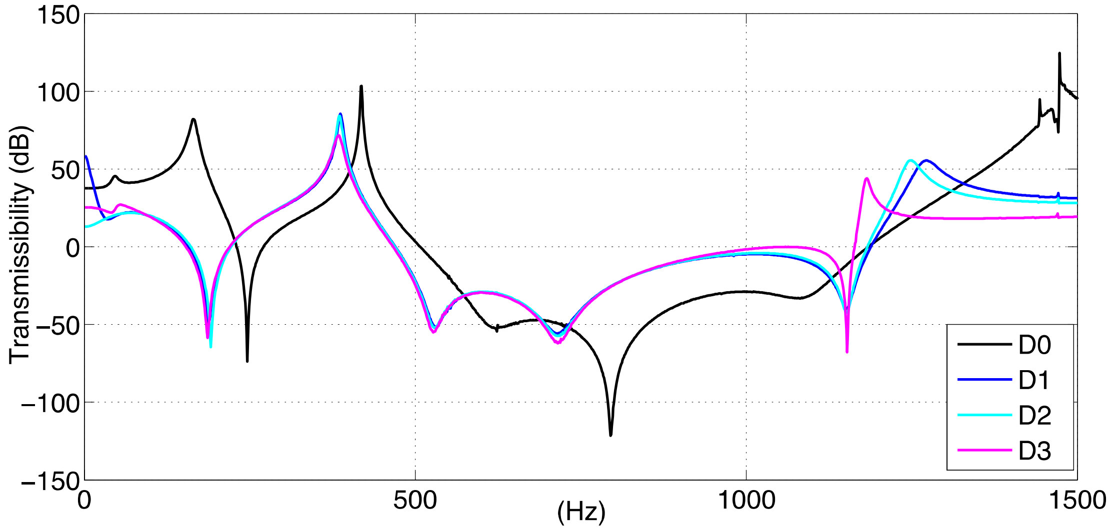

Fig. 2 Transmissibility T(15, 4) under D1-D3 along with D0.

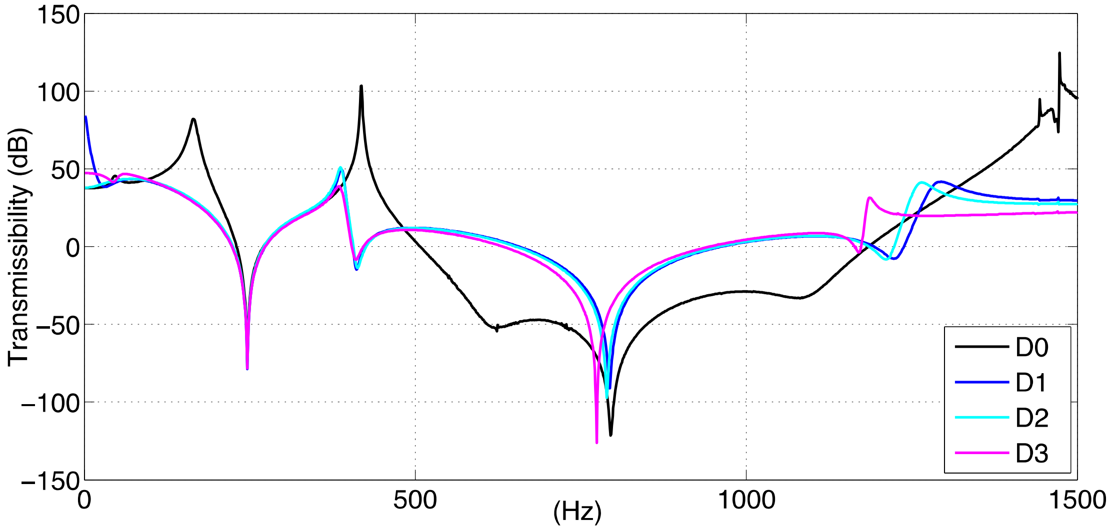

Fig. 3 Transmissibility T(11, 3) under D1-D3 along with D0.

Considering the MAC value defined in Equation (4), Table 3 shows the MAC calculated for each damage scenario.

From the Table 3, it can be found that:

(i) For all the cases, no matter how the frequency band is chosen, the MAC value can detect the damage, while if the frequency band is not well chosen, the difference might be little, like T(11,3) under frequency band [800, 1000] Hz.

(ii) If the entire frequency band is used, then even small damage occurs, the MAC value will decrease a lot.

(iii) In both T (15, 4), T (11, 3), if the entire frequency band is used, the MAC value did not change monotonically in accordance to the damage severity.

(iv) If the frequency band is well chosen, like T(15, 4) under [480, 500] Hz, T (11, 3) under [800, 1000] Hz, the MAC value can change monotonically in respect to the damage severity.

Table 3 MAC value of each damage scenario

Scenario	MAC value for T (15, 4)		MAC value for T (11, 3)	
	[0, 2048] (Hz)	[480, 500] (Hz)	[0, 2048] (Hz)	[800,1000] (Hz)
D0	1.0000	1.0000	1.0000	1.0000
D1	0.1604	0.9941	0.2349	0.9983
D2	0.1428	0.9934	0.3403	0.9980
D3	0.1471	0.9926	0.2751	0.9936

For better understanding the performance of MAC value, Fig. 4 and Fig. 5 show the comparison between T(15, 4), T(11, 3) under the entire frequency band, and under each own well fitting frequency band, respectively. Herein, note that the fitting frequency band is a critical issue to choose, while it will determine the performance of the MAC result.

From Fig. 4, it is clear that the MAC results did not hold a straight relation with the damage severity, while when damage happened, it changed a lot. And in Fig. 5, one can find that the MAC value decreased small as damage happened, however, one can find that the MAC value decreased monotonically in according to the damage severity. This suggests that if the frequency band is well chosen, the MAC value might used to assess the damage severity.

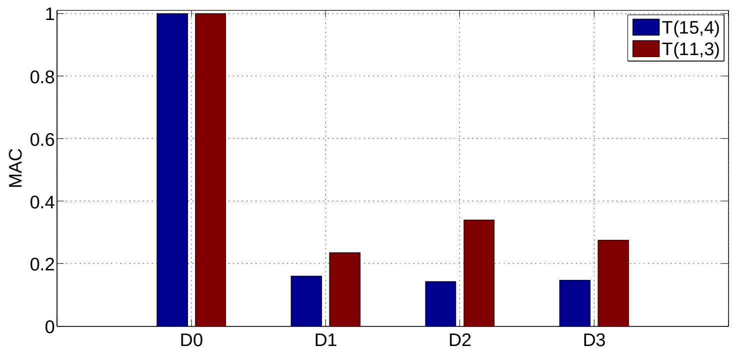

Fig. 4 MAC value of T(15,4), T(11, 3) under D1-D3 along with D0 with frequency band [0,2048] Hz.

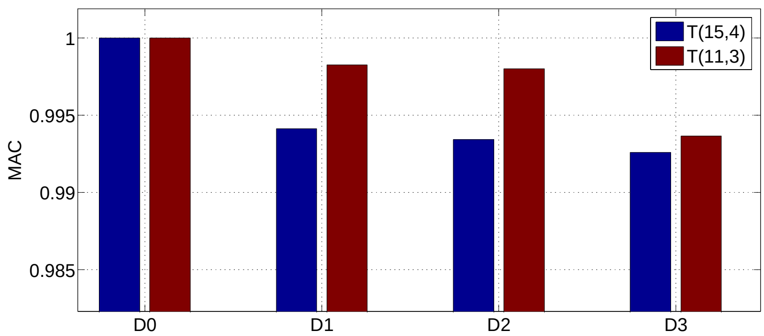

Fig. 5 MAC value of T(15,4) [480, 500] Hz, T(11, 3) [800, 1000] Hz under D1-D3 along with D0.

5 CONCLUSIONS

In this study, a new methodology for detecting damage in beam-like structures is proposed with a clear inference. Note that this proposed methodology is for Euler-Bernoulli beam-like structures. The numerical analysis results show the well performance in damage detecting, while if the frequency band is well chosen, it might also be used for assess the damage severity. Further investigation is needed in order to test the feasibility of the proposed methodology in noisy environmental experiment data.

6 ACKNOWLEDGEMENTS

The first author thanks CWO (Commissie Wetenschappelijk Onderzoek), Faculty of Engineering and Architecture, Ghent University for providing financial support for a research stay at Soete Laboratory.

7 REFERENCES

[1] M. Abdel Wahab, The Mechanics of Adhesives in Composite and Metal Joint: Finite Element Analysis using ANSYS, first ed., DEStech Publications, Inc., 2014.

[2] M. Abdel Wahab, Simulating mode I fatigue crack propagation in adhesively-bonded composite joints. Fatigue and fracture of adhesively-bonded composite joints. Elsevier; 2015. p. 323-44.

[3] Yun-Lai Zhou, M. Abdel Wahab, R. Perera, N. Maia, R. Sampaio, E. Figueiredo, Single side damage simulations and detection in beam-like structures, in: Proceeding of 11th International Conference on Damage Assessment of Structures (DAMAS 2015), Ghent University, Belgium, August 2015.

[4] A.M.R. Ribeiro, On The Generalization Of The Transmissibility Concept, in: Proceedings of NATO/ASI Conference on Modal Analysis and Testing, Sesimbra, Portugal, May 1998.

[5] N.M.M. Maia, J.M.M. Silva, A.M.R. Ribeiro, The Transmissibility Concept in Multi-Degree-of-Freedom Systems, Mechanical Systems and Signal Processing, 15(1), 129-137, 2001.

[6] Yun-Lai Zhou, E. Figueiredo, N. Maia, R. Sampaio, R. Perera, Damage detection in structures using a transmissibility-based Mahalanobis distance. Structural Control and Health Monitoring, DOI: 10.1002/stc.1743 (In press).

[7] N. M.M. Maia, R. Almeida, A. Urgueira, R. Sampaio, Damage detection and quantification using transmissibility, Mechanical Systems and Signal Processing, (25), 2475-2483.

[8] Yun-Lai Zhou, E. Figueiredo, Nuno M. Maia, R. Perera, Damage detection and quantification using transmissibility coherence analysis, Shock and Vibration, (2015), ID 290714.

[9] Yunlai Zhou, R. Perera, E. Sevillano, Damage identification from power spectrum density transmissibility, in: Proceedings of 6th European Workshop on Structural Health Monitoring and 1th European Conference of the Prognostics and Health Management (PHM) Society; Dresden, July 2012.

[10] Y. E. Lage, N. M. M. Maia, M. M Neves, Force Magnitude Reconstruction Using the Force Transmissibility Concept. Shock and Vibration, (2014), ID 905912.

[11] Yun Lai Zhou, Ricardo Perera, Transmissibility based damage assessment by optimizing intelligent algorithm, in: Proceedings of the 9th European Conference on Structural Dynamics (EURODYN 2014); June 2014, Oporto, Portugal.

Proceedings of the 4th International Conference On
Fracture Fatigue and Wear, pp. 260-264, 2015

FATIGUE DESIGN BASED ON FATIGUE MECHANISM OF FLAK GRAPHITE CAST IRON

K. Shirato[1], T. Nishimizu[2], Y. Miyashita[2], K. Takahashi[1] and Y. Otsuka[2]

[1]Isuzu Motors, Fujisawa, Japan
[2]Nagaoka University of Technology, Nagaoka, Japan

Abstract: In order to improve reliability and performance of an automotive engine, fatigue design method based on fatigue mechanism of flak graphite cast iron was studied. Rotating bending fatigue test was carried out at room temperature. The fatigue test specimen was cut from an actual component of an automotive engine. Fatigue crack initiation and propagation behaviour were observed during the fatigue test by replication technique. Fatigue crack growth test was also carried out under four-point bending condition. Fatigue crack was initiated early stage of the total fatigue life at flake graphite. Fatigue crack passed through aggregative region of the flake graphite. Multiple cracking and coalescence of the cracks were also observed. Different values of threshold stress intensity factor for fatigue crack propagation were obtained in a small surface crack and a long through thickness crack. It was considered that the difference in fatigue crack growth curves between surface crack and through thickness crack might be due to three dimensional shape and distribution of flake graphite. Fatigue strength was well predicted by threshold stress intensity factor obtained in a small surface crack and the maximum graphite size assumed as defect size according to result of evaluation in graphite size with extreme value statistics. It is considered that fracture mechanics approach is an effective way for fatigue design of an engine component produced by flake cast ion.

Keywords: Fatigue strength, Fatigue crack initiation, Fatigue crack propagation, Flake graphite cast ion

1 INTRODUCTION

Due to environmental problem and saving energy, higher performance is strongly required in an automotive engine. Therefore, development of new material and new structure is important, but certainly with high reliability. In order to improve reliability of the structure, fatigue design is one of the most important tasks. In case of conventional fatigue design method, reliability for fatigue is evaluated based on fatigue strength data such as S-N curve of the material used. On the other hand, material property and microstructure are not uniform in a component and is depending on the production process, for example cast material widely used in automotive component. In order to develop rational fatigue design method for an engine component, application of fracture mechanics was considered in the present study. Fatigue crack initiation and propagation behaviour was studied with a specimen cut from an engine component produced with flake graphite cast iron. Fatigue strength was evaluated based on fatigue mechanism observed in the present experiment.

2 EXPERIMENTAL PROCEDURE

Material used in the present study was flak graphite cast iron cut from an actual engine component. Microstructure and mechanical property of the material used are shown in Fig.1 and Table1. Flake graphite was observed in the substrate of pearlitic steel. According to classification of cast iron, the material is categorized as type I graphite cast iron that can be considered as a homogeneous material [1]. Geometry

Fig. 1 Microstructure of material used.

Table 1 Mechanical property of material used.

Tensile strength MPa	Young's modulus GPa	Vickers Hardness
300	110	216

of fatigue test specimen is shown in Fig.2 (a). Specimen surface was polished in loading direction to obtain mirror surface. Rotating bending fatigue test was carried out with frequency of 40 Hz in laboratory air. Fatigue crack initiation and propagation behaviour were observed by replication technique with interrupted fatigue test at stress amplitude of 120 and 130 MPa. Fatigue crack propagation test was also carried out in four-point bending condition with inner and outer span lengths of 10 and 30 mm, respectively. Geometry of specimen for fatigue crack growth test is shown in Fig.2 (b). A V-shape notch with depth of 3 mm was machined at the centre of the specimen. Fatigue pre-crack with length of 2 mm was introduced by applying cyclic loading with frequency of 20 Hz and stress ratio, R=0.1. Fatigue crack growth test was conducted with stress ratio, R=0.1 and frequency of 20 Hz at laboratory air. Threshold stress intensity factor was obtained with K-decreasing test. Crack length was measured by using a traveling microscope. Crack closure behaviour was also evaluated by elastic compliance method with measuring of strain ahead of crack tip by using a strain gage.

3 RESULT AND DISCUSSION

Result of the fatigue test is shown in Fig.3. S-N curve showed the knee around 10^6 cycles and fatigue strength at 10^7 cycles was 120 MPa as shown in the figure. Figure 4 shows observation of fatigue crack by replication technique at stress amplitude of 130 MPa. Fatigue cracks were initiated at flake graphite in plural positions. Relationship between crack length, 2a observed at the specimen surface and cycle ratio (N/N_f) is shown in Fig.5. Fatigue crack was initiated early stage of the total fatigue life, therefore it can be said that fatigue crack propagation life is dominant to the total fatigue life. During the fatigue test, interruption of crack propagation was observed in some cracks, however, those cracks were connected and propagate again to final failure in later stage of the total fatigue life as shown in Fig.5. Fracture surface of a specimen tested at stress amplitude of 130 MPa is shown in Fig.6. Roughness of fracture surface is large as not as fracture surface usually observed in metallic material. Graphite was observed in many places in the fracture surface. Figure 7 shows observation of specimen surface by replication technique during the fatigue test with applied stress amplitude of 120 MPa. Crack initiation was not observed at this stress level. According to the results shown in above, it is speculated that crack did not stop to propagate but continuously grown inside the specimen in case of applied stress amplitude of 130 MPa.

Fatigue crack growth curves obtained for a surface crack in rotating bending condition (R=-1) and for a through thickness crack in four-point bending condition at stress ratio, R=0.1 are shown in Fig .8(a) and (b), respectively. Fatigue crack growth curves for a through thickness crack were arranged by stress intensity factor range, ΔK and the maximum stress intensity factor, K_{max} and effective stress intensity factor range,

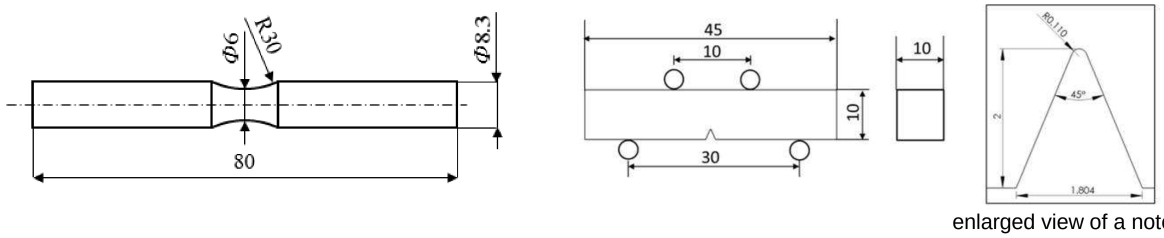

(a) Rotating bending fatigue test (b) Four-point bending fatigue crack growth test

Fig. 2 Geometries for specimens used (in mm).

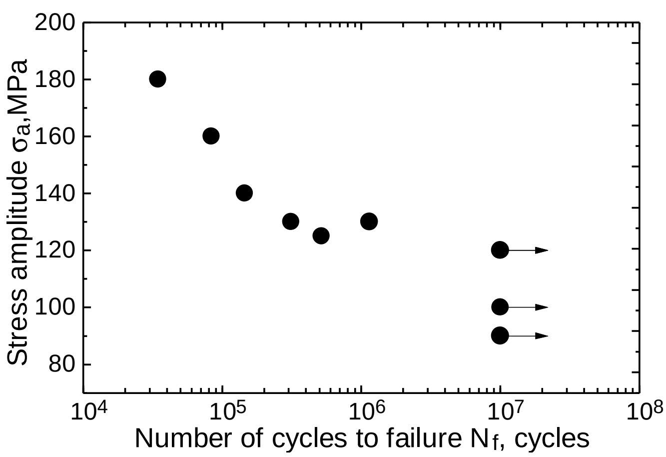

Fig. 3 S-N curve of flake graphite cast iron obtained by rotating bending fatigue test (R=-1).

ΔK_{eff}. Crack closure was observed in a through thickness crack as shown in the Fig. 8 (b). According to Fig.8 (a) and (b), crack growth curves for a surface crack and a through thickness crack show significant difference in lower stress intensity factor region. Threshold stress intensity factor for a surface crack shows lower value compared to that obtained for a through thickness crack even the effect of crack closure was taken into account. Yamabe et al. studied effect of crack length on threshold stress intensity factor range in spheroidal cast iron [2]. They also observed difference in threshold stress intensity factor range between small crack and long crack. However, effective threshold stress intensity factor ranges were almost the same regardless of crack length. It was considered that the difference in threshold stress intensity factor was mainly due to difference in crack closure effect in small and long crack. However, it was different from the present result as shown in Fig.8. Figure 9 shows fatigue crack growth path for through thickness crack

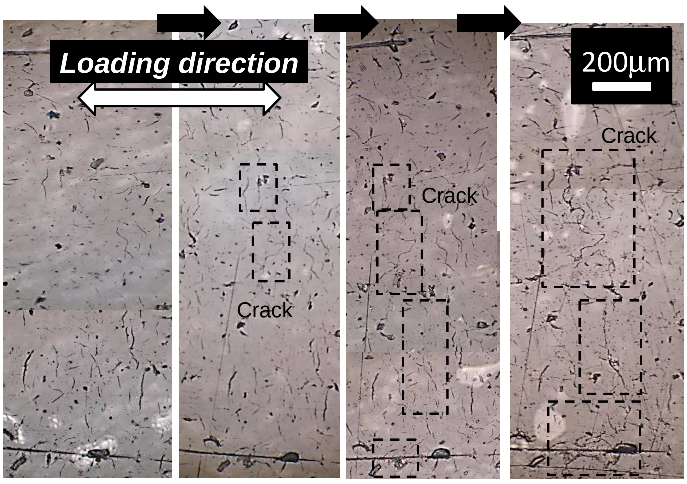

$N/N_f=0$ $N/N_f=0.1$ $N/N_f=0.5$ $N/N_f=0.9$

Fig. 4 Observation of fatigue crack initiation and propagation behaviour of a specimen tested with stress amplitude of 130MPa in rotating bending fatigue test ($N_f=1.14\times10^6$ cycles).

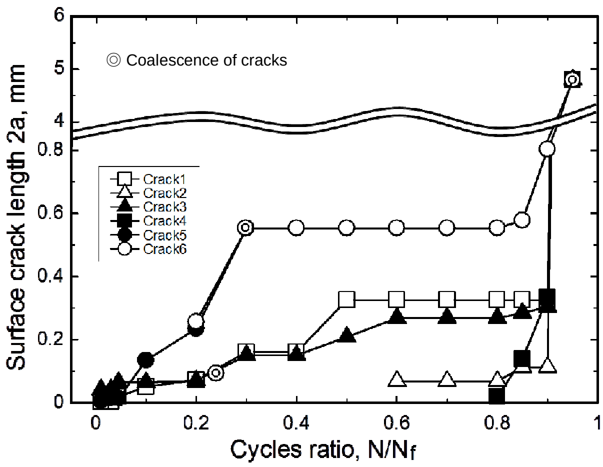

Fig.5 Relationship between cycle ratio, N/N_f and crack length, 2a for surface cracks observed in rotating bending fatigue test.

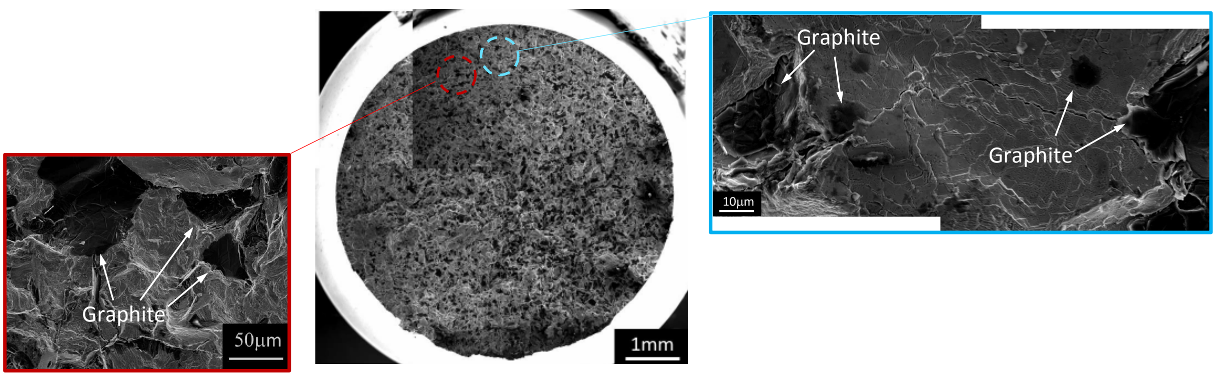

Fig. 6 Fracture surface observation of a specimen tested in rotating bending fatigue test (σ_a=130MPa, $N_f=1.14\times10^6$ cycles).

observed during the four-point bending test. Fatigue rack mainly propagated along the graphite. The study in detail is necessary, however, it is considered that significant difference in crack growth curve between a surface crack and a through thickness crack observed in the present study is due to effect of flake graphite. Flake graphite has complex shape and is distributed randomly in three dimensions ahead of crack. It could be difficult to uniformly propagate in all region of crack front in a through thickness crack.

Fatigue crack initiation and propagation behaviour of the present material was strongly affected by flake graphite distributed inside the material. Iguchi et al. studied effect of geometry and distribution of graphite on strength of flake graphite cast iron [3]. According to the result, stress near the void for the one void model was difference from that for the plural voids model. Moreover, they proposed that threshold intensity factor, ΔK_{th} was evaluated by following equation.

$$\Delta\sigma_{\max(i)} = \frac{\Delta K_{th}}{6.27\sqrt{\pi a_{\max}}} \quad (1)$$

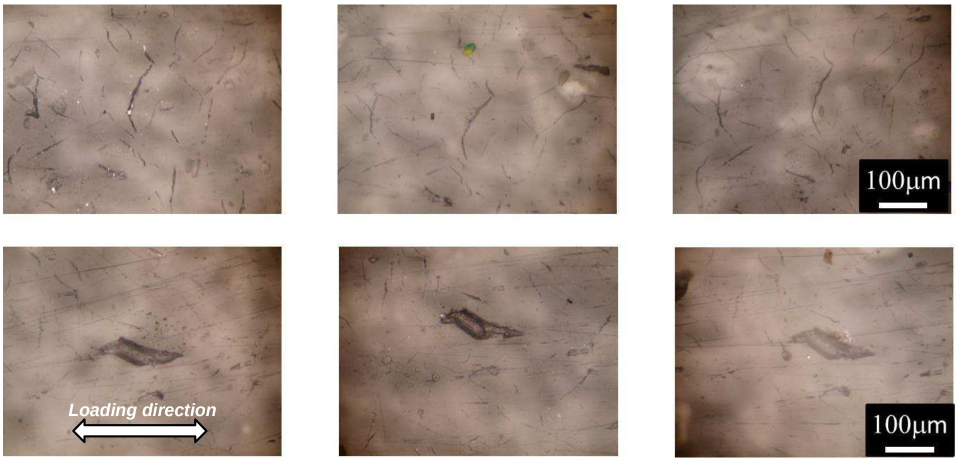

N=0 cycle N=5.0×10^6 cycles N=1.0×10^7 cycles

Fig. 7 Observation of surface for a specimen survived for 10^7 cycles at stress amplitude of 120MPa

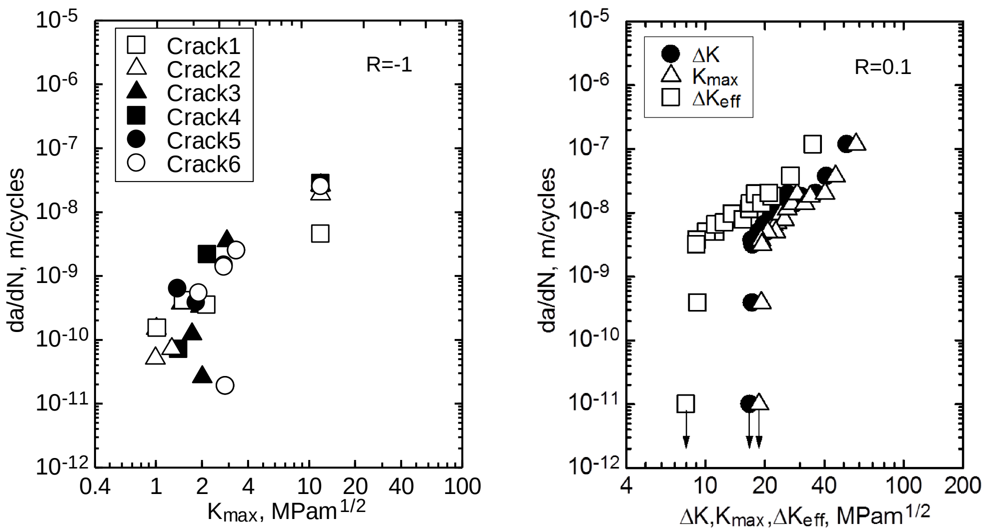

(a) Surface crack (b) Through thickness crack

Fig. 8 Fatigue crack growth curves.

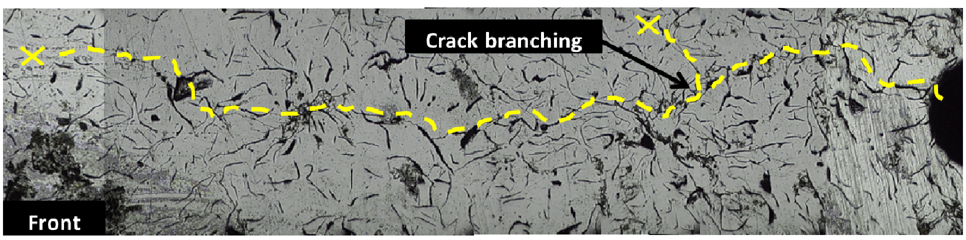

Fig. 9 Crack path observation of a through thickness crack tested in four-point bending test.

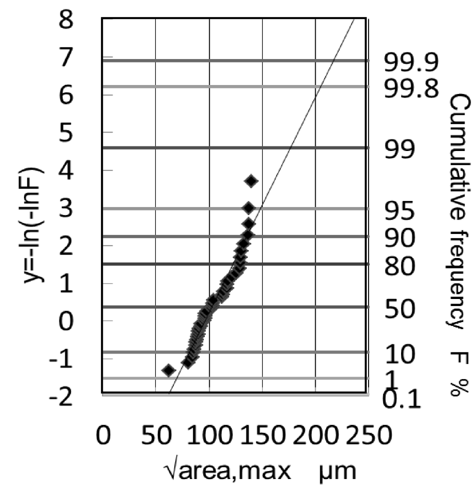

Figure 10 Distribution of the maximum graphite size by using extreme value statistics.

Where, a_{max} is the maximum length of graphite and $\sigma_{max(i)}$ is fatigue limit. In the present study, The maximum graphite length, $2a_{max}$ observed and the maximum threshold stress intensity factor, K_{max} were 210 μm and 18 MPam$^{1/2}$. Therefore. $\sigma_{max(i)}$ was calculated 164 MPa according to equation (1) and was higher than fatigue strength obtained at 10^7 cycle in the present experiment. It may be due to difference in distribution of flake graphite. Correction factor for stress in equation (1) would not be 6.27 in the present materials.

Figure 10 shows distribution of the maximum graphite size evaluated by using extreme value statistics. In the figure, root area parameter proposed by Y. Murakami was used as the size [4]. The evaluated area for the maximum graphite size was 393.9×10^{-3} mm^2 and number of evaluation was 40. In case of surface crack, fatigue limit is predicted by equation (2) with the maximum size of graphite in √area parameter and threshold stress intensity factor.

$$\sigma = \frac{K_{th}}{0.65\sqrt{\pi\sqrt{area}}} \tag{2}$$

Fatigue strength was calculated 131 MPa, where√area =175μm at cumulative frequency, F=99% and K_{th}=2 MPam$^{1/2}$ obtained with a surface crack. This value is the similar with fatigue strength obtained at 10^7 cycles as shown in the S-N curve in Fig.3.

4 CONCLUSIONS

Fatigue strength of flake graphite cast iron was evaluated by using a specimen cut from an actual engine component. Fatigue strength obtained at 10^7 cycles for the material used was 120MPa. Flake graphite significantly affected the initiation and the propagation behaviour. Multiple cracking was observed and those cracks were initiated at flake graphite. Fatigue crack mainly propagated along the graphite. Fatigue crack growth curves obtained for a surface crack and a through thickness crack showed significantly difference. It was considered that the difference in fatigue crack growth curves was induced by complex shape and distribution of flake graphite. Fatigue strength was well predicted by using threshold stress intensity factor obtained for a surface crack and the maximum graphite size arranged by √area parameter.

5 REFERENCES

[1] Japan Industrial Standard (JIS) G5505 “Compacted vermicular graphite cast irons” (2013).

[2] J. Yamabe and M. Kobayashi, Effect of Hardness and Stress Ration on Threshold Stress Intensity Factor Ranges for Small Cracks and Long Cracks in Spheroidal Cast Irons, Transactions of the Japan Society of Mechanical Engineers, Series A, Vol.71, No.711, (2005)pp.88-96.

[3] K. Iguchi, N. Tada and I. Shimizu. Evaluation of Strength of Diesel Engine Cylinder Block by Finite Element Analysis Based on Microstructure of Gray Cast Iron, Transactions of the Japan Society of Mechanical Engineers, Series A,Vol.79,No.799, (2013)pp.68-80.

[4] “Metal Fatigue; Effects of Small Defects and Nonmetallic Inclusions” by Y. Murakami, Yokendo Ltd., (1993).

Proceedings of the 4th International Conference On
Fracture Fatigue and Wear, pp. 265-271, 2015

AN EFFICIENT COMPUTATIONAL APPROACH FOR NONLINEAR ANALYSIS OF SMART PIEZOELECTRIC PLATES

P. Phung-Van[1], Loc V. Tran[1], M. Abdel-Wahab[1], H. Nguyen-Xuan[2]

[1]Department of Mechanical Construction and Production, Faculty of Engineering and Architecture, Ghent University, Belgium
[2]Faculty of Mathematics & Computer Science, University of Science, Vietnam National University, Ho Chi Minh City, Vietnam

Abstract: In this paper, a simple and effective formulation based on isogeometric finite elements (IGA) for geometrically nonlinear analysis of FGM plates integrated with sensors and actuators is investigated. The nonlinear formulation is based on a generalized five-parameter displacement field of higher order shear deformation (HSDT) and the von Kármán strains, which includes thermo-piezoelectric effects. The electric potential of each piezoelectric layer is assumed linearly through the thickness of each piezoelectric layer. The material properties of FGM are assumed to vary through the thickness by the rule of mixture and the Mori–Tanaka scheme. The accuracy and reliability of the proposed method is verified by comparing its numerical solutions with those of available other numerical results.

Keywords: geometrically nonlinear, isogeometric analysis (IGA), functionally graded material plates (FGM), sensors and actuators.

1 INTRODUCTION

The integration of piezoelectric and FGM has many practical applications such as smart material systems, the medical, micro-electromechanical systems (MEMS) and aerospace industries [1], etc. Because of properties of thermo-electro-mechanical coupling, many methods have been proposed He et al. [2] developed a finite element model based on variational principle and linear piezoelectricity theory. The active control of FGM integrated with piezoelectric sensors and actuators was studied by Liew et al. [3]. The behaviour of a FGM piezoelectric plate in thermal environments using HSDT was investigated in Refs. [4,5]. Yang et al. [6] examined the nonlinear thermo-electro-mechanical bending response of piezoelectric FGM plates. The FE formulations based HSDT for nonlinear analysis of functionally graded piezoelectric plates were also reported in [7]. Recently, isogeometric analysis (IGA) of the piezoelectric composite plates using HSDT was studied by Ref. [8]. However, nonlinear transient analysis has not taken into account for their previous work. So far, there are few published materials related to geometrically nonlinear analysis using IGA for composite plates. Apparently, there are no study on nonlinear analysis based on isogeometric analysis using the generalized shear deformation theory for the piezoelectric FGM plates. So, this paper hence tries to fill this gap by using IGA based on the generalized shear deformation theory for geometrically nonlinear transient analysis of the piezoelectric FGM plates. The nonlinear formulation is based on a generalized higher order shear deformation (HSDT) and the von Kármán strains, which includes thermo-piezoelectric effects. The electric potential of each piezoelectric layer is assumed linearly through the thickness of each piezoelectric layer. The material properties of FGM are assumed to vary through the thickness by the rule of mixture and the Mori–Tanaka scheme. The accuracy and reliability of the proposed method is verified by comparing its numerical solutions with those of available other numerical results.

2 THE GENERALIZED HSDT FOR SMART PIEZOELECTRIC PLATES

2.1 The piezoelectric FGM model

A sandwich plate shown in Figure 1a has the volume fraction of ceramic and metal phase across thickness as follows

$$V_c(z) = \left(\frac{1}{2} + \frac{z_c}{h_c}\right)^n, \quad V_m(z) = 1 - V(z) \tag{1}$$

where c and m refer to the ceramic and metal, respectively; $z_c \in [z_2, z_3]$ and $h_c = z_3 - z_2$ is thickness of core which are displayed in Figure 1b. The material constituents of piezoelectric FGM can be obtained as:

$$V_c(z) = 1, \quad h_c \in [z_1, z_2];\ V_c(z) = \left(\frac{1}{2} + \frac{z_c}{h_c}\right)^n, \quad h_c \in [z_2, z_3] \text{ for core}$$
$$V_c(z) = 1, \quad h_c \in [z_3, z_4];\ V_m(z) = 1 - V_c(z) \tag{2}$$

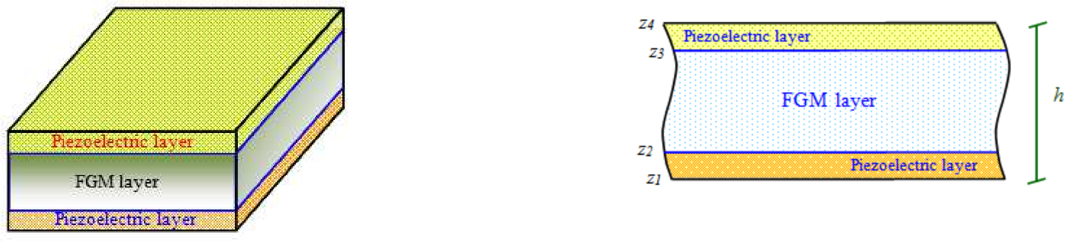

(a) (b)

Fig. 1 (a) Configuration of a piezoelectric FGM plate; (b) The sandwich plate with piezoelectric skins and FGM core

The material properties including Young's modulus (E), Poisson's ratio (v) and density (ρ) based on the mixture rule are defined by:

$$P = P_c V_c(z) + P_m V_m(z) \tag{3}$$

where P_c, P_m represent the individual properties of material of ceramic and metal. To consider the interactions among the constituents, the Mori-Tanaka scheme is used in this paper.

2.2 The generalized higher order shear deformation theory for piezoelectric FGM plates

In the piezoelectric FGM plates, there are two field variables including a mechanical displacements field and an electrical field that need to be approximated. The mechanical displacements are approximated by the generalized higher order shear deformation theory and expressed as follows

$$u = u_0 - z\partial w/\partial x + f(z)\beta_x;\ v = v_0 - z\partial w/\partial y + f(z)\beta_y;\ w = w \tag{4}$$

where u_0, v_0, β_x, β_y and w are displacement variables. The function $f(z)$ is a continuous function through the plate thickness and chosen as $f(z) = h\arctan(2z/h) - z$ as in Thai *et al.* [9]

For a bending plate, the Green's strain vector can be presented by

$$\varepsilon_{ij} = \frac{1}{2}\left(\frac{\partial u_i}{\partial x_j} + \frac{\partial u_j}{\partial x_i}\right) + \frac{1}{2}\frac{\partial u_k}{\partial x_i}\frac{\partial u_k}{\partial x_j} \tag{5}$$

The material behaviour of piezoelectric FGM is expressed as following [10]

$$\begin{bmatrix} \boldsymbol{\sigma} \\ \mathbf{D} \end{bmatrix} = \begin{bmatrix} \mathbf{c} & -\mathbf{e}^T \\ \mathbf{e} & \mathbf{g} \end{bmatrix} \begin{bmatrix} \bar{\boldsymbol{\varepsilon}} \\ \mathbf{E} \end{bmatrix} \tag{6}$$

where $\boldsymbol{\sigma}$ and $\bar{\boldsymbol{\varepsilon}} = [\boldsymbol{\varepsilon}\ \ \boldsymbol{\gamma}]^T$ are the stress and strain vectors, respectively; **D** is the dielectric displacement; **e** is the piezoelectric constant matrix and **g** denotes the dielectric constant matrix; **E** is the electric field vector that is defined as

$$\mathbf{E} = -\text{grad}\,\phi \tag{7}$$

in which ϕ is the electric potential field; and **c** is the elasticity matrix and defined as

$$\mathbf{c}=\begin{bmatrix}\mathbf{A} & \mathbf{B} & \mathbf{N} & \mathbf{0}\\ \mathbf{B} & \mathbf{C} & \mathbf{F} & \mathbf{0}\\ \mathbf{N} & \mathbf{F} & \mathbf{H} & \mathbf{0}\\ \mathbf{0} & \mathbf{0} & \mathbf{0} & \mathbf{D}^S\end{bmatrix} \tag{8}$$

where

$$A_{ij}, B_{ij}, C_{ij}, N_{ij}, F_{ij}, H_{ij}=\int_{-h/2}^{h/2}\left(1, z, z^2, f(z), zf(z), f^2(z)\right)\frac{E_e}{1-\nu_e^2}\begin{bmatrix}1 & \nu_e & 0\\ \nu_e & 1 & 0\\ 0 & 0 & \frac{1-\nu_e}{2}\end{bmatrix}\mathrm{dz}\ ,\quad i,j=1,2,6$$

$$D_{ij}^S=\int_{-h/2}^{h/2}[f'(z)]^2\frac{E_e}{2(1+\nu_e)}\begin{bmatrix}1 & 0\\ 0 & 1\end{bmatrix}\mathrm{dz}\ ,\qquad i,j=4,5 \tag{9}$$

And the piezoelectric constant matrix **e** and the dielectric constant matrix **g** are defined

$$\mathbf{e}=\begin{bmatrix}0 & 0 & 0 & 0 & d_{15} & 0\\ 0 & 0 & 0 & d_{15} & 0 & 0\\ d_{31} & d_{32} & d_{33} & 0 & 0 & 0\end{bmatrix}\ ;\quad \mathbf{g}=\begin{bmatrix}p_{11} & 0 & 0\\ 0 & p_{22} & 0\\ 0 & 0 & p_{33}\end{bmatrix} \tag{10}$$

3 THE SMART PIEZOELECTRIC PLATE FORMULATION BASED ON NURBS BASIC FUNCTION

Using Cox-de Boor algorithm, the univariate B-spline basis functions $N_{i,p}(\xi)$ are defined in Les Piegl and Wayne (1997) on the corresponding knot vector start with order p = 0

$$N_{i,0}(\xi)=\begin{cases}1 & \text{if}\quad \xi_i\le\xi<\xi_{i+1}\\ 0 & \text{otherwise}\end{cases} \tag{11}$$

as p + 1 the basis functions are obtained from

$$N_{i,p}(\xi)=\frac{\xi-\xi_i}{\xi_{i+p}-\xi_i}N_{i,p-1}(\xi)+\frac{\xi_{i+p+1}-\xi}{\xi_{i+p+1}-\xi_{i+1}}N_{i+1,p-1}(\xi) \tag{12}$$

To present exactly some conic sections, e.g., circles, cylinders, spheres, etc., non-uniform rational B-splines (NURBS) need to be used. Being different from B-spline, each control point of NURBS has an additional value called an individual weight $\zeta_A>0$.

$$R_A(\xi,\eta)=\frac{N_A(\xi,\eta)\zeta_A}{\sum_{A=1}^{m\times n}N_A(\xi,\eta)\zeta_A} \tag{13}$$

And the B-spline function is recovered as the individual weight of control point is constant.

3.1 Mechanical displacements

The displacement field **u** of the plate using NURBS basic function is approximated as

$$\mathbf{u}^h(\xi,\eta)=\sum_{I=1}^{m\times n}R_I(\xi,\eta)\mathbf{d}_I \tag{14}$$

where $\mathbf{d}_I=\begin{bmatrix}u_{0I} & v_{0I} & \beta_{xI} & \beta_{yI} & w_I\end{bmatrix}^T$ is the vector of degrees of freedom associated with the control point I, and R_I is the shape function as defined in Eq. (13).

The strains can be expressed as

$$\bar{\boldsymbol{\varepsilon}}=[\boldsymbol{\varepsilon}\ \ \boldsymbol{\gamma}]^T=\sum_{I=1}^{m\times n}\left(\mathbf{B}_I^L+\frac{1}{2}\mathbf{B}_I^{NL}\right)\mathbf{d}_I \tag{15}$$

where $\mathbf{B}_I^L=\left[\left(\mathbf{B}_I^m\right)^T\ \left(\mathbf{B}_I^{b1}\right)^T\ \left(\mathbf{B}_I^{b2}\right)^T\ \left(\mathbf{B}_I^s\right)^T\right]^T$, in which

$$\mathbf{B}_I^m = \begin{bmatrix} R_{I,x} & 0 & 000 \\ 0 & R_{I,y} & 000 \\ R_{I,y} & R_{I,x} & 000 \end{bmatrix}, \mathbf{B}_I^{b1} = -\begin{bmatrix} 00 & R_{I,xx} & 00 \\ 00 & R_{I,yy} & 00 \\ 00 & 2R_{I,xy} & 00 \end{bmatrix}, \mathbf{B}_I^{b2} = \begin{bmatrix} 000\,R_{I,x} & 0 \\ 000 \;\; 0 & R_{I,y} \\ 000\,R_{I,y} & R_{I,x} \end{bmatrix}, \mathbf{B}_I^{s} = \begin{bmatrix} 000\,R_I & 0 \\ 000 \;\; 0 & R_I \end{bmatrix} \tag{16}$$

and $\mathbf{B}_I^{NL}$ is calculated by

$$\mathbf{B}_I^{NL}(\mathbf{d}) = \begin{bmatrix} w_{I,x} & 0 \\ 0 & w_{I,y} \\ w_{I,y} & w_{I,x} \end{bmatrix} \begin{bmatrix} 0 & 0 & R_{I,x} & 0 & 0 \\ 0 & 0 & R_{I,y} & 0 & 0 \end{bmatrix} = \mathbf{A}_\theta \mathbf{B}_I^g \tag{17}$$

3.2 Electric potential field

The electric potential field of each piezoelectric layer is approximated through the thickness as

$$\phi^i(z) = \mathbf{R}_\phi^i \boldsymbol{\phi}^i \tag{18}$$

where $\mathbf{R}_\phi^i$ is the shape functions for the electric potential which is defined in Eq. (13) with $p = 1$, and $\boldsymbol{\phi}^i$ is the vector containing the electric potentials at the top and bottom surfaces.

The electric field **E** in Eq. (7) can be rewritten as [10]

$$\mathbf{E} = -\nabla \mathbf{R}_\phi^i \boldsymbol{\phi}^i = -\mathbf{B}_\phi \boldsymbol{\phi}^i \tag{19}$$

3.3 Governing equations of smart piezoelectric plates

The governing equations for piezoelectric FGM plates can be written by

$$\underbrace{\begin{bmatrix} \mathbf{M}_{uu} & 0 \\ 0 & 0 \end{bmatrix}}_{\bar{\mathbf{M}}} \underbrace{\begin{bmatrix} \ddot{\mathbf{d}} \\ \ddot{\boldsymbol{\phi}} \end{bmatrix}}_{\ddot{\mathbf{q}}} + \underbrace{\begin{bmatrix} \mathbf{K}_{uu} & \mathbf{K}_{u\phi} \\ \mathbf{K}_{\phi u} & \mathbf{K}_{\phi\phi} \end{bmatrix}}_{\bar{\mathbf{K}}} \underbrace{\begin{bmatrix} \mathbf{d} \\ \boldsymbol{\phi} \end{bmatrix}}_{\mathbf{q}} = \underbrace{\begin{bmatrix} \mathbf{f} \\ \mathbf{q} \end{bmatrix}}_{\bar{\mathbf{f}}} \quad \Leftrightarrow \quad \bar{\mathbf{M}}\ddot{\mathbf{q}} + \bar{\mathbf{K}}\mathbf{q} = \bar{\mathbf{f}} \tag{20}$$

where

$$\begin{aligned} &\mathbf{K}_{uu} = \int_\Omega (\mathbf{B}^L + \mathbf{B}^{NL})^T \mathbf{c} (\mathbf{B}^L + \tfrac{1}{2}\mathbf{B}^{NL}) \mathrm{d}\Omega \quad ; \quad \mathbf{K}_{u\phi} = \int_\Omega (\mathbf{B}^L)^T \mathbf{e}^T \mathbf{B}_\phi \mathrm{d}\Omega \\ &\mathbf{K}_{\phi\phi} = \int_\Omega \mathbf{B}_\phi^T \mathbf{p} \mathbf{B}_\phi \mathrm{d}\Omega \quad ; \quad \mathbf{M}_{uu} = \int_\Omega \tilde{\mathbf{N}}^T \mathbf{m} \tilde{\mathbf{N}} \mathrm{d}\Omega \quad ; \quad \mathbf{f} = \int_\Omega \bar{q}_0 \bar{\mathbf{R}} \mathrm{d}\Omega \end{aligned} \tag{21}$$

in which $\bar{q}_0$ is a uniform load; $\bar{\mathbf{R}} = [0\,0\,0\,0\,R_I]$; **m** is defined by

$$\mathbf{m} = \begin{bmatrix} I_1 & I_2 & I_4 \\ I_2 & I_3 & I_5 \\ I_4 & I_5 & I_7 \end{bmatrix}, \quad (I_1, I_2, I_3, I_4, I_5, I_7) = \int_{-h/2}^{h/2} \rho \left(1, z, z^2, f(z), zf(z), f^2(z)\right) \mathrm{d}z \tag{22}$$

and

$$\tilde{\mathbf{N}} = \begin{Bmatrix} \tilde{\mathbf{N}}_1 \\ \tilde{\mathbf{N}}_2 \\ \tilde{\mathbf{N}}_3 \end{Bmatrix}, \tilde{\mathbf{N}}_1 = \begin{bmatrix} R_I & 0 & 0\,0\,0 \\ 0 & R_I & 0\,0\,0 \\ 0 & 0 & R_I\,0\,0 \end{bmatrix}; \tilde{\mathbf{N}}_2 = -\begin{bmatrix} 0\,0\,R_{I,x}\,0\,0 \\ 0\,0\,R_{I,y}\,0\,0 \\ 0\,0 \;\; 0 \;\; 0\,0 \end{bmatrix}; \tilde{\mathbf{N}}_3 = \begin{bmatrix} 0\,0\,0\,R_I & 0 \\ 0\,0\,0\,0 & R_I \\ 0\,0\,0\,0 & 0 \end{bmatrix} \tag{23}$$

4 NUMERICAL EXAMPLES

4.1 Free vibration analysis

Consider a square Al2O3/Ti-6Al-4V plate (400mm × 400mm) with the thickness of the plate, *h*, is 5mm and thickness of each piezoelectric layer, *h_pie*, is 0.1mm. Figure 2 displays frequencies of the CCCC and SSSS plate. We can see that the frequencies of the present method match well with those of He et al. (2001) and those of the CCCC plate are larger than those of the SSSS plate.

4.2 Nonlinear analysis

4.2.1 An orthotropic plate

This example aims to verify the accuracy of the present method for geometrically nonlinear analysis. Consider a SSSS square plate subjected to a uniform loading of q_0 = 1 MPa. Material properties and the geometry are given E_1 = 525 GPa, E_2 = 21 GPa, $G_{12} = G_{23} = G_{13}$ = 10.5 GPa, v = 0.25, ρ = 800 kg/m^3, length L = 250 mm, thickness h = 5 mm. The normalized central deflection, $\bar{w} = w/h$, is shown in Figure 3. It can be observed that deflection responses of IGA match well with those of finite strip method (FSM) [11].

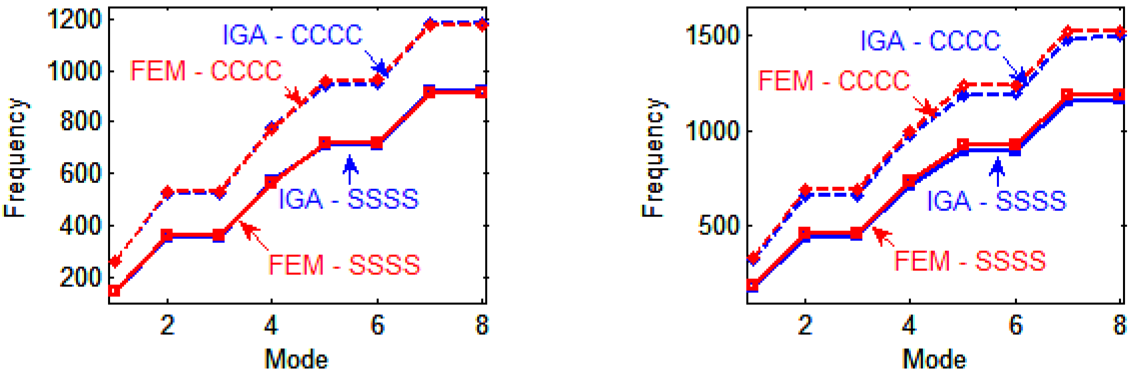

Fig. 2 The first lowest eight natural frequencies of the simply supported (SSSS) and clamped (CCCC) piezoelectric FGM plate with the different volume fraction exponents

4.2.2 A smart piezoelectric plate

Now we consider the square piezoelectric FGM plate with length L = 1, $h_{FGM} = L/20$ and $h_{piezo} = h_{FGM}/10$. The boundary condition of the plate is SSSS.

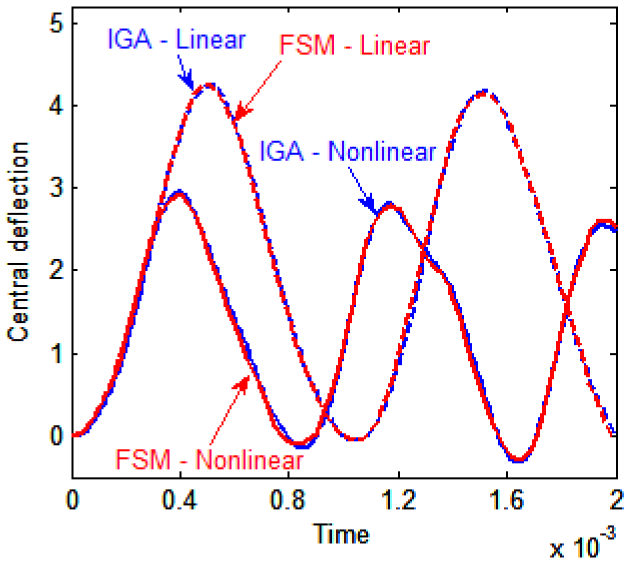

Fig. 3 Displacement of the plate under step uniform load

Figure 4a displays the effect of volume fraction exponent n to deflection of piezoelectric FGM (Al/ZrO2-2) plates under mechanical load (parameter load $\bar{q} = q_o \times 10^5$). It is seen that magnitude of deflection of nonlinear analysis is smaller than that of linear analysis. Next, effect of temperature to nonlinear deflection of the plate under thermo-mechanical load with n = 5 is displayed in Figure 4b. It is observed that the behaviour of deflection subjected to thermo-mechanical load is different from the pure mechanical loading. When the mechanical load is zero, the deflection of the plate is not zero. This is because of thermal expansion phenomenon. Also, the deflection decreases correspondingly to the increase of the temperature.

5 CONCLUSIONS

The paper presents a simple and effective formulation based on isogeometric finite elements (IGA) for geometrically nonlinear analysis of FGM piezoelectric plates. The nonlinear formulation is based on a generalized five-parameter displacement field of higher order shear deformation (HSDT) and the von Kármán strains, which includes thermo-piezoelectric effects. The electric potential of each piezoelectric layer is assumed linearly through the thickness of each piezoelectric layer. The material properties of FGM are assumed to vary through the thickness by the rule of mixture and the Mori–Tanaka scheme. The accuracy and reliability of the proposed method is verified by comparing its numerical solutions with those of available other numerical results.

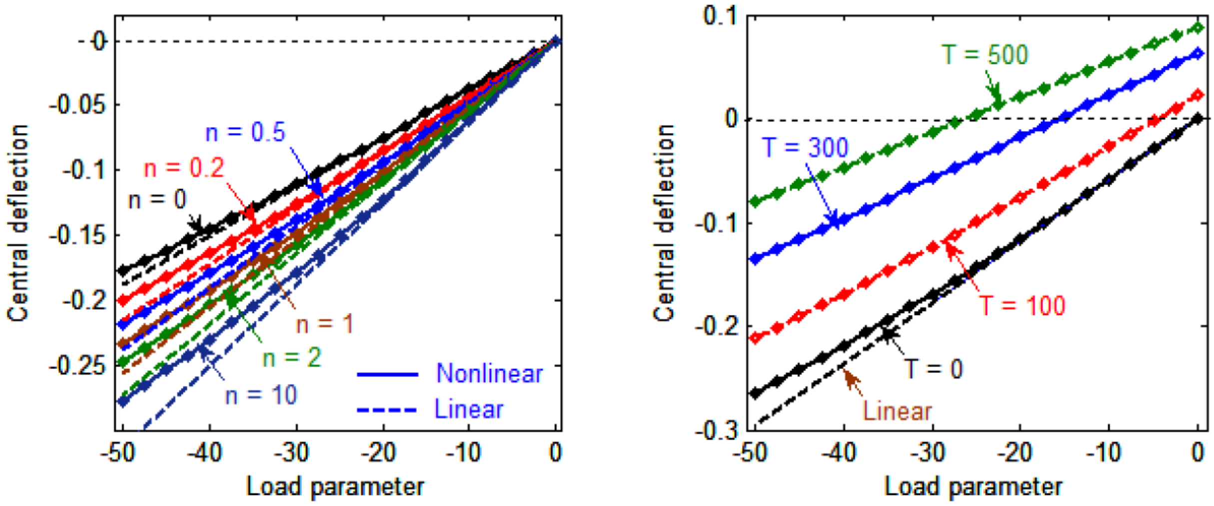

(a) (b)

Fig.4 The first lowest eight natural frequencies of the simply supported (SSSS) and clamped (CCCC) piezoelectric FGM plate with the different volume fraction exponents

6 REFERENCES

[1] K. Takagi, JF. Li, S. Yokoyama, R. Watanabe, Fabrication and evaluation of PZT/Pt piezoelectric composites and functionally graded actuators, Journal of the European Ceramic Society, 23, 1577–1583, 2003

[2] XQ. He, TY. Ng, S. Sivashanker, KM. Liew, Active control of FGM plates with intergrated piezoelectric sensors and actuators, International Journal of Solids and Structures, 38, 1641-1655, 2001

[3] KM. Liew, XQ. He, TY. Ng, S. Kitipornchai, Finite element piezothermo-elasticity analysis and active control of FGM plates with integrated piezoelectric sensors and actuators, Computational Mechanics, 31, 350–358, 2003.

[4] P. Phung-Van, T Nguyen-Thoi, H Luong-Van, Q Lieu-Xuan, Geometrically nonlinear analysis of functionally graded plates using a cell-based smoothed three-node plate element (CS-MIN3) based on the C0-HSDT, Computer Methods in Applied Mechanics and Engineering, 270, 15-36, 2014.

[5] XL. Huang, HS. Shen, Vibration and dynamic response of functionally graded plates with piezoelectric actuators in thermal environments. Journal of Sound Vibration, 289, 25–53, 2006.

[6] J. Yang, S. Kitipornchai, KM. Liew, Non-linear analysis of thermo-electro-mechanical behaviour of shear deformable FGM plates with piezoelectric actuators. International Journal for Numerical Methods in Engineering, 59, 1605–1632, 2004.

[7] B. Behjat, MR. Khoshravan, Geometrically nonlinear static and free vibration analysis of functionally graded piezoelectric plates. Composites Structures, 94, 874–882, 2012.

[8] P. Phung-Van, L. De Lorenzis, Chien H. Thai, M. Abdel-Wahab, H. Nguyen-Xuan, Analysis of laminated composite plates integrated with piezoelectric sensors and actuators using higher-order shear deformation theory and isogeometric finite elements. Computational Materials Science, 96, 496-505, 2015.

[9] Chien H. Thai, AJM. Ferreira, SPA Bordas, T Rabczuk, H. Nguyen-Xuan, Isogeometric analysis of laminated composite and sanwich plates using a new inverse trigometic shear deformation theory, European Journal of Mechanics – A/Solids, 43, 89-108, 2014.

[10] P. Phung-Van, T. Nguyen-Thoi, T. Le-Dinh, H. Nguyen-Xuan, Static and free vibration analyses and dynamic control of composite plates integrated with piezoelectric sensors and actuators by the cell-based smoothed discrete shear gap method (CS-FEM-DSG3), Smart Materials and Structures, 22, 095026, 2013.

[11] J. Chen, DJ. Dawe, S. Wang, Nonlinear transient analysis of rectangular composite laminated plates, Composite Structures, 49, 129-139, 2000.

Proceedings of the 4th International Conference On
Fracture Fatigue and Wear, pp. 272-278, 2015

MULTISCALE MODELLING OF ROUGHNESS EFFECT IN FRETTING WEAR

K. Pereira, T. Yue and M. A. Wahab

Ghent University, Laboratory Soete, Belgium

Abstract: This paper is a literature review of multiscale techniques and their possible applications to fretting wear simulations. Firstly, a brief introduction on fretting phenomenon is given, followed by an overview of the recent FEM modelling techniques used in fretting wear. The surface roughness effects is neglected on the majority of the FEM fretting wear models, mainly because modelling all the small geometrical details of the surface is very computationally demanding. Therefore, the use of methodologies that could provide information about these small-scale features to the macro-scale model is of great interest. Multiscale techniques (hierarchical, semi-concurrent and concurrent), discussed in this paper, may be a viable option. More specifically, the use of hierarchical homogenization techniques to contact problems and a possible application in fretting wear are discussed in detail.

Keywords: fretting wear, multiscale techniques, homogenization

1 INTRODUCTION

Fretting happens when two contacting surfaces, normally loaded, are submitted to small amplitude oscillatory relative movement. The amplitude generally varies from 5 to 100 µm [1]. However, it can be as low as, or even below, 1 µm [2].

This phenomenon can be observed in many mechanical assemblies such as dovetail joints, bearings and gears, or more generally in situations where contacting surfaces may be subjected to sliding motion. Depending on the conditions (surface finishing, coefficient of friction, normal load, slip amplitude), fretting may lead to catastrophic failure due to fatigue (known as fretting fatigue), may produce loss of fitting due to wear (fretting wear) or a combination of both. Therefore, in order to design and predict service life of mechanical components, it is important to be able to control and anticipate the effects of fretting.

The type of failure that may happen depends primarily on the fretting regime that the component is subjected to. Vingsbo and Söderberg [2] used a “fretting map" to describe the behaviour of the wear volume and fatigue life as function of the slip displacement for different fretting regimes. They defined three different fretting regimes: stick, mixed stick-slip and gross slip, as shown in Figure 1. At stick conditions, the surfaces are considered to be stuck to each other and no visible damage is generated. As the slip displacement increases, the fretting is characterized by mixed stick-slip conditions, the fatigue life decreases and the wear rate is reasonably low. This indicates that the main failure here is due to fretting fatigue. For even higher slip displacements, the regime changes to gross slip conditions where a considerable increase of the wear rate can be noticed. Fretting fatigue is not significant at this regime, because the cracks nucleated are removed by the intense amount of wear.

It is important to notice the difference between reciprocating wear and fretting wear. Different from reciprocating regime, the slip displacement at fretting wear conditions is small with respect to the contact width between the surfaces, causing the wear debris to be kept inside the contact region. This makes the fretting wear very hard to be noticeable, since it is necessary to disassemble the structure to have access to the affected region.

As shown by the Kubiak et al. [3], the effect of surface roughness in the fretting wear profile can be significant and must, therefore, be considered. However, most of the finite element (FE) models that are used to predict fretting wear do not take into consideration the effect of roughness. Since it is very computationally demanding to add all small surfaces features in a macro FE model, another techniques that allow the roughness information to be analysed are of great importance.

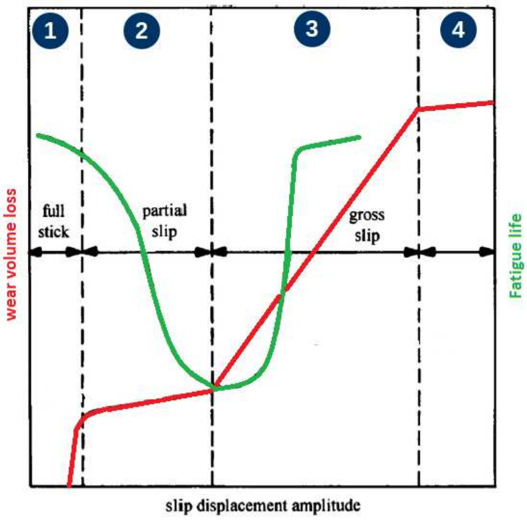

Fig. 1 Fretting map used by Vingsbo and Söderberg [2], showing the stick (1), mixed stick-slip(2) and gross slip (3) fretting regimes and also the reciprocating regime (4).

2 MULTISCALE MODELLING TECHNIQUES

The multiscale modelling techniques are used to connect results from models at different scales, sharing the efficiency of the macroscopic models with the accuracy of microscopic models. Aboudi et al. [4] classify the multiscale techniques in three main groups: hierarchical, concurrent and semi-concurrent.

2.1 Hierarchical homogenization

The hierarchical, or sequential, methodology is used to transfer information from a small scale to a larger model as a boundary condition or as an effective property. In order to do that, constitutive relations are precomputed by homogenizing (averaging) the material response at micro level and then this response is used on a large scale model. It is important to notice that the micro and macro models are independent from each other, i.e., the hierarchical approach deals with a one-way coupling (bottom-up or top-down), but not both of them.

In fracture analysis, Talebi et al. [5] applied hierarchical multi-scaling to estimate the material behaviour of nanocomposites. Figure 2 shows the procedure used to estimate material properties using homogenization. In their work, they predicted the elastic modulus of a clay/epoxy nanocomposite using a representative volume element (RVE) and then used this property in a macro model simulation. Eftekhari et al. [6] studied the fracture behaviour of CNT-reinforced concrete in a tree scale sequential scheme. The material properties of carbon nanotubes were extracted from molecular dynamics simulations and used in a micromodel, where a FE model is conducted to acquire the mechanical and damage properties. Finally, the response of the micromodel is upscale to the macro-model, where an extended finite element analysis is done.

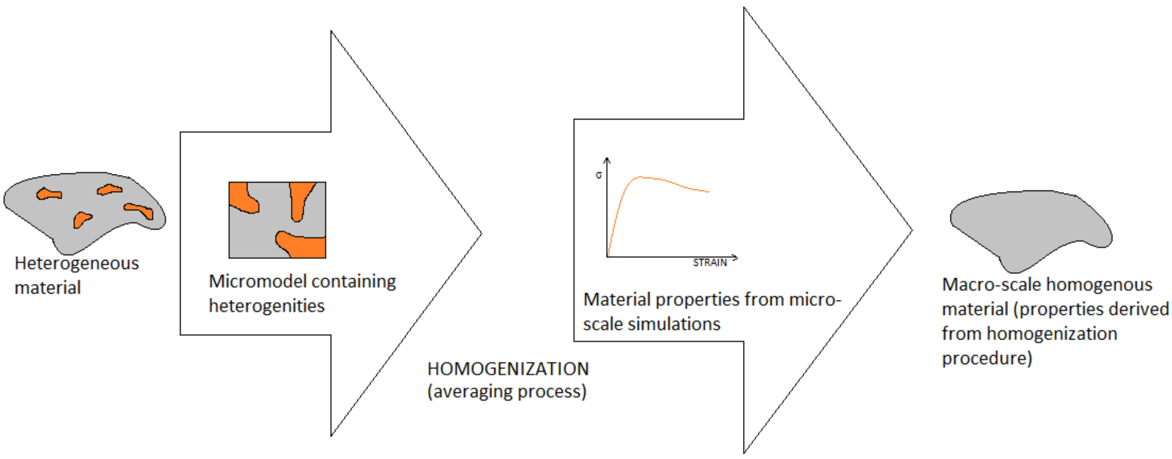

Fig. 2 Homogenization procedure adopted by Talebi et al. [5]

2.2 Semi-concurrent approach

In a semi-concurrent approach, the fine scale model is analysed at each integration point of the coarse scale model. Therefore, the semi-concurrent approach may produce better results than the homogenization method, but with a higher computational cost.

The deformation at macro level is sent to the micro model as boundary conditions and a homogenized stress tensor is calculate. This information is then sent back to the coarse model. In this way, the semi-concurrent technique can be considered as a two-way coupling [4], i.e., in order to solve the micro-model, the input from macro-model is necessary and vice-versa. The scales are interlaced in a parallel way (see Figure 3 for a schematic of the method).

Talebi et al. [5], Silani et al. [7] and Feyel and Chaboche [8] used semi-coupled schemes to connect the response of the micromodel to the macro model in a semi-concurrent way. They were interested in considering the materials heterogeneities impact in the response of the macroscale composite structures.

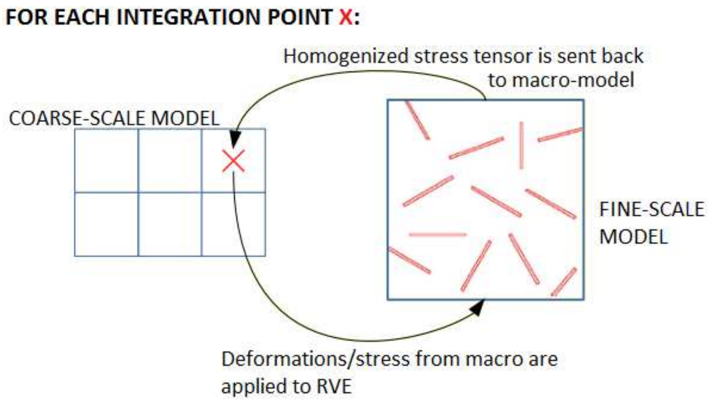

Fig. 3 Schematic of the semi-concurrent analysis of a nanocomposite done by Talebi et al. [5]

2.3 Concurrent technique

According to Aboudi et al. [4], concurrent techniques are fully coupled, which means that all scales are handled at once in the same numerical model. This technique provides the highest fidelity among all the other ones, but with the lowest computational efficiency. Figure 4 shows a comparison between the multiscale techniques.

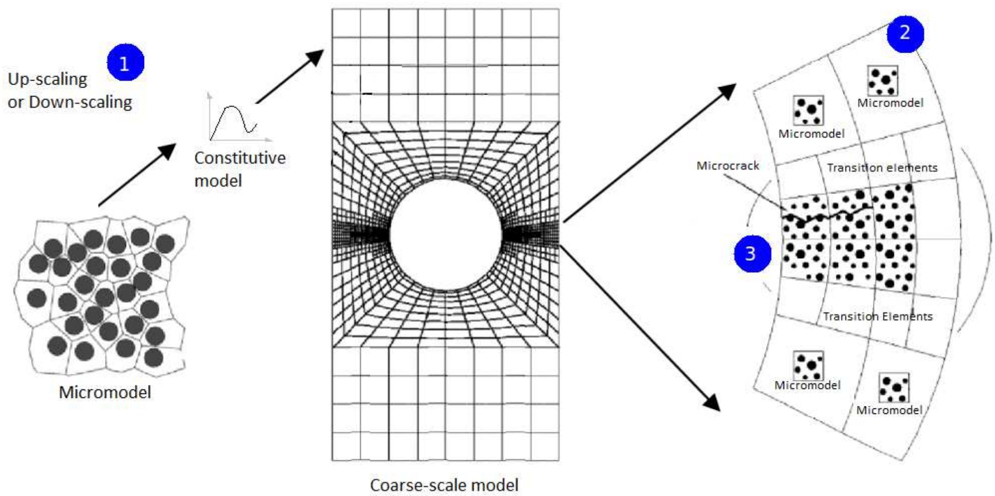

Fig. 4 Schematic of the types of multiscale analysis by Known et al. [9]: (1) homogenization, (2) semi-concurrent and (3) concurrent.

It is possible to couple different continuum to continuum and also atomistic to continuum scales in the same model. Silani et al. [10] illustrated a method to couple two continuum domains in different scales using concurrent technique. Aubertin et al. [11], Guo-Wu and Tie-Gang [12] and Yamakov et al. [13] presented results for crack propagation in a concurrent fashion, where the region near the crack tip was modelled with molecular dynamics (MD), while the region distant from the crack was modelled with finite element method (FEM). There are many other works done in the crack propagation analysis using concurrent technique. For instance, Talebi et al. [14] coupled molecular dynamics to extended finite element method (XFEM) and Yang et al. [15] coupled molecular dynamics to meshless method.

Concurrent approach is also applicable in contact mechanics, when nanoscale features of the interface are modelled using molecular dynamics and the region far from it using continuous mechanics, e.g. Luan et al. [16] did a 2D analysis of the contact, while Anciaux and Molinari [17, 18] considered a 3D problem. Figure 5 shows details of their models.

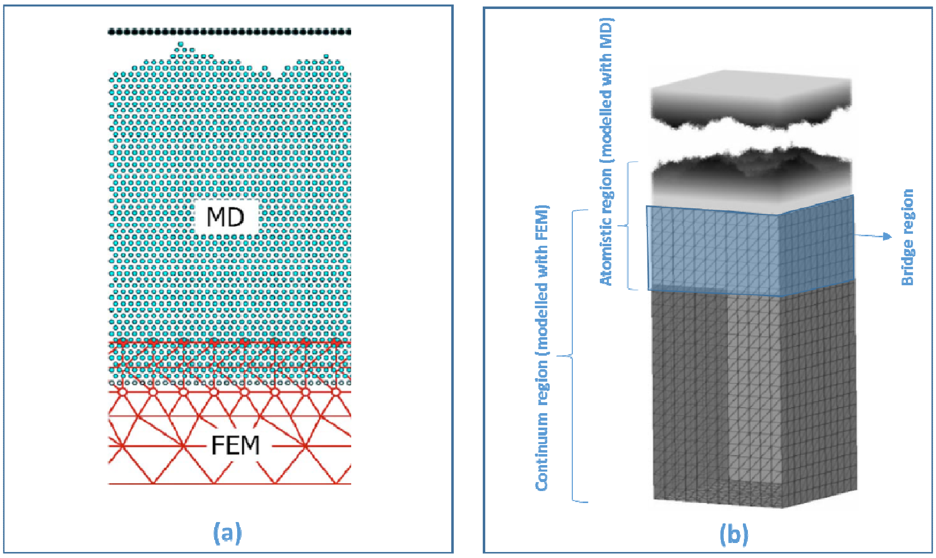

Fig. 5 Multiscale models using concurrent technique to model contact interactions. (a) model developed by Luan et al. [16] (b) model done by Anciaux and Molinari [18]

3 MULTISCALE IN FRETTING WEAR PROBLEMS

In fretting wear problems, some work have been done using multi-scaling techniques. Gallego et al. [19] presented a computational method, with three scales, for analysing dovetail joint (titanium-titanium) on blade/disk interface. Their goals was to obtain wear kinetics and worn out profile on a fast computational analysis. The scales used for analysis were: micro-scale and meso-scale, using a semi-analytical model to calculate the wear depth increments based on the solicitations derived by the forces and moments at a given point of the contact, and complete model of the blade/disk. The complete FE analysis for the whole system provided information regarding the forces and moments for calculation at meso-scale.

Leonard et al. [20] combined finite-discrete method to model the effect of third bodies in fretting. The third body is modelled as discrete elements, while the first bodies are modelled with finite elements.

Note that little or none work has been done to consider the roughness effect on fretting wear using multiscale analysis.

4 HOMOGENIZATION TECHNIQUES FOR CONTACT PROBLEMS

Hierarchical homogenization has been widely used for contact problems, as elucidated by Stupkiewicz et al. [21]. Homogenization is used in contact as a tool to derive a macroscopic constitutive relations for the contact stiffness based on microscopic simulations. It counts with the advantage of low computational cost, being able to incorporate many physical phenomena in the contact analysis. It is possible to consider many different effects, such as: hysteretic effects of rubber contact (Wriggers and Reinelt [22]), inelastic contact considering effect of third bodies (Temizer and Wriggers [23]) and also friction of soft matter (Temizer [24]).

Regarding the effect of roughness on the contact, Jerier and Molinari [25] presented a methodology to analyse the nonadhesive and frictionless contact between a flat elastic body and a rigid surface with fractal roughness (modelled by spheres). They used discrete element method and homogenization techniques in order to study the real contact area.

Another simpler way to deal with contact of rough surfaces is to model the rough surface in a micro-scale model and then upscale the results to a macro-model. Wriggers and Nettingsmeier [26] presented a methodology to derive a homogenized constitutive equations for normal frictionless contact based on those micro-scale models. This equation would have information regarding the effect of the roughness and then could be used on the macro-model. Their methodology is described in more detail in the following.

The macroscopic constitutive equation for normal frictionless contact can be written as:

$$p = c_n\delta^m. \quad (1)$$

where p is the average normal pressure, δ the normal approach between the two bodies and c_n and m are contact stiffness parameters. The normal approach δ can be replaced by maximum asperities height ξ and mean plane distance d.

The homogenization technique allows the estimation of the parameters c_n and m of Eq.1. They are obtained by the average response of the two deformable bodies in contact with rough surfaces modelled at microscale. One body is positioned on the top of the other and the bottom one is fixed. The top body is then moved downwards by a set of given displacements. The average contact pressure and the normal approach δ (see Fig. 6 for details) are calculated for each displacement of the top body. The simulation ends when the mean distance plane is relatively close to zero.

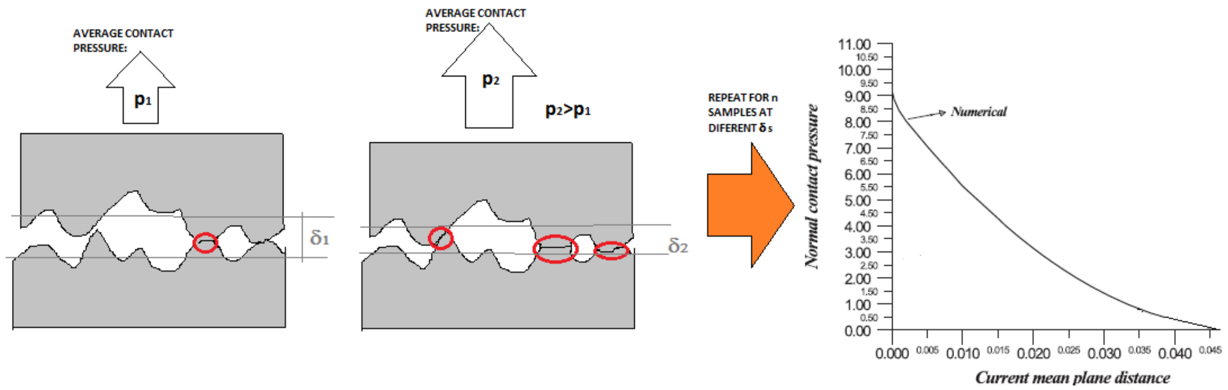

Fig. 6 Analysis process to estimate the parameters c_n and m of Eq. 1, based on Wriggers & Nettingsmeier [26].

In order to consider the randomness effect of the roughness and the geometry of the real surface, the above procedure is repeated for a large number of micro-models, each one with a different distribution of asperities, but with the same maximum asperities height. The results are statistically analysed and the parameters for the constitutive equation 1 are estimated. This equation can then be used as an input in the macro-model.

An elastoplastic analysis of the contact at micro-scale was considered in Bandeira et al. [27], which can be treated as an extension of the work discussed above.

5 CONCLUSIONS

This review presented a possible methodology to take into account the effect of roughness in contact problems. This approach could be used in computational simulations of fretting wear, providing better understanding of the fretting phenomenon and more accurate wear profile predictions.

As future work, we intend to apply the discussed methodology in fretting simulations and validate the results with experimental (or literature) data. Firstly, we intend to develop a micro-scale model in which all the small features of the rough surfaces are considered. Then, after an estimation of the contact stiffness parameters, we intend to use the average normal pressure from the micro model in a macro model simulation. This would enable us to calculate the wear depth profile in a fretting wear situation considering the effect of roughness.

This homogenization technique would be a simple approach and, in the future, a more detailed analysis may be needed. If that is the case, we may also try to implement a concurrent approach, considering even nano-features of the surface and its impact on fretting wear or may be a coupled continuum to continuum model with different scales or even a coupled atomistic to continuum analysis.

6 REFERENCES

[1] J. Ding, S. B. Leen, and I. R. McColl. The effect of slip regime on fretting wear-induced stress evolution. *International Journal of Fatigue*, 26:521–531, 2004.

[2] O. Vingsbo and S. Söderberg. On fretting maps. *Wear*, 126:131–147, 1988.

[3] K. J. Kubiak, T. W. Liskiewicz, and T. G. Mathia. Surface morphology in engineering applications: Influence of roughness on sliding and wear in dry fretting. *Tribology International*, 44:1427–1432, 2011.

[4] Jacob Aboudi, S. M. Arnold, and Brett A. Bednarcyk. *Micromechanics of Composite Materials: A Generalized Multiscale Analysis Approach*. Butterworth-Heinemann, 2012.

[5] Hossein Talebi, Mohammad Silani, Stphane P. A. Bordas, Pierre Kerfriden, and Timon Rabczuk. A computational library for multiscale modeling of material failure. *Computational Mechanics*, 53:1047–1071, 2014.

[6] M. Eftekhari, S. Ardakani, and S. Mohammadi. An xfem multiscale approach for fracture analysis of carbon nanotube reinforced concrete. *Theoretical and Applied Fracture Mechanics*, 72:64–75, 2014.

[7] M. Silani, S. Ziaei-Rad, H. Talebi, and T. Rabczuk. A semi-concurrent multiscale approach for modeling damage in nanocomposites. *Theoretical and Applied Fracture Mechanics*, 74:30–38, 2014.

[8] F. Feyel and J. L. Chaboche. Fe 2 multiscale approach for modelling the elastoviscoplastic behaviour of long fibre sic/ti composite materials. *Computer methods in applied mechanics and engineering*, 183(3):309–330, 2000.

[9] Young W. Kwon, David H. Allen, and R. Talreja. *Multiscale Modeling and Simulation of Composite Materials and Structures*. Springer, 2007.

[10] M. Silani, H. Talebi, S. Ziaei-Rad, M. A. Hamouda, G. Zi, and T. Rabczuk. A three dimensional extended arlequin method for dynamic fracture. *Computational Materials Science*, 96:425–431, 2015.

[11] Pascal Aubertin, Julien Rthor, and Ren de Borst. *A Multiscale Molecular Dynamics / Extended Finite Element Method for Dynamic Fracture*. Springer, 2010.

[12] R. Guo-Wu and T. Tie-Gang. Coupling of two-dimensional atomistic and continuum models for dynamic crack. *Chinese Physics B*, 23(11):118704, 2014.

[13] V. I. Yamakov, D. H. Warner, R. J. Zamora, E. Saether, W. A. Curtin, and E. I. Glaessgen. Investigation of crack tip dislocation emission in aluminum using multiscale molecular dynamics simulation and continuum modeling. *Journal of the Mechanics and Physics of Solids*, 65:35–53, 2014.

[14] H. Talebi, M. Silani, and T. Rabczuk. Concurrent multiscale modeling of three dimensional crack and dislocation propagation. *Advances in Engineering Software*, 80:82–92, 2015.

[15] S. W. Yang, P. R. Budarapu, D. R. Mahapatra, S. Bordas, G. Zi, and T. Rabczuk. A meshless adaptive multiscale method for fracture. *Computational Materials Science*, 96:382–395, 2015.

[16] B.Q. Luan, S. Hyun, J.F. Molinari, N. Bernstein, and M. O. Robbins. Multiscale modeling of two-dimensional contacts. *Physical Review E*, 74(4):046710, 2006.

[17] G. Anciaux and J. F. Molinari. Contact mechanics at the nanoscale, a 3d multiscale approach. *International journal for numerical methods in engineering*, 79(9):1041–1067, 2009.

[18] G. Anciaux and J. F. Molinari. Sliding of rough surfaces and energy dissipation with a 3d multiscale approach. *International Journal for Numerical Methods in Engineering*, 83(8-9):1255–1271, 2010.

[19] L. Gallego, B. Fulleringer, S. Deyber, and D. Nlias. Multiscale computation of fretting wear at the blade/disk interface. *Tribology International*, 43:708–718, 2010.

[20] Benjamin D. Leonard, Arnab Ghosh, Farshid Sadeghi, Sachin Shinde, and Marc Mittelbach. Third body modeling in fretting using the combined finite-discrete element method. *International Journal of Solids and Structures*, 51: 1375–1389, 2014.

[21] S. Stupkiewicz, M. J. Lewandowski, and J. Lengiewicz. Micromechanical analysis of friction anisotropy in rough elastic contacts. *International Journal of Solids and Structures*, 51(23):3931–3943, 2014.

[22] P. Wriggers and J. Reinelt. Multi-scale approach for frictional contact of elastomers on rough rigid surfaces. *Computer Methods in Applied Mechanics and Engineering*, 198(21):1996–2008, 2009.

[23] I. Temizer and P. Wriggers. Inelastic analysis of granular interfaces via computational contact homogenization. *International Journal for Numerical Methods in Engineering*, 84(8):883–915, 2010.

[24] I. Temizer. Computational homogenization of soft matter friction: Isogeometric framework and elastic boundary layers. *International Journal for Numerical Methods in Engineering*, 100(13):953–981, 2014.

[25] J. F. Jerier and J. F. Molinari. Normal contact between rough surfaces by the discrete element method. *Tribology International*, 47:1–8, 2012.

[26] P. Wriggers and J. Nettingsmeier. *Computational Contact Mechanics - CISM courses and lectures*. Springer, 2007.

[27] A. A. Bandeira, P. Wriggers, and P. M. Pimenta. Numerical derivation of contact mechanics interface laws using a finite element approach for large 3d deformation. *International Journal for numerical methods in Engineering*, 59(2): 173–195, 2004.

International Journal of Fracture Fatigue and Wear, Volume 3
Proceedings of the 4th International Conference On
Fracture Fatigue and Wear, pp. 279-286, 2015

BRAKING CONDITION OPTIMISATION OF SEMI-METALLIC EPOXIDISED NATURAL RUBBER ALUMINA NANOPARTICLES (ENRAN) FRICTION MATERIALS PRODUCED BY RADIATION CURING VIA RESPONSE SURFACE METHODOLOGY

A. Almaslow[1], M. J. Ghazali[1], C. T. Ratnam[2], R. J. Talib[3], and C. H. Azhari[1]

[1]Department of Mechanical & Materials Engineering, University Kebangsaan Malaysia, 43600 UKM, Bangi, Selangor, Malaysia
[2]Radiation Processing Technology Division, Malaysian Nuclear Agency, 43000 Bangi, Selangor, Malaysia
[3]AMREC, SIRIM Bhd, Lot 34, Jalan Hi-Tech 2/4, Kulim Hi-Tech Park, 09000 Kulim, Malaysia

Abstract: This study investigates braking conditions of semi-metallic epoxidised natural rubber alumina nanoparticle friction materials produced by radiation curing consisting of steel wool as the main fibre reinforcement, graphite as the lubricant, epoxidised natural rubber with 50 mol% epoxidation (ENR 50)-alumina nanoparticles (ENRAN) composites as the friction modifier, and benzoxazine resin as the binder. The braking conditions of applied load (200, 500, and 800 N) and braking time (3, 7.5, and 12 minutes) with tribological properties using a two-level factorial experimental design was optimised. The applied load and braking time were found to have significant effects on the friction characteristics, the specific wear rates and surface roughness. The resulting morphological changes of the material surface after braking were observed using Scanning Electron Microscopy (SEM). Friction coefficient was highest on the onset of braking due to ploughing of harder asperities and enlargement of the contact area. Thereafter, friction slowly decreased with braking time due to shearing of the peak asperities and formation of a friction film. Wear volume increased with increasing applied load as well as braking time. This was due to the microstructural changes and the decomposition of organic materials. Sample under the applied load of 200N and 4.12 minutes of braking time showed the best tribological properties.

Keywords: Friction Materials, Applied Loads, Braking Times, Wear, Friction Coefficient

1 INTRODUCTION

Brake friction materials have a crucial effect on the braking system. These materials produce thermal energy from the kinetic energy of a moving car using friction during braking. Brake friction materials are required to have a constant coefficient of friction under different operating conditions, such as applied loads, temperature, speed, mode of braking, and also in dry and wet conditions to preserve the braking features of a vehicle. It is also necessary to have several suitable attributes including resistance to heat, water, and oil, have low wear rate and high thermal stability, exhibit low noise, and should not have any harmful effects on the brake disc. However, having all of these features at the same time is not achievable and some features have to be compromised to have the other features. Each friction material formulation technically has its own unique frictional and wear-resistant attributes.

A friction material is a heterogeneous material having four main components: reinforcing fibers, binders, fillers, and frictional additives. Each element posses its own function, such as improving friction properties at low and high temperature, improve strength and rigidity, extend life, decrease porosity, and decrease noise. Any modification in the element type or proportion of the elements in the formulation will result in changes in the physical, mechanical, and chemical characteristics of brake friction materials [1-4]. Earlier scholars have demonstrated that no simple relationship exists between the friction and wear properties of a friction material with physical and mechanical properties [5-7]. Therefore, new formulations are subjected to series of tests to determine its friction and wear properties.

In this study, response surface methodology using a Two-level factorial design experiment central composite design was used to optimise braking conditions of semi-metallic epoxidised natural rubber alumina nanoparticles (ENRAN) friction materials produced by radiation curing.

2 EXPERIMENTAL METHOD

2.1 Preparation of Friction Materials

The composite obtained from Haake Rheomix Polydrive R 600/610 were then compression molded into 6-mm thick sheets under a pressure of 14.7 MPa at 150 ^{0}C for 30 min. The sheets were immediately cooled between two plates of a cold press at 25 ^{0}C.

The molded samples were irradiated in air at room temperature using 3.0 MeV Cockroft Walton type electron beam accelerator (model NHV EPS-3000) at a dose of 150 kGy. The acceleration energy, beam current and dose rate were 3 MeV, 5 mA and 50 kGy per pass.

2.2 Testing

Test samples for friction and wear test were cut from the brake pad backing plate with dimension of 25mm×25mm×6mm according to MS 474 PART10:2003 using LINK CHASE machine. Each sample was subjected to different braking times (3, 7.5 and 12 minutes) and applied loads (200, 500 and 800 N) according to Design Expert for optimising the braking conditions. Five samples were subjected for each types of braking conditions and the average friction result was calculated from the recorded result. In addition; the surface roughness was measured using a Taylor–Hobson (Surtronic 3+) roughness tester and repeated five times for each specimen after the friction test.

The weight of the pads for each sample was taken before and after the each test, and the wear was determined with the mass method following the standard of TSE 555 (1992) and calculated using the following equation:

$$w = (1/2\pi R) \times (1/f_m\, n) \times ((m_1-m_2)/\rho)) \qquad (1)$$

Where w is the specific wear rate (cm^3/Nm), R is the distance between the centre of specimen and the centre of the rotating disk, m_1 and m_2 are the average weight of specimen before and after the test (g), ρ is the density of the brake lining (g/cm^3), and f_m is the average friction force (N).

2.3 Fractional factorial

Design experiments were carried out using Design Expert software (Statistics Made Easy, version 6.0.10, Stat-Ease, Inc., Minneapolis, MN). Response surface methodology [8] was used to show the statistical significance of the applied load (X1) and braking time (X2). A 2^3 factorial design for two independent variables with three replications at the centre points leading to a total of 7 sets of experiments was carried out in this study (Table 1). The low, middle, and high levels of each variable are given in Table 2. From the experimental findings, the effects of the independent variables on friction coefficient, specific wear rate and roughness were studied using a half-normal graph and an effect list. A factorial model was chosen and analysed with analysis of variance (ANOVA) to determine the adequacy of the model. Each response was modelled on the two parameters using the following equation:

$$Yi = b_0 + b_1X1 + b_2X2 + b_{12}X1X2 \qquad (2)$$

where Yi is the theoretical response function [19].

Table 1 2^3Factorial Design Matrix Used for the Screening Factors.

Sample	Applied Load (N) X1	Braking Time (min) X2	Friction Coefficient (µ) Y1	Specific Wear Rate (cm^3/N.m) Y2	Ra (µm) Y5
S1	-1	-1	0.6	0.204	4.54
S2	+1	-1	0.455	0.412	2.21
S3	-1	+1	0.545	0.213	1.65
S4	+1	-1	0.34	0.455	2.12
S5	0	0	0.47	0.37	4.54
S6	0	0	0.44	0.4	4.54
S7	0	0	0.455	0.34	4.54

Table 2 Levels of Variables Chosen for Trial

Independent parameters	Range (coded level)		
	Low (-1)	Central point (0)	High (+1)
Applied Load (X1) N	200	500	800
Braking Time (X2) Min	3	7.5	12

3 RESULTS AND DISCUSSION

The sum of square (SS), coefficients of the models, and probability (P) value for the two factorial designs are presented in Table 3. The P-value represents the probability of error involved in accepting the observed value [9]. A P-value smaller than 0.05 indicates that the model is significant, with 95% degree of confidence. Applied load and braking time and their interactions exhibited significant effect on the friction coefficient, wear rates and surface roughness. The final models in coded parameters, with the exception of the insignificant terms (with P > 0.05), are given in Eqs. (3)– (5), respectively.

$$Y1 = 4.90E\text{-}01 - 8.8E\text{-}02\ X1 - 4.2E\text{-}02\ X2 \quad (3)$$

$$Y2 = 3.20E\text{-}01 + 1.10E\text{-}01\ X1 \quad (4)$$

$$Y3 = 2.63 - 4.70E\text{-}01\ X1 - 7.5E\text{-}01\ X2 + 7.0E\text{-}01\ X1X2 \quad (5)$$

Table 3 Full 2^2 factorials design (Coefficient are given in coded unit).

	SS	Coefficient	P value
(a) For Y1			
X1	3.1E-02	– 8.8E-02	0.0064
X2	7.2E-03	– 4.2E-02	0.0037
(b) For Y2			
X1	5.1E-02	1.10E-01	0.001
(c) For Y3			
X1	8.6E-01	– 4.70E-01	< 0.0001
X2	2.22	– 7.5E-01	< 0.0001
X1X2	1.96	7.0E-01	< 0.0001

3.1 Effects on friction coefficient

The half-normal graph shown in Figure 1 illustrates the significant main and interaction effects on the friction coefficient of optimised sample. This is also stated in equation (3) where we can see that both applied load and braking time are the significant negative effect influencing the friction coefficient of SMFC.

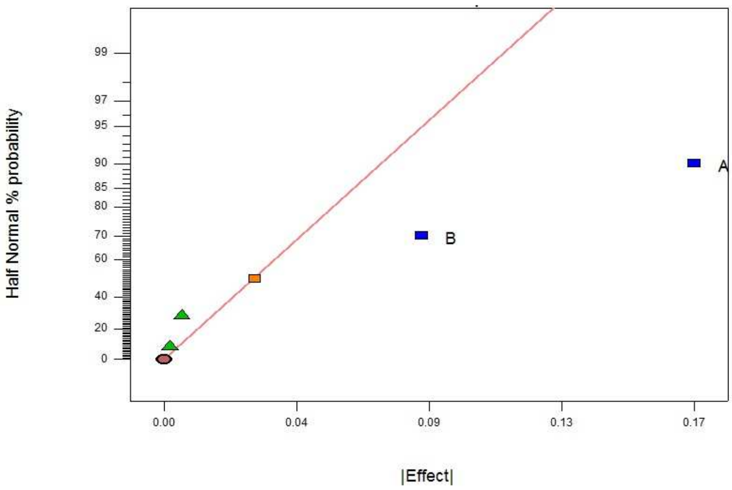

Fig. 1 Half-normal graph used for selecting the main effects for friction coefficient.

The brake is pressed against a rotating drum during braking, resulting in resistance to motion. The friction coefficient reaches its maximum value with the increase in braking time. It then decreases with braking time and reaches a steady state thereafter (Figure 2). The increase in the friction coefficient at the beginning of braking is due to the hard asperities being ploughed into the wear surfaces and also to the enlargement of the contact area.

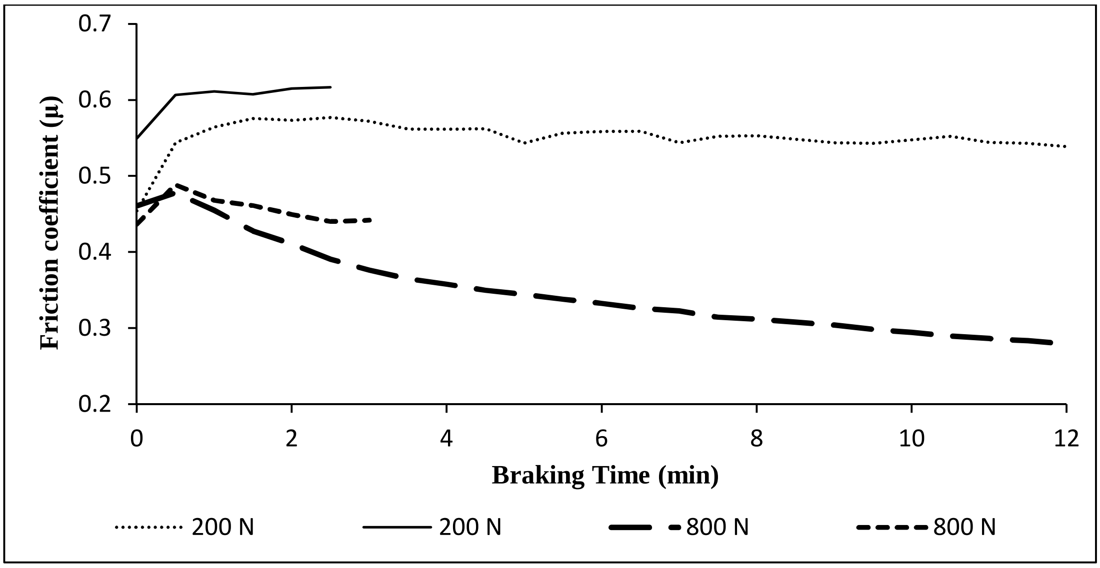

Fig. 2 Graph of friction coefficient versus braking time.

At the early stage of braking, the hard asperities are ploughed into the wear surfaces as shown in Figure 3 to Figure 7. The ensuing reduction in the friction coefficient of the samples at the load of 800 N may be explained by (i) the shearing of the peak asperities, (ii) formation of a friction film, and (iii) decomposition of the organic compounds. Figure 4 and Figure 5 show the detachment of wear fragments from the wear surface at the early stage of braking. The asperities are sheared and blunted during sliding with subsequent braking. Figure 7 shows the transfer layer or friction film formed on the worn surface. The formation of the transfer layer is the result of wear debris compaction between the brake pad and the disc surface [10].

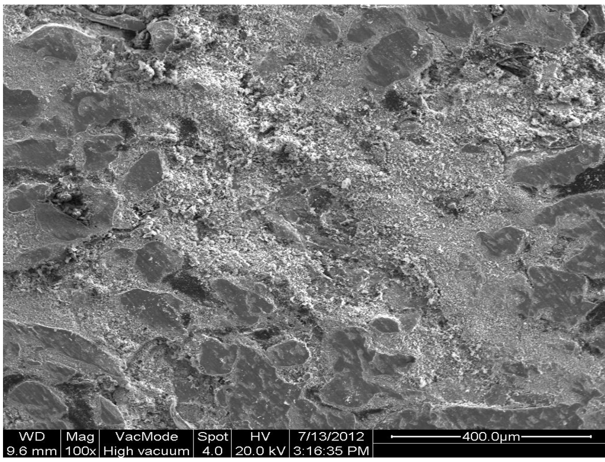

Fig. 3 The peak asperities ploughing on the surface of the sample. Load 200 N, time 3 minutes.

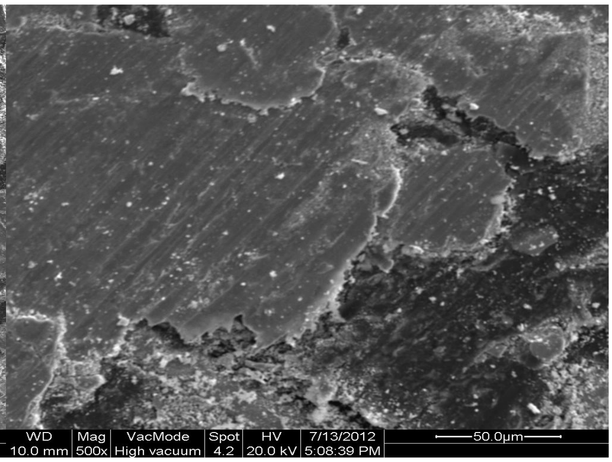

Fig. 4 The peak asperities ploughing on the surface of the sample. Load 800 N, time 3 minutes.

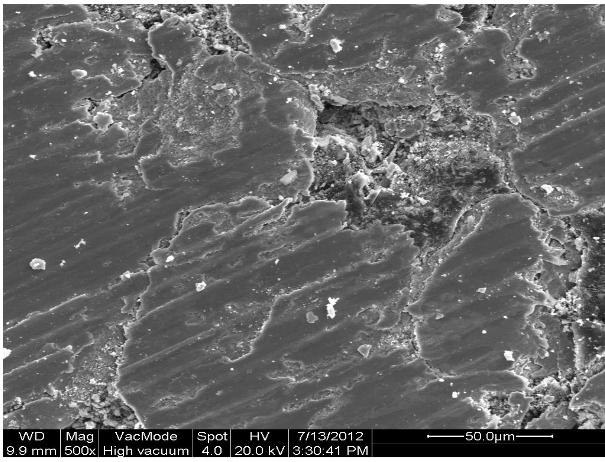

Fig. 5 The peak asperities ploughing on the surface of the sample. Load 500 N, time 7.5 minutes.

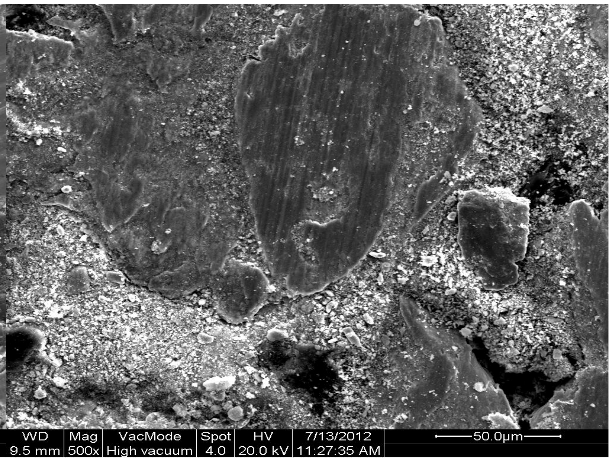

Fig. 6 The peak asperities ploughing on the surface of the sample. Load 200 N, time 12 minutes.

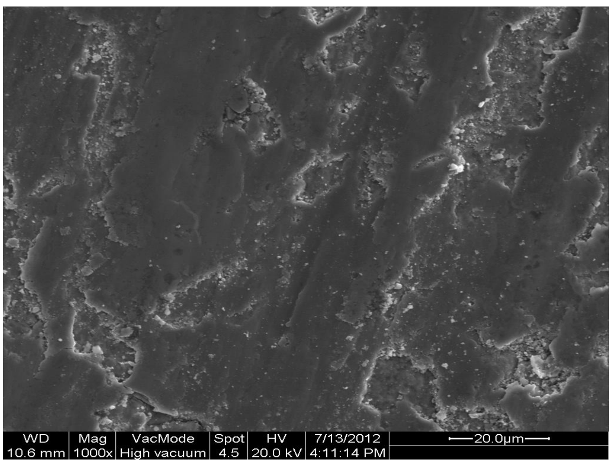

Fig. 7 The peak asperities ploughing on the surface of the sample. Load 800 N, time 12 minutes.

3.2 Effects on specific wear rate

Wear depends on several factors, such as temperature, speed, applied load, nature of interactions between the two friction surfaces in contact, and the environment [11]. Figure 8 shows applied load is effective factor on specific wear rate. This was also found in Equation (4).

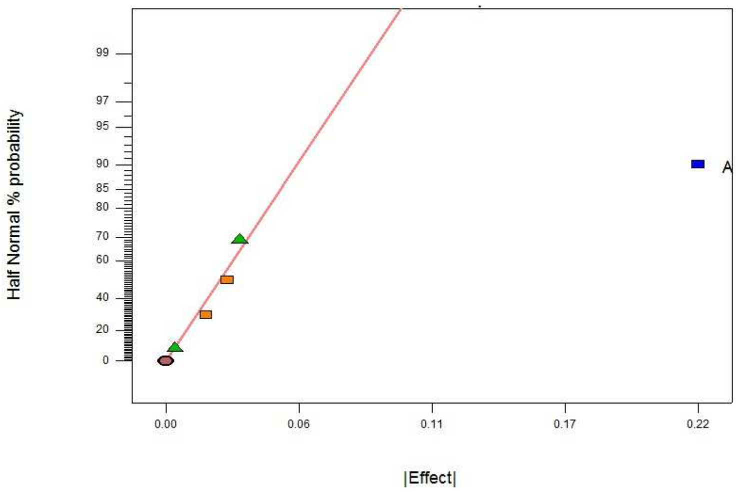

Fig. 8 Half-normal graph used for selecting the main effects for specific wear rate of optimised sample (A: applied load, B: braking time).

Figure 9 with the corresponding Eq. (4) shows the influence of varying the applied load from 200 to 800 N with 3 to 12 min of braking time on friction coefficient values of the composites in a 3D graph. Specific wear rate increases when the applied load increased. This occurrence is due to the following phenomena: (i) decomposition of organic materials, and (ii) microstructural changes. The degradation of the organic components in the brake pad composition increases with surface temperature, resulting in the reduction in composition bonding and structure integrity. This process is known to increase the rate of surface failure, thereby increasing wear rate as observed in the present study. This finding is similar to the results reported by other researchers [12 & 13].

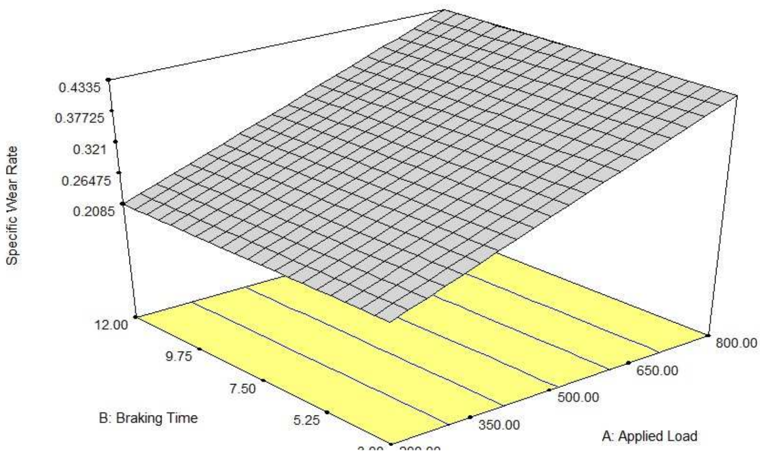

Fig. 9 Effects of applied load and braking time on specific wear rate.

3.3 EFFECTS ON SURFACE ROUGHNESS (R_a)

The half-normal graph shown in Figure 10 illustrates the significant main and interaction effects on the average surface roughness (R_a) of the optimised SMFC. This is also stated in equation (5). Figure 10 shows applied load and braking time are effective factors on surface roughness.

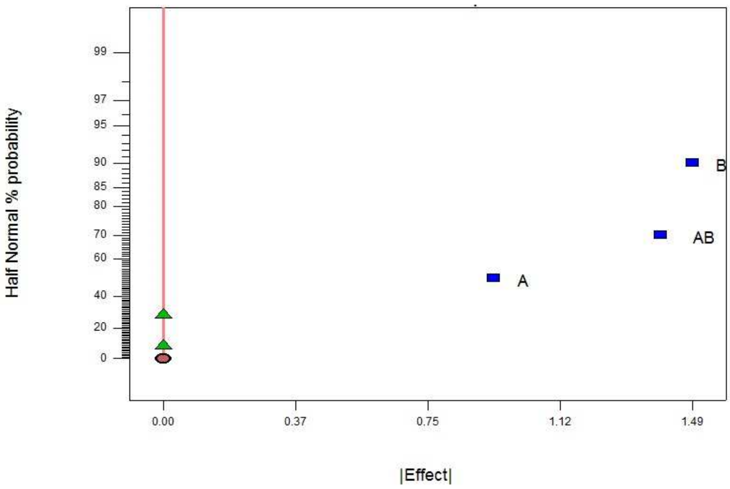

Fig. 10 Half-normal graph used for selecting the main effects for average surface roughness (R_a) of optimised sample (A: applied load, B: braking time).

Increasing the applied load and braking time would decrease the surface roughness of the SMFC as shown in Figure 11. The reduction in the surface roughness of the sample may be explained by the shearing of the peak asperities. The asperities are sheared and blunted during sliding with subsequent braking [10].

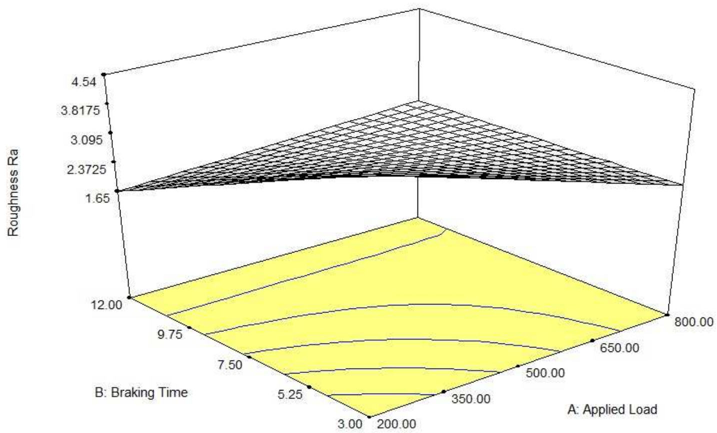

Fig. 11 The effect of applied load and braking time on the surface roughness.

4 CONCLUSION

- Friction coefficient was highest on the onset of braking due to ploughing of harder asperities and enlargement of the contact area. Thereafter, friction slowly decreased with braking time due to shearing of the peak asperities and formation of a friction film.
- Wear volume increased with increasing applied load as well as braking time. This was due to the transition of wear mechanism, in correspondence with the microstructural changes and the decomposition of organic materials.
- Increasing the applied load and braking time would decrease the surface roughness of the SMFC. The reduction in the surface roughness of the sample may be explained by the shearing of the peak asperities.

- Sample under the applied load of 200 N and 4.12 min of braking time showed the best tribological properties.

5 ACKNOWLEDGMENTS

We would like to thank the Universiti Kebangsaan Malaysia (Bangi, Selangor, Malaysia) for funding this research (UKM-GUP-2011-040). We also sincerely thank the Malaysian Nuclear Agency (Bangi, Selangor, Malaysia) and Advanced Materials Research Center, SIRIM Bhd (Kulim, Kedah, Malaysia) for providing the expertise, equipment, and technical assistance during our experiments.

6 REFERENCES

[1] Lu, Y. 2006. A combinatorial approach for automotive friction materials: Effects of ingredients on friction performance. *Composites Science and Technology* **66**: 591-598.

[2] Cho, M. H., Kim, S. J., Kim, D. & Jang, Ho. 2005, Effects of ingredients on tribological characteristics of a brake lining: an experimental case study. *Wear* **258**: 1682-1687.

[3] Mutlu, I., Eldogan, O. and Findik, F. 2006. Tribological properties of some phenolic composites suggested for automotive brakes. *Tribology International* **39**: 317-325.

[4] Jang, H., Ko, K., Kim, S.J., Basch, R.H. & Fash, J.W. 2004. The effect of metal fibers on the friction performance of automotive brake friction materials. *Wear* **256**: 406-414.

[5] Tanaka, K.; Ueda, S. & Noguchi, N. 1973. Fundamental studies on the brake friction of resin based friction materials. *Wear* **23**: 349-365.

[6] Todorovic, J., Duboka, C. & Arsenic, Z. 1987. Modelling of the Tribological Properties of Friction Materials Used in Motor Vehicle Brakes. *Mechanical Engineering Publications*: 911-916.

[7] Hsu, S. M., Shen, M. C. & Ruff, A. W. 1997. Wear prediction for metals. *Tribology International* **30**: 377-383.

[8] Myers RH, Montgomery DC. Response Surface Methodology, Process and Product Optimization Using Designed Experiments, 2nd ed; Wiley: New York, 2002.

[9] Jarrah NA. Studying the influence of process parameters on the catalytic carbon nanofibers formation using factorial design. Chem Eng J 2009; 151: 367–71.

[10] Filip, P., Weiss, Z. & Rafaja, D. 2002. On friction layer formation in polymer matrix composite materials for brake applications. *Wear* **252**: 189-198.

[11]Talib, R. J., Ramlan, K. & Azhari, C. H. 2001.Wear of friction materials for passenger cars. *Solid State Science and Technology* **10**(1, 2): 292-298.

[12] Zhigao, X. & Xiaofei, L. 1990. A Research for the Friction and Wear Properties of a Metal-fiber-reinforced Composite Material. *Mechanical Properties Materials Design. International Symposia Proceedings*.

[13] Talib, R. J. 1995. Investigation on the Wear Mechanism of Brake Pads. MSc Thesis.

International Journal of Fracture Fatigue and Wear, Volume 3
Proceedings of the 4th International Conference On
Fracture Fatigue and Wear, pp. 287-292, 2015

SOLUTION TO FATIGUE LIFE PREDICTION NEAR YIELD POINT BASED ON DAMAGE ACCUMULATION METHOD

J. Huo[1], X. You[1], G. Wang[2] and K. Cheng[2]

[1]School of Aerospace Engineering, Tsinghua University, Beijing 100084, China
[2]Shanghai Turbine Works Co. Ltd. Shanghai Electric, Shanghai, 200240, China

Abstract: Near yield point, SN method and EN method predict quite different results. Manson and Hirschberg proposed a formula, known as the EN method, based on the superposition of strain amplitude. Under the same fatigue life, they add plastic strain with elastic strain to get the relation between total strain and fatigue life. Such superposition is not inconsistent with the constitutive law. Moreover, it contradicts the negative correlation between strain amplitude and fatigue life, so that EN curve will generate significant error near yield point. A new solution is proposed, based on damage accumulation concept, which can solve these weaknesses, and better fit the experiment data.

Keywords: EN method; strain amplitude; yield point; damage accumulation; fatigue life.

1 INTRODUCTION

As the kernel component in a power producing system [1], the turbine transforms the steam's heat into kinetic energy, and its efficiency is greatly affected by the area of exhaust. It has become a general trend to improve the turbine capacity. Consequently, the blade height will be increased [2], which will cause the maximum stress in the critical section to approach the yield point during the steady-state phase [1]. Therefore, the precise determination of the fatigue life near the yield point seems to be an urgent problem in blade engineering.SN method refers to the equation found by Basquin [3] from the stress-controlled fatigue test in 1910, which indicates that the stress amplitudes and fatigue life, also known as number of reversals to failure, presents linear relation in log-log coordinates.

In 1954, Manson [4] and Coffin [5] respectively proposed fatigue life prediction method based on plastic strain amplitude parameter ($\varepsilon_{a,pl}$). For metals, plastic strain amplitude $\varepsilon_{a,pl}$ and fatigue $2N_f$ also shows better linear relation in log-log coordinates. Manson and Hirschberg proposed that a metal's resistance to total strain cycling can be obtained by a superposition of the elastic strain and plastic strain resistance as follows [6-8], but there are some problems for the expression.

$$\varepsilon_{a,total} = \frac{\sigma_f^{'}}{E}(2N)^b + \varepsilon_f^{'}(2N)^c. \tag{1}$$

2 THE CONTRADICTION OF EN AND SN METHOD NEAR YIELD POINT

We conduct two groups of tests, stress-controlled test under relatively low load condition, and strain-controlled test. After the test, we fit the test data in log-log coordinates to get the SN and EN expressions [9]. Then we extend the SN and EN curves in log-log coordinates to yield. At the yield point, the stress is 959MPa and strain is 0.48%, but we get two different fatigue lives for this point. This big discrepancy is unacceptable, and is shown in Fig. 1.

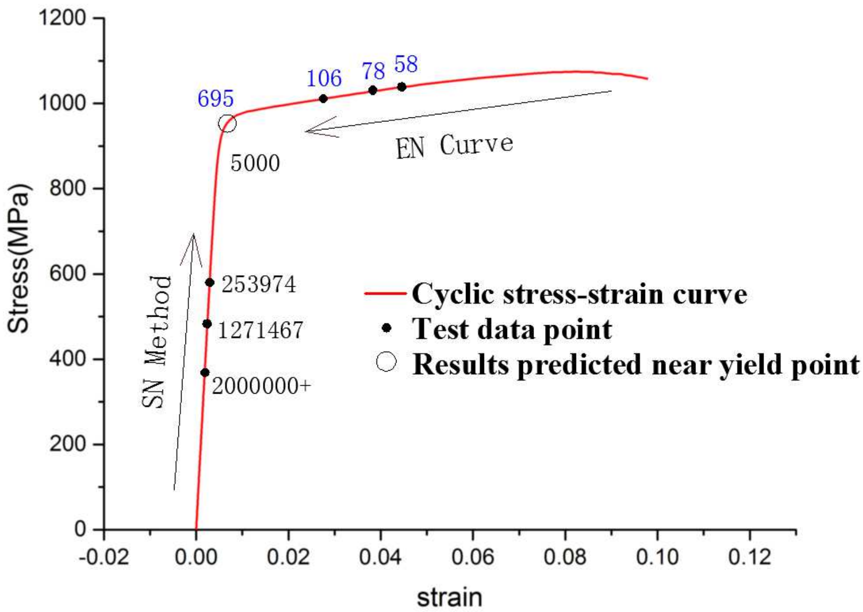

Fig. 1 The conflict of EN and SN methods near yield point

It is difficult to decide which method is reliable and reasonable for practical engineering problems. Therefore, we analyze this big discrepancy, and attempt to find a reliable method for fatigue life prediction near yield point.

3 THE WEAKNESS OF EN METHOD NEAR YIELD POINT

Based on the superposition of elastic strain and plastic strain, Manson and Hirschberg proposed the EN method. By superposing the Coffin-Manson and Basquin expressions in log-log coordinates, we can get the EN expression. Considering the same fatigue life, this superposition leads to a point which doesn't actually exist on the EN curve.

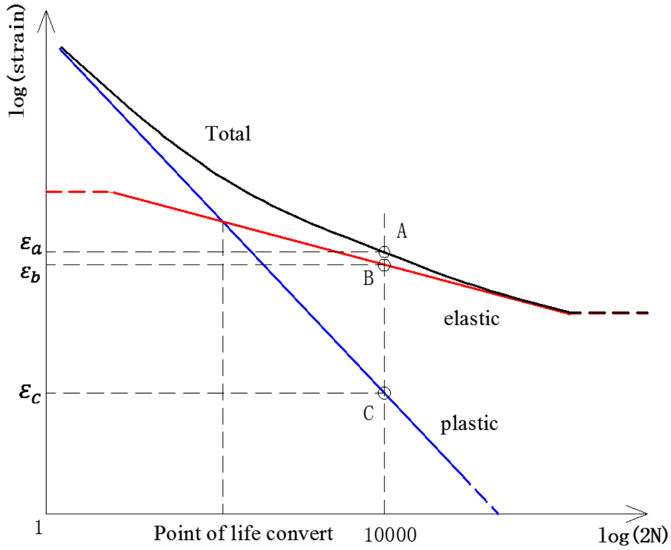

Fig. 2 The illustration of superimposition for EN method

In log-log coordinates, Basquin expression is also called elastic line, the red line in Fig. 2, and Coffin-Manson expression is also called plastic line, the blue line in Fig. 2. EN curve is also called total strain line, the black line shown in Fig. 2. For example, in Fig. 2 point C and point B can be added to obtain point A. The fatigue life calculation of point A depends on elastic strain of point B and plastic strain of point C, but this dependence is not reliable, because point A truly includes elastic strain that is σ_a/E , and plastic strain that is $\left(\varepsilon_a - \sigma_a/E\right)$. Total strain ε_a includes the elastic strain and plastic strain, and they should conform to Constitutive Law. Moreover, the fatigue life and strain amplitude have a negative correlation. This superposition of strain amplitudes doesn't consider this, because after superposition the strain increases but the fatigue life doesn't decrease. This causes the result of EN method to be higher than real fatigue life.

4 NEW APPROACH FOR LIFE PREDICTION NEAR YIELD POINT

In order to solve the aforementioned problems and give a better expression of total strain amplitude and fatigue, we divide the whole strain range into three stages.

When $\varepsilon_f \le \varepsilon \le \varepsilon_{e,\lim}$, stress state of material is near yield point. In order to solve this conflict, we propose a method based on damage accumulation. When fatigue life is 2N, we suppose that the damage is $D = \left(2N\right)^{-1}$ for each cycle, and when the total damage reaches 1, the material fails [10, 11]. We assume that damage caused by elastic strain plus damage caused by plastic strain equals total damage caused by total strain, shown as follows.

$$\mathrm{D}_t = \mathrm{D}_e + \mathrm{D}_p . \tag{2}$$

For example, introducing $\varepsilon_{a,el}$ into Basquin expression to get fatigue life $2N_e$, so the damage caused by elastic strain is $\left(2N_e\right)^{-1}$. By the same way, introducing $\varepsilon_{a,el}$ into the Coffin-Manson expression we get the fatigue life $2N_p$, such that the damage caused by plastic strain is $\left(2N_p\right)^{-1}$. Therefore, total damage is $\left(2N_t\right)^{-1}=\left(2N_e\right)^{-1}+\left(2N_p\right)^{-1}$ for each cycle, which is considered as the damage caused by the total strain [12].

The damage caused by elastic strain for each cycle can be expressed as follows:

$$\mathrm{D}_e=(2N_e)^{-1}=\left(\varepsilon_{a,el}\frac{E}{\sigma_f^{'}}\right)^{-\frac{1}{b}}. \tag{3}$$

The damage caused by plastic strain for each cycle can be expressed as follows:

$$\mathrm{D}_p=(2N_p)^{-1}=\left(\frac{\varepsilon_{\mathrm{ap}}}{\varepsilon_f^{'}}\right)^{-\frac{1}{c}}. \tag{4}$$

For the total strain, the total damage equals $\mathrm{D}_t=\mathrm{D}_e+\mathrm{D}_p$, which can be expressed as follows

$$\mathrm{D}_t=\left(\varepsilon_{a,el}\frac{E}{\sigma_f^{'}}\right)^{-\frac{1}{b}}+\left(\frac{\varepsilon_{\mathrm{ap}}}{\varepsilon_f^{'}}\right)^{-\frac{1}{c}}. \tag{5}$$

We obtain an expression for total strain amplitude and fatigue life can be written as follows

$$2N_f=\left[\left(\frac{E}{\sigma_f'}\right)^{-\frac{1}{b}}\left(\frac{\sigma_a}{E}\right)^{-\frac{1}{b}}+\left(\frac{1}{\varepsilon_f'}\right)^{-\frac{1}{c}}\left(\varepsilon_{a,t}-\frac{\sigma_a}{E}\right)^{-\frac{1}{c}}\right]^{-1}. \tag{6}$$

We call the proposed Eq. 6 Damage Accumulation Method.

5 EXPERIMENTAL RESULTS AND VERIFICATION

In order to find the effectiveness and precision of Eq. 6 for fatigue life prediction near yield point, we conduct a group of strain-controlled tests over 5 strain levels. The strain amplitude is from 0.5% to 1% and R=-1, and 3 samples are tested for each strain level. Then the test data is compared with the results of different methods near yield point, which is shown in Fig. 3.

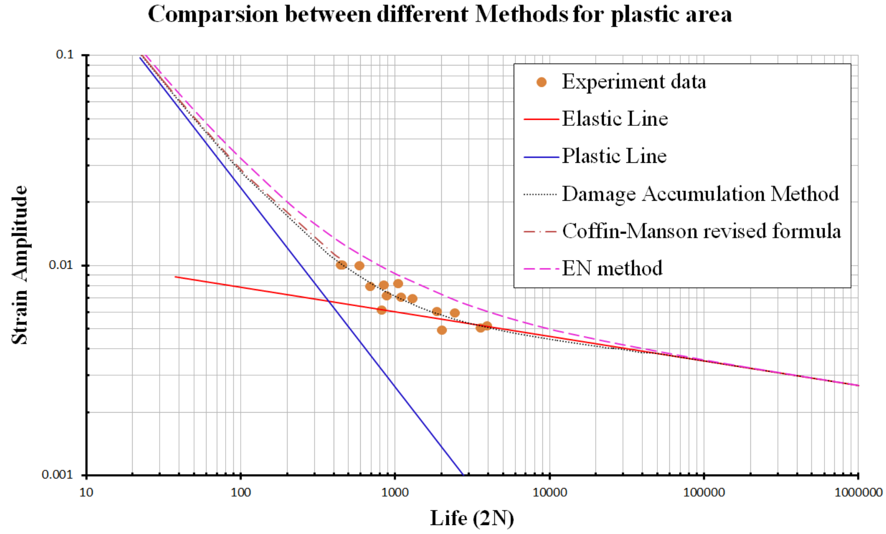

Fig. 3 Verification of different methods near yield point

Observing Fig. 3, it is easy to find that the Damage Accumulation Method can fit the test data much better than EN method, and the results predicted by EN method are relatively higher than the test data near yield point.

6 CONCLUSIONS

This paper proposes a new method, based on the damage accumulation concept, to enhance the prediction of fatigue life near yield point. After conducting some relevant experiments, it is obvious to find that the Damage Accumulation Method can better fit the test data. This paper also compares the precision of three different methods: Damage Accumulation Method, Revised Coffin-Manson Formula and EN method, and find that they show little difference in the plastic stage, and Damage Accumulation Method is effective from elastic stage to plastic stage.

7 NOMENCLATURE

R : Stress ratio or strain ratio

σ_u : Ultimate strength , the Maximum stress value of the material

σ_a : Stress amplitude, $(\sigma_{\max} - \sigma_{\min})/2$

$\sigma_f^{'}$: Fatigue strength coefficient, for Basquin expression

b : Strength exponent, for Basquin expression

S_f : Stress for endurance limit. When stress less than S_f , there is no fatigue failure

ε_f : Strain as infinite fatigue life $\varepsilon_f = S_f / E$. when $\varepsilon < \varepsilon_f$, $2N_f \to \infty$

$\varepsilon_f^{'}$: Fatigue ductility coefficient, for Coffin-Manson expression

c : Fatigue ductility exponent, for Coffin-Manson expression

$\varepsilon_{e,\lim}$: The corresponding strain for elastic limit. when $\varepsilon > \varepsilon_{e,\lim}$, plastic strain start to exist

$\varepsilon_{e,u}$: The corresponding strain for ultimate strength, $\varepsilon_{e,u} = \sigma_u / E$

ε_{con} : Strain of the Point of life convert

$\varepsilon_{a,t}$: Total strain amplitude $\left(\varepsilon_{\max} - \varepsilon_{\min}\right)/2$

$\varepsilon_{a,pl}$: Plastic strain amplitude

$\varepsilon_{a,el}$: Elastic strain amplitude

8 ACKNOWLEDGEMENTS

This work was supported by Shanghai Turbine Works Co. Ltd.

9 REFERENCES

[1] Poursaeidi E, Arhani M R M. Failure investigation of an auxiliary steam turbine. ENGINEERING FAILURE ANALYSIS. 2010, 17(6): 1328-1336.
[2] Xie Y H, Zhang D. Optimal design for damper of long blade in steam turbine based on dynamic analysis. NEW YORK:AMER SOC MECHANICAL ENGINEERS, 2007, 245-253.
[3] Basquin O. The exponential law of endurance tests. 1910(10): 625-630.
[4] Manson SS. Fatigue: a complex subject—some simple approximations. Exp Mech J Soc Exp Stress Anal. 1965, 7(5): 193-226.
[5] Coffin L F. CITATION CLASSIC - A STUDY OF THE EFFECTS OF CYCLIC THERMAL-STRESSES ON A DUCTILE METAL. CURRENT CONTENTS/ENGINEERING TECHNOLOGY & APPLIED SCIENCES. 1982(8): 22.
[6] Manson Ss H. Fatigue behavior in strain cycling in the low-and intermediate -cycle range. In fatigue, An interdisciplinary Approach, J.J. Burke, N. L. Reed and V. Weiss(Eds). Syracuse University Press, 1964: 133.
[7] Coffin L F, Tavernelli J F. THE CYCLIC STRAINING AND FATIGUE OF METALS. TRANSACTIONS OF THE AMERICAN INSTITUTE OF MINING AND METALLURGICAL ENGINEERS. 1959, 215(5): 794-807.
[8] Manson Ss H. FATIGUE - AN INTERDISCIPLINARY APPROACH. JOURNAL OF METALS. 1966, 18(5): 548.
[9] Ong J H. An evaluation of existing methods for the prediction of axial fatigue life from tensile data. International Journal of Fatigue. 1993, 15(1): 13-19.
[10] Golos K, Ellyin F. GENERALIZATION OF CUMULATIVE DAMAGE CRITERION TO MULTILEVEL CYCLIC LOADING. THEORETICAL AND APPLIED FRACTURE MECHANICS. 1987, 7(3): 169-176.
[11] Miner M A. Cumulative damage in fatigue. Journal of Applied Mechanics. 1945, A(67): 159-164.
[12] Chaboche J L, Lesne P M. A NON-LINEAR CONTINUOUS FATIGUE DAMAGE MODEL. FATIGUE & FRACTURE OF ENGINEERING MATERIALS & STRUCTURES. 1988, 11(1): 1-17.

International Journal of Fracture Fatigue and Wear, Volume 3
Proceedings of the 4th International Conference On
Fracture Fatigue and Wear, pp. 293-303, 2015

ADVANCED METHODS FOR EXPERIMENTAL CHARACTERIZATION OF RUBBER FAILURE WITH RESPECT TO REAL LOADING CONDITIONS OF RUBBER PRODUCTS IN THE FIELD

R. Stoček[1,2], O. Kratina[2,3], E. Euchler[4], R. Kipscholl[5]

[1]PRL Polymer Research Lab., s.r.o., Zlín, Czech Republic
[2]Centre of Polymer Systems, University Institute, Tomas Bata University in Zlín, Zlín, Czech Rep.
[3]Tomas Bata University Zlín, Faculty of Technology, Department of Polymer Engineering, Zlín, Czech Rep.
[4]Chemnitz University of Technology, Professorship of Plastics Engineering, Chemnitz, Germany
[5]Coesfeld GmbH & Co. KG, Dortmund, Germany

Abstract: Rubber is a widely used material in industry because of the unique viscoelastic behavior of rubber matrix. In practice, rubber products are exposed to complex dynamic loading conditions caused due to various effects. Technical rubber products are mainly used for high dynamic applications especially in automotive as well as mechanical engineering, thus the factors affecting the rubber matrix behavior mostly are the dynamic inertia, profile of a contact surface of solid parts affecting rubber as well as influence of ozone concentration, solar radiation, different temperature etc. These complex processes constitute the initiation of micro-cracks, which is the fundamental fracture element of rubber-matrix responsible for various failure mechanisms of rubber products. Tests and determination of rubber product failure in the real usage are time and money consuming and thus effective testing methods in laboratory condition are highly appreciated. This work focuses on advanced methods for experimental characterization of complex rubber fracture mechanisms and parameters in the laboratory with respect to real loading conditions of rubber products in the field. Thus the rubber product failure in the real usage could be predicted. Finally, we have introduced theoretical approaches, new methods and testing equipment for characterization of complex rubber failure process from the phase of the crack initiation, its propagation up to the total rupture of rubber matrix.

Keywords: Rubber, Failure, Fracture, Crack, Testing Equipment

1. INTRODUCTION

Rubber materials exhibit excellent damping behaviour and thereby the rubber has a broad range of applications in industry and technique. Rubber is mainly used in the applications where high dynamically loading is applied on the product, such as conveyor belts, transmission belts, shock absorbers, tires, hoses etc. In practice, these rubber parts are exposed to complex dynamic loading conditions. The exemplary rubber failure process is demonstrated in the Figure 1 using two important high dynamically loaded technique of rubber parts, which are conveyor belt (left) and tire (right). In the case of conveyor belts used in mining minerals, the part mostly affected is the outer tread of the belt, which is dynamically loaded and exposed to the dynamic impact of hard and sharp edged materials and their stochastic movements on the tread. This effects lead to substantial abrasion of the rubber surface. In the case of the other example of important high dynamically loaded rubber products, tires, the most affected part is the tire tread, because of its dynamic contact with the rough surface of the road or with the asperity of a hard terrain. Real dynamic loading conditions of tires are based on the load at the region provided by the tire footprint (abrasion) or the region with a high level of asperity (sharp stones, roots of trees, as well as thrusting parts) over which the tire rolls. The dynamic load of the affected zone is applied in milliseconds, after that the contact is enable and the zone relaxes until the next contact (impact from specific asperity, revolution of tire/ belt, etc.) occurs.

It is well known that high dynamic loading conditions have an extreme effect on crack initiation, its propagation, wear properties and in the end on the failure of product. These processes lead to a degradation of the mechanical performance of the rubber matrix. The unstable state of rubber products is caused particularly by micro-crack initiation, and its propagation could have fatal consequences caused by its final collapse. Generally, the fracture process starts due to micro-crack initiation, whereby the reason for its mechanical initiation is a foreign object (specific asperity, minerals, profile of the road surface, etc.), which has a considerable higher E-modulus in comparison with the rubber product tread.

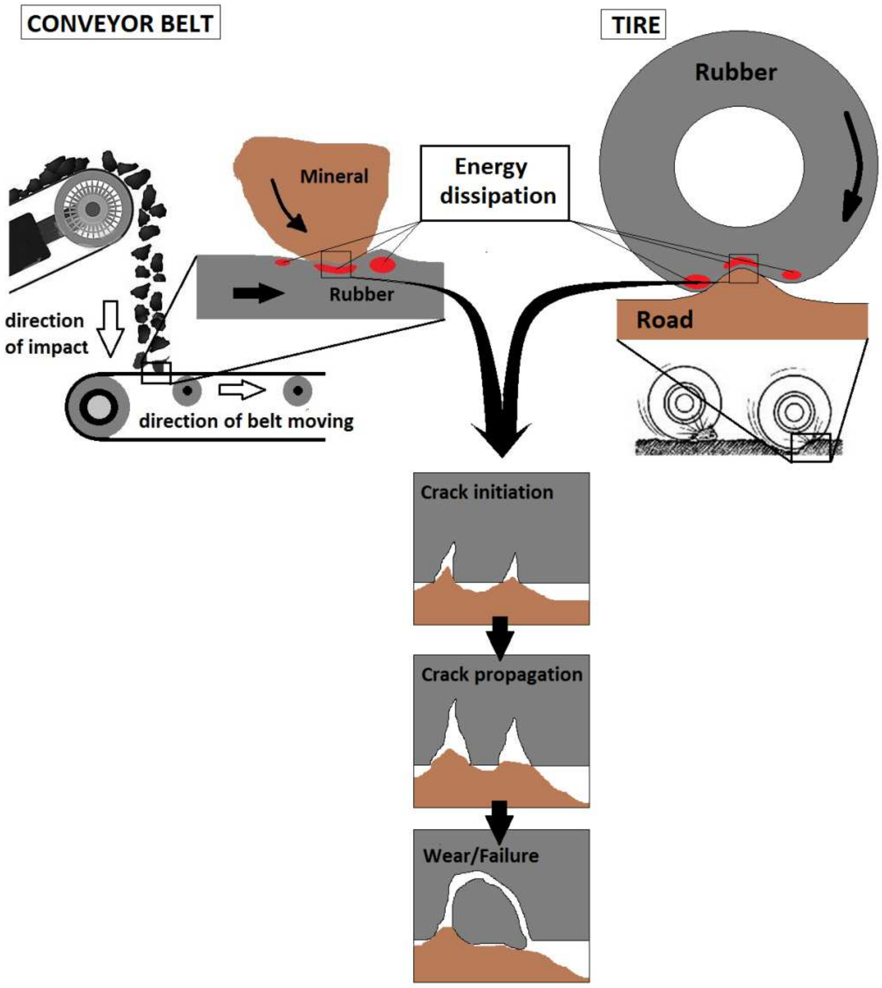

Fig. 1 Rubber failure process at dynamic loading conditions in the field shown in the case of conveyor belt (left) and tire tread (right).

The main fracture processes (crack nucleation respective initiation, propagation, wear) leading to total failure of real rubber products can be seen in the Figure 1. The tests of the real rubber products in common conditions would be the most suitable analysis for description of their mechanics as well as fracture behavior, whereas these tests are time and money consuming. In the case of characterization of conveyor belt's top layer, the stochastic loading conditions are necessary to be applied, whereas tire rolling is characterized due to Gause-pulse loading, where the width of the pulse is given by tire outer radius, running speed and tire footprint. With respect to the critical loading of these rubber products in the field, very hard parameters of lab test are necessary to be applied, whereas the pulse wide is lower than 20 milisecond followed by relaxation time dependent upon loading frequency. Thus an effective testing methodology as well as methods in laboratory condition, which will experimentally describe the complex rubber failure process from the crack initiation up to rubber matrix failure in dependence on various dynamic loading conditions as well as different stress conditions are highly appreciated.
The understanding of the crack initiation and its propagation in rubber matrix in the dependence on the complex stress loading conditions is a subject of high scientific interest, therefore its description will improve the safety, higher durability and life service of the tire as well. The observation of the crack nucleation so far is not realisable from the experimental point of view. Because of the main factor influencing the fracture properties is the crack nucleation respective initiation on micro-scale an experimental method, which would be able to determine the nucleation parameters with respect to the mechanics of rubber matrix, is highly appreciated to be developed.

As soon as the crack is initiated, its propagation starts due to applied loading conditions. The observation of a crack growth is commonly realized with using of standard testing method, whereas only quasi-static loading conditions can be applied during the analysis. In the case of requirement on cyclic fatigue loading conditions, the advanced methods and testing equipment is necessary to be used. The Tear Analyzer produced by Co. Coesfeld GmbH & Co is a unique testing equipment, which is industrially used for quantitative description of dynamic crack propagation under real loading conditions. The measuring methodology has been established by Eisele et al [1], whereas the advanced development for characterisation of fracture properties independent on test specimen geometry has been elaborated by Stoček et al.

The final phase of rubber failure is defined due to accelerated unstable crack growth up to the total rupture. From the theoretical point of view this phase of the process can be simulated due to high dynamic impact with simultaneously chipping of the rubber matrix. Thus a complete separation induced by unstable crack growth has been attained. This process can be denoted as a dynamic abrasion or wear process respectively. Beatty & Miksch [2] both developed laboratory equipment and established a measuring methodology for the characterization of abrasion in accordance with the practical use of rubber products. This procedure is based on a simulation of impacted rolling test specimens, and Beatty and Miksch termed this process the “chip and cut” effect (CC). This publication [2] was used by Maňas et al. [3] as a basis for designing new testing equipment, enabling in the first place the test parameters to be varied. However these both methods are based only on qualitative measurement. Because of the very high acceleration of crack growth in the very final rupture phase, there is necessary to be used an instrumented measuring method, which is able to precisely observe the fracture parameters. The advanced analysis with respect to the experimental simulation of the real loading conditions of rubber product has been introduced by Stoček et al [4], whereas this method was based on not instrumented testing equipment. This work firstly demonstrated relationship between crack propagation and total rupture of rubber matrix due to dynamic wear process.

Therefore this work deals with description of newly developed as well as industrially used advanced lab methods for experimental characterization of rubber failure with respect to real loading conditions of rubber products in the field based on different phase of fracture process and varied stress conditions of rubber test specimen. We concentrated our work on a demonstration of complex view on fracture process in practice with using of lab methods. Thus a characterization of fracture behavior with respect to real loading conditions of rubber product in the field could be firstly simulated and realized in laboratory.

2. THEORETICAL BACKGROUND

2.1 Energy fracture criterion dependent on test specimen geometry

An important quantity for fracture mechanical investigations is the tearing energy T, i.e. the energy released per unit area of crack surface growth. It was first introduced by Griffith [5] for metallic materials and Rivlin & Thomas [6] formulated the tearing energy for elastomers. It proposes that the strain energy release rate is the controlling parameter for crack growth and it is mathematically defined as,

$$T = -(\delta W / \delta A). \tag{1}$$

Where, T is tearing energy, W is the elastic strain energy, A is the interfacial area of crack and partial derivative denotes that no external work is done on the system.

In the language of geometry they defined the tearing energy for rubber material in Single Edge Notched Tensile (SENT) test specimen as well as in pure-shear test specimens. The more details are given in the work by Ghosh et al [7] as well as by Stoček et al [8-9].

2.2 Energy fracture criterion independent on test specimen geometry

Energy balance can be evaluated from both, the experimental and the numerical side. Experimental characterization is related to the evaluation of energy taken from loading and unloading curves, whereas numerical evaluation can be either taken from loading and unloading curves or by determining of energy J-Integral [10]:

$$J_k = \int_R (w n_k + \sigma_{ji} n_j \frac{\partial u_i}{\partial x_k}) ds \,. \tag{2}$$

Where, w is the strain elastic energy density, n is the outer normal unit vector of R, σ is the stress tensor, u is the displacement vector and s is the element length.

The path independent of the J-integral allows an integration path, taken sufficiently far from the crack tip and thus the fracture parameters calculated with using J-integral are independent on the direction of the crack propagation [10]. The commonly using of the on- or off-line calculation of fracture parameters at the fatigue dynamic fracture tests are not state-of the-art, therefore the tearing energy criterion is commonly used for the fatigue dynamic fracture analysis.

2.3 Fracture mechanical treatment of failure

With respect to the tearing energy criterion, Gent, Lindley and Thomas [11] determined experimentally an approach for description of the crack growth rate in dependence of the tearing energy. This approach represents a theoretical basis for description of fracture behaviour of rubber matrix with respect to the real loading conditions of rubber product by using in the field.

The typical relationship for a rubber material on a double logarithmic plot is shown in the Figure 2. Lake & Lindley [12] divided this plot into 4 regions which characterise different tear behaviours. The crack growth rate *da/dn* depends on the tearing energy T in each of the 4 regions in a characteristic manner:

- crack nucleation,
- initiation,
- propagation,
- total rupture.

As long as the value of tearing energy T is lower than T_0, crack growth proceeds at a constant rate r and the crack growth is independent of the dynamical loading, but affected by the environmental attack.

$$T \le T_0 \;\Rightarrow\; \frac{da}{dn} = r \tag{3}$$

In the region II between T_0 and T_1 one finds a transition between a nucleation and propagation of crack growth:

$$T_0 \le T \le T_I \;\Rightarrow\; \frac{da}{dn} = A(T - T_0) + r \tag{4}$$

After this transient state the crack propagates in a region between T_1 and T_C of stable crack growth which is denoted as region III. The relationship between fatigue crack growth rate *da/dn* and tearing energy describe Paris & Erdogan [13] with the power-law:

$$T_I \le T < T_C \;\Rightarrow\; \frac{da}{dn} = b \cdot \Delta T^{m} \,, \tag{5}$$

where b and m are material constants.

In the last region IV the tearing energy T_C proceeds to the unstable state of crack growth and the crack growth rate will become essentially infinite.

$$T \approx T_C \;\Rightarrow\; \frac{da}{dn} = \infty \tag{6}$$

The region III was utilised as the region that corresponds most closely to crack growth rates found in the engineering fatigue range.

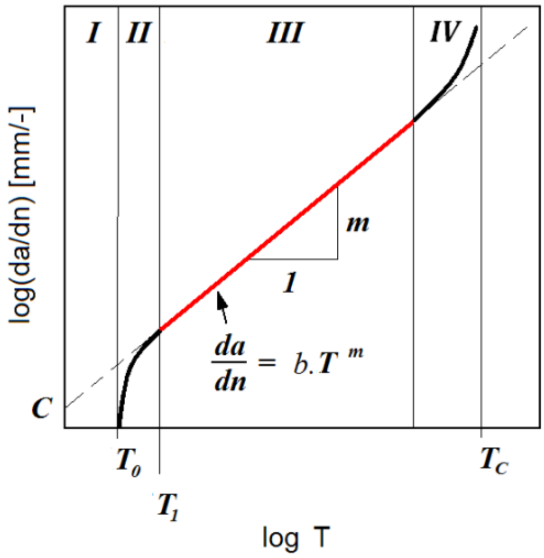

Fig. 2 Double logarithmic plot of crack growth rate da/dn vs. tearing energy T for rubber material [12].

3. EXPERIMENTAL METHODS FOR COMPLEX RUBBER FAILURE CHARACTERISATION IN LABORATORY

The most important question from the rubber producing industry as well as from the scientific domain is: *"Which methods could lead to the exact prediction and quantitative characterization of complex fracture behaviours of rubber matrix respective product with respect to the real loading conditions of rubber product in the field?"* Thus an efficient approach characterizing the complete mechanical behaviour of rubber matrix/product during all of fracture phases is necessary to be based on the development of new interconnected lab methods and equipments for physical material testing of rubber matrix with respect to the real loading conditions of rubber product. The schematic visualization of the interconnection between the complex fracture methodology is shown in the Figure 3.

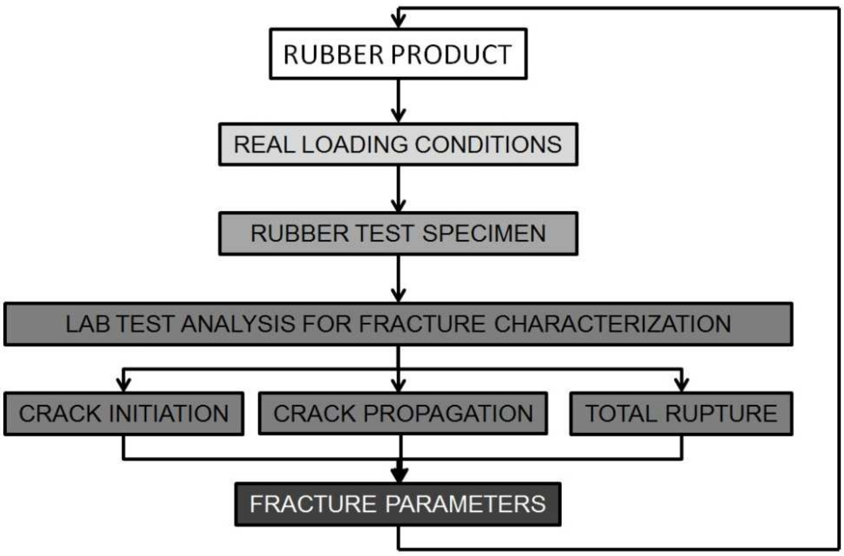

Fig. 3 Visualization of interconnection between complex fracture methodology.

There will be introduced three new methods and newly developed full instrumented testing equipment, which are able to simulate real loading conditions of rubber product by using of rubber test specimen, in the next chapters.

3.1 Analysis of crack initiation

The new fracture experimental approach to rubber resistance against crack initiation is based on newly developed instrumental testing equipment, which is measuring the resistance of prestressed rubber test specimen against cutting by sharp objects. Thus the effect of crack tip sharpness given by the geometry of cutting object can be used as simulation of crack initiation, whereas an special razor blade as cutting object has been implemented. The fracture mechanic's phenomena of crack initiation is based on the definition of test specimen geometry with respect to the geometry ratio L_0/W (length/width), whereas the common SENT- (single edge notched tensile) as well as pure-shear test specimens can be used for the observation. A schematic function diagram of the testing principle as well as the visualisation of the real testing machine is shown in Figure 4. The electrically driven testing equipment is able to apply the varied loading waveform working statically as well as dynamically. The test specimen holds in a clamping system is pre-stressed by given force or waveform in a strain direction X. The tip of razor blade actuates the loaded test specimen in an orthogonal direction Y to the main stress. During the actuating of the test specimen due to razor blade, the cutting force is observed respectively energy is calculated and simultaneously the tearing energy, which is responsible for the rubber test specimen fracture process in dependence on cutting depth is evaluated according to Rivlin & Thomas energy criterion [6].

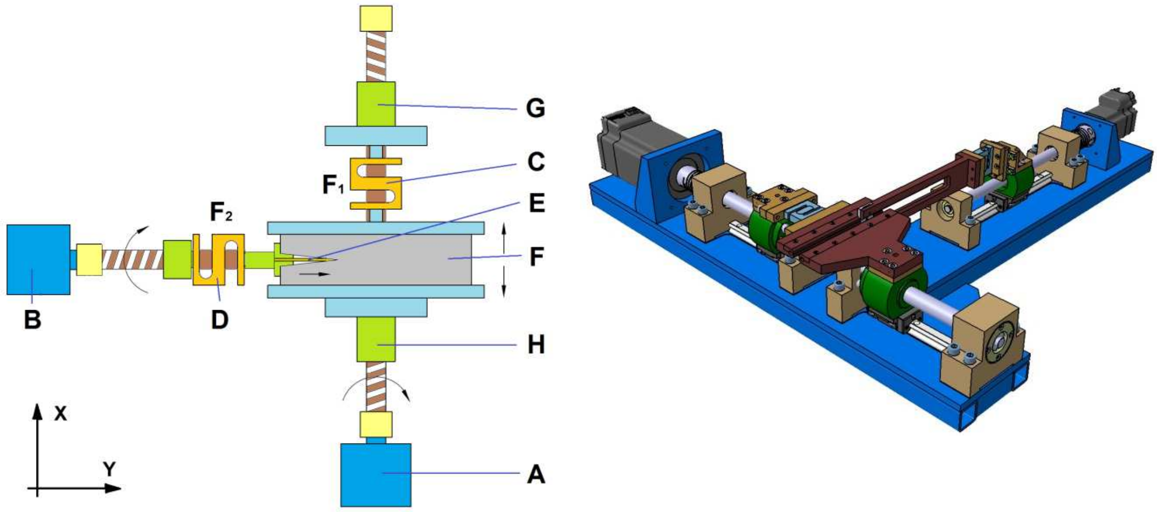

Fig. 4 Functional principle and visualization of testing equipment for experimental characterization of crack initiation, where: A – actuator of the axis X; B – actuator of the axis Y; C – loading cell of the axis X; D – loading cell of the axis Y; E – razor blade; F – test specimen; G – upper clamping system of test specimen; H – bottom clamping system of test specimen.

The results, shown in the Figure 5, demonstrate the Power law behavior of fatigue crack growth rate vs. tearing energy for the dynamically loaded pure-shear test specimens based on NR (natural rubber) without any reinforcement at simultaneously cutting with different razor blades. The loading conditions of test specimen have been defined due to sinusoidal waveform, frequency 1 Hz, room temperature, variation of the strain 5 and 8 %. For very sharp crack, there were found very higher crack growth rate due to lower radius of razor blade, whereas the higher radius of razor blade decrease the crack growth rate. The crack growth exponent m (see equation 4) slightly increases in dependence on decrease of razor blade radius. Thus the phase of crack initiation can be evaluated.

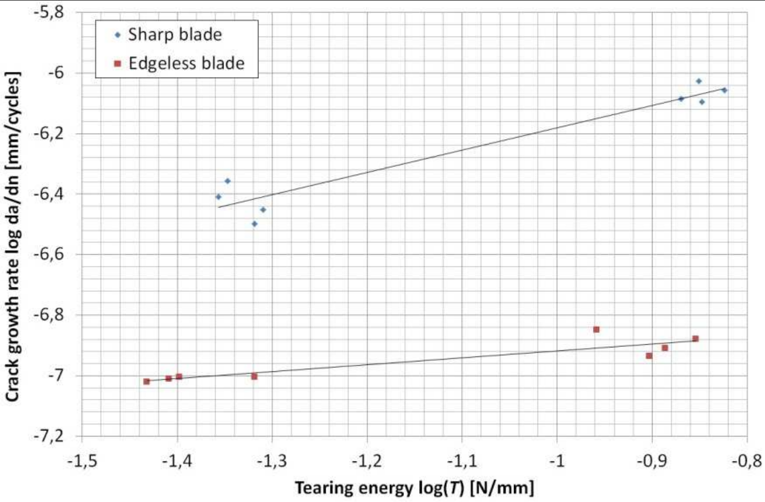

Fig. 5 Power law behavior of fatigue crack growth rate vs. tearing energy based on dynamically loaded test specimens with simultaneously cutting by razor with sharp and edgeless blades.

3.2 Analysis of crack growth

In Figure 6 a schematic function diagram/principle shows the Tear Analyzer for investigating the fatigue crack growth of rubber independent on test specimen geometry, whereas the method based on SENT and pure-shear mode testing can be simultaneously applied. The hydraulically driven testing equipment can apply the varied loading waveform, within the frequency range 0,1 - 50 Hz on the test specimens, whereas up to 10 test specimens can simultaneously be analysed. The crack growth of each rubber specimen is on-line monitored through an optical image processing system. After the capture of the picture, the software localizes in-situ the crack position and determines the contour length. Thus the infinitesimal enlargement of crack surface area can be determined according to Rivlin & Thomas energy criterion [6].

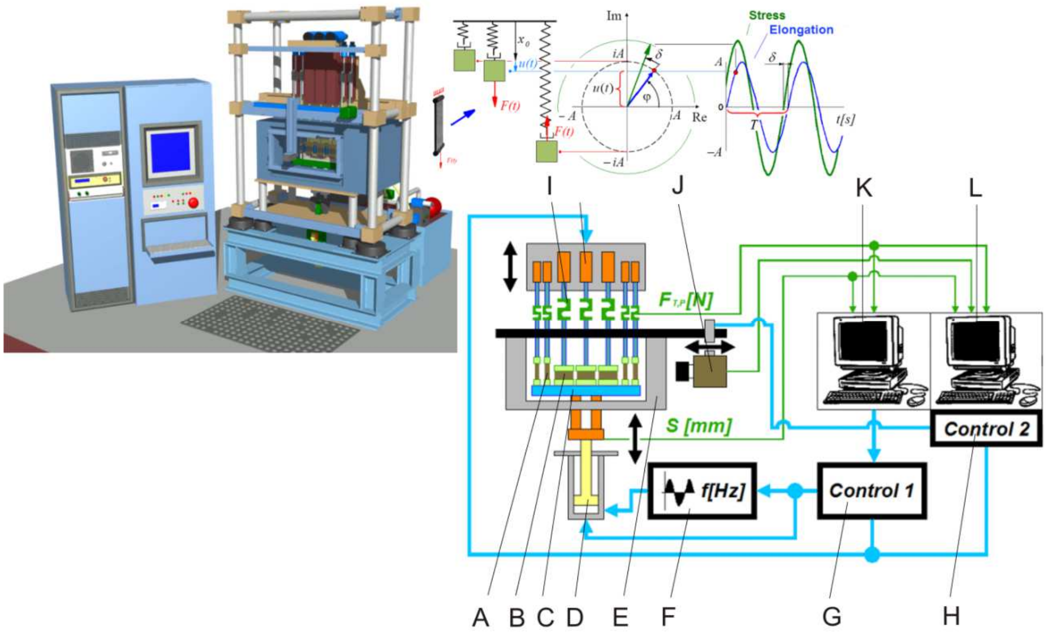

Fig. 6 Schematic and functional diagram of the tear analyzer: A-tensile test piece; B-pure-shear test piece; C-traverse; D-hydropulzer; E-isolated chamber; F-frequency generator; G-control unit 1; H-control unit 2; I-load cells; J-CCD monochrome camera; K-PC1; L-PC2.

The example of the results analysed with Tear Analyser is shown in Figure 7, where the influence of the volume of carbon black in NR on crack growth rate becomes apparent. Measurements were performed with preloading force 1N under sinusoidal loading conditions with frequency 1 Hz at room temperature. The content of carbon black type N234 has been varied from 0 up to 60 phr. We found that the crack growth rate at a given tearing energy decreases significantly with an increase in the volume of carbon black, whereas the crack growth exponent *m* (see equation 5) slightly increases with a higher amount of carbon black in rubber test specimens based on NR. The increase of tear strength independent from carbon black concentration induces the higher crack growth rate. This indicates the positive reinforcement of NR by carbon black. The comparison of the results determined in SENT as well as in pure-shear test specimens visualized in Figure 6, shows that the crack growth rate at a given tearing energy is higher in the pure-shear in comparison to the SENT test specimen, as observed in the non-reinforced and reinforced NR with a concentration of 20 phr of carbon black. The trends of the crack growth rate at the given tearing energy of NR reinforced by the concentration of 40 phr of carbon black are identical, as evaluated in SENT as well as in pure-shear test specimens.

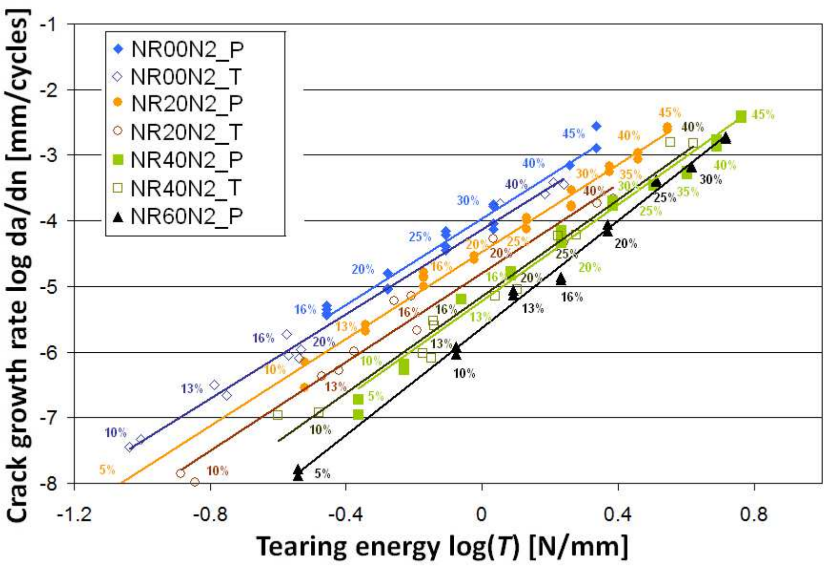

Fig. 7 Power law behavior of fatigue crack growth rate vs. tearing energy for the SENT (denoted T) as well as pure-shear (denoted P) test specimens based on carbon black filled NR [8].

3.3 Analysis of total rupture

The newly developed methodology and the measuring process of the total rupture analysis in laboratory is based on controlled impacting force or energy respectively. A schematic function diagram of the testing principle as well as the visualisation of the real testing machine is shown in Figure 8. The test equipment works automatically. It controls the user specified loading conditions in a wide field. Thus it is possible to simulate the rupture behaviour under conditions which are seen by the rubber products while operation in a precise and reproducible manner. It correlates the data to make them available for analytical purposes. The testing equipment works with a following principle: the cylindrical test specimen rotates with required velocity and simultaneously a penetrator impacts the surface of the test specimen with defined energy. The penetrator dynamically impacts the test specimen and chipps its surface. The constant presure is applied on the penetrator during exact defined time. During the measurement the normal and tangential forces as well as the depth of impact in to the test specimen and the length of chipping are measured. Thus the energies for high dynamic rupture process according to the fracture phase IV given by equation 6 firstly can be evaluated.

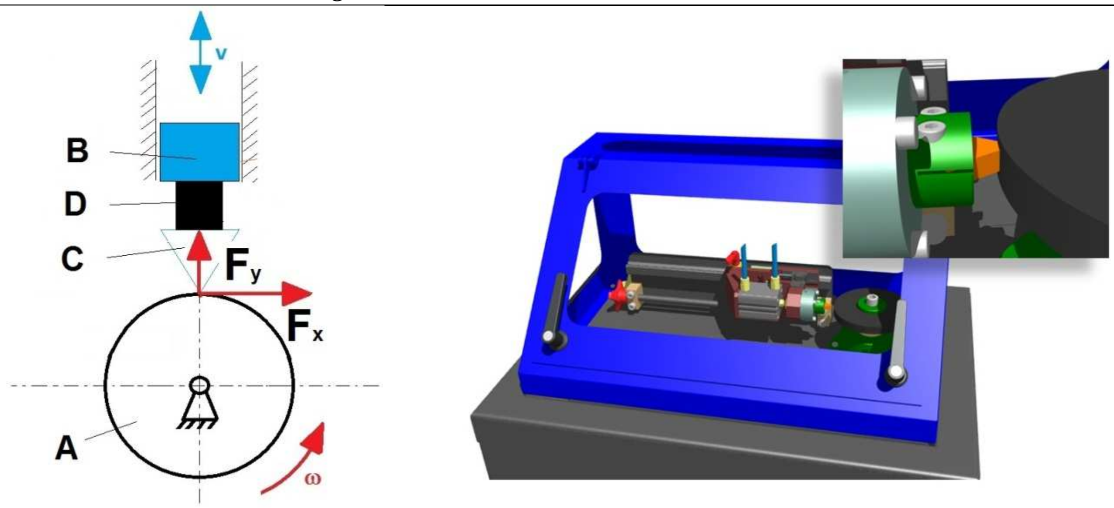

Fig. 8 Functional principle and visualization of testing equipment for experimental characterization of total rupture phenomenon.

In this exemplary study, the loading condition defined on the basis of pulse width 100 ms, frequency 1 Hz and rotation speed n_r = 100 rev.min^{-1} was used. The unique normal load was applied directly on the loading cylinder F_y = 60 N. The standard cylindrical test specimens with the diameter 55 mm and thickness 13 mm were analyzed over a broad period. During the measurement the normal and tangential forces in dependence on the depth of impacting tools into the surface of rubber test specimen have been measured. The relationships for the normal and tangential forces in dependence on the depth of impacting tools based on one loading cycle are shown in the Figure 9, whereas the both of directions F_x (left) and F_y (right) are visualized. We found that the tangential force F_x is higher in comparison to the normal force F_y, because of the additional rotation of the test specimen and chipping of the test specimen surface in the tangential direction. This indicates the high influence of test specimen rotation on the total rupture. During the reverse movement of the impacting tool, the trends decrease exponentially over the complete tool shifting. Thus the energies for high dynamic rupture process according to the fracture phase IV given by equation 6 can be evaluated in the normal and tangential directions. The final algorithm is an subject of the present work of the research team and thus its implementation to the approach describing the complex fracture rubber behavior including the phases of crack initiation, propagation and total rupture is an objective of next publication.

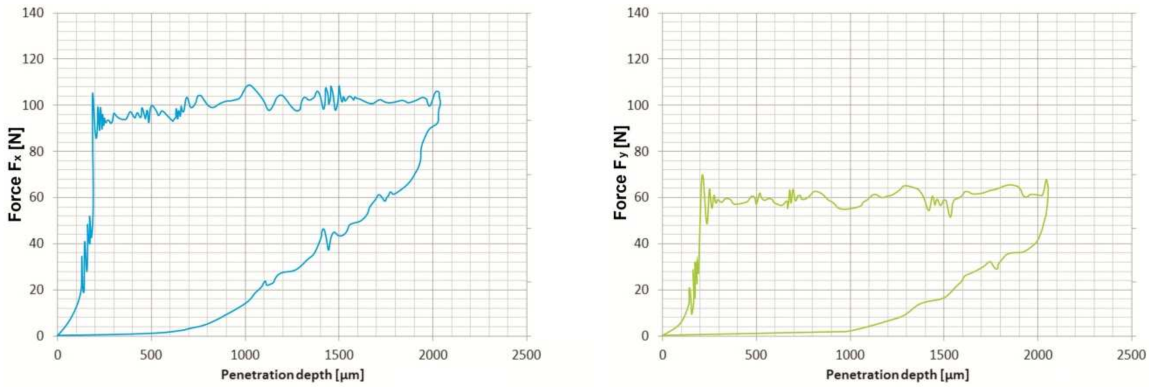

Fig. 9 Relationship between impacting force in dependence on penetration depth of rubber material in the both of directions F_x (left) and F_y (right) at the experimental measurement of total rubber rupture.

The fracture parameters evaluated due to introduced advanced testing methods and equipment demonstrate the possible observation of the complex fracture behaviour over the broad range of loading conditions or tearing energy respectively. The measuring methods are based on lab simulation of real loading conditions of rubber product in the field. Thus an experimental approach for analysis of the complete mechanical behaviour of rubber matrix during all of fracture phases could be established and firstly efficiently used. Because of the interconnection between the given experimental analyses and fracture parameters, the rubber product failure in the real usage could be predicted from the crack initiation up to the total rupture. The fully instrumented experimental methods on fracture behaviour targeted evaluated parameters give an exact basis of fracture data for future numerical characterisation and simulation of rubber product behaviour.

4. CONCLUSION

The work is concerning with the introduction of theoretical approaches, new methods and testing equipment for characterization of complex rubber failure process from the phases of the crack initiation, its propagation up to the total rupture of test specimen. This approach is based on the description of the crack growth rate in dependence on the tearing energy. We demonstrate the request of rubber industry as well as scientists for an establishment of a complex fracture methodology including experimental analyses, which could be able to evaluate the exact fracture parameters in lab conditions. We introduce three advanced interconnected lab methods and equipments for physical material testing of rubber matrix with respect to the real loading conditions of rubber product. Firstly the newly developed testing equipment for analysis of crack initiation based on measuring of the resistance of prestressed rubber test specimen against cutting by sharp objects has ben introduced. The advanced testing equipment Tear Analyzer has been demonstrated as a most efficient tool for observation of the crack propagation phase. The fracture process in the phase of total rupture has experimentally been desribed due to the newly developed measuring process and equipment based on controlled cyclically impacting force or energy respectively. Thus the complex methodology and testing equipment for evaluation of complex fracture parameters in lab conditions, which can be used for prediction of rubber product failure process, have been demonstrated.

5. ACKNOWLEDGEMENT

This article was written with support of Operational Program Research and Development for Innovations co-funded by the European Regional Development Fund (ERDF) and National Budget of Czech Republic, within the framework of project Centre of Polymer Systems (Reg. number: CZ.1.05/2.1.00/03.0111).

Furthermore, the authors are grateful for financial support for this research from the Internal Grant Agency of the TBU no. IGA/FT/2015/007, which is financed from the research at universities.

6. REFERENCES

[1] Eisele, U.; Kelbch, S.A.; Engels, H.-W.: The Tear Analyzer – A New Tool for Quantitative Measurements of the Dynamic Crack Growth of Elastomers, Kautschuk, Gummi, Kunststoffe 45, 1992, p. 1064-1069.

[2] Beatty, J.; Miksch, B.: A Laboratory Cutting and Chipping Tester for Evaluation Off-the-road and Heavy-duty Tire Treads, Rubber Chemistry and Technology, 55, 1982, p. 1531.

[3] Manas, D.; Manas, M.; Staněk, M.; Pata, V.: Wear of tyre treads, JAMME, 37, 2, 2009, p. 538-543.

[4] Stoček, R.; Kipscholl, R.; Euchler, E.; Heinrich, G.: Study of the Relationship between Fatigue Crack Growth and Dynamic Chip & Cut behavior of reinforced Rubber MaterialsKautschuk-Gummi-Kunststoffe, 67, 2014, p. 26-29.

[5] Griffith, A.A: The phenomena of rupture and flow in solids, Philos. Trans. R. Soc. Lond., Ser. A 221, 1920, p. 163.

[6] Rivlin, R.S.; Thomas, A.G.: Rupture of rubber. I. Characteristic energy for tearing, Journal of Polymer Science, 1953, 10, p. 291-318.

[7] Ghosh, P.; Stocek, R.; Gehde, M.; Mukhopadhyay, R.; Krishnakumar, R.:Investigation of fatigue crack growth characteristics of NR/BR blend based tyre tread compoundsInternational Journal of Fracture, Vol. 188, Issue 1, 2014, p. 9-21.

[8] Stoček, R.; Heinrich, G. Gehde, M., Kipscholl, R.: Analysis of Dynamic Crack Propagation in Elastomers by Simultaneous Tensile- and Pure-Shear-Mode TestingIn: W. Grellmann et al. (Eds.): Fracture Mechanics & Statistical Mech., LNACM 70, 2013, p. 269-301.

[9] Stoček, R.; Heinrich, G.; Gehde, M; Kipscholl, R.: A New Testing Concept for Determination of Dynamic Crack Propagation in Rubber Materials, Kautschuk-Gummi-Kunststoffe, 65, 2012, p. 49-53.

[10] Rice, J. R.; Rosengren, G. F.: Plane strain deformation near a crack tip in a power-law hardening material, J. Mech. Phys. Solids, Vol. 16, 1968, p. 1 - 12.

[11] Gent, A.N.; Lindley, P.B.; Thomas, A.G.: Cut Growth and Fatigue of Rubbers. I. The Relationship between Cut Growth and Fatigue, Journal of Applied Polymer Science, 1964, p. 455-466.

[12] Lake, G.J.; Lindley, P.B.: The Mechanical Fatigue Limit for Rubber, Journal of Applied Polymer Science, 9, 1965, p. 1233-1251.

[13] Paris, P.; Erdogan, F.: A critical analysis of crack propagation laws, Journal of Basic Engineering, Transactions of the American Society of Mechanical Engineers, 1963, p. 528-534.

International Journal of Fracture Fatigue and Wear, Volume 3
Proceedings of the 4th International Conference On
Fracture Fatigue and Wear, pp. 304-310, 2015

DAMAGE PREDICTION OF CARBON-EPOXY COMPOSITE LAMINATES USING FINITE ELEMENT ANALYSIS

K.M. Karumbaiah[1], R. Das[1] and S. Campbell[2]

[1]Centre for Advanced Composite Materials, Department of Mechanical Engineering, University of Auckland, Auckland, New Zealand
[2]Defence Technology Agency, Auckland, New Zealand

Abstract: Continuous growth in the use of composite materials in advanced structural applications, such as aerospace, marine, and automotive, has been observed in the past two decades. This has motivated efficient design and manufacturing of composite products so as to obtain lighter structures with higher strength, durability and life. To contribute to develop an efficient design methodology, the present research has been undertaken. The accuracy and predictive capabilities of finite element models and failure analysis of a specific composite material using the commercial finite element program ABAQUS are evaluated. A set of unidirectional carbon-epoxy composite laminates are modelled under monotonic tensile and compressive loading, and their failure is assessed using the Hashin's failure criterion. The numerical results are compared against carefully conducted experimental test data. The differences between the experimental and numerically predicted values of the maximum principle stress are used to evaluate the accuracy of the finite element models. In the unidirectional (0-degree) composite laminates after the initial ply failure, a varied damage pattern is observed with a difference of 17.7% and 10.5% under tension and compression, respectively. The unidirectional composites under transverse loading (90-degree) show a difference of 10.8% and 0.4% under tensile and compressive loading, respectively. The variations between the experimental and the modelled results are mainly due to approximating and analysing the model in its 2D behaviour, which excludes delamination. Specifically, a composite tested under compression suffers from Brooming Gage Bottom (BGB); so the variation is expected. The Hashin's damage criterion is not suitable when delamination occurs as a dominant failure mode.

Keywords: Carbon-epoxy; Composite materials; Failure criteria; Damage prediction.

1 INTRODUCTION

Specific properties, such as stiffness and strength, are high in synthetic fibre composites. These composites are incorporated in the areas, which require weight reduction and/or good load and impact bearing capacities. Since composites exhibit a complex failure behaviour, the failure behaviour has been studied by many researchers. The prediction of failure has been carried out using different failure criteria suited to for various types of composites. Since the composites are anisotropic and heterogeneous in nature, the failure may involve a combination of different failure modes, such as fibre and matrix failure, interface failure, delamination, fibre pullout and debonding, and microbucking. These failure modes result in the formation of cracks/damaged areas. Additionally, the combination of these failure modes can result in local defects, these local defects can interact with each other and lead to the failure of the composite material catastrophically.

Failure theories are broadly classified into (a) Fracture mechanics-based, (b) Strength-based, or (c) Damage-based. Damage-based analysis involves considering the composite material equivalent to progressively fracturing solids, resulting in the degradation of certain elements of the structure. The degraded elements do not carry loads, and the loads are redistributed to the adjacent components of the structure. The redistribution and degradation process are carried out till the structure has failed. The composite material is capable of accumulating a certain amount of damage before failure. Hence, damage based analysis will aid the designer to design the structure more efficiently.

Damage-based analysis is associated with the design or modelling the damage of materials for predicting the initiation and propagation of defects or cracks [1]. Damage-based analysis demonstrates the classic engineering methodology to model and simulate the complex phenomena observed in composite materials, such as the anisotropic and heterogeneous behaviour. One of the final goals is to convey the understanding of the examined phenomenon and to deliver a rational predictive tool appropriate to design [1]. In damage-based analysis, there is a need of failure criterion to predict the initiation of the local damage and to analyse its propagation and interaction with other local damage, such as matrix cracking, fibre kinking, and delamination leading to failure.

Prediction of failure in composite materials can be performed by implementing failure theories [2-6]. The failure criteria are not only for predicting the instigation of failure but in some cases it can also be used for progressive failure up to the ultimate load. The acceptance of some failure theories over others seems to be related to their ease of use. The theories, such as the maximum stress, maximum strain, Hashin's, Tsai–Wu, and Tsai–Hill failure criteria are still widely used despite their limitations. Because, they are easy to comprehend and implement in a Finite Element analysis [4, 5]. The maximum strain and maximum stress criteria are typical examples of theories that have been shown to produce poor predictions in general [7]. Failure theories that allow interaction between stress components, such as the Tsai–Hill and Tsai-Wu criteria can aid in good failure prediction [8, 9]. Different failure criteria were implemented to predict the progressive failure process of the composite laminates in a review [4]. Additionally, the residual strength, the maximum load attainable, the occurrence of First Ply Failure (FPF), and Last Ply Failure (LPF) can be predicted. The review also deliberates that a well-reported agreement of Finite Element Analysis with experiment results are observed under tensile loading. Additionally, relatively poor agreement in compressive loading has been observed. Similar inferences were made in another review of failure theories [4, 5].

One approach to predict failure that is adopted here is the damage mechanics based theory that can be implemented to degrade the elastic property of the composite owing to matrix cracking and fibre breakage. Additionally, a plasticity theory can be incorporated considering permanent deformations induced under loading [10]. Puck and Schurmann have comprehended Hashin's stress-based failure criterion [11] and recommended a failure criterion to degrade elastic parameters of the lamina subsequent to the initiation of damage [12]. Hassan and Batra have used several variables, such as material properties (specific strength, Poisson's ratio and shear modulus), loads and ply stacking sequence to analyse the performance of composite after the commencement of damage [13]. Plastic deformations of a composite material can lead to plastic damage based on the stresses induced [14]. Damage development is expressed in terms of fracture energy and stress, critical strain, and a characteristic local dimension. This allows to reduce the dependence of finite element results upon the mesh used to analyse the problem. To model the failure of composite laminates under monotonic tensile and compressive loads, the Hashin's failure criterion is used here. The damage developed at any point can be categorised by different modes of failure, such as fibre breakage and matrix cracking in tension and compression. The internal variables used to characterise different modes of failure at a point depend on the values of stresses at that point which are used in Hashin's failure criteria. The variables are expressed in terms of the strength parameters for the composite, longitudinal and transverse compressive strength, longitudinal and transverse tensile strength, and shear strengths.

The objective of this work is to develop an FE model for unidirectional composite laminates tested under monotonic loads and validate it against the experimental results provided by US Air Force Research Laboratory (AFRL) [15]. The idea was to focus on the initiation and propagation of damage in composite laminates. Since, these phenomena are well associated with the nature and interaction of the elementary degradation mechanisms. The examples presented in this paper are predominantly appropriate for an in-depth model validation, leading to the development of a well-validated tool, which could be used to design and analyse the composite structures efficiently.

2 FINITE ELEMENT MODELLING

Computational models were developed using the commercial software ABAQUS. Finite element modelling of composites can be used for, such as prediction of damage, residual strength, stiffness degradation, or failure. There are numerous methods for composite modelling, such as macroscopic modelling, microscopic modelling, mixed modelling, discrete reinforcement modelling and sub modelling. However, the most common approach used in finite element simulations of composite material is the use of conventional shell elements. A different set of the unidirectional composite laminates (0-degree and 90-degree composite laminates) were tested under monotonic loading conditions (tensile and compressive). For all the analyses conducted in this work, thin shell elements were used as the specimens were considered thin.

The model was established to characterise the failure behaviour of a balanced composite laminate. Different layup configurations were tested at ply level, and the damage modes were selected through review of previous works. Tensile and compressive failure models were applied to different composite laminates. Specifically, in the case of tensile damage, degradation of material properties could be the result of fibre matrix debonding, matrix cracking, fibre failure or a combination of these. The model, although not classifying these discrete damage types, signifies the collective effect of them through calibration from the physical tests. The simulation and subsequent validation authenticate the accuracy of the model developed.

The model implements global ply damage and failure mechanisms. Hashin's failure criterion is used to degrade when the element reaches the failure criterion limit.

Material Systems

The IM7/977-3 carbon epoxy composite materials are widely used in aerospace applications. Wide applications of this composite have resulted to analyse and predict the specific properties of the composite to obtain the long service life with minimum maintenance or repair cost. Table 1 shows the properties of the composite used to analyse the composite under monotonic tensile and compressive loads.

Table 1 Properties of unidirectional IM7/977-3 carbon/epoxy composites [15]

Property	Magnitude	Description
$E_{1T}\,(GPa)$	164.3	Modulus in fibre direction in tension
$S_{11}^{+}\,(MPa)$	2905	Maximum stress in fibre direction in tension
ε_{1T}	0.01610	Maximum strain in fibre direction in tension
v_{12}	0.3197	Poisson's ratio in fibre direction in tension
$E_{2T}\,(GPa)$	8.977	Modulus in 90-degree direction in tension
$S_{22}^{+}\,(MPa)$	44.4	Maximum stress in 90-degree direction in tension
ε_{2T}	0.00499	Maximum strain in 90-degree direction in tension
v_{21}	0.0175	Poisson's ratio in 90-degree direction in tension
$E_{1C}\,(GPa)$	137.4	Modulus in fibre direction in compression
$S_{11}^{-}\,(MPa)$	1274	Maximum stress in 0-degree direction in compression
$E_{2C}\,(GPa)$	8.694	Modulus in 90-degree fibre direction in compression
$S_{22}^{-}\,(MPa)$	247.6	Maximum stress in 90-degree direction in compression
$G_{12}\,(GPa)$	4.880	Shear modulus calculated from ±45-degree tension test
$\alpha 1$ (/°C)	0.01e-06	Coefficient of thermal expansion in fibre direction [16]
$\alpha 2 = \alpha 3$ (/°C)	32.73-06	Coefficient of thermal expansion in transverse direction [16]

Failure theory

Hashin [17] proposed a three-dimensional failure criterion for unidirectional fibre reinforced composites. The criteria were established in terms of quadratic stress polynomials that are formulated in terms of the transversely isotropic invariants of the applied average stress state. The four failure modes taken into account are tensile fibre failure, compressive fibre failure, tensile matrix failure, and compressive matrix failure.

The Hashin's formulations include two user-specified parameters, α and S_{23}; where α is a user-specified coefficient that determines the contribution of the longitudinal shear stress to fibre tensile failure ($0.0 \le \alpha \le 1.0$), S_{23} is the transverse shear strength of the composite material. During modelling, the value of α is set to be unity based on the Hashin's model proposed in 1980 [11], and the value of S_{23} was extracted from the literature [16]. The accuracy and predictive capability of the Hashin's failure criterion have been evaluated in this work under monotonic tensile and compressive loading, and the damage behaviour of the composite laminates is analysed.

Convergence study

A mesh convergence study was undertaken to determine the suitable mesh size required to produce a converged stress-strain behaviour and failure patterns. The set criteria was a maximum difference of 5% between two successively refined meshes. The mesh convergence study was carried out in two different layup configurations, unidirectional composite laminates loaded in the fibre direction under tension and unidirectional composite laminates loaded in the transverse direction under compression.

Under constant displacement tensile loading in a unidirectional composite (0-degree), a difference of 4.2% in the maximum principal stress can be observed between two FE models with mesh sizes of 0.5 and 0.25

mm (Fig. 1a). For the 0-degree composite loaded compressively, the difference was 4.6% between the models with mesh sizes of 0.5 and 0.25 mm (Fig. 1b). The coarser model of mesh size of 0.5 mm was chosen over the finer model with 0.25 mm mesh size, because the difference in results was below 5% and selecting the coarser mesh saves computational time.

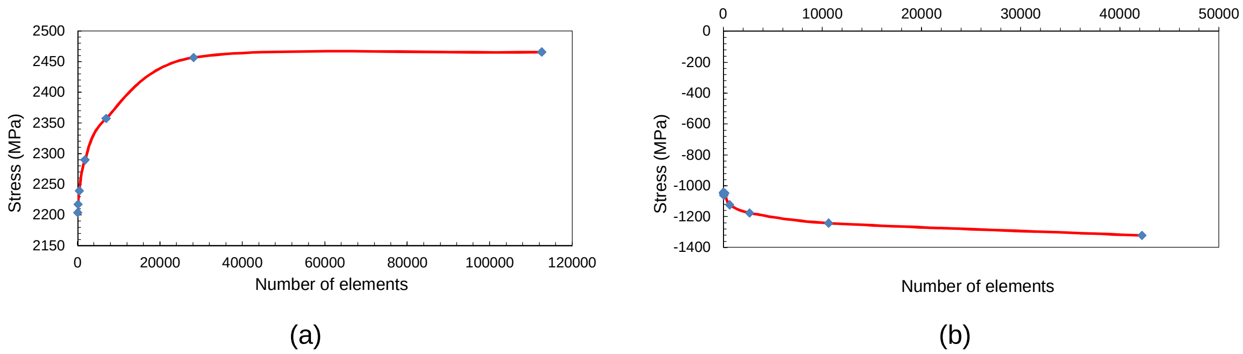

Fig. 1 Mesh convergence study (a) 0-degree composite laminate, and (b) 90-degree composite laminate

3 RESULTS AND DISCUSSIONS

Different layup configurations, e.g. 0-degree and 90-degree composite laminates, were analysed and validated with the experimental results. These composites were tested numerically under monotonic tension and compression.

Unidirectional composite laminates loaded in longitudinal (fibre) direction under tension

A typical stress–strain behaviour of composite laminates loaded in the longitudinal direction under tension is shown in Fig. 2. It can be observed that a significant stiffness reduction occurs under tension due to the local damage in the laminate. The strength of the laminate is taken as the magnitude of the stress which reaches the maximum value and causes the laminate to fail by cracking of matrix and splitting of fibres. Based on the comparison of the numerically predicted and experimental results [15], a difference of 17.7% can be observed in the maximum principal stress developed (Fig. 2b). The failure mode of the laminates observed in the experiments is brittle failure directly across the laminate near the fixed edge [15]. The matrix damage initiates from the lower and upper edges near the fixed support, which represents the matrix cracking. Fibre damage at the top and bottom corners propagates towards the centre in a slightly curved manner as shown in (Fig. 2a). Overall, a matrix dominated failure can be observed, as the matrix fails at the early stages due to cracking, and consequently fibres take the load and fail by fibre splitting.

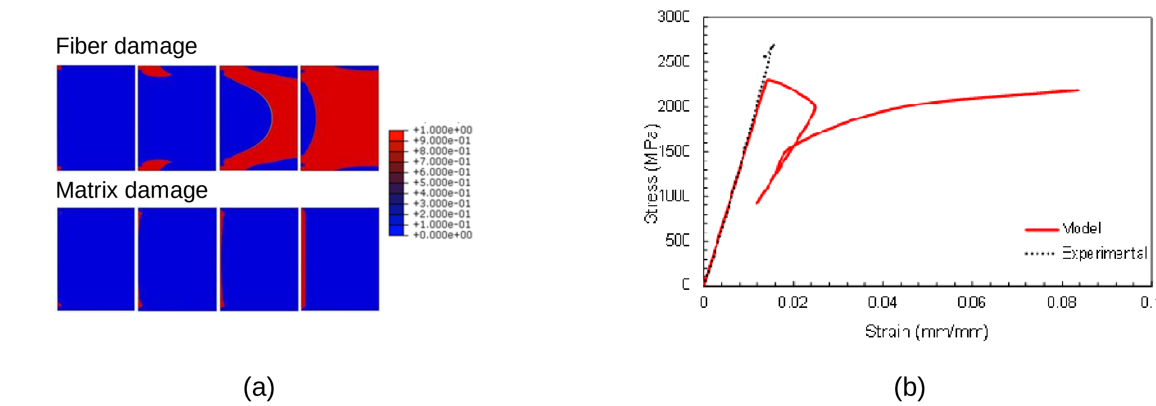

Fig. 2 0-degree composite laminate under tension (a) damage propagation pattern and (b) stress-strain behaviour

Unidirectional composite laminates loaded in longitudinal (fibre) direction under compression

Under compression, a significant reduction in the stiffness can be observed after the FPF. Based on the simulated results, a distinct degradation pattern can be observed, but this entire degradation occurs in the rapidly [9, 18]. Hence, the composite failure is catastrophic in nature. The observed failure modes are the crushing of matrix and buckling of fibres, as shown in [19]. The matrix damage initiates from the lower and upper edges near the fixed support and an accumulation of damage can be observed in the corners that are the regions where the matrix crushing can be observed. Fibre damage in the top and bottom corners propagates towards the centre in a slightly curved manner as shown in Fig. 3a, and the fibres present in the damaged region will suffer from fibre buckling [19]. Additionally, when the fibres are fully damaged, the matrix is nearly 8% damaged (Fig. 3b). Hence the failure is dominated by fibre failure.

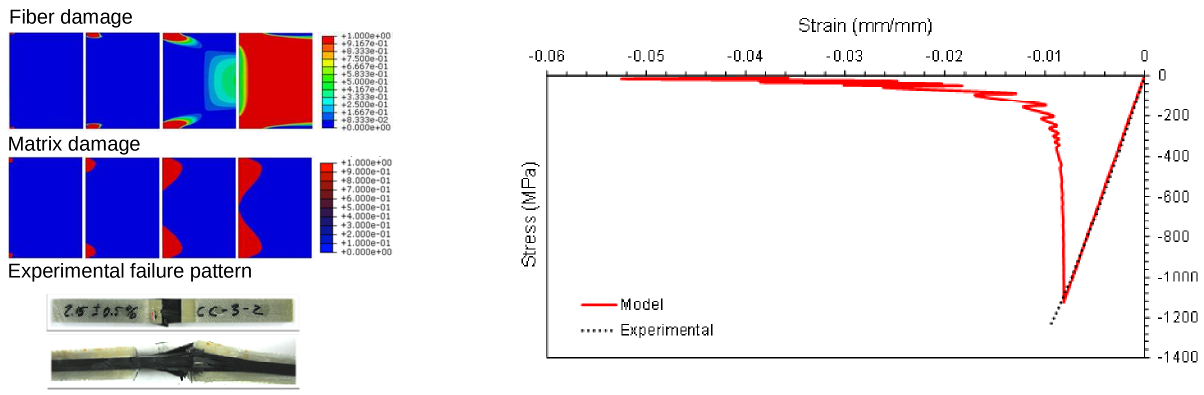

(a) (b)

Fig. 3 0-degree composite laminate under compression (a) damage propagation pattern, and (b) stress-strain behaviour

Unidirectional composite laminates loaded in transverse direction under tension

Composite laminates with a 90-degree layup under tensile loading exhibit a similar stress-strain behaviour. Since the fibres are oriented in the transverse direction to loading, they will not carry major loads. The strength of the composite is thus dominantly dependent on the matrix strength. Based on the finite element results, the strength of the composite was determined to be 46 MPa. A difference of 10.8% in the maximum principal stress developed can be noted between the simulated and the experimental results (Fig. 4b). The observed failure mode was matrix cracking. The matrix damage initiates from the lower and upper edges near the fixed support and propagates towards the centre near the fixed edge (Fig. 4a). With a continuous increment of the load, the damage is accumulated near the edge and the composite fails catastrophically by cracking of the matrix.

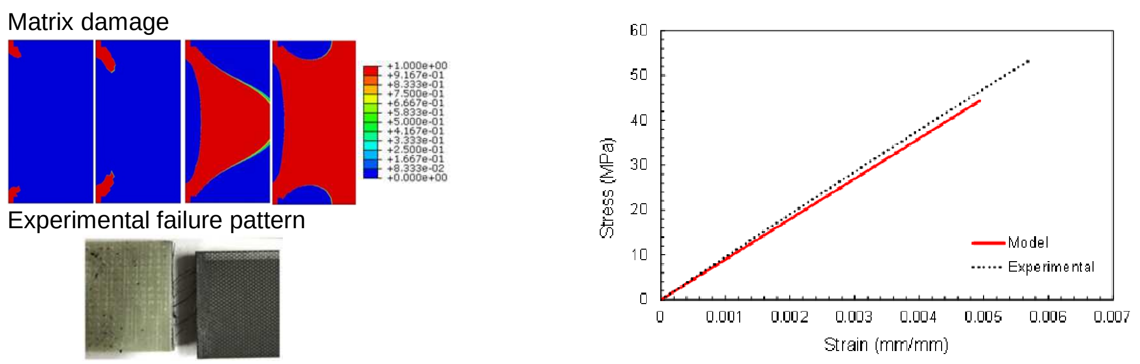

(a) (b)

Fig. 4 90-degree composite laminate under tension (a) damage propagation pattern, and (b) stress-strain behaviour

Unidirectional composite laminates loaded in transverse direction under compression

Under compression, the composites with 90-degree fibre orientation suffer from matrix crushing. The finite element model predicts the initiation and accumulation of damage starting from the corners of the fixed edge (Fig. 5a). When the 90-degree composite laminates are loaded under compression, the matrix takes the majority of the loads. As a result, kinking of composite lamina and generation of cracks leading to delamination can be generally observed [19]. Fig.5 shows the accumulation of damage, finally leading to the failure of the composite. A difference of 0.4% can be observed between the predicted and experimental maximum principal stress values (Fig. 5b).

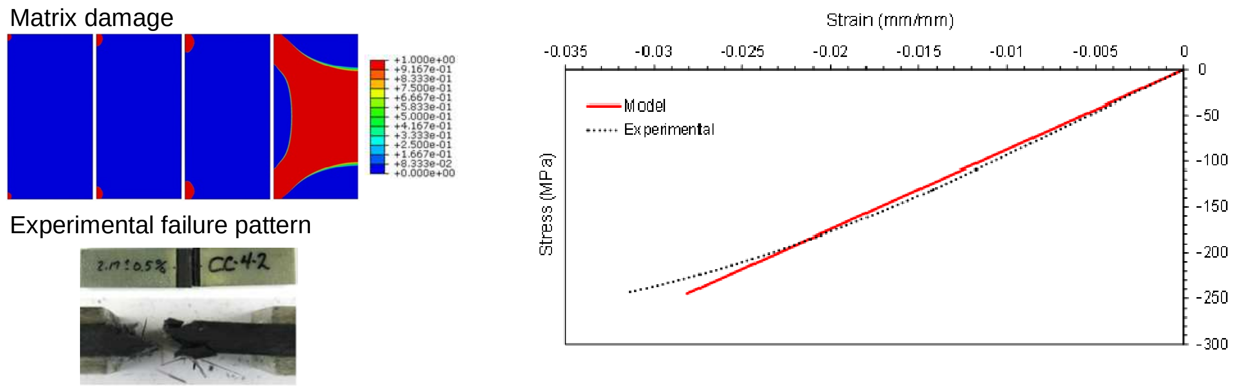

(a) (b)

Fig. 5 90-degree composite laminate under compression (a) damage propagation pattern, and (b) stress-strain behaviour

4 CONCLUSIONS

The finite element modelling has predicted stress-strain responses and damage patterns that correlate well with the experimental data. The values of the maximum principal stresses are 2301 and 1121 MPa in the unidirectional (0-degree) composite laminates loaded under tension and compression, respectively. In the unidirectional (90-degree) composite laminates, the maximum principal stresses are 46 and 243 MPa under tension and compression, respectively. The unidirectional (0-degree) composite laminates tested under tensile and compressive loading show differences in the maximum principal stress of 17.7% and 10.5%, respectively, between the model prediction and the experimental result. The unidirectional composite laminates under transverse loading (90-degree) show differences of 10.8% and 0.4% under tensile and compressive loadings, respectively. It has also been observed that as the fibre orientation decreases from 90 to 0-degree, the load taken by the fibre increases. Hence, the composite laminates consisting of more 0-degree plies are more prone to fibre failure. Fibre failure modes, such as breaking and buckling of fibres, are commonly observed in fibre dominated failures. When the fibres are 90-degree aligned to the loading direction in a transverse layup, the load carried by the fibres is less. Hence, the composite failure is more dominated by matrix failure. Matrix failure modes, such as matrix cracking, are dominantly observed in unidirectional composites loaded in the transverse direction. Moreover, it has been observed that the Hashin's criterion provides good agreement with experimental results only till the first ply failure.

5 REFERENCE

[1] D. Krajcinovic, S. Mastilovic, Some Fundamental Issues of Damage Mechanics, Mechanics of Materials, 21 (3), 217-230, 1995.

[2] M.J. Hinton, A.S. Kaddour, P.D. Soden, Failure Criteria in Fibre Reinforced Polymer Composites: The World-Wide Failure Exercise. Elsevier, 2004.

[3] M. Hinton, A. Kaddour, P. Soden, A Comparison of the Predictive Capabilities of Current Failure Theories for Composite Laminates, Judged against Experimental Evidence, Composites Science and Technology, 62 (12), 1725-1797, 2002.

[4] I. Daniel, Failure of Composite Materials, Strain, 43 (1), 4-12, 2007.

[5] U. Icardi, S. Locatto, A. Longo, Assessment of Recent Theories for Predicting Failure of Composite Laminates, Applied Mechanics Reviews, 60 (2), 76-86, 2007.

[6] M. Hinton, A. Kaddour, P. Soden, A Further Assessment of the Predictive Capabilities of Current Failure Theories for Composite Laminates: Comparison with Experimental Evidence, Composites Science and Technology, 64 (3), 549-588, 2004.

[7] R.M. Jones, Mechanics of Composite Materials, CRC Press, 1998.

[8] S.W. Tsai, E.M. Wu, A General Theory of Strength for Anisotropic Materials, Journal of Composite Materials, 5 (1), 58-80, 1971.

[9] F.-K. Chang, K.-Y. Chang, A Progressive Damage Model for Laminated Composites Containing Stress Concentrations, Journal of Composite Materials, 21 (9), 834-855, 1987.

[10] P. Ladeveze, E. LeDantec, Damage Modelling of the Elementary Ply for Laminated Composites, Composites Science and Technology, 43 (3), 257-267, 1992.

[11] Z. Hashin, Analysis of Composite Materials—A Survey, Journal of Applied Mechanics, 50 (3), 481-505, 1983.

[12] A. Puck, H. Schürmann, Chapter 5.6 - Failure Analysis of FRP Laminates by means of Physically based Phenomenological Models, In Failure Criteria in Fibre-Reinforced-Polymer Composites, M.J.H.S.K.D. Soden, Editor, Elsevier: Oxford. 832-876. 2004.

[13] N.M. Hassan, R.C. Batra, Modeling Damage in Polymeric Composites, Composites Part B: Engineering, 39 (1), 66-82, 2008.

[14] W.J. Clegg, I. Horsfall, J.F. Mason, L. Edwards, The Tensile Deformation and Fracture Of Al-"Saffil" Metal-Matrix Composites, Acta Metallurgica, 36 (8), 2151-2159, 1988.

[15] S. Clay, Assess and Quantify the Benefits of Applying Damage Tolerant Design Principles to Advanced Composite Aircraft Structures, FA8650-08-D-3858, U.S.A.F.R. Laboratory, Editor. 2014.

[16] T. Tay, G. Liu, V. Tan, X. Sun, D. Pham, Progressive Failure Analysis of Composites, Journal of Composite Materials, 2008.

[17] Z. Hashin, Failure Criteria for Unidirectional Fiber Composites, Journal of Applied Mechanics, 47 (2), 329-334, 1980.

[18] Y.K. Boey, Y.W. Kwon, Progressive Damage and Failure Strength of Notched Woven Fabric Composites under Axial Loading with Varying Strain Rates, Composite Structures, 96 (0), 824-832, 2013.

[19] C. Chaplin, Compressive Fracture in Undirectional Glass-Reinforced Plastics, Journal of Materials Science, 12 (2), 347-352, 1977.